Technische Universität München

TUM School of Natural Sciences

Highly Selective Inhibitors of Fibroblast-Activation-Protein for Imaging and Therapy of Oncological Diseases

Markus Frederik Fahnauer

Vollständiger Abdruck der von der TUM School of Natural Sciences der Technischen Universität München zur Erlangung des akademischen Grades eines
Doktors der Naturwissenschaften (Dr. rer. nat.)
genehmigten Dissertation.

Vorsitzende: Prof. Dr. Angela Casini

Prüfer der Dissertation:

1. Prof. Dr. Wolfgang Weber
2. Prof. Dr. Jason P. Holland
3. Prof. Dr. Michael Sattler

Die Dissertation wurde am 25.08.2022 bei der Technischen Universität München eingereicht und durch die TUM School of Natural Sciences am 28.11.2022 angenommen.

Eidesstattliche Erklärung

Ich, **Markus Fahnauer**, erkläre an Eides statt, dass ich die bei der promotionsführenden Einrichtung der **Fakultät für Chemie** der TUM zur Promotionsführung vorgelegte Arbeit mit dem Titel:

Highly Selective Inhibitors of Fibroblast-Activation-Protein for Imaging and Therapy of Oncological Diseases

am **Lehrstuhl für Pharmazeutische Radiochemie**

unter der Anleitung und Betreuung durch: **Prof. Dr. med. Wolfgang Weber** ohne sonstige Hilfe erstellt und bei der Abfassung nur die gemäß § 7 Abs. 6 und 7 angegebenen Hilfsmittel benutz habe.

- ☒ Ich habe keine Organisation eingeschaltet, die gegen Entgelt Betreuer*innen und Betreuer für die Anfertigung von Dissertationen sucht, oder die mir obliegenden Pflichten hinsichtlich der Prüfungsleistungen für mich gang oder teilweise erledigt.
- ☒ Ich habe die Dissertation in dieser oder ähnlicher Form in keinem anderen Prüfungsverfahren als Prüfungsleistung vorgelegt.
- ☒ Ich habe den angestrebten Doktorgrad noch nicht erworben und bin nicht in einem früheren Promotionsverfahren für den angestrebten Doktorgrad endgültig gescheitert.
- ☒ Ich habe keine Kenntnis über ein strafrechtliches Ermittlungsverfahren in Bezug auf wissenschaftsbezogene Straftaten gegen mich oder eine rechtskräftige strafrechtliche Verurteilung mit Wissenschaftsbezug.

Die öffentlich zugängliche Promotionsordnung sowie die Richtlinien zur Sicherung guter wissenschaftlicher Praxis und für den Umgang mit wissenschaftlichem Fehlverhalten der TUM sind mir bekannt, insbesondere habe ich die Bedeutung von § 27 PromO (Nichtigkeit der Promotion) und § 28 PromO (Entzug des Doktorgrades) zur Kenntnis genommen. Ich bin mir der Konsequenzen einer falschen Eidesstattlichen Erklärung bewusst.

Mit der Aufnahme meiner personenbezogenen Daten in die Alumni-Datei bei der TUM bin ich **einverstanden.**

München, 03. August 2022, Unterschrift

Acknowledgments

Mein Dank gebührt Herrn **Prof. Dr. Hans-Jürgen Wester**, welcher mir diese Arbeit an seinem Lehrstuhl ermöglicht hat und mir dieses spannende und vielseitige Thema überließ. Zudem bedanke ich mich für die exzellente fachliche und herzliche Förderung, sowie das entgegengebrachte Vertrauen, ohne welches diese Arbeit nicht zustande gekommen wäre.

Mein besonderer Dank gebührt Frau **Prof. Dr. Angela Casini** und Herrn **Prof. Dr. Wolfgang Weber**, welche die Beendigung meiner Doktorarbeit durch Übernahme meiner Betreuung ermöglicht haben. Ich möchte mich hier vor allem für die offene und vertrauensvolle Kommunikation und die tatkräftige Unterstützung bei der fachlichen Bewertung dieser Arbeit bedanken.

Im Weiteren danke ich Frau **Prof. Dr. Margret Schottelius** für das stets offene Ohr bei kleineren oder größeren wissenschaftlichen Fragestellungen, vor allem während meiner Masterarbeit.

Ein großes Dankeschön geht an Frau **Dr. Roswitha Beck** und Frau **Dr. Nicole Urtz-Urban** für die kompetente und tatkräftige Unterstützung bei allen durchgeführten *in vivo* Studien und das Beibringen des richtigen und artgerechten Umgangs mit Labortieren.

Ein spezieller Dank gebührt Herrn **Dr. Alexander Wurzer** für die Betreuung meiner Masterarbeit, welche schließlich dazu führte, Doktorand am Lehrstuhl für Pharmazeutische Radiochemie zu werden. Zudem bedanke ich mich für die stetige Unterstützung in jeglicher Hinsicht und die schöne gemeinsame Zeit am Lehrstuhl und außerhalb des Labors.

Ein herzlicher Dank gilt allen meinen Kollegen während der letzten drei Promotionsjahre. Vielen Dank **Dr. Veronika Felber**, **Mara Parzinger**, **Stefanie Färber**, **Dr. Stephanie Robu**, **Dr. Alexander Schmidt**, **Jan-Philip Kunert**, **Sebastian Fischer**, **Dr. Matthias Konrad**, **Dr. Thomas Günther**, **Daniel Di Carlo**, **Léon Stopper**, **Nadine Holzleitner**, **Jana Herbst** und **Tanja Reichhart** für die großartige Unterstützung und die vielen schönen Momente, gemeinsame Abende, wilde Wiesn Besuche. Danke, dass ihre diese Zeit unvergesslich gemacht habt.

Mein besonderer Dank geht an **Franziska Schuderer**, welche im Rahmen ihrer Masterarbeit unglaublich engagiert und zielführend an der Vollendung des tecFAPI Projektes in dieser Doktorarbeit beteiligt war.

Table of Content

Abstract

The reasons for the current dominance of ^{68}Ga-labeled tracers for PET imaging, also for addressing the fibroblast activation protein (FAP), need to be critically assessed. A major advantage of these radiopharmaceuticals is the lack or apparent lack of suitable alternatives, offering efficient and reliable technologies with proven clinical relevance for labeling with the superior isotope fluorine-18.

Primary aim of this work was the development of FAP inhibitors, which incorporate the radiohybrid concept (rhFAPI and transFAPI), allowing the ^{18}F-labelling by isotopic exchange at a Silicon-Fluoride Acceptor (SiFA). In this methodology the pronounced lipophilicity of the conjugates bearing the SiFA moieties is compensated by hydrophilic chelators, preventing the impairment of pharmacokinetics of corresponding radiopharmaceuticals, while allowing the complexation of radiometal for radioligand therapy. The radiohybrid concept offers the unique possibility to label one identical tracer either with fluorine-18 or a radiometal, resulting in the chemically identical pair of [^{18}F][M]-rhFAPI (M = metal) and [^{19}F][RM]-rhFAPI (RM = radiometal).

Another aim of this work was the development of a new group of FAP-addressing ligands (tecFAPI) for the labeling with technetium-99m through incorporation of the N4-chelator. Because of the presence of FAP in many different tumor entities, this group of tracers represent potential universal radiopharmaceuticals for SPECT imaging comparable to [^{18}F]FDG for PET imaging.

Several rhFAPI, transFAPI and tecFAPI ligands were synthesized by solid-phase and liquid-phase peptide synthesis. Human serum albumin (HSA) binding was measured by affinity high-performance liquid chromatography and albumin mediated size exclusion chromatography, while the lipophilicity of each tracer was determined by the shale-flask method in *n*-octanol and PBS buffer. *In vitro* experiments (affinity and internalization) were carried out on HT-1080hFAP cells. *In vivo* studies (biodistribution, µPET, metabolite analysis) were conducted on HT-1080hFAP tumor bearing female BALB/c nude mice.

On the laboratory scale, ^{18}F-labeling of rhFAPI and transFAPI ligands by isotopic exchange was completed in less than 20 min (radiochemical yield: 23.0 ± 12.1%, radiochemical purity: >95%, molar activities: 1-5 GBq/µmol) with a modified method based on the *Munich Method*, allowing impurity-free labeling. The ^{99m}Tc-labeling of tecFAPI ligands by complexation with the N4-chelator following a modified method based on a published procedure by *Nock et al.* was completed in less than 20 min, but still demonstrated unresolved difficulties regarding quantification and identification of impurities.

The radiohybrid ligands ([^{18}F][free]-rh/transFAPI-n, ([^{18}F][M_{1-2}]-rh/transFAPI-n were M = metal and ([^{18}F][RM_{1-2}]-rh/transFAPI-n were RM = radiometal) demonstrated similar but always lower

affinities to HT-1080hFAP cells, when compared to the reference ligand [^{177}Lu]Lu-FAPI-04. Moreover, all tracers showed medium-to-high lipophilicity and high binding to HSA. Biodistribution studies in HT-1080hFAP tumor-bearing mice revealed unfavorable high activity accumulation in nonspecific organs and low tumor uptakes with lower tumor-to-organ ratios compared to the reference. Only [^{177}Lu]Lu-rhFAPI-04+E, [^{18}F]F-Ga_2-transFAPI-02 and [^{18}F]F-Ga_2-transFAPI-03 showed improved tumor-to-organ ratios through higher tumor uptake and in the case of [^{18}F]F-Ga_2-transFAPI-03 also lower activity accumulation in nonspecific organs. Nevertheless, none of these ligands reached the favorable *in vivo* distribution of [^{177}Lu]Lu-FAPI-04 at early time points.

Regarding the tecFAPI ligands intended for labeling with technetium-99m, all compounds demonstrated similar, but always lower affinities to HT-1080hFAP cells, when compared to the reference ligand [^{177}Lu]Lu-FAPI-04. In comparison to the radiohybrid ligands all tracers showed medium-to-low lipophilicity and low binding to HSA. Internalization rates into HT-1080hFAP cells were increased compared to the reference. Biodistribution studies in HT-1080hFAP tumor-bearing mice revealed unfavorable high activity accumulation in nonspecific organs and very low tumor uptakes resulting in significantly inferior tumor-to-organ ratios. PET imaging revealed high activity accumulation in the thyroid glands for all evaluated tracers indicating stability issues of the ^{99m}Tc-N4-complex. These have been confirmed by stability studies in murine serum for [^{99m}Tc]Tc-Ga-tecFAPI-03 and [^{99m}Tc]Tc-Lu-tecFAPI-03.

In conclusion, rhFAPI and transFAPI ligands represent the first series of FAP-addressing radiopharmaceuticals incorporating the radiohybrid concept, while the tecFAPI ligands are the first FAP-addressing radiopharmaceuticals using the N4-chelator as moiety for ^{99m}Tc-labeling. Despite the unmatched simplicity of the ^{18}F-labeling *via* isotopic exchange and the possibility to produce identical ^{68}Ga- or ^{177}Lu-labeled tracers through the radiohybrid concept, the pharmacokinetic disadvantages introduced by the SiFA moiety led to ligands which could not compete against the state-of-the-art FAP-addressing tracer FAPI-04. The difficulties with ^{99m}Tc-labeling of the N4-chelator and issues with *in vivo* stability of the ^{99m}Tc-N4-chelate need to be overcome for tecFAPI ligands to be viable alternatives to existing compounds such as FAPI-04 or FAPI-34.

Zusammenfassung

Die Gründe für die derzeitige Dominanz von ^{68}Ga-markierten Tracern für die PET-Bildgebung, auch für die Untersuchung des Fibroblasten Aktivierungsproteins (FAP), müssen kritisch bewertet werden. Ein großer Vorteil dieser Radiopharmaka ist das Fehlen oder der scheinbare Mangel an geeigneten Alternativen, welche insbesondere effiziente und zuverlässige Technologien für die Markierung mit dem überlegenen Isotop Fluor-18 bieten und deren Relevanz klinisch nachgewiesen sind.

Hauptziel dieser Arbeit war die Entwicklung von FAP-Inhibitoren, die das Radiohybrid-Konzept (rhFAPI und transFAPI) beinhalten und die ^{18}F-Markierung durch Isotopenaustausch an einem Siliziumfluorid-Akzeptor (SiFA) ermöglichen. Bei dieser Methode wird die ausgeprägte Lipophilie der Konjugate, welche durch die verwendeten SiFA-Bausteine eingeführt wird, durch hydrophile Chelatoren kompensiert. Hierdurch wird eine Beeinträchtigung der Pharmakokinetik der entsprechenden Radiopharmaka vermieden, während gleichzeitig die Komplexierung von Radiometallen für die Radioligandentherapie ermöglicht wird. Das Radiohybrid-Konzept bietet die einzigartige Möglichkeit einen identischen Tracer entweder mit Fluor-18 oder einem Radiometall zu markieren, was zu dem chemisch identischen Paar [^{18}F][M]-rhFAPI (M = Metall) und [^{19}F][RM]-rhFAPI (RM = Radiometall) führt.

Ein weiteres Ziel dieser Arbeit war die Entwicklung einer neuen Gruppe von FAP-adressierenden Liganden (tecFAPI) für die Markierung mit Technetium-99m durch Einbau des N4-Chelators. Aufgrund des Vorkommens von FAP in vielen verschiedenen Tumorentitäten stellt diese Gruppe von Tracern potenzielle universelle Radiopharmaka für die SPECT-Bildgebung dar, vergleichbar mit [^{18}F]FDG für die PET-Bildgebung.

Mehrere rhFAPI, transFAPI und tecFAPI Liganden wurden durch Festphasen- und Flüssigphasenpeptidsynthese hergestellt. Die Bindung an humanem Serumalbumin (HSA) wurde durch Affinitäts-Hochleistungsflüssigkeitschromatographie und Albumin-vermittelter Größenausschlusschromatographie gemessen, während die Lipophilie jedes Tracers durch die Schüttelkolbenmethode in *n*-Octanol und PBS-Puffer bestimmt wurde. *In vitro*-Experimente (Affinität und Internalisierung) wurden an HT-1080hFAP-Zellen durchgeführt. *In vivo*-Studien (Biodistribution, µPET, Metabolitenanalyse) wurden an HT-1080hFAP Tumor tragenden weiblichen BALB/c-Nacktmäusen durchgeführt.

Im Labormaßstab war die ^{18}F-Markierung von rhFAPI- und transFAPI-Liganden durch Isotopenaustausch in weniger als 20 Minuten abgeschlossen (radiochemische Ausbeute: 23,0 ± 12,1%, radiochemische Reinheit: >95%, molare Aktivitäten: 1-5 GBq/µmol). Diese wurden mit einer modifizierten Methode auf der Grundlage der *Munich Method* durchgeführt,

die eine verunreinigungsfreie Markierung ermöglicht. Die ^{99m}Tc-Markierung von tecFAPI-Liganden durch Komplexierung mit dem N4-Chelator wurde nach einem modifizierten Verfahren nach der Methode von *Nock et al.* durchgeführt und konnte in weniger als 20 Minuten abgeschlossen werden, wies jedoch noch ungelöste Schwierigkeiten bei der Quantifizierung und Identifizierung von Verunreinigungen auf.

Die radiohybriden Liganden ([^{18}F][frei]-rh/transFAPI-n, ([^{18}F][M_{1-2}]-rh/transFAPI-n mit M = Metall und ([^{18}F][RM_{1-2}]-rh/transFAPI-n mit RM = Radiometall) wiesen verglichen mit dem Referenzliganden [177Lu]Lu-FAPI-04 ähnliche, aber stets geringere Affinitäten zu HT-1080hFAP-Zellen auf. Außerdem zeigten alle Tracer eine mittlere bis hohe Lipophilie und eine hohe Bindung an HSA. Biodistributionsstudien an Mäusen, die einen HT-1080hFAP Tumor trugen, ergaben eine ungünstige hohe Aktivitätsakkumulation in unspezifischen Organen und eine geringe Tumoraufnahme mit einem im Vergleich zur Referenz geringeren Tumor-zu-Organ Verhältnis. Nur [^{177}Lu]Lu-rhFAPI-04+E, [^{18}F]F-Ga_2-transFAPI-02 und [^{18}F]F-Ga_2-transFAPI-03 zeigten ein verbessertes Tumor-zu-Organ Verhältnis durch eine höhere Tumoraufnahme und im Falle von [^{18}F]F-Ga_2-transFAPI-03 auch eine geringere Aktivitätsanreicherung in unspezifischen Organen. Dennoch erreichte keiner dieser Liganden die günstige *in vivo*-Verteilung von [^{177}Lu]Lu-FAPI-04 zu frühen Zeitpunkten.

Was die tecFAPI-Liganden betrifft, die für die Markierung mit Technetium-99m bestimmt sind, so zeigten alle Verbindungen ähnliche, aber stets geringere Affinitäten zu HT-1080hFAP-Zellen im Vergleich zum Referenzliganden [^{177}Lu]Lu-FAPI-04. Im Vergleich zu den Radiohybrid-Liganden wiesen alle Tracer eine mittlere bis geringe Lipophilie und eine geringe Bindung an HSA auf. Die Internalisierungsraten in HT-1080hFAP-Zellen waren höher als bei der Referenz. Biodistributionsstudien an Mäusen, die einen HT-1080hFAP Tumor trugen, ergaben eine ungünstige hohe Aktivitätsakkumulation in unspezifischen Organen und eine sehr geringe Tumoraufnahme, was zu einem deutlich schlechteren Tumor-zu-Organ Verhältnis führte. Die PET-Bildgebung ergab für alle untersuchten Tracer eine hohe Aktivitätsakkumulation in den Schilddrüsen, was auf Stabilitätsprobleme des ^{99m}Tc-N4-Komplexes hinweist. Dies wurde durch Stabilitätsstudien in murinem Serum für [^{99m}Tc]Tc-Ga-tecFAPI-03 und [^{99m}Tc]Tc-Lu-tecFAPI-03 bestätigt.

Zusammenfassend lässt sich sagen, dass die rhFAPI- und transFAPI-Liganden die erste Reihe von FAP-adressierenden Radiopharmazeutika darstellen, die das Radiohybrid-Konzept beinhalten, während die tecFAPI-Liganden die ersten FAP-adressierenden Radiopharmazeutika sind, die den N4-Chelator als Modalität für die ^{99m}Tc-Markierung verwenden. Trotz der unübertroffenen Simplizität der ^{18}F-Markierung durch Isotopenaustausch und der Möglichkeit, identische ^{68}Ga- oder ^{177}Lu-markierte Tracer durch das Radiohybrid-Konzept herzustellen, führten die pharmakokinetischen Nachteile, die durch den SiFA-Baustein entstehen, zu Liganden, die nicht mit dem FAP-adressierenden Tracer FAPI-04 konkurrieren konnten, welcher den aktuellen Stand der Technik darstellt. Die Schwierigkeiten bei der ^{99m}Tc-Markierung des N4-Chelators und die Probleme mit der *in vivo*-

Stabilität des ^{99m}Tc-N4-Chelats müssen überwunden werden, damit die tecFAPI-Liganden eine brauchbare Alternative zu bestehenden Verbindungen wie FAPI-04 oder FAPI-34 darstellen.

1 Introduction

1.1 Tumor Microenvironment

Any injury to a functional parenchyma cell results in a host response, which is the repair of the cellular damage and restoration of homeostasis. Wound healing of this kind occurs as a response to divers types of acute injury such as mechanical trauma, radiation, toxins, etcetera.[1-5] The typical healing response recruits inflammation, immune cells and fibroblasts to promote angiogenesis and deposition of the extracellular matrix (ECM).[2,6,7] If the cell damage is perpetual, the repair response continues unrestrained and leads to a chronic wound healing condition that is also known as tissue fibrosis. As for this condition, the chronic tissue repair response also occurs in the setting of genetic damage in cancer. In this regard, tumors are considered as "wounds that do not heal".[7]

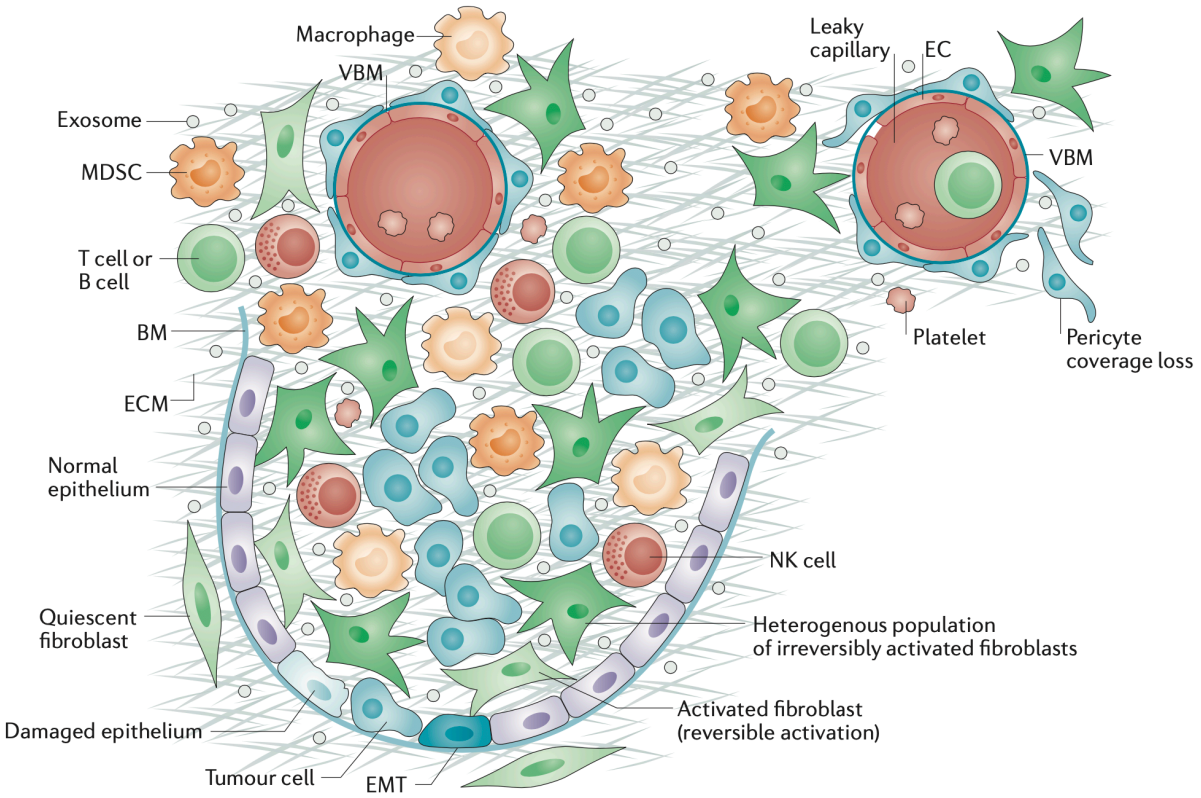

Figure 1: The tumor microenvironment (TME) consists of not only tumor cells but many non-tumor cells. The TME is composed of immune cell infiltrates, normal and injured epithelium, neoplastic epithelial cells, and blood vessels, which include endothelial cells, pericytes and the vascular basement membrane (VBM). Cancer-associated fibroblasts (CAFs) are a heterogeneous population of irreversibly activated fibroblasts with distinct functions. BM = basement membrane; EC = endothelial cell; EMT = epithelial to mesenchymal transition; MDSC = myeloid-derived suppressor cell; NK = natural killer. Figure taken from *Kalluri et al.: The biology and function of fibroblasts in cancer*.[8] License Number: 5456931401190

The host's response to evolving cancer cells leads to the formation of tumor tissue that not only contain cancer cells but also components of healthy organs as shown in Figure 1.[9-12] This results in heterotypic interactions between cancer cells and healthy cells, that are known

as desmoplastic reaction, tumor stroma and tumor microenvironment (TME), respectively.[12-15] As tumors grow and become invasive, its stromal content also increases. Tumor stroma in advanced stages of cancer contains increased amounts of immune cells, capillaries, basement membrane, activated fibroblasts and ECM surrounding the cancer cells.[10,13,16] These type of cells and cellular components of the TME can represent up to 90% of the tumor tissue in frequently occurring carcinomas of breast, colon and pancreas. The TME also significantly determines the malignant phenotype of cancer cells and contribute to the tumor evolution and progression.[12,17-19] Especially through the production of various growth factors, these non-cancerous stromal cells promote various actions as ECM remodeling, induction of angiogenesis, cellular migration, drug resistance, and evasion of immunosurveillance facilitating invasion and the development of metastasis.[9,13,20,21]

A dominant component of the TME are fibroblasts and many studies in the past decade suggest an important functional role of these cell types in tumor progression and metastasis, but also in tumor restraining actions.[6,22-24] These fibroblasts associated with cancerous diseases have been termed as activated fibroblasts or cancer-associated fibroblasts (CAFs).[24,25]

1.2 CAFs and their Marker Protein Expression

As concluded in the previous chapter, cancer-associated fibroblasts are an important and dominant cell type found in the TME of tumors, whether it is at the beginning of tumor growth or during the end-stage of the metastatic spread.[8,26] Because CAFs are a dynamically heterogeneous population of cells of mesenchymal lineage with a wide range of exhibited features, their precise functional role in cancer is not fully understood.[27,28] Fibroblasts in general are a resting cell type capable of responding to extrinsic signals, such as growth factors, cytokines and mechanical stress and are activated through these.[29,30] The injury associated with a growing tumor is such a signal and can lead to the activation of normal or tissue resident fibroblasts, thereby transforming to CAFs in the TME of expanding tumors.[31] The functions of CAFs are distinct from those of their origin fibroblasts. This makes them producers of a wide range of cytokines, chemokines, metabolites, enzymes, and ECM molecules (see Figure 2), which either limit or fuel cancer cell growth and tumor progression.[26,28]

The origin of CAFs in a tumor is likely mixed and as diverse as their expressed markers. When cancer cells arise in adult organs quiescent fibroblasts residing in the tissue are expanding as a responds to the injury caused by the developing neoplasm.[32] Additionally, CAFs can be recruited to the tumor from a distant source, such as the bone marrow.[33] As shown in Figure 2, CAFs can also emerge from trans-differentiation of pericytes, endothelial and epithelial cells through endothelial-to-mesenchymal (EndMT) and epithelial-to-mesenchymal transition (EMT).[34,35] Similar to cancer cells, CAFs can spread into the blood circulation and to metastatic sites, suggesting an additional complex role in metastasis.[23,36] The difficulty to clearly identify the biological origin of CAFs is mostly due to the lack of specific markers of CAFs as their function and therefore their markers can dynamically shift and change during cancer progression, reflecting their flexibility in adapting to a changing microenvironment.[37-39] Identification of CAFs therefore was mostly based on microscopic analyses of tissue sections and their spindle shape and elongated cytoplasmic processes (Figure 2).[40]

After an injury, activated fibroblasts accumulate in the affected area and facilitate many aspects of the tissue remodeling cascade, through secretion of several signaling molecules. They thereby initiate the repair process and prevent further tissue damage. The initial recruitment of CAFs to a neoplastic lesion therefore can reflect their role in the early antitumor response.[6,37,41] However, as the tumor growth progresses, this repair process might promote further growth, as cancer cells utilize the CAF-secreted growth factors to facilitate their own survival and proliferation. This pro-tumorigenic activity of CAFs may evolve gradually over time (see Figure 2) and the kinetics of such changes can be different for different tumor entities, because of the organ-specific transcriptomic profiles of the CAFs origins.[42,43]

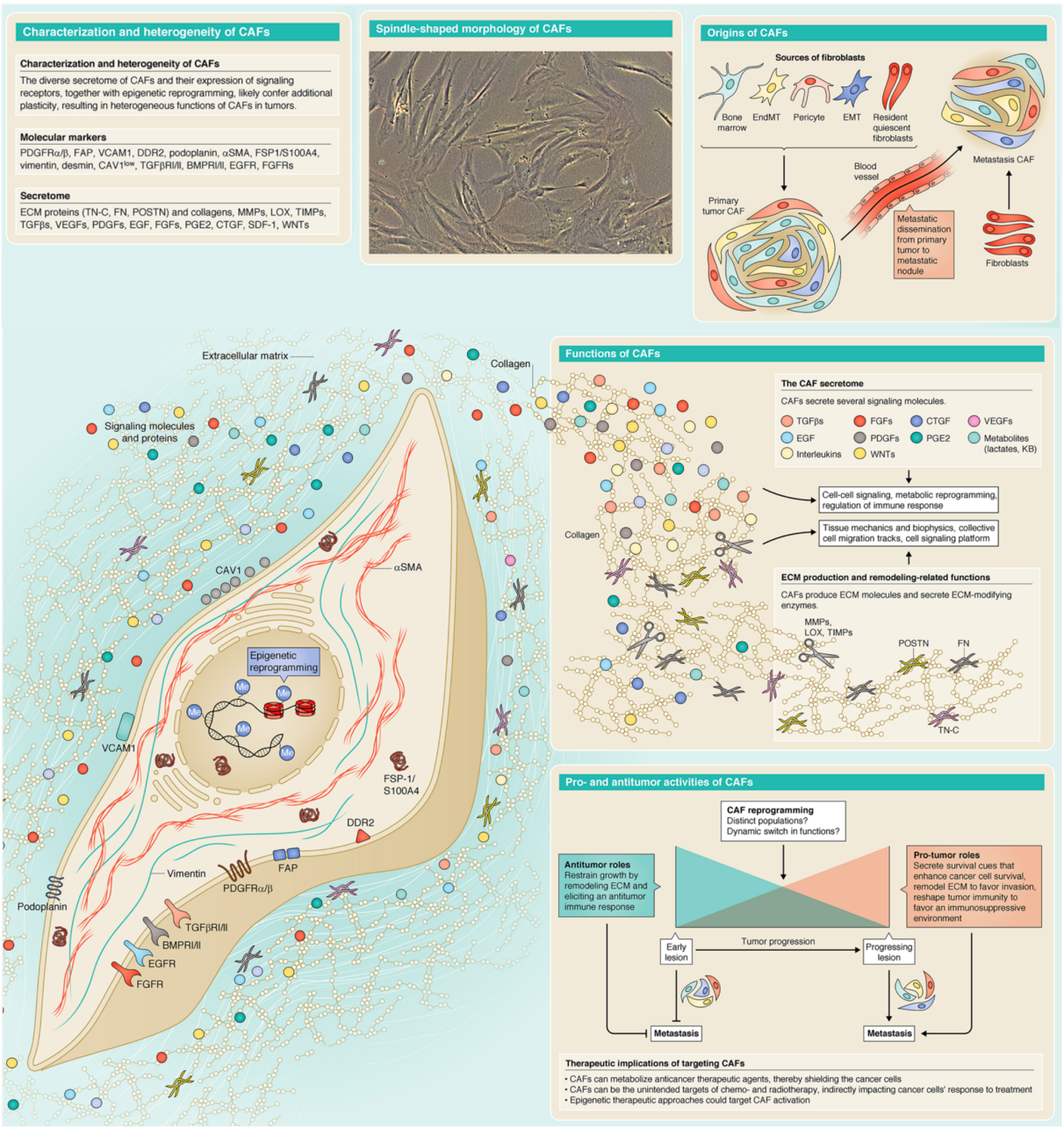

Figure 2: Systematic representation of CAFs and their marker proteins with additional information on their characterization, morphology, origin, function, and the pro- and antitumor activities. αSMA = alpha smooth muscle actin, BMPR I/II = bone morphogenetic protein receptor I/II, CAV1 = caveolin-1, CTGF = connective tissue growth factor, DDR2 = discoidin domain-containing receptor 2, EGFR = epidermal growth factor receptor, EGF = epithelial to mesenchymal program, FAP = fibroblast activation protein, FGF = fibroblast growth factor, FGFR = fibroblast growth factor receptor, FN = fibronectin, FSP1/S100A4 = fibroblast specific protein-1, INFγ = interferon γ, KB = ketone bodies, LOX = lysyl oxidase, MMPs = matrix metalloproteinases, PDGF = platelet-derived growth factor, PDGFR α/β = platelet-derived growth factor receptor α/β, PGE2 = prostaglandin E2, POSTN = periostin, SDF-1 (CXCL 12) = stromab cell-derived factor 1, TGFβ = transforming growth factor β, TGFβR I/II = transforming growth factor β receptor I/II, TIMPs = tissue inhibitor of metalloproteinases, TN-C = tenacin-C, TNFα = tumor necrosis factor α, VCAM1 = vascular cell adhesion protein 1, VEGF = vascular endothelial growth factor, WNTs = wingles-related integration site, protein ligands in the WNT signaling pathway. Figure taken from *Lebleu et al.: A peek into cancer-associated fibroblasts: origins, functions, and translational impact,* © 2018. Published by The Company of Biologists Ltd, doi: 10.1242/dmm.029447.[44] No licensing needed.

The cancer progression associated with the accumulation of CAFs often is directly linked to their markers which include:

- ECM components, such as collagen I and II, fibronectin, tenascin C and remodeling enzymes, such as LOX, LOX1, MMPs and TIMPS.[23,45]
- Growth factors and cytokines, such as TGFβs, VEGFs, PDGFs, EGFs, FGFs, SDF-1 (CXCL12) and WNTs.[45-47]
- Receptors and other membrane-bound proteins, such as PDGFRα/β, VCAM1, DDR2, TGFβR I/II, EGFR, FGFRs, podoplanin and FAP.[12,29,48]
- Cytoskeleton components and other cytoplasmic proteins, such as desmin, vimentin, αSMA and FSP1/S100A4.[12,49]

The heterogeneity of the above-mentioned markers in different tumor types and the expression of some of these markers in healthy tissues are especially challenging when studying the role and biological properties of CAFs in cancer.[27,50] However, new insights on the functional heterogeneity of CAFs, including the function of their markers are offered through genetically engineered mouse models. Hereby, it could be shown that the paracrine signaling between cancer cells and CAF-secreted growth factors and cytokines, such as CXCL12, CCL7, TGFβs, FGFs, HGFs, periostin and TN-C, directly and positively impact tumor progression by enhancing the survival, proliferation, stemness, and the metastasis-initiating capacity of cancer cells, promoting cancer progression and also enhancing resistance to therapy.[46,47,51-60] Other CAF secretomes as VEGFs, TNFα and ECM proteins promote tumor angiogenesis and the survival, proliferation and migration of cancer cells and generate an immunosuppressive microenvironment that limits antitumor immunity.[61,62] Looking at all this in summary, it can be said that most tumor-promoting functions of CAFs are due to “collateral damage” from their otherwise protective wound repair activities. Cancer cells hijack and benefit from the CAF secretome and additionally can mediate the epigenetic modifications of CAFs to further enhance their pro-tumorigenic functions.[63] This leads to a pronounced role of cancer-associated fibroblasts in reprogramming and shaping the metabolic microenvironment of tumors.[64]

The development of anticancer compounds for diagnostic and therapeutic targeting of CAFs has become more and more of interest in recent years. For this purpose, specific markers that do not occur in healthy or in non-cancer associated fibroblasts, were investigated, yielding the membrane-bound fibroblast activation protein (FAP) as a promising target.

1.3 Fibroblast Activation Protein

1.3.1 Structure and Function of FAP

As described above, activated fibroblasts express a series of proteins that can serve as tumor-specific markers. One of the most important proteins for drug targeting of CAFs is the fibroblast activation protein (FAP), which is also called seprase because of its function as a serine protease. It is an integral type II transmembrane protein and belongs to the post prolyl-dipeptidyl-aminopeptidase family (subfamily S9b).[65] Human FAP has a high structural homology to the related dipeptidyl peptidase IV (DPP IV), with which it shares 52% of its amino acid sequence, exhibits a DDP IV-like fold and has a molecular weight and an enzymatic activity comparable to DPP IV.[66,67] Murine FAP also shows high structural similarity to the human protein analogue, with a sequence identity of 90%.[68] This simplifies the translation of preclinical results of FAP-addressing drugs from animal studies to their behavior in humans.

FAP was first discovered in 1986 in cultured fibroblasts using the monoclonal antibody F19.[66,69] Crystal structure analysis of the protease revealed that it is a homodimer and the presence of the dimerized form is a prerequisite for enzymatic activity as shown in Figure 3.[65]

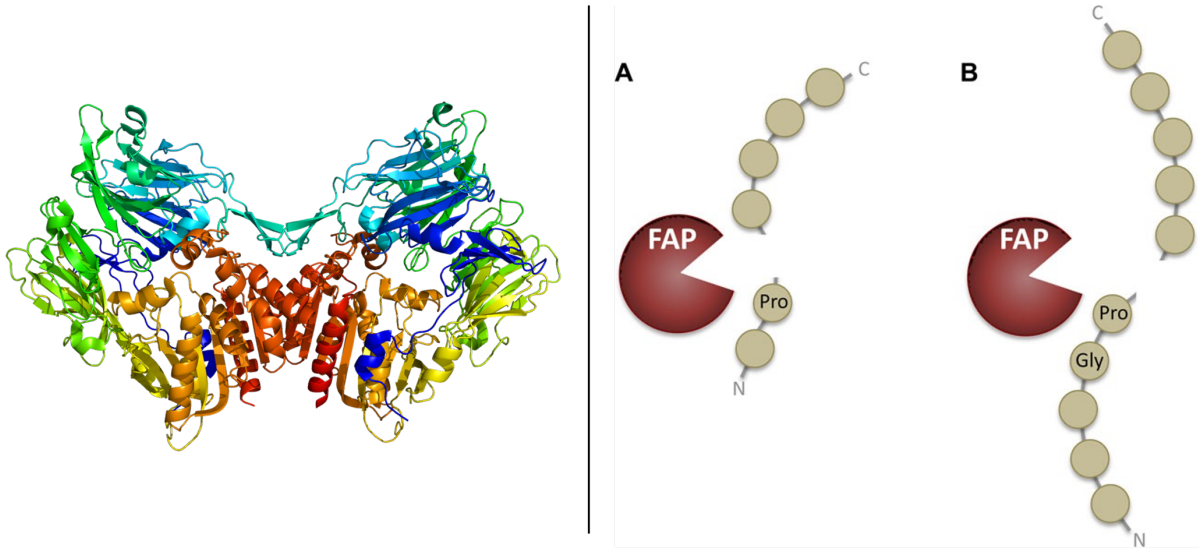

Figure 3: Overall 3D structure of the FAP dimer depicted on the left. Active site residues Ser^{624}, Asp^{702} and His^{734} are located at the interface of the two monomers in the α/β-hydrolase domain of each monomer and the β-propeller domain (red region); based on PyMOL rendering of PDB 1z68.[70] Dual-enzyme activity of FAP highlighted on the left. (A) Dipeptidyl peptidase activity of FAP. (B) Endopeptidase activity of FAP. Figure taken from *Hamson et al.: Understanding fibroblast activation protein (FAP): Substrates, activities, expression and targeting for cancer therapy, © 2013.*[71]

The catalytic triad, Ser^{624}, Asp^{702} and His^{734}, is located in a small pocket within the large cavity at the interface of the α/β-hydrolase and the β-propeller domain. The glycosylated form of the protein exhibits dipeptidyl peptidase, endopeptidase, and gelatinase properties while the non-glycosylated analogue does not possess any enzymatic activity. As shown in part A of Figure 3, the dipeptidyl peptidase activity of FAP allows for cleavage of two amino acids at

the *N*-terminus of a protein. This cleavage occurs at the *C*-terminal side of a proline (Pro) residue. As seen in part B, the endopeptidase activity of FAP enables cleavage that is more than two amino acids away from the *N*-terminus of a protein. However, cleavage is restricted to the post-Pro bond after a glycine-proline (Gly-Pro) motif.[71] Therefore, the proline residue of substrates is accommodated in a hydrophilic pocket, whereas the *N*-terminal end of substrate peptides is recognized by two glutamate moieties that are necessary for to the exopeptidase activity. Unlike the negatively charged Asp^{663} in the DPP IV active site, FAP has a neutral Ala^{657} residue at the corresponding position. Reduced acidity of the active site most likely explains the additional endopeptidase activity and substrate preference of FAP.[65,70,72-74] As will be described later, this unique enzymatic activity and the glycine-proline substrate sequence are important for innovative FAP-addressing drug design.

The enzymatic activity of this integral membrane protease contributes significantly to ECM degradation, which facilitates tumor cell metastasis. For this reason, high intratumoral expression of the protein is associated with poor tumor prognosis.[65] This has been shown particularly for colorectal carcinoma as well as ovarian, pancreatic, and hepatic tumors.[33,75] FAP is selectively expressed in over 90% of tumors of epithelial origin. The protein has also been discovered in some bone and soft tissue sarcomas and melanomas. Furthermore, expression occurs during embryonic development, in wound healing tissue and chronic inflammation, as well as in fibrotic tissue, for example in both liver cirrhosis and idiopathic pulmonary fibrosis. Unlike the related DDP IV, FAP is not expressed in benign lesions or healthy adult tissue and is thus suitable as a target in various malignant tumors.[76]

1.3.2 Development of Drugs Targeting FAP

Due to the selective expression of FAP in the TME of numerous tumors, its unique enzymatic activity, the importance of FAP-positive stromal cells (e.g., CAFs) in the development of TME and its presumed role in various aspects of cancer progression, the membrane protein represents an ideal target structure for imaging and targeted tumor therapy. As shown in Figure 4, a variety of different strategies for targeting FAP have been explored. These include the inhibition of FAP's enzymatic activity, ablation of FAP-positive cells, the exploitation of the selective expression of the protein in the activation or targeted delivery of cytotoxins, or the destruction of FAP-negative cells (for example cancer cells) in the proximity of FAP-positive cells through a bystander effect. The latter strategy has been particularly successful in recent years using FAP-addressing small molecule radiopharmaceuticals that specifically bind to cells of the TME and irradiate them.[77-79]

In the past, there have been different approaches for FAP-specific antitumor therapy, which are shown in Figure 4. In the following, the chronological development of some of the most important and most promising approaches and compounds to date will be elucidated. As such, the murine monoclonal antibody F19, which was originally used for the identification of the protein, was also used clinically for imaging and therapy. Two phase I studies with ^{131}I-labeled F19 in patients with colorectal carcinoma and soft tissue sarcomas demonstrated

selective activity accumulation in the tumor.[80] Based on these successful studies, a humanized analogue of the antibody, sibrotuzumab, was developed and investigated in patients with various epithelial tumors, including breast, colon and non-small cell lung tumors (NSCLC). However, in these studies, activity was cleared very slow from healthy organs, such as liver and spleen, which resulted in increased radiation exposure to the corresponding tissues. As no clinical benefit could be demonstrated, further clinical investigation of sibrotuzumab was discontinued.[75,80-82]

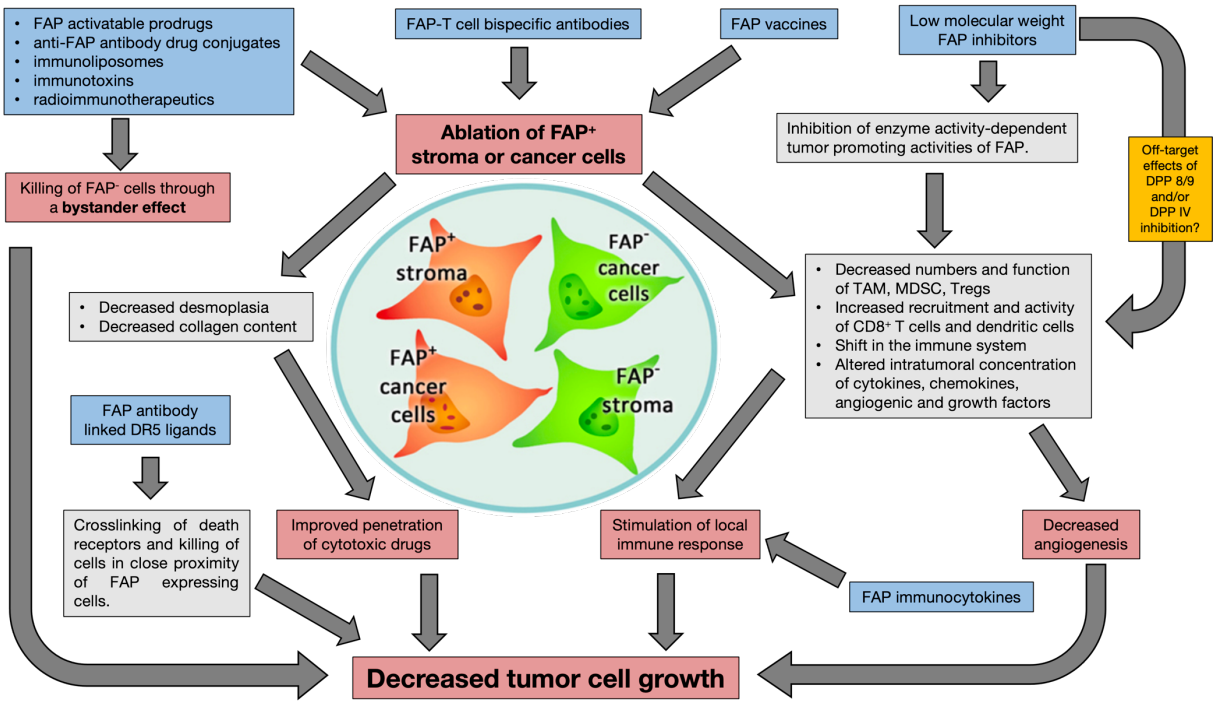

Figure 4: FAP-targeting therapeutics and their expected impact on tumors with heterogeneous FAP expression. Both FAP enzyme activity inhibition and ablation of FAP-positive cells lead to changes in the tumor microenvironment, including alleviation of immunosuppression, decreased neovascularization, and changes in ECM content and composition. This improves the effect of standard chemotherapeutics and potentiates endogenous and/or the therapeutically induced antitumor immune responses. FAP-activatable prodrugs, anti-FAP immunotoxins, and radioimmunotherapeutics can also achieve the killing of FAP-negative cancer cells by a bystander effect. DR5 = death receptor 5, DPP = dipeptidyl peptidase, TAM = tumor-associated macrophages, MDSC = myeloid-derived suppressor cells. Figure inspired by *Busek et al.: Targeting fibroblast activation protein in cancer – Prospects and caveats, 2018.*[77]

Other therapeutic strategies were based on the use of radiolabeled single-chain antibodies[83-85] and human antibody fragments (Fabs) that were identified using an antibody phage library.[86] In addition, immunologic approaches using a bispecific antibody with T-cell stimulation[87], CAR- T-cells (chimeric antigen receptor)[88], or the development of FAP-associated DNA and peptide vaccines[89,90] have been pursued. Nevertheless, none of these strategies have resulted in satisfactory therapeutic efficacy yet.

Another approach for FAP-mediated tumor targeting was described by *Brennen et al.*, who applied inactive prodrugs that are composed of a potent cytotoxic compound and a peptide moiety, which can be cleaved by FAP, the so-called *FAP cleavage site*. Prior to cleavage by

FAP, this peptide group prevents penetration of the cytostatic drug through the cell membrane, so that the substance circulates in its inactive form without damaging healthy tissue. After binding to FAP has occurred, the peptide moiety is proteolytically cleaved and the cytostatic can reach its intracellular target. Since the cytostatic itself has no target specificity, it can be taken up by all surrounding cells and thus addresses particularly tumor cells, CAFs and endothelial cells, resulting in a higher antitumor effect (bystander effect).[91] A similar approach for the selective transport of cytotoxic agents was also used by *Ostermann et al*. Inhibition of tumor growth in tumor-bearing mice was demonstrated by administration of an antibody-drug conjugate, consisting of a monoclonal FAP antibody and the maytansinoid DM1.[92]

An alternative FAP-specific therapeutic approach is based on direct inhibition of the enzymatic function of the protein. For this purpose, the small molecule inhibitor talabostat (Val-boroPro) was used and investigated in a first clinical study in 28 patients with metastatic colorectal carcinoma. However, although significant but not complete enzyme inhibition was demonstrated, an objective response rate was not achieved in these patients.[93] Other studies investigated the antitumoral effect of tolobostat in combination with other drugs such as the cytostatic drug docetaxel in patients with advanced NSCLC[94], the chemotherapeutic agent cis-platinum in patients with stage II melanoma[95], and the CD-20 antibody rituximab for the treatment of patients with chronic lymphocytic leukemia (CLL) or non-Hodgkin lymphoma[96]. None of these combined therapies exhibited a significant beneficial effect of the FAP inhibitor on overall treatment outcome. Although combined treatment with rituximab resulted in partial remission of the tumor in some patients, this is probably less due to direct inhibition of the enzyme and more the result of an immunologic effect. As shown in animal studies, administration of talabostat leads to an enhancement of tumor-specific T-cell immunity by increasing cytokine and chemokine release in both lymphoid organs and tumor. T-cell-independent stimulation of antitumor activity of neutrophils, macrophages, and natural killer cells was also observed.[96,97] Notwithstanding, talabostat is not observed to add a relevant benefit either as a monotherapeutic or in combination with a clinically established chemotherapeutic agents. Moreover, in addition to FAP, the compound also inhibits the related membrane protein DPP IV, which is expressed in numerous healthy tissues.[65,96]
The different effects of the FAP-specific therapies to date are attributed to the fact that different fibroblast subtypes have opposing effects on tumor progression and can not only suppress it, but in some cases also promote it, so that a reliable prognosis about the course of a targeted therapy in principle cannot be made. Meanwhile, no serious, dose-limiting side effects have been observed in any of the studies performed yet, although FAP expression is also discussed on multipotent bone marrow stem cells (BMSCs).[98] Moreover, a soluble form of the protein, known as antiplasmin-cleaving enzyme (APCE)[99,100], circulates in blood plasma. Thus, FAP inhibition, regardless of its effect on tumor progression, appears to be possible in principle, at least without increased risk of toxicity.

1.3.3 FAP-Addressing Drugs and Inhibitors in Nuclear Medicine

As mentioned previously, there are different strategies for targeting FAP, some of which are applied in nuclear medicine with varying degrees of success. As already discussed, the clinical studies with the ^{131}I-labeled antibody sibrotuzumab did not lead to a desired therapeutical outcome.[81] Recently, *Pandya et al.* conjugated this antibody with a desferrioxamine (DFO) chelator for the complexation of the positron emitter zirconium-89 and *Hintz et al.* followed the same chelator-isotope strategy with a newly identified antibody, which revealed accelerated blood clearance compared to the previously used humanized mAb F19 antibody.[101,102] Although these radiolabeled antibodies offered high target affinity and selectivity, the long circulation and slow clearance as a consequence of their high molecular weight led to unfavorable non-target accumulations and generally hampered a broader applicability in nuclear medicine.

To overcome these drawbacks, peptides are used often in nuclear medicine, as they usually show more rapid accumulation and clearance kinetics compared to antibodies. In the case of FAP, *3B-Pharmaceuticals GmbH* (Berlin, Germany) described a series of peptides in 2020 containing a cyclic heptapeptide core with nanomolar FAP affinity.[103] The clinical candidate of this series, FAP-2286, cannot be further described in this work, as the exact structures of most of these compounds are not published yet. However, a decelerated tumor washout of FAP-2286 as well as the successful radioligand therapy in patient-derived xenografts have been reported.[104]

Since recently, mostly small molecule-derived radiotracers were developed, which further reduce the molecular weight and thus potentially improve pharmacokinetics. As FAP belongs to the family of serine proteases, most new radiotracers described in the literature are based on already described FAP inhibitors. A selection of these is shown in Figure 5, while their FAP affinity and affinities to related proteases are depicted in Table 1.

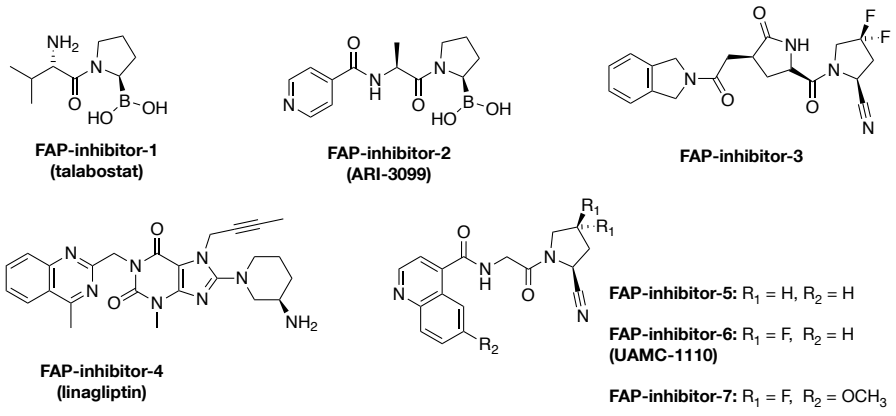

Figure 5: Structures of relevant FAP inhibitors with different inhibitory scaffolds.[105,106]

As will be seen, the selectivity of inhibitors to FAP over related proteases is crucial for selecting one as an inhibitory binding scaffold for radiotracers. Selectivity is inextricably linked to target-to-non-target ratios and therefore to the quality of imaging and the therapeutic

efficacy of a radiopharmaceutical. As can be seen in Table 1, talabostat is a nonselective boronic acid inhibitor that not only shows affinity to FAP, but also to various other proteases, which are expressed in healthy tissue. Because of this, the inhibitor was withdrawn for both safety and efficacy reasons, after previously reaching phase II clinical trials for several cancer types.[93-95] *Bachovchin et al.* recently published new boronic acid inhibitors like ARI-3099, which displayed higher selectivity to FAP over related proteases, especially over proteases of the DPP family.[105,107,108] Linagliptin is a clinically approved DPP IV inhibitor but also displayed substantial FAP affinity. Nevertheless, due to its primarily high DPP IV affinity, off-target accumulation might be a potential issue preventing its use case as a radiopharmaceutical.[109] FAP-inhibitor-3 is a representative of a series of pyroglutamyl(2-cyanopyrrolidine) derivatives reported by *Jiaang et al.*[110] and FAP-inhibitor-4 to -6 are part of the quinolinoylglycyl(2-cyanopyrrolidine) class of FAP inhibitors reported by *Jansen et al.*[105,106] Both classes showed sufficient selectivity to FAP over PREP and low affinities to proteases of the DPP family. Especially FAP-inhibitor-7 revealed that 6-quinolyl modification of UAMC-1110 is possible without a drastic reduction of selectivity, making it a promising starting point for the development of FAP-addressing radiopharmaceuticals.

Table 1: IC_{50} values of relevant inhibitors reported in the literature against FAP and similar proteases; SI stands for "selectivity index" (calculated as [IC_{50}(PREP)/IC_{50}(FAP)]).[105,106]

FAP-inhibitor	IC_{50} (µM) FAP	IC_{50} (µM) PREP	IC_{50} (µM) DPP IV	IC_{50} (µM) DPP 9	IC_{50} (µM) DDP 2	SI (FAP/PREP)
1	0.066 ± 0.011	0.98 ± 0.06	0.022 ± 0.001	ND	0.086 ± 0.007	14.8
2	0.025 ± 0.001	0.99 ± 0.04	> 100	> 50	> 100	39.6
3	0.017 ± 0.001	> 100	> 100	> 100	> 100	5882.4
4	0.37 ± 0.002	> 100	0.002 ± 0.0002	> 100	> 100	> 250
5	0.0103 ± 0.0004	0.86 ± 0.07	> 100	> 100	> 100	83.4
6	0.011 ± 0.0004	> 50	> 100	> 100	> 100	> 4500
7	0.0085 ± 0.0009	8.3 ± 0.7	19 ± 1.3	27.2 ± 0.8	> 100	976.4

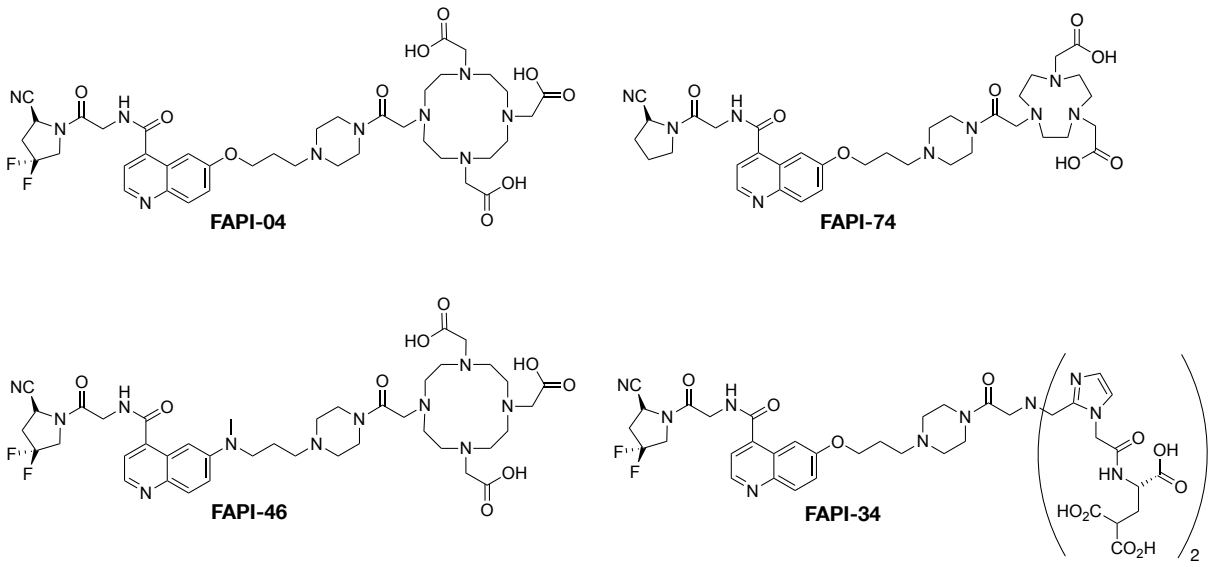

Figure 6: FAPI-tracers developed by *Haberkorn et al.*: FAPI-04 as the first theragnostic and currently the most investigated FAP inhibitor. FAPI-46 offers improved pharmacokinetics and thus tumor retention. FAPI-74 can be labeled with [^{18}F]aluminum fluoride or gallium-68 at ambient temperature. FAPI-34 is suitable for labeling with the theragnostic pair technetium-99m and rhenium-186 or rhenium-188.[79]

The field of FAP targeting radiopharmaceuticals is mainly dominated by 6-quinolyl modified UAMC-1110 derivatives, which are called FAPI's. They were developed by the *Heidelberg group* (*Haberkorn et al.*) with either a quinolinoylglycyl(2-cyanopyrrolidine) inhibitor as binding motif or its difluorinated analogue. The name "FAPI" was chosen as an acronym for "FAP inhibitor" and was adapted by other groups for the discerption of radiotracers that exhibit the structural characteristics of this group of compounds (Figure 6). Main goal of the development of different FAPI's was the optimization of the linker region between the inhibitory binding motif and the chelator moiety, especially to optimize tumor uptake and retention.[111] The most promising results were obtained with a 1,3-propylene spacer between a *N*-piperazine and an ether oxygen or a methylamino group bound to the quinoline moiety (Figure 6). Shorter linker sections resulted in drastically reduced *in vitro* cell uptake of the tracers, while for example a 4-piperidine instead of the *N*-piperazine led to higher background accumulation in xenotransplants.[111,112]

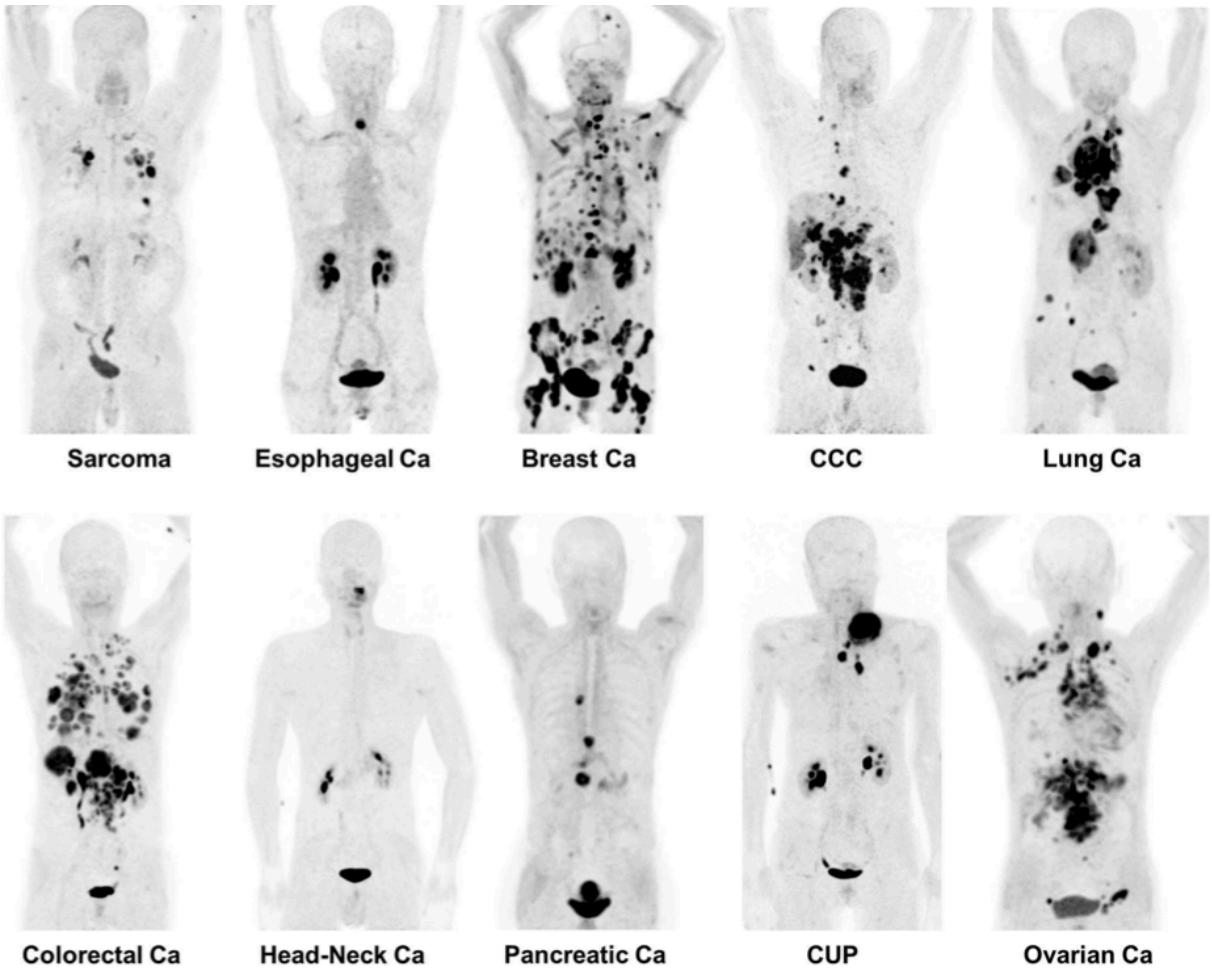

Figure 7: Maximum intensity projections of [^{68}Ga]Ga-FAPI-04-PET/CT in patients reflecting 10 different, histologically proven tumor entities (sorted by uptake in descending order from left to right and top to bottom). By targeting the cancer-associated fibroblasts while providing a low activity uptake in non-target organs as well as rapid clearance kinetics, the FAPI-tracers allowed for the detection of different tumor entities with a high specificity. Ca = carcinoma; CCC = cholangiocellular carcinoma; CUP = carcinoma of unknown primary. Picture sections were taken from *Kratochwil et al.*; © Society of Nuclear Medicine & Molecular Imaging.[113]

As can be seen in Figure 7, early PET imaging studies of [^{68}Ga]Ga-FAPI-04 in patients with 28 different kinds of cancer by *Kratochwil et al.* showed that FAP-targeting tracers have a pan-tumor applicability and even demonstrated potentially superior PET imaging contrast compared to [^{18}F]2-fluoro-2-deaoxyglucose ([^{18}F]FDG). This was particularly observed for important tumor entities, such as breast, lung, head-and-neck, or colorectal cancers as these are some of the most frequently occurring tumor entities.[113] Results from these studies led to initial therapeutic applications of [^{90}Y]Y-FAPI-04. Moreover, experiments in a pancreatic cancer xenograft model using copper-64 and actinium-225 for imaging and a proof-of-concept therapeutic study, respectively, have been reported.[111,114]

Despite the promising studies with [^{68}Ga]Ga-FAPI-04, the compound still suffers from a fast activity washout from tumor tissue, which might be limiting its therapeutic efficacy. Hence, FAPI-46 was developed together with a series of other compounds to further prolong tumor retention while maintaining the diagnostic benefit of a fast initial clearance from non-tumor

organs. This was achieved by additional modifications in the linker region substituting the bridging oxygen at the 6-quinoline position with a methylated nitrogen. This showed that with slight changes of the chemical properties of the linker region, new structure-activity relationships can be identified, which might lead to compounds with improved therapeutic efficacy.[78,112]

Since fluorine-18 offers benefits such as a longer half-life and a lower positron energy than gallium-68, as well as larger batch sizes, the use of this radionuclide for FAPI tracers is an important subject of research. *Toms et al.* first reported a ^{18}F-labeled tracer, FGly-FAPI (Figure 8), which was synthesized *via* triazole formation (*Click* chemistry) of a ^{18}F-labeled 6-deoxy-6-[^{18}F]fluoroglycosyl azide and an alkyne precursor similar to FAPI-04. Despite promising *in vitro* results, a pronounced hepatobiliary excretion and a low tumor uptake were observed in animal studies.[115] In order to benefit from the excellent pharmacokinetics of [^{68}Ga]Ga-FAPI-04 for imaging, *Lindner et al.* developed the homologous tracer FAPI-42, the NOTA derivative of FAPI-04, which is offering the possibility of the formation of an aluminum fluoride-NOTA chelate, which can be used for ^{18}F-labeling. However, this compound displays hepatobiliary excretion, which is why an analogue tracer, FAPI-74 (Figure 6) that lacks the difluoro substitution at the pyrrolidine ring, was developed. The corresponding radiotracer [^{18}F]AlF-FAPI-74 showed a comparable performance in first-in-man PET/CT studies compared to [^{68}Ga]Ga-FAPI-04.[116,117] However, no final conclusion can be given to which compound is superior to the other, as imaging performance of [^{18}F]AlF-FAPI-74 and [^{68}Ga]Ga-FAPI-04 was highly depended on the origin of the tumor tissue and the progress of disease. Nevertheless, because of the superior physicochemical properties of fluorine-18 compared to gallium-68 the general development direction of FAPI's is shifting to ^{18}F-labeled tracers for imaging.
Besides PET/CT, SPECT/CT imaging with FAPI analogs in combination with the enhanced availability of the radionuclide technetium-99m *via* ^{99}Mo/^{99m}Tc-generators are also attractive. Noteworthy, as there is no pan-tumoral tracer available for SPECT/CT like [^{18}F]FDG for PET, ^{99m}Tc-labeled FAPI tracer could represent a more affordable and highly interesting tracer group for imaging, which might even enable therapeutic application with rhenium-186/188. *Linder et al.* designed various compounds that possess a bisimidazole chelator, with [^{99m}Tc]Tc-FAPI-34 (Figure 6) being the most successful candidate, as it compensates for the elevated lipophilicity of the ^{99m}Tc-tricarbonyl core through its several carboxyl groups.[118] An alternative ^{99m}Tc-labeled tracer, [^{99m}Tc]Tc-FL-L3 (Figure 8) using a tripeptide moiety (2,3-diaminopropanoic acid- aspartate-cysteine) to form a complex with technetium-99m and uses a different binding motif compared to the *Haberkorn* group, was published by *Roy et al.* This tracer showed high activity levels in the kidneys and less favorable tumor-to-background ratios compared to [^{99m}Tc]Tc-FAPI-34.[119]

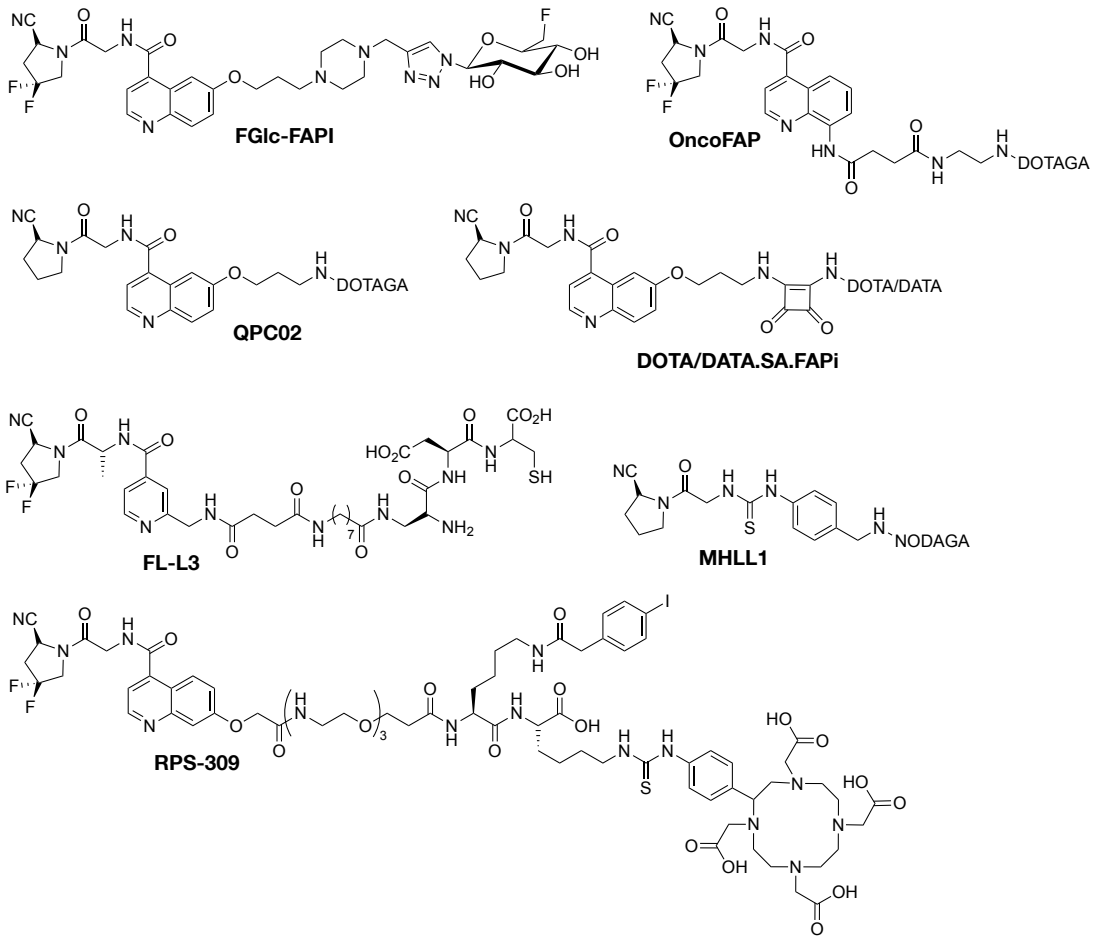

Figure 8: Small molecule FAP-targeted radiotracers published by different groups with identical inhibitory motif or derivatives thereof. Tracers possess different labeling moieties for ^{18}F-fluorination, complexation with ^{99m}Tc or complexation with other metal radioisotopes.[115,119-124]

Recently, many other groups published new FAP-targeting tracers (Figure 8), which often are structurally related to FAPI-04. Most of them comprise only slight modifications in the linker region, a different chelator or using the non-fluorinated or difluorinated inhibitor motif of UAMC-1110. The tracer OncoFAP showed high tumor-to-background ratios in xenografted animals, despite that the 8-quinoline position was used for the attachment of its linker. This was surprising, as *Jansen et al.* reported a loss of potency and selectivity of the inhibitory binding motif when modifications were conjugated at this site.[106,120] *Pomper et al.* reported the tracer QPC01, which revealed a considerable washout of the tumor tissue and a hepatobiliary excretion in small animal studies. The tracer is structurally nearly identical to FAPI-04. The most important structural difference lies in the linker region, where QPC01 uses a 3-aminopropan-1-ol linker, leading to a less sterically demanding amide bond between linker and chelator. Hence, this leads to a lower stability of the linker in the enzymatic pocket of FAP. Therefore, confirming the importance of the linker region for the tracers pharmacokinetics in the tumor tissue.[121] The radiotracers DOTA/DATA.SA.FAPi reported by *Moon et al.* showed similar *in vivo* behavior compared to [^{68}Ga]Ga-FAPI-04, except for activity uptake in the gastrointestinal tract, which lowers the overall imaging contrast. Nevertheless, the derivative that contains the DATA chelator allows for efficient ^{68}Ga-labeling at room

temperature, which enables labeling of temperature-sensitive compounds and is thus an advantage over DOTA-containing compounds.[122,125] In order to increase dose delivery to the tumor, *Kelly et al.* developed RPS-309, which possesses an 4-iodophenyl albumin binding moiety to slow down activity clearance from tumor tissue. While this strategy was successful for other therapeutic radiotracers, higher non-target accumulation and accelerated tumor washout prohibits its use as a theranostic agent.[124] The only compound that does not comprise the inhibitory quinoline motif, MHLL1, was not tested in an oncological setup yet successfully enabled the monitoring of fibroblast activity after myocardial infarction by PET/CT imaging.[123]

It is too early to tell, which FAP-targeting tracer strategy will prevail, but it seems clear that optimization towards improved tumor retention and pharmacokinetics is more important than absolute tumor uptake. Many tracers competing with the current lead compound FAPI-04 showed higher tumor uptake, but lacked the favorable tumor-to-background ratios of [^{68}Ga]Ga-FAPI-04 due to a higher off-target accumulation or a faster tumor washout. Moreover, low absolute tumor uptake because of a lower target density compared to other radiopharmaceuticals addressing different targets (e.g., PSMA or SST2R) raise doubts about the usability of FAP as a target for therapeutic approaches. Therefore, research in FAP-targeting compounds shifted to the development of ^{18}F- and ^{99m}Tc-labeled tracers for a primarily use as imaging agents. In the case of fluorine-18, introducing superior physicochemical properties compared to other PET isotopes and in the case of technetium-99m, enabling the introduction of pan-tumoral imaging with SPECT/CT. This might be advantageous over conventional imaging applications in nuclear medicine.

1.4 Fluorine-18 in Nuclear Medicine

1.4.1 Why Fluorine-18?

In the past decades, positron emission tomography (PET) developed into the leading imaging modality in nuclear medicine.[126] In contrast to computed tomography or magnetic resonance tomography, which provides detailed anatomical information, PET provides information about physiological and biochemical processes in the body before any macroscopic signs of possible disease appear.[127]

For molecular imaging by PET, a variety of nuclides are available, either obtained from a generator or from cyclotron production. A list of some nuclides and their physiochemical properties can be found in Table 2. Which positron emitter is chosen depends on several factors:[128]

- **Half-life ($t_{1/2}$):** on the one hand, the half-life must fit the *in vivo* half-life of the applied ligand and on the other hand, allow radiolabeling of the respective ligand with sufficiently high specific activity.
- **Specific activity (Sp*A*):** the Sp*A* of the nuclide directly influences the Sp*A* of the final to be applied radiopharmaceutical. A low SpA_{max} negatively affects adequate imaging due to (partial) saturation of the target through the cold labeled compound.
- **Maximum positron energy (E β_{max}):** this should be as low as possible for optimal resolution and lowest possible radiation dose to surrounding tissue.
- **Labeling chemistry:** ideally, a labeling method should be available that allows rapid labeling with high Sp*A* and that can easily be transferred to routine clinical practice.
- **Availability:** while gallium-68 is conveniently available *via* a generator, most nuclides must be produced in a cyclotron. Availability therefore depends on access to a cyclotron or the existence of a suitable distribution network.

PET nuclides carbon-11, nitrogen-13 and oxygen-15 are not suitable for labeling with FAP analogues due to their short half-life, they might be compatible with their pharmacokinetics, but the short half-life of the nuclides limits the possibilities of their synthetic incorporation. Nuclides with long half-life (copper-64, zirconium-89, iodine-124, terbium-152), high positron energy (gallium-68, iodine-124, oxygen-15) and low positron yield (copper-64, zirconium-89, iodine-124, terbium-152) are also found to be less suitable. In addition, nuclides such as copper-64 or iodine-124 exhibit other decay modes besides the desired β^+ decay, which increase the radiation dose to the patient.[128,129]

In contrast, fluorine-18 has a suitable half-life of 109.7 min and a sufficiently low positron energy of 634 keV and can be produced in the cyclotron with a high Sp*A*. It has been shown that fluorine-18 provides better imaging resolution in comparison with ^{68}Ga due to its lower positron energy.[130] Nevertheless, gallium-68 based PET diagnostics are mainly found in routine clinical molecular imaging. One of the reasons often given in the literature is the fact

that gallium-68 can be conveniently obtained by a generator.[131] However, an extensive distribution system for fluorine-18 exists in many places and the cost of a gallium-68 generator is generally higher than the production of fluorine-18. A gallium-68 generator provides about 1.8 GBq with daily elution, while a low energy (18 MeV) cyclotron can produce as little as between 370 and 740 GBq of fluorine-18.[132]

Table 2: List of common isotopes for PET imaging. The list provides only a basic overview and does not represent the totality of all available β^+-emitters. The physicochemical data, with the exception of iodine-124 and terbium-152,[133,134] were taken from the *Table of Radionuclides of the Bureau International des Poids et Mesures*.[135-137]

Nuclide	**Half-life ($t_{1/2}$)**	**Proportion of β^+ in % (E β_{max} [keV])**	**Advantages**	**Disadvantages**
^{11}C	20.4 min	99.8 (961)	• high proportion of β^+ decay • moderate positron energy	• short $t_{1/2}$
^{13}N	9.98 min	99.0 (1199)	• high proportion of β^+ decay • moderate positron energy	• short $t_{1/2}$
^{15}O	2.04 min	99.9 (1735)	• high proportion of β^+ decay	• short $t_{1/2}$ • high positron energy
^{18}F	109.7 min	96.9 (634)	• high proportion of β^+ decay • low positron energy • suitable half-life	• synthetic accessibility of the radiopharmacon
^{64}Cu	12.7 h	17.9 (653)	• low positron energy	• long half-life • low proportion of β^+ decay • 39% β^- (579 keV)
^{68}Ga	67.8 min	88.9 (1899)	• production *via* generator	• high positron energy
^{89}Zr	3.27 d	22.8 (902)	• moderate positron energy	• long half-life • low proportion of β^+ decay
^{124}I	4.2 d	23.0 (2138)	-	• long half-life • low proportion of β^+ decay • high positron energy • γ-radiation (602, 722, 1691 keV)
^{152}Tb	17.5 h	17.0 (1080)	• moderate positron energy	• long half-life • low proportion of β^+ decay

Therefore, it may be assumed that the preference of gallium-68 over fluorine-18 is mainly due to the different labeling methods. While gallium-68 is incorporated in a simple complexation reaction and the radiopharmaceutical usually requires no further purification, many methods for labeling with fluorine-18 rely on pre-labeled prosthetic groups followed by time-consuming purification by RP-HPLC. These rather complicated synthetic routes proved to be unattractive for routine clinical use in the context of FAP.[129,132] Nonetheless, fluorine-18 exhibits superior physicochemical properties ($t_{1/2}$, positron energy, production volume), which is why intensive research made newer and more modern labeling methods available.

1.4.2 Production and Application

Fluorine-18 can be incorporated into a molecule *via* both nucleophilic and electrophilic reaction mechanisms. The labeling follows direct substitution reactions and indirect methods, for example *via* prosthetic groups. Depending on the case, fluorine-18 is required in different forms for the reaction and its production in a cyclotron must follow corresponding different routes (Table 3).[138,139]

Table 3: Possible production routes for the extraction of fluorine-18. The table only gives an overview, for a complete overview, see *Guillaume et al.*.[138,139]

	Reaction	Target	Product	Sp*A* [GBq/µmol]
1	$^{18}O(p,n)^{18}F$	$^{18}O_2$ (F_2 carried)	$[^{18}F]F_2$ (gas)	~0.6
2	$^{18}O(p,n)^{18}F$	$[^{18}O]H_2O$	$[^{18}F]F^-$ (aq)	~600
3	$^{16}O(^3He,p)^{18}F$	$[^{16}O]H_2O$	$[^{18}F]F^-$ (aq)	~50
4	$^{20}Ne(d,\alpha)^{18}F$	Ne (F_2 carried)	$[^{18}F]F_2$ (gas)	~0.1

For electrophilic radiolabeling, $[^{18}F]F_2$ is required to generate the electrophilic species in subsequent synthesis steps. The two most relevant production routes (Table 3, entries 1 and 4), are performed with ^{20}Ne or $^{18}O_2$ gas targets and yield low specific activities between ~0.1 and 0.6 GBq/µmol. Since $[^{18}F]F_2$ adsorbs strongly to vascular surfaces, the addition of $^{19}F_2$ is required, lowering Sp*A* and making electrophilic reaction mechanisms unattractive for molecular imaging. In the case of nucleophilic reaction pathways, ^{18}F is used as fluoride. The main production pathways occur with H_2O as the target, which is either enriched in $[^{18}O]H_2O$ (Table 3, entry 2), or used as $[^{16}O]H_2O$ (Table 3, entry 3). The latter reaction is of rather minor importance due to the cost-intensive ^3He irradiation and the comparatively low yields. Production using an $H_2{}^{18}O$ target is generally preferred due to the high resulting Sp*A* (~600 GBq/µmol) and high yields, even at low irradiation durations of 1 h, which is why nucleophilic reaction mechanisms are favored, like isotopic exchange reactions which will be discussed in a later chapter.[138-140]

In most cases, the formation of a C-F bond is desired, since fluorine can be used as a bioisoster for both hydrogen (size and valence electrons) and oxygen (size and electronegativity).[141] For small molecules, direct labeling methods such as aliphatic or aromatic nucleophilic substitutions are often used (e.g., $[^{18}F]$FDG, $[^{18}F]$FMISO, $[^{18}F]$FET). However, for biomolecules, these methods often prove to be inapplicable, due to high

temperatures, pH, or an unsuitable solution environment, respectively.[140,141] As an alternative, a wide range of prosthetic groups exist, which are commonly radiolabeled in advance and subsequently anchored to the biomolecule by alkylation, acylation, amidation, click chemistry, oxime ligation, or other methods. However, a subsequent purification of the prosthetic group is often required after labeling with fluoride-18 and the reaction with the biomolecule is usually followed by another time-consuming purification step by RP-HPLC to remove by-products or reactants.[129,141]

The given methods often do not fulfill the demands made on ^{18}F-labeling. These should be rapid due to the half-life - more than one purification step is therefore rather unsuitable - provide high radiochemical yields and specific activities and the reaction conditions should be mild enough not to damage the biomolecule (e.g., low temperatures, suitable pH range). In addition, few and simple reaction steps are required, especially in terms of transferability to routine clinical practice.[129,140,141]

1.4.3 Modern Fluorination Methods

In order to circumvent the problems mentioned in the previous chapter, the spectrum of C-F bonds has been extended to Al-F, B-F or even Si-F bonds.[141] In the following, the methods available for this purpose will be examined in more detail. Figure 9 gives an overview on the most relevant methods and the underlying building blocks.

The use of aluminum-bound fluorine followed by complexation using the NOTA chelator was first described in 2009 and is based on the strong coordination of fluoride ions to Al^{3+} (> 670 kJ/mol; Figure 9, entry A).[142] In this process, the $[^{18}F][AlF]^{2+}$ complex is formed prior to complexation, from $AlCl_3$ and ^{18}F-fluoride in target water ($[^{18}O]H_2O$). Subsequently, $[^{18}F][AlF]^{2+}$ is combined with the peptide carrying the chelator and complexed at high temperatures (90 to 110 °C). In this method, the fluoride-18 can be used in an aqueous environment without prior transfer to a pure organic solution environment, and RP-HPLC purification is also not required. The pH range is between 4 and 5. To optimize the RCY, the $[^{18}F][AlF]^{2+}$ complex is formed in an aqueous NaOAc buffer with the addition of organic solvents as DMSO. For this the ^{18}F-fluoride needs to be separated from the target water ($[^{18}O]H_2O$) through QMA cartridge purification. A potential problem with the method of complexation with a $[^{18}F][AlF]^{2+}$ complex is the high temperature range, which can have a negative effect on the stability, depending on the peptide structure.[142,143] To compensate for this and other difficulties of this labeling strategy, new state-of-the-art open chain chelators like (±)-H_3RESCA and 2-AMPTA have been developed, which show beneficial complexation properties (high RCY up to 90% at low temperatures) compared to classic chelators like NOTA.[144]

Trifluoroborates (Figure 9, entry B) can be prepared rapidly from aromatic boric acid esters in a substitution reaction.[145] In contrast to other substitution reactions, radiosynthesis can also be carried out in an aqueous environment, which means that azeotropic drying, for example, can be dispensed with. However, even with this method, the conversion of the leaving group

to a B-F bond increases especially at elevated temperatures and low pH. Therefore, this method relies on the concept of prior labeling of the prosthetic group and subsequent conjugation to the peptide, making RP-HPLC purification usually indispensable. In addition, for the formation of the trifluoroborates, fluoride-18 carried with fluoride-19 is required, lowering the specific activity of the product.[146-148]

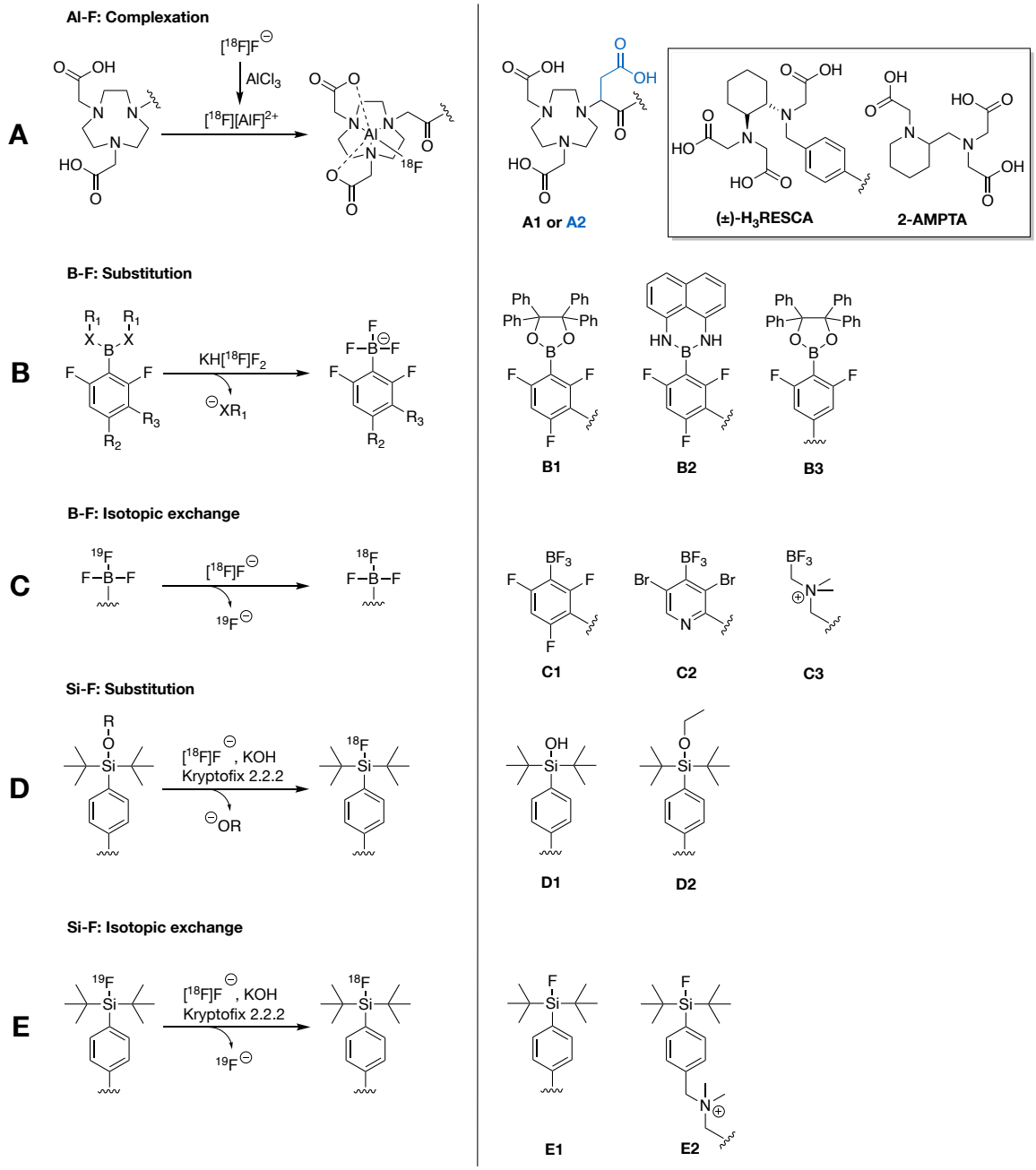

Figure 9: Overview of radiosynthesis using [^{18}F]fluoride (left in figure) and a selection of corresponding prostatic groups (right in figure, molecules **A1 – E3**) that can be used to generate Al-F, B-F or Si-F bonds. **A:** [^{18}F]Al-F by formation of [^{18}F][AlF]$^{2+}$ and subsequent complexation using suitable chelators; example **A1**, **A2**, **(±)-H$_3$RESCA** or **2-AMPTA**. **B:** [^{18}F]B-F by nucleophilic substitution on boric acid esters; examples **B1—B3**. **C**: [^{18}F]B-F by isotopic exchange on trifluoroborates; examples **C1—C3**. **D**: [^{18}F]Si-F by nucleophilic substitution on alkoxysilanes; examples **D1** and **D2**. **E**: [^{18}F]Si-F by isotopic exchange on SiFA moieties; examples **E1** and **E2**. Figure adapted from *Bernard-Gauthier et al.* and *Kumar et al*.[149,150]

Like trifluoroborates building blocks, Silicon-fluoride acceptors (SiFA) can be radiolabeled by both nucleophilic substitution (Figure 9, entry D) and isotopic exchange (Figure 9, entry E) with fluoride-18. The efficiency of the substitution reaction of alkoxysilanes or silanols (Figure 9, entry D) depends on the selected leaving group and the reaction conditions, nevertheless, it can be generalized that satisfactory conversions (radiochemical conversion (RCC) > 80%) are mainly achieved at temperatures above 65 °C and at low pH values. Furthermore, there is the problem of chemical purity since the reaction usually is carried out with carrier-free ^{18}F-fluoride and therefore purification by RP-HPLC is required to separate the unreacted precursor from the radiolabeled product.[151,152]

To compensate difficulties arising for both B-F and Si-F bond formation through substitution reactions, isotope exchange has become the preferred reaction pathway (Figure 9, entries C and E). The reaction conditions are milder, since radiosynthesis can be carried out at room temperature. The pH for trifluoroborates is between 1.5 and 2.5, while SiFA isotope exchange occurs even between pH 5.0 to 7.0. Provided that neither the formation of by-products nor decomposition are observed, RP-HPLC purification can be omitted since the precursor molecule and the radioactive species are chemically identical. Instead, solid phase extraction is performed to separate free ^{18}F-fluoride and organic solvents. The syntheses are mild, rapid, and feasible with low precursor amounts (< 25 nmol), allowing high radiochemical yields and specific activities of 40 to 111 GBq/µmol for trifluoroborates and 30 to 63 GBq/µmol for SiFAs.[149,153-155]

In this work, the focus lies on the application of radiolabeled SiFA moieties using isotopic exchange. This methodology will be discussed in more detail in subsequent chapters.

1.5 Silicon-Fluoride Acceptor (SiFA)

1.5.1 Development of SiFA Moieties

The strong affinity of fluorine for silicon is evident from the high binding energy of 576.4 ± 17 kJ/mol, which is higher than for a C-F bond with only 513.8 ± 10 kJ/mol. Because of this and the growing importance of fluorine-18 as a radionuclide for imaging, the use of a Si-F bond in radiopharmaceuticals is of considerable interest.[156] Due to the high difference in electronegativity between fluorine (4.1) and to silicon (1. 7), the bond is strongly polarized and can be considered rather ionic than covalent.[157] This ionic character is the reason for the kinetic instability of the Si-F bond with respect to other silophiles, resulting in the rapid hydrolysis of simple fluoroalkylsilanes in an aqueous environment.[158,159] At the same time, however, this instability allows nucleophilic substitution at the silicon atom by fluoride-18.[159] In addition, the larger atomic radius of silicon ensures that the SiFA moieties used for fluorination react more efficiently in a nucleophilic substitution compared to analogous carbon building blocks.[159,160]

An early mention of an [^{18}F]Si-F compound is found in a 1958 publication in which SiF_4 was combined with [^{18}F]metal fluorides.[161] Later, fluoroalkylsilanes were further investigated for their ^{19}F-^{18}F isotope exchange capability.[162,163] [^{18}F]Fluorotrimethylsilane ([^{18}F]FTMS) was the first [^{18}F]F-Si compound to be investigated in an *in vivo* study in rats. However, this simple fluoroalkylsilane proved to be hydrolytically unstable due to the highly polarized Si-F bond and resulted in a high accumulation of fluoride-18 in bone. Even back then, *Rosenthal et al.* postulated that steric shielding of the silicon atom by suitable substituents, could lead to a decrease in the hydrolysis rate.[158]

For radiopharmacy, the isotope exchange at silicon-fluorine bonds - or the Si-F bond in general - initially had no major significance. In contrast, ^{19}F-^{18}F isotopic exchange at carbon-fluorine bonds was investigated in more detail, for example, on the basis of the preparation of [^{18}F]haloperidol and [^{18}F]spiroperidol. Besides the harsh reaction conditions, such as high temperatures and long reaction times, it were mainly the poor yields and low specific activities that made this methodology unattractive. Depending on the publication, maximum specific activities of ~37—240 MBq/µmol can be found, which hardly allow for *in vivo* application.[164-166] These problematic issues are likely responsible for the widespread assumption that isotope exchange is not a viable tool for ^{18}F-labeling.[167]

It was not until 2006 that [^{18}F]Si-F compounds regained importance through the work of *Schirrmacher et al*. The three SiFA moieties [^{18}F]Ph_3SiF, [^{18}F]*t*$BuPh_2SiF$ and [^{18}F]*t*Bu_2PhSiF were subjected to a human serum study in which it could be shown that the hydrolysis stability can be increased by shielding the Si-F bond, using appropriate sterically demanding substituents such as phenyl or *tert*-butyl substituents as shown in Figure 10.[153]
These observations were also confirmed for alkoxysilanes labeled with fluoride-18 in a nucleophilic substitution as described in chapter 1.4.3 and shown in Figure 9.[168] In a study

by *Höhne et al.* a wide variety of substituents on the silicon atom were investigated, resulting in a clear correlation between steric shielding of the Si-F bond and hydrolysis stability. Therefore, *t*Bu$_2$PhSiF has now been established as the classical SiFA moiety.[169]

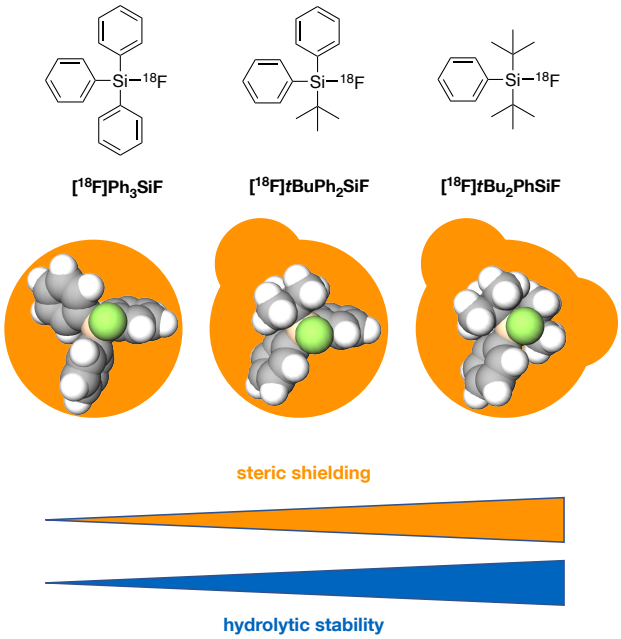

Figure 10: SiFA moieties developed by *Schirrmacher et al.* and their respective 3D-structure models. Bars imply increasing steric shielding (orange) and hydrolytic stability (blue) of a [^{18}F]Si-F bond in human serum from left to right.[153]

Another important insight from the publication of *Schirrmacher et al.* was, in addition to the considerations on stability, especially the results on isotope exchange reactions as shown in Scheme 1.

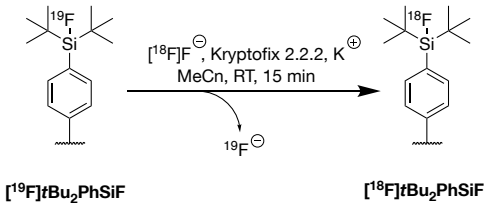

Scheme 1: Isotopic exchange reaction on [^{19}F]*t*BuPhSiF as described by *Schirrmacher et al.*.[153]

Isotopic exchange on [^{19}F]*t*Bu$_2$PhSiF occurred within 15 min at room temperature and with radiochemical yields between 80 and 95%. In addition, the specific activities of 190—230 GBq/µmol far exceeded previous results on C-F bonds.[153]
These promising results provided the basis for the development of various SiFA moieties that can be attached to peptides *via* appropriate conjugation methods and used for PET imaging.

1.5.2 Chemistry and Mechanistic Aspects of SiFA Labeling

To find out why the isotope exchange on SiFA moieties proceed within a few minutes at room temperature and approximately stoichiometrically, both theoretical calculations and experimental investigations were carried out.

Using density-functional theory (DFT), a reaction mechanism for the isotopic exchange was postulated to proceed *via* a 5-fold coordinated intermediate. This allows the substitution of fluoride, whereby starting from the intermediate, both fluoride-18 and fluoride-19 can be substituted as shown in Figure 11.[170] The trigonal-bipyramidal structure of the intermediate is consistent with the literature, which describes the formation of hypervalent 5- or even 6-coordinated structures for the substitution on tetravalent silanes.[171,172]

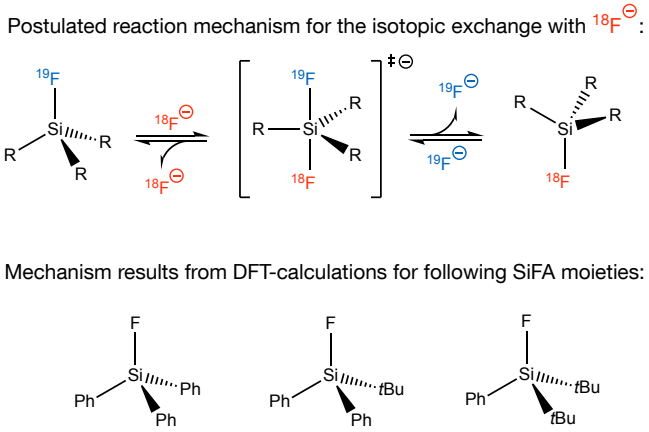

Figure 11: Reaction mechanism of isotope exchange with fluoride-18. Postulated for the SiFA moieties Ph_3SiF, $tBuPh_3SiF$ and tBu_2Ph_3SiF. Shown mechanism is generally valid for all SiFA moieties.[170]

According to the calculations for Ph_3SiF, $tBuPh_2SiF$ and tBu_2PhSiF, the pentacoordinate would be stable at least in the gas phase. However, for the calculations of the intermediates in the reaction medium acetonitrile, a low energy barrier of Gibbs free energy (ΔG) between 21 and 42 kJ/mol is shown. Accordingly, the formation of the intermediate $[^{18}F][^{19}F][R_3SiF_2]^-$ shown in Figure 11, is energetically less favorable and either $[^{18}F]R_3SiF$ or $[^{19}F]R_3SiF$ is formed upon release of a fluoride. The formation of both variants is equally likely, since $\Delta G = 0$ can be assumed for the isotope exchange. Thus, the uptake and release of a fluoride proceeds rapidly and approximately stoichiometrically. Despite the lack of energetic driving force toward the fluorine-18 product, an exchange of fluorine-18 with fluorine-19 is usually not observed. The latter is due to the stoichiometric excess of the $[^{19}F]$SiFA substrate, which makes a re-encounter of a fluoride-19 with a $[^{18}F]$SiFA species statistically improbable.[170]

Kostikov et al. performed experimental studies using the SiFA moiety $SiFAN^+$ and determined a low activation energy of $E_a = 65.6$ kJ/mol for the isotopic exchange and a value of 7.6×10^{13} $M^{-1}s^{-1}$ for the preexponential factor A as shown in Figure 12.[173] For a better classification of the results, they also calculated both values for the nucleophilic substitution of ethylene glycol-di-*p*-tosylate with fluoride-18, where *p*-tosylate is a commonly used prosthetic group

for ^{18}F-labeling. Typical of such substitutions on a carbon atom - and in contrast to the isotope exchange on SiFA moieties - this reaction must be carried out at elevated temperatures.[174] The activation energy E_a = 71.5 kJ/mol is slightly higher than for the isotope exchange reaction. However, the preexponential factor A of 2.9 × 10^9 $M^{-1}s^{-1}$ is significantly lower than for the reaction of SiFAN$^+$.[173] The preexponential factor A, describes the collision frequency of two reactants and thus represents a measure of the probability of the reaction.[175]

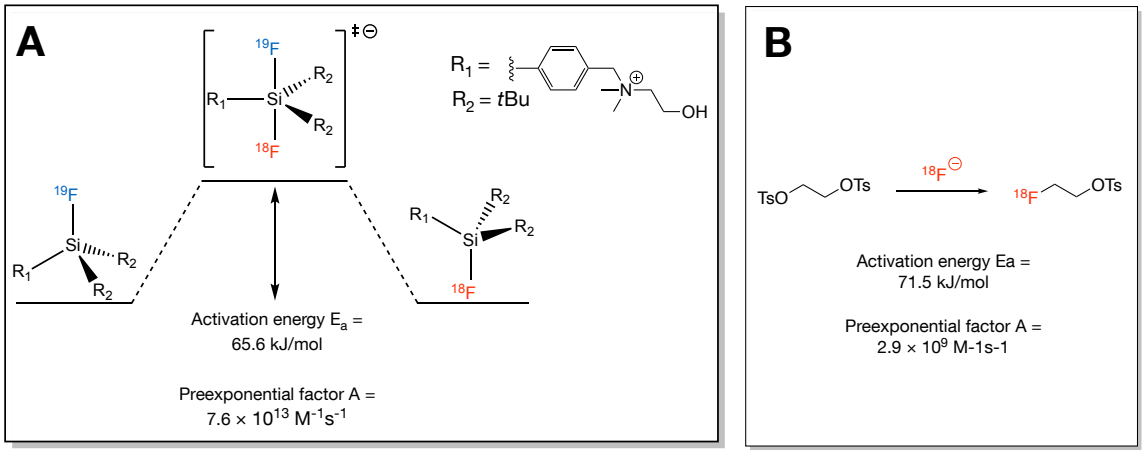

Figure 12: **A** Energetic profile for the isotope exchange at SiFAN$^+$. Activation energy E_a and the preexponential factor A calculated from using the Arrhenius plot. **B** Reaction equation for the nucleophilic substitution of ethylene glycol-di-*p*-tosylate. Activation energy E_a and the preexponential factor A calculated from using the Arrhenius plot.[154]

The lower E_a and the high preexponential factor A provide an explanatory basis for the efficient isotopic exchange reaction at SiFA moieties, even at low temperatures.[173]

1.5.3 SiFA Moieties for the Application in Peptide Chemistry

Various SiFA moieties are available for the usage in peptides or proteins as shown in Figure 13 and Figure 14. Due to the high stability towards hydrolysis of the Si-F bond, the *t*Bu$_2$PhSiF motif has prevailed for these building blocks and the functionality required for conjugation is mostly located in the *para*-position to the silicon unit.[153,176]

Starting from SiFA-alcohol, various building blocks can be prepared for different applications.[176] Oxidized to SiFA-aldehyde (SiFA-A), this can be linked to the peptide in an oximligation,[170] SiFA-benzoic acid (SiFA-BA) can be linked *via* a peptide bond, or converted in advance to a comparatively stable pentafluorophenyl active ester (SiFA-Pfp active ester).[176] The SiFA-Aldehyde (SiFA-A) can be used for the production of SiFA-benzoic acid (SiFA-BA) *via* oxidation.

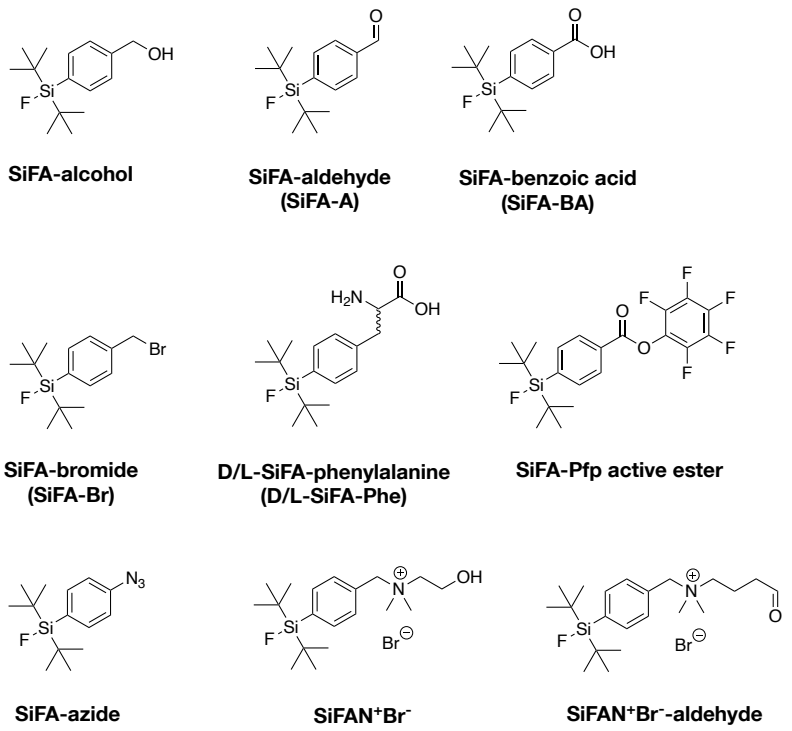

Figure 13: Selection of SiFA moieties based on the basic *t*Bu$_2$PhSiF motif, which are mainly used for incorporation in peptide synthesis.[170,173,176-178]

As a brominated variant, SiFA-bromide (SiFA-Br) is mainly used to produce further building blocks, such as SiFAN$^+$Br$^-$ or SiFAN$^+$Br$^-$-aldehyde. These, in contrast to the previously mentioned variants, carry an additional positive charge, which is intended to compensate for the high lipophilicity of SiFA moieties.[173,178] Also worth mentioning is the development of SiFA-phenylalanine (SiFA-Phe), which can be synthesized both racemically and isomerically pure, and is inserted directly into the peptide chain *via* classical peptide synthesis methods.[177]

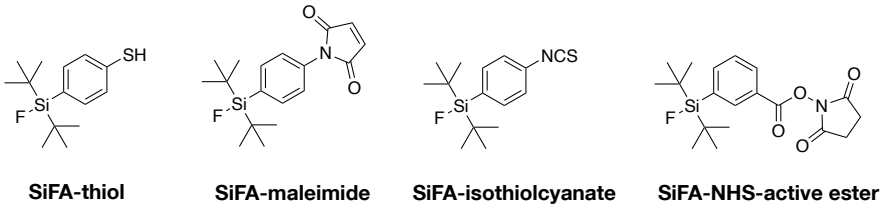

Figure 14: Selection of SiFA moieties based on the basic *t*Bu$_2$PhSiF motif, which are mainly used for incorporation in protein labeling.[176,179-182]

Using SiFA-thiol or SiFA-maleimide (Figure 14) in maleimide-sulfhydryl-reactions can be used for protein labeling. However, it must be considered that either a maleimide functionality has to be positioned in the protein, or cysteines potentially relevant for the biological activity, are no longer available after maleimide binding.[176,179,180] As an alternative, SiFA-isothiocyanate or the SiFA-NHS-active ester are available, which are reacted with lysine side chains.[181,182]

1.5.4 State-of-the-Art Design of SiFA-Containing Ligands

Due to the different possible functional groups on the *t*Bu$_2$PhSiF motif, SiFA building blocks can be incorporated into low molecular weight compounds, peptides, or proteins by the simplest synthetic steps. Thus, the main problem in the use of SiFA moieties is not synthetic considerations. Due to the *t*Bu residues on the silicon atom, these building blocks - and thus the final ligands - exhibit high lipophilicity. This can lead to hepatobiliary excretion, low accumulation at the target structure, and slow clearance, among other effects. Thus, in the development of SiFA containing ligands, the incorporation of hydrophilic moieties is the preferred approach to counteract these effects.[159,167,183,184]

The most prominent example of a SiFA ligand is SST2 receptor addressing [^{18}F]SiTATE, which is the result of a multi-step ligand optimization process.[178,185] This compound is an interesting example for the challenges in radioligand development when lipophilic SiFA-moieties are applied. The earlier developed SiFA-TATE, shown in Figure 15, was the first peptide ligand conjugated to the *t*Bu$_2$PhSiF-SiFA moiety.[153,170] In the *in vivo* mouse experiment, with AR42J tumor-bearing nude mice, no tumor accumulation was found for [^{18}F]SiFA-TATE 90 min p.i., but significant excretion *via* liver and intestine was observed. The authors explain this observation with the high log$D_{7.4}$ of 1.59 ± 0.01. The introduction of the saccharified amino acid L-Asn(AcNH-β-Glc) and a PEG$_1$ linker should lower the lipophilicity. The resulting derivatives SiFA-TATE-02 and SiFA-TATE-03 still exhibited high lipophilicity with log$D_{7.4}$ of 1.23 ± 0.05 and 0.96 ± 0.07, respectively. However, [^{18}F]SiFA-TATE-03 showed tumor accumulation of as much as 7.73 ± 1.90 %ID/g in mouse experiments in addition to hepatobiliary excretion (liver = 16.1 ± 3.80 %ID/g).[186]

To further increase the hydrophilicity, two additional L-Asp were inserted yielding SiFA-TATE-04 and lowering the log$D_{7.4}$ to about -1.1* (values marked with * are not published in figures and were therefore estimated graphically)[178]. The introduction of the aspartates thus provided the largest contribution to hydrophilicity to date.[178] Further derivatives showed that neither longer PEG linkers nor the incorporation of further aspartates, could significantly lower the lipophilicity.[178,185] Due to the negative log$D_{7.4}$ for [^{18}F]SiFA-TATE-04, tumor accumulation 60 min p.i. is close to 30 %ID/g, however, the ligand still exhibits high liver accumulation, although lower than for [^{18}F]SiFA-TATE-03.[178]

Instead of the previously used SiFA aldehyde (SIFA-TATE to -04), the SiFAN$^+$ building block, with a positive charge neighboring the aromatic phenyl of the SiFA moiety, was used in the further ligand development (SiTATE).[178,185] This building block, although specifically developed to increase hydrophilicity, only slightly reduces lipophilicity to a log$D_{7.4}$ of -1.21 ± 0.02.[178,187] In the *in vivo* mouse experiment 60 min p.i. however, [^{18}F]SiTATE exhibited 18.5 ± 4.89 %ID/g in the tumor and is thus comparable to [^{68}Ga]DOTA-TATE with 14.1 ± 4.84 %ID/g. Most surprising is the predominantly renal excretion, with liver accumulation in the low single-digit %ID/g range and this despite the still moderate hydrophilicity. The authors already suspected that this drastic influence on liver excretion

cannot be attributed solely to the minor difference in hydrophilicity of SiFA-TATE-04 compared to SiTATE, but must be related to the structure of the different SiFA moieties.[178] The promising preclinical data of SiTATE meanwhile resulted in initial patient studies.[188]

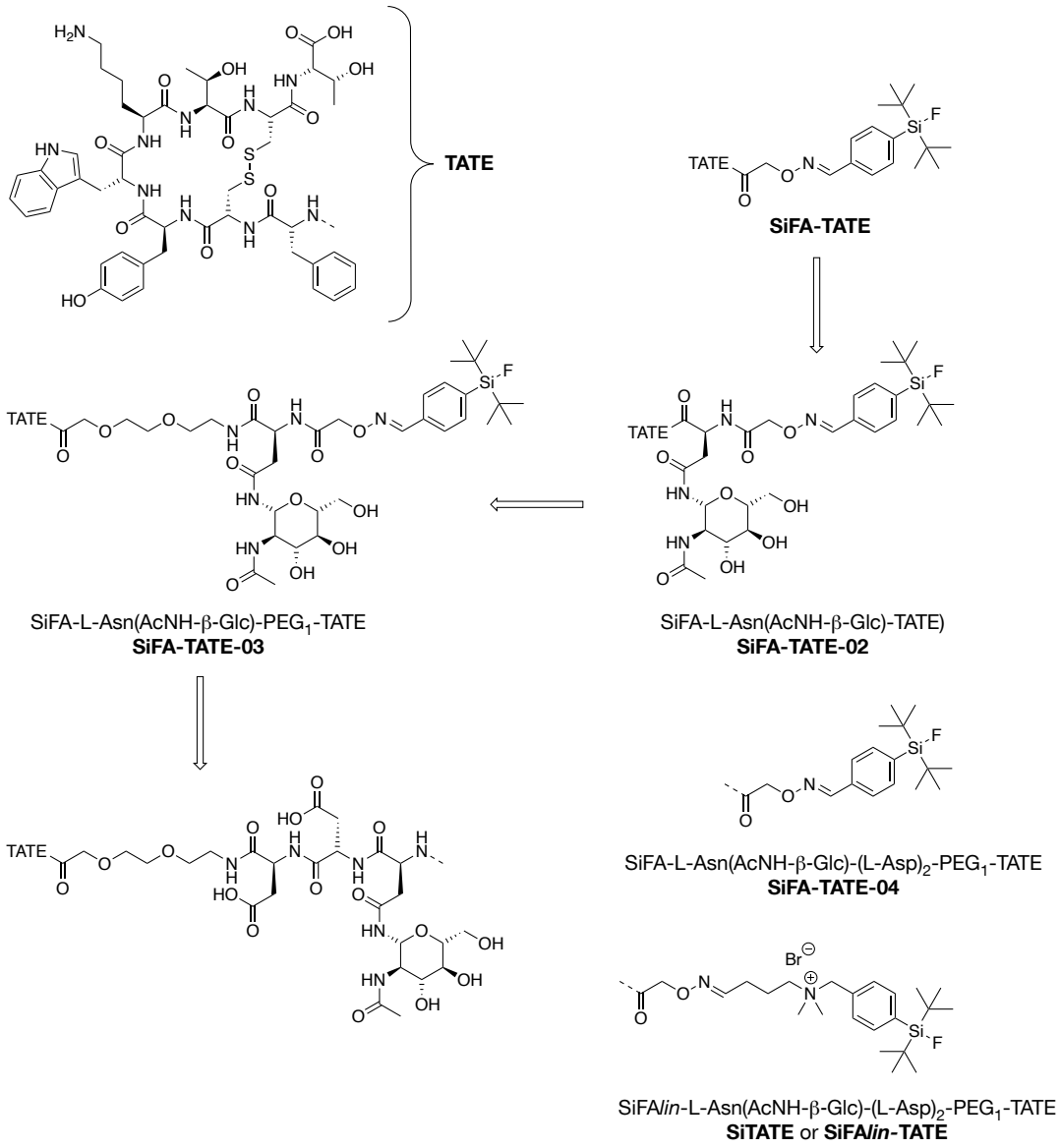

Figure 15: Development of SiTATE starting from SiFA-TATE with stepwise improvement of hydrophilicity and pharmacokinetics.[178]

The development of SiTATE has shown that the lipophilicity of the SiFA moiety, with respect to the excretion pathway and accumulation at the target structure, is a problem that can be partially circumvented by hydrophilic groups. Here it should be mentioned that lipophilicity optimizations must be seen as dedicated structural optimizations, because contributions of individual structural components are not necessarily cumulative. At the same time, especially modified SiFA building blocks such as the SiFAN$^+$, can significantly affect excretion, accumulation, and clearance.

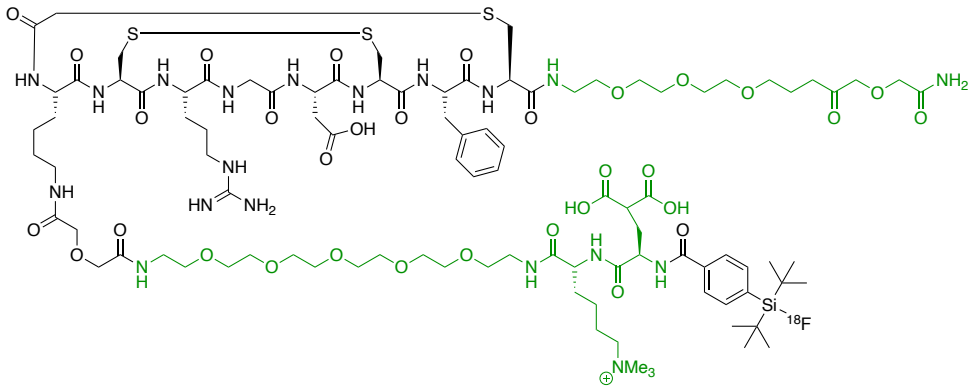

[^{18}F]SiFA-LysMe$_3$-γ-carboxy-D-Glu-RGD (example derivative)

Figure 16: Chemical structure of an exemplary integrin ligand according to *Lindner et al*. and based on the classical RGD motif. Areas highlighted in green serve to enhance hydrophilicity.[189]

The development of SiFA ligands for other target structures, however, focused primarily on the modulation of the log$D_{7.4}$ value. For the $\alpha_5\beta_3$ and $\alpha_5\beta_5$ integrins, *Lindner et al.* presented different RGD-based derivatives structurally based on the clinically applied [^{18}F]fluciclatide as shown in Figure 16.[184,189] Only by using the L-Lys(Me$_3$)-γ-carboxy-D-Glu sequence, a sufficient hydrophilicity could be achieved (log$D_{7.4}$ = -1.97 ± 0.12), which provided promising clearance and tumor accumulation in the mouse model. In contrast, the structurally analogous derivative lacking the L-Lys(Me$_3$)-γ-carboxy-D-Glu sequence exhibited hepatobiliary excretion, most likely due to the higher log$D_{7.4}$ of -1.10 ± 0.03.[189]

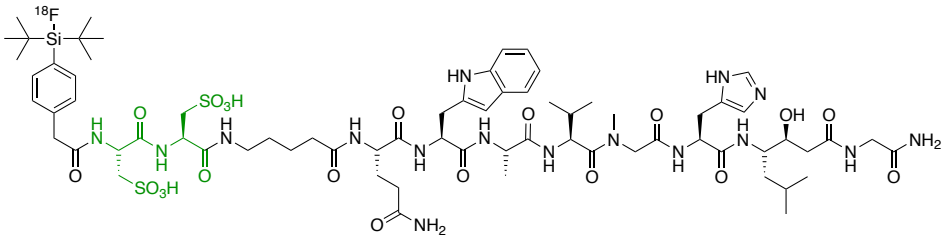

[^{18}F]SiFA-Bombesin (example derivative)

Figure 17: Chemical structure of an exemplary GRPr ligand according to *Dialer et al.* and based on the classical bombesin motif. Areas highlighted in green serve to enhance hydrophilicity.[190]

Various bombesin-based SiFA ligands have also been developed in gastrin releasing peptide receptor (GRPr) imaging (exemplified in Figure 17).[190] To date, it has not been possible to develop derivatives of sufficiently low lipophilicity. Slow clearance, hepatic excretion, and low tumor accumulation in mouse models are still unsolved problems.[190-192]

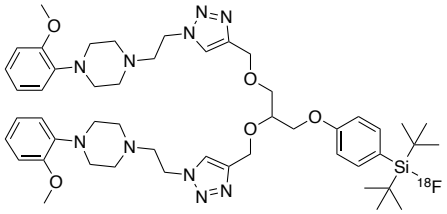

[^{18}F]BMPP-SiF

Figure 18: Chemical structure of [^{18}F]BMPP-SiF, a low molecular weight, dimeric ligand for the D2 receptor.[193]

For the dopamine receptor D_2, the low-molecular compound [^{18}F]BMPP-SiF, among others, has been developed as shown in Figure 18.[193,194] Since this class of compounds has to cross the blood-brain barrier, the increased lipophilicity is advantageous in this case. However, in principle, low molecular weight ligands can be influenced more strongly by additional modifications, which may affect biological activity and complicate their incorporation into the molecule.[183,184]

Apart from [^{18}F]SiTATE, the SiFA-PSMA ligand [^{18}F][^{nat}Ga]rhPSMA-7, shown in Figure 19, is also currently being investigated in initial clinical trials.[188,195-198] The peculiarity of this compound is the choice of hydrophilicity enhancing moiety. Instead of a PEG linker, hydrophilic amino acids or sugars, the chelator *(R)/(S)*-DOTAGA was used in [^{18}F][^{nat}Ga]rhPSMA-7 and complexed with ^{nat}Ga-gallium. In this way, the lipophilicity was lowered to the lowest range yet for a SiFA containing ligand (log$D_{7.4}$ between -2.0 and -3.5; see Wurzer et al.[199]). Since the labeling with fluoride-18 takes place in the form of an isotope exchange, the uncomplexed precursor compound can also be labeled with gallium-68, while the SiFA moiety contains stable fluorine-19 instead of fluorine-18. In each case, these are simply different isotopes, so [^{18}F][^{nat}Ga]rhPSMA-7 and [^{nat}F][^{68}Ga]rhPSMA-7 exhibit the same pharmacological properties. This is of interest to hospitals that have a gallium-68 generator but do not have access to a cyclotron for fluorine-18 production. Also of interest is the possibility to use the combination of fluorine and lutetium. The latter allows, for the first time, ^{18}F-diagnostics and ^{177}Lu-therapy with the same molecular compound and enables accurate, pretherapeutic dosimetry.[184,199]

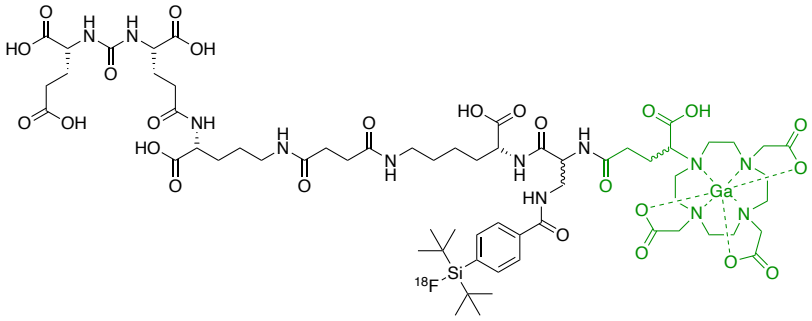

[^{18}F][^{nat}Ga]rhPSMA-7

Figure 19: Chemical structure of [^{18}F][^{nat}Ga]rhPSMA-7. Green highlighted regions serve to enhance hydrophilicity.[200]

The combination of a SiFA moiety and a chelator resulted in the so-called radiohybrid concept as shown in Figure 20 and is further described in chapter 1.6.

1.6 Radiohybride Concept in Nuclear Medicine

In recent years, the Chair for Pharmaceutical Radiochemistry at the Technical University of Munich has developed the radiohybrid concept (rh) for labeling of biomolecules, which is the alternative labeling of a universal precursor molecule with fluorine-18 (for PET) or a trivalent radiometal (including gallium-68 for PET, lutetium-177 for the peptide radionuclide receptor therapy (PRRT)). This novel class of compounds combine a Silicon-Fluoride-Acceptor for $^{19}F/^{18}F$-isotopic exchange radiolabeling and a chelator for complexation. This concept was first introduced with rhPSMA-7, as shown in Figure 19. When a radiohybrid ligand is labeled with fluoride-18, the cold metal is complexed elsewhere in the molecule - when labeled with a radiometal, cold fluorine-19 is included. Therefore, the ^{18}F-labeled peptide and the corresponding radiometal-labeled analog possess the same chemical structure and thus identical *in vitro* and *in vivo* properties (affinity, lipophilicity, pharmacokinetics, etc.), thereby allowing the generation of structurally identical theranostic tracers with the same *in vivo* properties of the diagnostic and therapeutic tracers (e.g., $^{18}F/^{177}Lu$ analogs). This behavior of a rh-ligand counteracts problems arising from the classical nuclide pair gallium-68 for diagnostics and lutetium-177 for therapy.[201,202] For instance in the case of [^{68}Ga]DOTATATE and [^{177}Lu]DOTATATE, where this nuclide pair results in chemically different ligands with different *in vivo* behavior, from which the accuracy of dosimetry suffers.[184,199] Additional benefits of the radiohybrid concept is the fact, that complexation of a trivalent metal such as gallium or lutetium further increases hydrophilicity, which counteracts the lipophilicity introduced by the SiFA moiety as described in chapter 1.5.[200]

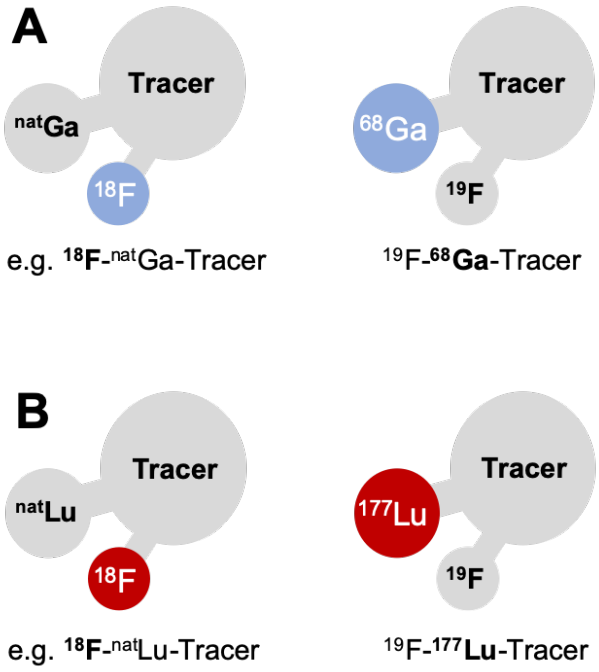

Figure 20: The radiohybrid concept: a molecular species that offers two binding sites for radionuclides, here a silicon fluorine acceptor (SiFA) for ^{18}F-fluoride and a chelator for radio metalation.[200] Note: ^{68}Ga in **A** and ^{177}Lu in **B** are examples that can be substituted by other (radio)metals.

This concept is shown in Figure 20, where just one of the binding sites is labeled with a radioisotope while the other binding site incorporates a nonradioactive isotope. The resulting tracer pair can be applied either for a pure imaging purpose (A) or a theranostic approach (B).[199]

The group led *by Perrin et al.* has since extended this concept to the trifluoroborate method, combining $AMBF_3$ with DOTA.[203] The introduction of a DOTA chelator adjacent to the $AMBF_3$ group significantly improved the biodistribution of the previously developed tracer [^{18}F]$AMBF_3$-PEG_2-LLP2A (Figure 21, top). The DOTA-modified tracer [^{18}F]DOTA-$AMBF_3$-PEG_2-LLP2A (Figure 21, bottom) showed a 10-fold reduction of accumulation in the intestine compared to previously investigated LLP2A tracers and a 2—3-fold higher tumor uptake with 9.46 ± 2.19 %ID/g resulting in higher tumor-to-background ratios and better imaging contrast.[203,204]

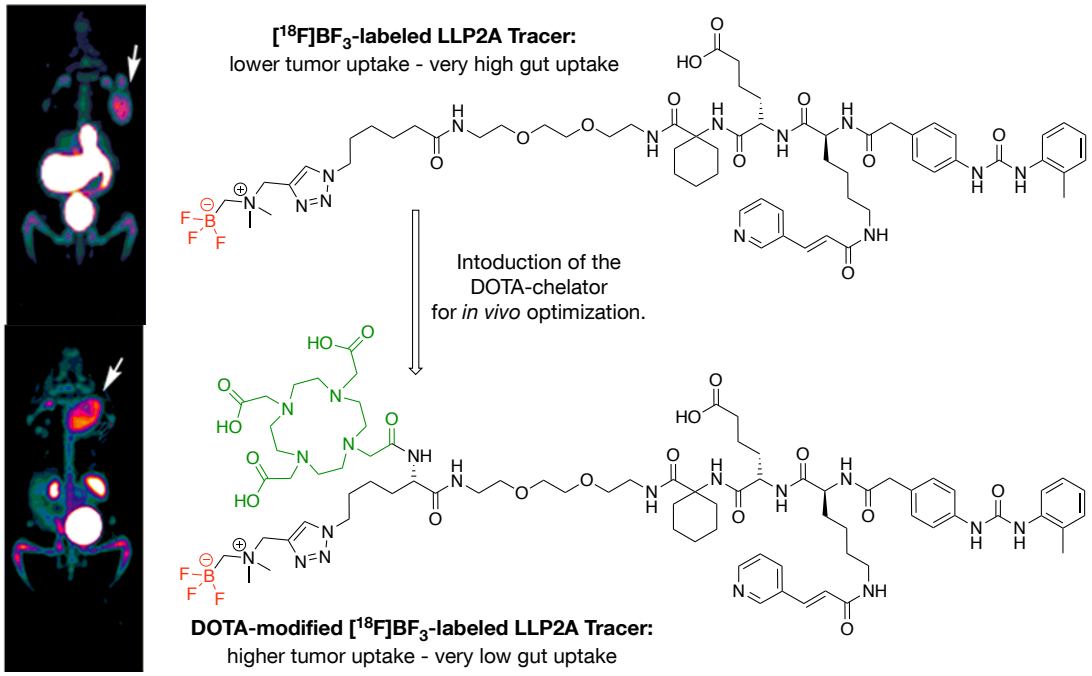

Figure 21: Chemical structure of [^{18}F]BF_3-labeled (red) LLP2A tracers (right) developed by *Perrin et al.* with introduction of a DOTA chelator (green) for optimized *in vivo* pharmacokinetics and PET imaging of both tracers in male C57BL/6J mice bearing B16-F10 melanoma tumors (left).[203,204]

The higher tumor uptake and reduced accumulation in the intestine are results of an increased hydrophilicity through incorporation of the DOTA chelator next to the ^{18}F-labeling site as was shown for rhPSMA-7 and the rh concept. *Perrin et al.* concluded that the logical further development is the incorporation of ^{nat}Lu/^{177}Lu-lutetium to obtain a “hot-cold/cold-hot” paired isotopologs (e.g., ^{18}F/^{nat}Lu and ^{nat}F/^{177}Lu) to produce a truly theranostic tracer and completely extending the rh concept to trifluoroborate compounds.[203]

This was done by translation of the structural DOTA-$AMBF_3$ moiety previously used for LLP2A tracers into the basic structure of PSMA-617, a clinical approved prostate cancer radio

pharmakon, as shown in Figure 22.[205,206] The only difference between DOTA-AMBF$_3$-PSMA and PSMA-617 is the incorporation of Lys(AMBF$_3$) resulting in similar *in vitro* data of both compounds. Historically, DOTA had been used to chelate different radiometals, most notably lutetium-177 for therapy, and either gallium-68 or copper-64 for PET.[207-210] *Lepage et al.* selected copper-64 and lutetium-177 for the evaluation of DOTA-AMBF$_3$-PSMA in *ex vivo* studies as shown in Figure 22, even with the knowledge from previous reports that Cu-DOTA-complexes suffer from transchelation from DOTA to liver proteins resulting in relatively high liver uptake.[207-210]

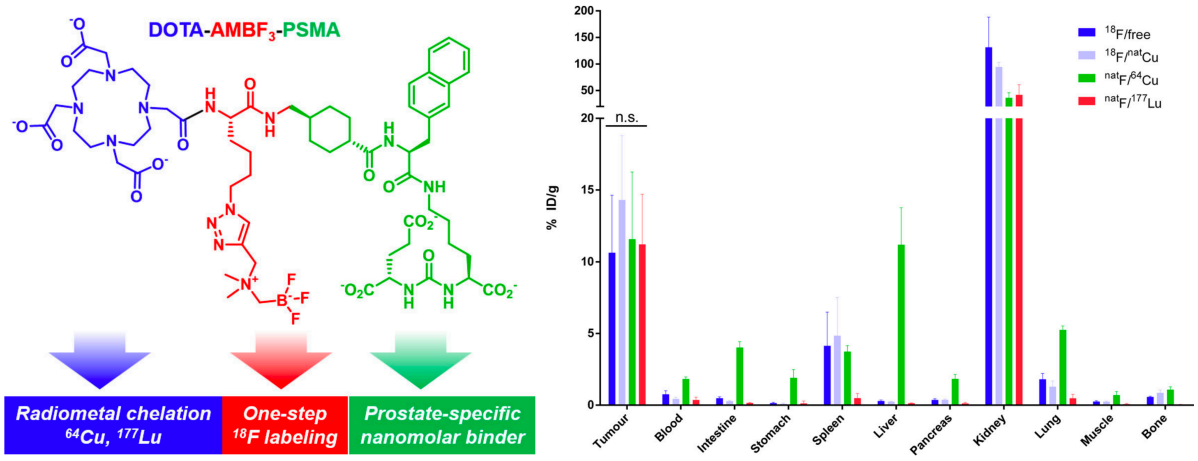

Figure 22: **Left:** Concept of a theranostic tracer for use with multiple radioisotopes: DOTA-AMBF$_3$; synthesis incorporates LysAMBF$_3$ (red) as a latent fluorine-18 radioprosthetic group and a DOTA chelator (blue) into the core PSMA-617 pharmacophore.[206] **Right:** *Ex vivo* biodistribution of (^{18}F/free), (^{18}F/^{nat}Cu), (^{nat}F/^{64}Cu) and (^{nat}F/^{177}Lu) at 1 h p.i.[205]

As seen in the biodistribution data shown in Figure 22 there was no significant difference in tumor uptake values, suggesting generally consistent affinity to the target structure across the different combinations of tracer and radioisotope. In addition, all tracers show accumulation in the kidneys which is known for PSMA targeting compounds as well as compounds with high number of charged groups (e.g., a carboxyl group).[211,212] As expected the metal-free DOTA-AMBF$_3$-PSMA showed the highest kidney accumulation resulting from the three free negative charges from the DOTA chelator. [^{nat}F][^{64}Cu]DOTA-AMBF$_3$-DOTA showed comparable liver uptake to the structural similar ^{64}Cu-PSMA-617.[207-210] As already mentioned, this arises from the known metastability of Cu-DOTA-complexes *in vivo*.[213-215] The ^{nat}F/^{177}Lu-tracer shows overall promising biodistribution data with a high tumor uptake and low accumulation in background organs and the liver confirming the well-known high metabolic stability of the Lu-DOTA-complex.[205]

In conclusion, the group led *by Perrin et al.* could successfully extend the rh concept to the trifluoroborate method. This is giving more options for single-molecule chemical identical theranostic tracers without the negative influence of high lipophilicity introduced by the SiFA moiety. However, it must be considered that despite the lipophilic character of SiFA moieties, these building blocks allow radiolabeling in much milder reaction conditions and with

significantly higher radiochemical yields (chapter 1.4.3).[149,153-155] Therefore, including SiFA moieties in the radiohybrid concept is still preferable to other ^{18}F-labeling methods.

2 Research Aims and Objectives

The widespread expression of FAP in the tumor microenvironment of different tumor entities led to the development of highly optimized FAP-targeting inhibitors and furthermore to FAP-targeting radiopharmaceuticals for the diagnostic and therapeutic applications, and their rapid bench-to-bed translation. An emerging demand for new PET imaging ligands arose especially for ^{18}F-labeled radiopharmaceuticals due to the possibility of large-scale production and favorable nuclide properties. However, a major disadvantage of these ^{18}F-labeled tracers lies in commonly elaborate and time-consuming radiolabeling procedures, which usually result in low radiochemical yields and molar activities. To circumvent these limitations, new labeling strategies like for example, the ^{18}F-^{19}F isotopic exchange reaction at SiFA moieties, which allow for facile and rapid ^{18}F-labeling with high yields and molar activities, have been developed. The main drawback of this labeling method is the high lipophilicity of the SiFA building blocks, which derives from the necessity of bulky groups at said moiety to ensure sufficient *in vivo* stability of the Si-F bond. This mostly leads to unfavorable biodistribution profiles of SiFA-containing ligands, preventing their clinical translation. For that reason, the SiFAN$^+$ moiety and the radiohybrid concept were developed as a universally applicable methodology to increase the hydrophilicity of SiFA conjugates.
The prime objective of this work was to develop a new group of FAPI ligands for the labeling with fluorine-18 based on the current lead compound for FAP imagining, [^{68}Ga]Ga-FAPI-04, and the promising labeling strategy for fluorine-18 being the ^{18}F-^{19}F isotopic exchange reaction at SiFA moieties.

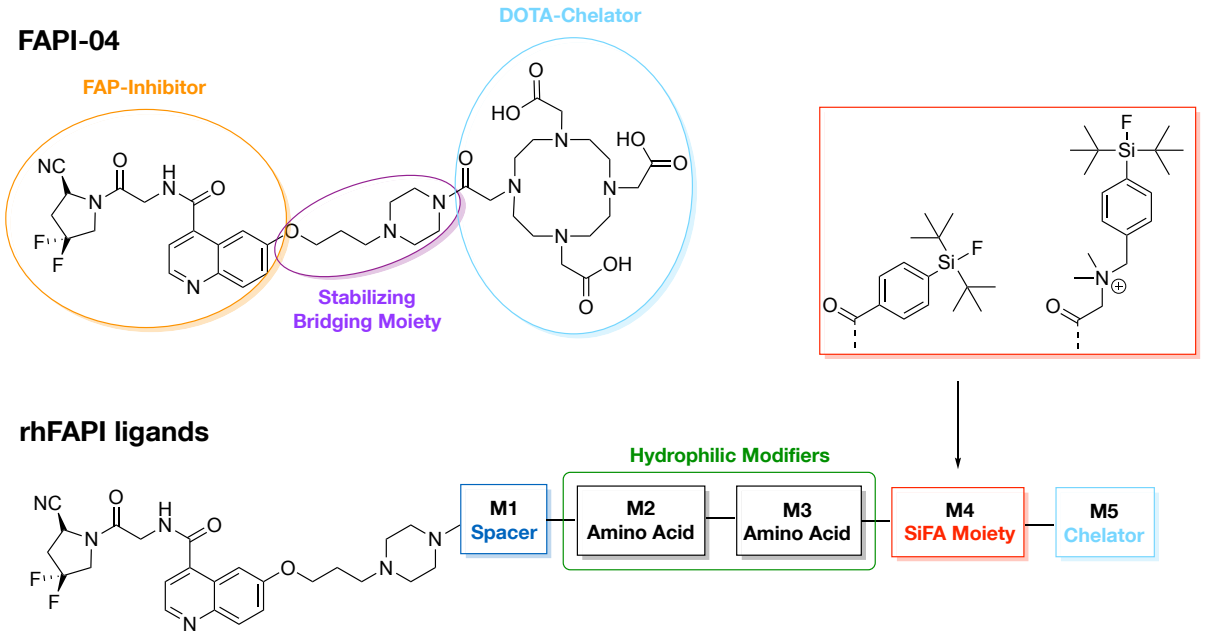

Figure 23: Chemical structure of FAPI-04 developed by *Haberkorn et al.* and conceptual structure of rhFAPI ligands containing the shown FAP inhibitor (orange) and stabilizing bridging moiety (purple). rhFAPI ligands have the variable modification sites **M1** to **M5**, where **M1** is a spacer (blue), **M2** and **M3** are amino acids which act as hydrophilic modifiers (green), **M4** is a SiFA moiety (red), being either SiFA-BA or a SiFAN$^+$ moiety and **M5** is a chelator (turquoise) for metal complexation.

For this reason, the radiohybrid (rh) concept was implemented into the structure of FAPI-04 as shown in Figure 23, where a SiFA moiety being either a SiFA-BA group or a SIFAN$^+$ moiety was positioned between the stabilizing birding moiety and a hydrophilic chelator. Optionally, a linker and additional hydrophilic groups can be introduced to further improve the pharmacokinetics of the new ligands. This rh concept should initially be validated for FAPI ligands with lutetium-177 as a complexed metal cation enabling a theranostic approach. Therefore, either the ^{18}F-labeled [^{nat}Lu]rhFAPI or the ^{177}Lu-labeled [^{19}F]rhFAPI ligand can be clinically applied either for PET imaging, dosimetry and follow-up imaging or PRRT. Due to their chemical indistinguishability, the data obtained for one ligand can be transferred to its "twin" (Figure 20). Theranostic radiohybrid tracers could therefore further advance personalized medicine by providing one probe, which would truly bridge PET-based imaging and therapy.

A secondary objective of this work was to develop a new group of FAPI ligands for the labeling with technetium-99m through incorporation of the N4-chelator. Here, a radiohybrid-like concept should be explored through optional addition of a chelator or a SiFA moiety. Because of the presence of FAP in many different tumor entities the goal of the secondary objective was to achieve a universal radiopharmaceutical for SPECT imaging comparable to [^{18}F]FDG for PET imaging. As of today, there is no universal tracer for SPECT imaging despite the advantages of being more affordable compared to PET and being a widespread application worldwide, especially in less developed countries. Therefore, a tecFAPI ligand might have the potential to become a universal SPECT tracer in the future, even providing clinics with the opportunity of a theranostic ^{99m}Tc/$^{186/188}$Re-pair enabling PRRT with the rhenium isotopes.

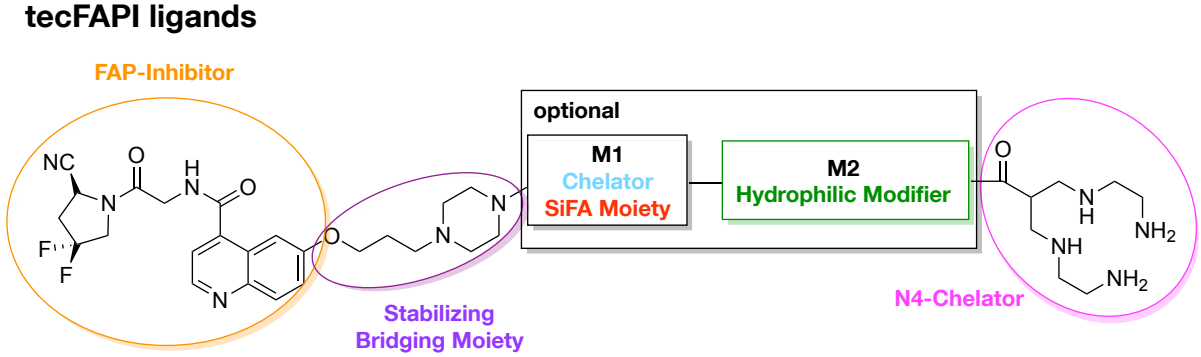

Figure 24: Conceptual structure of tecFAPI ligands containing the shown FAP inhibitor (orange), stabilizing bridging moiety (purple) and N4-chelator (pink) for complexation with ^{99m}Tc-technetium. The variable modification sites **M1** and **M2** are optional, where **M1** is a SiFA moity (red) or a chelator (turquoise) for metal complexation and **M2** is a hydrophilic modifier (green).

Additional objectives of this work were the establishment of a cell-based assay for the FAP-transfected fibrosarcoma cell line HT-1080hFAP and the optimization of the procedure described in literature for ^{18}F-fluorination of SiFA-containing compounds. Moreover, optimization of complexation of technetium-99m *via* the N4 chelator was addressed to enable labeling of rhFAPI and tecFAPI ligands in high yield.

3 Materials and Methods

3.1 Synthesis Protocols

3.1.1 General Information for Synthesis

Unless otherwise stated, reagents and solvents were used directly without further purification. All air or water sensitive reactions were carried out under an argon atmosphere in preheated reaction vessels using the *Schlenk* technique. Anhydrous solvents and water sensitive liquid chemicals were transferred to the reaction vessels using argon flooded syringes.

The solvents used were obtained from *VWR International* (Buchsal, Germany), *Alfa Aesar* (Karlsruhe, Germany) or *Sigma-Aldrich* (Munich, Germany). Water for the HPLC solvents was obtained from the in-house Millipore Barnsted MicroPure-System from *Thermo Fischer Scientific Inc.* (Waltham MA, USA), while trace pure water came from *Merck Millipore* (Darmstadt, Germany). Amino acids were obtained from *IRIS Biotech GmbH* (Marktredewitz, Germany), *Sigma-Aldrich* (Munich, Germany), *Carbolution Chemicals GmbH* (St. Ingbert, Germany) or *Merck Millipore* (Darmstadt, Germany). Coupling reagents came from *Sigma-Aldrich* (Munich, Germany), *Molekula GmbH* (Garching, Germany) and *Macrocyclics Inc.* (Dallas, United States). Chemicals for the synthesis of the inhibitor and the SiFA moieties were purchased from *Fluorochem* (Hadfield, United Kingdom), *TCI Deutschland GmbH* (Eschborn, Germany) and *Alfa Aesar* (Karlsruhe, Germany). *Chematech* (Dijon, France) delivered the chelators DOTA, DOTA-GA and derivatives thereof. All other reagents for synthesis were obtained from *Sigma-Aldrich* (Munich, Germany), *Merck Millipore* (Darmstadt, Germany) and *VWR* (Darmstadt, Germany).

Solide-phase peptide synthesis (SPPS) was carried out by manual operation using a syringe shaker (Intelli-Mixer, *Neolab*, Heidelberg, Germany). Analytical and preparative high-performance liquid chromatography (HPLC) was performed using Shimadzu gradient systems (*Shimadzu*, Neufahrn, Germany), each equipped with a SPD-20A UV/Vis detector (220 nm, 254 nm). A Nucleosil 100 C18 (125 × 4.6 mm, 5 µm paricle size) or MultoKrom 100-5 C18 (125 × 4.6 mm, 5 µm paricle size) column (*CS Chromatographie Servie*, Langerwehe, Germany) was used for analytical measurements at a flow rate of 1 mL/min. Specific gradients, the corresponding retention time (t_R) and the capacity factors (K') are cited in the text. Purification of compounds *via* preparative PLC was done with MultoHigh 100 RP-18 (250 × 10 mm, 5 µm paricle) and MultoKrom 100-5 C18 (250 × 10 mm, 5 µm paricle) columns (*CS Chromatographie Servie*) at a constant flow rate of 5 mL/min, also the respective 250 × 20 mm columns with a constant flow rate of 10 ml/min were used for high-throughput purification. Eluents for all HPLC operations were water (solvent A) and acetonitrile (solvent B), both containing 0.1% trifluoroacetic acid (TFA). Flash chromatography for purification was completed on an Isolera™ Prime System (*Biotage*, Uppsala, Sweden) coupled to a Biotage 09474 Rev. E. Bio pump. A Biotage™ SNAP KP-C18 (12 g column material, 93 Å pore diameter, 382 m^2/g surface area) column was used with the eluents water (solvent A) and

acetonitrile (solvent B), both containing 0.1% trifluoroacetic acid (TFA). Lyophilization of products was conducted with an Alpha 1-2 lyophilization system (*Christ*, Osterode am Harz, Germany) coupled to a RZ-2 vacuum pump (*Vacuubrand GmbH*, Wertheim, Germany). For characterization of substances electrospray ionization mass spectrometry (ESI-MS) was used. Spectra were acquired on an Expression^{L} CMS mass spectrometer (*Advison*, Harlow, United Kingdom). Nuclear magnetic resonance (NMR) spectra were recorded on *Bruker* (Billerica, United States) AVHD-300, -400 or -500 spectrometers at 300 K.

3.1.2 Solide-Phase Peptide Synthesis

2-CTC Resin Loading (General Synthesis Procedure 1 (GSP1))

For the loading of the 2-Chlorotrityl chloride (2-CTC) resin with a Fmoc-protected amino acid (AA) a suspension of the resin (1.60 mmol/g), Fmoc-AA-OH (2.0 eq.) and *N*,*N*-diisopropyl-ethylamine (DIPEA) (5.0 eq.) in anhydrous DMF was shaken at rt for 2 h. Remaining 2-CTC was capped by the addition of methanol (MeOH) (2 mL/g resin) for 15min. Afterwards the resin was filtered an washed with DMF (2 × 5 mL/g resin), MeOH (2 × 5 mL/g resin), dichloromethane (DCM) (2 × 5 mL/g resin) and dried *in vacuo*. Final AA loading *l* of the resin was determined using following equation:

$$l\left[\frac{mmol}{g}\right] = \frac{(m_2 - m_1) \times 1000}{(M_{AA} - M_{HCl}) \times m_2}$$

m_1 = mass of loaded resin [g]
m_2 = mass of unloaded resin [g]
M_w = molecular weight of AA [g/mol]
M_{HCl} = molecular weight of HCl [g/mol]

On-Resin Amide Bond Formation (GSP2)

For coupling of a building block to an unprotected amine of the resin-bound peptide, a reaction mixture of *O*-(benzotriazol-1-yl)-*N*,*N*,*N*′,*N*′-tetramethyluronium tetrafluoroborate (TBTU) with 1-hydroxybenzotriazol (HOBt) or 1-hydroxy-7-azabenzotriazol (HOAt) was used for pre-activation of a carboxylic acid with DIPEA or 2,4,6-trimethylpyridine (*sym*-collidine). Based on the equivalents of the swollen resin conjugation was executed after 15 min of pre-activation with 1.5 eq. AA, 1.5 eq. TBTU, 1.5 eq. HOBt/HOAt and 4.5 eq. DIPEA or 6.0 eq. *sym*-collidine at rt. Reaction time and stoichiometry of non-standard conjugation steps are given in the respective synthesis protocols. After the reaction, the resin was washed with DMF (6 × 5mL/g resin).

On-Resin Fmoc-Deprotection (GSP3)

For fluorenylmethoxycarbonyl (Fmoc) deprotection the resin-bound Fmoc-peptide was treated with 20% piperidine in DMF (*v*/*v*, 8 mL/g resin) for 5 min and subsequently for 15 min. Thereafter, the resin was thoroughly washed with DMF (8 × 5 mL/g resin).

On-Resin Dde-Deprotection (GSP4)

For *N*-[1-(4,4-dimethyl-2,6-dioxocyclohex-1-ylidene)ethyl] (Dde) deprotection the resin-bound peptide was shaken in 2% hydrazine monohydrate in DMF (*v*/*v*, 5 mL/g resin) for 20 min (**GSP4a**). In case of a present Fmoc-group, deprotection was performed by adding a solution of imidazole (0.92 g/g resin) and hydroxylamine hydrochloride (1.26 g/g resin) in *N*-

methyl-2-pyrrolidone (NMP) and dimethylformamide (DMF) (5:1, 5 mL/g resin) for 3 h at rt (**GSP4b**). After the reaction, the resin was washed with DMF (8 × 5 mL/g resin).

On-Resin Allyl-Deprotection (GSP5)

Removal of allyl groups was carried out by treating the protected compound with $Pd(PPh_3)$ (0.1 eq.) and phenylsilane (24 eq.) in 5 mL DCM for 220 min with protection from light. Afterwards, the resin was thoroughly washed alternately with 0.5 wt% DDTC in DMF and 0.5 vol% DIPEA in DMF (3 × 5 mL for 5 min each).

*t*Bu/Boc-Deprotection (GSP6)

Removal of *tert*-butyl (*t*Bu) and *tert*-butyloxycarbonyl (Boc) groups was performed by dissolving the crude product in a mixture of TFA/triisopropylsilane (TIPS)/water (*v*/*v*/*v*, 95/2.5/2.5) and stirring for 1 to 6 h at rt. Formation of the unprotected product was monitored by analytically RP-HPLC. The solvent was evaporated under a nitrogen stream and the residue was solved in *tert*-butanol and water (*v*/*v*, 1/1). After lyophilization the crude product was obtained for further purification.

Peptide Cleavage from the Resin (GSP7)

Preservation of acid label protection groups while cleavage (**GSP7a**):
The resin-bound peptide was treated with a mixture of 20% hexafluoroisopropanol (HFIP) in DCM (*v*/*v*, 8 mL/g) for 30 min. After filtering of the solution containing the fully protected peptide, the resin was again treated with the cleavage solution for 30 min. All fractions were combined, and solvents were removed under reduced pressure. Afterwards, lyophilization yielded the fully protected crude peptide.

Deprotection of acid label protection groups while cleavage (**GSP7b**):
The resin-bound peptide was treated with a mixture of TFA/TIPS/water (*v*/*v*/*v*, 95/2.5/2.5) and shaken for 30 min. The solution was filtered off and the resin was again treated with the cleavage solution for 30 min. All filtrates were combined and stirred for additional 1 to 6 h at rt while product formation was monitored by RP-HPLC. After removing TFA under a stream of nitrogen, the residue was dissolved in a mixture of *tert*-butanol and water and freeze-dried.

3.1.3 Synthesis of FAP-Inhibitor (7) as Binding Motif

Synthesis of FAP-inhibitor **7** was carried out following a previously published procedure with slight modifications.[105,106,111,112] The synthetic pathway is shown in Scheme 2.

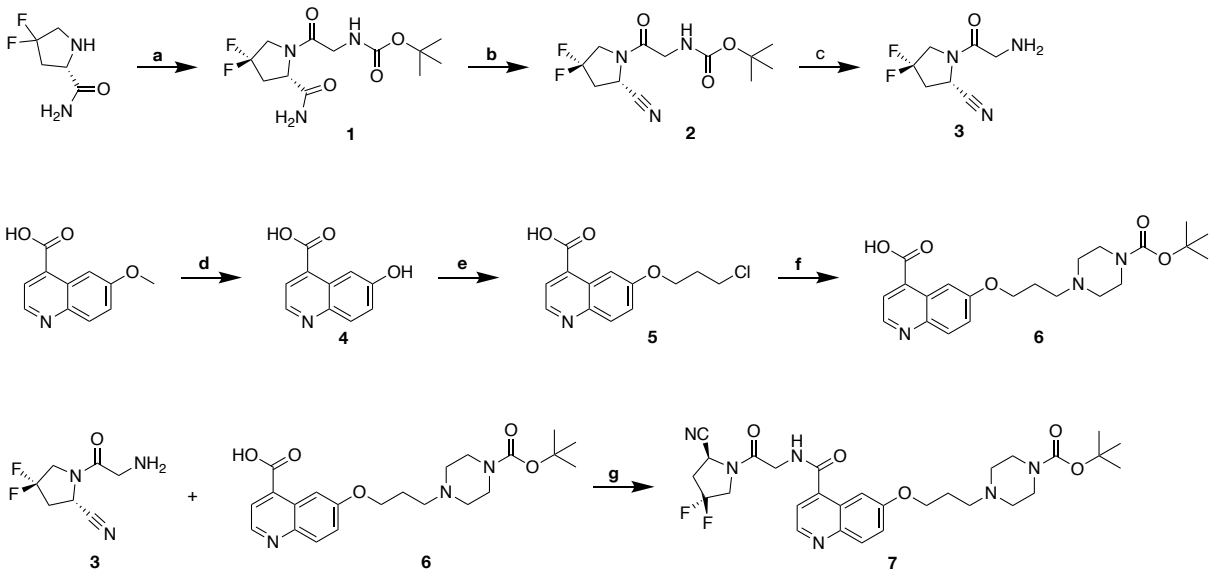

Scheme 2: Synthesis of FAP-inhibitor **7**: a) Boc-Gly-OH, HATU, DIPEA (DCM); b) TFAA, pyridine (THF); c) TsOH (MeCN); d) HBr (H_2O); e) 1-bromo-3-chloropropane, Cs_2CO_3 (DMF); f) *N*-*tert*-butoxycabonylpiperazine, KI (DMF); g) HATU, HOAt, DIPEA (DMF).

tert-butyl-*(S)*-(2-(2-carbamoyl-4,4-difluoropyrrolidin-1-yl)-2-oxoethyl)carbamate (1)

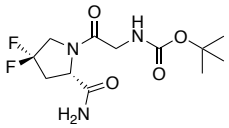

Chemical Formula: $C_{12}H_{19}F_2N_3O_4$
Molecular Weight: 307.30

1-[Bis(dimethylamino)methylene]-1H-1,2,3-triazolo[4,5-b]pyridinium-3-oxide hexafluorophosphate (HATU) (489 mg, 1.29 mmol, 1.2 eq.) and 2-(*tert*-butoxycarbinylamino)acetic acid (225 mg, 1.29 mmol, 1.2 eq.) were dissolved in 0.8 mL DMF and added to DIPEA (449 µL, 2.57 mmol, 2.4 eq.) in 1.2 mL DCM. After 15 min, a solution of (*S*)- 4,4-difluoropyrrolidine-2-carboxamide hydrochloride (200 mg, 1.07 mmol, 1.0 eq.) and DIPEA (224 µL, 1.29 mmol, 1.2 eq.) in 2 mL DCM was added. After stirring at ambient temperature for 3 h the cloudy mixture was filtrated, and the residue was washed with DCM. The filtrate was cooled and filtrated again, and the combined residues were recrystallized from ethyl acetate. Compound **1** was isolated as a white solid (74%).

RP-HPLC (10 to 90% B in 15 min): t_R = 6.24 min.
ESI-MS: Calculated monoisotopic mass ($C_{12}H_{19}F_2N_3O_4$): 307.3; found: m/z = 308.4 $[M+H]^+$.

tert-butyl-*(S)*-(2-(2-cyano-4,4-difluoropyrrolidin-1-yl)-2-oxoethyl)carbamate (2)

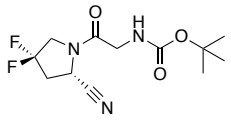

Chemical Formula: $C_{12}H_{17}F_2N_3O_3$
Molecular Weight: 289.28

Compound **1** (243 mg, 0.78 mmol, 1.0 eq.) was dissolved in dry THF at -15 °C in an argon atmosphere. Then pyridine was added, followed by the dropwise addition of a solution of 2,2,2-trifluoroacetic anhydride (547 µg, 3.93 mmol, 5.0 eq.) in 5 mL of dry DCM. After the complete addition, the mixture was allowed to reach rt and was stirred for 90 min. The reaction mixture was washed with 1 M solution of aqueous hydrochloric acid. Afterwards, the organic layer was washed with sat. aq. sodium bicarbonate ($NaHCO_3$) (3 × 30 mL) and brine (30 mL), dried over Mg_2SO_4, filtered, and concentrated *in vacuo*. The crude product was purified by flash column chromatography (silica, hexane in EtOAc, 2:3) yielding **2** as a yellow oil (71%).

RP-HPLC (10 to 90% B in 15 min): t_R = 12.5 min.
ESI-MS: Calculated monoisotopic mass ($C_{12}H_{17}F_2N_3O_3$): 289.3; found: m/z = 290.0 $[M+H]^+$.

(S)-4,4-difluoro-1-glycylpyrrolidine-2-carbonitrile (3)

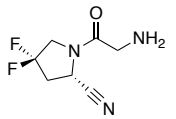

Chemical Formula: $C_7H_9F_2N_3O$
Exact Mass: 189.07

p-Toluenesulfonic acid (224 mg, 1.18 mmol, 1.5 eq.) was added to a cooled (0 °C) solution of **2** (227 mg, 0.79 mmol, 1.0 eq.) in 5 mL of dry MeCN. The reaction mixture was slowly warmed to rt and stirred for 24 h. The solution was concentrated *in vacuo* and the residue was washed with cold ether and ethyl acetate and dried. Compound **3** was isolated as a white solid (90%).

RP-HPLC (10 to 90% B in 15 min): t_R = 10.3 min.
ESI-MS: Calculated monoisotopic mass ($C_7H_9F_2N_3O$): 189.1; found: m/z = 190.0 $[M+H]^+$.

6-hydroxyquinoline-4-carboxylic acid (4)

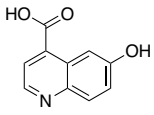

Chemical Formula: $C_{10}H_7NO_3$
Molecular Weight: 189.17

6-Methoxyquinoline-4-carboxylic acid (200 mg, 0.98 mmol) is dissolved in 4 mL of 48% HBr in water and heated to 130 °C for 4 h. After reaching rt, the cloudy mixture was diluted with water and centrifuged. The residue was washed with water and the filtrate was brought to a slightly basic pH with 6 M NaOH. The filtrate was purified through automated flash column chromatography (Biotage™ Sfär C18 D-Duo 100 Å catridge, 0 to 10% B in 10 min) followed by concentration *in vacuo*. Residue from purification and filtration were combine yielding **4** as a white-yellowish solid (90%).

RP-HPLC (0 to 40% B in 15 min): t_R = 4.88 min.
ESI-MS: Calculated monoisotopic mass ($C_{10}H_7NO_3$): 189.1; found: m/z = 189.9 $[M+H]^+$.

6-(3-chloropropoxy)quinoline-4-carboxylic acid (5)

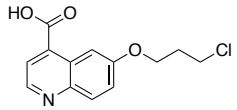

Chemical Formula: $C_{13}H_{12}ClNO_3$
Molecular Weight: 265.69

1-Bromo-3-chloropropane (341 µL, 3.45 mmol, 3.5 eq.) was added to a suspension of **4** (186 mg, 0.98 mmol, 1.0 eq.) and potassium carbonate (1.6 g, 4.93 mmol, 5.0 eq.) in 8 mL DMF and heated to 60 °C for 24 h. After reaching rt, the reaction mixture was diluted with 5 mL water and 5 mL MeCN before 2 mL of 6 M NaOH are added. The reaction was monitored through analytic HPLC and the reaction mixture was directly purified through automated flash column chromatography (Biotage™ Sfär C18 D-Duo 100 Å catridge, 0 to 30% B in 20 min) after the complete ester hydrolysis was accomplished. After concentration *in vacuo*, **5** was isolated as a yellowish solid (83%).

RP-HPLC (0 to 40% B in 15 min): t_R = 11.6 min.
ESI-MS: Calculated monoisotopic mass ($C_{13}H_{12}ClNO_3$): 265.7; found: m/z = 265.9 $[M+H]^+$.

6-(3-(4-(*tert*-butoxycarbonyl)piperazin-1-yl)propoxy)quinoline-4-carboxylic acid (6)

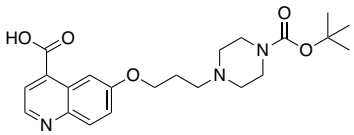

Chemical Formula: $C_{22}H_{29}N_3O_5$
Molecular Weight: 415.49

N-tert-butoxycabonylpiperazine (916 mg, 4.92 mmol, 5.0 eq.), potassium iodide (981 mg, 5.91 mmol, 6.0 eq.) and **5** (262 mg, 0.99 mmol, 1.0 eq.) were dissolved in 8 mL DMF and heated to 60 °C for 24 h. The resulting suspension was concentrated *in vacuo* and the crude product was dissolved in 6 mL water/MeCN (2:1, *v/v*). The purification was carried out through

automated flash column chromatography (Biotage™ Sfär C18 D-Duo 100 Å catridge, 10 to 30% B in 20 min). Product **6** was isolated as a yellow crystalline solid (95%).

RP-HPLC (0 to 40% B in 15 min): t_R = 10.6 min.
ESI-MS: Calculated monoisotopic mass ($C_{22}H_{29}N_3O_5$): 415.5; found: m/z = 415.8 $[M+H]^+$.

tert-butyl-*(S)*-4-(3-((4-((2-(2-cyano-4,4-difluoropyrrolidin-1-yl)-2-oxoethyl)carbamoyl)-quinolin-6-yl)oxy)propyl)piperazine-1-carboxylate (7)

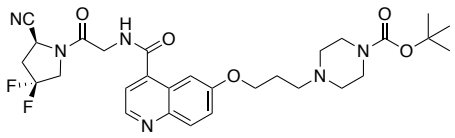

Chemical Formula: $C_{29}H_{36}F_2N_6O_5$
Molecular Weight: 586.64

HATU (38.0 mg, 0.1 mmol, 1.0 eq.), HOAt (15.0 mg, 0.11 mmol, 1.1 eq.), DIPEA (51.0 µL, 0.3 mmol, 3.0 eq.) and **6** (41.5 mg, 0.1 mmol, 1.0 eq.) were dissolved in 5 mL DMF and stirred for 15 min. Afterwards, **3** (20.98 mg, 0.11 mmol, 1.1 eq.) in 1.0 mL DMF was added and the reaction mixture was stirred at rt for 3 h. The reaction was quenched by addition of 1.0 mL water, followed by the purification through purified by RP-HPLC (35 to 45% B in A in 30 min). Concentration *in vacuo* and freeze drying provided **7** as a yellowish solid (75%).

RP-HPLC (10 to 70% B in A in 15 min): t_R = 8.2 min.
ESI-MS: Calculated monoisotopic mass ($C_{29}H_{36}F_2N_6O_5$): 486.6; found: m/z = 487.5 $[M+H]^+$.

3.1.4 Synthesis of Silicon Fluoride Acceptors

Synthesis of all *para*-SiFA moieties were performed following previously published procedures with slight modifications.[173,176,178] All water- and oxygen-sensitive reactions were conducted under *Schlenk*-technique with heat-dried reaction vessels and under argon atmosphere. The synthetic pathways of *para*-SiFA moieties are shown in Scheme 3.

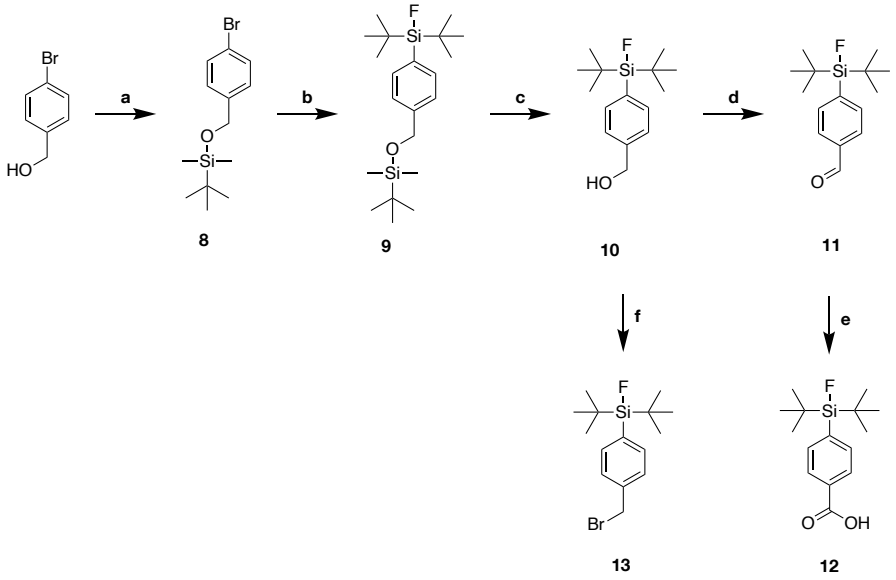

Scheme 3: Synthesis of SiFA moieties SiFA-benzoeic acid (**12**) and SiFA-bromide (**13**): a) TBDMSCl, imidazole (DMF); b) *t*BuLi, di-*tert*-butyldifluorosilane (THF); c) HCl (MeOH); d) pyridinium chlorochromate (DCM); e) $KMnO_4$ (DCM, *tert*-butanol, NaH_2PO_4 buffer); f) tetrabromomethane, triphenylphosphine (DCM).

The synthetic pathway of the IPA-SiFA moiety is shown in Scheme 4 and was performed following a procedure developed at the Chair of Pharmaceutical Radiochemistry at the Technical University Munich.

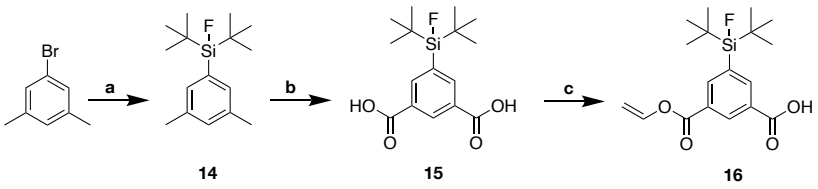

Scheme 4: Synthesis of IPA-SiFA (**15**) and allyl-IPA-SiFA (**16**): a) *t*BuLi, di-*tert*-butyldifluorosilane (THF); b) KMnO4 (DCM, tert-butanol, NaH2PO4 buffer); c) allyl bromide, K_2CO_3 (DMF).

((4-bromobenzyl)oxy)(*tert*-butyl)dimethylsilane (8)

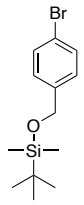

Chemical Formula: $C_{13}H_{21}BrOSi$
Molecular Weight: 301.30

To a stirred solution of (4-bromophenyl)methanol (4.68 g, 25.0 mmol, 1.0 eq.) in anhydrous DMF (70 mL), imidazole (2.04 g, 30.0 mmol, 1.2 eq.) and *tert*-butyldimethylsilyl chloride (4.52 g, 30.0 mmol, 1.2 eq.) were added and the resulting mixture was stirred for 16 h at rt. The reaction mixture was diluted with cold water (250 mL) and extracted with diethyl ether (Et_2O) (5 × 50 mL). The combined organic fractions were washed with sat. aq. sodium bicarbonate ($NaHCO_3$) (2 × 100 mL) and brine (100 mL), dried, filtered and concentrated *in vacuo*. The crude product was purified by flash column chromatography (silica, 5 % EtOAc in petrol, *v/v*). Compound **8** was isolated as a colorless oil (95%).

RP-HPLC (50 to 100% B in 15 min): t_R = 15 min.
^{1}H-NMR (400 MHz, $CDCl_3$, 300 K): δ = 7.46 (2H, d, C_6H_4), 7.21 (2H, d, C_6H_4), 4.69 (2H, s, CH_2OSi), 0.95 (9H, s, $SiMe_2tBu$), 0.10 (6H, s, $SiMe_2tBu$) ppm.

di-*tert*-butyl(4-(((tert-butyldimethylsilyl)oxy)methyl)phenyl)fluorosilane (9)

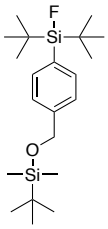

Chemical Formula: $C_{21}H_{39}FOSi_2$
Molecular Weight: 382.71

At -78° C under stirring, a solution of *t*BuLi in pentane (7.29 mL, 1.7 mol/L, 12.4 mmol, 2.4 eq.) was added to a solution of **8** (1.56 g, 5.18 mmol, 1.0 eq.) in dry tetrahydrofuran (THF) (15 mL) over a period of 30 min in small portions. After the reaction mixture was stirred for 30 min at -78° C, the suspension was added dropwise over a period of 30 min to a cooled (-78° C) solution of di-*tert*-butyldifluorosilane (1.12 g, 6.23 mmol, 1.2 eq.) in dry THF (10 mL). The reaction mixture was allowed to warm to rt over a period of 12 h and afterwards hydrolyzed with brine (100 mL). The organic layer was separated, and the aqueous layer was extracted with Et_2O (3 × 50 mL). The combined organic layers were dried over magnesium sulfate and filtered. The filtrate was concentrated *in vacuo* to give **9** as a yellow oil (95%). It was used for further reactions without additional purification.

RP-HPLC (50 to 100% B in 15 min): t_R = 17 min.

(4-(di-*tert*-butylfluorosilyl)phenyl)methanol (10)

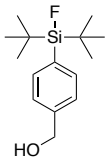

Chemical Formula: $C_{15}H_{25}FOSi$
Molecular Weight: 268.45

A catalytic amount of concentrated aq. HCl (0.5 mL) was added to a suspension of **9** (1.88 g, 4.92 mmol, 1.0 eq.) in MeOH (50 mL). The reaction mixture was stirred for 18 h at rt and the solvent was removed *in vacuo*. The residue was dissolved in Et_2O (40 mL) and washed with sat. aq. $NaHCO_3$ (80 mL). The aqueous layer was extracted with Et_2O (3 × 50 mL) and the combined organic layers were dried over magnesium sulfate and filtered. The filtrate was concentrated *in vacuo* to give **10** as a yellow oil (98%). It was used for further reactions without additional purification.

RP-HPLC (50 to 100% B in 15 min): t_R = 8.2 min.

4-(di-*tert*-butylfluorosilyl)benzaldehyde (11)

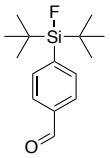

Chemical Formula: $C_{15}H_{23}FOSi$
Molecular Weight: 266.43

A solution of **10** (1.37 g, 5.10 mmol, 1.0 eq.) in dry DCM (20 mL) was dropwise added to a stirring ice-cold suspension of pyridinium chlorochromate (2.75 g, 12.8 mmol, 2.5 eq.) in dry DCM (60 mL). After stirring the reaction mixture for 30 min at 0 °C and 2.5 h at rt, anhydrous diethyl ether (40 mL) was added, and the solution was decanted from a black residue. The insoluble material was washed thoroughly with diethyl ether and the combined organic phases were passed through a short pad of silica gel (10 cm per g crude product) for filtration. The solvents were removed *in vacuo* to yield **11** as a yellow oil (96%).

RP-HPLC (50 to 100% B in 15 min): t_R = 10.5 min.

4-(di-*tert*-butylfluorosilyl)benzoic acid (12)

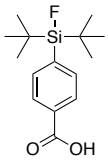

Chemical Formula: $C_{15}H_{23}FO_2Si$
Molecular Weight: 282.43

At rt, 1 M aq. $KMnO_3$ (30 mL) was added to a mixture of **11** (1.31 g, 4.92 mmol, 1.0 eq.) in *tert*-butanol (*t*BuOH) (30 mL), DCM (3.3 mL), and 1.25 M aq. $NaH_2PO_4 \cdot H_2O$ buffer (20 mL) at pH 4.0-4.5. After stirring the mixture for 25 min at rt, it was cooled to 0° C and an excess of $KMnO_4$ (0.78 g, 4.93 mmol, 1.0 eq.) was added. Subsequently the reaction was quenched by the addition of sat. aq. Na_2SO_3 (50 mL). Upon addition of 2 M aq. HCL, all the developed MnO_2 was dissolved. The resulting solution was extracted with diethyl ether (3 × 50 mL) and the combined organic layers were washed with sat. aq. $NaHCO_3$ (100 mL), dried over $MgSO_4$, filtered, and concentrated *in vacuo*. The residue was purified by recrystallization from diethyl ether/*n*-hexane (1:3, *v/v*), yielding **12** (60%) as a colorless solid

RP-HPLC (50 to 100% B in 15 min): t_R = 8.5 min.
ESI-MS: Calculated monoisotopic mass ($C_{15}H_{23}FO_2Si$): 282.4; found: m/z = 281.1 $[M-H]^-$, 235.1 $[M-COOH]^-$.
^{1}H-NMR (300 MHz, $CDCl_3$, 300 K): δ = 8.10 (2H, d, C_6H_4), 7.74 (2H, d, C_6H_4), 1.07 (18H, s, Si(*t*Bu)$_2$) ppm.
^{13}C-NMR (75 MHz, $CDCl_3$, 300 K): δ = 171.00 (a, COOH), 141.37 (d, C_p), 134.22 (d, C_m), 129.03 (d, $C_{i,o}$), 27.40 (d, CCH_3), 20.36 (d, CCH_3) ppm.

(4-(bromomethyl)phenyl)di-*tert*-butylfluorosilane (13)

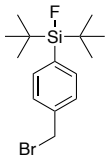

Chemical Formula: $C_{15}H_{24}BrFSi$
Molecular Weight: 331.34

To a 0° C cooled solution of **10** (3.08 g, 11.5 mmol, 1.0 eq.) and tetrabromomethane (4.18 g, 12.6 mmol, 1.1 eq.) in 100 mL DCM, triphenylphosphine (3.30 g, 12.6 mmol, 1.1 eq.) was added over a period of 30 min in small portions. The solution was stirred for 2 h at rt. Solvents were removed *in vacuo* and the residue was washed with cold *n*-hexane (3 × 50 mL). A white precipitate was removed by filtration and the solution was concentrated *in vacuo*. Purification was conducted by flash column chromatography (silica, pentane). Compound **13** was isolated as a colorless oil (3.06 g, 9.2 mmol, 80%).

RP-HPLC (50 to 100% B in 15 min): t_R = 9.2 min.

^{1}H-NMR (400 MHz, $CDCl_3$, 300 K): δ = 7.58 (2H, d, C_6H_4), 7.40 (2H, d, C_6H_4), 4.49 (2H, s, CH_2Br), 1.05 (18H, s, Si(*t*Bu)$_2$) ppm.

Di-*tert*-butyl(3,5-dimethylphenyl)fluorosilane (14)

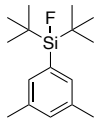

Chemical Formula: $C_{16}H_{27}FSi$
Molecular Weight: 266,48

A solution of 4.54 g 1-bromo-3,5-dimethylbenzene (25.1 mmol, 1.0 eq.) in 70 mL dry THF was cooled to -78 °C. To this 34.7 mL of a 1.6 M solution of *t*BuLi in pentane (55.5 mmol, 2.2 eq.) was added dropwise at -78 °C and stirred for 30 min. The solution then was added to di-*tert*-butyldifluorosilane (5.0 g, 27.7 mmol, 1.1 eq.) in 50 mL THF at -78 °C and stirred over night at room temperature with pressure control. To this, 100 mL of aqueous saturated NaCl-solution was added. Afterwards the solution was extracted with Et_2O (3 × 100 mL), combined organic phases were dried over $MgSO_4$ and the solvent was removed under reduced pressure to obtain **14** (6.6 g, 24.8 mmol, 99 %) as a colorless solid.

RP-HPLC (50 to 100 in 15 min): t_R = 16.5 min.
^{1}H-NMR (500 MHz, $CDCl_3$, 300 K): δ = 7.19 (2H, s, H_O), 7.04 (1H, s, H_p), 2.33 (6H, s, CH_3), 1.06 (18H, s, Si(*t*Bu)$_2$) ppm.

5-(di-*tert*-butylfluorosilyl)isophthalic acid (15)

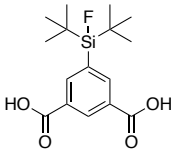

Chemical Formula: $C_{16}H_{23}FO_4Si$
Molecular Weight: 326,44

To a solution of **14** (1.1 g, 4.0 mmol, 1.0 eq.) in 16.8 mL *t*BuOH in DCM (*v*/*v* 3.5/1) a 2.5 M aqueous NaH_2PO_4 (16.0 mL, 40.0 mmol, 10.0 eq.) buffer solution was added. To this, $KMnO_4$ (7.6 g, 48.0 mmol, 12.0 eq.) was added and the solution was stirred for 24 h at 75 °C. The reaction was stopped by adding an aqueous saturated solution of $NaSO_3$ until there were no traces of violet $KMnO_4$ (ca. 50 mL) left. MnO_2 was dissolved with conc. HCl (ca. 10 mL) until the solution turns slightly pink. The solution was extracted with Et_2O (3 × 100 mL), the combined organic phases were dried over $MgSO_4$ and the solvent was removed under reduced pressure to obtain **15** (1.3 g, 4.0 mmol, 100%) as a colorless solid.

RP-HPLC (50 to 100 in 15 min): t_R = 5.7 min (Mono acid: 9.6 min).
ESI-MS: Calculated monoisotopic mass ($C_{16}H_{23}FO_4Si$): 326.13; found: m/z = 327.2 $[M+H]^+$, 309.2 $[M-H_2O+H]^+$.

^{1}H-NMR (400 MHz, DMSO-D_6, 300 K): δ = 8.53 (t, 1 H, $^{4}J(^{1}H,^{1}H)$ = 1.7 Hz; H_{Ar-2}), 8.32 (d, 2 H, $^{4}J(^{1}H,^{1}H)$ = 1.6 Hz; $H_{Ar-4,-6}$), 1.03 (s, 18 H; CH_3).
^{13}C[^{1}H]-NMR (101 MHz, DMSO-D_6): δ [ppm] = 166.5 (s; COOH), 137.9 (d, $^{3}J(^{13}C,^{19}F)$ = 4 Hz; $C_{Ar-4,-6}$), 134.0 (d, $^{2}J(^{13}C,^{19}F)$ = 14 Hz; C_{Ar-5}), 131.4 (s; C_{Ar-2}), 130.8 (s; $C_{Ar-1,-3}$), 26.8 (s; C*C*H_3), 19.7 (d, $^{2}J(^{13}C,^{19}F)$ = 12 Hz; *C*CH_3).
^{19}F[^{29}Si]-NMR (376 MHz, DMSO-D_6): δ = –187.1 ppm.
^{29}Si[^{1}H]INEPT-NMR (79 MHz, DMSO-D_6): δ = 13.8 (d, $^{1}J(^{19}F,^{29}Si)$ = 299 Hz) ppm.

3-(di-*tert*-butylfluorosilyl)-5-((vinyloxy)carbonyl)benzoic acid (16)

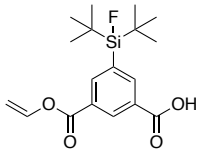

Chemical Formula: $C_{18}H_{25}FO_4Si$
Molecular Weight: 352,48

A solution of **15** (1.0 g, 3.1 mmol, 1.0 eq.) and K_2CO_3 (1.3 g, 9.2 mmol, 3.0 eq.) in 300 mL DMF was cooled to 0 °C and a solution of allyl bromide (185.0 mg, 132.0 µL, 1.5 mmol, 0.5 eq.) in 10 mL DMF was slowly added over a period of 20 min. The mixture was stirred over night at rt. The solution was filtered, and the solvent was removed under reduced pressure. The residue was solved in 100 mL 1 M HCl, extracted with Et_2O (3 × 200 mL), the combined organic phases were dried over $MgSO_4$ and the solvent was removed under reduced pressure. The residue was solved in DMF and purified with a flash chromatography purification system (Biotage™ Sfär C18 D-Duo 100 Å catridge, 20 to 50% B in 20 min). The product 16 was obtained as a colorless solid (250.9 mg, 684.6 mmol, 18.6 %).

RP-HPLC (50 to 100 in 15 min): t_R = 10.4 min.
^{1}H-NMR (400 MHz, DMSO-D_6): δ = 8.57 (t, 1H, $^{4}J(^{1}H,^{1}H)$ = 1.5 Hz; H_{Ar-6}), 8.36 (t, 1H, $^{4}J(^{1}H,^{1}H)$ = 1.5 Hz; H_{Ar-2}), 8.34 (t, 1H, $^{4}J(^{1}H,^{1}H)$ = 1.5 Hz; H_{Ar-4}), 6.07 (ddt, 1H, $^{3}J(^{1}H,^{1}H)$ = 17.3, 10.7, 5.5 Hz; CH_2–C*H*=CH_2), 5.41 (dd, 1H, $^{3}J(^{1}H,^{1}H)$ = 17.2 Hz, $^{2}J(^{1}H,^{1}H)$ = 1.7 Hz; CH_2–CH=CH_2 (*E*)), 5.30 (dd, 1H, $^{3}J(^{1}H,^{1}H)$ = 10.3 Hz, $^{2}J(^{1}H,^{1}H)$ = 1.6 Hz; CH_2–CH=CH_2 (*Z*)), 4.85 (d, 2H, $^{3}J(^{1}H,^{1}H)$ = 5.6 Hz; CH_2–CH=CH_2), 1.03 (s, 18H; CCH_3) ppm.
^{13}C[^{1}H]-NMR (101 MHz, DMSO-D_6): δ = 166.3 (COOH), 164.6 (*C*O-OAll), 138.3 (d, $^{3}J(^{13}C,^{19}F)$ = 4 Hz; C_{Ar-4}), 137.6 (d, $^{3}J(^{13}C,^{19}F)$ = 4 Hz; C_{Ar-6}), 134.3 (d, $^{2}J(^{13}C,^{19}F)$ = 14 Hz; C_{Ar-5}), 132.4 (CH_2–*C*H=CH_2), 131.2 (C_{Ar-2}), 131.0 (C_{Ar-1}), 129.7 (C_{Ar-3}), 118.2 (CH_2–CH=*C*H_2), 65.6 (*C*H_2–CH=CH_2), 26.8 (s; C*C*H_3), 19.7 (d, $^{2}J(^{13}C,^{19}F)$ = 12 Hz; *C*CH_3) ppm.
^{19}F[^{29}Si]-NMR (376 MHz, DMSO-D_6): δ = –187.0 ppm.
^{29}Si[^{1}H]INEPT-NMR (79 MHz, DMSO-D_6): δ = 13.8 (d, $^{1}J(^{19}F,^{29}Si)$ = 299 Hz) ppm.

3.1.5 Synthesis of SiFA Containing Bridging Motifs

For the synthesis of symmetric SiFA containing bridging motifs 1,4,7-triazaheptane (DETA) was used as the basic structural motif. Following the reaction pathways shown in Scheme 5 three different symmetric SiFA building blocks where synthesized. For the synthesis of *N,N*-bis(2-aminoethyl)-4-(di-*tert*-butylfluorosilyl)benzamide (**19**, DETA(SiFA)) **12** (SiFA-BA) was used. For the synthesis of Vinyl-3-(bis(2-aminoethyl)carbamoyl)-5-(di-*tert*-butylfluorosilyl)benzoate (**20**, DETA(IPA-SiFA)) **16** (IPA-SiFA) was used, which provides an additional acid functionality after allyl-deprotection when compared to DETA(SiFA). To provide a symmetric SiFA building block with a permanent positive charge **13** (SiFA-Br) was used for the synthesis of 2-(Bis(2-aminoethyl)amino)-*N*-(4-(di-*tert*-butylfluorosilyl)benzyl)-*N,N*-dimethyl-2-oxoethan-1-aminium (**23**, DEMTA(SiFA*lin*)). Mono-Fmoc-protection of **18** and **23,** as shown in Scheme 6, provided SiFA containing bridging motifs for simple application in SPPS.

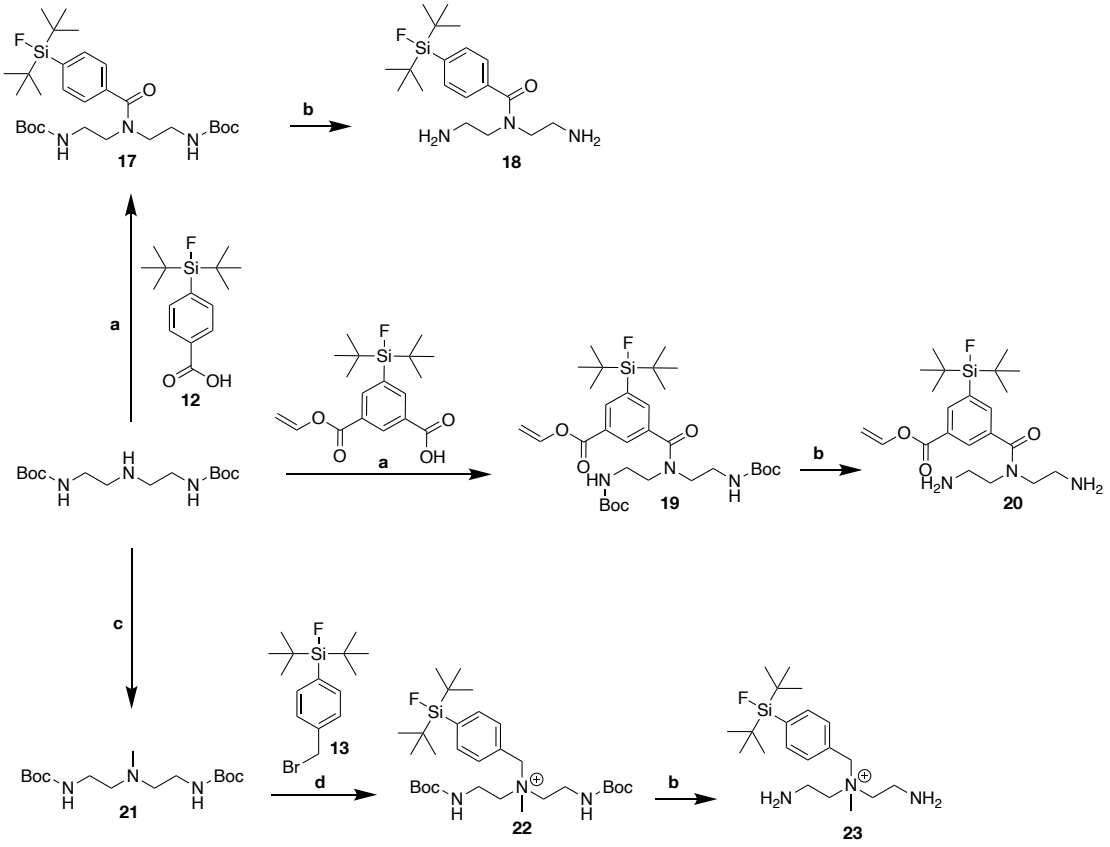

Scheme 5: Synthesis of SiFA containing bridging motifs **18**, **20** and **23**: a) TBTU, HOAt, DIPEA (DMF); b) TFA/TIPS/water (*v/v/v*, 95/2.5/2.5); c) formaldehyde, acetic acid, sodium cyanotrihydroborate (dry MeOH/DCM (*v/v*, 1/1)); d) DCM/DMF (*v/v*, 5/1).

Synthesis of DETA(SiFA) (18)

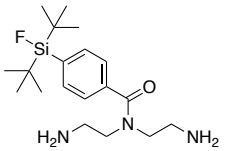

Chemical Formula: $C_{19}H_{34}FN_3OSi$
Molecular Weight: 367,58

For the synthesis of **18**, first SiFA-BA (140 mg, 495 µmol, 1.5 eq.) together with TBTU (159 mg, 495 µmol, 1.5 eq.), HOAt (68 mg, 495 µmol, 1.5 eq.) and DIPEA (260 µL, 1.49 mmol, 4.5 eq.) are dissolved in 5 mL DMF and stirred for 20 min. Afterwards, 1,7-Bis-Boc-1,4,7-triazaheptane (100 mg, 330 µmol, 1.0 eq.) in 5 mL DMF was added and the reaction mixture was stirred for 4 h. **17** was achieved by precipitating the reacting mixture in water. After lyophilization, the crude product was stirred for 1 h in TFA/TIPS/water (*v*/*v*/*v*, 95/2.5/2.5). Following the removal of the deprotection solution under a stream of nitrogen, the residue was purified by RP-HPLC (38 to 55% B in A in 20 min). Concentration *in vacuo* and freeze drying provided **18** as a yellowish solid (98%).

RP-HPLC (10 to 90% B in 15 min): t_R = 8.4 min.
ESI-MS: Calculated monoisotopic mass ($C_{19}H_{34}FN_3OSi$): 367.6; found: m/z = 368.2 $[M+H]^+$.

Synthesis of DETA(IPA-SiFA) (20)

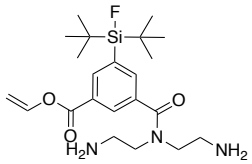

Chemical Formula: $C_{22}H_{36}FN_3O_3Si$
Molecular Weight: 437,63

For the synthesis of **20**, first 5-(di-*tert*-butylfluorosilyl)isophthalic acid (Allyl-IPA-SiFA, **15**) (116 mg, 330 µmol, 1.0 eq.) together with TBTU (105 mg, 330 µmol, 1.0 eq.), HOAt (44.8 mg, 330 µmol, 1.0 eq.) and DIPEA (224 µL, 1.31 mmol, 4.0 eq.) were dissolved in 4 mL DMF and stirred for 20 min. Afterwards, 1,7-Bis-Boc-1,4,7-triazaheptane (100 mg, 330 µmol, 1.0 eq.) in 5 mL DMF was added and the reaction mixture was stirred for 4 h. **19** was achieved by precipitating the reacting mixture in water. After lyophilization, the crude product was stirred for 1 h in TFA/TIPS/water (*v*/*v*/*v*, 95/2.5/2.5). Following the removal of the deprotection solution under a stream of nitrogen, the residue was purified by RP-HPLC (34 to 60% B in A in 30 min). Concentration *in vacuo* and freeze drying provided **20** as a yellowish solid (5%).

RP-HPLC (10 to 90% B in 15 min): t_R = 8.9 min.
ESI-MS: Calculated monoisotopic mass ($C_{22}H_{36}FN_3O_3Si$): 437.6; found: m/z = 438.5 $[M+H]^+$.

Synthesis of DEMTA(SiFA*in*) (23)

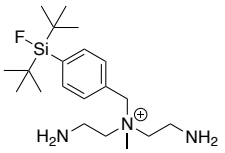

Chemical Formula: $C_{20}H_{39}FN_3Si^+$
Molecular Weight: 368,64

For the synthesis of **21**, 1,7-Bis-Boc-1,4,7-triazaheptane (100 mg, 330 µmol, 1.0 eq.), formaldehyde (29.7 mg, 990 µmol, 3.0 eq.), acetic acid (38 µL, 660 µmol, 2.0 eq.) and sodium cyanotrihydroborate (82.9 mg, 1.32 mmol, 4.0 eq.) were dissolved in 16 mL dry MeOH/DCM (*v*/*v*, 1/1) and stirred at rt for 24 h. Concentration *in vacuo* and freeze drying provided a yellowish crude product which was used without further purification. **22** was achieved by dissolving the crude product of **21** (105 mg, 330 µmol, 1.0 eq.) and SiFA-Br (**13**) (157 mg, 473 µmol, 1.43 eq.) in 10 mL DCM/DMF (*v*/*v*, 5/1) and stirring at 40 °C for 24 h. Afterwards, concentration *in vacuo*, Boc-deprotection (**GSP6**), the removal of the deprotection solution under a stream of nitrogen and the purification by RP-HPLC (30 to 50% B in A in 30 min) were done. Concentration *in vacuo* and freeze drying provided **23** as a yellowish solid (83.3 mg, 266 µmol, 81%).

For 22:
RP-HPLC (10 to 90% B in 15 min): t_R = 14.59 min.
ESI-MS: Calculated monoisotopic mass ($C_{30}H_{55}FN_3O_4Si^+$): 568.9; found: m/z = 568.4 $[M]^+$.

For 23:
RP-HPLC (10 to 90% B in 15 min): t_R = 7.72 min.
ESI-MS: Calculated monoisotopic mass ($C_{20}H_{39}FN_3Si^+$): 368.3; found: m/z = 368.2 $[M]^+$.

Mono-Fmoc-Protection of SiFA Containing Bridging Motifs

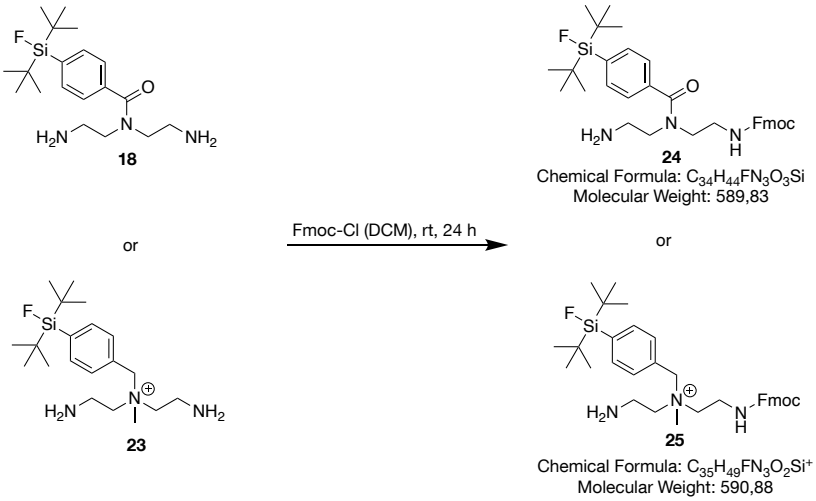

Scheme 6: Mono-Fmoc-protection of SiFA containing bridging motifs **18** and **23** with Fmoc-chloride.

For the mono-Fmoc-protection of SiFA containing bridging motifs, **18** (173 mg, 471 µmol, 1.0 eq.) or **23** (173 mg, 471 µmol, 1.0 eq.) together with Fmoc-chloride (122 mg, 471 µmol, 1.0 eq.) were dissolved in 10 mL DCM and stirred at rt for 24 h. Afterwards, the resulting suspension was concentrated *in vacuo* and the crude product is dissolved in 6 mL water/MeCN (1:2, *v/v*). The purification is carried out through automated flash column chromatography (Biotage™ Sfär C18 D-Duo 100 Å catridge, 20 to 50% B in 20 min). Concentration *in vacuo* and freeze drying provided products **24** or **25** isolated as a white crystalline solid (40%).

For 24:
RP-HPLC (10 to 90% B in 15 min): t_R = 13.99 min.
ESI-MS: Calculated monoisotopic mass ($C_{34}H_{44}FN_3O_3Si^+$): 589.9; found: m/z = 590.7 $[M]^+$.

For 25:
RP-HPLC (10 to 90% B in 15 min): t_R = 12.22 min.
ESI-MS: Calculated monoisotopic mass ($C_{35}H_{49}FN_3O_2Si^+$): 590.9; found: m/z = 590.5 $[M]^+$.

3.1.6 Synthesis of the N4 Chelator

The chelator N4 was synthesized following an improved reaction pathway based on a previously published route by *Meacke et al.*.[216]

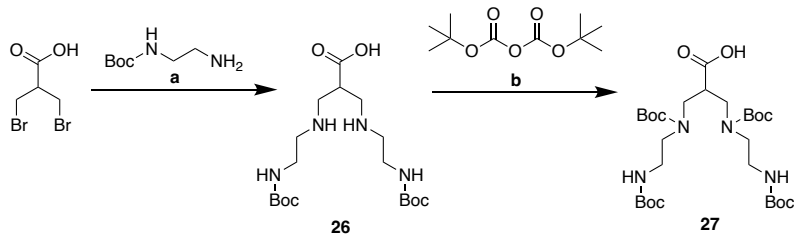

Scheme 7: Reaction pathway for the synthesis of Boc-protected N4 (**27**): a) rt, 4 h (THF); b) 3.0 eq. NEt_3, 0 °C to rt over 15 h (MeCN/H_2O, 1/1, *v/v*).

Synthesis of 3-((2-((tert-butoxycarbonyl)amino)ethyl)amino)-2-(((2-((tert-butoxycarbonyl)amino)ethyl)amino)methyl)propanoic acid (26)

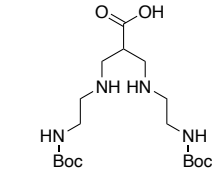

Chemical Formula: $C_{18}H_{36}N_4O_6$
Molecular Weight: 404,51

3-bromo-2-(bromomethyl)propinoic acid (1.0 g, 4.10 mmol, 1.0 eq.) was dissolved in THF (102.5 mL, 25 mL/mmol). Afterwards, *N*-boc-ethylenediamine (2.63 g, 16.4 mmol, 4.0 eq.) was added slowly under vigorous stirring, the reaction mixture was stirred at rt for 4 h. The reaction progress was monitored via ESI-MS. The solvent was removed under reduced pressure at rt and the resulting colorless oil was directly utilized in the next synthesis step.

ESI-MS of reaction control: Calculated monoisotopic mass ($C_{18}H_{36}N_4O_6$): 404.51; found: m/z = 405.7 $[M+H]^+$.

Synthesis of (3-((*tert*-butoxycarbonyl)(2-((*tert*-butoxycarbonyl)amino)ethyl)amino)-2-(((tert-butoxycarbonyl)(2-((*tert*-butoxycarbonyl)amino)ethyl)amino) methyl)propanoic acid) (N4(Boc)$_4$, 27)

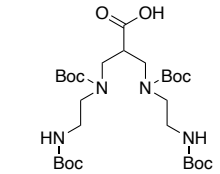

Chemical Formula: $C_{28}H_{52}N_4O_{10}$
Molecular Weight: 604,74

26 was dissolved in 102.5 mL acetone/H_2O (1/1, *v/v* [25 mL/mmol]) and cooled to 0 °C. NEt_3 (1.71 mL, 12.3 mmol, 3.0 eq.) was added to the solution. After 5 min di-*tert*-butyl-dicarbonate (3.51 mL, 16.4 mmol, 4.0 eq.) was added. The reaction mixture was stirred for 24 h, whereby

a white solid precipitated. The white precipitate was immediately dissolved by adding additional acetone. As the reaction control via ESI-MS revealed that the reaction was not completed, additional 4.0 eq. (3.51 mL, 16.4 mmol) di-tert-butyl-dicarbonate were added (pH 8). The reaction mixture was stirred for another 15 h. A reaction control via ESI-MS was performed before the solvent was removed under reduced pressure at rt. If the reaction control showed that Boc-anhydride was formed at the acid group (m/z = 705.0 $[M+H]^+$), this side product does not need to be separated, as partial Boc deprotection could be carried out directly before the chelator was coupled. The solvent was removed in vacuo and the crude product was dissolved in DMF to be purified via flash chromatography. After removal of the solvent, 539.6 mg (0.893 mmol, 22%) of **27** were obtained as a white solid.

RP-flash chromatography (35-71% B, 18 min, Biotage ®SNAP Cartridge KP-C18-HS 30 g, 30 mL/min): t_R =14.5 min.
ESI-MS: Calculated monoisotopic mass ($C_{28}H_{52}N_4O_{10}$): 604.37; found: m/z = 505.2 $[M-Boc+H]^+$, 605.2 $[M+H]^+$, 706.4 $[M+Boc+H]^+$, 1231.5 $[2M+Na]^+$.

3.1.7 Synthesis of a *trans-tert*-Butyl Protected FAPI-04 Building Block

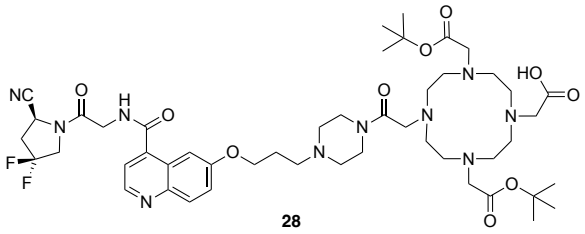

28
Chemical Formula: $C_{48}H_{70}F_2N_{10}O_{10}$
Molecular Weight: 985,14

For the synthesis of **28**, firstly Boc-deprotection of **7** (30 mg, 50 µmol, 1.0 eq.) is carried out as described in **GSP8**. The resulting deprotected inhibitory sequence **29** is diluted in 6 mL DMF and the pH value is adjusted to pH 8 by adding DIPEA. Afterwards, DOTA(*t*Bu)$_2$ (264 mg, 510 µmol, 10 eq.), TBTU (32.8 mg, 100 µmol, 2.0 eq.) and HOAt (69.6 mg, 510 µmol, 10.0 eq.) are dissolved in 8 mL DMF. After addition of DIPEA (261 µL, 1.53 mmol, 30 eq.) and preactivation for 15 min, the solution is added to **29** and stirred at rt for 6 h. Following a successful reaction control, the solution is concentrated *in vacuo* and the crude product is purified by RP-HPLC (10 to 60% B in A in 30 min). Concentration *in vacuo* and freeze drying provides **28** as a yellowish solid (43.7 mg, 44.4 µmol, 87%).

RP-HPLC (10 to 60% B in 30 min, Multospher 100 RP 18-5µ, 10 mL/min): t_R = 22.3 min.
ESI-MS: Calculated monoisotopic mass ($C_{48}H_{70}F_2N_{10}O_3$): 984.52; found: m/z = 985.5 $[M+H]^+$, 493.4 $[M+2H]^{2+}$.

3.2 Synthesis of rhFAPI, transFAPI and tecFAPI Ligands

Synthesis of FAPI ligands was generally achieved by coupling of the previously synthesized inhibitor **7** or *trans-tert*-butyl protected FAPI-04 building block **28** and a protected peptide containing hydrophilic modifications and labeling moieties for radiolabeling with fluoride-18, technetium-99m and radiometals such as e.g., lutetium-177. These peptides were synthesized *via* SPPS following **GSP1** to **GSP10**. Deprotection was conducted following **GSP6**, thereafter the crude product is purified by HPLC.

Coupling of Building Block and Inhibitor (GSP8)

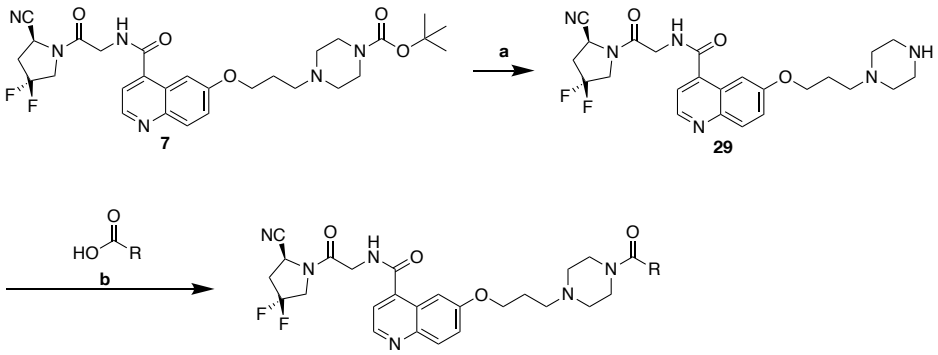

Scheme 8: Synthesis of FAPI ligand through coupling of building block with acid functionality and inhibitor (**29**): a) TsOH (MeCN); b) TBTU, HOAt, DIPEA (DMF).

Coupling of a building block with acid functionality and inhibitor followed the reaction pathway shown in Scheme 8. Here, the previously synthesized Boc-protected inhibitor **7** was deprotected by dissolving 1.0 eq. of **7** and 6.5 eq. of *p*-toluenesulfonic acid in dry MeCN and heating the solution to 45 °C for 3 h. Afterwards, the reaction mixture was brought to a slightly basic pH with DIPEA, followed by concentration *in vacuo*. The crude product (**29**) was used without further purification. Thereafter, the building block with acid functionality (1.0 eq.) together with TBTU (1.0 eq.), HOAt (1.0 eq.) and DIPEA (3.0 eq.) were dissolved in 2.5 mL DMF and stirred for 15 min. Then, **29** (1.0 eq.) dissolved in 2.5 mL DMF was added and the reaction mixture was stirred at rt for 3 to 6 h. The reaction was monitored through analytic HPLC and was ended by removing the solvent *in vacuo* after the complete coupling was accomplished.

Coupling of Building Block and trans-*tert*-Butyl Protected FAPI-04 Building Block (GSP9)

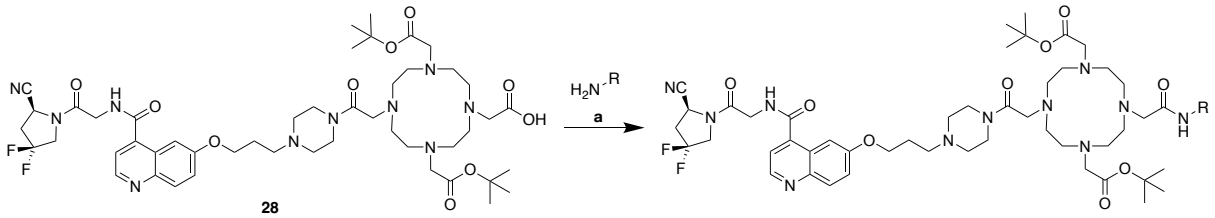

Scheme 9: Synthesis of FAPI ligands through coupling of building blocks with amine functionality and *trans-tert*-butyl protected FAPI-04 building block **28**: a) TBTU, HOAt, DIPEA (DMF).

Coupling of a building block with amine functionality and *trans-tert*-butyl protected FAPI-04 building block **28** followed the reaction pathway shown in Scheme 9. Here, the previously synthesized **28** (1.0 eq.) was preactivated and stirred for 15 min in 2.5 mL DMF with TBTU (1.0 eq.), HOAt (1.0 eq.) and DIPEA (3.0 eq.). Then, the building block with amine functionality (1.0 eq.) dissolved in 2.5 mL DMF was added to the reaction mixture and stirred at rt for 3 to 6 h. The reaction is monitored through analytic HPLC and was ended by removing the solvent *in vacuo* after the complete coupling was accomplished.

Synthesis of the dap(NMe$_2$-Gly-SiFA*lin*) Moiety (GSP10)

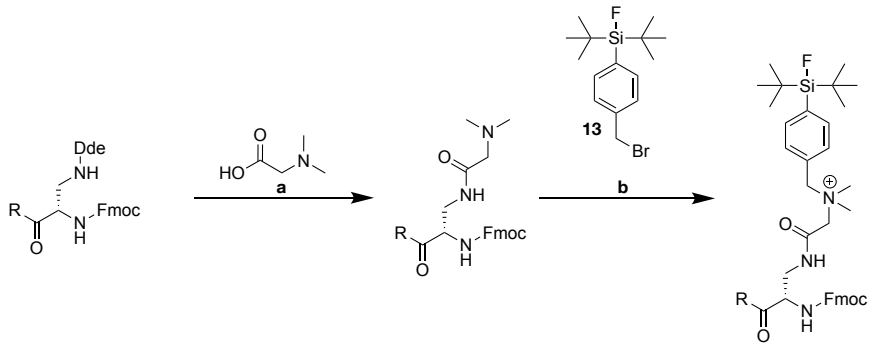

Scheme 10: Synthesis of the dap(NMe$_2$-Gly-SiFA*lin*) moiety starting from peptide bound Fmoc-dap(Dde): a) 1. **GSP4a**, 2. TBTU, HOAt, DIPEA (DMF); b) DIPEA (DCM).

Synthesis of the dap(NMe$_2$-Gly-SiFA*lin*) moiety was carried out following the reaction pathway shown in Scheme 10. Starting from peptide bound Fmoc-dap(Dde), Dde deprotection was carried out following **GSP4**. Afterwards, dimethylglycine (NMe$_2$-Gly) was coupled as described in **GSP2**. For the nucleophilic substitution with **13** the resign bound peptide first was washed with DCM (8 × 5 mL/g resin) followed by the addition of **13** (3.0 eq.) and DIPEA (6.0 eq.) in DCM (5.0 mL) and reaction for 24 h. The reaction was monitored through analytic HPLC and was ended by washing the reaction reactor with DMF (8 × 5 mL/g resin).

3.2.1 General Synthesis Strategy and Structural Modification of rhFAPI Ligands

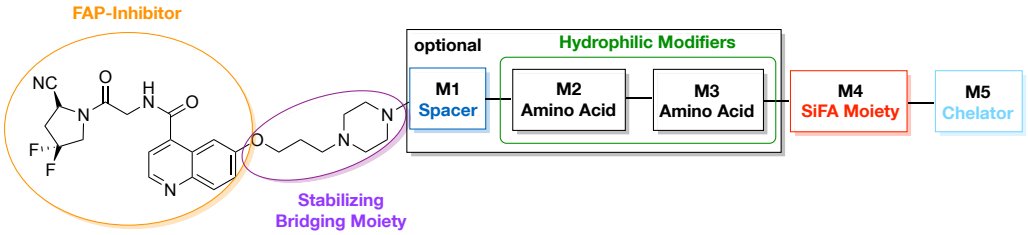

Figure 25: General structure of rhFAPI ligands containing the shown FAP inhibitor (orange) and stabilizing bridging moiety (purple) and the variable modification sites **M1** to **M5**, where **M1** is a spacer (blue), **M2** and **M3** are amino acids which act as hydrophilic modifiers (green), **M4** is a SiFA moiety (red) and **M5** is a chelator (turquoise) for metal complexation.

The general structure of rhFAPI Ligands is shown in Figure 25, whereas their respective detailed structural modification sites are specified in Table 4.

Table 4: Listing of all rhFAPI Ligands and their respective variable modification sites **M1** to **M5.**

rhFAPI Ligand	M1	M2	M3	M4	M5
rhFAPI-01	δ-D-glu	D-cit	D-lys	D-dap(SiFA)	(*R*)-DOTAGA
rhFAPI-02	δ-D-glu	D-cit	D-cit	D-dap(SiFA)	(*R*)-DOTAGA
rhFAPI-03	δ-D-glu	D-lys	D-lys	D-dap(SiFA)	(*R*)-DOTAGA
rhFAPI-04	δ-D-glu	D-asp	D-asp	D-dap(SiFA)	(*R*)-DOTAGA
rhFAPI-04+E	δ-D-glu	D-asp	(D-asp- D-glu)	D-dap(SiFA)	(*R*)-DOTAGA
rhFAPI-05	GABA	D-cit	D-lys	D-dap(SiFA)	(*R*)-DOTAGA
rhFAPI-06	GABA	D-cit	D-cit	D-dap(SiFA)	(*R*)-DOTAGA
rhFAPI-07	GABA	D-lys	D-lys	D-dap(SiFA)	(*R*)-DOTAGA
rhFAPI-08	GABA	D-asp	D-asp	D-dap(SiFA)	(*R*)-DOTAGA
rhFAPI-09	GABA	D-dap	D-dap	D-dap(SiFA)	(*R*)-DOTAGA
rhFAPI-10	GABA	D-ser	D-ser	D-dap(SiFA)	(*R*)-DOTAGA
rhFAPI-11	GABA	D-asn	D-asn	D-dap(SiFA)	(*R*)-DOTAGA
rhFAPI-12	GABA	D-glu	D-glu	D-dap(SiFA)	(*R*)-DOTAGA
rhFAPI-13	GABA	D-lys	D-cit	D-dap(SiFA)	(*R*)-DOTAGA
rhFAPI-14	GABA	D-dap	D-cit	D-dap(SiFA)	(*R*)-DOTAGA
rhFAPI-15	GABA	D-cit	D-dap	D-dap(SiFA)	(*R*)-DOTAGA
rhFAPI-16	GABA	D-cit	D-asp	D-dap(SiFA)	(*R*)-DOTAGA
rhFAPI-17	GABA	D-cit	D-lys	D-dap(NMe_2-Gly-SiFA*lin*)	(*R*)-DOTAGA
rhFAPI-18	GABA	D-cit	D-lys	D-dap(NMe_2-Gly-SiFA*lin*)	DOTA
rhFAPI-19	GABA	D-cit	D-asp	D-dap(NMe_2-Gly-SiFA*lin*)	DOTA
rhFAPI-20	GABA	D-cit	D-lys	D-dap(NMe_2-Gly-SiFA*lin*)	(D-asp-DOTA)
rhFAPI-21	GABA	D-cit	(D-glu- D-lys)	D-dap(NMe_2-Gly-SiFA*lin*)	DOTA

All ligands contain the (*R*)-*N*-(2-(2-cyano-4,4-difluoropyrrolidin-1-yl)-2-oxoethyl)quinoline-4-carboxamide based FAP-inhibitor (orange) developed by *Jansen et al.*[105,106] and the 3-(piperazin-1-yl)propan-1-ol based stabilizing bridging moiety introduced by *Lindner et al.*[111,112]. Following the stabilizing bridging moiety δ-D-glu or *gamma*-aminobutyric acid

(GABA) was introduced as a spacer (**M1**, blue). Afterwards different amino acids (**M2** and **M3**, green) were coupled to serve as a hydrophilic counterpart to the lipophilic SiFA moiety (**M4**, red), which can be dap(SiFA) or dap(NMe_2-Gly-SiFA*lin*). Lastly a chelator (**M5**, turquoise) like DOTA or (*R*)-DOTAGA was inserted.

Synthesis of rhFAPI-01 (FAPI-δ-e-cit-k-dap(SiFA)- (*R*)-DOTAGA)

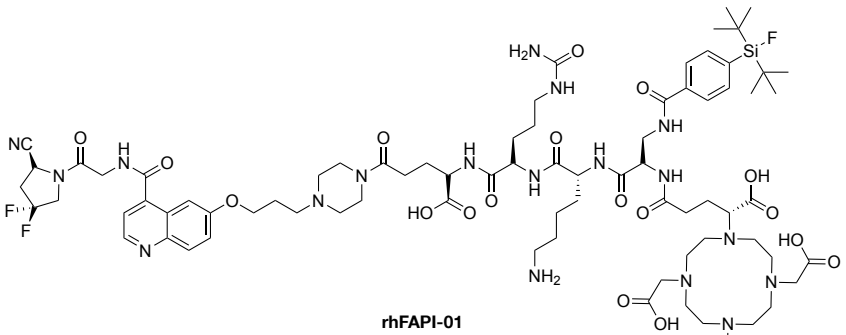

rhFAPI-01
Chemical Formula: $C_{78}H_{115}F_3N_{18}O_{20}Si$
Exact Mass: 1708,83
Molecular Weight: 1709,96

The synthesis of **rhFAPI-01** was started by resin loading (**GSP1**) with Fmoc-D-glu-O(*t*Bu). After Fmoc-deprotection (**GSP3**), Fmoc-D-cit-OH, Fmoc-D-lys(Boc)-OH and Fmoc-D-dap(Dde)-OH were coupled following **GSP2**. The SiFA moiety was introduced by Dde-deprotection (**GSP4**) of the sidechain of D-dap and coupling (**GSP2**) of SiFA-BA. The chelator was introduced by Fmoc-deprotection (**GSP3**) followed by coupling (**GSP2**) of (*R*)-DOTAGA(*t*Bu)$_4$. This peptidic building block was cleaved from the resin preserving all acid sensitive protection groups (**GSP7a**) and the crude product was purified by RP-HPLC (60 to 80% B in A in 30 min, t_R = 21.8 min). Concentration *in vacuo* and freeze drying provided a white solid (19%).
The received building block was coupled to the inhibitor following **GSP8**. After *t*Bu-/Boc-deprotection (**GSP6**), the crude product was purified by RP-HPLC (35 to 50% B in A in 30 min, t_R = 10.3 min). Concentration *in vacuo* and freeze drying provided **rhFAPI-01** as a white solid (26%).

RP-HPLC (10 to 90% B in 15 min): t_R = 7.99 min.
ESI-MS: Calculated monoisotopic mass ($C_{78}H_{115}F_3N_{18}O_{20}Si$): 1708.83; found: m/z = 1710.5 $[M+H]^+$, 855.6 $[M+2H]^{2+}$, 570.7 $[M+3H]^{3+}$.

Synthesis of rhFAPI-02 (FAPI-δ-e-cit-cit-dap(SiFA)-(*R*)-DOTAGA)

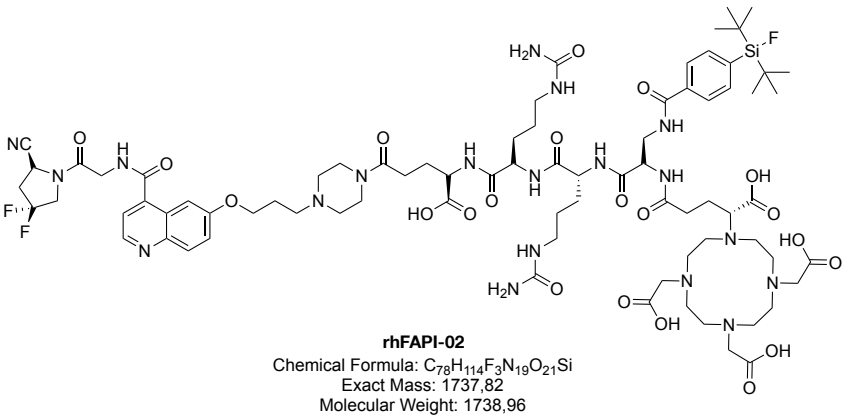

rhFAPI-02
Chemical Formula: $C_{78}H_{114}F_3N_{19}O_{21}Si$
Exact Mass: 1737,82
Molecular Weight: 1738,96

The synthesis of **rhFAPI-02** was started by resin loading (**GSP1**) with Fmoc-D-glu-O(*t*Bu). After Fmoc-deprotection (**GSP3**), Fmoc-D-cit-OH, Fmoc-D-cit-OH and Fmoc-D-dap(Dde)-OH were coupled following **GSP2**. The SiFA moiety was introduced by Dde-deprotection (**GSP4**) of the sidechain of D-dap and coupling (**GSP2**) of SiFA-BA. The chelator was introduced by Fmoc-deprotection (**GSP3**) followed by coupling (**GSP2**) of (*R*)-DOTAGA(*t*Bu)$_4$. This peptidic building block was cleaved from the resin preserving all acid sensitive protection groups (**GSP7a**) and the crude product was purified by RP-HPLC (55 to 80% B in A in 30 min, t_R = 17.3 min). Concentration *in vacuo* and freeze drying provided a white solid (20%).
The received building block was coupled to the inhibitor following **GSP8**. After *t*Bu-/Boc-deprotection (**GSP6**), the crude product was purified by RP-HPLC (35 to 50% B in A in 30 min, t_R = 12.5 min). Concentration *in vacuo* and freeze drying provided **rhFAPI-02** as a white solid (28%).

RP-HPLC (10 to 90% B in 15 min): t_R = 8.10 min.
ESI-MS: Calculated monoisotopic mass ($C_{78}H_{114}F_3N_{19}O_{21}Si$): 1737.82; found: m/z = 1739.2 $[M+H]^+$, 870.2 $[M+2H]^{2+}$, 580.4 $[M+3H]^{3+}$.

Synthesis of rhFAPI-03 (FAPI-δ-e-k-k-dap(SiFA)-(*R*)-DOTAGA)

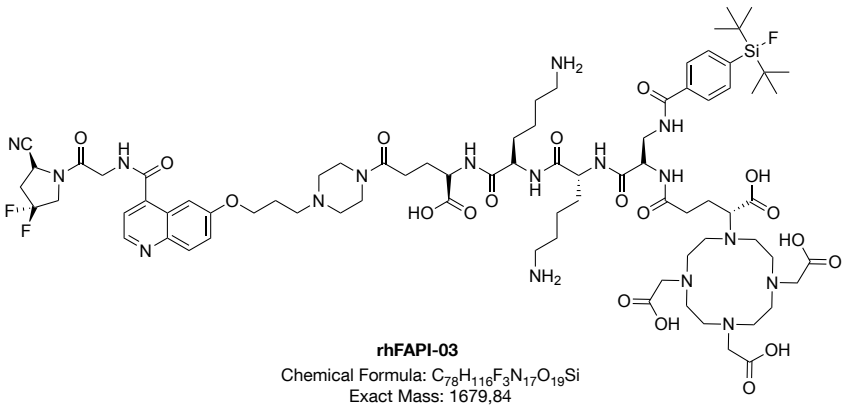

rhFAPI-03
Chemical Formula: $C_{78}H_{116}F_3N_{17}O_{19}Si$
Exact Mass: 1679,84
Molecular Weight: 1680,97

The synthesis of **rhFAPI-03** was started by resin loading (**GSP1**) with Fmoc-D-glu-O(*t*Bu). After Fmoc-deprotection (**GSP3**), Fmoc-D-lys(Boc)-OH, Fmoc-D-lys(Boc)-OH and Fmoc-D-dap(Dde)-OH were coupled following **GSP2**. The SiFA moiety was introduced by Dde-deprotection (**GSP4**) of the sidechain of D-dap and coupling (**GSP2**) of SiFA-BA. The chelator was introduced by Fmoc-deprotection (**GSP3**) followed by coupling (**GSP2**) of (*R*)-DOTAGA(*t*Bu)$_4$. This peptidic building block was cleaved from the resin preserving all acid sensitive protection groups (**GSP7a**) and the crude product was purified by RP-HPLC (75 to 80% B in A in 30 min, t_R = 16.3 min). Concentration *in vacuo* and freeze drying provided a white solid (23%).
The received building block was coupled to the inhibitor following **GSP8**. After *t*Bu-/Boc-deprotection (**GSP6**), the crude product was purified by RP-HPLC (30 to 45% B in A in 30 min, t_R = 16.4 min). Concentration *in vacuo* and freeze drying provided **rhFAPI-03** as a white solid (25%).

RP-HPLC (10 to 90% B in 15 min): t_R = 7.60 min.
ESI-MS: Calculated monoisotopic mass ($C_{78}H_{116}F_3N_{17}O_{19}Si$): 1679.84; found: m/z = 1681.5 $[M+H]^+$, 841.2 $[M+2H]^{2+}$, 561.2 $[M+3H]^{3+}$.

Synthesis of rhFAPI-04 (FAPI-δ-e-d-d-dap(SiFA)-(*R*)-DOTAGA)

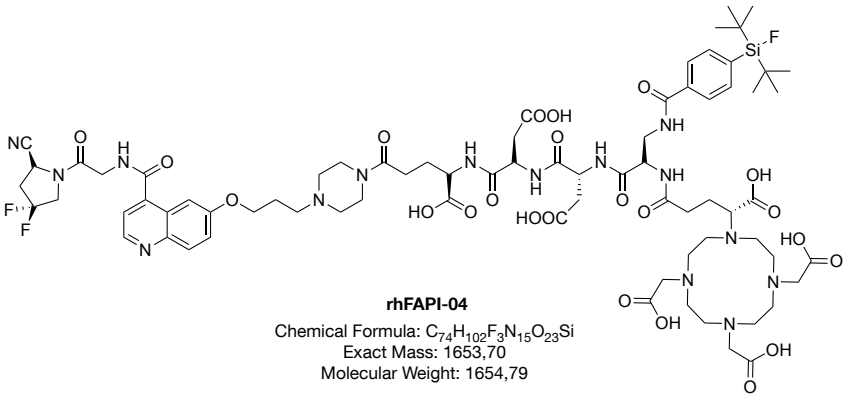

The synthesis of **rhFAPI-04** was started by resin loading (**GSP1**) with Fmoc-D-glu-O(*t*Bu). After Fmoc-deprotection (**GSP3**), Fmoc-D-asp(*t*Bu)-OH, Fmoc-D-asp(*t*Bu)-OH and Fmoc-D-dap(Dde)-OH were coupled following **GSP2**. The SiFA moiety was introduced by Dde-deprotection (**GSP4**) of the sidechain of D-dap and coupling (**GSP2**) of SiFA-BA. The chelator was introduced by Fmoc-deprotection (**GSP3**) followed by coupling (**GSP2**) of (*R*)-DOTAGA(*t*Bu)$_4$. This peptidic building block was cleaved from the resin preserving all acid sensitive protection groups (**GSP7a**) and the crude product was purified by RP-HPLC (70 to 80% B in A in 30 min, t_R = 15.7 min). Concentration *in vacuo* and freeze drying provided a white solid (17%).
The received building block was coupled to the inhibitor following **GSP8**. After *t*Bu-/Boc-deprotection (**GSP6**), the crude product was purified by RP-HPLC (35 to 40% B in A in 30 min,

t_R = 12.4 min). Concentration *in vacuo* and freeze drying provided **rhFAPI-04** as a white solid (33%).

RP-HPLC (10 to 90% B in 15 min): t_R = 8.02 min.
ESI-MS: Calculated monoisotopic mass ($C_{74}H_{102}F_3N_{17}O_{23}Si$): 1653.7; found: m/z = 1655.2 $[M+H]^+$, 828.1 $[M+2H]^{2+}$, 552.4 $[M+3H]^{3+}$.

Synthesis of rhFAPI-04+E (FAPI-δ-e-d-d-e-dap(SiFA)-(*R*)-DOTAGA)

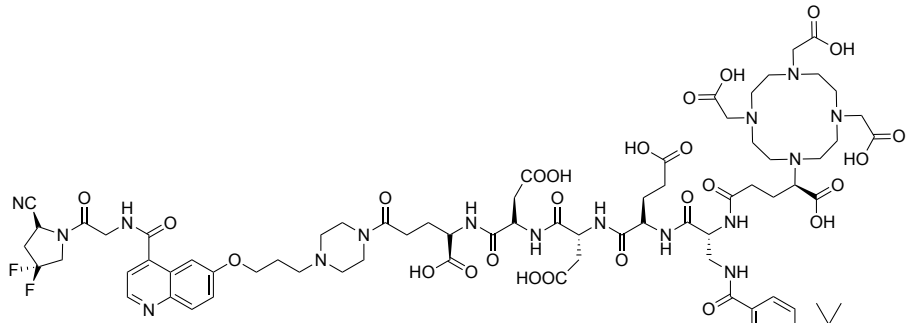

rhFAPI-04+E
Chemical Formula: $C_{79}H_{109}F_3N_{16}O_{26}Si$
Exact Mass: 1782,74
Molecular Weight: 1783,91

The synthesis of **rhFAPI-04+E** was started by resin loading (**GSP1**) with Fmoc-D-glu-O(*t*Bu). After Fmoc-deprotection (**GSP3**), Fmoc-D-asp(*t*Bu)-OH, Fmoc-D-asp(*t*Bu)-OH, Fmoc-D-glu(*t*Bu)-OH and Fmoc-D-dap(Dde)-OH were coupled following **GSP2**. The SiFA moiety was introduced by Dde-deprotection (**GSP4**) of the sidechain of D-dap and coupling (**GSP2**) of SiFA-BA. The chelator was introduced by Fmoc-deprotection (**GSP3**) followed by coupling (**GSP2**) of (*R*)-DOTAGA(*t*Bu)$_4$. This peptidic building block was cleaved from the resin preserving all acid sensitive protection groups (**GSP7a**) and the crude product was purified by RP-HPLC (70 to 80% B in A in 30 min, t_R = 15.9 min). Concentration *in vacuo* and freeze drying provided a white solid (24%).
The received building block was coupled to the inhibitor following **GSP8**. After *t*Bu-/Boc-deprotection (**GSP6**), the crude product was purified by RP-HPLC (35 to 40% B in A in 30 min, t_R = 11.8 min). Concentration *in vacuo* and freeze drying provided **rhFAPI-04+E** as a white solid (25%).

RP-HPLC (10 to 90% B in 15 min): t_R = 7.95 min.
ESI-MS: Calculated monoisotopic mass ($C_{79}H_{109}F_3N_{16}O_{26}Si$): 1782.74; found: m/z = 1784.2 $[M+H]^+$, 892.6 $[M+2H]^{2+}$, 595.4 $[M+3H]^{3+}$.

Synthesis of rhFAPI-05 (FAPI-GABA-cit-k-dap(SiFA)-(*R*)-DOTAGA)

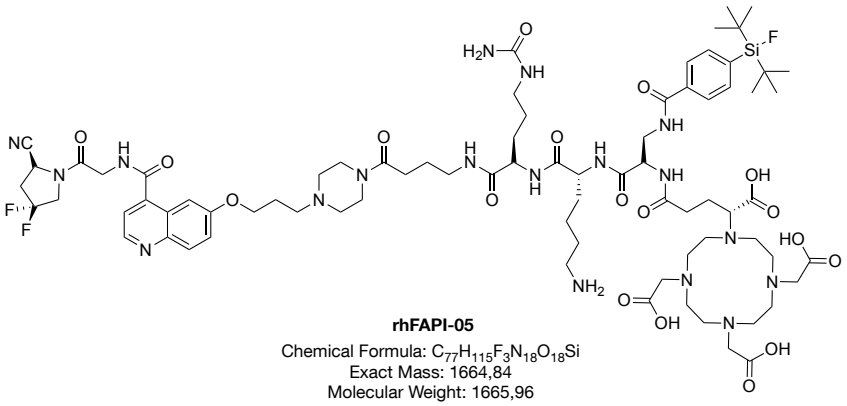

rhFAPI-05
Chemical Formula: $C_{77}H_{115}F_3N_{18}O_{18}Si$
Exact Mass: 1664,84
Molecular Weight: 1665,96

The synthesis of **rhFAPI-05** was started by resin loading (**GSP1**) with Fmoc-GABA-OH. After Fmoc-deprotection (**GSP3**), Fmoc-D-cit-OH, Fmoc-D-lys(Boc)-OH and Fmoc-D-dap(Dde)-OH were coupled following **GSP2**. The SiFA moiety was introduced by Dde-deprotection (**GSP4**) of the sidechain of D-dap and coupling (**GSP2**) of SiFA-BA. The chelator was introduced by Fmoc-deprotection (**GSP3**) followed by coupling (**GSP2**) of (*R*)-DOTAGA(*t*Bu)$_4$. This peptidic building block was cleaved from the resin preserving all acid sensitive protection groups (**GSP7a**) and the crude product was purified by RP-HPLC (62 to 67% B in A in 20 min, t_R = 10.1 min). Concentration *in vacuo* and freeze drying provided a white solid (15%).
The received building block was coupled to the inhibitor following **GSP8**. After *t*Bu-/Boc-deprotection (**GSP6**), the crude product was purified by RP-HPLC (32 to 37% B in A in 20 min, t_R = 10.4 min). Concentration *in vacuo* and freeze drying provided **rhFAPI-05** as a white solid (29%).

RP-HPLC (10 to 90% B in 15 min): t_R = 7.75 min.
ESI-MS: Calculated monoisotopic mass ($C_{77}H_{115}F_3N_{18}O_{18}Si$): 1664.84; found: m/z = 1666.7 $[M+H]^+$, 833.4 $[M+2H]^{2+}$, 556.0 $[M+3H]^{3+}$.

Synthesis of rhFAPI-06 (FAPI-GABA-cit-cit-dap(SiFA)-(*R*)-DOTAGA)

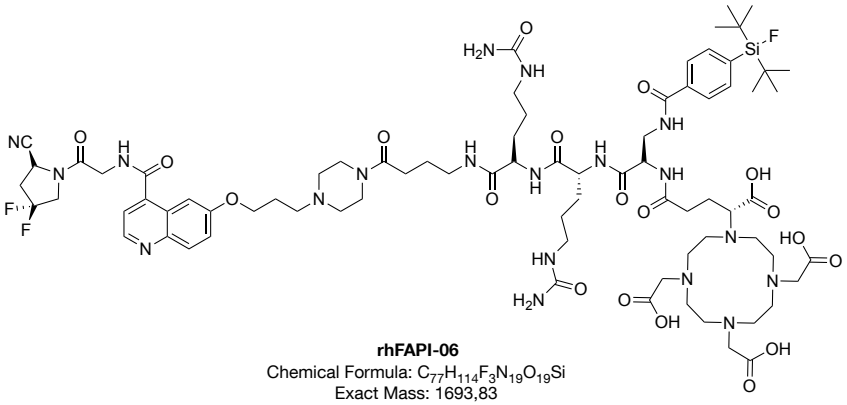

rhFAPI-06
Chemical Formula: $C_{77}H_{114}F_3N_{19}O_{19}Si$
Exact Mass: 1693,83
Molecular Weight: 1694,95

The synthesis of **rhFAPI-06** was started by resin loading (**GSP1**) with Fmoc-GABA-OH. After Fmoc-deprotection (**GSP3**), Fmoc-D-cit-OH, Fmoc-D-cit-OH and Fmoc-D-dap(Dde)-OH were coupled following **GSP2**. The SiFA moiety was introduced by Dde-deprotection (**GSP4**) of the sidechain of D-dap and coupling (**GSP2**) of SiFA-BA. The chelator was introduced by Fmoc-deprotection (**GSP3**) followed by coupling (**GSP2**) of (*R*)-DOTAGA(*t*Bu)$_4$. This peptidic building block was cleaved from the resin preserving all acid sensitive protection groups (**GSP7a**) and the crude product was purified by RP-HPLC (70 to 80% B in A in 20 min, t_R = 8.1 min). Concentration *in vacuo* and freeze drying provided a white solid (23%).
The received building block was coupled to the inhibitor following **GSP8**. After *t*Bu-/Boc-deprotection (**GSP6**), the crude product was purified by RP-HPLC (35 to 42% B in A in 20 min, t_R = 14.4 min). Concentration *in vacuo* and freeze drying provided **rhFAPI-06** as a white solid (35%).

RP-HPLC (10 to 90% B in 15 min): t_R = 7.99 min.
ESI-MS: Calculated monoisotopic mass ($C_{77}H_{114}F_3N_{19}O_{19}Si$): 1693.83; found: m/z = 847.9 $[M+2H]^{2+}$, 565.9 $[M+3H]^{3+}$.

Synthesis of rhFAPI-07 (FAPI-GABA-k-k-dap(SiFA)-(*R*)-DOTAGA)

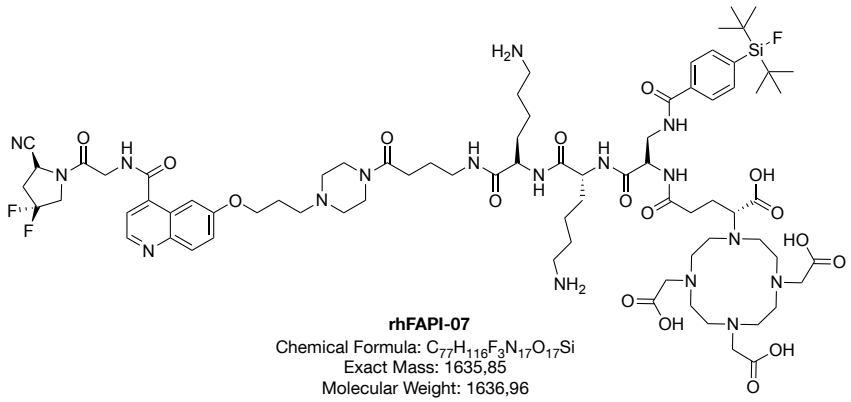

rhFAPI-07
Chemical Formula: $C_{77}H_{116}F_3N_{17}O_{17}Si$
Exact Mass: 1635,85
Molecular Weight: 1636,96

The synthesis of **rhFAPI-07** was started by resin loading (**GSP1**) with Fmoc-GABA-OH. After Fmoc-deprotection (**GSP3**), Fmoc-D-lys(Boc)-OH, Fmoc-D-lys(Boc)-OH and Fmoc-D-dap(Dde)-OH were coupled following **GSP2**. The SiFA moiety was introduced by Dde-deprotection (**GSP4**) of the sidechain of D-dap and coupling (**GSP2**) of SiFA-BA. The chelator was introduced by Fmoc-deprotection (**GSP3**) followed by coupling (**GSP2**) of (*R*)-DOTAGA(*t*Bu)$_4$. This peptidic building block was cleaved from the resin preserving all acid sensitive protection groups (**GSP7a**) and the crude product was purified by RP-HPLC (70 to 80% B in A in 20 min, t_R = 10.0 min). Concentration *in vacuo* and freeze drying provided a white solid (22%).
The received building block was coupled to the inhibitor following **GSP8**. After *t*Bu-/Boc-deprotection (**GSP6**), the crude product was purified by RP-HPLC (32 to 37% B in A in 20 min, t_R = 10.9 min). Concentration *in vacuo* and freeze drying provided **rhFAPI-07** as a white solid (31%).

RP-HPLC (10 to 90% B in 15 min): t_R = 7.54 min.
ESI-MS: Calculated monoisotopic mass ($C_{77}H_{116}F_3N_{17}O_{17}Si$): 1635.85; found: m/z = 1636.9 $[M+H]^+$, 818.9 $[M+2H]^{2+}$, 546.3 $[M+3H]^{3+}$.

Synthesis of rhFAPI-08 (FAPI-GABA-d-d-dap(SiFA)-(*R*)-DOTAGA)

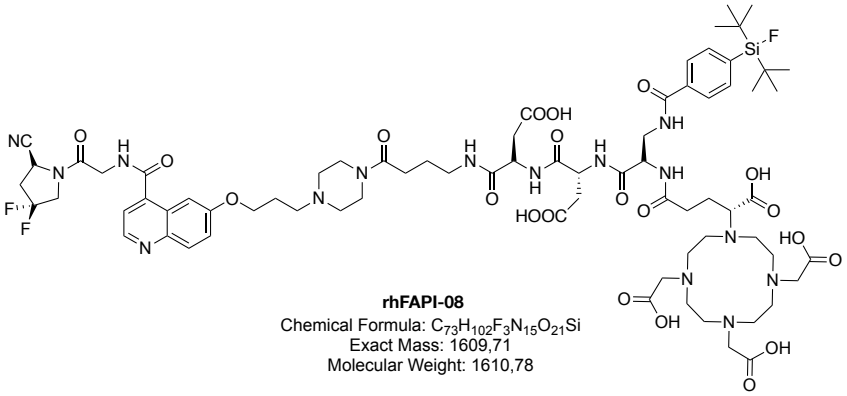

The synthesis of **rhFAPI-08** was started by resin loading (**GSP1**) with Fmoc-GABA-OH. After Fmoc-deprotection (**GSP3**), Fmoc-D-asp(*t*Bu)-OH, Fmoc-D-asp(*t*Bu)-OH and Fmoc-D-dap(Dde)-OH were coupled following **GSP2**. The SiFA moiety was introduced by Dde-deprotection (**GSP4**) of the sidechain of D-dap and coupling (**GSP2**) of SiFA-BA. The chelator was introduced by Fmoc-deprotection (**GSP3**) followed by coupling (**GSP2**) of (*R*)-DOTAGA(*t*Bu)$_4$. This peptidic building block was cleaved from the resin preserving all acid sensitive protection groups (**GSP7a**) and the crude product was purified by RP-HPLC (70 to 85% B in A in 20 min, t_R = 12.5 min). Concentration *in vacuo* and freeze drying provided a white solid (16%).
The received building block was coupled to the inhibitor following **GSP8**. After *t*Bu-/Boc-deprotection (**GSP6**), the crude product was purified by RP-HPLC (30 to 35% B in A in 20 min, t_R = 11.9 min). Concentration *in vacuo* and freeze drying provided **rhFAPI-08** as a white solid (29%).

RP-HPLC (10 to 90% B in 15 min): t_R = 10.1 min.
ESI-MS: Calculated monoisotopic mass ($C_{73}H_{102}F_3N_{15}O_{21}Si$): 1609.71; found: m/z = 1610.8 $[M+H]^+$, 805.7 $[M+2H]^{2+}$.

Synthesis of rhFAPI-09 (FAPI-GABA-dap-dap-dap(SiFA)-(*R*)-DOTAGA)

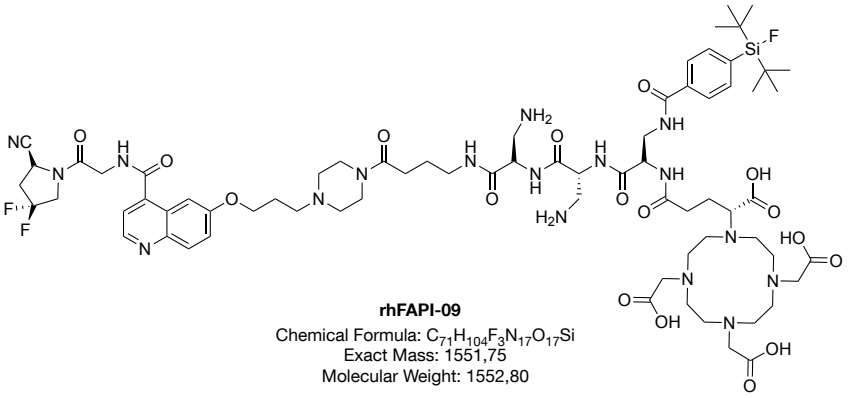

rhFAPI-09
Chemical Formula: $C_{71}H_{104}F_3N_{17}O_{17}Si$
Exact Mass: 1551,75
Molecular Weight: 1552,80

The synthesis of **rhFAPI-09** was started by resin loading (**GSP1**) with Fmoc-GABA-OH. After Fmoc-deprotection (**GSP3**), Fmoc-D-dap(Boc)-OH, Fmoc-D-dap(Boc)-OH and Fmoc-D-dap(Dde)-OH were coupled following **GSP2**. The SiFA moiety was introduced by Dde-deprotection (**GSP4**) of the sidechain of D-dap and coupling (**GSP2**) of SiFA-BA. The chelator was introduced by Fmoc-deprotection (**GSP3**) followed by coupling (**GSP2**) of (*R*)-DOTAGA(tBu)$_4$. This peptidic building block was cleaved from the resin preserving all acid sensitive protection groups (**GSP7a**) and the crude product was purified by RP-HPLC (70 to 80% B in A in 20 min, t_R = 9.1 min). Concentration *in vacuo* and freeze drying provided a white solid (24%).

The received building block was coupled to the inhibitor following **GSP8**. After tBu-/Boc-deprotection (**GSP6**), the crude product was purified by RP-HPLC (32 to 37% B in A in 20 min, t_R = 15.7 min). Concentration *in vacuo* and freeze drying provided **rhFAPI-09** as a white solid (32%).

RP-HPLC (10 to 90% B in 15 min): t_R = 7.93 min.
ESI-MS: Calculated monoisotopic mass ($C_{71}H_{104}F_3N_{17}O_{17}Si$): 1551.75; found: m/z = 1552.9 $[M+H]^+$, 776.8 $[M+2H]^{2+}$, 531.9 $[M+3H]^{3+}$.

Synthesis of rhFAPI-10 (FAPI-GABA-s-s-dap(SiFA)-(*R*)-DOTAGA)

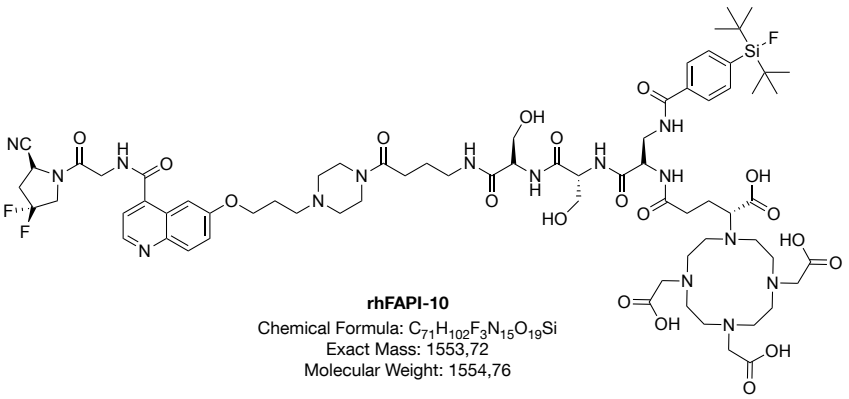

rhFAPI-10
Chemical Formula: $C_{71}H_{102}F_3N_{15}O_{19}Si$
Exact Mass: 1553,72
Molecular Weight: 1554,76

The synthesis of **rhFAPI-10** was started by resin loading (**GSP1**) with Fmoc-GABA-OH. After Fmoc-deprotection (**GSP3**), Fmoc-D-ser(*t*Bu)-OH, Fmoc-D-ser(*t*Bu)-OH and Fmoc-D-dap(Dde)-OH were coupled following **GSP2**. The SiFA moiety was introduced by Dde-deprotection (**GSP4**) of the sidechain of D-dap and coupling (**GSP2**) of SiFA-BA. The chelator was introduced by Fmoc-deprotection (**GSP3**) followed by coupling (**GSP2**) of (*R*)-DOTAGA(*t*Bu)$_4$. This peptidic building block was cleaved from the resin preserving all acid sensitive protection groups (**GSP7a**) and the crude product was purified by RP-HPLC (80 to 83% B in A in 30 min, t_R = 10.1 min). Concentration *in vacuo* and freeze drying provided a white solid (20%).
The received building block was coupled to the inhibitor following **GSP8**. After *t*Bu-/Boc-deprotection (**GSP6**), the crude product was purified by RP-HPLC (35 to 45% B in A in 20 min, t_R = 12.6 min). Concentration *in vacuo* and freeze drying provided **rhFAPI-10** as a white solid (27%).

RP-HPLC (10 to 90% B in 15 min): t_R = 9.83 min.
ESI-MS: Calculated monoisotopic mass ($C_{71}H_{102}F_3N_{15}O_{19}Si$): 1553.72; found: m/z = 1554.7 $[M+H]^+$, 778.0 $[M+2H]^{2+}$, 519.3 $[M+3H]^{3+}$.

Synthesis of rhFAPI-11 (FAPI-GABA-n-n-dap(SiFA)-(*R*)-DOTAGA)

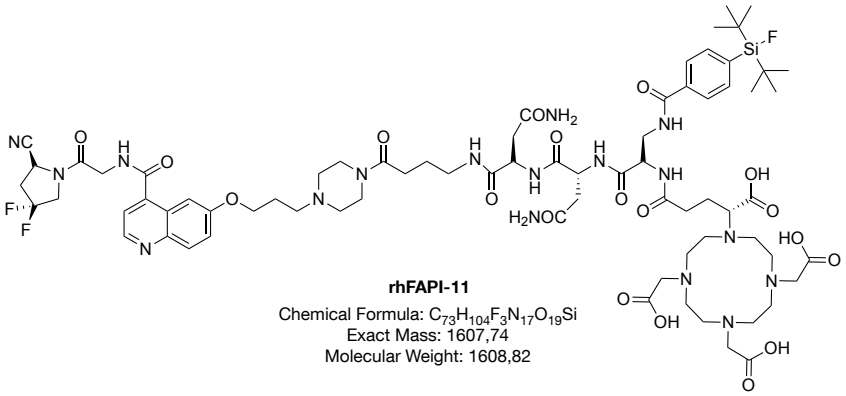

The synthesis of **rhFAPI-11** was started by resin loading (**GSP1**) with Fmoc-GABA-OH. After Fmoc-deprotection (**GSP3**), Fmoc-D-asn(Trt)-OH, Fmoc-D-asn(Trt)-OH and Fmoc-D-dap(Dde)-OH were coupled following **GSP2**. The SiFA moiety was introduced by Dde-deprotection (**GSP4**) of the sidechain of D-dap and coupling (**GSP2**) of SiFA-BA. The chelator was introduced by Fmoc-deprotection (**GSP3**) followed by coupling (**GSP2**) of (*R*)-DOTAGA(*t*Bu)$_4$. This peptidic building block was cleaved from the resin preserving all acid sensitive protection groups (**GSP7a**) and the crude product was purified by RP-HPLC (85 to 90% B in A in 30 min, t_R = 18.9 min). Concentration *in vacuo* and freeze drying provided a white solid (18%).
The received building block was coupled to the inhibitor following **GSP8**. After *t*Bu-/Boc-deprotection (**GSP6**), the crude product was purified by RP-HPLC (35 to 45% B in A in 20 min,

t_R = 12.7 min). Concentration *in vacuo* and freeze drying provided **rhFAPI-11** as a white solid (32%).

RP-HPLC (10 to 90% B in 15 min): t_R = 9.74 min.
ESI-MS: Calculated monoisotopic mass ($C_{73}H_{104}F_3N_{17}O_{19}Si$): 1607.74; found: m/z = 805.1 $[M+2H]^{2+}$, 537.3 $[M+3H]^{3+}$.

Synthesis of rhFAPI-12 (FAPI-GABA-e-e-dap(SiFA)-(*R*)-DOTAGA)

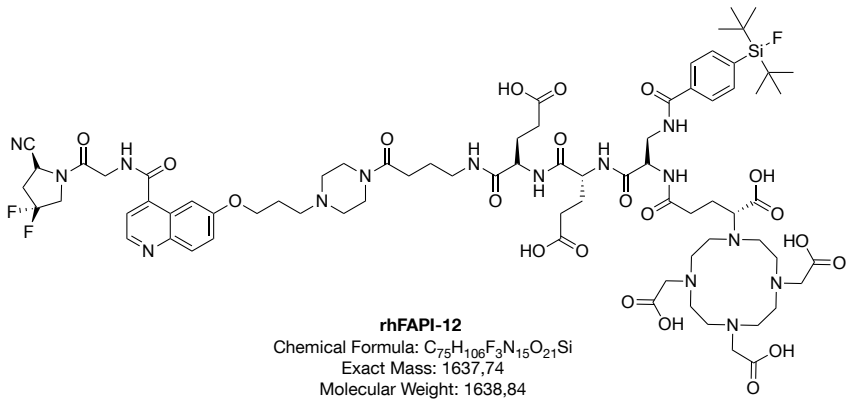

The synthesis of **rhFAPI-12** was started by resin loading (**GSP1**) with Fmoc-GABA-OH. After Fmoc-deprotection (**GSP3**), Fmoc-D-glu(*t*Bu)-OH, Fmoc-D-glu(*t*Bu)-OH and Fmoc-D-dap(Dde)-OH were coupled following **GSP2**. The SiFA moiety was introduced by Dde-deprotection (**GSP4**) of the sidechain of D-dap and coupling (**GSP2**) of SiFA-BA. The chelator was introduced by Fmoc-deprotection (**GSP3**) followed by coupling (**GSP2**) of (*R*)-DOTAGA(*t*Bu)$_4$. This peptidic building block was cleaved from the resin preserving all acid sensitive protection groups (**GSP7a**) and the crude product was purified by RP-HPLC (70 to 85% B in A in 20 min, t_R = 13.5 min). Concentration *in vacuo* and freeze drying provided a white solid (25%).
The received building block was coupled to the inhibitor following **GSP8**. After *t*Bu-/Boc-deprotection (**GSP6**), the crude product was purified by RP-HPLC (30 to 35% B in A in 20 min, t_R = 10.9 min). Concentration *in vacuo* and freeze drying provided **rhFAPI-12** as a white solid (34%).

RP-HPLC (10 to 90% B in 15 min): t_R = 10.2 min.
ESI-MS: Calculated monoisotopic mass ($C_{75}H_{106}F_3N_{15}O_{21}Si$): 1637.74; found: m/z = 1638.6 $[M+H]^+$, 819.7 $[M+2H]^{2+}$.

Synthesis of rhFAPI-13 (FAPI-GABA-k-cit-dap(SiFA)-(*R*)-DOTAGA)

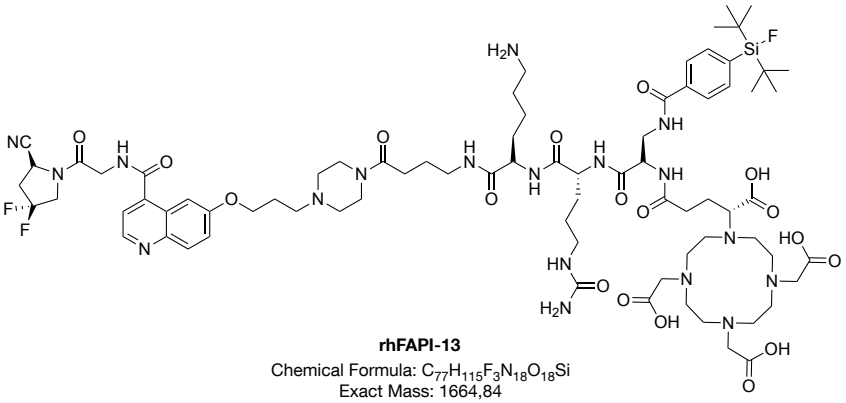

rhFAPI-13
Chemical Formula: $C_{77}H_{115}F_3N_{18}O_{18}Si$
Exact Mass: 1664,84
Molecular Weight: 1665,96

The synthesis of **rhFAPI-13** was started by resin loading (**GSP1**) with Fmoc-GABA-OH. After Fmoc-deprotection (**GSP3**), Fmoc-D-lys(Boc)-OH, Fmoc-D-cit-OH and Fmoc-D-dap(Dde)-OH were coupled following **GSP2**. The SiFA moiety was introduced by Dde-deprotection (**GSP4**) of the sidechain of D-dap and coupling (**GSP2**) of SiFA-BA. The chelator was introduced by Fmoc-deprotection (**GSP3**) followed by coupling (**GSP2**) of (*R*)-DOTAGA(*t*Bu)$_4$. This peptidic building block was cleaved from the resin preserving all acid sensitive protection groups (**GSP7a**) and the crude product was purified by RP-HPLC (65 to 70% B in A in 20 min, t_R = 8.89 min). Concentration *in vacuo* and freeze drying provided a white solid (19%).
The received building block was coupled to the inhibitor following **GSP8**. After *t*Bu-/Boc-deprotection (**GSP6**), the crude product was purified by RP-HPLC (32 to 37% B in A in 20 min, t_R = 10.4 min). Concentration *in vacuo* and freeze drying provided **rhFAPI-13** as a white solid (30%).

RP-HPLC (10 to 90% B in 15 min): t_R = 7.79 min.
ESI-MS: Calculated monoisotopic mass ($C_{77}H_{115}F_3N_{18}O_{18}Si$): 1664.84; found: m/z = 1665.8 $[M+H]^+$, 833.4 $[M+2H]^{2+}$, 556.0 $[M+3H]^{3+}$.

Synthesis of rhFAPI-14 (FAPI-GABA-dap-cit-dap(SiFA)-(*R*)-DOTAGA)

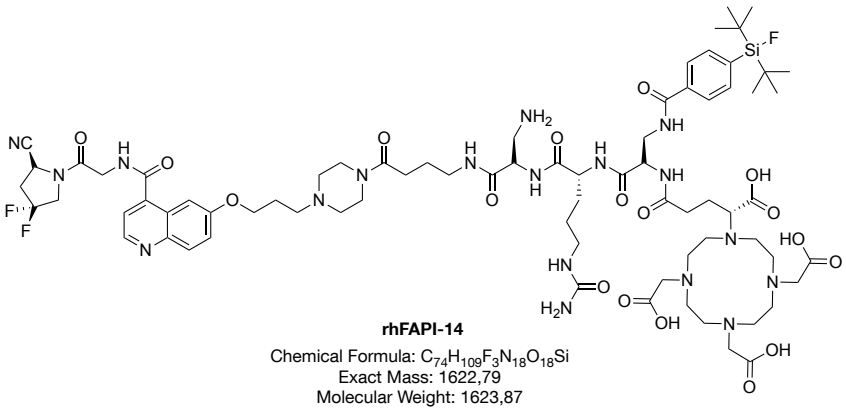

rhFAPI-14
Chemical Formula: $C_{74}H_{109}F_3N_{18}O_{18}Si$
Exact Mass: 1622,79
Molecular Weight: 1623,87

The synthesis of **rhFAPI-14** was started by resin loading (**GSP1**) with Fmoc-GABA-OH. After Fmoc-deprotection (**GSP3**), Fmoc-D-dap(Boc)-OH, Fmoc-D-cit-OH and Fmoc-D-dap(Dde)-OH were coupled following **GSP2**. The SiFA moiety was introduced by Dde-deprotection (**GSP4**) of the sidechain of D-dap and coupling (**GSP2**) of SiFA-BA. The chelator was introduced by Fmoc-deprotection (**GSP3**) followed by coupling (**GSP2**) of (*R*)-DOTAGA(tBu)$_4$. This peptidic building block was cleaved from the resin preserving all acid sensitive protection groups (**GSP7a**) and the crude product was purified by RP-HPLC (65 to 70% B in A in 20 min, t_R = 8.21 min). Concentration *in vacuo* and freeze drying provided a white solid (15%).
The received building block was coupled to the inhibitor following **GSP8**. After tBu-/Boc-deprotection (**GSP6**), the crude product was purified by RP-HPLC (32 to 37% B in A in 20 min, t_R = 11.4 min). Concentration *in vacuo* and freeze drying provided **rhFAPI-14** as a white solid (33%).

RP-HPLC (10 to 90% B in 15 min): t_R = 7.96 min.
ESI-MS: Calculated monoisotopic mass ($C_{74}H_{109}F_3N_{18}O_{18}Si$): 1622.79; found: m/z = 1624.0 $[M+H]^+$, 812.4 $[M+2H]^{2+}$, 541.9 $[M+3H]^{3+}$.

Synthesis of rhFAPI-15 (FAPI-GABA-k-cit-dap(SiFA)-(*R*)-DOTAGA)

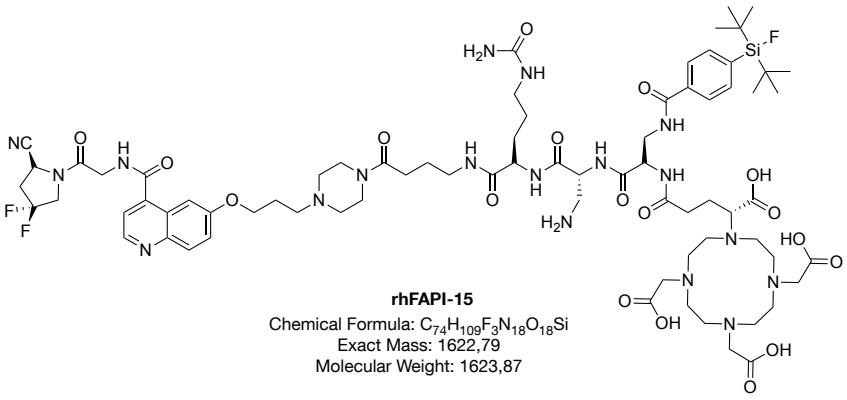

The synthesis of **rhFAPI-15** was started by resin loading (**GSP1**) with Fmoc-GABA-OH. After Fmoc-deprotection (**GSP3**), Fmoc-D-cit-OH, Fmoc-D-dap(Boc)-OH and Fmoc-D-dap(Dde)-OH were coupled following **GSP2**. The SiFA moiety was introduced by Dde-deprotection (**GSP4**) of the sidechain of D-dap and coupling (**GSP2**) of SiFA-BA. The chelator was introduced by Fmoc-deprotection (**GSP3**) followed by coupling (**GSP2**) of (*R*)-DOTAGA(tBu)$_4$. This peptidic building block was cleaved from the resin preserving all acid sensitive protection groups (**GSP7a**) and the crude product was purified by RP-HPLC (62 to 67% B in A in 20 min, t_R = 10.4 min). Concentration *in vacuo* and freeze drying provided a white solid (21%).
The received building block was coupled to the inhibitor following **GSP8**. After tBu-/Boc-deprotection (**GSP6**), the crude product was purified by RP-HPLC (32 to 37% B in A in 20 min, t_R = 11.4 min). Concentration *in vacuo* and freeze drying provided **rhFAPI-15** as a white solid (34%).

RP-HPLC (10 to 90% B in 15 min): t_R = 7.75 min.
ESI-MS: Calculated monoisotopic mass ($C_{74}H_{109}F_3N_{18}O_{18}Si$): 1622.79; found: m/z = 1623.9 $[M+H]^+$, 812.2 $[M+2H]^{2+}$, 541.9 $[M+3H]^{3+}$.

Synthesis of rhFAPI-16 (FAPI-GABA-cit-d-dap(SiFA)-(*R*)-DOTAGA)

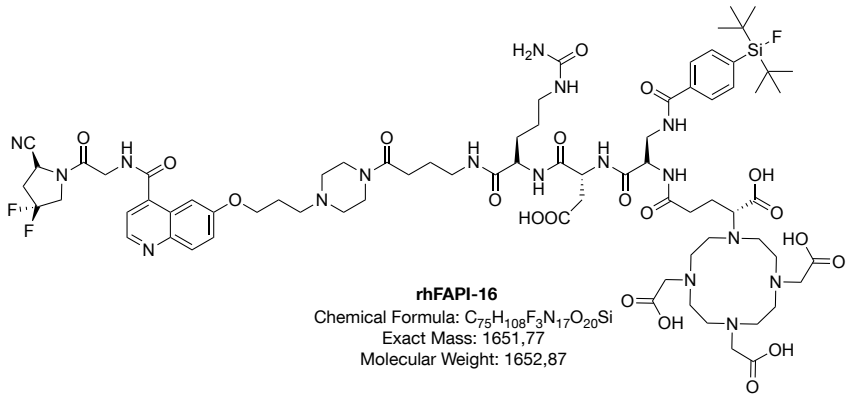

The synthesis of **rhFAPI-16** was started by resin loading (**GSP1**) with Fmoc-GABA-OH. After Fmoc-deprotection (**GSP3**), Fmoc-D-cit-OH, Fmoc-D-asp(*t*Bu)-OH and Fmoc-D-dap(Dde)-OH were coupled following **GSP2**. The SiFA moiety was introduced by Dde-deprotection (**GSP4**) of the sidechain of D-dap and coupling (**GSP2**) of SiFA-BA. The chelator was introduced by Fmoc-deprotection (**GSP3**) followed by coupling (**GSP2**) of (*R*)-DOTAGA(*t*Bu)$_4$. This peptidic building block was cleaved from the resin preserving all acid sensitive protection groups (**GSP7a**) and the crude product was purified by RP-HPLC (65 to 80% B in A in 30 min, t_R = 14.0 min). Concentration *in vacuo* and freeze drying provided a white solid (17%).
The received building block was coupled to the inhibitor following **GSP8**. After *t*Bu-/Boc-deprotection (**GSP6**), the crude product was purified by RP-HPLC (35 to 50% B in A in 30 min, t_R = 14.8 min). Concentration *in vacuo* and freeze drying provided **rhFAPI-16** as a white solid (35%).

RP-HPLC (10 to 90% B in 15 min): t_R = 8.31 min.
ESI-MS: Calculated monoisotopic mass ($C_{75}H_{108}F_3N_{17}O_{20}Si$): 1651.77; found: m/z = 1653.3 $[M+H]^+$, 827.0 $[M+2H]^{2+}$, 551.7 $[M+3H]^{3+}$.

Synthesis of rhFAPI-17 (FAPI-GABA-cit-k-dap(NMe$_2$-Gly-SiFA*lin*)-(*R*)-DOTAGA)

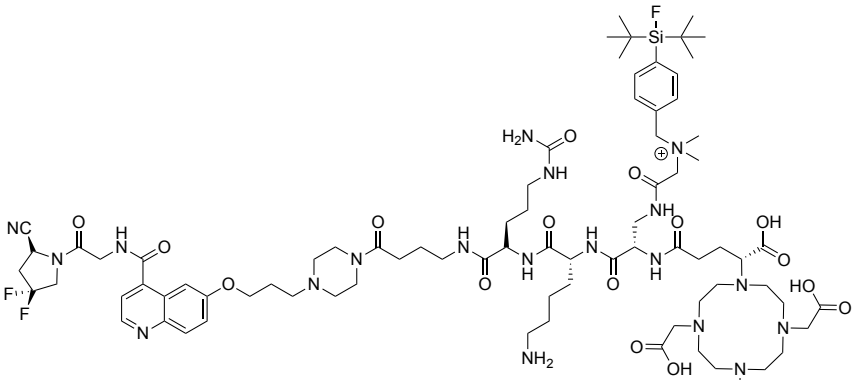

rhFAPI-17
Chemical Formula: $C_{81}H_{125}F_3N_{19}O_{18}Si^+$
Exact Mass: 1736,92
Molecular Weight: 1738,09

The synthesis of **rhFAPI-17** was started by resin loading (**GSP1**) with Fmoc-GABA-OH. After Fmoc-deprotection (**GSP3**), Fmoc-D-cit-OH, Fmoc-D-lys(Boc)-OH and Fmoc-D-dap(Dde)-OH were coupled following **GSP2**. The dap(NMe$_2$-Gly-SiFA*lin*) moiety was introduced as described in **GSP10**. The chelator was introduced by Fmoc-deprotection (**GSP3**) followed by coupling (**GSP2**) of (*R*)-DOTAGA(*t*Bu)$_4$. This peptidic building block was cleaved from the resin preserving all acid sensitive protection groups (**GSP7a**) and the crude product was purified by RP-HPLC (55 to 85% B in A in 30 min, t_R = 18.9 min). Concentration *in vacuo* and freeze drying provided a white solid (17%).
The received building block was coupled to the inhibitor following **GSP8**. After *t*Bu-/Boc-deprotection (**GSP6**), the crude product was purified by RP-HPLC (35 to 45% B in A in 30 min, t_R = 18.4 min). Concentration *in vacuo* and freeze drying provided **rhFAPI-17** as a white solid (33%).

RP-HPLC (10 to 90% B in 15 min): t_R = 8.12 min.
ESI-MS: Calculated monoisotopic mass ($C_{81}H_{125}F_3N_{19}O_{18}Si^+$): 1736.92; found: m/z = 1737.8 $[M+H]^+$, 869.4 $[M+2H]^{2+}$, 579.9 $[M+3H]^{3+}$.

Synthesis of rhFAPI-18 (FAPI-GABA-cit-k-dap(NMe$_2$-Gly-SiFA*lin*)-DOTA)

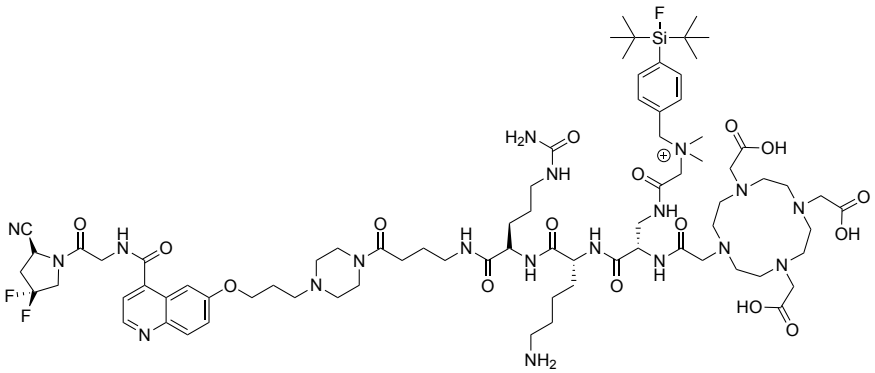

rhFAPI-18
Chemical Formula: $C_{78}H_{121}F_3N_{19}O_{16}Si^+$
Exact Mass: 1664,90
Molecular Weight: 1666,02

The synthesis of **rhFAPI-18** was started by resin loading (**GSP1**) with Fmoc-GABA-OH. After Fmoc-deprotection (**GSP3**), Fmoc-D-cit-OH, Fmoc-D-lys(Boc)-OH and Fmoc-D-dap(Dde)-OH were coupled following **GSP2**. The dap(NMe_2-Gly-SiFA*lin*) moiety was introduced as described in **GSP10**. The chelator was introduced by Fmoc-deprotection (**GSP3**) followed by coupling (**GSP2**) of DOTA(tBu)$_3$. This peptidic building block was cleaved from the resin preserving all acid sensitive protection groups (**GSP7a**) and the crude product was purified by RP-HPLC (50 to 75% B in A in 30 min, t_R = 11.0 min). Concentration *in vacuo* and freeze drying provided a white solid (24%).
The received building block was coupled to the inhibitor following **GSP8**. After tBu-/Boc-deprotection (**GSP6**), the crude product was purified by RP-HPLC (35 to 45% B in A in 30 min, t_R = 9.4 min). Concentration *in vacuo* and freeze drying provided **rhFAPI-18** as a white solid 26%).

RP-HPLC (10 to 90% B in 15 min): t_R = 7.91 min.
ESI-MS: Calculated monoisotopic mass ($C_{78}H_{121}F_3N_{19}O_{16}Si^+$): 1664.90; found: m/z = 1666.1 $[M+H]^+$, 833.5 $[M+2H]^{2+}$, 555.9 $[M+3H]^{3+}$.

Synthesis of rhFAPI-19 (FAPI-GABA-cit-d-dap(NMe_2-Gly-SiFA*lin*)-DOTA)

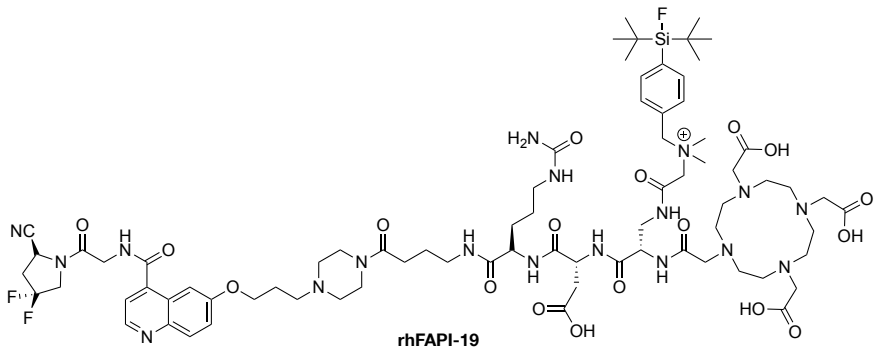

rhFAPI-19
Chemical Formula: $C_{76}H_{114}F_3N_{18}O_{18}Si^+$
Exact Mass: 1651,83
Molecular Weight: 1652,94

The synthesis of **rhFAPI-19** was started by resin loading (**GSP1**) with Fmoc-GABA-OH. After Fmoc-deprotection (**GSP3**), Fmoc-D-cit-OH, Fmoc-D-asp(tBu)-OH and Fmoc-D-dap(Dde)-OH were coupled following **GSP2**. The dap(NMe_2-Gly-SiFA*lin*) moiety was introduced as described in **GSP10**. The chelator was introduced by Fmoc-deprotection (**GSP3**) followed by coupling (**GSP2**) of DOTA(tBu)$_3$. This peptidic building block was cleaved from the resin preserving all acid sensitive protection groups (**GSP7a**) and the crude product was purified by RP-HPLC (50 to 70% B in A in 30 min, t_R = 11.3 min). Concentration *in vacuo* and freeze drying provided a white solid (17%).
The received building block was coupled to the inhibitor following **GSP8**. After tBu-/Boc-deprotection (**GSP6**), the crude product was purified by RP-HPLC (35 to 45% B in A in 30 min, t_R = 21.8 min). Concentration *in vacuo* and freeze drying provided **rhFAPI-19** as a white solid (32%).

RP-HPLC (10 to 90% B in 15 min): t_R = 8.6 min.
ESI-MS: Calculated monoisotopic mass ($C_{76}H_{114}F_3N_{18}O_{18}Si^+$): 1651.83; found: m/z = 1652.9 $[M+H]^+$, 826.0 $[M+2H]^{2+}$, 551.0 $[M+3H]^{3+}$.

Synthesis of rhFAPI-20 (FAPI-GABA-cit-k-dap(NMe$_2$-Gly-SiFA*lin*)-d-DOTA)

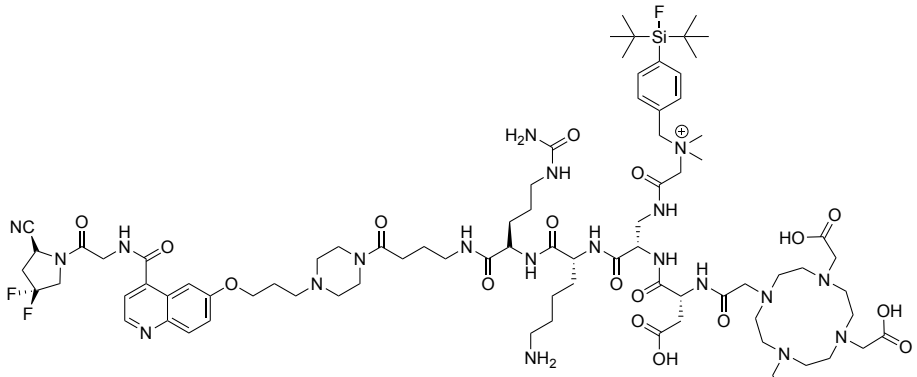

rhFAPI-20
Chemical Formula: $C_{82}H_{126}F_3N_{20}O_{19}Si^+$
Exact Mass: 1779,92
Molecular Weight: 1781,11

The synthesis of **rhFAPI-20** was started by resin loading (**GSP1**) with Fmoc-GABA-OH. After Fmoc-deprotection (**GSP3**), Fmoc-D-cit-OH, Fmoc-D-lys(Boc)-OH and Fmoc-D-dap(Dde)-OH were coupled following **GSP2**. The dap(NMe$_2$-Gly-SiFA*lin*) moiety was introduced as described in **GSP10**. After Fmoc-deprotection (**GSP3**) followed by coupling (**GSP2**) of Fmoc-D-asp(*t*Bu)-OH, the chelator was introduced by Fmoc-deprotection (**GSP3**) followed by coupling (**GSP2**) of DOTA(*t*Bu)$_3$. This peptidic building block was cleaved from the resin preserving all acid sensitive protection groups (**GSP7a**) and the crude product was purified by RP-HPLC (50 to 70% B in A in 30 min, t_R = 21.3 min). Concentration *in vacuo* and freeze drying provided a white solid (25%).
The received building block was coupled to the inhibitor following **GSP8**. After *t*Bu-/Boc-deprotection (**GSP6**), the crude product was purified by RP-HPLC (35 to 45% B in A in 30 min, t_R = 14.3 min). Concentration *in vacuo* and freeze drying provided **rhFAPI-20** as a white solid (27%).

RP-HPLC (10 to 90% B in 15 min): t_R = 7.8 min.
ESI-MS: Calculated monoisotopic mass ($C_{82}H_{126}F_3N_{20}O_{19}Si^+$): 1779.92; found: m/z = 1780.4 $[M+H]^+$, 890.3 $[M+2H]^{2+}$, 593.7 $[M+3H]^{3+}$.

Synthesis of rhFAPI-21 (FAPI-GABA-cit-e-k-dap(NMe$_2$-Gly-SiFA*lin*)-DOTA)

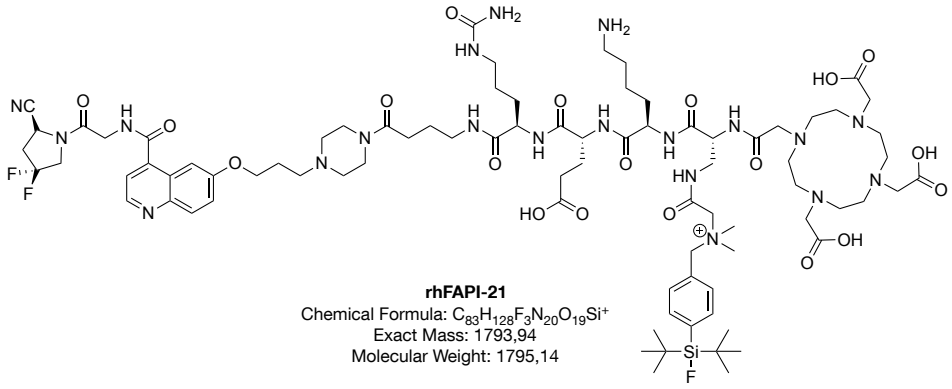

rhFAPI-21
Chemical Formula: $C_{83}H_{128}F_3N_{20}O_{19}Si^+$
Exact Mass: 1793,94
Molecular Weight: 1795,14

The synthesis of **rhFAPI-21** was started by resin loading (**GSP1**) with Fmoc-GABA-OH. After Fmoc-deprotection (**GSP3**), Fmoc-D-cit-OH, Fmoc-D-lys(Boc)-OH and Fmoc-D-dap(Dde)-OH were coupled following **GSP2**. The dap(NMe$_2$-Gly-SiFA*lin*) moiety was introduced as described in **GSP10**. After Fmoc-deprotection (**GSP3**) followed by coupling (**GSP2**) of Fmoc-D-asp(*t*Bu)-OH, the chelator was introduced by Fmoc-deprotection (**GSP3**) followed by coupling (**GSP2**) of DOTA(*t*Bu)$_3$. This peptidic building block was cleaved from the resin preserving all acid sensitive protection groups (**GSP7a**) and the crude product was purified by RP-HPLC (50 to 75% B in A in 30 min, t_R = 15.0 min). Concentration *in vacuo* and freeze drying provided a white solid (24%).
The received building block was coupled to the inhibitor following **GSP8**. After *t*Bu-/Boc-deprotection (**GSP6**), the crude product was purified by RP-HPLC (35 to 45% B in A in 30 min, t_R = 16.5 min). Concentration *in vacuo* and freeze drying provided **rhFAPI-21** as a white solid (33%).

RP-HPLC (10 to 90% B in 15 min): t_R = 7.85 min.
ESI-MS: Calculated monoisotopic mass ($C_{83}H_{128}F_3N_{20}O_{19}Si^+$): 1793.94; found: m/z = 1794.8 $[M+H]^+$, 898.0 $[M+2H]^{2+}$, 599.0 $[M+3H]^{3+}$.

3.2.2 General Synthesis Strategy and Structural Modification of transFAPI Ligands

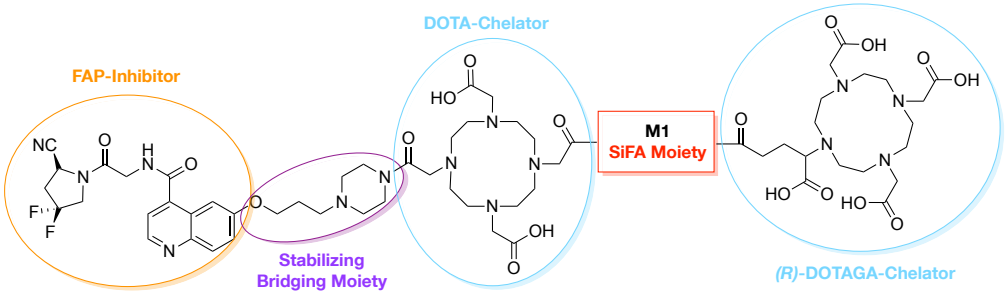

Figure 26: General structure of transFAPI ligands containing the shown FAP inhibitor (orange), stabilizing bridging moiety (purple) and a DOTA and (*R*)-DOTAGA chelator (turquoise) for metal complexation. The variable modification site **M1** is a symmetric SiFA moiety (red).

The general structure of transFAPI Ligands is shown in Figure 26, whereas their respective detailed structural modification sites are specified in Table 5. All ligands contain the (*R*)-*N*-(2-(2-cyano-4,4-difluoropyrrolidin-1-yl)-2-oxoethyl)quinoline-4-carboxamide based FAP-Inhibitor (orange) developed by *Jansen et al.*[105,106] and the 3-(piperazin-1-yl)propan-1-ol based stabilizing bridging moiety introduced by *Lindner et al.*[111,112] as well as a DOTA and (*R*)-DOTAGA chelator for complexation of two metals. Between the DOTA and (*R*)-DOTAGA chelator different symmetric SiFA moieties (**M1**, red) were introduced. These could be IPA-SiFA, DETA(SiFA) and DEMTA(SiFA*lin*).

Table 5: Listing of all transFAPI Ligands and their respective variable modification sites **M1**.

transFAPI Ligand	M1
transFAPI-01	EDA-IPA-SiFA-EDA
transFAPI-02	DETA(SiFA) **(18)**
transFAPI-03	DEMTA(SiFA*lin*) **(23)**

Synthesis of transFAPI-01 (FAPI-DOTA-EDA-IPA-SiFA-EDA-(*R*)-DOTAGA)

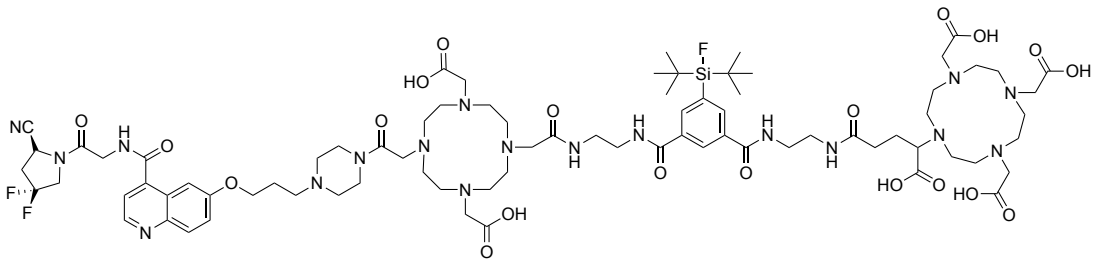

transFAPI-01
Chemical Formula: $C_{79}H_{117}F_3N_{18}O_{20}Si$
Exact Mass: 1722,84
Molecular Weight: 1723,99

The synthesis of **transFAPI-01** was started by resin loading (**GSP1**) with DOTA(*t*Bu)$_2$. After Fmoc-deprotection (**GSP3**), ethylenediamine (EDA) and **16** were coupled following **GSP2**.

Following an allyl-deprotection (**GSP5**) EDA was again coupled (**GSP2**) and the (*R*)-DOTAGA chelator was introduced by Fmoc-deprotection (**GSP3**) followed by coupling (**GSP2**) of (*R*)-DOTAGA(*t*Bu)$_4$. This peptidic building block was cleaved from the resin preserving all acid sensitive protection groups (**GSP7a**) and the crude product was purified by RP-HPLC (50 to 70% B in A in 30 min, t_R = 15.6 min). Concentration *in vacuo* and freeze drying provided a white solid (15%).
The received building block was coupled to the inhibitor following **GSP8**. After *t*Bu-/Boc-deprotection (**GSP6**), the crude product was purified by RP-HPLC (30 to 60% B in A in 30 min, t_R = 12.7 min). Concentration *in vacuo* and freeze drying provided **transFAPI-01** as a white solid (31%).

RP-HPLC (10 to 90% B in 15 min): t_R = 7.06 min.
ESI-MS: Calculated monoisotopic mass ($C_{79}H_{117}F_3N_{18}O_{20}Si$): 1722.84; found: m/z = 862.6 $[M+2H]^{2+}$, 575.4 $[M+3H]^{3+}$.

Synthesis of transFAPI-02 (FAPI-DOTA-DETA(SiFA)-(*R*)-DOTAGA)

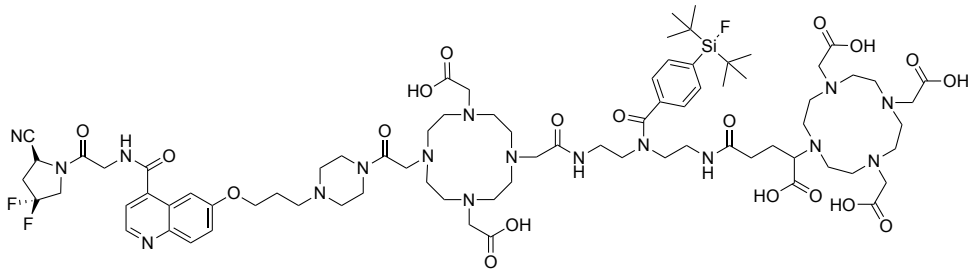

transFAPI-02
Chemical Formula: $C_{78}H_{116}F_3N_{17}O_{19}Si$
Exact Mass: 1679,84
Molecular Weight: 1680,97

The synthesis of **transFAPI-02** was started by resin loading (**GSP1**) with DOTA(*t*Bu)$_2$. After Fmoc-deprotection (**GSP3**), Fmoc-DETA(SiFA) was coupled following **GSP2**. Following a Fmoc-deprotection (**GSP3**) the (*R*)-DOTAGA chelator was introduced by coupling (**GSP2**) of (*R*)-DOTAGA(*t*Bu)$_4$. This peptidic building block was cleaved from the resin preserving all acid sensitive protection groups (**GSP7a**) and the crude product was purified by RP-HPLC (55 to 70% B in A in 30 min, t_R = 12.0 min). Concentration *in vacuo* and freeze drying provided a white solid (25%).
The received building block was coupled to the inhibitor following **GSP8**. After *t*Bu-/Boc-deprotection (**GSP6**), the crude product was purified by RP-HPLC (30 to 60% B in A in 30 min, t_R = 15.8 min). Concentration *in vacuo* and freeze drying provided **transFAPI-02** as a white solid (35%).

RP-HPLC (10 to 90% B in 15 min): t_R = 7.55 min.
ESI-MS: Calculated monoisotopic mass ($C_{78}H_{116}F_3N_{17}O_{19}Si$): 1679.84; found: m/z = 841.1 $[M+2H]^{2+}$, 561.2 $[M+3H]^{3+}$.

Synthesis of transFAPI-03 (FAPI-DOTA-DEMTA(SiFA*lin*)-(*R*)-DOTAGA)

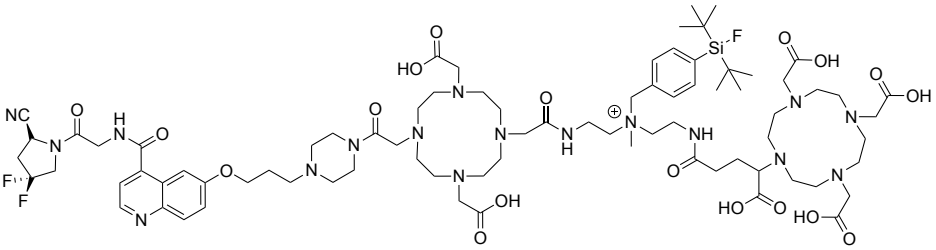

transFAPI-03
Chemical Formula: $C_{79}H_{121}F_3N_{17}O_{18}Si^+$
Exact Mass: 1680,88
Molecular Weight: 1682,02

The synthesis of **transFAPI-03** was started by resin loading (**GSP1**) with DOTA(*t*Bu)$_2$. After Fmoc-deprotection (**GSP3**), Fmoc-DEMTA(SiFA*lin*) was coupled following **GSP2**. Following a Fmoc-deprotection (**GSP3**) the (*R*)-DOTAGA chelator was introduced by coupling (**GSP2**) of (*R*)-DOTAGA(*t*Bu)$_4$. This peptidic building block was cleaved from the resin preserving all acid sensitive protection groups (**GSP7a**) and the crude product was purified by RP-HPLC (55 to 85% B in A in 30 min, t_R = 15.3 min). Concentration *in vacuo* and freeze drying provided a white solid (21%).
The received building block was coupled to the inhibitor following **GSP8**. After tBu-/Boc-deprotection (**GSP6**), the crude product was purified by RP-HPLC (30 to 60% B in A in 30 min, t_R = 19.2 min). Concentration *in vacuo* and freeze drying provided **transFAPI-03** as a white solid (25%).

RP-HPLC (10 to 90% B in 15 min): t_R = 7.74 min.
ESI-MS: Calculated monoisotopic mass ($C_{79}H_{121}F_3N_{17}O_{18}Si^+$): 1680.88; found: m/z = 1679.4 $[M+H]^+$, 840.0 $[M+2H]^{2+}$, 560.5 $[M+3H]^{3+}$.

3.2.3 General Synthesis Strategy and Structural Modifications of tecFAPI Ligands

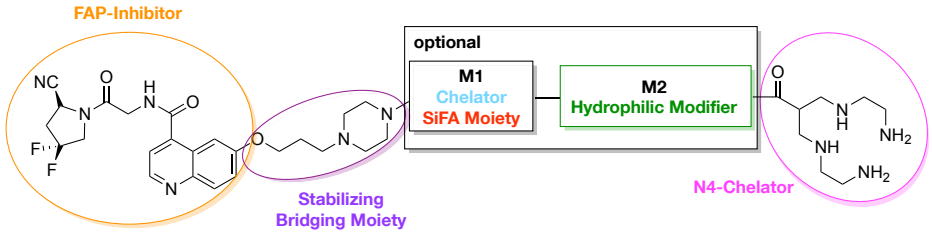

Figure 27: General structure of tecFAPI ligands containing the shown FAP inhibitor (orange), stabilizing bridging moiety (purple) and N4-chelator (pink) for complexation with ^{99m}Tc-technetium. The variable modification site **M1** is a SiFA moity (red) or a chelator (turquoise) for metal complexation and **M2** is a hydrophilic modifier (green).

The general structure of tecFAPI Ligands is shown in Figure 27, whereas their respective detailed structural modification sites are specified in Table 6. All ligands contain the (*R*)-*N*-(2-(2-cyano-4,4-difluoropyrrolidin-1-yl)-2-oxoethyl)quinoline-4-carboxamide based FAP-Inhibitor (orange) developed by *Jansen et al.*[105,106] and the 3-(piperazin-1-yl)propan-1-ol based stabilizing bridging moiety introduced by *Lindner et al.*[111,112] as well as N4 chelator (pink) for complexation of ^{99m}Tc-technetium at the *N*-terminus. Following the stabilizing bridging moiety, a chelator (**M1**, turquoise) or a SiFA moiety (**M1**, red) was introduced following a hydrophilic moiety (**M2**, green).

Table 6: Listing of all tecFAPI Ligands and their respective variable modification sites **M1** and **M2**.

tecFAPI Ligand	M1	M2
tecFAPI-01	-	-
tecFAPI-02	D-dap(SiFA)	-
tecFAPI-03	DOTA	D-asp-D-dap
tecFAPI-04	DOTA	D-asp-D-asp-D-dap
tecFAPI-05	DOTA	D-asp-D-asp-D-asp-D-dap

Synthesis of tecFAPI-01 (FAPI-N4)

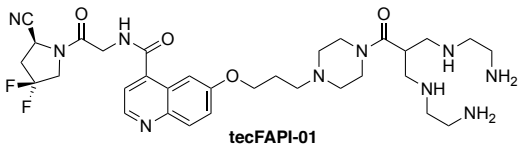

tecFAPI-01
Chemical Formula: $C_{32}H_{46}F_2N_{10}O_4$
Exact Mass: 672,37
Molecular Weight: 672,78

The synthesis of **tecFAPI-01** was carried out by coupling the N4 chelator to the FAP inhibitor following **GSP8**. After Boc-deprotection (**GSP6**), the crude product was purified by RP-HPLC (5 to 25% B in A in 30 min, t_R = 25.0 min). Concentration *in vacuo* and freeze drying provided **tecFAPI-01** as a white solid (7%).

RP-HPLC (10 to 30% B in 15 min): t_R = 8.01 min.
ESI-MS: Calculated monoisotopic mass ($C_{32}H_{46}F_2N_{10}O_4$): 672.37; found: m/z = 673.5 $[M+H]^+$, 337.1 $[M+2H]^{2+}$.

Synthesis of tecFAPI-02 (FAPI-d-dap(SiFA)-N4)

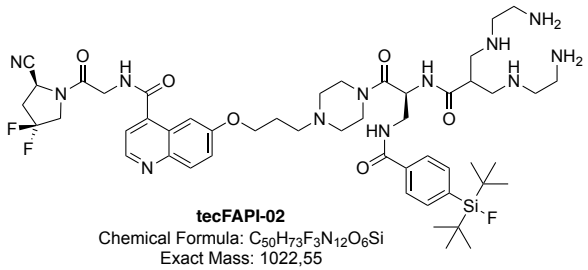

tecFAPI-02
Chemical Formula: $C_{50}H_{73}F_3N_{12}O_6Si$
Exact Mass: 1022,55
Molecular Weight: 1023,29

The synthesis of **tecFAPI-02** was started by resin loading (**GSP1**) with Fmoc-D-dap(Boc)-OH. After Dde-deprotection (**GSP4**) of the sidechain of D-dap, SiFA-BA was coupled (**GSP2**). The chelator was introduced by Fmoc-deprotection (**GSP3**) followed by coupling (**GSP2**) of $N4(Boc)_4$. This peptidic building block was cleaved from the resin preserving all acid sensitive protection groups (**GSP7a**) and the crude product was purified by RP-HPLC (85 to 100% B in A in 30 min, t_R = 11.8 min). Concentration *in vacuo* and freeze drying provided a white solid (7%).
The received building block was coupled to the inhibitor following **GSP8**. After *t*Bu-/Boc-deprotection (**GSP6**), the crude product was purified by RP-HPLC (10 to 70% B in A in 30 min, t_R = 25.2 min). Concentration *in vacuo* and freeze drying provided **tecFAPI-02** as a white solid (50%).

RP-HPLC (10 to 90% B in 15 min): t_R = 9.87 min.
ESI-MS: Calculated monoisotopic mass ($C_{50}H_{73}F_3N_{12}O_6Si$): 1022.55; found: m/z = 1023.6 $[M+H]^+$, 512.4 $[M+2H]^{2+}$.

Synthesis of tecFAPI-03 (FAPI-DOTA-d-dap-N4)

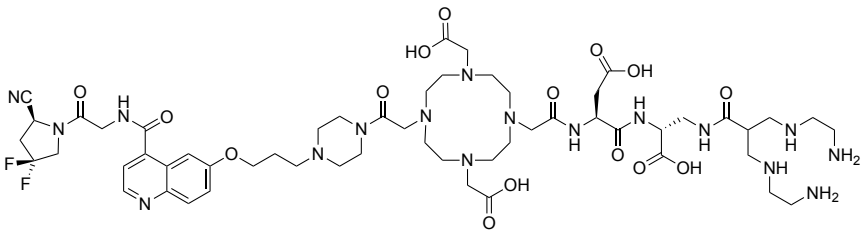

tecFAPI-03
Chemical Formula: $C_{55}H_{83}F_2N_{17}O_{15}$
Exact Mass: 1259,62
Molecular Weight: 1260,37

The synthesis of **tecFAPI-03** was started by resin loading (**GSP1**) with Fmoc-D-dap(Boc)-OH. Following Dde-deprotection (**GSP4**) of the sidechain of D-dap, the chelator N4 was introduced

by coupling of N4(Boc)$_4$ as described in **GSP2**. After Fmoc-deprotection (**GSP3**) Fmoc-D-asp(*t*Bu)-OH was coupled followed by another Fmoc-deprotection and coupling of the *trans-tert*-butyl protected FAPI-04 building block **28** as described in **GSP9**. The ligand was cleaved from the resin with simultaneous cleavage of all protection groups (**GSP7b**) and the crude product was purified by RP-HPLC (10 to 40% B in A in 30 min, t_R = 17.8 min). Concentration *in vacuo* and freeze drying provided **tecFAPI-03** as a white solid (13%).

RP-HPLC (10 to 30% B in 15 min): t_R = 7.081 min.
ESI-MS: Calculated monoisotopic mass ($C_{55}H_{83}F_2N_{17}O_{15}$): 1259.62; found: m/z = 1260.6 $[M+H]^+$, 630.8 $[M+2H]^{2+}$, 420.6 $[M+3H]^{3+}$.

Synthesis of tecFAPI-04 (FAPI-DOTA-d-d-dap-N4)

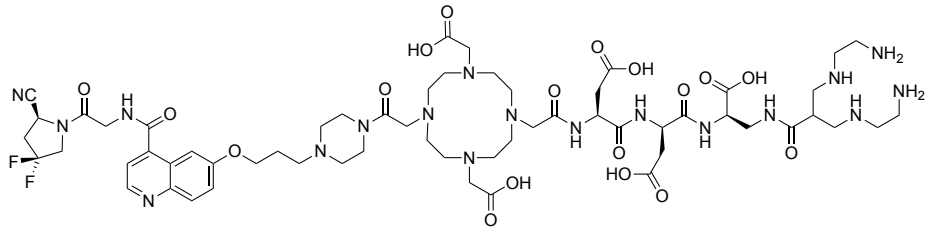

tecFAPI-04
Chemical Formula: $C_{59}H_{88}F_2N_{18}O_{18}$
Exact Mass: 1374,65
Molecular Weight: 1375,46

The synthesis of **tecFAPI-04** was started by resin loading (**GSP1**) with Fmoc-D-dap(Boc)-OH. Following Dde-deprotection (**GSP4**) of the sidechain of D-dap, the chelator N4 was introduced by coupling of N4(Boc)$_4$ as described in **GSP2**. After Fmoc-deprotection (**GSP3**), Fmoc-D-asp(*t*Bu)-OH was coupled and this step was repeating one time, followed by another Fmoc-deprotection, and coupling of the *trans-tert*-butyl protected FAPI-04 building block **28** as described in **GSP9**. The ligand was cleaved from the resin with simultaneous cleavage of all protection groups (**GSP7b**) and the crude product was purified by RP-HPLC (12 to 40% B in A in 30 min, t_R = 16.4 min). Concentration *in vacuo* and freeze drying provided **tecFAPI-04** as a white solid (6%).

RP-HPLC (10 to 30% B in 15 min): t_R = 6.77 min.
ESI-MS: Calculated monoisotopic mass ($C_{59}H_{88}F_2N_{18}O_{18}$): 1374.65; found: m/z = 1376.0 $[M+H]^+$, 688.5 $[M+2H]^{2+}$, 459.4 $[M+3H]^{3+}$.

Synthesis of tecFAPI-05 (FAPI-DOTA-d-d-d-dap-N4)

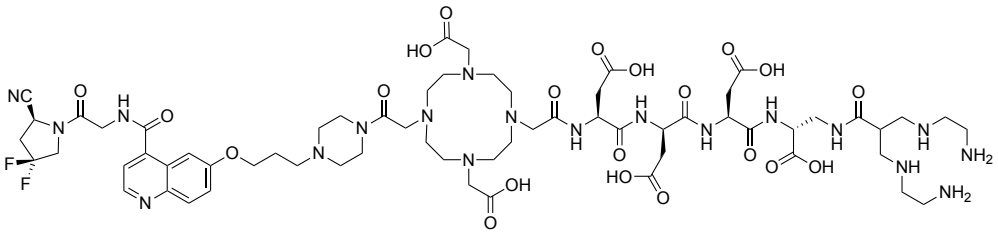

tecFAPI-05
Chemical Formula: $C_{63}H_{93}F_2N_{19}O_{21}$
Exact Mass: 1489,68
Molecular Weight: 1490,55

The synthesis of **tecFAPI-05** was started by resin loading (**GSP1**) with Fmoc-D-dap(Boc)-OH. Following Dde-deprotection (**GSP4**) of the sidechain of D-dap, the chelator N4 was introduced by coupling of N4(Boc)$_4$ as described in **GSP2**. After Fmoc-deprotection (**GSP3**), Fmoc-D-asp(*t*Bu)-OH was coupled and this step was repeating two times, followed by another Fmoc-deprotection, and coupling of the *trans*-*tert*-butyl protected FAPI-04 building block **28** as described in **GSP9**. The ligand was cleaved from the resin with simultaneous cleavage of all protection groups (**GSP7b**) and the crude product was purified by RP-HPLC (12 to 40% B in A in 30 min, t_R = 16.1 min). Concentration *in vacuo* and freeze drying provided **tecFAPI-05** as a white solid (18%).

RP-HPLC (10 to 30% B in 15 min): t_R = 6.91 min.
ESI-MS: Calculated monoisotopic mass ($C_{63}H_{93}F_2N_{19}O_{21}$): 1489.68; found: m/z = 745.9 $[M+2H]^{2+}$, 497.8 $[M+3H]^{3+}$.

3.2.4 Synthesis of Cold Metal Complexes of FAPI Ligands

Synthesis of ^{nat}Ga-DOTA and ^{nat}Ga-(*R*)-DOTAGA Complexes (GSP11)

For ^{nat}Ga-complexation 100 µL of a 2 mM rhFAPI precursor solution (1.0 eq.) in DMSO were combined with 10 µL of a 20 mM $Ga(NO_3)$ solution (1.5 eq.) in water (Tracepur®, Merck, Darmstadt, Germany). After filling up DMSO to achieve a concentration of 1 mM the reaction mixture was heated for 30 min at 75° C. Outcome of the reaction was monitored by RP-HPLC and subsequent mass spectrometry. If required, the complexed ligand was purified by RP-HPLC. Upscale complexations were carried out by maintaining the used concentrations and equivalents.

[^{nat}Ga]Ga-rhFAPI-04: RP-HPLC (10 to 90% B in 15 min): t_R = 8.3 min. ESI-MS: Calculated monoisotopic mass ($C_{74}H_{99}F_3GaN_{15}O_{23}Si$): 1721.49; found: m/z = 1722.5 $[M+H]^+$, 861.3 $[M+2H]^{2+}$.
[^{nat}Ga]Ga-rhFAPI-04+E: RP-HPLC (10 to 90% B in 15 min): t_R = 8.2 min. ESI-MS: Calculated monoisotopic mass ($C_{79}H_{106}F_3GaN_{16}O_{26}Si$): 1850.61; found: m/z = 1851.3 $[M+H]^+$, 926.3 $[M+2H]^{2+}$.
[^{nat}Ga]Ga$_2$-transFAPI-01: RP-HPLC (10 to 90% B in 15 min): t_R = 7.32 min. ESI-MS: Calculated monoisotopic mass ($C_{79}H_{114}F_3Ga_2N_{18}O_{20}Si$): 1857.67; found: m/z = 1859.8 $[M+H]^+$, 929.5 $[M+2H]^{2+}$, 620.0 $[M+3H]^{3+}$.
[^{nat}Ga]Ga$_2$-transFAPI-02: RP-HPLC (10 to 90% B in 15 min): t_R = 7.320 min. ESI-MS: Calculated monoisotopic mass ($C_{78}H_{112}F_3Ga_2N_{17}O_{19}Si$): 1813.66; found: m/z = 1814.4 $[M+H]^+$, 907.8 $[M+2H]^{2+}$, 605.6 $[M+3H]^{3+}$.
[^{nat}Ga]Ga$_2$-transFAPI-03: RP-HPLC (10 to 90% B in 15 min): t_R = 7.82 min. ESI-MS: Calculated monoisotopic mass ($C_{79}H_{116}F_3Ga_2N_{17}O_{18}Si$): 1813.70; found: m/z = 907.2 $[M+2H]^{2+}$, 605.1 $[M+3H]^{3+}$.
[^{nat}Ga]Ga-tecFAPI-03: RP-HPLC (10 to 30% B in 15 min): t_R = 7.3 min. ESI-MS: Calculated monoisotopic mass ($C_{55}H_{81}F_2GaN_{17}O_{15}$): 1326.53; found: m/z = 1328.4 $[M+H]^+$, 664.1 $[M+2H]^{2+}$, 443.2 $[M+3H]^{3+}$.
[^{nat}Ga]Ga-tecFAPI-04: RP-HPLC (10 to 60% B in 15 min): t_R = 7.3 min. ESI-MS: Calculated monoisotopic mass ($C_{59}H_{86}F_2GaN_{18}O_{18}$): 1441.56; found: m/z = 1443.0 $[M+H]^+$, 722.3 $[M+2H]^{2+}$, 481.6 $[M+3H]^{3+}$.
[^{nat}Ga]Ga-tecFAPI-05: RP-HPLC (10 to 30% B in 15 min): t_R = 7.2 min. ESI-MS: Calculated monoisotopic mass ($C_{63}H_{91}F_2GaN_{19}O_{21}$) 1556.59; found: m/z = 779.6 $[M+2H]^{2+}$, 520.0 $[M+3H]^{3+}$.

Synthesis of ^{nat}Lu-DOTA and ^{nat}Lu-(*R*)-DOTAGA Complexes (GSP12)

The corresponding ^{nat}Lu-complexes were prepared with 100 µL of a 2 mM rhFAPI precursor solution (1.0 eq.) in DMSO and 5 µL of a 20 mM $LuCl_3$ solution (1.5 eq.) in water (Tracepur®, Merck, Darmstadt, Germany). After filling up DMSO to achieve a concentration of 1 mM the reaction mixture was heated for 30 min at 90° C. Formation of the ^{nat}Lu-complexe was confirmed using RP-HPLC and MS. If required, the complexed ligand was purified by RP-

HPLC. Upscale complexations were carried out by maintaining the used concentrations and equivalents.

[^{nat}Lu]Lu-rhFAPI-01: RP-HPLC (10 to 90% B in 15 min): t_R = 8.477 min. ESI-MS: Calculated monoisotopic mass ($C_{78}H_{112}F_3LuN_{18}O_{20}Si$): 1880.74; found: m/z = 1882.4 $[M+H]^+$, 941.5 $[M+2H]^{2+}$, 628.0 $[M+3H]^{3+}$.
[^{nat}Lu]Lu-rhFAPI-02: RP-HPLC (10 to 90% B in 15 min): t_R = 8.511 min. ESI-MS: Calculated monoisotopic mass ($C_{78}H_{111}F_3LuN_{19}O_{21}Si$): 1909.73; found: m/z = 1911.4 $[M+H]^+$, 956.1 $[M+2H]^{2+}$, 637.8 $[M+3H]^{3+}$.
[^{nat}Lu]Lu-rhFAPI-03: RP-HPLC (10 to 90% B in 15 min): t_R = 8.122 min. ESI-MS: Calculated monoisotopic mass ($C_{76}H_{113}F_3LuN_{17}O_{19}Si$): 1851.75; found: m/z = 1853.3 $[M+H]^+$, 927.0 $[M+2H]^{2+}$, 618.4 $[M+3H]^{3+}$.
[^{nat}Lu]Lu-rhFAPI-04: RP-HPLC (10 to 90% B in 15 min): t_R = 8.7 min. ESI-MS: Calculated monoisotopic mass ($C_{74}H_{99}F_3LuN_{15}O_{23}Si$): 1825.49; found: m/z = 1826.5 $[M+H]^+$, 913.7 $[M+2H]^{2+}$.
[^{nat}Lu]Lu-rhFAPI-04+E: RP-HPLC (10 to 90% B in 15 min): t_R = 8.6 min. ESI-MS: Calculated monoisotopic mass ($C_{79}H_{106}F_3GaN_{16}O_{26}Si$): 1955.85; found: m/z = 1956.2 $[M+H]^+$, 978.5 $[M+2H]^{2+}$.
[^{nat}Lu]Lu-rhFAPI-05: RP-HPLC (10 to 90% B in 15 min): t_R = 8.5 min. ESI-MS: Calculated monoisotopic mass ($C_{77}H_{112}F_3LuN_{18}O_{18}Si$): 1835.75; found: m/z = 1836.9 $[M+H]^+$, 919.3 $[M+2H]^{2+}$, 613.3 $[M+3H]^{3+}$.
[^{nat}Lu]Lu-rhFAPI-06: RP-HPLC (10 to 90% B in 15 min): t_R = 8.8 min. ESI-MS: Calculated monoisotopic mass ($C_{77}H_{111}F_3LuN_{19}O_{19}Si$): 1865.90; found: m/z = 1865.8 $[M+H]^+$, 933.7 $[M+2H]^{2+}$, 622.6 $[M+3H]^{3+}$.
[^{nat}Lu]Lu-rhFAPI-07: RP-HPLC (10 to 90% B in 15 min): t_R = 8.1 min. ESI-MS: Calculated monoisotopic mass ($C_{77}H_{113}F_3LuN_{17}O_{17}Si$): 1807.90; found: m/z = 1807.7 $[M+H]^+$, 904.6 $[M+2H]^{2+}$, 603.3 $[M+3H]^{3+}$.
[^{nat}Lu]Lu-rhFAPI-08: RP-HPLC (10 to 90% B in 15 min): t_R = 10.708 min. ESI-MS: Calculated monoisotopic mass ($C_{73}H_{99}F_3LuN_{15}O_{21}Si$): 1781.63; found: m/z = 1783.1 $[M+H]^+$, 892.0 $[M+2H]^{2+}$.
[^{nat}Lu]Lu-rhFAPI-09: RP-HPLC (10 to 90% B in 15 min): t_R = 8.5 min. ESI-MS: Calculated monoisotopic mass ($C_{71}H_{101}F_3LuN_{17}O_{17}Si$): 1723.74; found: m/z = 1724.0 $[M+H]^+$, 862.5 $[M+2H]^{2+}$, 575.3 $[M+3H]^{3+}$.
[^{nat}Lu]Lu-rhFAPI-10: RP-HPLC (10 to 90% B in 15 min): t_R = 9.0 min. ESI-MS: Calculated monoisotopic mass ($C_{71}H_{99}F_3LuN_{15}O_{19}Si$): 1725.71; found: m/z = 1726.3 $[M+H]^+$, 863.9.5 $[M+2H]^{2+}$.
[^{nat}Lu]Lu-rhFAPI-11: RP-HPLC (10 to 90% B in 15 min): t_R = 8.9 min. ESI-MS: Calculated monoisotopic mass ($C_{73}H_{101}F_3LuN_{17}O_{19}Si$): 1779.76; found: m/z = 1780.0 $[M+H]^+$, 891.0 $[M+2H]^{2+}$, 594.3 $[M+3H]^{3+}$.
[^{nat}Lu]Lu-rhFAPI-12: RP-HPLC (10 to 90% B in 15 min): t_R = 11.456 min. ESI-MS: Calculated monoisotopic mass ($C_{75}H_{103}F_3LuN_{15}O_{21}Si$): 1809.66; found: m/z = 1811.3 $[M+H]^+$, 906.1 $[M+2H]^{2+}$.

[^{nat}Lu]Lu-rhFAPI-13: RP-HPLC (10 to 90% B in 15 min): t_R = 8.5 min. ESI-MS: Calculated monoisotopic mass ($C_{77}H_{112}F_3LuN_{18}O_{18}Si$): 1835.75; found: m/z = 1837.1 $[M+H]^+$, 919.3 $[M+2H]^{2+}$, 613.2 $[M+3H]^{3+}$.

[^{nat}Lu]Lu-rhFAPI-14: RP-HPLC (10 to 90% B in 15 min): t_R = 8.7 min. ESI-MS: Calculated monoisotopic mass ($C_{74}H_{106}F_3LuN_{18}O_{18}Si$): 1794.82; found: m/z = 1794.8 $[M+H]^+$, 898.1 $[M+2H]^{2+}$, 599.1 $[M+3H]^{3+}$.

[^{nat}Lu]Lu-rhFAPI-15: RP-HPLC (10 to 90% B in 15 min): t_R = 8.7 min. ESI-MS: Calculated monoisotopic mass ($C_{74}H_{106}F_3LuN_{18}O_{18}Si$): 1794.82; found: m/z = 1795.1 $[M+H]^+$, 898.3 $[M+2H]^{2+}$, 599.2 $[M+3H]^{3+}$.

[^{nat}Lu]Lu-rhFAPI-16: RP-HPLC (10 to 90% B in 15 min): t_R = 8.756 min. ESI-MS: Calculated monoisotopic mass ($C_{75}H_{105}F_3LuN_{17}O_{20}Si$): 1823.69; found: m/z = 1825.3 $[M+H]^+$, 913.0 $[M+2H]^{2+}$, 609.0 $[M+3H]^{3+}$.

[^{nat}Lu]Lu-rhFAPI-17: RP-HPLC (10 to 90% B in 15 min): t_R = 8.115 min. ESI-MS: Calculated monoisotopic mass ($C_{81}H_{122}F_3LuN_{19}O_{18}Si$): 1908.83; found: m/z = 1909.9 $[M+H]^+$, 955.1 $[M+2H]^{2+}$, 637.1 $[M+3H]^{3+}$.

[^{nat}Lu]Lu-rhFAPI-18: RP-HPLC (10 to 90% B in 15 min): t_R = 7.861 min. ESI-MS: Calculated monoisotopic mass ($C_{78}H_{118}F_3LuN_{19}O_{16}Si$): 1836.81; found: m/z = 1837.9 $[M+H]^+$, 919.2 $[M+2H]^{2+}$, 613.1 $[M+3H]^{3+}$.

[^{nat}Lu]Lu-rhFAPI-19: RP-HPLC (10 to 90% B in 15 min): t_R = 8.4 min. ESI-MS: Calculated monoisotopic mass ($C_{76}H_{111}F_3LuN_{18}O_{18}Si$): 1823.74; found: m/z = 912.2 $[M+2H]^{2+}$.

[^{nat}Lu]Lu-rhFAPI-20: RP-HPLC (10 to 90% B in 15 min): t_R = 7.8 min. ESI-MS: Calculated monoisotopic mass ($C_{82}H_{123}F_3LuN_{20}O_{19}Si$): 1956.12; found: m/z = 976.0 $[M+2H]^{2+}$.

[^{nat}Lu]Lu-rhFAPI-21: RP-HPLC (10 to 90% B in 15 min): t_R = 7.848 min. ESI-MS: Calculated monoisotopic mass ($C_{83}H_{125}F_3LuN_{20}O_{19}Si$): 1965.86; found: m/z = 1966.6 $[M+H]^+$, 984.0 $[M+2H]^{2+}$, 656.2 $[M+3H]^{3+}$.

[^{nat}Lu]Lu$_2$-transFAPI-01: RP-HPLC (10 to 90% B in 15 min): t_R = 7.69 min. ESI-MS: Calculated monoisotopic mass ($C_{79}H_{112}F_3Lu_2N_{18}O_{20}Si$): 2067.68; found: m/z = 1034.5 $[M+2H]^{2+}$, 690.1 $[M+3H]^{3+}$.

[^{nat}Lu]Lu$_2$-transFAPI-02: RP-HPLC (10 to 90% B in 15 min): t_R = 8.31 min. ESI-MS: Calculated monoisotopic mass ($C_{78}H_{111}F_3Lu_2N_{17}O_{19}Si$): 2024.68; found: m/z = 1012.9 $[M+2H]^{2+}$, 675.6 $[M+3H]^{3+}$.

[^{nat}Lu]Lu$_2$-transFAPI-03: RP-HPLC (10 to 90% B in 15 min): t_R = 8.62 min. ESI-MS: Calculated monoisotopic mass ($C_{79}H_{116}F_3Lu_2N_{17}O_{18}Si$): 2025.72; found: m/z = 1011.8 $[M+2H]^{2+}$, 675.0 $[M+3H]^{3+}$.

[^{nat}Lu]Lu-tecFAPI-03: RP-HPLC (10 to 30% B in 15 min): t_R = 7.4 min. ESI-MS: Calculated monoisotopic mass ($C_{55}H_{81}F_2LuN_{17}O_{15}$): 1432.55; found: m/z = 716.7 $[M+2H]^{2+}$, 478.2 $[M+3H]^{3+}$.

3.3 Radiolabeling

3.3.1 General Information for Radiolabeling

Aqueous fluoride-18 (approx. 0.6-2.0 GBq/mL) for manual ^{18}F-labeling was provided by the *Klinikum rechts der Isar* (Munich, Germany). For ^{177}Lu-labeling $^{177}LuCl_3$ (specific activity (S_A) > 3000 GBq/mg, 740 MBq/mL, 0.04 M HCl) from *ITG* (Garching, Germany) was used. Measurement of pH values were conducted with a SevenEasy pH-meter from *Mettler Toledo* (Gießen, Germany). Radio-thin layer chromatography (TLC) was carried out using silica gel coated aluminium (silica gel 60 RP-18 F_{254S}) or cellulose from *Agilent Technologies* (Waldbronn, Germany) as stationary phase. A 3:2 mixture (*v/v*) of MeCN in water, supplemented with 10% of 2 m NaOAc solution and 1% of TFA, or a 0.1 M aqueous citrate solution was used as mobile phase. Analysis of radio-TLC was carried out with a Scan-RAM detector from *LabLogic* (Sheffield, United Kingdom) using the corresponding *Laura* software. Analytical and preparative radio-HPLC was performed using Shimadzu gradient systems (*Shimadzu*, Neufahrn, Germany) which have been previously described. Radioactivity was detected through connection of the outlet of the UV-photometer to a HERM LB 500 NaI detector from *Berthold Technologies* (Bad Wildbad, Germany).

3.3.2 ^{18}F-Labeling

^{18}F-Labeling *via* Munich Method (GSP13)

Manual ^{18}F-labeling was conducted following a previously published method with minor modifications.[154,186,199,217] Aqueous fluoride-18 was passed through a SAX cartridge (Sep-Pak Accell Plus QMA Carbonate Plus Light, 46 mg, 40 µg, Waters), which first was preconditioned with 10 mL of water. After removing most of the water by passing 20 mL air through the cartridge, residual water was removed by rinsing with 10 mL of anhydrous acetonitrile (for DNA synthesis, max. 10 ppm H_2O, VWR) followed by 20 mL of air. A solution of $[K^+\subset 2.2.2]OH^-$ cryptate in 500 µL of anhydrous acetonitrile was used for cartridge elution, which was freshly prepared by dissolution of lyophilized cryptate prior to the elution process. The cryptate was prepared by lyophilization of a solution of 2.2.2-cryptand (Kryptofix® 222, 91 µmol, 1.1 eq., Sigma Aldrich) and KOH (83 µmol, 1.0 eq., 99.99% semiconductor grade, Sigma Aldrich) in 1.0 mL of water.

The eluate was partly neutralized with 30 µL of a 1 M solution of oxalic acid (99.999%, trace metals basis, Sigma Aldrich) in anhydrous acetonitrile. The labeling solution (eluate and oxalic acid) or an aliquot thereof was used for fluorination of 10-150 nmol of respective SiFA-conjugated labeling precursor (1 mM solutions in anhydrous DMSO, > 99.9%, Sigma Aldrich) for 5 min at rt. Purification by solid phase extraction was conducted with Oasis HLB Plus Light cartridges (30 mg, 30 µL, Waters) preconditioned with 10 mL of ethanol and 10 mL of water. The labeling mixture was diluted with 9 mL PBS (pH 3, adjusted with 1 M aq. HCl) and passed through the cartridge followed by 10 mL PBS (pH 5) and 10 mL of air. The labeled product and the unlabeled precursor were eluted from the HLB cartridge with 0.3–2.0 mL of a 1:1

mixture (*v*/*v*) of EtOH and water. Radiochemical purity of the ^{18}F-labeled compound was determined by radio-RP-HPLC and radio-TLC.

^{18}F-Labeling *via* Di Carlo Method (GSP14)

Manual ^{18}F-labeling of ligands, which showed building of byproducts through labeling following **GSP13**, were performed using a modified protocol based on the *Munich Method*. Prior to ^{18}F-labeling, an elution cocktail kit was prepared by dissolving ammonium formate (40.0 mg) in anhydrous DMSO. In order to obtain dry labeling conditions for radio fluorination, aq. fluoride-18 was retained onto a SAX cartridge (Sep-Pak Accell Plus QMA Carbonate Plus Light, 46 mg, 40 µg, Waters), which was preconditioned with water (10 mL). After drying with air (2 × 20 mL), the cartridge was slowly rinsed with anhydrous DMSO (8 mL) and subsequently dried with air (2 × 20 mL) again. Dried fluoride-18 was eluted from the cartridge using the previously prepared elution cocktail kit. The eluate was incubated with an anhydrous DMSO solution of the SiFA-bearing compound (1 mM, 0.5 – 150 nmol, 0.5 – 150 µL) for 10 min at a ligand specific temperature between rt and 95°C. The reaction mixture was further diluted with PBS (pH 3, adjusted with 1 M aq. HCl, 10 mL) and passed through an Oasis HLB Plus Light cartridge (30 mg sorbent, 30 µm particle size) previously preconditioned with abs. EtOH (10 mL) and water (10 mL). Finally, the cartridge was rinsed with PBS (10 mL) and dried with air (20 mL), followed by the elution of the radio fluorinated compound with a mixture of abs. EtOH and PBS (1:1, *v*/*v*, 300 µL).

3.3.3 ^{177}Lu-Labeling (GSP15)

Labeling with lutetium-177 was conducted following a previously published procedure with minor modifications.[218,219] The labeling precursor (e.g., rhFAPI ligand, 1.0 nmol, 1.0 µL, 1 mM in DMSO) was added to 10 µL of 1.0 M aq. NaOAc buffer (pH 4.5). Subsequently, 10 to 50 MBq $^{177}LuCl_3$ were added and the mixture was filled up to a total volume of 100 µL with 0.04 M HCl. The labeling mixture was heated for 15 to 30 min at 95 °C and the radiochemical purity was determent using radio-RP-HPLC and radio-TLC. To prevent radiolysis 10% (*v*/*v*, 10 µL) of a 0.1 M sodium ascorbate solution was added to the labeling product.

3.3.4 ^{99m}Tc-Labeling (GSP16)

The labeling with technetium-99m was based on a procedure published by *Nock et al*.[220] A variable volume of 0.05 M Na_2HPO_4 buffer (pH 9.24), depending on the used peptide, 3 µL of 0.1 M $Na_2Cit{\cdot}1.5\ H_2O$ in H_2O, 5 µL of a freshly prepared solution of $SnCl_2$ (1 mg/mL) and sodium ascorbate (3 mg/mL) in 0.01 M HCL and 7.5 µL 1 mM peptide solution in DMSO were prepared in a protein LoBind Eppendorfer reaction tube. 0.5-1.0 mL (45-100 MBq) ^{99m}Tc-eluate in 0.9 w% NaCl in H_2O were added. Complexation was carried out for 10 min at 95 °C. Reaction control was performed via radio-TLC with 0.9 w% NaCl as eluant, radio-RP-TLC with sat. NH_4Cl/DMF (3/1, *v*/*v*) as eluant and radio-RP-HPLC (1-2 MBq complexation solution with a gradient of 10-90% B in 15 min).

3.4 *In Vitro* Experiments

3.4.1 General Information for *In Vitro* Experiments

Cells were cultivated in a HERAcell 150i incubator from *Thermo Fisher Scientific* (Waltham, United States). All cell preparations were conducted with a sterile laminar flow hood from *Thermo Fisher Scientific* (Waltham, United States). All equipment used in the laminar flow hood were previously sterilized in a Varioklav 400-E autoclave from *H+P Labortechnik AG* (Oberschleißheim, Germany). To supervise the cell grows and to determine the cell number an adjustable Inverse microscope AE 2000 from *Motic Deutschland GmbH* (Wetzlar, Germany) was used. Precipitation of cells to pellets were done using a Heraeus Megafuge 16R centrifuge from *Thermo Fisher Scientific* (Waltham, United States). Activity quantification was performed using a 2480 WIZARD^2 automatic gamma counter from *PerkinElmer* (Waltham, Unites States).

3.4.2 Cell Culture

For all cell-based experiments the stably FAP-transfected fibrosarcoma cell line HT-1080hFAP was used, which was kindly provided by Prof. Uwe Haberkorn from the Department of Nuclear Medicine at University of Heidelberg. The cells were cultivated in Dulbecco's modified Eagle's medium (DMEM, *Thermo Fisher Scientific*, Waltham, United States) with GlutaMAX supplementals containing 10% fetal bovine serum (FBS, *FBS Zellkultur*, Berlin, Germany) at 37 °C in a humidified CO_2 atmosphere (5%). A mixture of trypsin and EDTA (0.05%, 0.02%) in phosphate buffered saline (PBS, *Biochrom,* Berlin, Germany) was used in order to harvest cells. Cells were counted with a Neubauer hemocytometer (*Paul Marienfeld*, Lauda-Königshofen, Germany). If not stated otherwise, all cell-based experiments were performed in 24-well plates with a final confluence of 80-100%.

3.4.3 Affinity Determination (IC_{50})

Determination of IC_{50}

Quantification of the binding affinity to FAP was measured by determination of the half-maximal inhibitory concentration (IC_{50}) of each inhibitor using [^{177}Lu]Lu-FAPI-04 as radioactive reference ligand. Therefore, the respective ligand was diluted (serial dilution 10^{-4} to 10^{-10} M) in Hank´s balanced salt solution (HBSS, *Biochrom*) containing 1% (*v/v*) bovine serum albumin (BSA, *Biowest*, Nuaillé, France). In the case of metal-complexed ligands, the crude complexation mixture containing the purified metal-complexed inhibitor and remaining metal chloride/nitrate was diluted analogously without further purification. Cells were harvested 24 ± 2 h prior to the experiment and seeded into 24-well plates (2.5×10^5 cells in 1 mL/well). Following the removal of the culture medium, the cells were carefully washed with 500 µL of DMEM and left on ice for 15 min in 200 µL DMEM to equilibrate. Afterwards, 25 µL per well of solution containing either HBSS (1% BSA, control) or the respective ligand in increasing concentration (10^{-10} to 10^{-4} M in HBSS with 1% BSA) were added with subsequent addition of 25 µL of [^{177}Lu]Lu-FAPI-04 (0.7 pmol/well, SA: 40 GBq/µmol) in DMEM. Following incubation on ice for 120 min, the experiment was terminated by removal of the medium and consecutive

rinsing with 250 µL of ice-cold PBS. The medium of both steps was combined in one fraction and represent the amount of free radioligand. Next, the cells were lysed with 250 µL of 1 M aq. NaOH for at least 15 min. After removing the lysate and a consecutive washing step (250 µL of 1 M aq. NaOH), both fractions representing the amount of bound ligand were combined. Quantification of all collected fractions was accomplished in a gamma counter. All IC_{50} experiments were carried out with at least threefold repetition per ligand.

Determination of Inverse IC_{50}

The measurement of inverse IC_{50} values of each inhibitor was performed analog to the determination of classic IC_{50} values and was used to test ^{99m}Tc-labeled inhibitors as there is no non-radioactive technetium isotope for cold metal-complexation of tecFAPI ligands. The difference of both methods was the concentration of the reference ligand Lu-FAPI-04, the concentration of the tested inhibitor and which compound was labeled radioactively. For inverse IC_{50} determination the reference ligand FAPI-04 was complexed with cold lutetium and diluted (serial dilution 10^{-4} to 10^{-10} M) in HBSS containing 1% (*v*/*v*) BSA. The 25 µL per well of the reference ligand in increasing concentration (10^{-10} to 10^{-4} M in HBSS with 1% BSA) were added to a 24-well plate with subsequent addition of 25 µL of [^{99m}Tc]Tc-tecFAPI ligand (0.7 pmol/well, SA: 40 GBq/µmol) in DMEM. All previous and following steps were performed analogous to the determination of the standard IC_{50}.

3.4.4 Cell Uptake and Internalization Studies

Quantification of the cell uptake and internalization of FAP-addressing ligands was measured for each inhibitor using [^{177}Lu]Lu-FAPI-04 as radioactive reference Ligand. Therefore, the respective ligand was solved in HBSS containing 1% (*v*/*v*) BSA. In the case of metal-complexed ligands, the crude complexation mixture containing the purified metal-complexed inhibitor and remaining metal chloride/nitrate was diluted analogously without further purification. Cells were harvested 24 ± 2 h prior to the experiment and seeded into 24-well plates (2.5×10^5 cells in 1 mL/well). Following the removal of the culture medium, the cells were carefully washed with 500 µL of DMEM and left on ice for 15 min in 225 µL DMEM to equilibrate. Afterwards, 25 µL per well solution containing 0.7 pmol of the respective radiolabeled ligand or the reference [^{177}Lu]Lu-FAPI-04 were added to 6 wells per compound onto three different plates. For incubation, the plates were transferred into the incubator at 37 °C. Incubation time differs for each plate (30 min, 60 min and 120 min). Following incubation each plate was put on ice and the experiment was terminated by removal of the medium and consecutive rinsing with 250 µL of ice-cold PBS. The medium of both steps was combined in one fraction and represent the amount of free radioligand. Afterwards, 250 µL acid wash solution (1 M glycine-HCL, pH 2.2) are added per well. After 10 min on ice, the acid wash was terminated by removal of the solution and consecutive rinsing with 250 µL of ice-cold PBS. The solution of both steps was combined in one fraction and represent the amount of cell surface bound ligand. Next, the cells were lysed with 250 µL of 1 M aq. NaOH for at least 15 min. After removing the lysate and a consecutive washing step (250 µL of 1 M aq. NaOH), both fractions representing the amount of internalized ligands were combined. Quantification of all collected fractions was accomplished in a gamma counter.

3.4.5 *n*-Octanol-PBS Partition Coefficient

Determination of lipophilicity was conducted by dissolving approximately 1 MBq of the labeled tracer in 1 mL of a 1:1 mixture (*v/v*) of *n*-octanol and PBS in a reaction vial (1.5 mL). After intensive mixing of the suspension for 3 min at rt, the vials were centrifuged at 9000 rpm for 5 min. Subsequently, 100 µL aliquots of both phases were taken and measured in a gamma counter. The experiment was repeated at least eight times and a log $D_{7.4}$ value was determined for each tracer.

3.4.6 Determination of Human Serum Albumin Binding

HSA Column Method

Binding of FAP-addressing tracers to human serum albumin (HSA) was determined following a previously published procedure *via* high performance affinity chromatography (HPAC).[221] A Chiralpak HSA column (50 × 3 mm, 5 µm, H13H-2433, *Daicel*, Tokyo, Japan) was used with a constant flow rate of 0.5 mL/min at rt. Eluent A was a freshly prepared 50 mM aqueous solution of NH_4OAc (pH 6.9) and eluent B was isopropanol (HPLC grade). The applied gradient for all experiments was 100% A (0 to 3 min), followed by 80% A (3 to 40 min). Before carrying out an experiment the column was calibrated using nine reference substances with known HSA binding in the range of 13 to 99%.[221,222] Calibration substances and investigated FAPI tracers were dissolved in a 1:1 mixture (*v/v*) of A and B with a final concentration of 0.5 mg/mL. Non-linear regression was calculated with the OriginPro 2016G software (Northampten, United States) as shown in Table 7 and Figure 28.

Table 7: The HSA binding values were obtained from literature (lit. HSA [%]) and the respective logarithmic value of the affinity constant (log K HSA) was calculated.[221,222] Log t_R: logarithmic value of experimentally determined retention time. K': capacity factor.

reference	t_R	K'	log t_R	Lit. HSA [%]	Log K HSA
p-benzyl alcohol	2.50	0.25	0.40	13.15	-0.82
aniline	2.83	0.42	0.45	14.06	-0.79
phenol	3.35	0.68	0.52	20.69	-0.59
benzoic acid	3.92	0.96	0.59	34.27	-0.29
carbamazepin	4.14	1.08	0.62	75.00	0.46
p-nitrophenol	5.45	1.73	0.74	77.65	0.52
estradiol	7.71	2.86	0.89	94.81	1.19
probenecid	7.78	2.89	0.89	95.00	1.20
glibenclamide	30.76	14.38	1.49	99.00	1.69

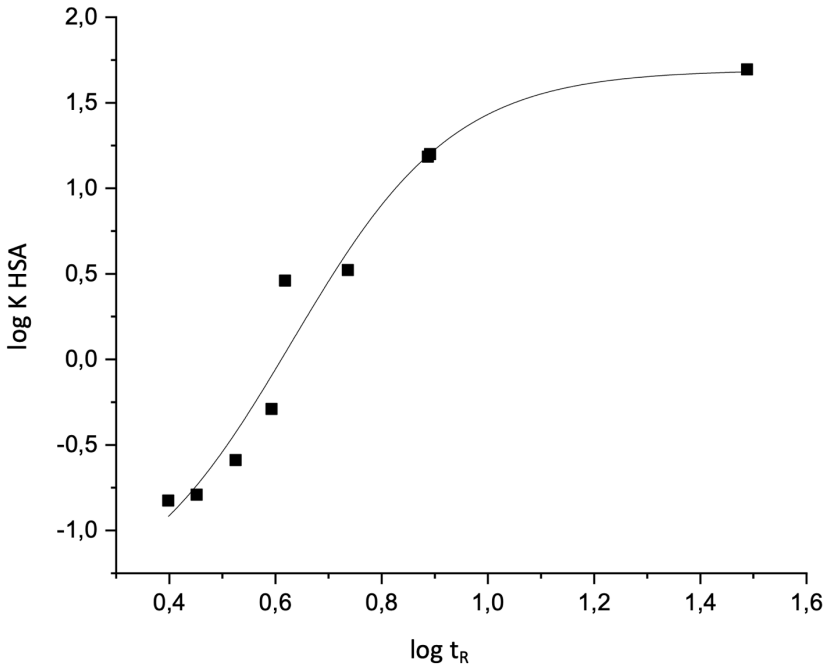

Figure 28: Exemplary sigmoidal plot, showing the correlation between human serum albumin (HSA) binding of selected reference substances and their retention time (t_R) on a Chiralpak HSA column (*Daicel*, Tokyo, Japan). The HSA binding values and calculated and logarithmic values of the affinity constant are shown in Table 7.

AMSEC Method

Binding of FAP-addressing tracers to HSA additionally was determined following the albumin mediated size exclusion chromatography (AMSEC) method described in the following. AMSEC was performed on a radio-RP-HPLC equipped with a Superdex™ 75 Increase 10/300 GL column (*Global Life Science Solutions USA LLC*, Marlborough, USA). The eluent used for the isocratic gradient was 700µM HSA in PBS (pH = 4.7) with a flow rate of 0.8 mL/min. Calibration was performed by using the low molecular weight (LMW) kit from *Global Life Science Solutions*.

Table 8: Reference compounds used for the determination of a calibration line in the AMSEC method for the determination of the HSA binding of radiolabeled FAP-addressing tracers.

reference compound	reference mass M_r [Da]
Aprotinin	6,500
Ribonuclease A	13,700
Carbonic anhydrase	29,000
Ovalbumin	43,000
Conalbumin	75,000
Blue Dextran 2000	>2,000,000

Following the calibration, the retention time of a tracer can be used to calculate the apparent molecular weight of the tracer-HSA adduct. For this purpose, 1–2 MBq (150 pmol) of the radiolabeled ligands were injected directly from the labeling solution. The higher the retention time, the lower the calculated mass and therefore the lower the HSA binding of the used tracer.

3.5 *In Vivo* Experiments

3.5.1 General Information for *In Vivo* Experiments

All animal experiments were conducted in accordance with general animal welfare regulations in Germany (German animal protection act, as amended on 18.05.2018, Art. 141 G v. 29.03.2017 I 626, approval no. 55.2-1-54-2532-71-13) and the institutional guideline for the care and use of animals. To establish tumor xenografts, HT-1080hFAP cells (approx. 10^5 cells) were suspended in 200 µL of 1:1 mixture (*v/v*) of DMEM with GlutaMAX-I and Matrigel (*BD Biosciences*, Germany), and inoculated subcutaneously onto the right shoulder of 6-8 weeks old female BALB/c mice (*Charles River*, Sulzfeld, Germany). Mice were used for experiments when tumors had grown to a diameter of 5-10 mm (1-2 weeks after inoculation).

3.5.2 µSPECT/CT and µPET/CT Imaging

Imaging studies were performed using a MILabs VECTor4 small-animal SPECT/PET/OI/CT. The resulting data were analyzed by the associated PMOD (version 4.0) software. For imaging studies mice were anesthetized with isoflurane and injected with 5-15 MBq (0.15-0.40 nmol) of ^{18}F-, ^{99m}Tc- or ^{177}Lu-labeled tracer into the tail vein. Static images were recorded 1 h post injection (p.i.) with an acquisition time of 15 min and blood samples for later biodistribution studies were taken by cardiac puncture before image acquisition. Static images were acquired with 45 min acquisition time using the HE-UHR-M collimator and a stepwise spiral bed movement. All images were reconstructed using the MILabs Rec software (version 10.02) and a pixel-based Similiarity-Regulated Ordered Subsets Expectation Maximization (SROSEM) algorithm, with a window-based scatter correction (20% below and 20% above the photopeak, respectively). Voxel size CT: 80 µm, 1.6 mm Gaussian blurring, with calibration factor in kBq/mL and decay correction.

3.5.3 Biodistribution Studies

For biodistribution studies approximately 1-5 MBq (0.2 nmol) of ^{18}F-, ^{99m}Tc- or ^{177}Lu-labeled FAPI ligands were injected into the tail vein of HT-1080hFAP tumor-bearing female BALB/c nude mice and sacrificed after 1 h p.i.. Selected organs were removed, weighted, and measured in a gamma counter.

3.5.4 Serum Studies

Blood from a healthy mouse model was collected and centrifuged for 5 min at 13000 rpm to separate the serum from other blood components. 30 MBq of a ^{99m}Tc-labeled ligand was added to the murine serum, to obtain a final volume of 700 µL. The mixture was incubated for 24 h at 37 °C in an incubator. Ice cold MeCN (0 °C, 1.125 mL) was added to the serum to precipitate residual serum components. After stirring, the mixture was transferred into Eppendorf reaction tubes with ultracentrifuge filters. Ultrafiltration was carried out for 20 min at 13000 rpm. About 1 MBq of the obtained filtrate was injected into and analyzed by radio-RP-HPLC.

3.5.5 Metabolite Studies

Processing of organ samples and body fluids was performed according to the hereafter described procedures. Organ samples and body fluids were taken from biodistribution studies or from tumor-bearing or non-tumor-bearing BALB/c nude or CB-17 SCID mice receiving 2-20 MBq (0.2 nmol) of radioactively labeled FAPI ligands injected into the tail vein. The urine sample was centrifuged for 5 min at 13000 rpm yielding a clear solution which directly was subjected to radio-RP-HPLC analysis. The blood sample was diluted to 1 mL with water and centrifuged twice at 13000 rpm for 5 min. The supernatant was collected and loaded on a Strata X cartridge (33 µm Polymeric Reversed Phase, 500 mg, *Phenomernex*, Aschaffenburg, Germany) earlier preconditioned with 5 mL MeOH followed by 5 mL water. After washing with 5 mL water, the cartridge was eluted with a 3:2 mixture (*v*/*v*) of MeCN in water supplemented with 1% TFA. Collected eluate was diluted with water and analyzed by radio-RP-HPLC. Tumor, kidney, and liver samples were homogenized using either a Potter-Elvehjem tissue grinder (*Kontes Glass*, Vineland, United States) or a MM-400 ball mill (*Retsch*, Haan, Germany).

Extraction *via* the Potter-Elvehjem Tissue Grinder

The organ samples (tumor, kidney, liver) were separately homogenized with 1 mL of extraction buffer (850 µL 1 M HEPES pH 7.4 and 150 µL 1 M NaCl) for 30 min. Resulting homogenate was collected and centrifuged at 13000 rpm for 5 min. Subsequently, the supernatant was collected, centrifuged again (13000 rpm for 5 min) and loaded on a Strata X cartridge (33 µm Polymeric Reversed Phase, 500 mg) preconditioned with 5 mL MeOH and 5 mL of water. After washing with 5 mL water, the cartridge was eluted with a 3:2 mixture (*v*/*v*) of MeCN in water supplemented with 1% TFA. For radio-RP-HPLC analysis the eluates were diluted with water.

Extraction *via* the MM-400 Ball Mill

The organ samples (tumor, kidney, liver) were separately homogenized in a 2 mL tube together with Lysis Tube W beads (ceramic and steal beads with a size of 1.4 and 3.5 mm, *Analytic Jena AG*, Jena, Germany) and 1 mL of extraction buffer (850 µL 1 M HEPES pH 7.4 and 150 µL 1 M NaCl) for 10 min at 30 Hz. The homogenate was centrifuged at 13000 rpm for 5 min and the supernatant was collected. Subsequently, the pellet was suspended in 1 mL of extraction buffer and homogenized again with the ball mill for 10 min at 30 Hz. After centrifugation (13000 rpm for 5 min), both supernatants were combined and loaded on a Strata X cartridge (33 µm Polymeric Reversed Phase, 500 mg) preconditioned with 5 mL MeOH and 5 mL of water. Following washing and elution steps, the analysis was performed as described above for the procedure using the Potter-Elvehjem tissue grinder.

4 Results and Discussion

4.1 rhFAPI Ligands

Since its introduction in 2018, radiolabeled FAPI-04 by *Haberkorn et al.* proved to be a valuable tool as a pan-tumor tracer, especially for diagnostic applications.[113] Due to its excellent selectivity and FAP-targeting properties including favorable pharmacokinetics with high tumor-to-organ ratios, the general peptide scaffold of FAPI-04 was used for the design of first radiohybrid FAP-addressing rhFAPI ligands. These compounds suffered from low affinity, high lipophilicity, strong binding to HSA and thermal instability when positioning amino acids capable of imide formation (e.g., asp, glu) next to the piperazine moiety. However, the latter entity is needed for pharmacokinetics benefits regarding tumor retention of the ligands.[112] These findings led to the development strategy shown in Figure 29, with stepwise optimizations of the modification sites following the FAP-inhibitor and stabilizing bridging moiety found in FAPI-04.

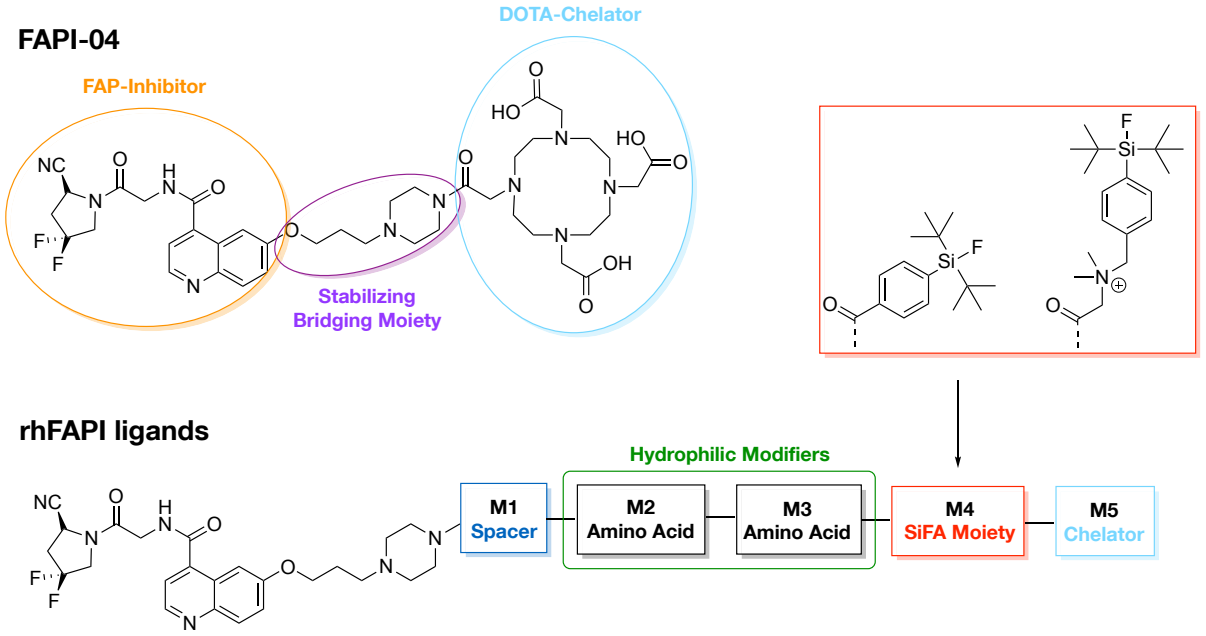

Figure 29: Chemical structure of FAPI-04 developed by *Haberkorn et al.* and conceptual structure of rhFAPI ligands containing the shown FAP inhibitor (orange) and stabilizing bridging moiety (purple). rhFAPI ligands have the variable modification sites **M1** to **M5**, where **M1** is a spacer (blue), **M2** and **M3** are amino acids which act as hydrophilic modifiers (green), **M4** is a SiFA moiety (red), being either SiFA-BA or a SiFAN$^+$ moiety and **M5** is a chelator (turquoise) for metal complexation.

For this development strategy, the peptide scaffold of FAPI-04 was extended by several modification sites (M1 to M4), while also positioning the chelator at the end of the molecule at M5. This design strategy was also used by other groups (Figure 8) for FAP-addressing ligands which were developed in parallel to the ligands described here.[115,119-124] To retain the classical radiohybrid concept (chapter 1.6) a bifunctional amino acid with a SiFA moiety at its side chain was positioned at M4, where resulting proximity to the chelator additionally is

beneficial to compensate the high lipophilicity of the SiFA moiety. This distant positioning of the radiohybrid (M4+M5) to the FAP-inhibitor was done with the intention to avoid steric repulsion from the bulky SiFA moiety within the sensitive binding region of FAP. Variations in the modification sites M1, M2 and M3 are discussed in detail in the following chapters. Shortly, M1 is an additional spacer to lower unwanted interactions of functional groups with the FAP binding motif and M2 and M3 are hydrophilic modifiers to counteract against the lipophilicity introduced through the SiFA moiety and to further modulate the pharmacokinetics of the ligands. All ligands could be prepared *via* a mixed solid-phase/solution-phase synthesis strategy and were obtained after subsequent purification in yields between 5 to 15%. Here, all utilized building blocks (FAP-inhibitor and SiFA moieties) were synthesized according to procedures described in chapter 3. For all ligands FAP-affinity (IC_{50}, competitive binding assay on HT-1080hFAP cells), lipophilicity (log $D_{7.4}$, by means of the distribution in *n*-octanol and PBS at pH 7.4), as well as binding to human serum albumin of the (radio)metal chelates were determined and later compared to the reference compound [$^{nat/177}$Lu]Lu-FAPI-04. All rhFAPI ligands were evaluated as their respective $^{nat/177}$Lu-chelate as a theranostic approach with structurally identical tracers with the same *in vitro* and *in vivo* properties of the diagnostic ([^{18}F]^{nat}Lu-rhFAPI) and therapeutic ([^{177}Lu]Lu-^{nat}F-rhFAPI) tracer was the main goal of this work.

4.1.1 Optimization of Modification Site M1

For the first generation of rhFAPI ligands variations between compounds were limited to the modification sites M1, M2 and M3 as the main goal was the development of radiohybrid ligands with a classic D-dap(SiFA-BA)-*(R)*-DOTAGA moiety. As can be seen in Figure 30, the spacer (M1) can either be a δ-bridged D-glutamate or GABA and the hydrophilic modifiers (M2+M3) can be amino acids with positively or negatively charged or neutral polar side chain functionalities. The hydrophilic modifiers were chosen to compensate the high lipophilicity and strong binding to HSA introduced by the SiFA moiety. Generally, high lipophilicity and strong binding to HSA leads to slow clearance and long circulation of tracers in blood resulting in decreased imaging contrast and higher proportions of hepatobiliary excretion. Detailed investigation into optimized modifiers is discussed later. Here, the main goal of the variations depicted was the optimization of the modification site M1.

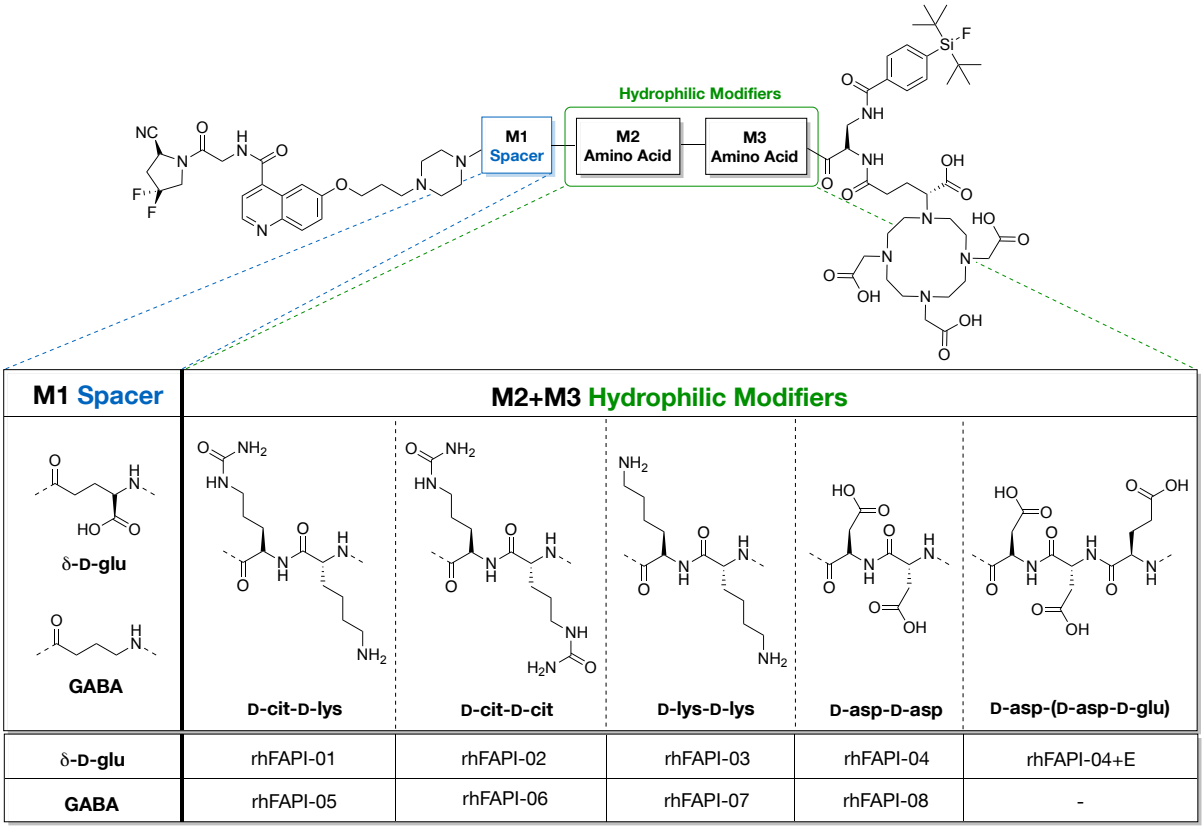

δ-D-glu	rhFAPI-01	rhFAPI-02	rhFAPI-03	rhFAPI-04	rhFAPI-04+E
GABA	rhFAPI-05	rhFAPI-06	rhFAPI-07	rhFAPI-08	-

Figure 30: Structure of ligands rhFAPI-01 to -08 with shown variations at **M1** (spacer) and **M2** and **M3** (hydrophilic modifiers). **M1** can either be a side chain δ-bridged D-glutamate or GABA. **M2** and **M3** can be one or two of following amino acids: D-citrulline, D-lysine, D-aspartate, or D-glutamate.

For M1, δ-bridged D-glutamate was chosen as a spacer to investigate the influence of negative charges near to the FAP binding motif on affinity, hydrophilicity and to investigate if there are interactions with the physiologically positively charged piperazine group in its proximity. GABA was chosen as an alternative with no functional group but the same chain length as δ-bridged D-glutamate. The used selection of amino acids (D-citrulline, D-lysine, D-aspartate, or D-glutamate) was chosen because of their strong influence on increasing the hydrophilicity of compounds they are introduced to. Additionally, in previous projects these

groups proved to compensate the negative effects a SiFA moiety can have on the pharmacokinetics of ligands, especially on blood clearance through high lipophilicity and binding to HSA.[223,224] All ligands carry a “classic” radiohybrid moiety consisting of 2,3-diaminopropionic acid as a bifunctional amino acid with a SiFA-benzoic acid as SiFA moiety coupled to its side chain and (*R*)-DOTAGA as chelator at the *N*-terminus.

In Vitro Characterization

All results from the *in vitro* characterizations of the reference [$^{nat/177}$Lu]Lu-FAPI-04 and [$^{nat/177}$Lu]Lu-rhFAPI-01 to -08 are shown in Figure 31 to Figure 33.

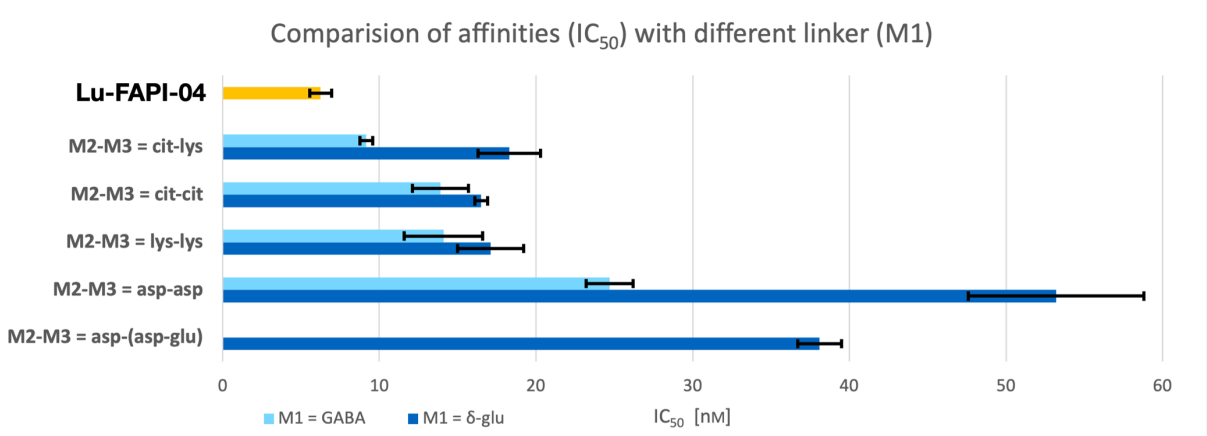

Figure 31: Affinities to FAP (IC_{50} [nM]) on HT-1080hFAP cells (2 h, 4 °C, n = 3) of Lu-FAPI-04 and Lu-rhFAPI ligands with different spacers (M1) and hydrophilic modifiers (M2 and M3); mean values ± SD.

Compared to Lu-FAPI-04 all Lu-rhFAPI ligands displayed 1.5 to 9-fold decreased affinities to FAP. The most obvious explanation for the lower affinities of the rhFAPI ligands would be the more complex structure, which might lead to repulsive interactions of functional groups in the M1, M2 or M3 modification sites with the binding cavity of FAP. An influence on the affinity of the respective spacer used at the M1 position can be clearly stated. In comparison, using GABA as spacer results in a 1.2 to 2.0-fold increased affinity compared to using δ-bridged D-glutamate. Additionally, hydrophilic modifiers (M2+M3) with neutral polar (D-cit) or positively charged (D-lys) side chains seem to be advantageous compared to using negatively charged modifiers (D-asp, D-glu). The highest affinity was achieved for Lu-rhFAPI-05 (M1 = GABA and M2-M3 = cit-lys, IC_{50} = 9.17 ± 0.4 nM) with only a 1.5-fold decreased affinity compared to Lu-FAPI-04 (IC_{50} = 6.25 ± 0.7 nM). This result led to the conclusion that having no charges in proximity to the FAP binding motif was beneficial for a high affinity. Another interesting result was the increased affinity of Lu-rhFAPI-04+E (M1 = δ-glu, M2+M3 = asp-(asp-glu)) compared to Lu-rhFAPI-04 (M1 = δ-glu, M2+M3 = asp-asp), with the only difference between the compounds being an additional D-glutamate. The most obvious explanation for these findings

would be the increased distance between the binding motif and the radiohybrid moiety with its sterically demanding SiFA moiety.

Considering the lipophilicity (Figure 32) of all evaluated ligands, it could be seen that [^{177}Lu]Lu-FAPI-04 (log $D_{7.4}$ = -3.36 ± 0.002) had a lower lipophilicity than all rhFAPI ligands most likely due to the lack of the highly lipophilic SiFA moiety. Especially, rhFAPI ligands with neutral polar (D-cit) or positively charged (D-lys) hydrophilic modifiers showed 2 to 7-fold higher lipophilicity compared to [^{177}Lu]Lu-FAPI-04. In contrast, compounds with negatively charged modifiers (D-asp, D-glu) like [^{177}Lu]Lu-rhFAPI-04 (M1 = δ-glu, M2+M3 = asp-asp, log $D_{7.4}$ = -2.64 ± 0.03) and [^{177}Lu]Lu-rhFAPI-04+E (M1 = δ-glu, M2+M3 = asp-(asp-glu), log $D_{7.4}$ = -2.97 ± 0.05) showed similar low lipophilicities as [^{177}Lu]Lu-FAPI-04. This led to the conclusion, that negatively charged modifiers have a stronger influence on lowering the lipophilicity of rhFAPI ligands compared to other modifications. This was also evident in the spacer variations (M1), where the switch from δ-bridged D-glutamate to GABA was accompanied by a 1.4 to 3.5-fold increase in lipophilicity.

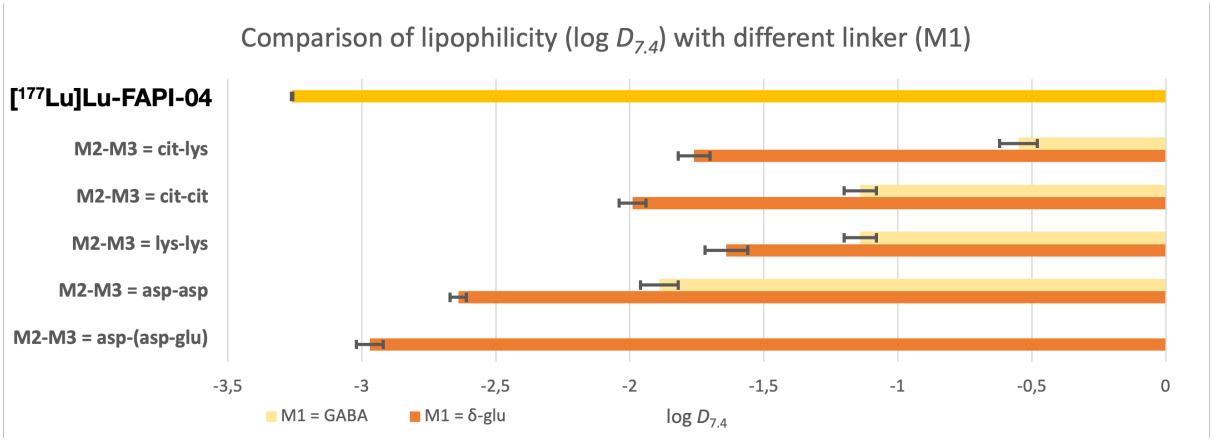

Figure 32: Lipophilicity as octanol/PBS (pH 7.4) partition coefficient (log $D_{7.4}$, n = 8) of [^{177}Lu]Lu-FAPI-04 and [^{177}Lu]Lu-rhFAPI ligands with different spacers (M1) and hydrophilic modifiers (M2 and M3); mean values ± SD.

The characterization of tracer binding to HSA was determined by two different methods (AMSEC and HPAC). While the AMSEC method is a more dynamic system presumably more comparable with realistic *in vivo* binding behavior of ligands to HSA, the HPAC method is a more established method to predict binding to HSA. Nevertheless, both methods will be discussed together, and differences will be interpreted. Generally, all rhFAPI ligands showed stronger binding to HSA compared to [^{177}Lu]Lu-FAPI-04. Reason for this was the SiFA moiety, which has classical structural characteristics of HSA-binding compounds like a *para*-substituted arene ring and lipophilic alkyl groups like the *tert*-butyl group.[225,226] *Wurzer et al.* showed higher HSA binding of the SiFA containing PSMA ligand rhPSMA-7.3 in comparison to structural similar PSMA ligands, which further confirmed the influence of the SiFA moiety on HSA binding.[199,200] The results from the performed HSA binding studies showed a strong influence of the groups in proximity to the SiFA moiety. It seemed that neutral polar (D-cit) or positively charged (D-lys) groups at M3 decreased the HSA binding by a factor of 2 to 3

compared to negatively charged groups (D-asp, D-glu). Additionally, the range of motion of the functional group - here the length of the amino acid side chain – had an influence. This was seen for [^{177}Lu]Lu-rhFAPI-04 (M1 = δ-glu, M2+M3 = asp-asp, MW (HSA) = 20.7 kDa and HSA binding = 96.6%) and [^{177}Lu]Lu-rhFAPI-04+E (M1 = δ-glu, M2+M3 = asp-(asp-glu), MW (HSA) = 28.9 kDa and HSA binding = 98.6%), were the longer side chain length of D-glutamate compared to D-aspartate resulted in stronger binding to HSA. The influence of charged groups nearby to an HSA binding moiety was described by *Deberle et al.* for PSMA ligands with ibuprofen as an albumin-binding entity. *Deberle et al*. showed, that negatively charged groups result in stronger binding to HSA, whereby positively charged groups weakened the binding.[227] Similar findings were described by *Martínez-Gómez et al.*, where negatively charged and neutral lipophilic groups can interact with binding sites at HSA.[228] These finding match with the results obtained by the *in vitro* studies.

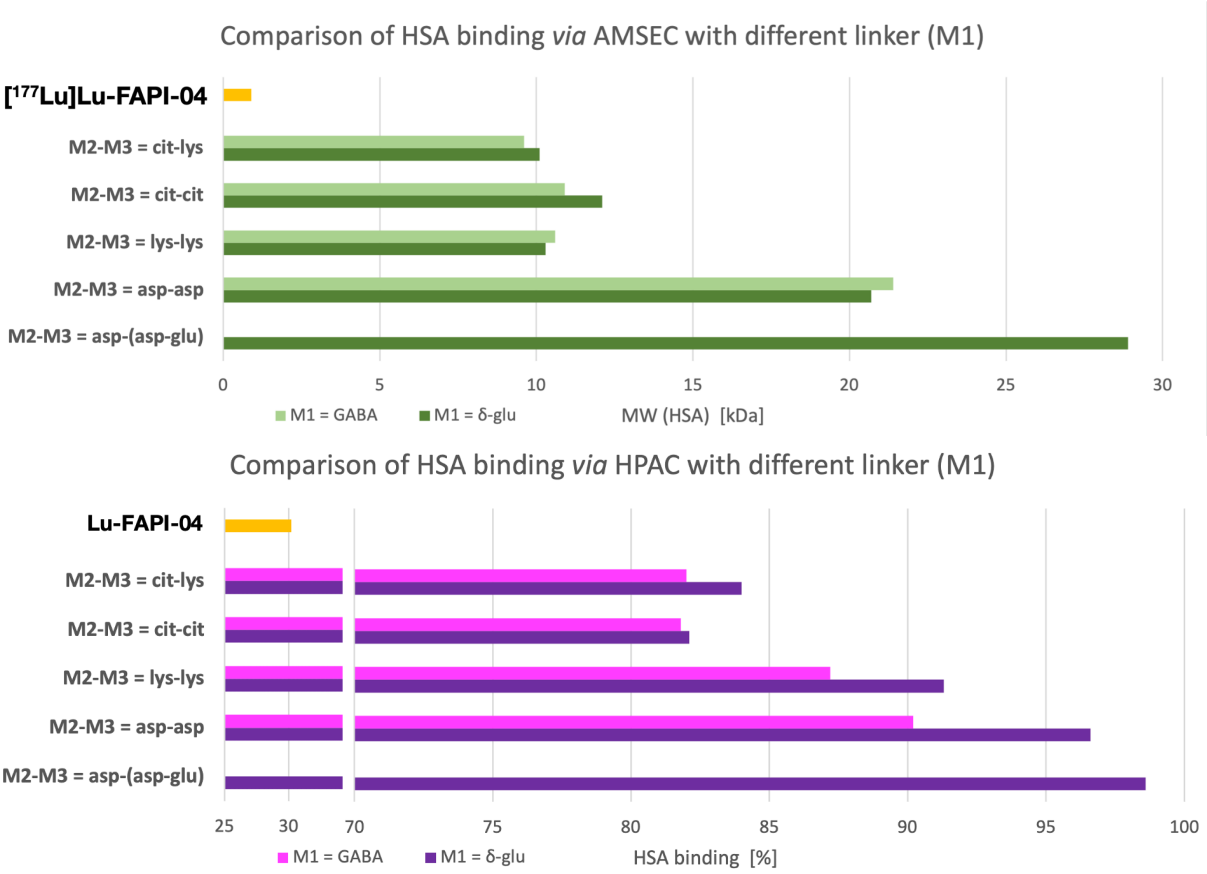

Figure 33: Binding to human serum albumin (HSA) at the upper panel as apparent molecular weight (MW) determined following the albumin mediated size exclusion chromatography (AMSEC) method (determined on a Superdex™ 75 Increase 10/300 GL column) and at the lower panel as in percent of literature-known calibration-compounds (determined on a Chiralpak HSA column *via* HPAC method) of [$^{nat/177}$Lu]Lu-FAPI-04 and [$^{nat/177}$Lu]Lu-rhFAPI ligands with different spacers (M1) and hydrophilic modifiers (M2 and M3).

Interestingly, the choice of the spacer had little influence on the binding to HSA. This most likely was because of the distant positioning of the spacer to the SiFA moiety, lowering the impact of the negatively charged functional group of δ-bridged D-glutamate on the HSA binding of the SiFA moiety. Therefore, the choice of the spacer was not important for defining

the binding properties of future rhFAPI ligands to HSA, rather of importance was the choice of the group at modification site M3. In general, it was observed that ligands with strong binding to HSA had the lowest affinities, while ligands with high affinities demonstrated lowest hydrophilicities. Especially the latter observation complicated the project in the further course of development. An influence of HSA binding towards ligand affinity to FAP in the used cell assay could be eliminated during assay development (chapter 4.5).

In Vivo Characterization

Considering the results of the *in vitro* characterization, only a selection of rhFAPI ligands were chosen for further *in vivo* evaluation, consisting of [^{177}Lu]Lu-rhFAPI-02 (IC_{50} = 16.5 ± 0.4 nM, log $D_{7.4}$ = -1.99 ± 0.05, MW (HSA) = 12.1, HSA binding = 82.1%), [^{177}Lu]Lu-rhFAPI-04+E (IC_{50} = 38.1 ± 0.7 nM, log $D_{7.4}$ = -2.97 ± 0.05, MW (HSA) = 28.9, HSA binding = 98.6%) and [^{18}F]F-Lu-rhFAPI-05 (IC_{50} = 9.17 ± 0.4 nM, log $D_{7.4}$ = -0.55 ± 0.07, MW (HSA) = 9.6, HSA binding = 82.0%). For the biodistribution studies all ligands were either labeled with lutetium-177 or fluorine-18 and injected into HT-1080hFAP tumor-bearing female BALB/c mice (Figure 34), evaluated after 1 h p.i. and compared to the lutetium-177 complexed reference ligand [^{177}Lu]Lu-FAPI-04 (IC_{50} = 6.25 ± 0.7 nM, log $D_{7.4}$ = -3.36 ± 0.02, MW (HSA) = 0.9, HSA binding = 30.2%).

The comparative biodistribution of the three rhFAPI ligands depicted in Figure 34 revealed similar pharmacokinetics with higher uptake in non-specific organs 1 h p.i. compared to the reference [^{177}Lu]Lu-FAPI-04. High uptake in bone and joints could be explained through FAP expression in these structures. This expression was described in literature by *Toms et al.* and could be blocked through addition of excess of non-labeled FAP addressing ligands.[115] All rhFAPI ligands showed high accumulation in blood, which indicated a not yet completed distribution of the ligands, probable through high binding to HSA. The ligands [^{177}Lu]Lu-rhFAPI-02 (log $D_{7.4}$ = -1.99 ± 0.05) and [^{18}F]Lu-rhFAPI-05 (log $D_{7.4}$ = -0.55 ± 0.07) showed high uptake in a variety of organs such as liver, the gastrointestinal system, but also lung, which was most probably a result of their high lipophilicity. The accumulation in the pancreas, resulted from an endogenous expression.[229] The so called Langerhans islet cells, micro-organs consisting of different cell types located in the pancreas, are FAP positive.[230] Unexpectedly, [^{177}Lu]Lu-rhFAPI-04+E showed the highest uptake in the tumor while having the lowest affinity (IC_{50} = 38.1 ± 1.4 nM) and [^{18}F]Lu-rhFAPI-05 showed the lowest tumor uptake while having the highest affinity (IC_{50} = 9.17 ± 0.4 nM) to FAP. Most likely, [^{177}Lu]Lu-rhFAPI-04+E benefited from its high hydrophilicity (log $D_{7.4}$ = -2.97 ± 0.05), which leads to a fast distribution and therefore higher accumulation in tumor tissue. The surprisingly high bone uptake of [^{18}F]F-Lu-rhFAPI-05 could not be explained with certainty. Free fluoride-18 could be a reason for elevated uptake; however, radio-RP-HPLC and radio-TLC conducted after labelling did not show any signs of free fluoride-18 and indicated a radiochemical purity of 96.7%. A possibility for free fluorine-18 could have been defluorination of the SiFA moiety which seems unlikely due to the reported high hydrolysis stability of the used SiFA-BA group.[153]

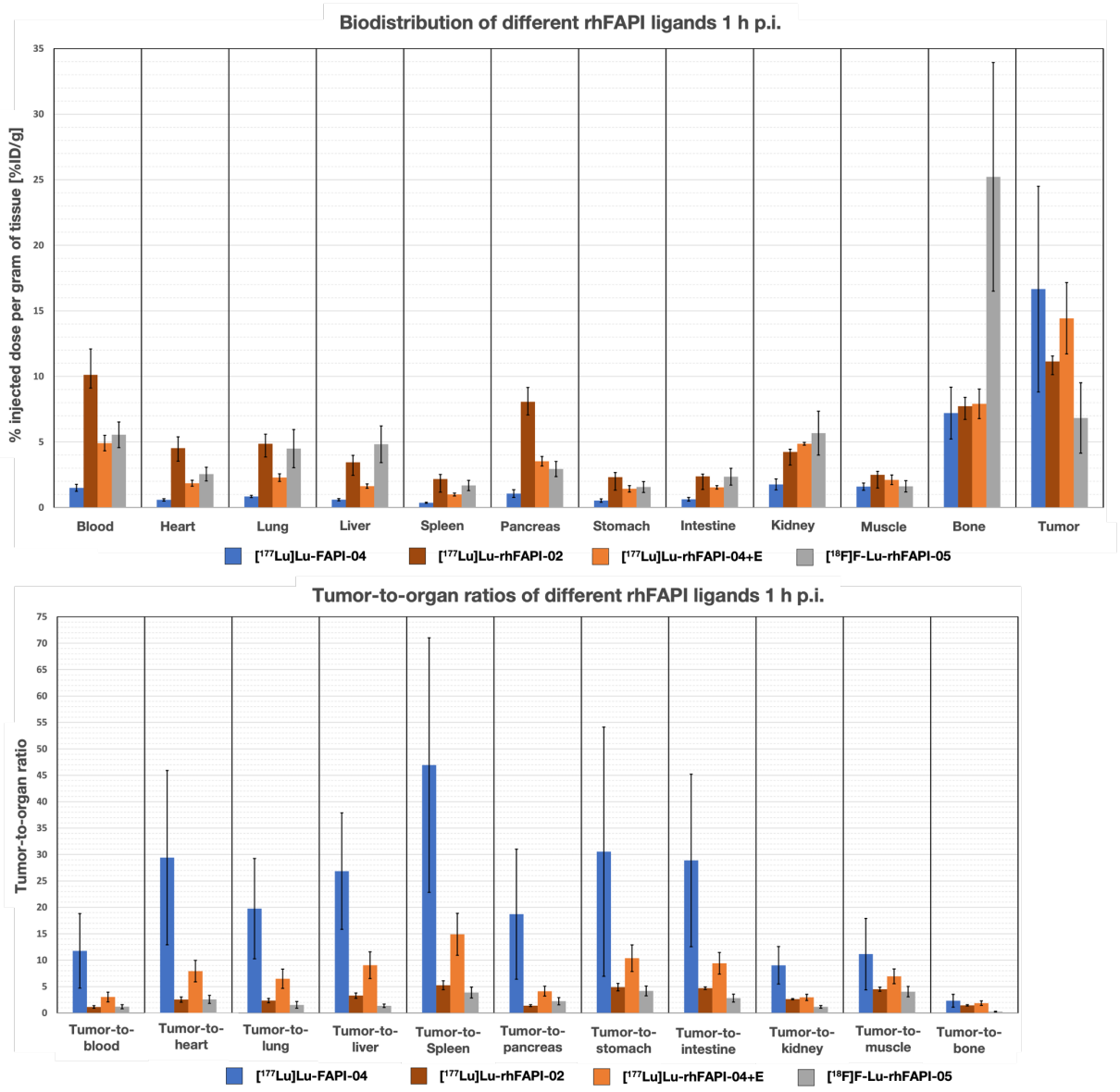

Figure 34: Biodistribution (top) and tumor-to-organ ratios (bottom) of the reference ligand [^{177}Lu]Lu-FAPI-04 and the rhFAPI ligands [^{177}Lu]Lu-rhFAPI-02, [^{177}Lu]Lu-rhFAPI-04+E and [^{18}F]F-Lu-rhFAPI-05 at 1 h p.i. in HT-1080hFAP tumor-bearing BALB/c mice (n = 4-5). Values for biodistributions are expressed as a percentage of injected dose per gram of tissue (%ID/g), mean ± SD. Values for tumor-to-organ ratios are expressed as ratios between accumulation in the tumor and accumulation in each organ, mean ± SD.

In conclusion, [^{177}Lu]Lu-rhFAPI-04+E performed best of all evaluated rhFAPI ligands with the highest tumor-to-organ ratios (Figure 34), however, combining the lowest affinity and strongest binding to HSA of this subset of ligands. Here, hydrophilicity seemed to be the most important parameter for favorable *in vivo* performance. Because of the fast clearance, low uptake in non-specific organs and high tumor uptake of [^{177}Lu]Lu-FAPI-04, the tumor-to-organ ratios of [^{177}Lu]Lu-rhFAPI-04+E still were 3 to 4-fold decreased compared to [^{177}Lu]Lu-FAPI-04.

Summary and Conclusion of M1 Optimizations

In summary, all rhFAPI ligands performed worse than $^{nat/177}$Lu-FAPI-04 in all conducted *in vitro* and *in vivo* characterizations. The ligand Lu-rhFAPI-05 showed the highest affinity (IC_{50} = 9.17 ± 0.4 nM) to FAP and hereby almost achieved the same affinity as Lu-FAPI-04 (IC_{50} = 6.25 ± 0.7 nM). Generally, the usage of GABA as spacer at modification site M1 was beneficial for increasing the affinity (1.2 to 2.0-fold) of ligands towards FAP. It was shown that the charge of hydrophilic modifiers at M2 and M3 have an influence on the binding to HSA, whereas positively charged and neutral polar modifiers showed decreased binding. The choice of spacer at modification site M1 only had a negligible influence on the binding to HSA. This most likely was because of its distance to the SiFA moiety, which was responsible for the high HSA binding compared to FAPI-04. The switch from δ-bridged D-glutamate to GABA was accompanied by a 1.4 to 3.5-fold increase in lipophilicity, which was unfavorable because of the strong influence of the lipophilicity on the pharmacokinetics of tracers. This was shown through biodistribution studies where [^{177}Lu]Lu-rhFAPI-04+E performed best, benefitting from its high hydrophilicity (log $D_{7.4}$ = -2.97 ± 0.05), which leads to a fast distribution and therefore higher accumulation in tumor tissue. Nevertheless, the decision was made to use GABA as spacer in all future ligands to benefit from its higher affinity and compensate its higher lipophilicity by additional modifications positioned more distant to the binding motif.

4.1.2 Optimization of Modification Site M2 and M3

Optimization of Hydrophilic Modifiers with Differently Charged Sidechains

Main goal of the following rhFAPI development process was to further investigate the behavior of positively or negatively charged and neutral polar modifiers at the modification site M2 and M3. The influence on the affinity towards FAP and the binding to HSA were of particular interest. Therefore, the compounds rhFAPI-09 to -12 (Figure 35) have been synthesized, evaluated, and compared to existing rhFAPI ligands.

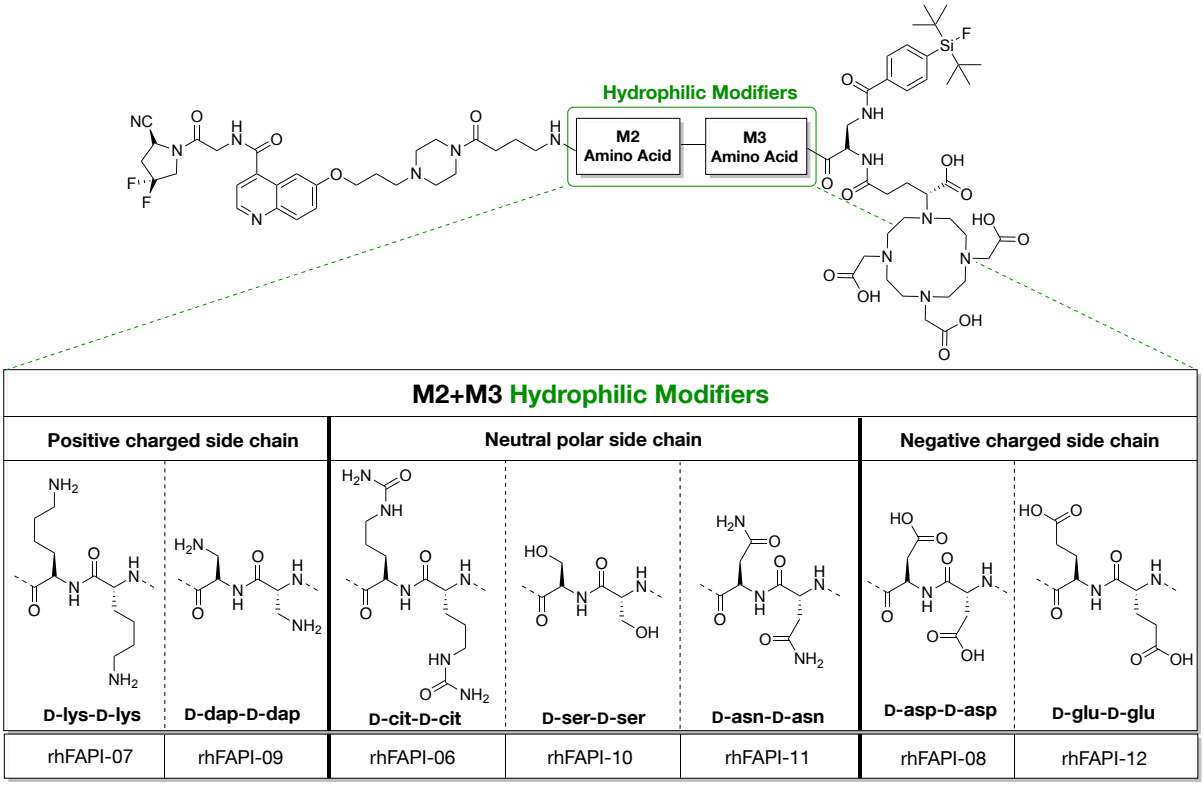

Figure 35: Structure of ligands rhFAPI-06 to -12 with shown variations at **M2** and **M3** (hydrophilic modifiers). Here, **M2** and **M3** were the same modifier from a selection of amino acids with positively charged (D-lysine or D-dap), neutral polar (D-citrulline, D-serine or D-asparagine) or negatively charged (D-aspartate or D-glutamate) side chain motifs.

As stated earlier, GABA was used as spacer for all future rhFAPI ligands, leaving only the modification sites M2 and M3 as locations for variations. Here, M2 and M3 were the same modifiers out of a selection of amino acids with positively charged (D-lys or D-dap), neutral polar (D-cit, D-ser or D-asn) or negatively charged (D-asp or D-glu) side chain functionalities.

In Vitro Characterization

All results from the *in vitro* characterizations of [$^{nat/177}$Lu]Lu-rhFAPI-06 to -12 are shown in Figure 36 to Figure 38. Here, already seen trends were confirmed by the wider variety of compounds. The affinity of rhFAPI ligands increased when using positively charged (D-lys or D-dap) and neutral polar (D-cit, D-ser or D-asn) groups and decreased when using negatively charged (D-asp or D-glu) groups as modifiers. Additionally, the length of the amino acid side chain amplified the observed tendencies.

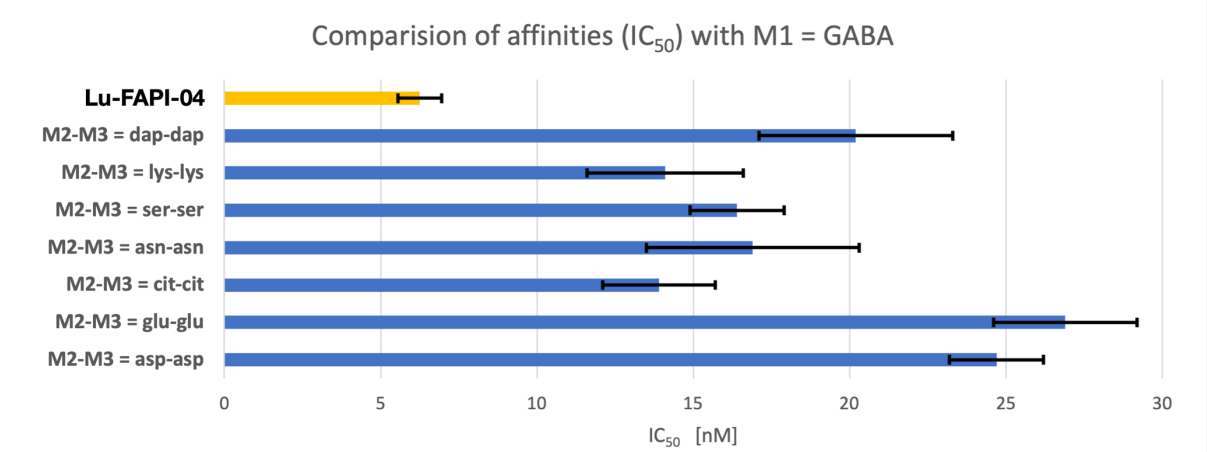

Figure 36: Affinities to FAP (IC_{50} [nM]) on HT-1080hFAP cells (2 h, 4 °C, n = 3) of Lu-FAPI-04 and Lu-rhFAPI ligands with GABA as spacer (M1) and different hydrophilic modifiers (M2 and M3); mean values ± SD.

This could be seen especially when comparing Lu-rhFAPI-07 (M2-M3 = lys-lys, IC_{50} = 14.1 ± 2.5 nM) with the shorter side-chain analogue Lu-rhFAPI-09 (M2-M3 = dap-dap, IC_{50} = 20.2 ± 3.1 nM), resulting in an increased affinity, as well as rhFAPI-08 (M2-M3 = asp-asp, IC_{50} = 24.7 ± 1.5 nM) compared to the longer side-chain analogue Lu-rhFAPI-12 (M2-M3 = glu-glu, IC_{50} = 26.9 ± 2.3 nM). A similar tendency can be assumed for ligands with neutral polar (D-cit, D-ser or D-asn) modifiers, where Lu-rhFAPI-06 (M2-M3 = cit-cit, IC_{50} = 13.9 ± 1.8 nM) had the longest side chain length and the highest affinity compared to Lu-rhFAPI-10 (M2-M3 = ser-ser, IC_{50} = 16.4 ± 1.5 nM) and Lu-rhFAPI-11 (M2-M3 = asn-asn, IC_{50} = 16.9 ± 3.4 nM). Altogether, the amino acids D-lys and D-cit appeared to be the most suitable modifiers for enhancing the affinity, although Lu-FAPI-04 still had a higher affinity towards FAP.

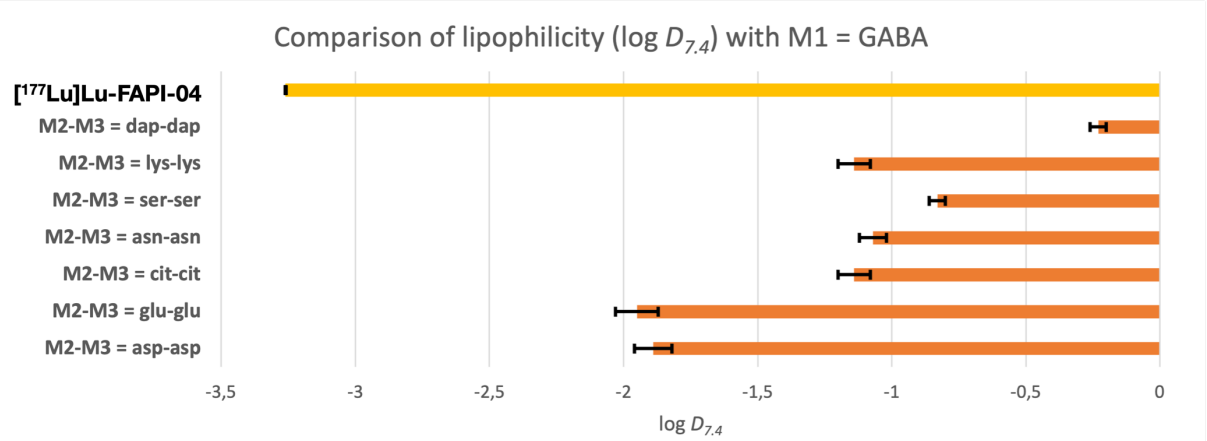

Figure 37: Lipophilicity as octanol/PBS (pH 7.4) partition coefficient (log $D_{7.4}$, n = 8) of [^{177}Lu]Lu-FAPI-04 and [^{177}Lu]Lu-rhFAPI ligands with GABA as spacer (M1) and different hydrophilic modifiers (M2 and M3); mean values ± SD.

Within the different modifier types, the previously observed tendencies on the lipophilicity were also amplified by the length of the amino acid side chain. Especially, this was shown for [^{177}Lu]Lu-rhFAPI-07 (M2-M3 = lys-lys, log $D_{7.4}$ = -1.14 ± 0.06) and [^{177}Lu]Lu-rhFAPI-09 (M2-M3 = dap-dap, log $D_{7.4}$ = -0.23 ± 0.03) with a 6-fold increase in lipophilicity for the ligand

bearing the short-chain modification. Compared to [^{177}Lu]Lu-FAPI-04 the ligands [^{177}Lu]Lu-rhFAPI-06 to -12 had a 1.7 to 16-fold increased lipophilicity, which raised concerns towards unfavorable *in vivo* distribution.

As for affinity and lipophilicity, a dependence also was shown between binding to HSA and length of the amino acid side chain. Here, a longer range of motion of the side chain functionalities leads to a decreased binding for positively charged (D-lys and D-dap) and neutral polar groups (D-cit, D-ser and D-asn), whereas negatively charged groups (D-asp and D-glu) increased binding to HSA. [^{177}Lu]Lu-rhFAPI-12 (M2-M3 = glu-glu) showed exceptional high HSA binding *via* the AMSEC method with an apparent molecular weight of 56 kDa. This nearly was the weight of HSA (66.5 kDa), which indicated almost complete binding. As this method expresses the binding strength to HSA through a calculated increase of the ligands own molecular weight towards the molecular weight of HSA. Altogether, the amino acids D-lys and D-cit again appeared to be the most suitable modifiers for lowering the binding to HSA when looking at results from the AMSEC method, whereas finding from the HPAC method indicate that D-cit was more favorable than D-lys.

Figure 38: Binding to human serum albumin (HSA) at the upper panel as apparent molecular weight (MW) determined following the albumin mediated size exclusion chromatography (AMSEC) method (determined on a Superdex™ 75 Increase 10/300 GL column) and at the lower panel as in percent of literature-known calibration-compounds (determined on a Chiralpak HSA column *via* HPAC method) of [$^{nat/177}$Lu]Lu-FAPI-04 and [$^{nat/177}$Lu]Lu-rhFAPI ligands with GABA as spacer (M1) and different hydrophilic modifiers (M2 and M3).

The rhFAPI ligand [$^{nat/177}$Lu]Lu-rhFAPI-06 (IC_{50} = 13.9 ± 1.8 nM, log $D_{7.4}$ = -1.14 ± 0.06, MW (HSA) = 10.9, HSA binding = 81.8%) with the hydrophilic modifier D-citrulline demonstrated overall beneficial results of all *in vitro* characterizations. Here, the best trade-off between improved hydrophilicity and still high affinity was achieved, while including a comparatively low HSA binding. Because of this [$^{nat/177}$Lu]Lu-rhFAPI-06 was chosen as lead compound for further investigations. These will be discussed in the following chapter, mainly focusing on the positioning of D-citrulline at modification site M2 or M3 and compatible additional modifiers for the second modification site.

Optimization of Hydrophilic Modifiers with Focus of Citrulline Positioning

Main goal of the following rhFAPI development process was to further investigate the ideal positioning of D-citrulline for improved *in vitro* properties. For this, the new ligands rhFAPI-13 to -16 (Figure 39) were synthesized, evaluated, and compared to the existing ligands rhFAPI-05 and -06.

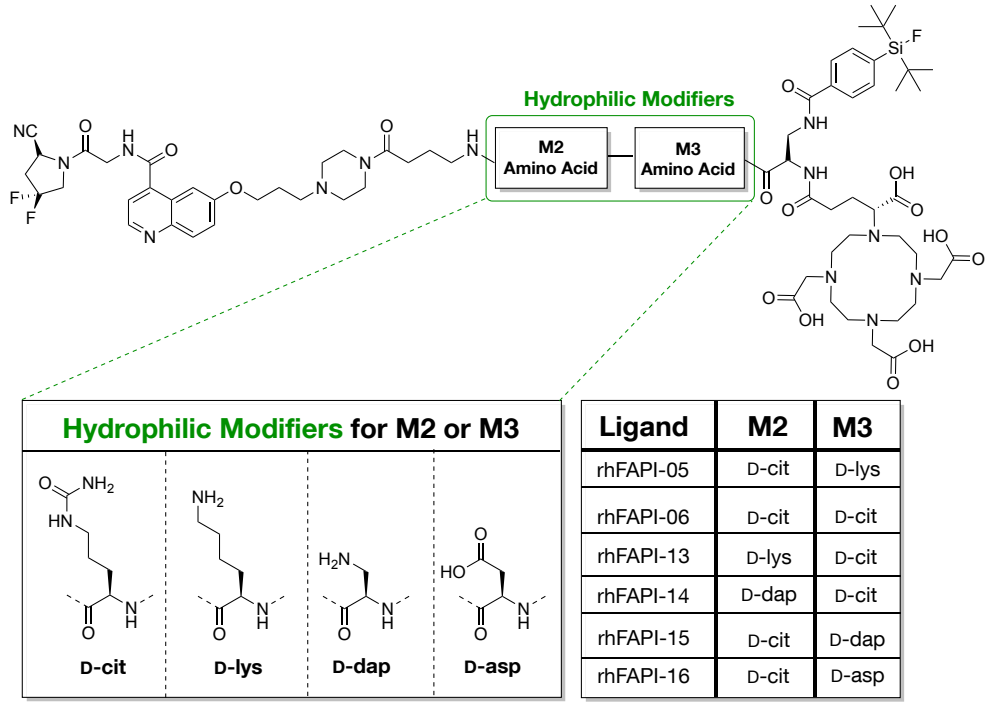

Ligand	M2	M3
rhFAPI-05	D-cit	D-lys
rhFAPI-06	D-cit	D-cit
rhFAPI-13	D-lys	D-cit
rhFAPI-14	D-dap	D-cit
rhFAPI-15	D-cit	D-dap
rhFAPI-16	D-cit	D-asp

Figure 39: Structure of ligands rhFAPI-05, -06 and -13 to -16 with shown variations at **M2** and **M3** (hydrophilic modifiers). Here, **M2** and **M3** were modifiers from a selection of amino acids, whereas either one of them is a D-citrulline and the other modifiers is a D-lysine, D-dap, or D-aspartate.

Here, D-citrulline was positioned either at modification site M2 or M3 while the other site was filled with a D-lysine, D-dap, or D-aspartate. Only the in Figure 39 shown combinations have been evaluated, because after first results a beneficial positioning for D-citrulline already was found.

In Vitro Characterization

All results from the *in vitro* characterizations of [$^{nat/177}$Lu]Lu-rhFAPI-06 to -12 are shown in Figure 40 to Figure 42. Comparing the binding affinities of Lu-rhFAPI-05 (M2-M3 = D-cit-D-lys, IC_{50} = 9.17 ± 0.4 nM) with Lu-rhFAPI-13 (M2-M3 = D-lys-D-cit, IC_{50} = 13.3 ± 2.0 nM) and rhFAPI-14 (M2-M3 = D-dap-D-cit, IC_{50} = 21.8 ± 1.0 nM) with Lu-rhFAPI-15 (M2-M3 = D-cit-D-dap, IC_{50} = 12.7 ± 0.6 nM) clearly showed a preference for a neutral polar modifier at modification site M2. The usage of D-citrulline at M2 instead of M3 compared to using D-lysine or D-dap in M2 instead of M3 led to a 1.5 to 1.7-fold increased affinity to FAP. Additionally, it was shown that especially a positively charged modifier at M3 was beneficial to further increase affinity. This can be seen when comparing Lu-rhFAPI-05 (M2-M3 = D-cit-D-lys, IC_{50} = 9.17 ± 0.4 nM), Lu-rhFAPI-06 (M2-M3 = D-cit- D-cit, IC_{50} = 13.9 ± 1.8 nM) and rhFAPI-16 (M2-M3 = D-cit-D-asp, IC_{50} = 12.5 ± 1.8 nM). Interestingly, using a negatively charged modifier at M3 seemed to be acceptable without decreasing the affinity compared

to using a neutral polar modifier. This supports the conclusion, that especially modification sites M1 and M2 are important for high affinities. Ligand Lu-rhFAPI-05 still showed the highest affinity with 9.17 ± 0.4 nM.

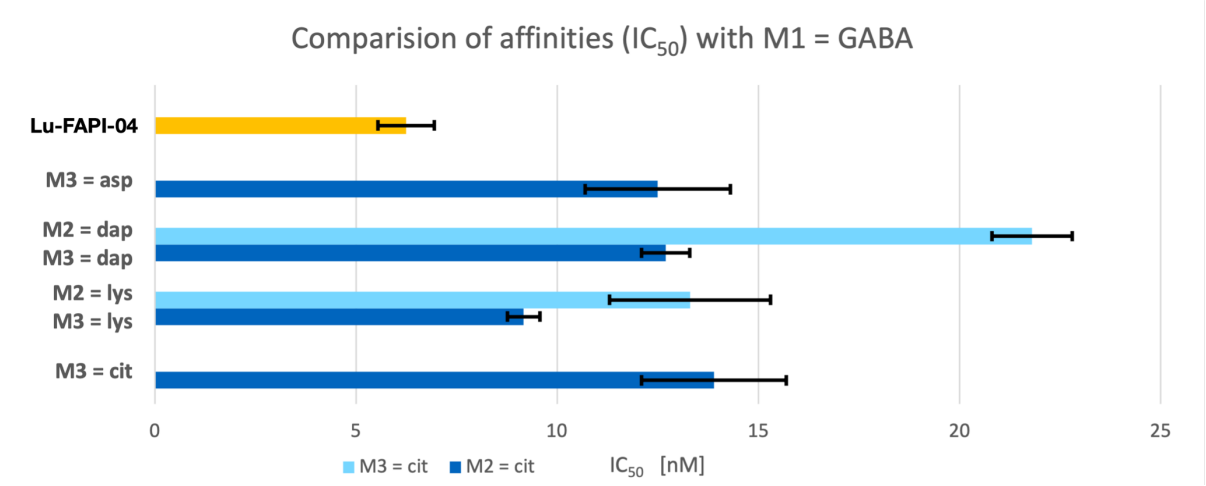

Figure 40: Affinities to FAP (IC_{50} [nM]) on HT-1080hFAP cells (2 h, 4 °C, n = 3) of Lu-FAPI-04 and Lu-rhFAPI ligands with GABA as spacer (M1) and different hydrophilic modifiers (M2 and M3) with D-citrulline either on modification site M2 or M3; mean values ± SD.

For the characterization of the lipophilicity already known results could be confirmed. Incorporating a negatively charged modifier next to the SiFA moiety ([^{177}Lu]Lu-rhFAPI-16, M3 = D-asp) resulted in a 1.4-fold decreased lipophilicity in comparison to a compound carrying a neutral polar modifier ([^{177}Lu]Lu-rhFAPI-06, M3 = D-cit) at the same position. Using a positively charged modifier (D-lys or D-dap) increased lipophilicity by 2 to 2.8-fold. Surprisingly, previous ligands with M2-M3 = D-cit-D-cit ([^{177}Lu]Lu-rhFAPI-06, log $D_{7.4}$ = -1.14 ± 0.06) and M2-M3 = D-lys-D-lys ([^{177}Lu]Lu-rhFAPI-07, log $D_{7.4}$ = -1.14 ± 0.06) showed a lower lipophilicity compared to the merged ligands, combining D-lys and D-cit in the linker.

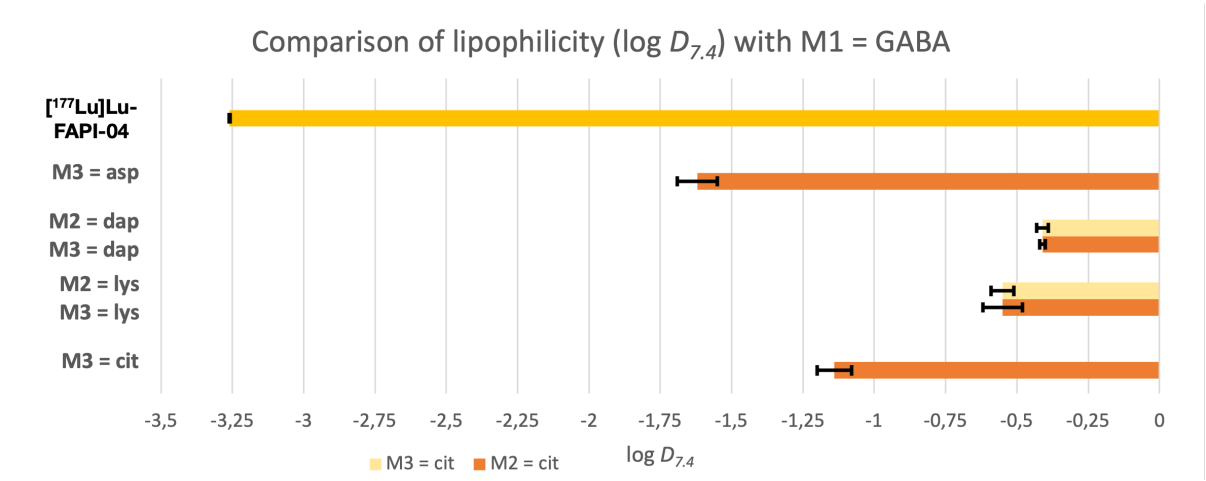

Figure 41: Lipophilicity as octanol/PBS (pH 7.4) partition coefficient (log $D_{7.4}$, n = 8) of [^{177}Lu]Lu-FAPI-04 and [^{177}Lu]Lu-rhFAPI ligands with GABA as spacer (M1) and different hydrophilic modifiers (M2 and M3) with D-citrulline either on modification site M2 or M3; mean values ± SD.

For the binding strength of rhFAPI ligands to HSA, already known correlations could be verified. Positioning of a positively charged modifier (D-lys or D-dap) at M3 next to the SiFA moiety decreased binding to HSA, while positioning a negatively charged modifier (D-asp) increased the binding strength. Compared to [$^{nat/177}$Lu]Lu-FAPI-04, all rhFAPI ligands showed significantly higher binding to HSA.

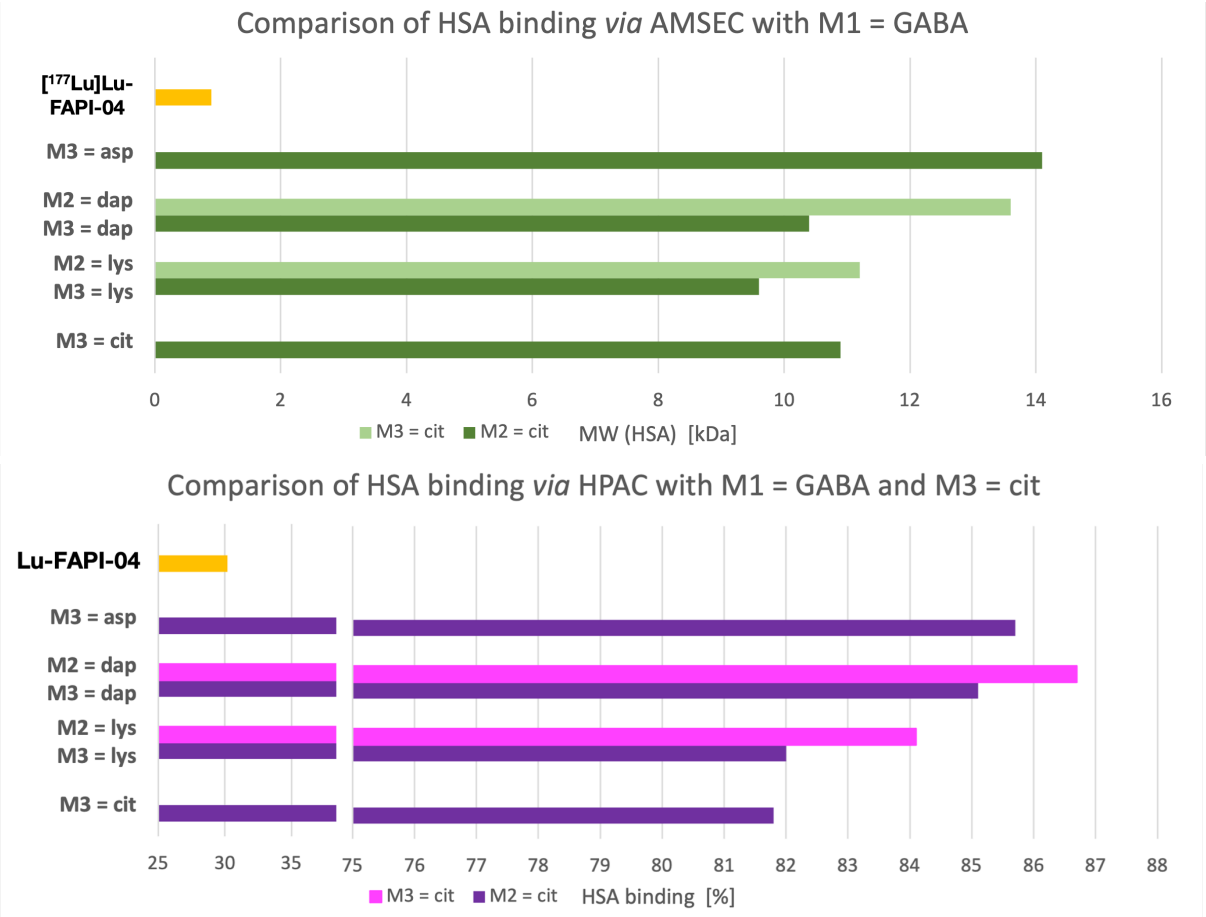

Figure 42: Binding to human serum albumin (HSA) at the upper panel as apparent molecular weight (MW) determined following the albumin mediated size exclusion chromatography (AMSEC) method (determined on a Superdex™ 75 Increase 10/300 GL column) and at the lower panel as in percent of literature-known calibration-compounds (determined on a Chiralpak HSA column *via* HPAC method) of [$^{nat/177}$Lu]Lu-FAPI-04 and [$^{nat/177}$Lu]Lu-rhFAPI ligands with GABA as spacer (M1) and different hydrophilic modifiers (M2 and M3) with D-citrulline either on modification site M2 or M3.

In Vivo Characterization

Considering the results of the *in vitro* characterization, only [^{177}Lu]Lu-rhFAPI-16 (M2 = D-cit and M3 = D-asp) was chosen for further *in vivo* evaluation because of its favorable higher hydrophilicity. For the biodistribution studies the ligand was injected into HT-1080hFAP tumor-bearing female BALB/c mice (Figure 43), evaluated after 1 h p.i. and compared to the lutetium-177 complexed reference ligand [^{177}Lu]Lu-FAPI-04. The comparative biodistribution of [^{177}Lu]Lu-rhFAPI-16 revealed similar pharmacokinetics to previously tested rhFAPI ligands. Surprisingly, [^{177}Lu]Lu-rhFAPI-16 (IC_{50} = 12.5 ± 1.8 nM, log $D_{7.4}$ = -1.62 ± 0.07) showed a lower tumor uptake and slower clearance compared to [^{177}Lu]Lu-rhFAPI-04+E (IC_{50} = 38.1 ± 1.4 nM,

log $D_{7.4}$ = -2.97 ± 0.05) and [^{18}F]F-Lu-rhFAPI-05 (IC_{50} = 9.17 ± 0.4 nM, log $D_{7.4}$ = -0.55 ± 0.07) despite having a higher affinity and a decreased lipophilicity, respectively. In general, [^{177}Lu]Lu-rhFAPI-16 showed high activity accumulation in blood, which indicated a not yet completed distribution of the ligand, despite having a lower HSA binding (MW (HSA) = 14.1 kDa, HSA binding = 85.7%) compared to [^{177}Lu]Lu-rhFAPI-04+E (MW (HSA) = 28.9 kDa, HSA binding = 98.6%). Additionally, [^{177}Lu]Lu-rhFAPI-16 showed high uptake in a variety of organs such as liver, the gastrointestinal system, but also lung, which was most probably a result of its high activity retention in blood and slow clearance.

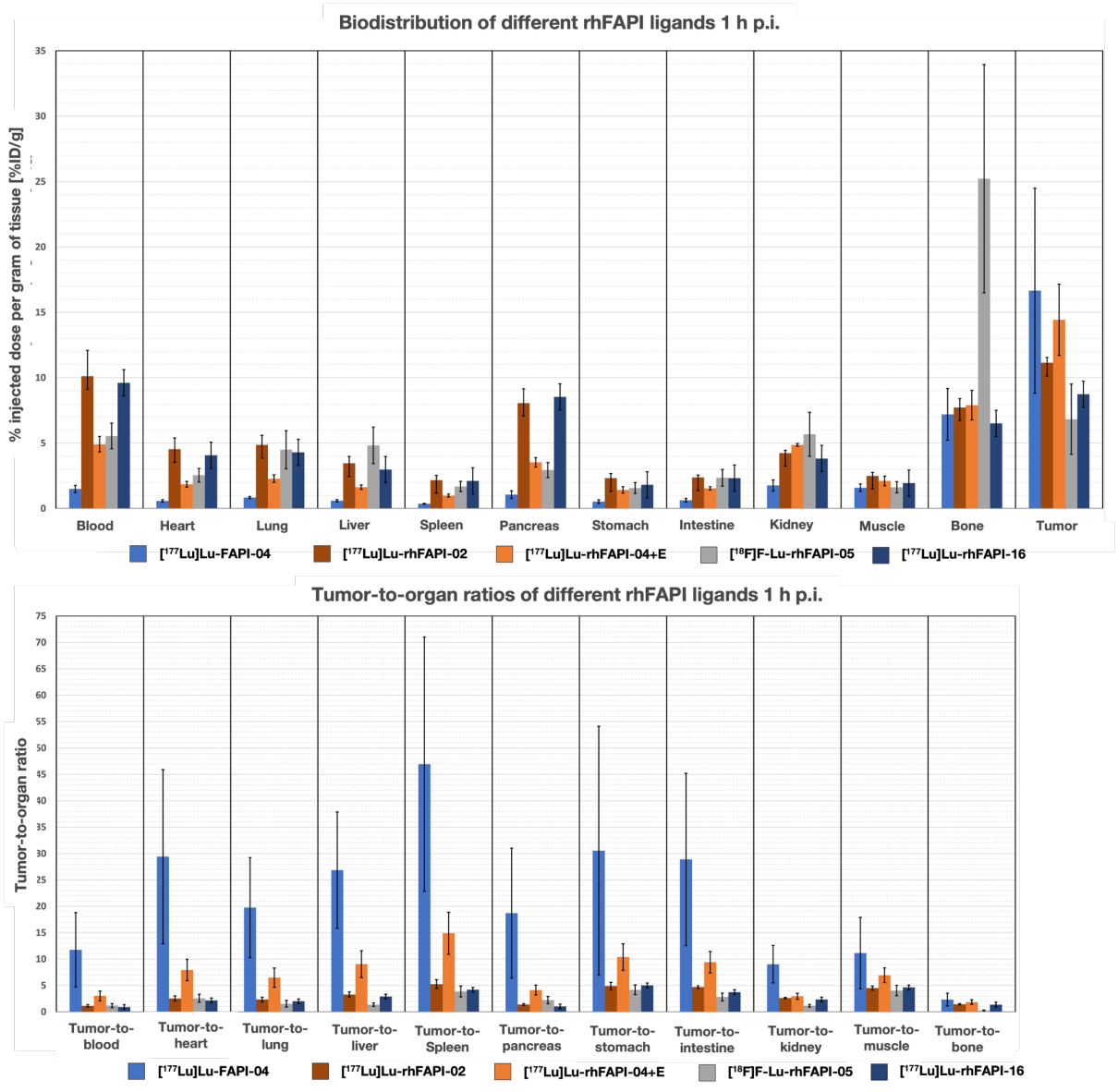

Figure 43: Biodistribution (top) and tumor-to-organ ratios (bottom) of the reference ligand [^{177}Lu]Lu-FAPI-04 and the rhFAPI ligands [^{177}Lu]Lu-rhFAPI-02, [^{177}Lu]Lu-rhFAPI-04+E, [^{18}F]F-Lu-rhFAPI-05 and [^{177}Lu]Lu-rhFAPI-16 at 1 h p.i. in HT-1080hFAP tumor-bearing BALB/c mice (n = 4-5). Values for biodistributions are expressed as a percentage of injected dose per gram of tissue (%ID/g), mean ± SD. Values for tumor-to-organ ratios are expressed as ratios between accumulation in the tumor and accumulation in each organ, mean ± SD.

Altogether, [^{177}Lu]Lu-rhFAPI-16 showed low tumor-to-organ ratios, an unfavorable *in vivo* distribution 1 h p.i. and therefore performed worse than [^{177}Lu]Lu-FAPI-04 and previously evaluated rhFAPI ligands. [^{177}Lu]Lu-rhFAPI-04+E still was the best performing rhFAPI ligand despite its low affinity and strong HSA binding, most likely due to the high hydrophilicity of the compound. [^{177}Lu]Lu-rhFAPI-02 and [^{177}Lu]Lu-rhFAPI-16 demonstrated an almost identical biodistribution and matching similar affinities and lipophilicities, which were higher for both when compared to [^{177}Lu]Lu-rhFAPI-04+E. Only the results of [^{18}F]F-Lu-rhFAPI-05 did not fit into the observed patterns as the fast blood clearance was not consistent with the extremely high lipophilicity of this ligand. Here, the high bone uptake through unlikely but possible *in vivo* ^{18}F-defluorination could be a reason for these difficult to classify results.

Summary and Conclusion of M2 and M3 Optimizations

In summary, all new rhFAPI ligands performed worse than FAPI-04 in all conducted *in vitro* and *in vivo* characterizations. When comparing differently charged modifiers for the modification sites M2 and M3, several lessons could be learned. First, using positively charged or neutral polar modifiers showed beneficial properties with regards to increasing affinity and decreasing binding to HSA of rhFAPI ligands. These characteristics were amplified when the functional group had higher range of motion through longer amino acid side chains. It could be demonstrated, that especially using D-citrulline and D-lysine as modifiers showed promising results. Through studies in which the position of D-citrulline varied, it was observed that the best placement of these modifiers was D-citrulline at modification site M2 and D-lysine at M3. An increased lipophilicity was accompanying the increased affinity and decreased binding to HSA when using these amino acids. As was discussed previously, the characterization of [^{18}F]F-Lu-rhFAPI-05 (M2-M3 = D-cit-D-lys) showed slow clearance of the compound from background tissues in biodistributions studies despite high affinity and low HSA binding most likely caused through its high lipophilicity. Therefore, [$^{nat/177}$Lu]Lu-rhFAPI-16 (M2-M3 = D-cit-D-asp) was investigated replacing the D-lysine at M3 with D-aspartate, leading to a 3-fold lower lipophilicity and only slightly decreased affinity (1.4-fold) but increased HSA binding (1.5-fold). Biodistribution studies showed only marginal improvements for tumor-to-organ ratios manly through a 1.3-fold increased tumor uptake. Despite lower lipophilicity, [^{177}Lu]Lu-rhFAPI-16 exhibited a 1.7-fold increased activity accumulation in blood compared to [^{18}F]F-Lu-rhFAPI-05, probably through its increased binding to HSA.

Summarizing, these results showed the limited ability to influence all relevant *in vitro* parameters with only varying the modification sites M2 and M3. Whatever modifier combinations have been used, only two out of three relevant *in vitro* characteristics could be optimized. Therefore, it was decided to focus on the optimization of the moieties at modification site M4 and M5 for all further rhFAPI developments. Despite showing the most favorable biodistribution, [$^{nat/177}$Lu]Lu-rhFAPI-04+E was not chosen as starting point for following optimization processes because of two reasons. Firstly, the *in vivo* studies were not conducted in parallel to the *in vitro* characterizations therefore, further development of the rhFAPI ligands was not always planned with the knowledge of the biodistribution results. Secondly, it seemed obvious to use a ligand as starting point were just the lipophilicity needed

improvement compared to choosing a ligand were two out of three parameters needed optimization. In the case of [$^{nat/177}$Lu]Lu-rhFAPI-04+E the low affinity and the strong binding towards HSA had to be enhanced. Therefore, [$^{nat/177}$Lu]Lu-rhFAPI-05 was selected because it already combined the highest affinity and lowest binding to HSA, only lacking a preferable high hydrophilicity.

4.1.3 Optimization of Modification Site M4 and M5

Main goal of the following rhFAPI development process was to further improve the existing rhFAPI ligands through modification of the moieties at M4 and M5. Therefore, rhFAPI-05 was selected as starting point because it already had the highest affinity and lowest binding to HSA, only lacking a preferable low lipophilicity. In a fist development step, the SiFA moiety D-dap(SiFA) was exchanged with the SiFAN$^+$ building block D-dap(NMe2-Gly-SiFA*lin*) as shown in Figure 44. The SiFAN$^+$ building block, with a positive charge neighboring the aromatic phenyl of the SiFA moiety, was specifically developed to increase hydrophilicity, and was discussed in more detail in chapter 1.5.3.[178,187] This building block was first used in the development of SiTATE to enhance the hydrophilicity of this SSTR2 addressing tracer, as was described in chapter 1.5.4.[178,185] Since the lipophilic character and strong binding to HSA of the previously developed rhFAPI ligands mainly originated from the SiFA moiety the introduction of the SiFAN$^+$ building block promised to improve both parameters. The benefits of positive charges next to HSA binding moieties to decrease binding strength was already shown in this work and in literature.[185,225]

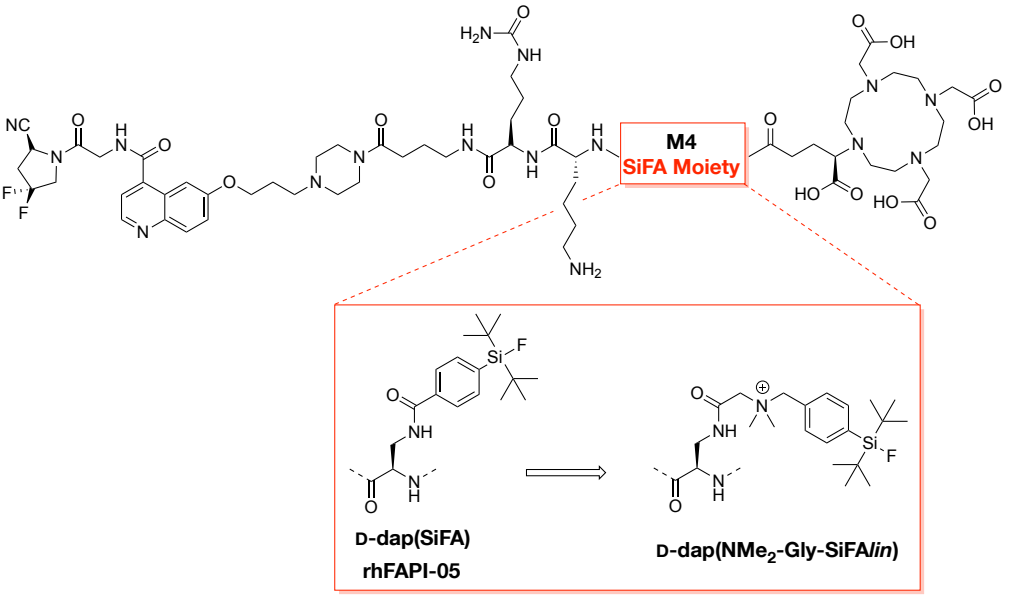

Figure 44: Structure of rhFAPI-05 and the strategic change of the SiFA moiety from a classic D-dap(SiFA) moiety to a SiFAN$^+$ moiety consisting of D-dap(NMe$_2$-Gly-SiFA*lin*).

For this reason, the compounds rhFAPI-17 to -21 (Figure 45) have been synthesized, evaluated, and compared to [$^{nat/177}$Lu]Lu-rhFAPI-05 and the reference [$^{nat/177}$Lu]Lu-FAPI-04. Here, all ligands had the SiFAN$^+$ building block D-dap(NMe2-Gly-SiFA*lin*) incorporated at modification site M4 and only were varied at position M3 or M4. The hydrophilic modifier at M3 can either be a D-lysine, D-aspartate or a double amino acid unit consisting of D-glutamate and D-lysine. Hereby, the influence of charged modifiers on the SiFAN$^+$ building block were investigated. For modification site M5 three different moieties were selected, being either (*R*)-DOTAGA, DOTA or D-asp-DOTA as suitable chelating agent for lutetium in a potential therapeutic application. With this selection the influence of the net charge of the complex and the positioning of negative charges ((*R*)-DOTAGA vs. D-asp-DOTA) in relation to the SiFAN$^+$ building block were investigated.

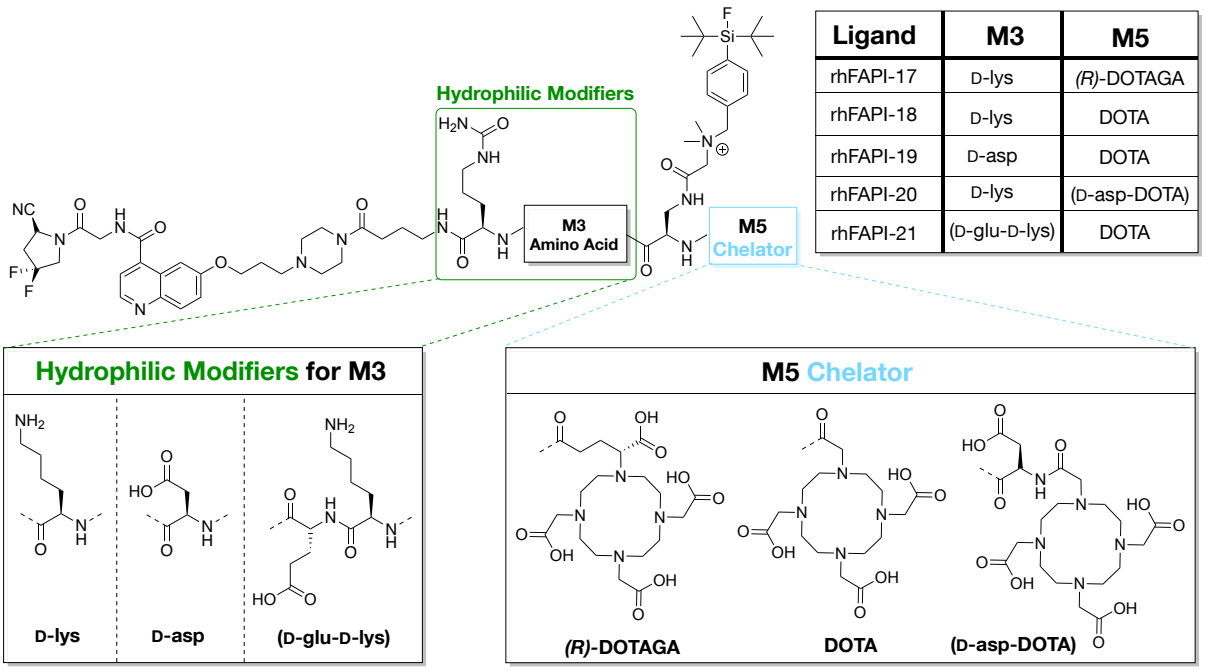

Ligand	M3	M5
rhFAPI-17	D-lys	*(R)*-DOTAGA
rhFAPI-18	D-lys	DOTA
rhFAPI-19	D-asp	DOTA
rhFAPI-20	D-lys	(D-asp-DOTA)
rhFAPI-21	(D-glu-D-lys)	DOTA

Figure 45: Structure of SiFAN⁺ containing ligands rhFAPI-17 to -21 with shown variations at **M3** (hydrophilic modifiers) and **M5** (chelator). Here, **M3** was a modifier from a selection of one or two amino acids (D-lysine, D-aspartate, or D-glutamate) and **M5** was a chelator ((*R*)-DOTAGA or DOTA) or a combination of hydrophilic modifier and chelator (D-asp-DOTA).

In Vitro Characterization

All results from the *in vitro* characterizations of [$^{nat/177}$Lu]Lu-rhFAPI-17 to -21 are shown in Figure 46 to Figure 48. Comparing the binding affinities of these ligands with Lu-rhFAPI-05 showed that introducing the SiFAN⁺ building block D-dap(NMe2-Gly-SiFA*lin*) leads to a 1.5-fold decreased affinity as can be seen for Lu-rhFAPI-17 (M3 = lys, M5 = (*R*)-DOTAGA, IC_{50} = 13.4 ± 1.4 nM), probably through a higher steric demand of the SiFAN⁺ moiety. The change of (*R*)-DOTAGA to DOTA for Lu-rhFAPI-18 (M3 = lys, M5 = DOTA, IC_{50} = 21.4 ± 1.0 nM) decreased affinity by 2.3-fold. This decrease was reverted by introducing a D-aspartate between the SiFAN⁺ building block and the DOTA chelator (Lu-rhFAPI-20 (M3 = lys, M5 = D-asp-DOTA, IC_{50} = 14.0 ± 2.5 nM)). Interestingly, introducing negative charges between the binding motif and the SiFAN⁺ moiety decreased affinity while this effect was enhanced for shorter distances between negative charge and the SiFAN⁺ moiety. Here, Lu-rhFAPI-19 (M3 = asp, M5 = DOTA, IC_{50} = 29.3 ± 5.0 nM) showed a 2.2-fold decreased affinity when compared to Lu-rhFAPI-17 (M3 = lys, M5 = (*R*)-DOTAGA) and a 2.3-fold decreased affinity when compared to Lu-rhFAPI-16, which was the analogous ligand with D-dap(SiFA) as a SiFA moiety. This suggests an electrostatic interaction between the two opposite charges which results in a negative impact on the affinity perhaps by provoking steric repulsion with the binding cavity induced by intramolecular salt bridging. This effect might be weakened with distance between negatively charged functionality and the SiFAN⁺ moiety, explaining why Lu-rhFAPI-21 (M3 = glu-lys, M5 = DOTA, IC_{50} = 23.2 ± 0.8 nM) had a higher affinity compared to Lu-rhFAPI-19 (M3 = asp, M5 = DOTA, IC_{50} = 29.3 ± 5.0 nM). This would also explain why Lu-rhFAPI-17 (M3 = lys, M5 = (*R*)-DOTAGA) and (Lu-rhFAPI-20 (M3 =

lys, M5 = D-asp-DOTA)) showed the best affinities in this series. Here, the negative net charge of the chelator-metal-complex might reduce steric interactions of the SiFAN$^+$ moiety with the binding cavity resulting in a higher affinity through a weakened steric repulsion by intramolecular salt bridging.

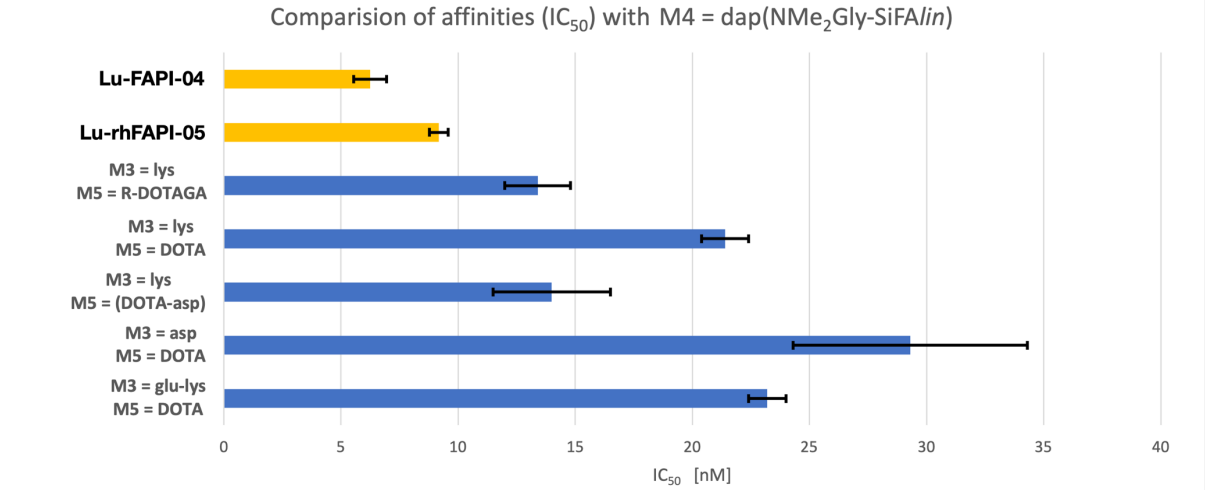

Figure 46: Affinities to FAP (IC_{50} [nM]) on HT-1080hFAP cells (2 h, 4 °C, n = 3) of Lu-FAPI-04 and Lu-rhFAPI-05 as reference and Lu-rhFAPI ligands with GABA as spacer (M1), D-citrulline as hydrophilic modifiers at modification site M2 and dap(Me_2Gly-SiFA*lin*) at modification site M4, with different hydrophilic modifiers at modification site M3 and different chelators (M5). ; mean values ± SD.

Goal of introducing the SiFAN$^+$ moiety was a potential decreased lipophilicity of the rhFAPI ligands. As hypothesized, all SiFAN$^+$-modified ligands showed significantly higher hydrophilicities compared to the SiFA-bearing [^{177}Lu]Lu-rhFAPI-05, where a direct comparison with [^{177}Lu]Lu-rhFAPI-17 (M3 = lys, M5 = (*R*)-DOTAGA, log $D_{7.4}$ = -1.53 ± 0.08) showed a 2.8-fold decreased lipophilicity.

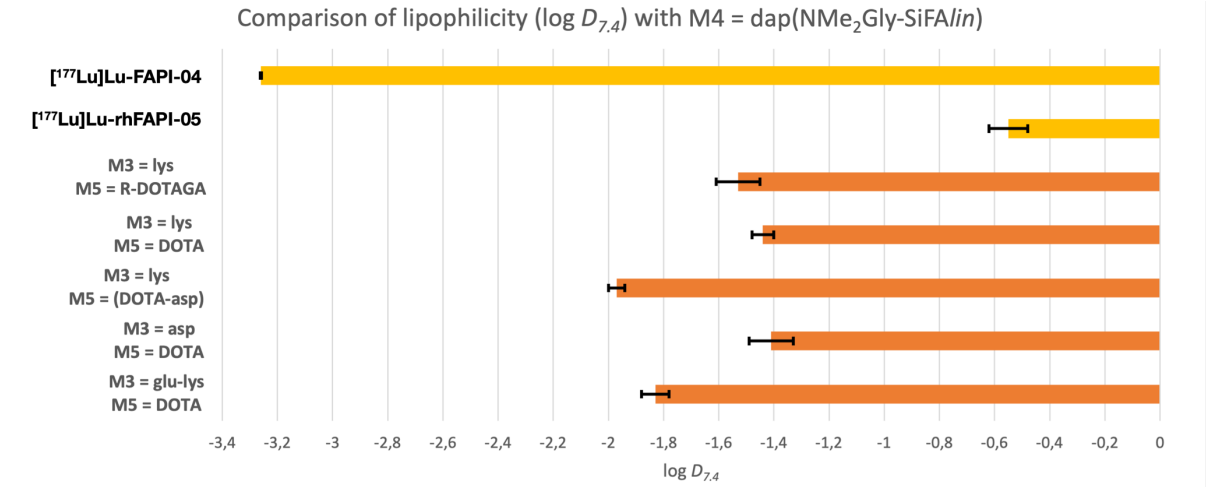

Figure 47: Lipophilicity as octanol/PBS (pH 7.4) partition coefficient (log $D_{7.4}$, n = 8) of [^{177}Lu]Lu-rhFAPI-05 as reference and [^{177}Lu]Lu-rhFAPI ligands with GABA as spacer (M1), D-citrulline as hydrophilic modifiers at modification site M2 and dap(Me_2Gly-SiFA*lin*) at modification site M4, with different hydrophilic modifiers at modification site M3 and different chelators (M5); mean values ± SD.

Nevertheless, the non-radiohybrid reference [^{177}Lu]Lu-FAPI-04 still demonstrated a more then 2-fold higher hydrophilicity. An additional change of the chelator from (*R*)-DOTAGA to DOTA gave only a slightly increased lipophilicity despite the loss of a negatively charged functionality (carboxyl group). Interestingly, the change from (*R*)-DOTAGA to D-asp-DOTA decreased lipophilicity by 1.3-fold. This was surprising because both moieties had the same negative net charge of the chelator-metal-complex. This behavior could be explained through the higher distance of the D-aspartate to the chelator-metal-complex in comparison to the carboxyl groups of (*R*)-DOTAGA. Therefore, having a larger influence on the overall lipophilicity through distributing hydrophilic functionalities over more surface of the ligand or being more exposed and therefore making a stronger contribution to solvation in the aqueous phase. Also, the closer position to the SiFAN$^+$ moiety could be a reason for the increased hydrophilicity.

Figure 48: Binding to human serum albumin (HSA) at the upper panel as apparent molecular weight (MW) determined following the albumin mediated size exclusion chromatography (AMSEC) method (determined on a Superdex™ 75 Increase 10/300 GL column) and at the lower panel as in percent of literature-known calibration-compounds (determined on a Chiralpak HSA column *via* HPAC method) of [$^{nat/177}$Lu]Lu-rhFAPI-05 as reference and [$^{nat/177}$Lu]Lu-rhFAPI ligands with GABA as spacer (M1), D-citrulline as hydrophilic modifiers at modification site M2 and dap(Me$_2$Gly-SiFA*lin*) at modification site M4, with different hydrophilic modifiers at modification site M3 and different chelators (M5).

When looking on the influence of the SiFAN$^+$ moiety on the binding to HSA, a contradictory situation was revealed. On one hand, HSA binding determined *via* the AMSEC method showed a 1.3 to 2.3-fold decreased binding strength, while HSA binding determined *via* the HPAC method showed a 1.1 to 1.2-fold increased binding to HSA, compared to SiFA-bearing [$^{nat/177}$Lu]Lu-rhFAPI-05. These incoherent results didn't allow a final conclusion on the influence of the SiFAN$^+$ moiety on the HSA binding and therefore, comparisons between SiFAN$^+$-containing ligands and [$^{nat/177}$Lu]Lu-FAPI-04 as well as rhFAPI ligands with the classic SiFA moiety D-dap(SiFA) have to be seen with caution. Here, only a comparison between the SiFAN$^+$-containing ligands was made, because the seen trends for these ligands between each other are similar for both methods. Shortly, it was shown that changing the chelator at M5 from (*R*)-DOTAGA to DOTA decreased HSA binding, while incorporating additional negative charges (rhFAPI-19 (M3 = asp, M5 = DOTA) and rhFAPI-20 (M3 = lys, M5 = D-asp-DOTA)) right next to the SiFAN$^+$ moiety did not influence the binding. Introducing a negative charge (rhFAPI-21 (M3 = glu-lys, M5 = DOTA)) with more distance to the SiFAN$^+$ moiety interestingly increased binding to HSA by 1.5-fold compared to (rhFAPI-19 (M3 = asp, M5 = DOTA). Reason for this could be an interaction between the D-glutamate and a functionality at the binding site of HSA where distance between the SiFAN$^+$ moiety and the negative charge was important. This also could explain the 1.7-fold higher binding strength of [$^{nat/177}$Lu]Lu-rhFAPI-17 (M3 = lys, M5 = (*R*)-DOTAGA) to HSA compared to rhFAPI-20 (M3 = lys, M5 = D-asp-DOTA), because here the negative charge of the (*R*)-DOTAGA-metal-complex was positioned further away from the SiFAN$^+$ moiety then the negative charge of the D-aspartate of rhFAPI-20 (M3 = lys, M5 = D-asp-DOTA).

In Vivo Characterization

Considering the results of the *in vitro* characterization, only [^{177}Lu]Lu-rhFAPI-20 (IC_{50} = 14.0 ± 2.5 nM, log $D_{7.4}$ = -1.97 ± 0.03, MW (HSA) = 4.4, HSA binding = 97.1%) was chosen for further *in vivo* evaluation because it combining favorable parameters within all categories including high affinity, above average hydrophilicity and one of the weakest bindings to HSA (AMSEC). For the biodistribution studies the ligand was injected into HT-1080hFAP tumor-bearing female BALB/c mice (Figure 49), evaluated after 1 h p.i. and compared to the reference ligand [^{177}Lu]Lu-FAPI-04. The comparative biodistribution of [^{177}Lu]Lu-rhFAPI-20 revealed similar pharmacokinetics to previously tested rhFAPI ligands. Compared to [^{177}Lu]Lu-rhFAPI-16 (IC_{50} = 12.5 ± 1.8 nM, log $D_{7.4}$ = -1.62 ± 0.07, MW (HSA) = 14.1, HSA binding = 85.7%), the tracer [^{177}Lu]Lu-rhFAPI-20 showed faster blood clearance and lower activity accumulations in non-specific organs like lung, liver, spleen and pancreas. This indicated that the 1.2-fold lower lipophilicity does seem to show an influence in the overall uptake in non-specific organs, while the 3.2-fold decreased binding to HSA significantly decreased (1.8-fold) activity accumulation in blood. This was also seen when comparing the result with the biodistribution of [^{18}F]F-Lu-rhFAPI-05 (IC_{50} = 9.17 ± 0.4 nM, log $D_{7.4}$ = -0.55 ± 0.07, MW (HSA) = 9.6, HSA binding = 82.0%). Here, blood uptake was similar, but the 3.6-fold lower lipophilicity resulted in 2 to 5-fold higher tumor-to-organ ratios for non-specific organs. Kidney uptake of [^{177}Lu]Lu-rhFAPI-20 was the highest for all evaluated rhFAPI ligands. This could be explained with the high amount of charged functionalities, which often

result in a higher uptake into the kidneys, especially for positively charged groups. This behavior was described in literature for different tracers and was subject of studies to reduce kidney uptake by saturating intake through co-administration of positively charged compounds.[231-233]

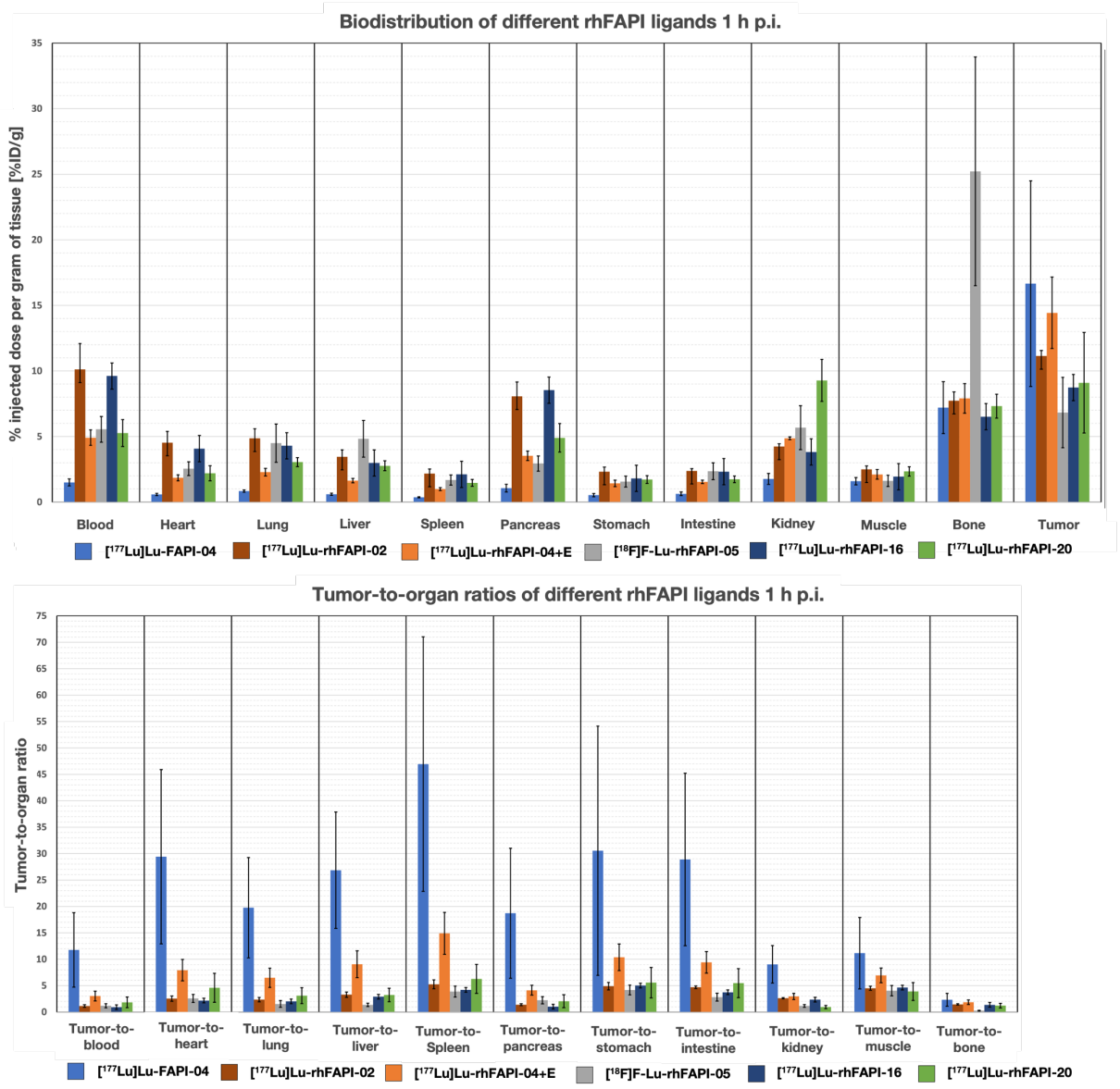

Figure 49: Biodistribution (top) and tumor-to-organ ratios (bottom) of the reference ligand [^{177}Lu]Lu-FAPI-04 and the rhFAPI ligands [^{177}Lu]Lu-rhFAPI-02, [^{177}Lu]Lu-rhFAPI-04+E, [^{18}F]F-Lu-rhFAPI-05, [^{177}Lu]Lu-rhFAPI-16 and [^{177}Lu]Lu-rhFAPI-20 at 1 h p.i. in HT-1080hFAP tumor-bearing BALB/c mice (n = 4-5). Values for biodistributions are expressed as a percentage of injected dose per gram of tissue (%ID/g), mean ± SD. Values for tumor-to-organ ratios are expressed as ratios between accumulation in the tumor and accumulation in each organ, mean ± SD.

Surprisingly, [^{177}Lu]Lu-rhFAPI-20 overall didn't outperform any other rhFAPI ligand despite combining favorable *in vitro* results in all relevant parameters. Here, [^{177}Lu]Lu-rhFAPI-04+E still performed best with the highest tumor uptake and lowest uptake in non-specific organs resulting in highest tumor-to-organ ratios of all rhFAPI ligands. Because [^{177}Lu]Lu-rhFAPI-04+E only performed favorable in one of the tested *in vitro* parameters it was assumed that

there are parameters more important than others for well *in vivo* performance. Looking at the *in vitro* results of the two best performing ligands [^{177}Lu]Lu-rhFAPI-20 (IC_{50} = 14.0 ± 2.5 nM, log $D_{7.4}$ = -1.97 ± 0.03, MW (HSA) = 4.4, HSA binding = 97.1) and [^{177}Lu]Lu-rhFAPI-04+E (IC_{50} = 38.1 ± 1.4 nM, log $D_{7.4}$ = -2.97 ± 0.05, MW (HSA) = 28.9, HSA binding = 98.6) it seemed obvious that lipophilicity was the most important parameter for a favorable *in vivo* distribution behavior. An affinity in the low to medium double digit nanomolar range was sufficient for high tumor uptake nearly reaching the tumor uptake of [^{177}Lu]Lu-FAPI-04. The binding to HSA seemed to be subordinate and strong binding to HSA could be compensated by sufficient high hydrophilicity. Thus, further investigations are necessary in order to fully understand the observed results and tracer differences and to draw conclusions for next FAPI ligand development steps.

Summary and Conclusion of M4 and M5 Optimizations

With the introduction of the SiFAN$^+$ moiety the main goal of the development process of further improving the existing rhFAPI ligands through modification of the moieties at M4 and M5 was successful. A 2.8 to 3.6-fold decreased lipophilicity was achieved while retaining high affinities towards FAP. Additionally, the binding to HSA was reduced by 1.3 to 2.3-fold when viewing at the results of the AMSEC method. But the incoherent results between AMSEC and HPAC method did not allow a conclusion on the influence of the SiFAN$^+$ moiety on the HSA binding and raised questions whether there are unknown interactions between the SiFAN$^+$ moiety and the column materials used for the methods. Further variations at M3 and M5 gave insight into interesting electrostatic interactions between negatively charged amino acids or chelator-metal-complexes with the SiFAN$^+$ moiety, especially influencing the affinity and HSA binding. Here, the distance between the negatively charged functionality and the SiFAN$^+$ moiety played a crucial role for the strength of the interaction. With [^{177}Lu]Lu-rhFAPI-20 (IC_{50} = 14.0 ± 2.5 nM, log $D_{7.4}$ = -1.97 ± 0.03, MW (HSA) = 4.4, HSA binding = 97.1) a ligand was obtained, which combined advantageous *in vitro* properties and was one of the best compounds of all rhFAPI ligands in every parameter of investigation. Subsequent *in vivo* biodistribution studies yielded in disappointing results with no benefit for [^{177}Lu]Lu-rhFAPI-20 at early time points compared to previously evaluated tracers. Although, these results should be treated with caution and should not be overrated as later time points would be necessary to completely understand the distribution and the pharmacokinetics of rhFAPI ligands. [^{177}Lu]Lu-rhFAPI-20 and also other evaluated rhFAPI ligands showed high activity accumulation in blood 1 h after injection. This slow blood clearance indicates the potential of an increased tumor uptake at later time points. Nevertheless, the high blood retention was accompanied by a slower whole-body clearance resulting in unfavorable tumor-to-organ ratios compared to the reference at 1 h p.i., but potentially higher tumor-to-organ ratios at later time points. This wouldn't be ideal for imaging with fluorine-18 but could be beneficial for a therapeutic application with lutetium-177. Nevertheless, further studies in preclinical models will be necessary.

4.1.4 Summary and Conclusion of rhFAPI Ligand Development

Over the course of the rhFAPI ligand development process numerous modification sites could successfully be optimized. Hereby, the in Table 9 listed ligands were synthesized and characterized in several different *in vitro* studies. The results of these comparative studies are shown in Figure 50 to Figure 52. Here, a red star indicates that a compound was additionally evaluated through *in vivo* biodistribution studies and data of [$^{nat/177}$Lu]Lu-rhFAPI-04+E is emphasized in gray indicating that it performed best in these studies.

Table 9: Summary of investigated *in vitro* parameters of the reference Lu-FAPI-04 and Lu-rhFAPI-01 to -21. FAP binding affinities (IC_{50} [nM]) on HT-1080hFAP cells (2 h, 4 °C, n=3). Lipophilicity as octanol/PBS (pH 7.4) partition coefficient (log $D_{7.4}$, n=8). Binding to human serum albumin (HSA) as apparent molecular weight (MW) determined following the albumin mediated size exclusion chromatography (AMSEC) method (determined on a Superdex™ 75 Increase 10/300 GL column) and binding to HSA as in percent of literature-known calibration-compounds (determined on a Chiralpak HSA column *via* HPAC method). Values are expressed as mean ± SD.

FAPI ligand	IC_{50} [nM]	log $D_{7.4}$	MW (HSA) [kDa]	HSA binding [%]
Lu-FAPI-04	6.25 ± 0.7	-3.36 ± 0.002	0.9	30.2
Lu-rhFAPI-01	18.3 ± 2.0	-1.76 ± 0.06	10.1	84.0
Lu-rhFAPI-02	16.5 ± 0.4	-1.99 ± 0.05	12.1	82.1
Lu-rhFAPI-03	17.1 ± 2.1	-1.64 ± 0.08	10.3	91.3
Lu-rhFAPI-04	53.2 ± 5.6	-2.64 ± 0.03	20.7	96.6
Lu-rhFAPI-04+E	38.1 ± 1.4	-2.97 ± 0.05	28.9	98.6
Lu-rhFAPI-05	9.17 ± 0.4	-0.55 ± 0.07	9.6	82.0
Lu-rhFAPI-06	13.9 ± 1.8	-1.14 ± 0.06	10.9	81.8
Lu-rhFAPI-07	14.1 ± 2.5	-1.14 ± 0.06	10.6	87.2
Lu-rhFAPI-08	24.7 ± 1.5	-1.89 ± 0.07	21.4	90.2
Lu-rhFAPI-09	20.2 ±3.1	-0.23 ± 0.03	13.3	92.5
Lu-rhFAPI-10	16.4 ± 1.5	-0.83 ± 0.03	17.5	84.9
Lu-rhFAPI-11	16.9 ± 3.4	-1.07 ± 0.05	13.6	83.8
Lu-rhFAPI-12	26.9 ± 2.3	-1.95 ± 0.08	56.0	94.4
Lu-rhFAPI-13	13.3 ± 2.0	-0.55 ± 0.04	11.2	84.1
Lu-rhFAPI-14	21.8 ± 1.0	-0.41 ± 0.02	13.6	86.7
Lu-rhFAPI-15	12.7 ± 0.6	-0.41 ± 0.01	10.4	85.1
Lu-rhFAPI-16	12.5 ± 1.8	-1.62 ± 0.07	14.1	85.7
Lu-rhFAPI-17	13.4 ± 1.4	-1.53 ± 0.08	7.6	98.6
Lu-rhFAPI-18	21.4 ± 1.0	-1.44 ± 0.04	4.6	98.4
Lu-rhFAPI-19	29.3 ± 5.0	-1.41 ± 0.08	4.1	92.4
Lu-rhFAPI-20	14.0 ± 2.5	-1.97 ± 0.03	4.4	97.1
Lu-rhFAPI-21	23.2 ± 0.8	-1.83 ± 0.05	6.0	98.0

Even though five different modification sites could be successfully optimized, none of the obtained [$^{nat/177}$Lu]Lu-rhFAPI ligands could achieve the superb results of [$^{nat/177}$Lu]Lu-FAPI-04 in any investigated *in vitro* parameter. Questioning the feasibility of introducing the rh concept into FAP-addressing compounds. Considering the affinity towards FAP, a ligand with high

affinity could be identified with Lu-rhFAPI-05 (IC_{50} = 9.17 ± 0.4 nM) with only a 1.5-fold decreased affinity compared to Lu-FAPI-04 (IC_{50} = 6.25 ± 0.7 nM). However, affinity does not appear to be the most important factor for a successful ligand, because Lu-rhFAPI-04+E (IC_{50} = 38.1 ± 1.4 nM) outperformed all other rhFAPI ligands tested in *in vivo* biodistribution studies, although it was the ligand with the lowest affinity. This was also shown for FAPI ligands developed by *Haberkorn et al.* where FAPI-04 outperformed other compounds with higher affinities in respective *in vivo* studies.[111,112,118] Therefore, further development steps concentrated on improving the lipophilicity and reducing the binding to HSA of future ligands.

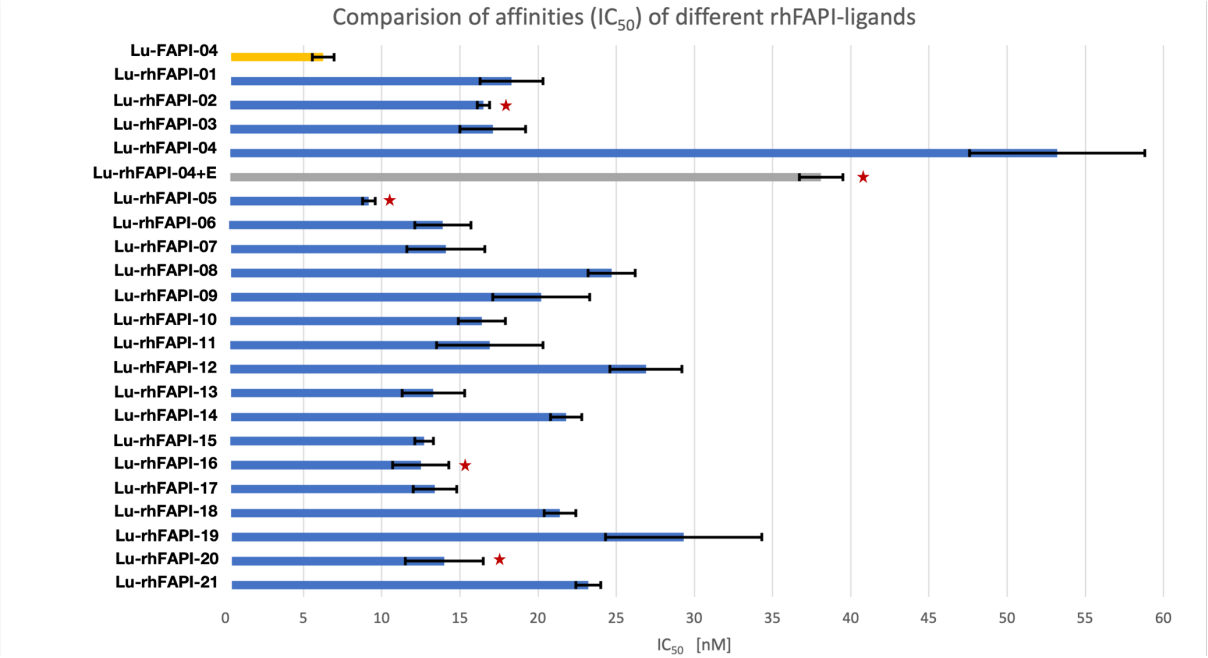

Figure 50: Affinities to FAP (IC_{50} [nM]) on HT-1080hFAP cells (2 h, 4 °C, n = 3) of Lu-FAPI-04 as reference and different Lu-rhFAPI ligands; mean values ± SD. Red stars indicate ligands evaluated by *in vivo* biodistribution studies and data of Lu-rhFAPI-04+E is emphasized in gray indicating that it performed best in these studies.

The structural motif which most affected the lipophilicity of the rhFAPI ligands was the SiFA moiety. Due to the *tert*-butyl residues on the silicon atom, these building blocks - and thus the final ligands - exhibit high lipophilicity. This can lead to hepatobiliary excretion, low accumulation at the target structure, and slow clearance, among other effects. Thus, in the development of SiFA containing ligands, the incorporation of hydrophilic moieties was the preferred approach to counteract these effects.[159,167,183,184] This approach was also used in the development of rhFAPI ligands. Here it was shown that the introduction of negatively charged modifiers (Lu-rhFAPI-04, Lu-rhFAPI-04+E, Lu-rhFAPI-08 and Lu-rhFAPI-12) or a modified SiFA moiety like the $SiFAN^+$ building block (Lu-rhFAPI-16 to -21) were the most promising approaches to counteract the high lipophilicity of the SiFA moiety. Interestingly, the lower the lipophilicity of a ligand the better it performed in *in vivo* biodistribution studies. This led to the conclusion that lipophilicity was the dominant characteristic which must be improved for better performing FAP-addressing ligands. This was underlined by the biodistribution study results of Lu-rhFAPI-04+E (log $D_{7.4}$ = -2.97 ± 0.05) which showed the highest tumor uptake (14.4 ± 2.7 %ID/g) and tumor-to-organ ratios of all evaluated rhFAPI

ligands. Nevertheless, Lu-FAPI-04 still showed favorable results in these studies which probably originate from the 1.1-decreased lipophilicity, but also from higher affinity and lower binding to HSA. The impact of the lipophilicity over the pharmacokinetics of a FAP-addressing compound was also shown for FAPI-34 and similar ^{99m}Tc-labled ligands in the past. Here, all compounds had similar *in vitro* parameters only differing in their lipophilicity, where ^{99m}Tc-FAPI-34 outperformed all compounds. Interestingly, ligands with higher lipophilicity showed higher uptake in non-specific organs and lower tumor uptake, while ligands with lower lipophilicity showed similar low uptake in non-specific organs but also lower tumor uptake compared to ^{99m}Tc-FAPI-34, independent of the other *in vitro* parameters.[118] This indicates that there might be a lipophilic "sweet spot" were too high lipophilicity leads to slow *in vivo* distribution and too low lipophilicity leads to fast clearance with low tumor uptake.

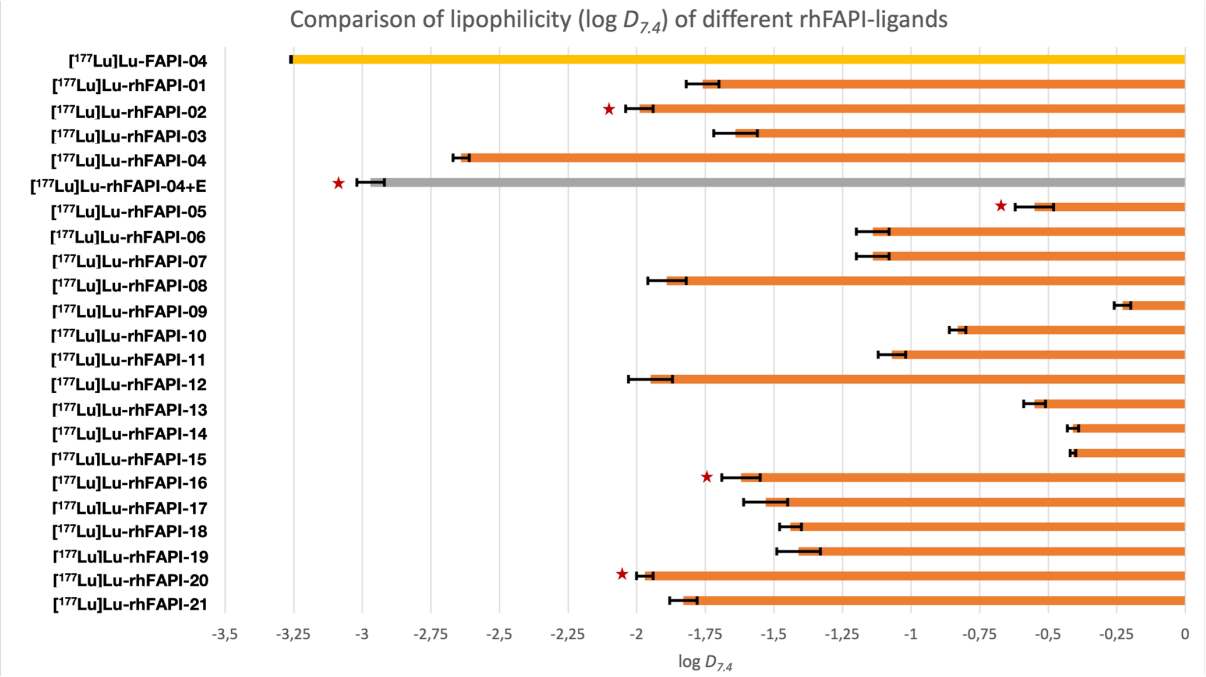

Figure 51: Lipophilicity as octanol/PBS (pH 7.4) partition coefficient (log $D_{7.4}$, n = 8) of [^{177}Lu]Lu-Lu-FAPI-04 as reference and different [^{177}Lu]Lu-rhFAPI ligands; mean values ± SD. Red stars indicate ligands evaluated by *in vivo* biodistribution studies and data of [^{177}Lu]Lu-rhFAPI-04+E is emphasized in gray indicating that it performed best in these studies.

As was seen in previous works of this chair, the SiFA moiety increases binding to HSA significantly.[200] Therefore, a goal of the rhFAPI development process was to decrease the binding strength of this interaction. The influence of charged groups nearby to an HSA binding moiety was describes by *Deberle et al.* for PSMA ligands with ibuprofen as an albumin-binding entity. *Deberle et al*. showed, that negatively charged groups result in stronger binding to HSA, whereby positively charged groups weakened the binding.[227] Similar findings were described by *Martínez-Gómez et al.*, where negatively charged and neutral lipophilic groups can interact with binding sites at HSA.[228] These findings match with the results obtained by the *in vitro* studies. Where the introduction of negatively charged modifiers (Lu-rhFAPI-04, Lu-rhFAPI-04+E, Lu-rhFAPI-08 and Lu-rhFAPI-12) led to a strong binding to HSA, while the

introduction of positively charged groups (Lu-rhFAPI-05, Lu-rhFAPI-06 or Lu-rhFAPI-13) and especially a SiFAN⁺ building block (Lu-rhFAPI-16 to -21) were the most promising approaches to reduce the binding to HSA. The latter was shown only for determination of the binding strength by the AMSEC method, since the HPAC method showed contradictory results.

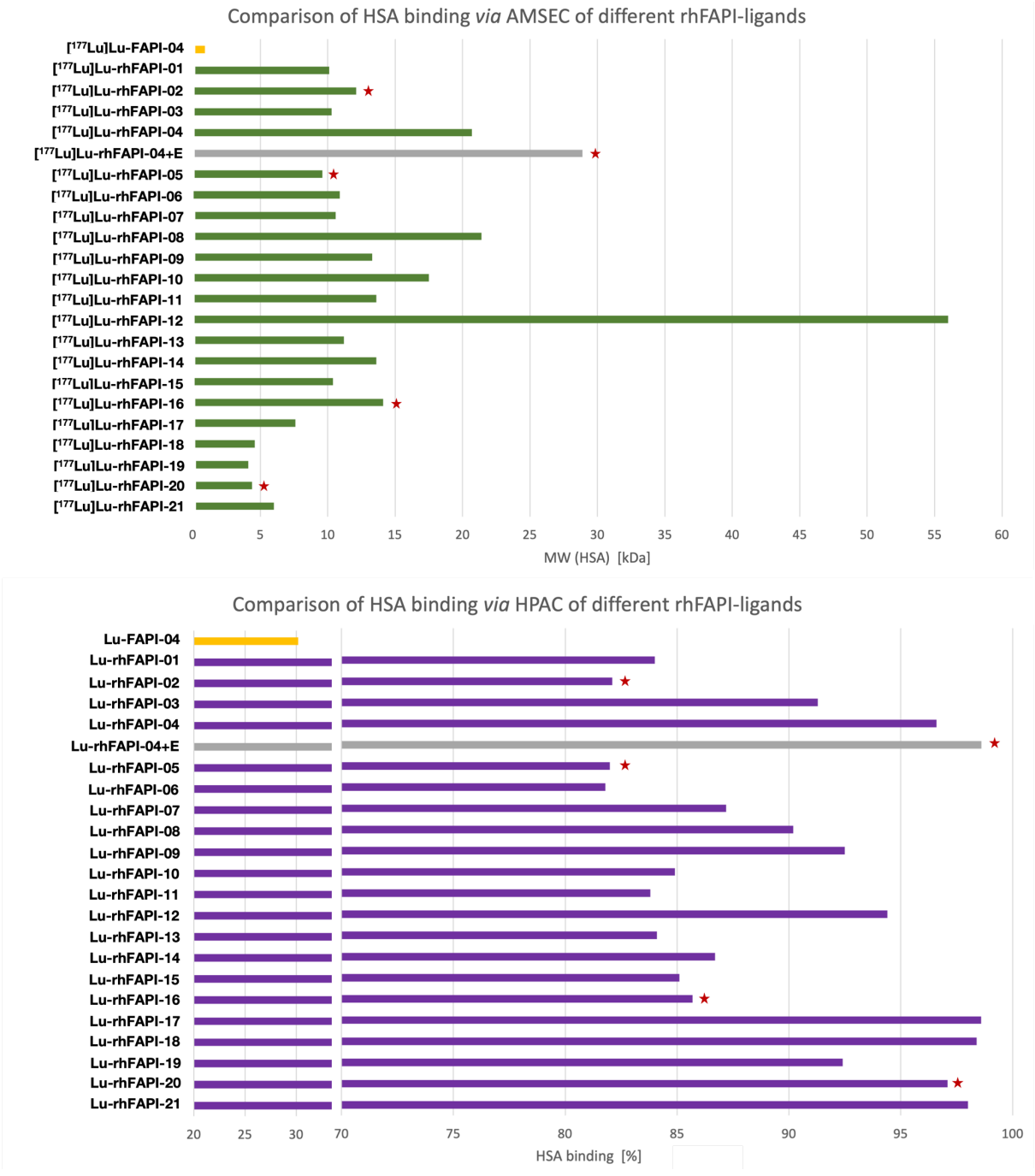

Figure 52: Binding to human serum albumin (HSA) at the upper panel as apparent molecular weight (MW) determined following the albumin mediated size exclusion chromatography (AMSEC) method (determined on a Superdex™ 75 Increase 10/300 GL column) and at the lower panel as in percent of literature-known calibration-compounds (determined on a Chiralpak HSA column *via* HPAC method) of [$^{nat/177}$Lu]Lu-FAPI-04 as reference and different [$^{nat/177}$Lu]Lu-rhFAPI ligands. Red stars indicate ligands evaluated by *in vivo* biodistribution studies and data of [$^{nat/177}$Lu]Lu-rhFAPI-04+E is emphasized in gray indicating that it performed best in these studies.

Because of the results of the *in vivo* biodistribution studies the impact of HSA binding for the performance of a FAP-addressing ligand seemed negligible. When investigating the tumor-to-organ ratios in Figure 49 it can be seen, that the stronger binding to HSA of [^{177}Lu]Lu-rhFAPI-02 (log $D_{7.4}$ = -1.99 ± 0.05, MW (HSA) = 12.1, HSA binding = 82.1) and [^{177}Lu]Lu-rhFAPI-16 (log $D_{7.4}$ = -1.62 ± 0.07, MW (HSA) = 14.1, HSA binding = 85.7) compared to [^{18}F]F-Lu-rhFAPI-05 (log $D_{7.4}$ = -0.55 ± 0.07, MW (HSA) = 9.6, HSA binding = 82.0) could be compensated by a decreased lipophilicity resulting in similar tumor-to-organ ratios. This can be demonstrated especially for [^{177}Lu]Lu-rhFAPI-04+E (IC_{50} = 38.1 ± 1.4 nM, log $D_{7.4}$ = -2.97 ± 0.05, MW (HSA) = 28.9, HSA binding = 98.6) and [^{177}Lu]Lu-rhFAPI-20 (IC_{50} = 14.0 ± 2.5 nM, log $D_{7.4}$ = -1.97 ± 0.03, MW (HSA) = 4.4, HSA binding = 97.1), where the lower lipophilicity of [^{177}Lu]Lu-rhFAPI-04+E led to a favorable *in vivo* performance despite being the ligand with the lowest affinity and strongest binding to HSA. This overall contradiction between *in vitro* and *in vivo* results was also shown for FAPI ligands developed by *Haberkorn et al.,* where FAPI-04 outperformed other compounds in *in vivo* biodistribution studies, while having worse results in *in vitro* studies.[111,112,118] This was not only limited to the ligands developed by *Haberkorn et al.* but also compounds published by other groups (Figure 8).[115,119-124] These compounds were developed in parallel to the ligands described here and used a similar design strategy were the main difference compared to the ligands by *Haberkorn et al.* were the incorporation of moieties for different labeling strategies or additional groups between binding motif and groups needed for labeling. All these compounds also showed less favorable *in vivo* behavior when compared to [^{68}Ga]Ga/[^{177}Lu]Lu-FAPI-04.[115,119-124]

Although, the *in vivo* results of these newly developed group of rhFAPI ligands should be treated with caution and should not be overrated as further later time points would be necessary to completely understand the distribution and the pharmacokinetics of rhFAPI ligands over a longer period. Compared to [^{177}Lu]Lu-rhFAPI-04+E, [^{177}Lu]Lu-rhFAPI-20 and also other evaluated rhFAPI ligands showed high activity accumulation 1 h p.i. in blood. Therefore, one could assume that distribution of these tracers was not finished. Hereby, providing the opportunity of further uptake in tumor tissue over time and higher tumor-to-organ ratios for later time points. This wouldn't be ideal for imaging with fluorine-18 but could be beneficial for a therapeutic application. However, current developed FAP ligands often demonstrate rather low SUVs for tumor tissue. This arises the question, if the activity, accumulated in the tumor, can get high enough to be suitable for a therapeutic application without causing excessive side effects through damaging healthy tissue and organs.[234] Here, especially therapeutic applications with actinium-225 could be of interest, because alpha decay provides high linear energy transfer and demonstrate higher cell-killing efficiencies even with smaller activities compared to β^--emitting isotopes like lutetium-177.[235-237] Therefore, the problem of low SUVs for FAP-addressing tracers in tumors could be overcome with ^{225}Ac-labeled compounds which provide sufficient activity accumulation to deliver high doses into the tumor or tumor microenvironment. Another promising new technology to overcome this problem would be the biology-guided radiotherapy (BgRT).[238-241] Here, the emission generated by an injected PET-tracer is used to guide an external radiotherapy beam

in real time. Therefore, this method could take advantage of the pan tumoral properties of FAP-addressing ligands without the need to develop therapeutic tracers with long tumor retention.

4.2 transFAPI Ligands

Since the previously developed rhFAPI ligands did not meet the required conditions for new promising FAP-addressing ligands that allowed labeling with fluorine-18, a new tracer concept was developed. For this, the design strategy shown in Figure 53 was chosen. The general scaffold of FAPI-04 was extended by the conjugation of a SiFA moiety and an additional chelator at the *N*-terminus positioning the SiFA moiety between the two sterically demanding hydrophilic chelators. This design strategy therefore represents a novel approach compared to other groups (Figure 8), that developed FAP-addressing ligands in parallel to the ligands described here.[115,119-124] These in parallel developed compounds used a similar design strategy compared to the rhFAPI ligands were the main difference to the ligands by *Haberkorn et al.* were the incorporation of moieties for different labeling strategies or additional groups between the binding motif and labeling moieties. Here, the most important goal of the development process was to limit and reduce the influence of the SiFA moiety on the ligands pharmacokinetics and to achieve the highest possible hydrophilicity while keeping a minimalistic structure. This parameter was suspected to be the most important for a favorable *in vivo* distribution of FAPI ligands.

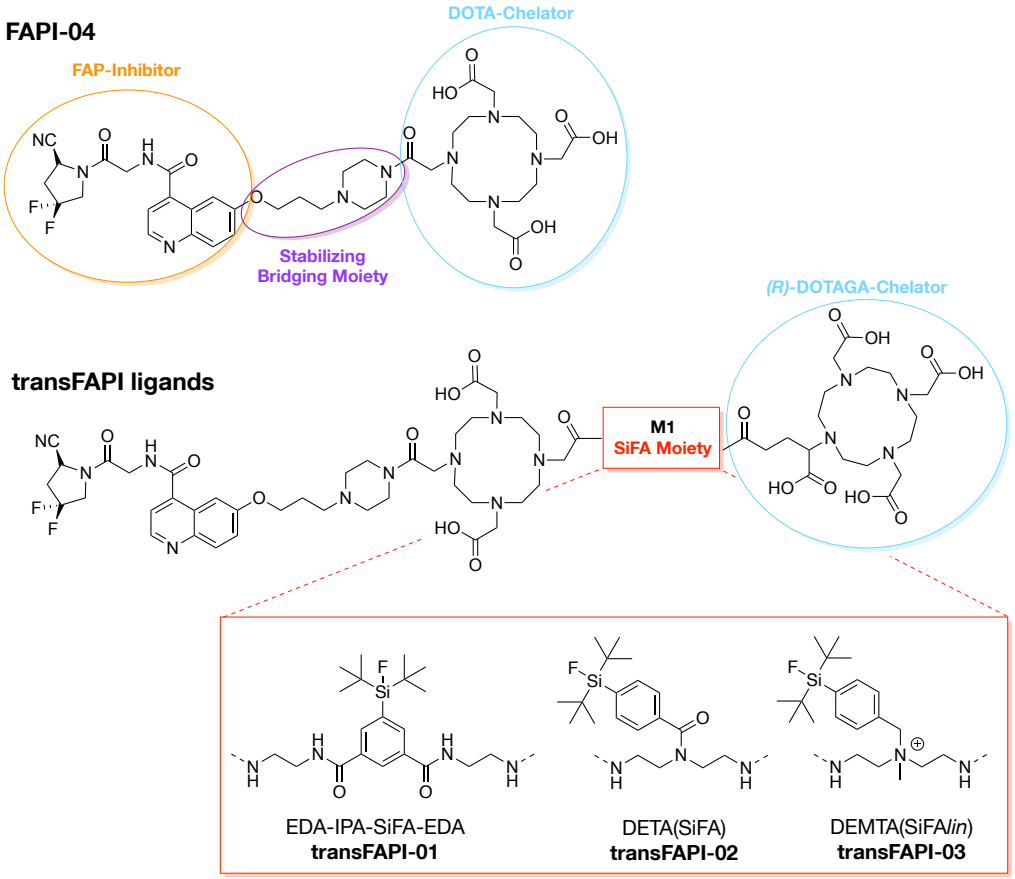

Figure 53: Chemical structure of FAPI-04 developed by *Haberkorn et al.* and conceptual structure of transFAPI ligands containing the shown FAP inhibitor (orange) and stabilizing bridging moiety (purple). As chelator (turquoise), FAPI-04 contains a DOTA, whereas the transFAPI ligands possess a DOTA and (*R*)-DOTAGA. The transFAPI ligands have the variable modification site **M1**, which is a symmetric SiFA moiety (red) either being EDA-IPA-SiFA-EDA (transFAPI-01), DETA(SiFA) (transFAPI-02), or DEMTA(SiFA*lin*) (transFAPI-03).

To achieve this goal three ligands were synthesized which differed only in the choice of the SiFA moiety. Here, a selection of symmetric fragments was developed as described in chapter 3.1.5. The IPA-SiFA building block used for transFAPI-01 differs from SiFA-BA and SiFA-Br, because it contains two linking sites at the *3,5*-positions instead of a single linking site at the *4*-position of the benzene ring. Initially, the synthesis of a DETA(IPA-SiFA) building block (Scheme 5) was planned, similar to DETA(SiFA) and DEMTA(SiFA*lin*), which would provide a negatively charged carboxylic acid next to the di-*tert*-butyl-fluoro-silane group of the SiFA moiety to compensate the lipophilic property of this group. This DETA(IPA-SiFA) building block could not be produced in sufficient quantities to manufacture a corresponding ligand. Instead, the two linking sites of the IPA-SiFA building block were used to incorporate it symmetrically between the DOTA and *(R)*-DOTAGA chelator through two bridging EDAs, resulting in the synthesis of transFAPI-01. Here, the SiFA moiety was integrated tightly into the ligand's backbone with relatively low range of motion, which was expected to result in a better compensation of its lipophilicity by the neighboring chelators. Compared to the DETA(IPA-SiFA) building block, the mono-Fmoc-protected analogs of DETA(SiFA) and DEMTA(SiFA*lin*) could be synthesized, allowing the development of transFAPI-02 and -03. These building blocks used a symmetric triamine building block, where the SiFA moiety was coupled to the central secondary amine. For DETA(SiFA) the already previously used SiFA-BA was used as SiFA moiety and for DEMTA(SiFA*lin*) a SIFAN$^+$ approach was followed. Here, the central secondary amine was methylated and coupled with SiFA-Br, which resulted in a SIFAN$^+$ moiety with a permanent positive charge next to the SiFA group. These symmetric SiFA containing building blocks were incorporated between the DOTA chelator of the FAPI-04 structure and an additional *(R)*-DOTAGA to allow highest possible shielding of the lipophilic *tert*-butyl groups of the SiFA moiety to achieve favorable hydrophilic properties for the transFAPI ligands. In general, all ligands could be prepared *via* a mixed solid-phase/solution-phase synthesis strategy and subsequent purification yielded between 5 to 15%. Here, all utilized building blocks (FAP-inhibitor and SiFA moieties) were synthesized according to procedures described in chapter 3. For all ligands FAP-affinity (IC_{50}, competitive binding assay on HT-1080hFAP cells), lipophilicity (log $D_{7.4}$, by means of the distribution in *n*-octanol and PBS at pH 7.4), as well as binding to human serum albumin were determined and later compared to the reference compound [$^{nat/177}$Lu]Lu-FAPI-04. All transFAPI ligands were evaluated in their respective fluoride-18 labeled form. Additionally, the DOTA/*(R)*-DOTAGA-gallium- and lutetium-chelates were also evaluated.

4.2.1 *In Vitro* Characterization

All results from the *in vitro* characterizations of the reference [$^{nat/177}$Lu]Lu-FAPI-04 and [$^{nat/18}$F]F-transFAPI-01 to -03 and their respective gallium- and lutetium-chelates are shown in Figure 54 to Figure 56. Compared to Lu-FAPI-04 all transFAPI ligands displayed 1.7- to 2.9-fold decreased affinities to FAP. Interestingly, affinities are increased for the metal-chelates of the transFAPI ligands, especially for transFAPI-01 and -02 with a 1.4- to 1.6-fold increase. This however was not the case for transFAPI-03, where upon metal complexation no significant increase in affinity was found. A reason for this could be the overall net charge of the respective ligand and the distribution of the respective charges. As previously shown for the rhFAPI ligands negative charges in the proximity of the binding site presumably resulted in lower affinities. Here, the doubly negatively charged, uncomplexed *trans*-bridged DOTA chelator could negatively affect the affinity towards FAP through repulsive interactions, while affinity increases again when DOTA was chelated with gallium or lutetium, leading to a net positive charge of the complex. This behavior was somewhat less pronounced for transFAPI-03, probably due to the permanent positive charge of the SIFAN$^+$ moiety next to the DOTA chelator, which could already offset the negative influence of a negatively charged group next to the binding site. This trend was also seen when comparing all three uncomplexed transFAPI ligands where transFAPI-03 demonstrated the highest affinity. Especially Ga_2-transFAPI-02 and Lu_2-transFAPI-02 showed promising results with only a 1.4-fold decreased affinity compared to Lu-FAPI-04.

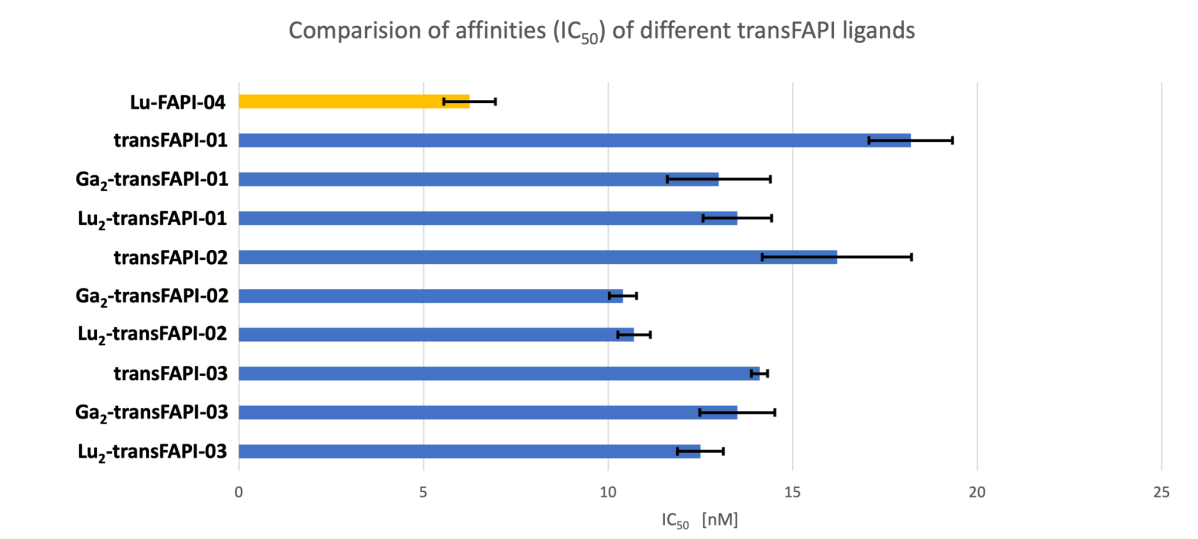

Figure 54: Affinities to FAP (IC_{50} [nM]) on HT-1080hFAP cells (2 h, 4 °C, n = 3) of Lu-FAPI-04 as reference and different transFAPI ligands either uncomplexed or complexed with gallium or lutetium; mean values ± SD.

Evaluation of the lipophilicity of the different transFAPI ligands resulted in surprisingly unfavorable properties. All compounds showed 1.7- to 2.4-fold increased lipophilicity compared to [^{177}Lu]Lu-FAPI-04, therefore not fulfilling the main goal of this ligand development process, which was to demonstrate higher hydrophilicities compared to the rhFAPI ligands. Here, all compounds show similar lipophilicity as the most rhFAPI ligands but a 1.5- to 2.1-fold increased lipophilicity when compared with the most hydrophilic tracer

[^{177}Lu]Lu-rhFAPI-04+E. Except for transFAPI-03, the lipophilicity further increased for the respective gallium- and lutetium-chelates. Here, the larger sized lutetium resulted in a higher lipophilicity compared to gallium when chelated with DOTA and *(R)*-DOTAGA. Reason therefore could be simply the larger size over which the net charge of the chelate was distributed or that gallium needs one acid group less for coordination. Therefore, the gallium-chelate has an acid group with relatively high freedom of movement allowing for additional solvation and herewith hydrophilicity. Interestingly, the lipophilicity of the ligands seemed to only be dependent on the overall net charge of the compound and the metal used for complexation.

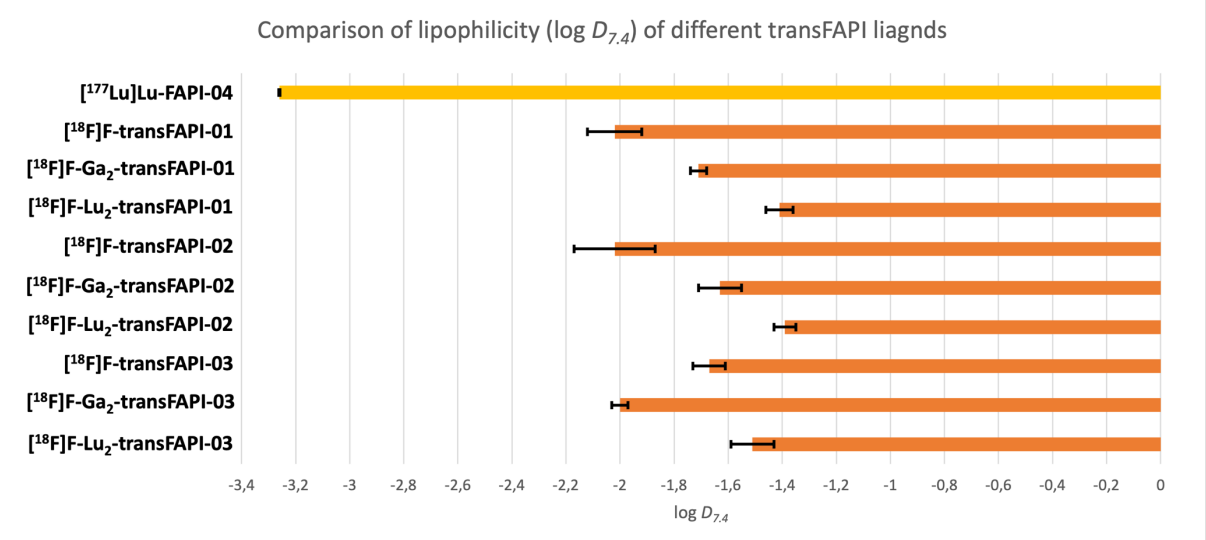

Figure 55: Lipophilicity as octanol/PBS (pH 7.4) partition coefficient (log $D_{7.4}$, n = 8) of [^{177}Lu]Lu-FAPI-04 as reference and different [^{18}F]F-transFAPI ligands either uncomplexed or complexed with gallium or lutetium; mean values ± SD.

This allowed the conclusion, that the chosen ligand design strategy was successful in the sense that the influence of the used SiFA moiety building block was negligible. For high negative net charges of -5 ([^{18}F]F-transFAPI-01 and -02) the lowest lipophilicities were determined. Lowering the net charge to -4 ([^{18}F]F-transFAPI-03) resulted in a higher lipophilicity. After complexation of transFAPI-01 and -02 with gallium or lutetium (net charge of +1) the lipophilicity further increases, thus strengthening the assumption that negative charges have a more pronounced effect on influencing the lipophilicity compared to positive charges. This was also found when investigating the previously developed rhFAPI ligands. The influence of the larger size of lutetium compared to gallium was already discussed above. The only compound not following this observation was transFAPI-03, where the respective gallium-chelate resulted in the lowest lipophilicity of this set of ligands. This most likely could be explained through electrostatic interactions of the permanent positive charge of the SIFAN$^+$ moiety with the neighboring negative charges of the uncomplexed ligand. Thus, this interaction was not present for the gallium-chelated *trans*-bridged DOTA probably resulting in overall favorable charge distribution over the whole length of the ligand. Despite the usage of two chelators and, in the case of transFAPI-03, a SIFAN$^+$ moiety to compensate the high

lipophilicity of the SiFA group the target of a similar lipophilicity compared to [^{177}Lu]Lu-FAPI-04 could not be achieved.

As for the binding strength of the transFAPI ligands towards HSA, there were several findings worth discussing. First, incoherent results were obtained for the determination of HSA binding *via* the AMSEC and the HPAC method. The metal derivatives of transFAPI-01 and -02 showed lower HSA binding compared to their free counterparts when determined *via* AMSEC however analysis *via* HPAC resulted in increased binding.

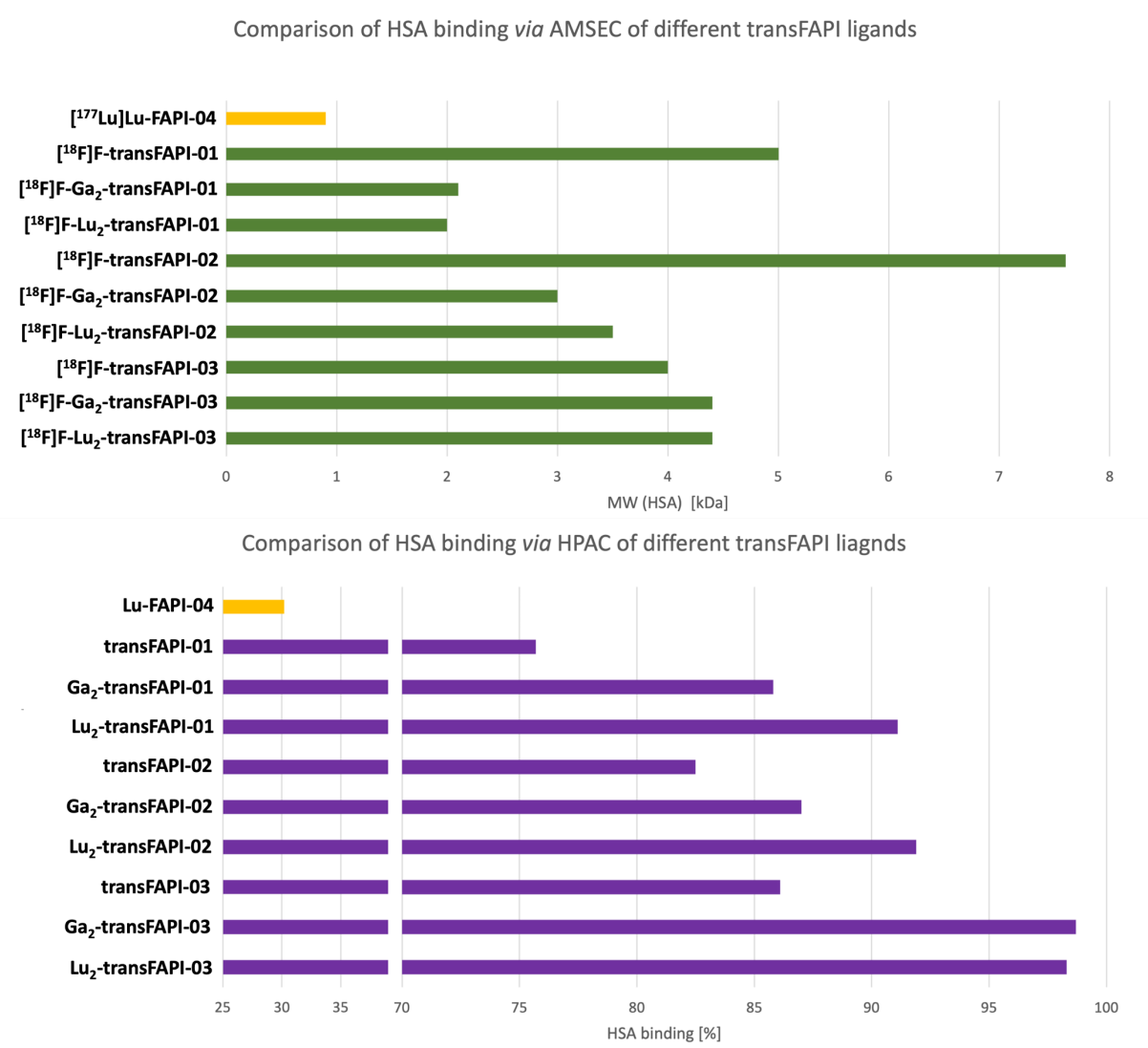

Figure 56: Binding to human serum albumin (HSA) at the upper panel as apparent molecular weight (MW) determined following the albumin mediated size exclusion chromatography (AMSEC) method (determined on a Superdex™ 75 Increase 10/300 GL column) and at the lower panel as in percent of literature-known calibration-compounds (determined on a Chiralpak HSA column *via* HPAC method) of [$^{nat/177}$Lu]Lu-FAPI-04 as reference and different [$^{nat/18}$F]F-transFAPI ligands either uncomplexed or complexed with gallium or lutetium.

For the AMSEC method the respective metal-chelates of transFAPI-01 and -02 (MW = 2.0 to 3.5 kDA) showed very low binding compared to the previously evaluated rhFAPI ligands (MW = 4.1 to 56.0 kDA), which indicated that the chosen ligand design strategy was

successful in reducing the influence of the used SiFA moiety on HSA binding. Surprisingly, as it was found for the rhFAPI ligands (chapter 4.1.3) the incorporation of the SIFAN$^+$ moiety into transFAPI-03 did not result in the expected, reduced binding strength towards HSA when looking at the results of the HPAC method. Here, transFAPI-03 and its respective metal-chelates showed the highest binding strength of the group of transFAPI ligands. When comparing the data obtained by the AMSEC method, transFAPI-03 showed lower binding compared to transFAPI-01 and -02, but for these compounds binding strength decreased when being complexed, while the binding strength towards HSA increased for the metal-chelates of transFAPI-03. As lower binding to HSA seemingly has not been significant for predicting *in vivo* behavior when evaluating the rhFAPI ligands no further investigations were conducted.

In summary, all transFAPI ligands and their metal-chelates showed higher binding towards HSA compared to [^{177}Lu]Lu-FAPI-04, but very low binding *via* AMSEC when compared to the previously developed rhFAPI ligands. Especially the metal-chelates of transFAPI-01 and -02 showed the lowest binding to HSA when measured by the AMSEC method and the metal-free analogs of transFAPI-01 showed the lowest binding to HSA when measured by the HPAC method.

4.2.2 *In Vivo* Characterization

For the biodistribution studies the ligands were injected into HT-1080hFAP tumor-bearing female BALB/c mice (Figure 57), evaluated after 1 h p.i. and compared to the reference ligand [^{177}Lu]Lu-FAPI-04. Considering the results of the *in vitro* characterization, only [^{18}F]F-Ga$_2$-transFAPI-02 (IC_{50} = 10.4 ± 0.4 nM, log $D_{7.4}$ = -1.63 ± 0.08, MW (HSA) = 3.0, HSA binding = 87.0%), [^{18}F]F-Ga$_2$-transFAPI-03 (IC_{50} = 13.5 ± 1.0 nM, log $D_{7.4}$ = -2.00 ± 0.03, MW (HSA) = 4.4, HSA binding = 98.7%) and [^{18}F]F-Lu$_2$-transFAPI-03 (IC_{50} = 12.5 ± 0.6 nM, log $D_{7.4}$ = -1.51 ± 0.08, MW (HSA) = 4.4, HSA binding = 98.3%) were chosen for further *in vivo* evaluation.

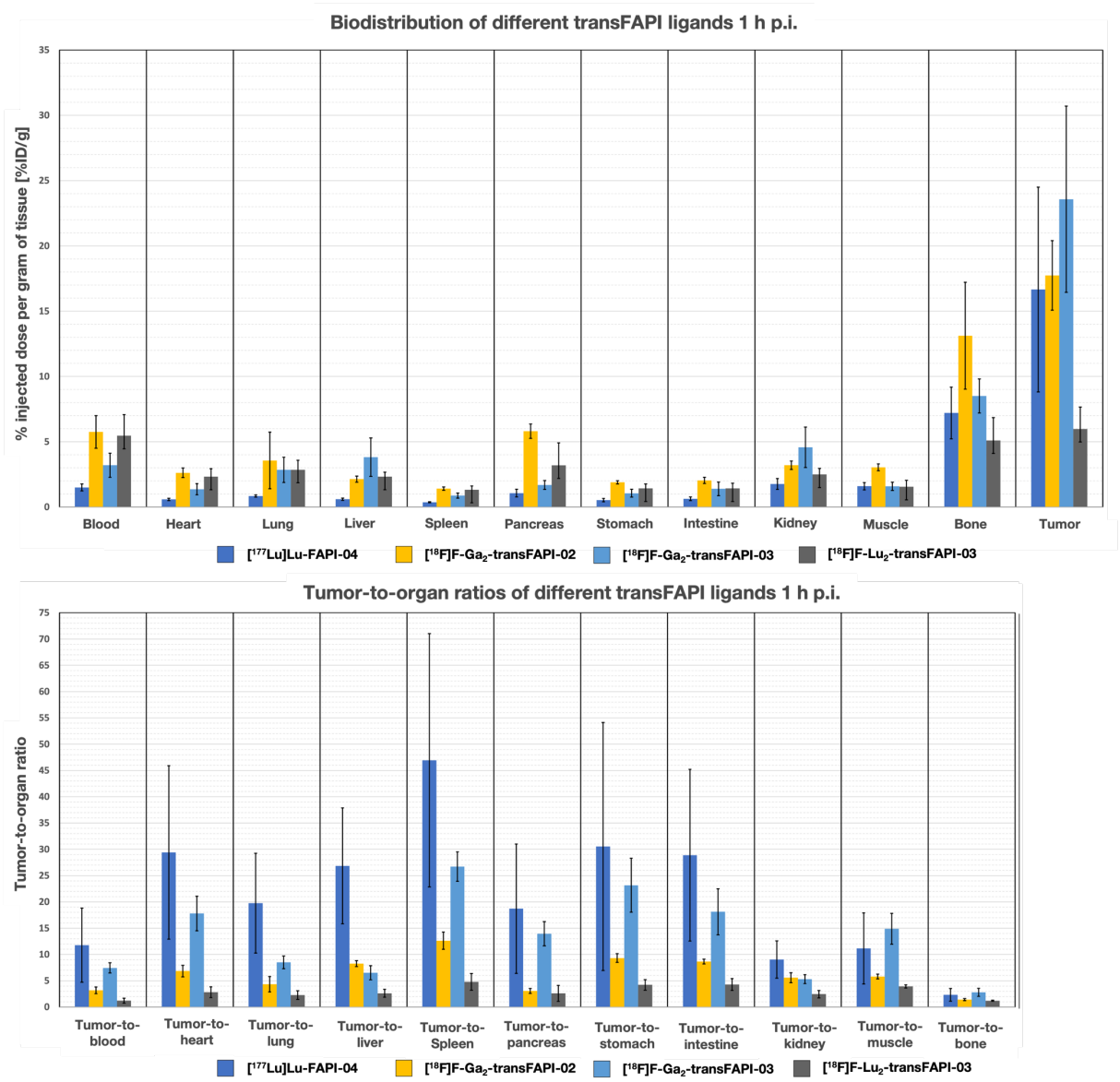

Figure 57: Biodistribution (top) and tumor-to-organ ratios (bottom) of the reference ligand [^{177}Lu]Lu-FAPI-04 and the transFAPI ligands [^{18}F]F-Ga$_2$-transFAPI-02, [^{18}F]F-Ga$_2$-transFAPI-03 and [^{18}F]F-Lu$_2$-transFAPI-03 at 1 h p.i. in HT-1080hFAP tumor-bearing BALB/c mice (n = 4-5). Values for biodistributions are expressed as a percentage of injected dose per gram of tissue (%ID/g), mean ± SD. Values for tumor-to-organ ratios are expressed as ratios between accumulation in the tumor and accumulation in each organ, mean ± SD.

These were selected for the following reasons. First, only metal-chelated ligands should be examined because tracers with free chelators could incorporate different metal ions *in vivo* leading to inconclusive results. Regarding the metal-chelates, [^{18}F]F-Ga$_2$-transFAPI-02 showed the highest affinity combined with the second lowest lipophilicity and low HSA binding. The analogs [^{18}F]F-Ga$_2$-transFAPI-03 and [^{18}F]F-Lu$_2$-transFAPI-03 were chosen because the first ligand showed the lowest lipophilicity, which was the goal of this ligand development process, and the second represents the therapeutic alternative to [^{18}F]F-Ga$_2$-transFAPI-03 enabling a theranostic approach with ^{18}F/^{177}Lu-tracer analogs. The comparative biodistribution of these ligands revealed surprisingly high tumor uptakes for [^{18}F]F-Ga$_2$-transFAPI-02 (17.74 ± 2.66 %ID/g) and [^{18}F]F-Ga$_2$-transFAPI-03 (23.57 ± 7.13 %ID/g) even surpassing the uptake of [^{177}Lu]Lu-FAPI-04 (16.66 ± 7.84 %ID/g). Despite possessing a higher affinity and lower binding to HSA [^{18}F]F-Ga$_2$-transFAPI-02 showed higher activity accumulation in nearly all non-specific organs, probably originating from the slower blood clearance seen at the high activity being available in the blood. In comparison to [^{18}F]F-Ga$_2$-transFAPI-03 (log $D_{7.4}$ = -2.00 ± 0.03) this most likely was due to its higher lipophilicity (log $D_{7.4}$ = -1.63 ± 0.08). Interestingly, [^{18}F]F-Lu$_2$-transFAPI-03 performed unexpectedly unfavorable compared to its gallium-chelate. A low uptake into the tumor (5.96 ± 1.68 %ID/g) and similar accumulation in other organs resulted in low tumor-to-organ ratios. This strong influence of the chelated metal was somewhat not surprising as this behavior was known for tracers applied for different targets when the complexed chelator was in proximity to the binding motif. Prominent examples are the theranostic pairs [^{68}Ga]Ga/[^{177}Lu]Lu-Pentixafor and [[^{68}Ga]Ga/[^{177}Lu]Lu -DOTATATE for which a lower affinity and different *in vivo* distributions were reported for the lutetium-chelate.[242-250] Due to the high tumor uptake of [^{18}F]F-Ga$_2$-transFAPI-03 and the relatively low uptake in other organs the corresponding tumor-to-organ ratios were the highest for this subset of ligands. Only the accumulation in the excretion organs liver and kidney were the highest in this comparative study. For the liver uptake this was surprising as [^{18}F]F-Ga$_2$-transFAPI-03 showed the lowest lipophilicity. The accumulation in the kidneys might be explainable due to a higher positive net charge of the ligand. This behavior was mentioned earlier and described in literature for different tracers and was subject of studies to reduce kidney uptake by saturating intake through addition of positively charged compounds.[231-233] High uptake in bone and joints could be explained through FAP expression in these structures. This expression is described in literature by *Toms et al.* and could be blocked through addition of excess of non-labeled FAP addressing ligands.[115] Despite the higher tumor uptake of [^{18}F]F-Ga$_2$-transFAPI-03 compared to [^{177}Lu]Lu-FAPI-04 the latter still showed much higher tumor-to-organ ratios making it superior against the developed transFAPI ligands for the chosen time point.

4.2.3 Summary and Conclusion of transFAPI Ligand Development

Over the course of the transFAPI ligand development process several tracers bearing a symmetric SiFA-containing bridging motif could successfully be synthesized. These ligands were characterized in several different *in vitro* studies which results are shown in Table 10. The new developed SiFA moieties (EDA-IPA-SiFA-EDA, DETA(SiFA) and DEMTA(SiFA*lin*)) could successfully be labeled with fluorine-18 in sufficient RCYs to perform all *in vitro* and *in vivo* characterizations.

Table 10: Summary of investigated *in vitro* parameters of the reference Lu-FAPI-04 and transFAPI-01 to -03 and their respective gallium or lutetium complexes. FAP binding affinities (IC_{50} [nM]) on HT-1080hFAP cells (2 h, 4 °C, n=3). Lipophilicity as octanol/PBS (pH 7.4) partition coefficient (log $D_{7.4}$, n=8). Binding to human serum albumin (HSA) as apparent molecular weight (MW) determined following the albumin mediated size exclusion chromatography (AMSEC) method (determined on a Superdex™ 75 Increase 10/300 GL column) and binding to HSA as in percent of literature-known calibration-compounds (determined on a Chiralpak HSA column *via* HPAC method). Values are expressed as mean ± SD.

FAPI ligand	IC_{50} [nM]	log $D_{7.4}$	MW (HSA) [kDa]	HSA binding [%]
Lu-FAPI-04	6.25 ± 0.7	-3.36 ± 0.002	0.9	30.2
transFAPI-01	18.2 ± 1.1	-2.02 ± 0.1	5.0	75.7
Ga_2-transFAPI-01	13.0 ± 1.4	-1.71 ± 0.03	2.1	85.8
Lu_2-transFAPI-01	13.5 ± 0.9	-1.41 ± 0.05	2.0	91.1
transFAPI-02	16.2 ± 2.0	-2.02 ± 0.15	7.6	82.5
Ga_2-transFAPI-02	10.4 ± 0.4	-1.63 ±0.08	3.0	87.0
Lu_2-transFAPI-02	10.7 ± 0.4	-1.39 ± 0.04	3.5	91.9
transFAPI-03	14.1 ± 0.2	-1.67 ±0.06	4.0	86.1
Ga_2-transFAPI-03	13.5 ± 1.0	-2.00 ± 0.03	4.4	98.7
Lu_2-transFAPI-03	12.5 ± 0.6	-1.51 ± 0.08	4.4	98.3

The main goal of this work was the improvement of the lipophilicity, which was suspected to be the most important parameter for favorable *in vivo* distribution of FAP-addressing ligands. This goal was not achieved, as the most hydrophilic rhFAPI ligand had a 1.5-fold increased hydrophilicity compared to the most hydrophilic transFAPI ligands. With respect to the affinity towards FAP and the binding strength to HSA the new transFAPI ligands were comparable to the best performing rhFAPI ligands in these two investigated parameters. This confirmed that the new design strategy allowed promising results in these *in vitro* characterizations while simplifying the overall structure of the compounds. Here, also the influence of the chelated metal ions was further investigated. For the rhFAPI ligands only few compounds were evaluated as their gallium-chelate and not all parameters were determined. There, first results suggested that the influence of the used metal-chelate was negligible. However, the evaluation of the different transFAPI ligands and their metal chelates showed a significant influence, especially for transFAPI-01 and -02. Here, affinity and lipophilicity increased with complexation of the chelators, while lipophilicity further increased when using lutetium instead of gallium. This influence might mainly come from the complexation of the *trans*-bridged DOTA-chelator next to the FAP binding motif as no influence was found for the rhFAPI

ligands lacking this chelator. The obtained *in vitro* data first did not suggest any big improvements compared to the previously developed rhFAPI ligands and despite the missed objective of further decrease lipophilicity, first *in vivo* biodistribution studies showed surprisingly favorable tumor-to-organ ratios and the highest tumor uptake for [^{18}F]F-Ga$_2$-transFAPI-03. The results of all comparative biodistribution studies performed for the rhFAPI and transFAPI ligands are displayed in Figure 58.

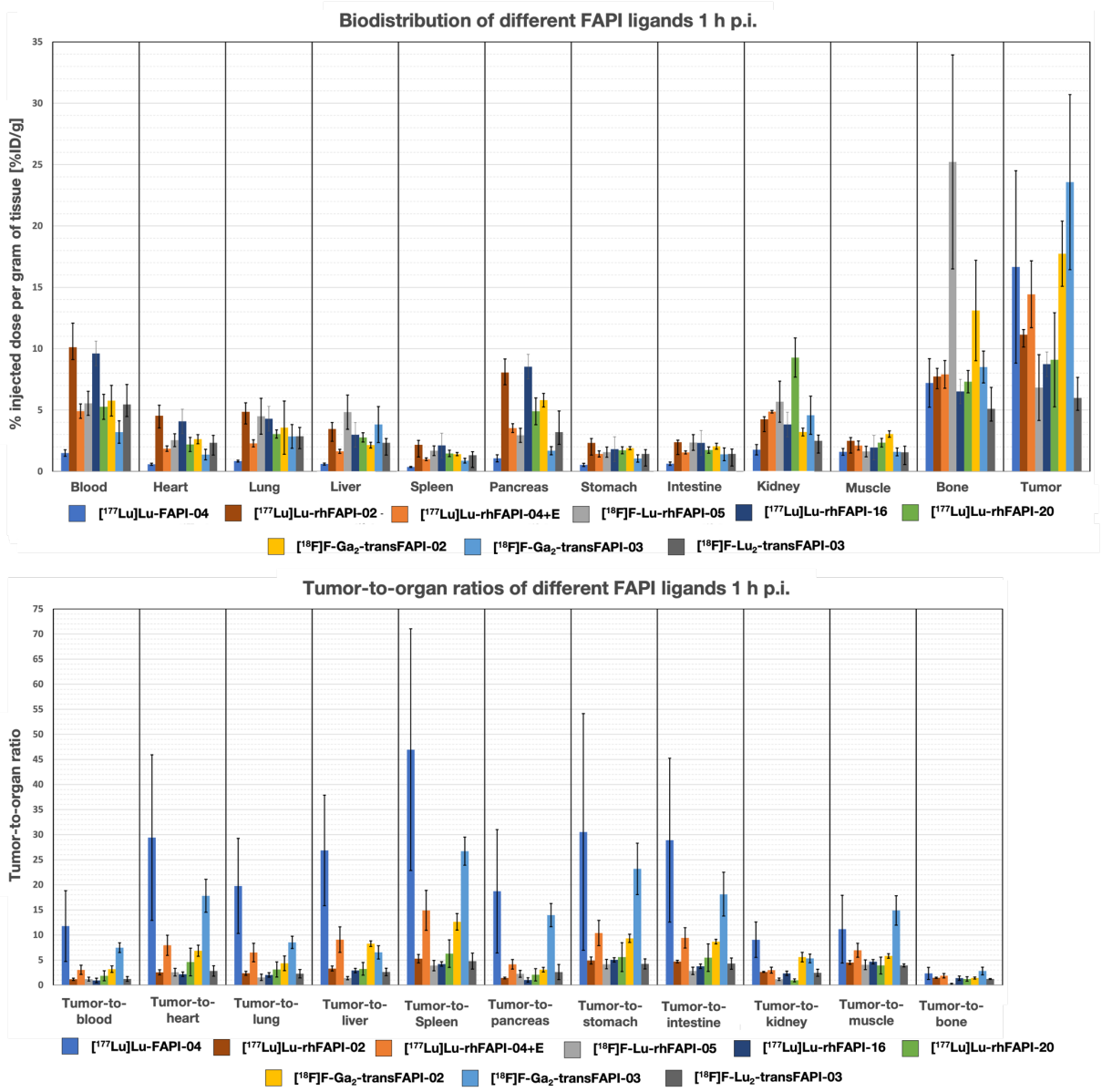

Figure 58: Biodistribution (top) and tumor-to-organ ratios (bottom) of the reference ligand [^{177}Lu]Lu-FAPI-04 and the rhFAPI ligands [^{177}Lu]Lu-rhFAPI-02, [^{177}Lu]Lu-rhFAPI-04+E, [^{18}F]F-Lu-rhFAPI-05, [^{177}Lu]Lu-rhFAPI-16 and [^{177}Lu]Lu-rhFAPI-20 as well as the transFAPI ligands [^{18}F]F-Ga$_2$-transFAPI-02, [^{18}F]F-Ga$_2$-transFAPI-03 and [^{18}F]F-Lu$_2$-transFAPI-03 at 1 h p.i. in HT-1080hFAP tumor-bearing BALB/c mice (n = 4-5). Values for biodistributions are expressed as a percentage of injected dose per gram of tissue (%ID/g), mean ± SD. Values for tumor-to-organ ratios are expressed as ratios between accumulation in the tumor and accumulation in each organ, mean ± SD.

In comparison to all evaluated ligands [^{18}F]F-Ga$_2$-transFAPI-02 and [^{18}F]F-Ga$_2$-transFAPI-03 showed the highest tumor uptakes, however while [^{18}F]F-Ga$_2$-transFAPI-02 also had higher

accumulation in other organs [^{18}F]F-Ga$_2$-transFAPI-03 had comparable or lower uptake in these organs. This resulted in the overall highest tumor-to-organ ratios, which was somewhat surprising as [^{18}F]F-Ga$_2$-transFAPI-03 (IC_{50} = 13.5 ± 1.0 nM, log $D_{7.4}$ = -2.00 ± 0.03, MW (HSA) = 4.4, HSA binding = 98.7) had a very similar *in vitro* performance as [^{177}Lu]Lu-rhFAPI-20 (IC_{50} = 14.0 ± 2.5 nM, log $D_{7.4}$ = -1.97 ± 0.03, MW (HSA) = 4.4, HSA binding = 97.1) but showed significantly favorable distribution *in vivo*. Therefore, again indicating the difficulties of drawing conclusions from *in vitro* data for the prediction of *in vivo* behavior as it was earlier discussed for the rhFAPI ligands. Here, other ligand properties must be of importance about which one can only speculate without further investigations. A reason might be steric shielding through the size of the *trans*-bridged DOTA incorporated into the structural design of the transFAPI ligands hindering interactions of the binding motif or the FAP binding site with groups positioned next to the chelator. Here, also the general structure of the pharmacophore of the transFAPI ligands, which is nearly identical to FAPI-04, could be a reason, where the binding motif including the DOTA-chelator might fit very well into the binding pocket of FAP. Another reason could be a better compensation of the lipophilicity of the SiFA moiety through the two neighboring hydrophilic chelators without changing the overall measurable lipophilicity of the ligands. The conclusion of the development process of the rhFAPI ligands, which was the assumption that lipophilicity was the most important parameter must be modified. Here, it seems that not the overall measured lipophilicity of a ligand was the most important property rather the compensation of the local lipophilicity of the SiFA moiety itself. This would also explain why [^{18}F]F-Ga$_2$-transFAPI-03 even outperformed [^{177}Lu]Lu-rhFAPI-04+E (IC_{50} = 38.1 ± 1.4 nM, log $D_{7.4}$ = -2.97 ± 0.05, MW (HSA) = 28.9, HSA binding = 98.6) in the biodistribution studies despite having a 1.5-fold increased lipophilicity. Surprisingly, [^{18}F]F-Lu$_2$-transFAPI-03 demonstrated an unexpectedly unfavorable biodistribution compared to its gallium-chelate. A low uptake into the tumor (5.96 ± 1.68 %ID/g) and similar accumulation in other organs resulted in low tumor-to-organ ratios. A reason therefore could be a missing acid group for a heptadentate coordination of lutetium in the *trans*-bridged DOTA-chelator. Here, an acid group of the (*R*)-DOTAGA-chelator could coordinate to the lutetium-DOTA-chelate resulting in an entangled ligand configuration hindering optimal binding into the FAP binding pocket. Despite these promising results for [^{18}F]F-Ga$_2$-transFAPI-03, [^{177}Lu]Lu-FAPI-04 still showed higher tumor-to-organ ratios 1 h p.i. and therefore exhibits advantages as an imaging agent when using the gallium-chelated analog [^{68}Ga]Ga-FAPI-04.

In summary, the goal of a better *in vivo* performing FAP-addressing ligand compared to the previously developed rhFAPI ligands was achieved with [^{18}F]F-Ga$_2$-transFAPI-03. Nevertheless, [^{177}Lu]Lu-FAPI-04 still performed favorable in all *in vitro* and *in vivo* studies, which overall questions the feasibility of introducing the radiohybrid concept into FAP-addressing ligands. The difficulties of high lipophilicity and high binding to HSA introduced through the SiFA moiety could not be compensated here through approaches previously used by this chair and published by *Wurzer et al.* for PSMA-addressing ligands.[199,200] Additionally, a lack of transferability between the data of the *in vitro* characterizations and biodistribution studies made predictions of the ligands *in vivo* distribution difficult. Therefore, making it nearly

impossible to select the most suitable ligands for further studies. In conclusion, to obtain an ideal SiFA-containing FAP-addressing ligand new characterization methods for the evaluation of new parameters need to be found and developed, as the used parameters seemed to not be sufficient to provide enough information for the decision which ligands needs to be evaluated in animal studies.

4.3 tecFAPI Ligands

Another objective of this work was to develop a new series of FAPI ligands for the labeling with technetium-99m through incorporation of the N4-chelator. Because of the presence of FAP in many different tumor entities the goal of this objective was to potentially achieve the development of a universal radiopharmaceutical for SPECT imaging comparable to [^{18}F]FDG for PET imaging, which represents an unmet need. As of today, there is no universal tracer for SPECT imaging despite the advantages of being more affordable compared to PET and being a widespread application, especially in less developed countries. Therefore, a tecFAPI ligand might have the potential to become a universal SPECT tracer in the future, even providing the opportunity of a theranostic ^{99m}Tc/$^{186/188}$Re-pair enabling PRRT with the rhenium isotopes. For this reason, novel ligands were developed according to the design strategy shown in Figure 59.

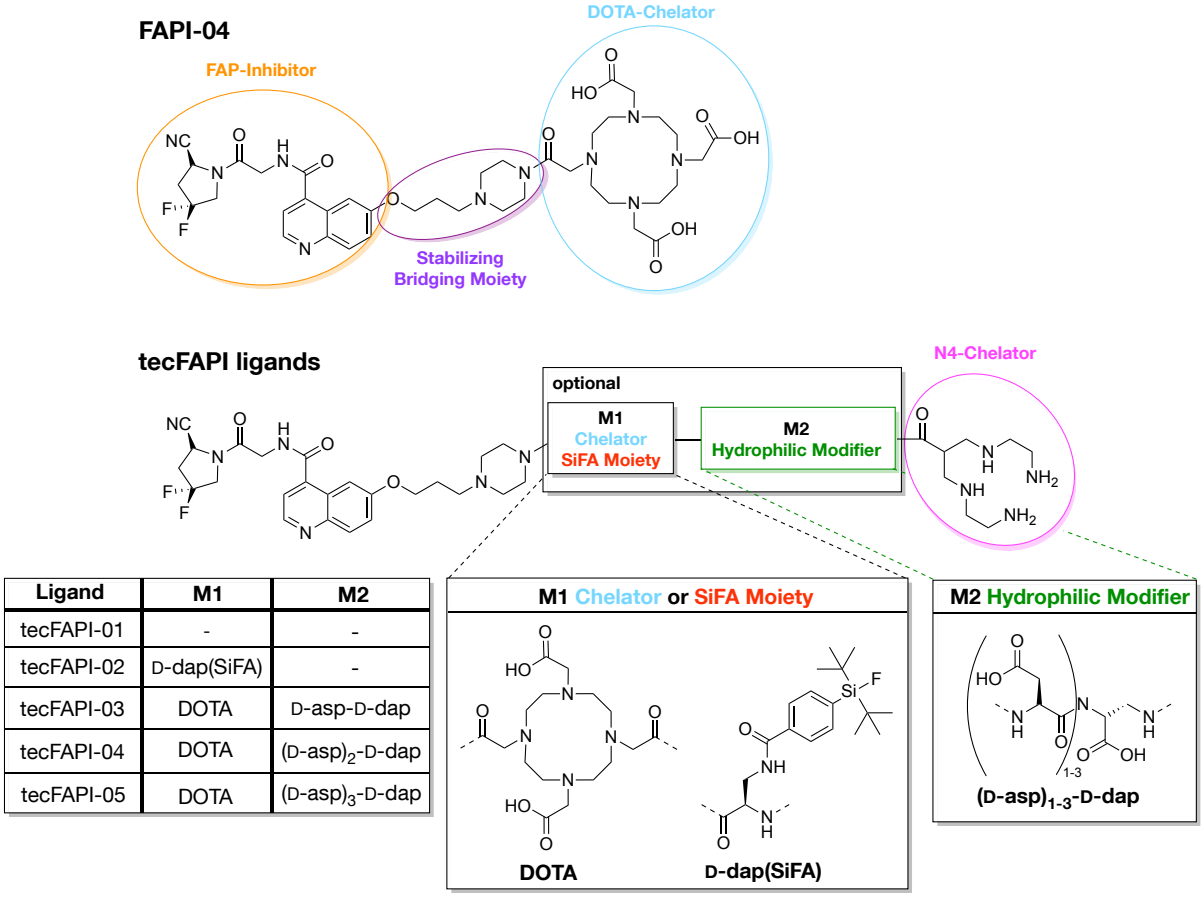

Ligand	M1	M2
tecFAPI-01	-	-
tecFAPI-02	D-dap(SiFA)	-
tecFAPI-03	DOTA	D-asp-D-dap
tecFAPI-04	DOTA	$(D\text{-asp})_2$-D-dap
tecFAPI-05	DOTA	$(D\text{-asp})_3$-D-dap

Figure 59: Chemical structure of FAPI-04 developed by *Haberkorn et al.* and conceptual structure of tecFAPI ligands containing a FAP inhibitor (orange) and a stabilizing bridging moiety (purple). As chelator (turquoise), FAPI-04 contains a DOTA, whereas the tecFAPI ligands possess a N4-chelator (pink) for complexation with ^{99m}Tc-technetium. The ligands tecFAPI-01 to -05 have the optional modification sites **M1** and **M2**, which were either a D-dap(SiFA) (SiFA moiety) or a DOTA (chelator) for metal complexation for **M1** or a hydrophilic modifier (green) consisting of $(D\text{-asp})_{1\text{-}3}$-D-dap for **M2**.

As it was also the case for rhFAPI and transFAPI ligands, the general peptide scaffold of FAPI-04 was used and combined with a N4-chelator at the *N*-terminus. The most important goal of the development process here was to achieve the highest possible hydrophilicity, as this parameter was shown to be the most important for favorable *in vivo* distribution when evaluating rhFAPI ligands. Until now only two groups published their work on FAP-addressing ligands which can be labeled with technetium-99m. One promising ligand is [^{99m}Tc]Tc-FAPI-34 (Figure 6) by *Linder et al.* which possess a bisimidazole chelator and compensates for the elevated lipophilicity introduced by the ^{99m}Tc-tricarbonyl core through its several carboxyl groups.[118] An alternative ^{99m}Tc-labeled tracer published by *Roy et al. is* [^{99m}Tc]Tc-FL-L3 (Figure 8) which uses a tripeptide moiety (2,3-diaminopropanoic acid-aspartate-cysteine) to form a complex with technetium-99m and holds a different binding motif compared to FAPI-34. This tracer showed high activity accumulation in the kidneys and less favorable tumor-to-background ratios compared to [^{99m}Tc]Tc-FAPI-34.[119] Both ligands allow some room for improvement, thereby here, the new series of tecFAPI ligands incorporates the N4-chelator. Reported in literature by *Meacke et al.*, this chelator demonstrates advantages for labeling and the pharmacokinetic behavior of compounds.[216]

Firstly, a minimalistic ligand was synthesized by only exchanging the DOTA-chelator of FAPI-04 with a N4-chelator (tecFAPI-01). Additionally, a radiohybrid-like concept was explored through optional addition of a SiFA moiety at modification site M1 between the FAP-inhibitor and the N4-chelator. To eliminate the main drawback of the rhFAPI and transFAPI ligands, their overall high lipophilicity compared to FAPI-04, three additional tecFAPI ligands were synthesized. These ligands incorporated a DOTA-chelator at modification site M1, mimicking the structure of FAPI-04 even closer, and hydrophilic modifiers at M2 to further enhance the hydrophilicity. These hydrophilic modifiers were composed of a D-dap and 1 to 3 additional D-aspartates, providing 2 to 4 negatively charged carboxyl groups to decrease lipophilicity. All ligands were prepared *via* a mixed solid-phase/solution-phase synthesis strategy and could be obtained after subsequent purification in yields between 5 to 15%. Here, all utilized building blocks (FAP-inhibitor and N4-chelator) were synthesized according to procedures described in chapter 3. For all ligands FAP-affinity (IC_{50}, competitive binding assay on HT-1080hFAP cells), lipophilicity (log $D_{7.4}$, by means of the distribution in *n*-octanol and PBS at pH 7.4), as well as binding to human serum albumin of the ligands and their metal chelates were determined and later compared to the reference compound [$^{nat/177}$Lu]Lu-FAPI-04. All tecFAPI ligands were evaluated as their respective technetium-99m chelate apart from the determination of standard IC_{50} values and binding to HSA by the HPAC method. Here, for laboratory reasons no radiolabeled ligands could be used and there is no non-radioactive isotope of technetium available. Additionally, the DOTA-gallium-chelates of tecFAPI-03 to -05 were also evaluated and for tecFAPI-03 also the DOTA-lutetium-chelate was characterized.

4.3.1 *In Vitro* Characterization

All results from the *in vitro* characterizations of tecFAPI-01 to -05 and their respective [^{99m}Tc]Tc-N4-complex are shown in Figure 60 to Figure 62. Affinities were determined *via* two different competitive cell assays, IC_{50} and inverse IC_{50} determination. The determination of standard IC_{50} values was executed with [^{177}Lu]Lu-FAPI-04 as reference and a serial dilution of the respective tecFAPI ligand as described in chapter 3.4.3. The methodical limitation here is, that there is no non-radioactive technetium isotope for cold metal-complexation of tecFAPI ligands. Therefore, IC_{50} values are evaluated for the ligands with free N4-chelator which, strictly spoken, might show an affinity profile that diverges from the ^{99m}Tc-complexed species for *in vivo* studies or applications in the clinic. To circumvent this limitation, inverse IC_{50} values were measured to assess the affinity of ^{99m}Tc-labeled tecFAPI ligands. For inverse IC_{50} determination the reference ligand FAPI-04 is complexed with cold lutetium and diluted (serial dilution 10^{-4} to 10^{-10} M) and then tested against a consistent concentration of [^{99m}Tc]Tc-tecFAPI ligand. Therefore, in contrast to standard IC_{50} determinations, where a low value corresponds to high affinity, high values correspond to high affinity in inverse IC_{50} determinations.

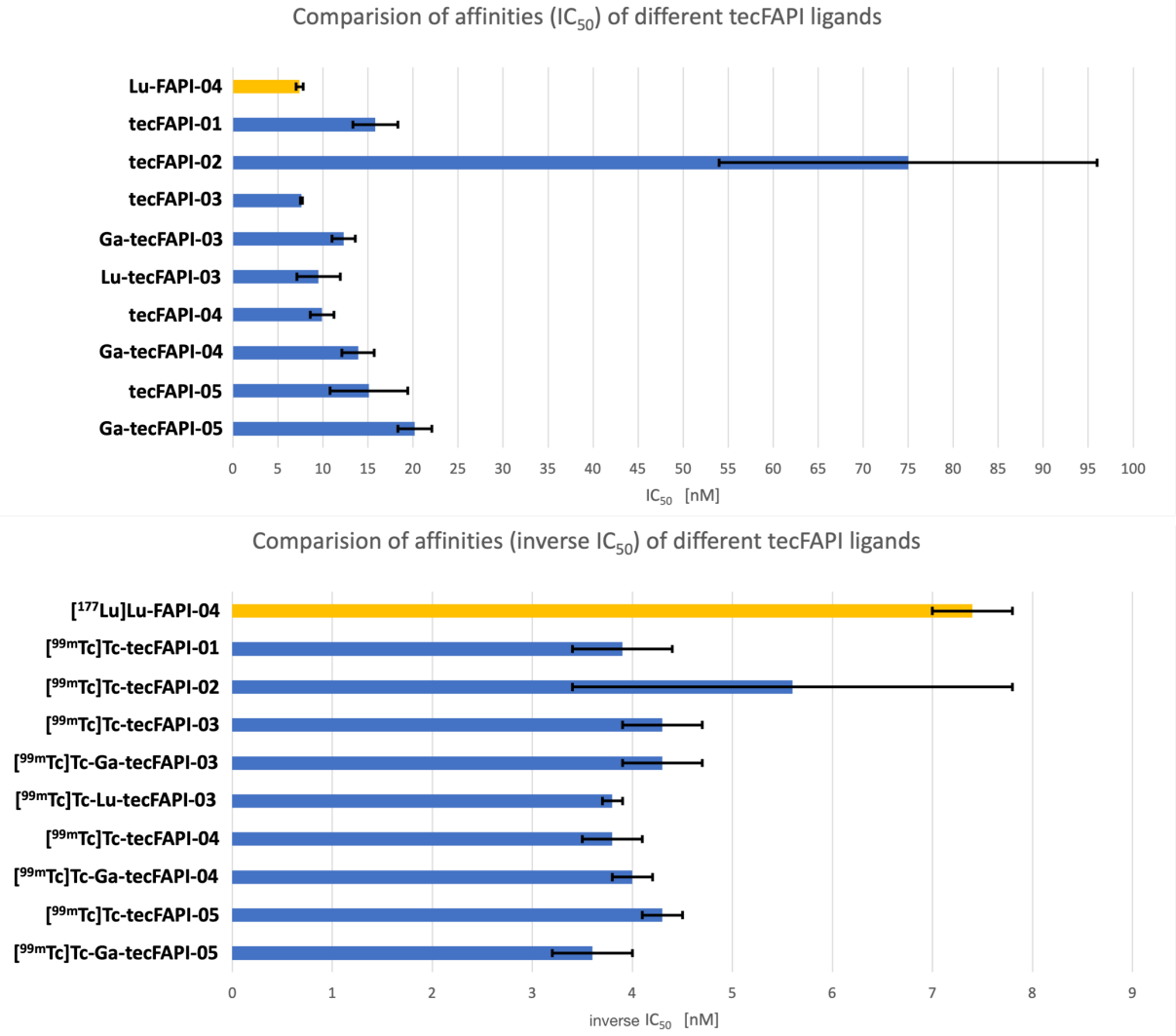

Figure 60: Affinities of tecFAPI-01 – 05 to FAP as IC_{50} [nM] (determined uncomplexed ligands) at upper panel and inverse IC_{50} [nM] (determined as [^{99m}Tc]Tc-tecFAPI ligands) at lower panel on HT-1080hFAP cells (2 h, 4 °C, n = 3)

of [$^{nat/177}$Lu]Lu-FAPI-04 as reference and different tecFAPI ligands either with free *trans*-bridged DOTA moiety or complexed with gallium or lutetium; mean values ± SD.

As shown in Figure 60, all tecFAPI ligands, with the exception of the SiFA-containing tecFAPI-02, showed high affinities below 20 nM with only 1.2 to 2.5-fold decreased affinity compared to [^{177}Lu]Lu-FAPI-04. Gallium complexation of the DOTA-chelator in tecFAPI-03, -04 and -05 led to a 1.3 to 1.6-fold decreased affinity, while complexation of tecFAPI-03 with lutetium led to a 1.2-fold decrease. Here it must be noted that only tecFAPI-03 was complexed with lutetium. This trend was also observed for FAPI-04, where the noncomplexed ligand showed an affinity of IC_{50} = 2.7 ± 0.2 nM, while Ga-FAPI-04 (IC_{50} = 7.9 ± 0.5 nM) showed lower affinity then Lu-FAPI-04 (IC_{50} = 6.2 ± 0.7 nM) compared to the metal free chelate. The SiFA-containing ligand tecFAPI-02 showed 10-fold decreased affinity compared to the reference, this was in accordance with previous data of SiFA-containing FAPI-ligands (see Figure 31). It can be assumed that the sterically demanding SiFA moiety most likely prevents optimal binding to FAP. Lastly, comparing tecFAPI-03, tecFAPI-04 and tecFAPI-05, it was shown that the affinity decreased with more aspartates in the spacer region. Thus, either a greater distance between N4 and the binding site was not favorable, or the carboxylic acid functionalities of the side chains were the reason for the decrease in affinity. The ligand tecFAPI-03 showed the highest affinity with an IC_{50} value of 7.6 ± 0.1 nM, which was comparable to the affinity of the reference.

When comparing the inverse IC_{50} values of the ^{99m}Tc-labeled tecFAPI ligands, nearly all compounds showed a similar affinity between 3.8 to 4.3 nM which is a 1.7 to 2.0-fold decreased affinity when compared to [^{177}Lu]Lu-FAPI-04. Interestingly, no drastic influence of the complexation of the *trans*-bridging DOTA-chelator was observed. This indicates that the labelling of the N4-chelator with technetium-99m might diminish affinity influencing interactions previously found for the unlabeled tecFAPI ligands. Here, the net charge of the chelator and metal-chelate might have an influence as uncomplexed N4 has a net charge of +4 while the ^{99m}Tc-N4-chelate has a net charge of +1.[216] Therefore, complexation of N4 had a strong influence of the overall net charge of the ligands. The affinity of [^{99m}Tc]Tc-tecFAPI-02 with an inverse IC_{50} values of 5.6 ± 2.2 nM was surprisingly high and not in accordance with the data obtained for the standard IC_{50} determination. Reason for this might be significant amounts of non-specific binding which was presumably caused by the high lipophilicity of the compound (Figure 61), which might have led to a wrongfully high affinity. Here, the higher net charge of the uncomplexed ligand might compensate this lipophilicity stronger, therefore not showing the same significant amount of non-specific binding for the IC_{50} determination. In the case of the determination of the inverse IC_{50} determination the radioactive stock solution of [^{99m}Tc]Tc-tecFAPI-02 was prepared without BSA, which serves the purpose of reducing non-specific binding. Therefore, a significant amount of substance might have been lost due to non-specific binding of the radioligand to reaction vessels and material surfaces. No further investigations into this matter were conducted hence this would have meant changing the assay conditions and loosing comparability to other affinity data. As it will be discussed later, the *in vitro* characterization of [^{99m}Tc]Tc-tecFAPI-02 overall showed

unfavorable properties, therefore the approach of SiFA containing tecFAPI ligands was not pursued further. In conclusion, tecFAPI ligands with high affinity could be developed, especially tecFAPI-03 showed promising results.

One goal of the development of the tecFAPI ligands was to optimize the lipophilicity of these compounds, because previous studies of rhFAPI and transFAPI ligands showed the significant importance of this parameter for *in vivo* applications. Here, [^{99m}Tc]Tc-tecFAPI-01 already showed reduced lipophilicity when compared to most rhFAPI (see Table 4) and transFAPI ligands (see Table 5) but still 1.6-fold increased lipophilicity compared to [^{177}Lu]Lu-FAPI-04. As expected, [^{99m}Tc]Tc-tcFAPI-02 showed increased lipophilicity of 0.42 ± 0.03. Such high lipophilicity will most likely lead to unfavorable *in vivo* behavior, like hepatobiliary excretion and therefore, this model compound of SiFA-containing FAPI ligands was not further optimized. As the high lipophilicity was mainly caused by the *tert*-butyl groups at the SiFA moiety, the radiohybrid approach was not suitable for the design of N4-based tecFAPI for *in vivo* application. The ligands [^{99m}Tc]Tc-tecFAPI-03 to -05 showed greatly improved lipophilicity between -2.5 and -3.0 with only a 1.1 to 1.2-fold increase when compared to the reference. This proved the positive impact of the applied design concept on the hydrophilicity of these ligands.

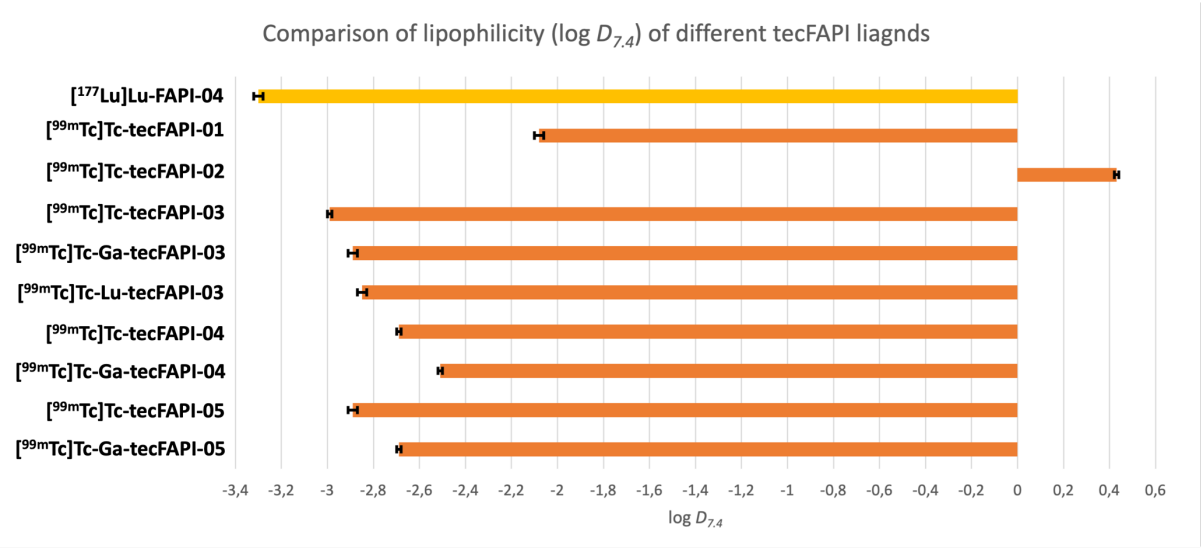

Figure 61: Lipophilicity as *n*-octanol/PBS (pH 7.4) partition coefficient (log $D_{7.4}$, n = 8) of [^{177}Lu]Lu-FAPI-04 as reference and different [^{99m}Tc]Tc-tecFAPI ligands either with free *trans*-bridged DOTA moiety or complexed with gallium or lutetium; mean values ± SD.

The introduction of a second D-aspartate in [^{99m}Tc]Tc-tecFAPI-04 led to a higher lipophilicity when compared to [^{99m}Tc]Tc-tecFAPI-03. This was contra intuitive, as D-aspartate bears a hydrophilic carboxyl group at the side chain. This observation was inverted for the introduction of the third D-asp ([^{99m}Tc]Tc-tecFAPI-05), which led to an increased hydrophilicity in comparison to [^{99m}Tc]Tc-tecFAPI-04, as expected. However, [^{99m}Tc]Tc-tecFAPI-05 still was not as hydrophilic as [^{99m}Tc]Tc-tecFAPI-03. As a second observation, lower hydrophilicities were generally observed for the ligands complexed with gallium or lutetium. This could be explained by the two carboxylic acid groups located at the DOTA which seem to contribute

less to the hydrophilicity when being bound to the metal compared to not being used for complexation. [^{99m}Tc]Tc-tecFAPI-03 showed the highest hydrophilicity (log $D_{7.4}$ = -2.99 ± 0.01) of all FAP-addressing ligands in this work and therefore was expected to show a favorable renal excretion and fast clearance in *in vivo* studies.

The HPAC method was conducted for all tecFAPI ligands. Here, the HSA binding for tecFAPI-01 was significantly higher than for Lu-FAPI-04. This should lead to a longer circulation time *in vivo* and thereby potentially a higher tumor accumulation, but also a higher background. As tecFAPI-01 was structurally analogous to FAPI-04 this result was surprising, indicating some HSA binding property of the N4-chelator. The high HSA binding of tecFAPI-02 was expected as binding of the SiFA moiety to HSA[199,228] was already known due to previous results during evaluation of the rhFAPI and transFAPI ligands.

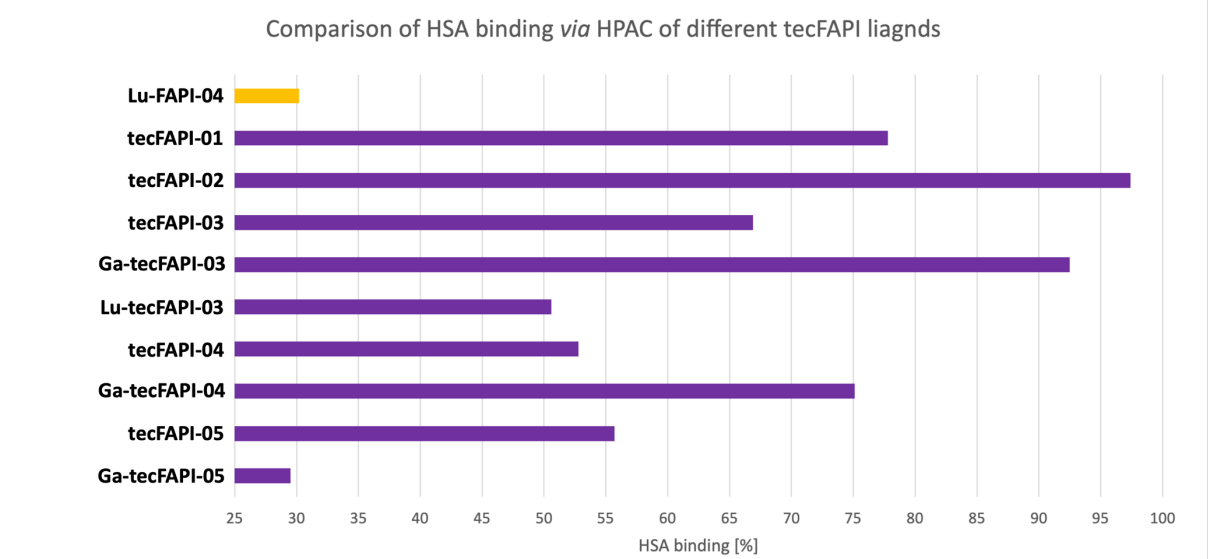

Figure 62: Binding to human serum albumin (HSA) expressed in percent of literature-known calibration-compounds (determined on a Chiralpak HSA column *via* HPAC method) of [$^{nat/177}$Lu]Lu-FAPI-04 as reference and different tecFAPI ligands either with free DOTA moiety or complexed with gallium or lutetium. All ligands had uncomplexed N4-chelators.

HSA binding determined for tecFAPI-03 to -05 and their respective gallium and lutetium complexes haven't revealed any clear trends. When comparing tecFAPI-03 and tecFAPI-04 it seemed that an additional D-aspartate in the backbone lowered HSA binding and complexation with gallium strengthened binding. However, tecFAPI-05 did not follow these observations as it showed higher HSA binding compared to tecFAPI-04 despite having an additional D-aspartate. Complexation with gallium lowered binding by 1.9-fold compared to the metal free analog which was an inverted behavior compared to what was found before. The HSA binding of Ga-tecFAPI-05 was the lowest achieved HSA binding strength of all investigated ligands in this work, even being lower than the HSA binding of Lu-FAPI-04.

However, it must be mentioned that ligands with uncomplexed N4-chelator were used as the method is not applicable for radioactive probes. This most likely led to ambiguous results,

especially when comparing discussed observations with results obtained by the AMSEC method. Because of their favorable lipophilicity [^{99m}Tc]Tc-tecFAPI-03 and its gallium and lutetium chelates, as well as [^{99m}Tc]Tc-tecFAPI-04 and [^{99m}Tc]Tc-tecFAPI-05 were evaluated *via* the AMSEC method. The apparent molecular weight of the [^{99m}Tc]Tec-tcFAPI ligands determined by the AMSEC method was lower than the calibrated range for this method, which is from 3000 to 70000 Da. The radioligands most likely show non-specific binding with the column material and only a weak interaction with HSA. Due to this unspecific binding and the fact, that the results were outside the optimal range for determination, the obtained values are not entirely reliable. Nevertheless, the general observation of low HSA binding of the [^{99m}Tc]Tc-tecFAPI ligands and [^{177}Lu]Lu-FAPI-04, as well, was visible.

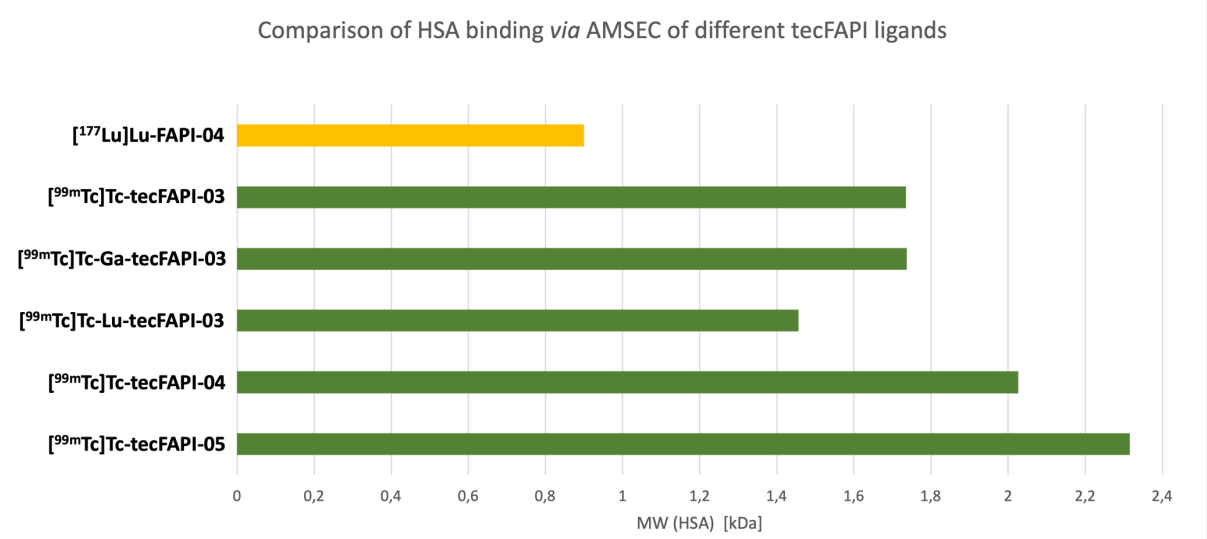

Figure 63: Binding to human serum albumin (HSA) expressed as apparent molecular weight (MW) determined by following the albumin mediated size exclusion chromatography (AMSEC) method (determined on a Superdex™ 75 Increase 10/300 GL column) of [$^{nat/177}$Lu]Lu-FAPI-04 as reference and different [^{99m}Tc]Tc-tecFAPI ligands either with free DOTA moiety or complexed with gallium or lutetium.

For the ligands [^{99m}Tc]Tc-tecFAPI-03, [^{99m}Tc]Tc-Ga-tecFAPI-03, [^{99m}Tc]Tc-Lu-tecFAPI-03 and [^{177}Lu]Lu-FAPI-04 cell uptake and internalization were determined after 30, 60 and 120 min of incubation at 37 °C. The results are visualized in Figure 64.

The cell uptake of all four ligands increased with a longer incubation time, even though the increase for [^{177}Lu]Lu-FAPI-04 was only marginal. The cell uptake of the reference ligand was also significantly lower, than for [^{99m}Tc]Tc-tecFAPI-03 and its metal chelates. The complexation with both gallium and lutetium increased the cell uptake of tecFAPI-03 and the effect was more pronounced with lutetium. Therefore, [^{99m}Tc]Tc-Lu-tecFAPI-03 exhibited the highest cell uptake. When the internalization was determined in relation to the cell uptake, an internalization rate of above 85% was observed for all four compounds at all evaluated time points. This value increased with a longer incubation time. [^{177}Lu]Lu-FAPI-04 reached an internalization of 97.4 ± 1.1%, [^{99m}Tc]Tc-tecFAPI-03 and [^{99m}Tc]Tc-Ga-tecFAPI-03 of 95.1 ± 0.3% and 94.9 ± 0.4% respectively. [^{99m}Tc]Tc-Lu-tecFAPI-03 with 90.9 ± 0.5%

internalization of its cell uptake has the lowest relative value. When considering the internalization in relation to the overall applied activity, [^{177}Lu]Lu-FAPI-04 displays only 26.0 ± 1.3% after 60 min and 27.8 ± 2.0% after 120 min. Obtained results were similar among all three [^{99m}Tc]Tc-tecFAPI ligands (36.3 ± 0.9% to 38.2 ± 1.5% after 1 h and 42.3 ± 0.5% to 43.4 ± 0.5% after 2 h) and significantly higher than for the reference. This relativized the results of the internalization in relation to the cell uptake in which [^{177}Lu]Lu-FAPI-04 reached the highest internalization rate of 97.4 ± 1.1%, hence eventually the absolute activity accumulation in the cells was higher for all tecFAPI ligands.

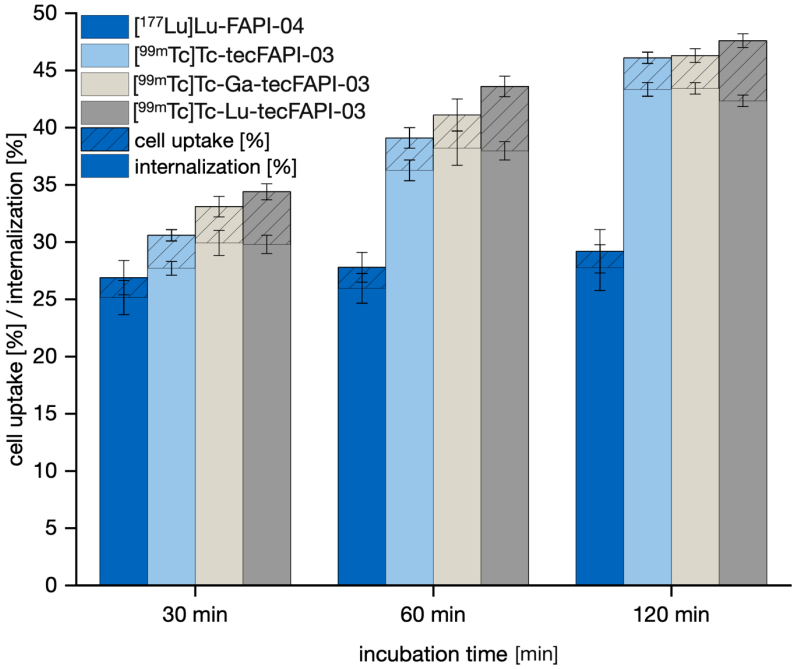

Figure 64: Cell uptake (striped) and FAP-mediated internalization in % of applied activity of [^{177}Lu]Lu-FAPI-04, [^{99m}Tc]Tc-tecFAPI-03, [^{99m}Tc]Tc-Ga-tecFAPI-03 and [^{99m}Tc]Tc-Lu-tecFAPI-03 on HT-1080hFAP cells (30 min to 2 h, 37 °C, n = 6).

In conclusion, all tested ligands had a high internalization rate. The reference ligand had by far the lowest cell uptake, but the highest percentage of internalization in relation to the cell uptake. Although complexation with gallium had a positive effect on the cell uptake, it did not influence the internalization of the ligand. Complexation with lutetium on the other hand led to an even higher cell uptake, however, internalization rates were similar. Thus, [^{99m}Tc]Tc-Lu-tecFAPI-03 either binds stronger to the extracellular catalytical center of FAP or exhibits more non-specific binding to the cell surface. As a slightly lower internalization was observed, the latter option is more likely. To be certain, this would need to be tested in a blocking experiment. As both, the cell uptake and the overall internalization increased over the observed time points, in would be beneficial to extend the experiments time frame to monitor longer incubation times. This could lead to realizations for optimal evaluation time frames for further studies.

4.3.2 *In Vivo* Characterization

Biodistribution studies

Considering the results of the *in vitro* characterization, only [^{99m}Tc]Tc-tecFAPI-03 (IC_{50} = 7.6 ± 0.1 nM, inverse IC_{50} = 4.3 ± 0.4 nM, log $D_{7.4}$ = -2.99 ± 0.01, MW (HSA) = 1.7, HSA binding = 66.9%) and its gallium (IC_{50} = 12.3 ± 1.3 nM, inverse IC_{50} = 4.3 ± 0.4 nM, log $D_{7.4}$ = -2.89 ± 0.02, MW (HSA) = 1.7, HSA binding = 92.5%) and lutetium (IC_{50} = 9.5 ± 2.4 nM, inverse IC_{50} = 3.8 ± 0.1 nM, log $D_{7.4}$ = -2.85 ± 0.02, MW (HSA) = 1.4, HSA binding = 50.6%) complexed analogs were chosen for further *in vivo* evaluation, primarily because of their high affinity and hydrophilicity. For the biodistribution studies the ligands were injected into HT-1080hFAP tumor-bearing female BALB/c mice (Figure 65), evaluated after 1 h p.i. and compared to the reference ligand [^{177}Lu]Lu-FAPI-04 (IC_{50} = 6.25 ± 0.7 nM, inverse IC_{50} = 7.4 ± 0.4 nM, log $D_{7.4}$ = -3.36 ± 0.002, MW (HSA) = 0.9, HSA binding = 30.2%).

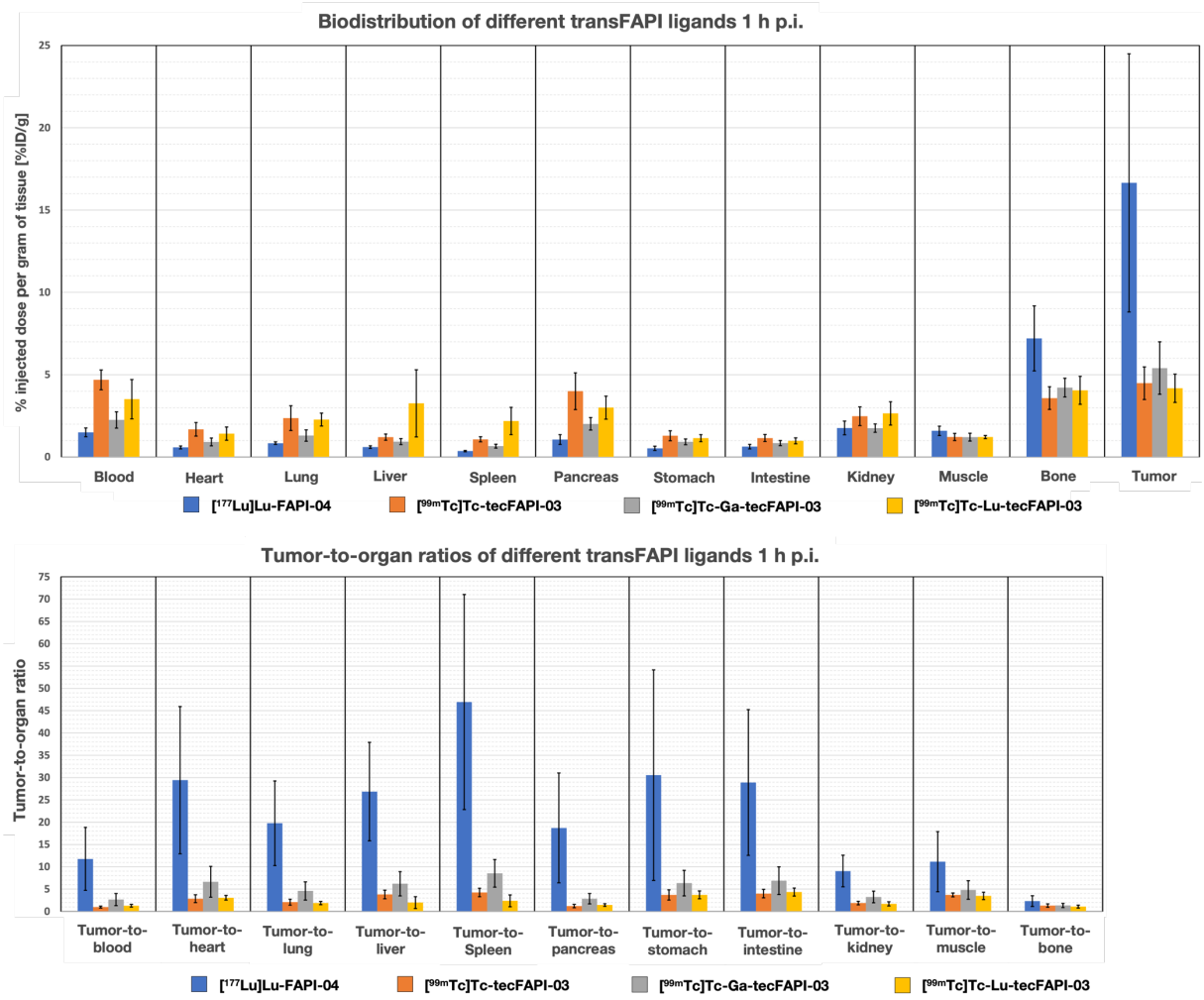

Figure 65: Biodistribution (top) and tumor-to-organ ratios (bottom) of the reference ligand [^{177}Lu]Lu-FAPI-04 and [^{99m}Tc]Tc-tecFAPI-03, [^{99m}Tc]Tc-Ga-tecFAPI-03 and [^{99m}Tc]Tc-Lu-tecFAPI-03 at 1 h p.i. in HT-1080hFAP tumor-bearing BALB/c mice (n = 4-5). Values for biodistributions are expressed as a percentage of injected dose per gram of tissue (%ID/g), mean ± SD. Values for tumor-to-organ ratios are expressed as ratios between accumulation in the tumor and accumulation in each organ, mean ± SD.

The comparative biodistribution of [^{99m}Tc]Tc-tecFAPI-03, [^{99m}Tc]Tc-Ga-tecFAPI-03 and [^{99m}Tc]Tc-Lu-tecFAPI-03 revealed 3 to 4-fold decreased tumor uptake compared to the reference and higher uptake in nearly all non-specific organs and blood leading to unfavorable tumor-to-background ratios. The increased activity accumulation in blood was noncompliant with the low HSA binding determined by the AMSEC method, as well as with the results of the HSA binding determined by the HPAC method. In these methods [^{99m}Tc]Tc-Ga-tecFAPI-03 presented the strongest binding, although it had the lowest blood accumulation in the biodistribution. Furthermore, it also was counter-intuitive, that [^{99m}Tc]Tc-tecFAPI-03, the tracer with the highest hydrophilicity exhibited the highest retention in blood. It is possible, that the binding to other plasma proteins, like human α_1-acid glycoprotein (α_1-AGP) or human transthyretin (hTTR), was responsible for this circumstance.[251] More likely and in accordance with results discussed in the following chapters, the high activity accumulation in the blood may account for the binding of [^{99m}Tc]TcO4$^-$ to red blood cells.[252] Free pertechnetate could be available in significant quantities due to an instability of the ligands [^{99m}Tc]Tc-N4 complex, which again will be discussed in more detail later. Colloidal technetium could also have led to activity accumulation in blood and despite excessive quality control procedures ideal conditions for quantifying impurities could not be developed (see chapter 4.4.2).

Another aspect was the increased activity accumulation in the bone. The origin of this accumulation was explained previously for biodistribution studies of rhFAPI and transFAPI ligands and originates from the endogenous expression of murine FAP in bones and joints.[115] The accumulation in the pancreas can be explained through endogenous expression as well, as the so called Langerhans islet cells, micro-organs consisting of different cell types, located in the pancreas, are FAP positive.[229,230]

[^{99m}Tc]Tc-Lu-tecFAPI-03 exhibited a significantly higher liver uptake compared to its analogous tracers. This observation was in accordance with the log $D_{7.4}$ values, as [^{99m}Tc]Tc-Lu-tecFAPI-03 (-2.85 ±0.02) was the most lipophilic amongst the tracers used for these biodistribution studies. The higher lipophilicity could lead to a partially hepatobiliary excretion instead of an exclusively renal excretion, which would explain the higher activity accumulation in the liver. However, such significant differences between the liver uptakes of the different tecFAPI ligands, were not expected, due to the very similar and relatively high hydrophilicities only showing a 1.1 to 1.2-fold increased lipophilicity compared to [^{177}Lu]Lu-FAPI-04.

In summary, all evaluated tecFAPI ligands performed surprisingly unfavorable at the early time point of 1 h p.i. despite showing highly promising results for all *in vitro* characterizations. In retrospect, one possible explanation for this could be the mentioned instability of the [^{99m}Tc]Tc-N4 complex, which will be discussed in the following chapters.

SPECT/CT Imaging

For each tecFAPI ligand, one mouse of the biodistribution cohort was imaged using µSPECT/CT. Maximum intensity projections (MIPs) are presented in Figure 66.

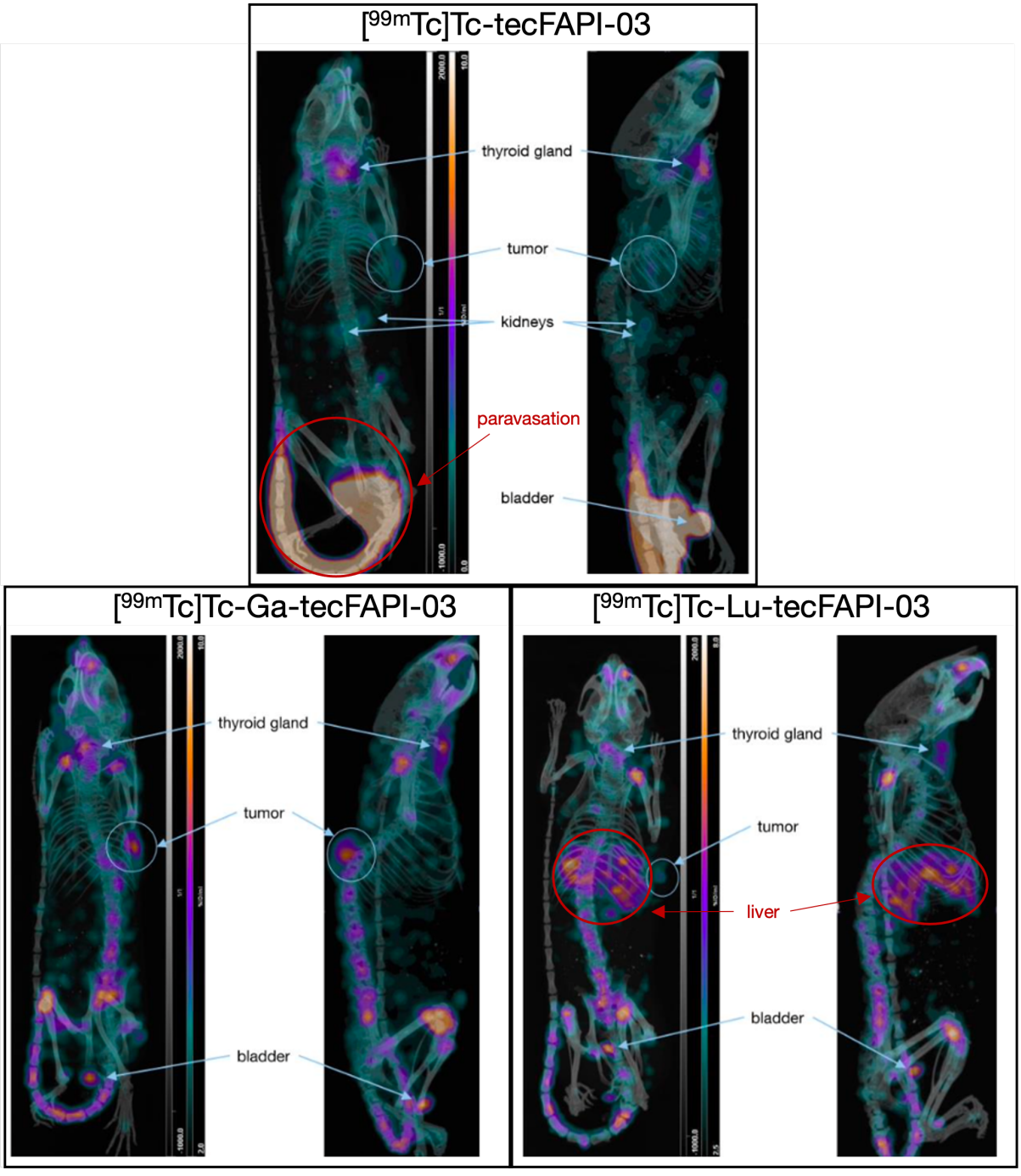

Figure 66: Maximum intensity projections (MIPs) of small animal SPECT/CT of [^{99m}Tc]Tc-tecFAPI-03, [^{99m}Tc]Tc-Ga-tecFAPI-03 and ^{99m}Tc]Tc-Lu-tecFAPI-03, 1 h p.i. Each scan is displayed from the top and from the right side of the mouse.

In the MIP of [^{99m}Tc]Tc-tcFAPI-03, firstly the high activity on the buttock and the top half of the tail stood out. A possible reason for an unusually high activity in the tail could be a paravasation during the injection in the tail vein, whereby a significant amount was injected in

the surrounding tissue. The high activity in the bladder, in the kidneys and negligible activity in liver and intestines led to the conclusion, that the ligand was excreted over the renal pathway. Due to a faster excretion and a lower resulting background activity, this is preferred over a hepatobiliary excretion. As already discussed for the biodistribution data, the accumulation in the tumor was rather low. In the MIP the tumor was visible with estimated 4% ID/mL (biodistribution: 4.99% ID/g). An interesting finding was the activity accumulation in the thyroid gland of about 7% ID/mL. As pertechnetate is transported into the thyroid gland by the sodium-iodide symporter (NIS)[253], the corresponding accumulation was an indication for the presence of this species and therefore an *in vivo* instability of [^{99m}Tc]Tc-tecFAPI-03 or the presence of free pertechnetate in the injected radioligand solution. Reason for this could be the lack of ideal conditions for quantifying impurities after labeling with technetium-99m as will be described in chapter 4.4.2.

Similar activity uptake in the thyroid gland was also present in the MIP of [^{99m}Tc]Tc-Ga-tecFAPI-03, pointing towards a common phenomenon within this series of ligands. The tumor accumulation was about 7-8% ID/mL (biodistribution: 4.43% ID/g) and therefore significantly higher than for [^{99m}Tc]Tc-tecFAPI-03 and generally higher than expected when compared to data from the biodistribution studies. High activity accumulation in the bladder, but low accumulation in liver or intestine, again indicated renal excretion of the tracer. Consistent with data from biodistribution studies, µSPECT/CT revealed uptake in bones and joints, which can be attributed to murine FAP expression in these tissues.

µSPECT/CT-imaging of [^{99m}Tc]Tc-Lu-tecFAPI-03 showed the same activity accumulations in the thyroid gland, shoulder and knee joints and the spine. Compared to the other ligands [^{99m}Tc]Tc-Lu-tecFAPI-03 demonstrated decreased tumor accumulation, showing only about 2% ID/mL (biodistribution 3.08% ID/g) uptake. This was lower than expected when comparing with the data of the biodistribution studies. The lower part of the thorax exhibited an extensive activity accumulation. This most likely derived from liver uptake and thereby a partially hepatobiliary excretion. This theory was supported by the high liver uptake also observed during the biodistribution studies.

Tracer Stability in Murine Serum

To further investigate the results of the biodistributions and µSPECT/CT imaging studies, which indicated suboptimal *in vivo* stability of all three ligands, stability studies in murine serum over 24 h at 37 °C were performed for [^{99m}Tc]Tc-Ga-tecFAPI-03 and [^{99m}Tc]Tc-Lu-tecFAPI-03 but not for the metal free [^{99m}Tc]Tc-tecFAPI-03. Reason for the chosen time span of 24 hours was the circumstance that processes in serum tend to take longer compared to in living organisms. The radio-RP-HPLC chromatograms of the labeled ligands before and after incubation in murine serum are visualized in Figure 67. Probes for radio-RP-HPLC chromatography before incubation were additionally spiked with [^{99m}Tc]TcO_4^- eluate to gain a reference retention time for this radioactive species, which is indicated in yellow in Figure 67.

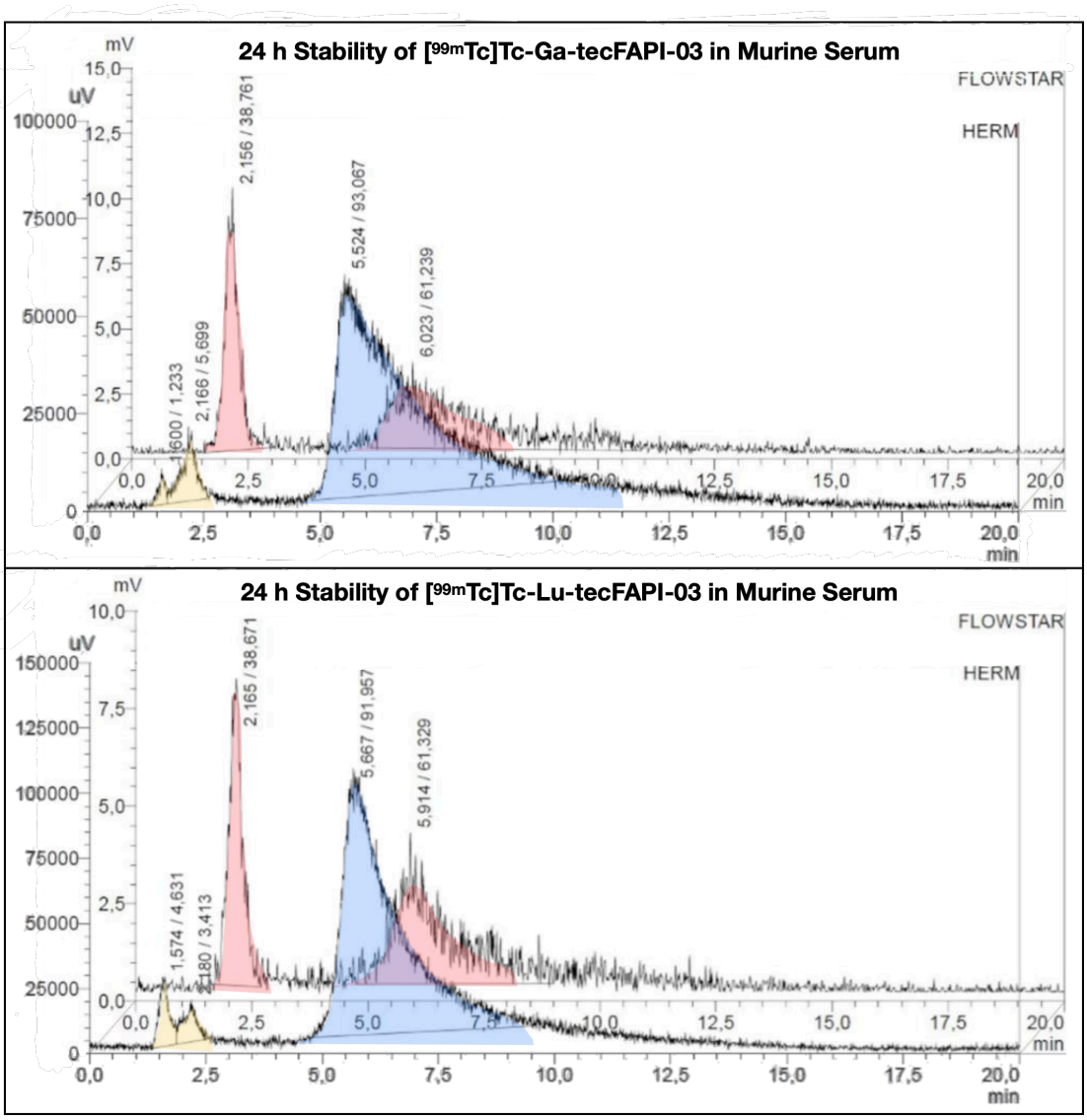

Figure 67: HPLC chromatogram of Ga-tecFAPI-03 (top) and [^{99m}Tc]Tc-Lu-tecFAPI-03 (bottom) before (front, blue) and after (back, red) incubation in murine serum for 24 h at 37 °C. Impurities after complexation with technetium-99m and before incubation of radioligands are shown in yellow.

Both evaluated ligands showed a significantly lower radiochemical purity after incubation in murine serum. The determined purity of the radiolabeling solution was 93% for [^{99m}Tc]Tc-Ga-tecFAPI-03 and 92% for [^{99m}Tc]Tc-Lu-tecFAPI-03. The HPLC chromatogram of the quality control after incubation in murine serum displayed 61.2% and 61.3% purity, respectively. In both cases, a peak with a retention time of 2.2 min corresponding to approximately 39% of the injected activity was observed. This radio-signal might either arise from a free technetium-99m species, which could originate due to an instability of the [^{99m}Tc]Tc-N4 complex, or from the formation of a hydrophilic metabolite. The first assumption was supported by the activity accumulation in the thyroid gland and in the blood shown in µSPECT/CT-imaging and biodistribution which is typical for free pertechnetate ([^{99m}Tc]TcO4$^-$). The retention time of the peak was also suitable for this species. A possible reason for this issue might be the two negative charges in proximity to the N4-chelator. The two carboxylic acids located at D-dap and D-aspartate may have weakened the binding of the [^{99m}Tc]TcO$_2$ species to the chelator

by coordination to the radiometal. The *in vivo* behavior of [^{99m}Tc]TcO_2 could be similar to pertechnetate or a further *in vivo* oxidization to [^{99m}Tc]TcO4$^-$ could be possible. The assumption of a weakened [^{99m}Tc]Tc-N4 complex was further supported by the observation of a pH-dependent instability of the labeled tecFAPI ligands discussed later in chapter 4.2.2.

4.3.3 Summary and Conclusion of tecFAPI Ligand Development

Over the course of the tecFAPI ligand development process several N4-bearing tracers could successfully be synthesized. These ligands were characterized in several *in vitro* studies and a summary of the results is shown in Table 11. The first generation of minimalistic ligands, consisting of tecFAPI-01 and -02, did not meet the desired requirements for further evaluation. Data obtained for tecFAPI-02 led to the conclusion, that the radiohybrid concept was not suitable for this research project, as the ligand had a high lipophilicity and a rather low affinity. The ligand tecFAPI-01, which only contains the inhibitor and the chelator, offered a significantly higher hydrophilicity and affinity. As both properties still needed improvement in order to be able to compete with the reference ligand FAPI-04, a second generation of tecFAPI ligands was developed with the main goal of optimized lipophilicity.

Table 11: Summary of the *in vitro* evaluation of the reference Lu-FAPI-04 and [^{99m}Tc]Tc-tecFAPI-01 to -05 and their respective gallium or lutetium complexes. FAP binding affinities as IC_{50} [nM] and inverse IC_{50} [nM] on HT-1080hFAP cells (2 h, 4 °C, n=3). Lipophilicity as *n*-octanol/PBS (pH 7.4) partition coefficient (log $D_{7.4}$, n=8). Binding to human serum albumin (HSA) as apparent molecular weight (MW) determined by the albumin mediated size exclusion chromatography (AMSEC) method (determined on a Superdex™ 75 Increase 10/300 GL column) and binding to HSA in percent of reference compounds (determined on a Chiralpak HSA column *via* HPAC method). Values are expressed as mean ± SD. ND = not determined; * = values determined with compounds with uncomplexed N4-chelator.

FAPI ligand	IC_{50} [nM]	Inverse IC_{50} [nM]	log $D_{7.4}$	MW (HSA) [kDa]	HSA binding [%]
Lu-FAPI-04	6.25 ± 0.7	7.4 ± 0.4	-3.36 ± 0.002	0.9	30.2
[^{99m}Tc]Tc-tecFAPI-01	15.8 ± 2.5*	3.9 ± 0.5	-2.08 ± 0.02	ND	77.8*
[^{99m}Tc]Tc-tecFAPI-02	75.0 ± 21*	5.6 ± 2.2	0.43 ± 0.01	ND	97.4*
[^{99m}Tc]Tc-tecFAPI-03	7.6 ± 0.1*	4.3 ± 0.4	-2.99 ± 0.01	1.7	66.9*
[^{99m}Tc]Tc-Ga-tecFAPI-03	12.3 ± 1.3*	4.3 ± 0.4	-2.89 ± 0.02	1.7	92.5*
[^{99m}Tc]Tc-Lu-tecFAPI-03	9.5 ± 2.4*	3.8 ± 0.1	-2.85 ± 0.02	1.4	50.6*
[^{99m}Tc]Tc-tecFAPI-04	9.9 ± 1.3*	3.8 ± 0.3	-2.69 ± 0.01	2.0	52.8*
[^{99m}Tc]Tc-Ga-tecFAPI-04	13.9 ± 1.8*	4.0 ± 0.2	-2.51 ± 0.01	ND	75.1*
[^{99m}Tc]Tc-tecFAPI-05	15.1 ± 4.3*	4.3 ± 0.2	-2.89 ± 0.02	2.3	55.7*
[^{99m}Tc]Tc-Ga-tecFAPI-05	20.2 ± 1.9*	3.6 ± 0.4	-2.69 ± 0.01	ND	29.5*

The next generation of tecFAPI ligands were structurally more closely modelled after FAPI-04 like the transFAPI ligands before. The general structure was extended by a *trans*-bridged DOTA-chelator, which serves as connection between the inhibitory sequence and a hydrophilic modifier moiety with a variable number of hydrophilic functional groups. With exception of Ga-tecFAPI-05, all members of this second generation showed a higher affinity and hydrophilicity, than the first generation of ligands.

As the best *in vitro* results were obtained for the ligands tecFAPI-03, Ga-tecFAPI-03 and Lu-tecFAPI-03, these derivatives were selected to undergo biodistribution studies and µSPECT/CT imaging. Unfortunately, the *in vivo* performances were not as favorable as expected based on the *in vitro* characterizations. The tumor accumulation of all three ligands was significantly lower than for [^{177}Lu]Lu-FAPI-04 which resulted in lower tumor-to-background ratios, as well. The best results were obtained for [^{99m}Tc]Tc-Ga-tecFAPI-03 with a tumor uptake of 5.40 ± 1.6 %ID/g. The novel ligands might possibly show improved *in vivo* results at later time points, as internalization studies revealed increasing cell uptake up to an incubation time of 2 h. Additionally, several indicators for unsatisfying stability of all three radioligands were observed, which might have caused high activity accumulation in the thyroid glands and blood. It most likely also effected the tumor uptake because less amount of intact ligand was available to accumulate in the tumor. Additionally, free technetium-99m or pertechnetate and more hydrophilic or lipophilic metabolites distort the tumor-to-background ratios. The stability studies in murine serum, which were performed to obtain deeper insight into the origin of the unfavorable *in vivo* behavior, revealed a significant degradation of radioligand with potential release of technetium-99m and metabolite formation for both evaluated ligands ([^{99m}Tc]Tc-Ga-tecFAPI-03 and [^{99m}Tc]Tc-Lu-tecFAPI-03). This was most likely due to an instability of the [^{99m}Tc]Tc-N4-complex. The interaction may be weakened by a coordination of negatively charged carboxylic acids to the TcO_2-core, located at the neighboring amino acids. The stability of the technetium-N4-complex could be investigated using the chemical similar rhenium-N4-complex. In this work rhenium complexes were not produced which in retrospective is a shortcoming of this work. In contrast to technetium, rhenium has non-radioactive isotopes which allow safe lab-based stability studies of the formed complex. With this system it also could have been investigated if technetium forms complexes with the present DOTA-chelator in the case of non-complex DOTA. This could also have an impact on the *in vivo* distribution of the investigated tecFAPI ligands. Another plausible reason for unfavorable biodistribution might be the formation of a different Tc-Oxo-species while labeling. Here, the additional electron donors (carboxylates) neighboring the N4-chelator might stabilize another oxidation state, hereby preventing the formation of the TcO_2-N4-complex.[254] Quantification of these two chelates *via* radio-HPLC most likely would fail because of the tailing of the peak as described later (chapter 4.4.2). These theories need to be verified in future research investigating the stability of similar ligands with neutral polar and non-polar, as well as with positively charged modifiers/neighboring groups. The obtained results could be of value for the development of N4-bearing ligands for other targets as well.

It was assumed, that the suboptimal instability was the main reason for the limited correlation between *in vitro* and *in vivo* results. This underlines the importance of biodistribution experiments before first in human application of newly developed pharmaceuticals, as most *in vitro* evaluations are not able to capture all relevant properties of a radioligand. Thereby, the tracers could have been excluded from biodistribution studies and the reason for their instability could have been investigated first. Although, the transferability of the results in murine or human serum to the stability in mice or humans and vice versa is not completely reliable due to species differences, it still could indicate similar behavior.

A general challenge for all FAPI development projects in this thesis was comparability with compounds from different groups. For the evaluation of the tecFAPI ligands, an independent synthesis of more reference compounds was beyond the scope of this work. The biggest problem for comparability was the circumstance that every group uses slightly or completely different *in vitro* characterization methods or investigates different parameter. While *Lindner et al.*[118] (FAPI-34, Figure 6) used the same HT-1080hFAP cell line, however, with different assay conditions, *Roy et al*.[119] (FL-L3, Figure 8) used the HEK293-hFAP cell line for *in vitro* studies and the MDA-MB231 cell line for *in vivo* studies. This was a general problem as many groups use different transfected cell lines, therefore complicating not only the comparison of *in vitro,* but also *in vivo* data. When comparing data of FAPI-34 (IC_{50} = 6.9 nM, log *P* = -1.54, plasma protein binding = 98%) to the overall state-of-the-art FAP-addressing tracer FAPI-04 (IC_{50} = 6.5 nM, log *P* = ND, plasma protein binding = ND) from the same group only the affinity was determined for both ligands.[112,118,255] Hence, not allowing an indirect comparison of data ratios between FAPI-04 and FAPI-34 with ratios of FAPI-04 with tecFAPI ligands. Additionally, not all groups stated which derivative of a compound was investigated. Here, it often was not clear if the labeled, cold complexed or free ligand was evaluated. When comparing the data of [^{99m}Tc]Tc-FAPI-34 directly with the best *in vivo* performing tecFAPI ligand in this work [^{99m}Tc]Tc-Ga-tecFAPI-03 (IC_{50} = 12.2 ± 1.3 nM, log $D_{7.4}$ = -2.89 ± 0.03, MW (HSA) = 1.7, HSA binding = 92.5) the presumed instability of the [^{99m}Tc]Tc-N4 complex was most likely the reason for the 2 to 4-fold higher tumor-to-background ratios of FAPI-34 for the same investigated time point (1 h p.i.).[118] Resolving the stability issue could lead to a promising ligand when just comparing *in vitro* data of these two compounds. This comparison of cause lacks transferability of the data, however, serves as an example of the general issue. Therefore, all data for the developed ligands from this work were compared to FAPI-04, which still is the state-of-the-art FAP-addressing tracer.

Interestingly, even if [^{99m}Tc]Tc-FAPI-34 was outperformed by [^{68}Ga]Ga-FAPI-04 after 1 h p.i. it showed increasing tumor uptake and tumor-to-background ratios up to 4h p.i., while [^{68}Ga]Ga-FAPI-04 showed sever tumor washout.[112,118] Therefore, offering the possibility of a therapeutic application using the corresponding ^{188}Re-labeled compound. However, current developed FAP ligands often demonstrate rather low SUVs for tumor tissue. This arises the question, if a sufficient high tumor dose suitable for a therapeutic application could be realized with the currently used binding motifs without causing excessive side effects through

damaging healthy tissue and organs.[234] Therefore, it is reasonable that further studies first set their focus on the improvement of FAPIs for imaging purposes and the research in new binding motifs enabling higher uptake in tumor tissue for therapeutic applications.[256-258]

4.4 Radiolabeling

In general, only compounds with a chemical purity of ≥95% were used for radiochemical labelling. Ligands were labelled with different amounts of activity or varying substance quantities resulting in different molar activities depending on the area of application being *in vitro* or *in vivo* studies. Here, only radioligands with a radiochemical purity of ≥95% were used for any type of cell based or animal studies. In the case of labelling with lutetium-177 or technetium-99m no purification was performed after labelling as ligands were used in significant excess to obtain quantitative radiochemical conversion. Therefore, radiochemical yield can be considered as 100%. For the labelling with fluorine-18 a cartridge purification was performed as no quantitative radiochemical conversion was obtained for the labelling reactions and radiochemical yields are given in chapter 4.4.3 and 4.4.4. HPLC chromatograms representing quality controls of representative labelling reactions for each radiolabeled FAPI ligand are shown in chapter 7.6 as supplemental information.

4.4.1 Radiometalation of rhFAPI Ligands with Lutetium-177

The ^{177}Lu-labeled rhFAPI ligands were prepared according to a standard protocol (GSP15) for complexation of DOTA- and *(R)*-DOTAGA-chelators.[218,219] Radiochemical purities were determined by radio-TLC and radio-RP-HPLC and were ≥95% for all ligands. The tracers were obtained in molar activity (A_M) of 20 to 110 GBq/µmol. As described in literature for rhPSMA ligands, radiometalation of rhFAPI ligands with lutetium-177 was not negatively affected by the radiohybrid ligand design and well-known literature protocols for DOTA/DOTAGA-based ligands could be applied for the labelling reactions.[217]

4.4.2 Radiometalation of tecFAPI Ligands with Technetium-99m

The ^{99m}Tc-labeled tecFAPI ligands were prepared according to a procedure (GSP16) adjusted from a published procedure by *Nock et al*.[220] Radiochemical purities were determined by radio-TLC and radio-RP-HPLC and were ≥95% for all ligands. Here, tailing of the peaks detected in radio-RP-HPLC was seen which could indicate unwanted Tc-species or impurities. This could not be fully solved as will be discussed later. The tracers were obtained in molar activity (A_M) of 8 to 30 GBq/µmol.

Due to low purities in quality controls with radio-RP-HPLC of first radiometalations, investigations were started leading to the conclusion that pH-dependent complex instability was the main reason for impurities. As visualized in Figure 68, HPLC chromatograms of the quality controls with probes of the same batch of [^{99m}Tc]Tc-tecFAPI-01 was performed under varying conditions for 10 min at 95 °C. Probes within a pH-range from 6.0 to 9.0 exhibit about 97% radiochemical purity. When diluted in MeCN/H_2O, resulting in a pH-value of 5.0, the complex was unstable. This results in a significantly lower radiochemical purity of only 69%. The purity may also be influenced by the low pH-value of the TFA-containing eluent system

used for radio-RP-HPLC. As it was not practical to perform a solvent change of the system for each quality control, this possibility was not investigated.

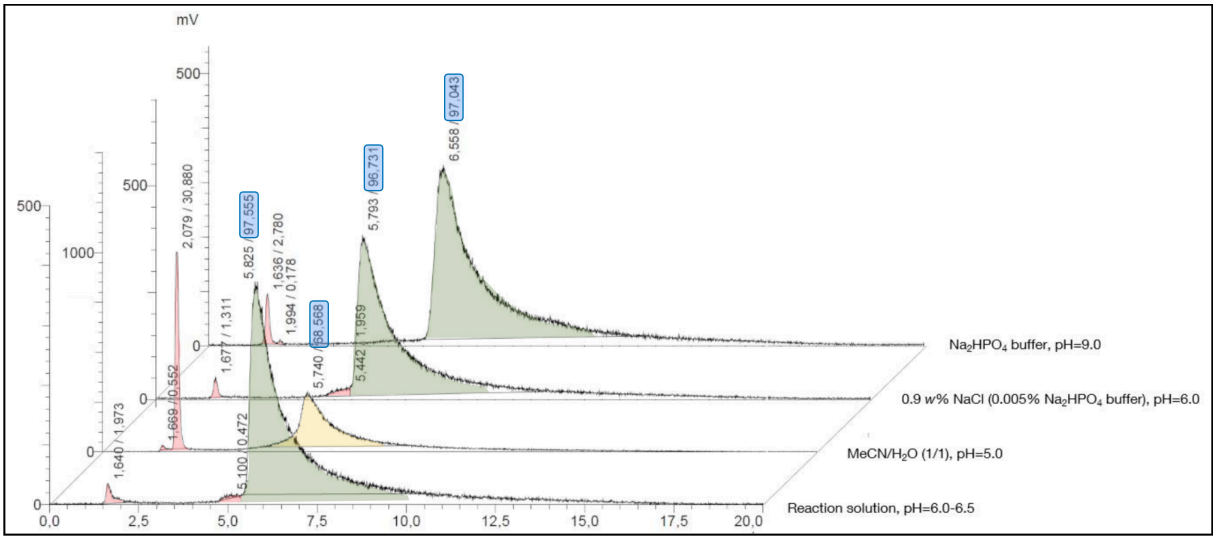

Figure 68: Investigations on pH-dependent stability of [^{99m}Tc]Tc-tecFAPI-01. Quality controls of the same batch were performed (from front to back) directly from the reaction solution (pH = 6.0-6.5), from a dilution in MeCN/H2O (1/1, pH = 5.0), from a dilution in 0.9 w% NaCl (0.005% Na_2HPO4 buffer) (pH = 6.0) and from a dilution in Na_2HPO_4 buffer (pH = 9.0). Red indicates impurities, green indicates quality controls with sufficient radiochemical purities (blue) and yellow quality controls with insufficient radiochemical purities.

After a pH dependency was determined, the complexation of every ligand was performed with variable amounts of buffer (0.005% Na_2HPO4 buffer), to identify the optimal conditions. For [^{99m}Tc]Tc-tecFAPI-01 this was obtained with 5 µL buffer in 1.0 mL generator-eluate (pH = 6.5). For [^{99m}Tc]Tc-tecFAPI-02 an amount of 25 µL buffer (pH = 7.0) in 1.0 mL generator-eluate was used. As only a limited quantity of [^{99m}Tc]TcO_4^- eluate was available per day, the applied volume per labeling was reduced for further studies. The labeling with technetium-99m of tecFAPI-03 to tecFAPI-05 was performed with 0.5 mL eluate and 35 µL of buffer (Na_2HPO_4), which resulted in pH values of about 7.5. Valid quality controls presented an ongoing problem, were the use of the standard radio-RP-HPLC system (chapter 3.3.1) showed severe tailing for all tecFAPI ligands. This resulted in inaccurate quantification of the impurities. Thus, two other HPLC column systems were tested to obtain better results.

The first system being tested was a SeQuant™ ZIC®-HILIC column (hydrophilic interaction liquid chromatography). This led to more defined peaks without significant tailing. Afterwards, the same batch of [^{99m}Tc]Tc-Ga-tecFAPI-04 was analyzed using the standard column (Multospher® column), the HILIC and Nucleosil system. The Nucleosil material is very similar to the normally used Multospher® column. The filling mainly differs by the form of the particles, which alters the separation performance. In this system the peaks also showed less tailing compared to the standard system while maintaining good separation and similar retention times. Separation of the SeQuant™ ZIC®-HILIC column seemed less favorable raising concerns towards recovery and quantification of impurities. Therefore, the Nucleosil column was used for all further quality controls of ^{99m}Tc-labeled tecFAPI ligands, which was also the

column used by *Abiraj et al.*, while *Fani et al.* used a Jupiter Proteo column not available at our chair.[216,259]

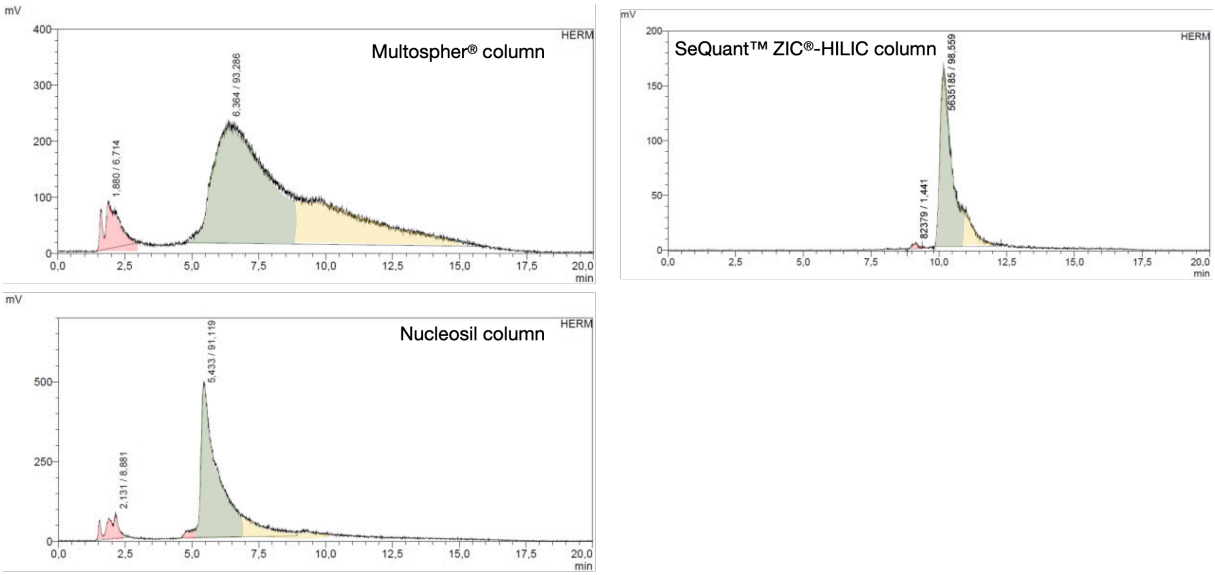

Figure 69: radio-HPLC of the labelling of [^{99m}Tc]Tc-Ga-tecFAPI-04 using the Multospher® (top left), ZIC®-HILIC (top right) and Nucleosil column (bottom left). Red indicates impurities, green indicates tracer peak and yellow indicates tailing of the tracer peak.

Radio-TLC was always performed to cross validate the purity of the ^{99m}Tc-labeled tecFAPI ligands. This was especially used to identify the two most common impurities during complexation with technetium-99m, which are free pertechnetate ([^{99m}Tc]TcO_4^-) and colloidal technetium-99m. A normal phase radio-TLC with 0.9 *w%* NaCl as mobile phase was used to test for pertechnetate. This system gave reproduceable and clear results, which correlated with the results received through radio-RP-HPLC. Colloidal technetium-99m on the other hand could not be quantified *via* radio-TLC, as no mobile phase was found to entirely separate the impurity from the ligand. To quantify this impurity, it is common to eluate a compound, while the colloid stays at the baseline of the radio-TLC. This separation did not take place completely, as the peak of the ligand showed severe fronting and therefore, the two peaks were not baseline separated. In this case, a valid quantification could not be performed. The best results were obtained with a combination of DMF/NH_4Cl_{sat} (3/1, *v/v*) as mobile phase and RP-radio-TLC as stationary phase.

Due to the various difficulties concerning the labelling of the tecFAPI ligands, an approach for future research should be to establish a cartridge purification, which would be performed prior to quality control and subsequent application of the radiolabeled ligands.

No investigations were conducted in the characterization of the present technetium core build for the labelling of the N4-chelator. *Abiraj et al.* suggests that a Tc(V)O_2 core is present in tetramine based chelator which exhibits high kinetic stability.[216,260] But as this was not analytically confirmed also other technetium cores could be present and therefore leading to

broader peak shapes in RP-HPLC analytic. Different technetium core species would lead to drastically different behavior *in vivo* and therefore could explain the unexpected unfavorable results of the biodistribution studies.

4.4.3 ^{18}F-Labeling of rhFAPI Ligands *via Munich* Method

In first ^{18}F-fluorinations of SiFA-derivatives described by *Schirrmacher* and co-workers, aqueous fluoride-18 was dried azeotropically under reduced pressure.[153] In order to circumvent this time-consuming process, the so-called *Munich Drying Method*, developed in our group in 2012 by *Wessmann et al.*[261], was successfully applied for SiFA-bearing compounds.[262] The described procedure was adapted for ^{18}F-labeling of rhFAPI ligands in this work (Figure 70).

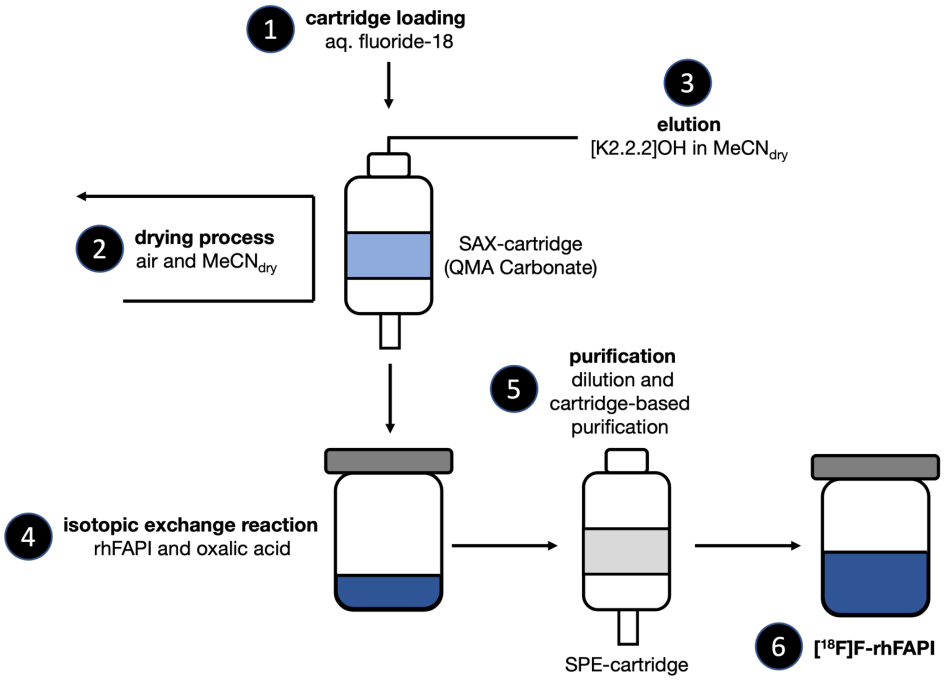

Figure 70: Schematic presentation of the ^{18}F-labeling procedure of [^{19}F]F-rhFAPI ligands by isotopic exchange via the *Munich Method*: Aqueous fluoride-18 was loaded on a strong anion exchange (SAX) cartridge preconditioned with carbonate (**1**) and dried with air and dry MeCN (**2**). After elution of fluoride-18 (**3**) by means of a solution of [$K^+ \subset$2.2.2]OH^- cryptate in dry MeCN and addition of oxalic acid, ^{18}F-for-^{19}F-isotopic exchange on the [^{19}F]F-rhFAPI ligands was carried out for 5 min at rt (**4**). A cartridge-based purification (solid-phase extraction, SPE) (**5**) yielded the ^{18}F-labeled rhFAPI ligand (**6**).

For this purpose, aqueous fluorid-18 is loaded onto a carbonate-based anion exchange cartridge (Sep-Pak Accell Plus QMA Carbonate Plus Light) and purged with air. Drying of the resin was subsequently carried out by purging the cartridge with 10 mL anhydrous MeCN (2 mL/min) and a few mL of air allowing efficient and rapid on-column drying. Thereafter, dried fluorid-18 can be eluted using a solution of [$K^+ \subset$2.2.2]OH^- cryptate (83 µmol KOH, 91 µmol Kryptofix 222) in 500 µL dry MeCN in almost quantitative yield (96 ± 2%). In order to partly neutralize the eluted alkaline solution, containing [$K^+ \subset$2.2.2]$^{18}F^-$, ([$K^+ \subset$2.2.2])$_2CO_3^{2-}$, and excess [$K^+ \subset$2.2.2]OH-, a precise amount of oxalic acid (30 µmol) was added, which was

found to be mandatory for a successful isotopic exchange reaction at the SiFA moiety or SiFA-conjugated radiopharmaceuticals.[262] After addition of 30 µL of a 1.0 M rhFAPI ligand solution in dry DMSO (30 nmol) the isotopic exchange was performed at rt for 5 min. In order to separate and purify the radiolabeled SiFA ligand from cryptate, acetonitrile or DMSO, and free ^{18}F- and ^{19}F-fluoride, a cartridge-based purification (SPE) step was required.[154] For solid-phase extraction, the organic reaction mixture has been diluted with a suitable slightly acidic aqueous buffer to prevent hydrolysis of the Si-F bond from aqueous basic conditions. With respect to clinical applications, a phosphate buffered saline (PBS, pH = 5) was used to dilute the reaction mixture. After purging the cartridge with the buffer, the [^{18}F]F-rhFAPI ligands were eluted in a 1:1 mixture (*v/v*) of ethanol and water (0.3 mL). Due to inefficient elution of the initially used C-18 cartridges (77 ± 11%), Oasis HLB cartridges (Oasis HLB Plus Light, 30 mg sorbent, 30 µm particle size) were employed, resulting in >90% elution efficiency and overall radiochemical yields of 25 ± 8%. Unfortunately, the radiochemical purity of the ^{18}F-labeled rhFAPI ligands was always below 92%, as determined by radio-RP-HPLC and radio-TLC. Reason for this most likely was the amount of oxalic acid added to partly neutralize the eluted alkaline solution. It has been speculated that oxalic acid is necessary to partly neutralize the basic milieu resulting from the high hydroxide and carbonate concentration after cartridge elution which would otherwise decompose the precursor and/or the labeled product.[154,189,262] With further addition of oxalic acid and therefore to high concentrations, the increasing acidity significantly reduces the nucleophilicity of fluoride-18. Due to the quantity of different functional groups with different pK_A values within the diverse rhFAPI ligands the amount of oxalic acid needs to be varied for every ligand. For this reason, labeling of rhFAPI ligands by means of the *Munich Method* would be accompanied by a large experimental workload. Therefore, future ^{18}F-fluorinations were performed following the *Di Carlo Method* where no oxalic acid was needed.

4.4.4 ^{18}F-Labeling of rhFAPI Ligands *via Di Carlo* Method

To avoid the process of individual optimization of oxalic acid quantity for each rhFAPI or transFAPI ligand when labeling with fluorid-18 *via* the *Munich Method*, an unpublished method was developed in our group by *Di Carlo et al.* in 2019. This procedure was adapted for ^{18}F-labeling of rhFAPI and transFAPI ligands in this work (Figure 71) and was performed analogously to the *Munich Method*. Therefore, only differences between the two methods will be discussed here, whereby the *Di Carlo Method* itself is described in detail in GSP14.

A small variation between the methods was the use of dry DMSO instead of dry MeCN as solution for the drying process and the elution cocktail, whereas the main difference was the elution process itself. Here, an elution cocktail kit was prepared by dissolving ammonium formate (40.0 mg) in anhydrous DMSO (500 µL), which then was used to eluate the dried fluorid-18 from the SAX-cartridge with a yield of 87.5 ± 6.6% elution efficiency. This was about 10% lower than for the *Munich Method* therefore leading to an allover reduced radiochemical yield of the labeling process. The elution efficiency could be increased by addition of water to the elution cocktail kit. An amount of 1-2% of water resulted in an elution

efficiency of 90.5 ± 2.0% and could even be increased further by more water. However, this also led to higher amounts of impurities, which could be identified as hydrolysed SiFA species. Therefore, no water was used in the elution cocktail kit to reduce the chances of impurities. Elution after the purification step (**5**) was done with a 1:2 mixture (*v/v*) of ethanol and PBS (0.3 mL). Especially rhFAPI and transFAPI ligands with a positive net charge showed higher radiochemical yields through higher elution efficiency when PBS was used instead of water. Here it was also shown that inverse loading of the SPE-cartridge led to an average of 20% higher elution efficiencies when compared to normal loading. Reason for this might be stronger interactions of ligands with higher amounts of positive charges and in general more lipophilic ligands with material inside the cartridge.

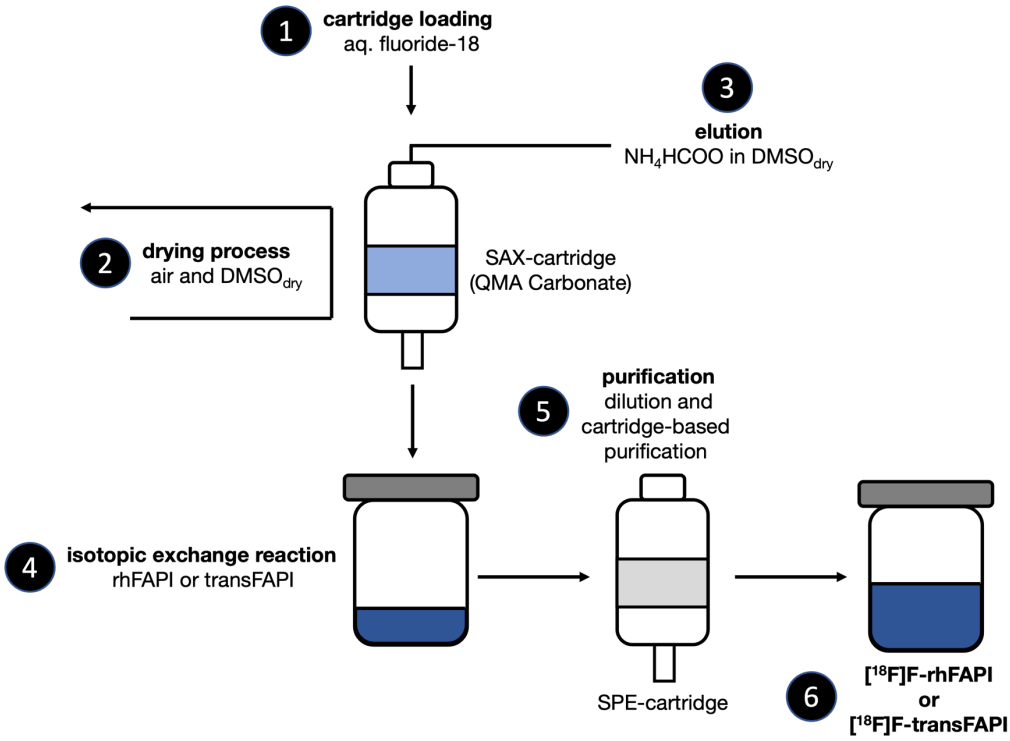

Figure 71: Schematic presentation of the ^{18}F-labeling procedure of [^{19}F]F-rhFAPI or [^{19}F]F-transFAPI ligands by isotopic exchange via the *Di Carlo Method*: Aqueous fluoride-18 was loaded on a strong anion exchange (SAX) cartridge preconditioned with carbonate (**1**) and dried with air and dry DMSO (**2**). After elution of fluoride-18 (**3**) by means of a solution of NH_4HCOO in dry DMSO, ^{18}F-for-^{19}F-isotopic exchange on the [^{19}F]F-rhFAPI ligands was carried out for 5 min at rt (**4**). A cartridge-based purification (solid-phase extraction, SPE) (**5**) yielded the ^{18}F-labeled rhFAPI or transFAPI ligand (**6**).

Overall radiochemical yield for the ^{18}F-labeling of rhFAPI and transFAPI ligands *via* the *Di Carlo Method* were 23.0 ± 12.1%, which was comparable to the yield achieved through labeling with the more established *Munich Method.* On average molar activities of 1-5 GBq/µmol were obtained with varying starting activities between 50 to 150 MBq. These yields were sufficient to perform all *in vitro* and *in vivo* studies but are low compared to results for other SiFA containing ligands with specific molar activities of 30 to 63 GBq/µmol.[149,153-155] Reason for this was lower radiochemical conversion for the isotopic exchange reactions and lower elution efficiencies. Test reactions showed a doubled radiochemical yield of about 45% when

performing the isotopic exchange reaction at 40 °C instead of room temperature. This was more consistent with yields reported by *Wurzer et al.* for the group of rhPSMA ligands.[199,200,217] This leads to the conclusion that further investigations into optimizing the conditions of the isotopic exchange reaction for labeling of rhFAPI and transFAPI ligands are needed to achieve highest possible radiochemical yields and molar activities. Here, especially temperature and reaction time should be investigated. These studies were not conducted in this work, because no developed FAPI tracer described so far showed the potential for a translation to first proof-of-concept studies in humans.

4.5 Development of a Cell Assay for the HT-1080hFAP Cell Line

Starting point for the development of a reliable cell assay, which was simple and fast to perform and that produces consistent results, were the assay conditions used by *Loktev et al.* for FAPI radioligand binding and competition studies.[112] For this purpose, HT-1080 cells transfected with the human FAP-gene (obtained by Stefan Bauer, *NCT Heidelberg*)[86] were cultivated in DMEM containing 10% fetal calf serum at 37 °C. To conduct studies, cells (1.2 to 2.0 million cells per well) were seeded in 6-well plates and cultivated for 48 h. Afterwards, the medium was replaced with 1.0 mL of fresh fetal calf serum free medium. Competition studies were performed by simultaneous exposure of unlabeled (10^{-5} to 10^{-10} M) and radiolabeled compound (12.5 pmol per well) for 60 min. Thereafter, the supernatant was collected, and cells were washed twice with PBS and subsequently lysed with lysis buffer (0.3 M NaOH, 0.2% SDS). Here, *Loktev et al.* never specified which temperature and radiolabeled compound was used for these studies.

Because the assay conditions were published incomplete, an entirely new assay was developed only adapting some aspect and transferring them to the standard way of working at our chair. Here, several changes had to be applied, resulting in an optimization process for each parameter that had to be carried out. The main difference was the use of 24-well plates, which by itself resulted in the question, which cell number per well should and could be used for efficient studies. To many cells in one well could lead to separation of the cell pellet from the well surface and a too small cell count could lead to an insufficient amount of available binding sites and therefore oversaturation by the added ligands. Advantages of the 24-well plates are a broader concentration range of the tested ligand (10^{-4} to 10^{-10} M) and three data points per concentration for each plate with a simplified workflow. In general, the same transfected HT-1080hFAP cell line was used as by *Loketv et al.*, which was also obtained by Stefan Bauer, and ^{177}Lu-labeled FAPI-04 was used as a reference ligand, as it was the state-of-the-art FAP-addressing tracer at that time.

4.5.1 Optimization of Cell-dependent Factors

The cell-based studies were conducted in 24-well plates, therefore the number of cells per well was the first parameter optimized for establishing a reliable cell assay. Here, an important condition can be the time cells are cultivating in the well plate after being seeded. A first investigation showed that cell uptake and therefore binding of the reference ligand was nearly independent of the cell count (1×10^4 to 4×10^4 cells per well) after 24 or 48 h. When seeding more than 5×10^4 cells per well, cultivating for 48 h led to separation of the cell pellet from the well surface most like due to overlapping growth of the cells. Therefore, all further optimization studies were performed 24 h after seeding the cells into the well plates. All optimization experiments were carried out with a total volume of 250 µL per well with at least threefold repetition per parameter.

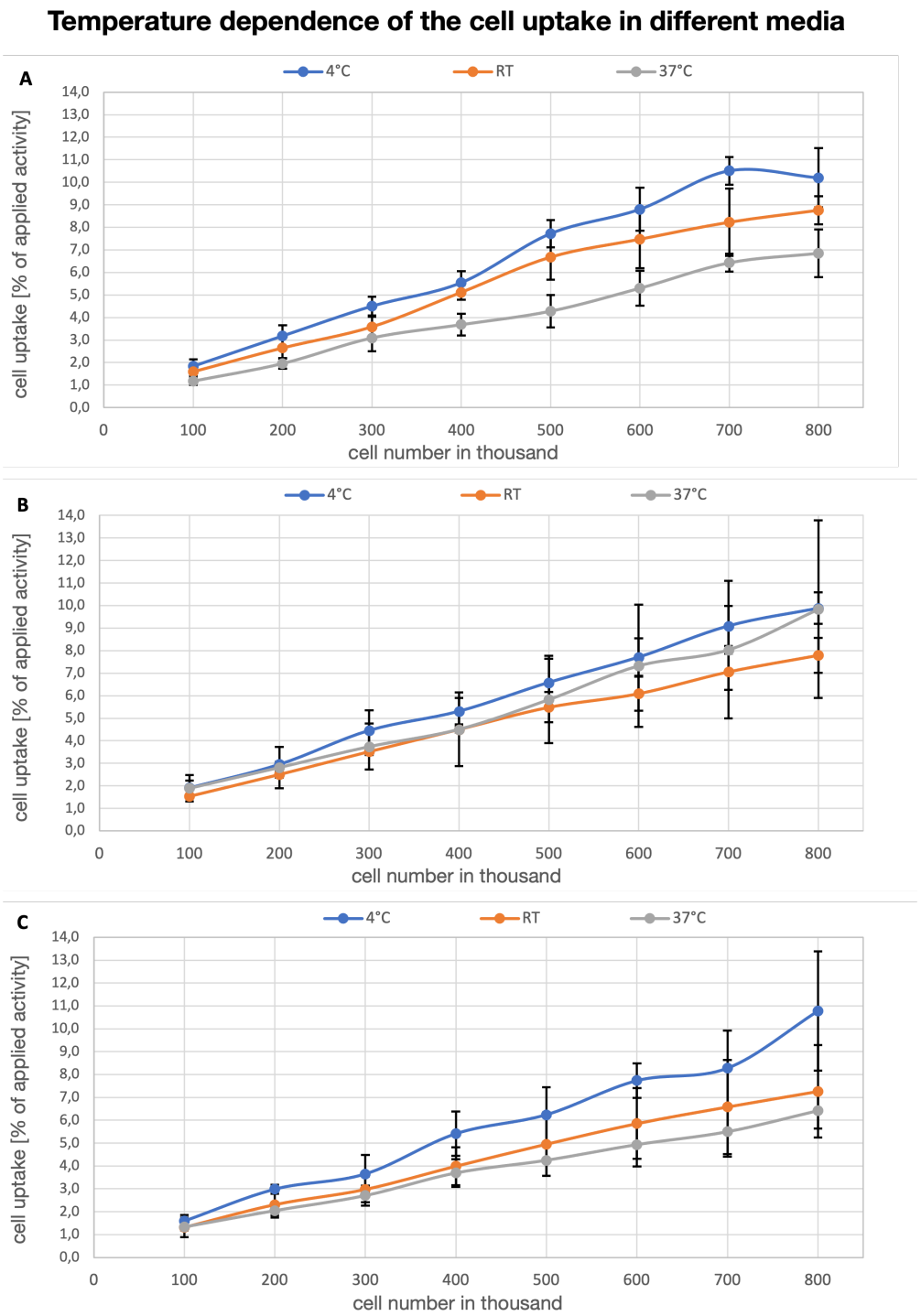

Figure 72: Cell uptake after 1 h incubation of [^{177}Lu]Lu-FAPI-04 at different temperatures (4 °C, RT and 37 °C) and cell numbers (1×10^4 to 8×10^4 cells per well) in various cell assay media: **A** DMEM GlutaMAX, **B** DMEM GlutaMAX + 1% BSA and **C** HBSS + 1% BSA.

For the optimization of the media condition of the cell assay 12.5 pmol of ^{177}Lu-labeled FAPI-04 was added per well, as this amount was also used by *Loktev et al.* in their assay. The temperature of the uptake studies was varied, performing the studies at 4 °C (on ice), room temperature and 37 °C. The cell number was also varied from 1×10^4 to 8×10^4 per well. Therefore, cell uptakes were determined after 1 h incubation in the cultivation medium DMEM with and without addition if 1% BSA and HBSS with 1% BSA. The results of these studies

are shown in Figure 72, where **A** is the uptake in DMEM, **B** in DMEM with addition of 1% BSA and **C** in HBSS with addition of 1% BSA for the three different chosen temperatures and cell numbers of 1×10^4 to 8×10^4 per well.

All studies showed an almost linear increasing uptake of [^{177}Lu]Lu-FAPI-04 with increasing cell numbers from 1–2% uptake with 1×10^4 cells per well to 6–11% uptake for 8×10^4 cells per well. The highest uptakes in all tested media were obtained for studies at 4 °C. When looking at the comparative results for this temperature (Figure 73), the highest uptake over the investigated area was obtained for DMEM GlutaMAX as an assay medium. Here, only studies in HBSS with 1% BSA for a cell number of 8×10^4 cells per well showed higher uptake. It could also be seen that standard deviation of the results for uptake in DMEM GlutaMAX with 1% BSA and HBSS with 1% BSA was significantly higher compared to DMEM GlutaMAX without addition of BSA. Here, unspecific binding of the reference ligand to the protein BSA could be responsible for the lower uptake into the HT-1080hFAP cells.

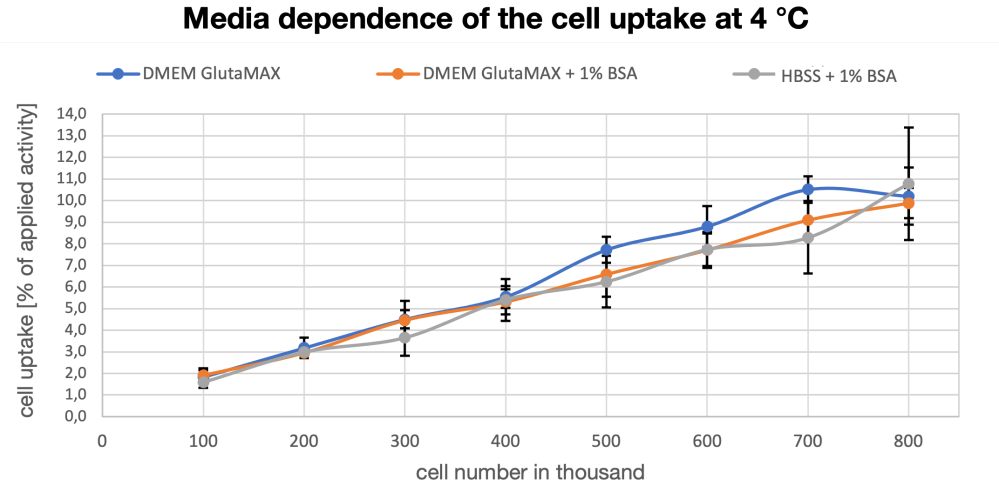

Figure 73: Cell uptake after 1 h incubation of [^{177}Lu]Lu-FAPI-04 at 4 °C and cell numbers (1×10^4 to 8×10^4 cells per well) in a various cell assay media (DMEM GlutaMAX, DMEM GlutaMAX + 1% BSA and HBSS + 1% BSA).

These results led to the decision to further investigate the other different parameters only in DMEM GlutaMAX medium at a temperature of 4 °C. Here, a temperature of 4 °C for the cell assay was desirable as ligand internalization is significantly reduced at these temperatures. Higher temperatures lead to internalization and therefore the possibility of ligands being released from the cells after internalization and again being available for binding. Another problem of internalization is that an internalized reference cannot be displaced from the receptor or binding site, which in result would influence competition studies. Hereby, distortion of the desired uptake study results could occur. To further simplify the handling of the cell assay, a cell number of 5×10^4 cells per well was seen as ideal, as here the uptake difference between the media were most pronounced and more studies could be conducted with the number of cells usually obtained by cultivation.

4.5.2 Optimization of the Incubation Time

The influence of the incubation time on the cell uptake was investigated for 12.5 pmol of [^{177}Lu]Lu-FAPI-04 per well at 4 °C and 5×10^4 cells per well in DMEM GlutaMAX from 1 up to 4 hours. The results are shown in Figure 74 and first indicated no time dependent influence on cell uptake as the increase over time was below 1%. Therefore, no further investigations were performed, and all subsequent studies were conducted with an incubation time of 1 h.

However, the time dependency was revisited after the results of chapter 4.5.3, where the amount of [^{177}Lu]Lu-FAPI-04 per well was reduced to 1.56 pmol. This was done because of reasons discussed in the following (chapter 4.5.3). It was shown that the cell uptake increased about 10% from 1 to 2 h incubation time, while further time points showed only a negligible uptake increase. Furthermore, for incubation times longer than 2 h it was observed that the cell pellets started to separate from the well surface, resulting in higher standard deviations and difficulties at washing steps while performing cell studies. Therefore, an incubation time of two hours was chosen for the final developed cell assay studies.

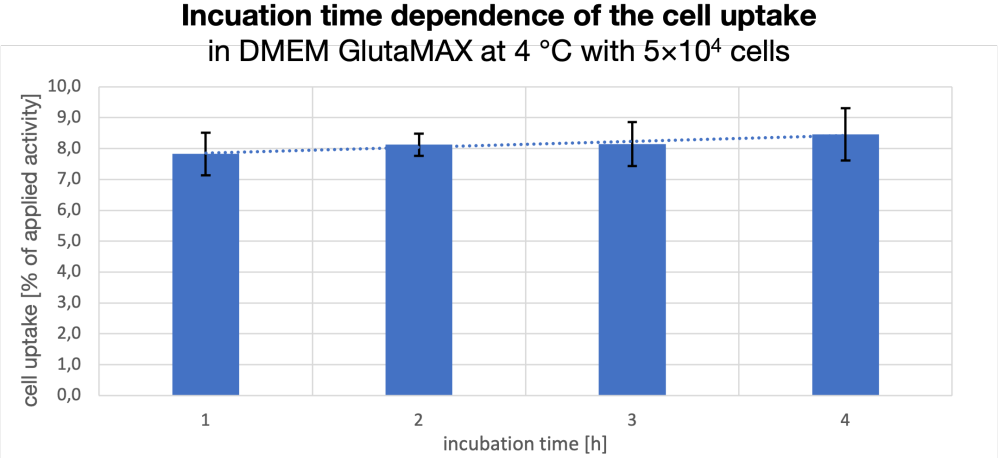

Figure 74: Cell uptake of [^{177}Lu]Lu-FAPI-04 at 4 °C and 5×10^4 cells per well in a DMEM GlutaMAX after increasing incubation time (1 to 4 h).

4.5.3 Optimization of the Reference Concentration

Lastly, the influence of the concentration of added radioligand [^{177}Lu]Lu-FAPI-04 was investigated first in uptake studies and later in first IC_{50} affinity determinations. Thus, different concentrations per well were added at 4 °C to 5×10^4 cells per well in DMEM GlutaMAX for 1 h incubation time. The results are shown in Figure 75, where the activity in counts per minute (CPM) for supernatant and lysate of each concentration and the respective cell uptakes [%] are displayed. In part **A** of Figure 75 the results of concentrations of 12.5, 6.25 and 3.125 pmol per well are shown. There, it was shown that reducing the amount of [^{177}Lu]Lu-FAPI-04 by half results in twice as high cell uptake (5.8% for 12.5 pmol, 11.3% for 6.25 pmol and 21% for 3.125 pmol). This occurred because the total CPM in the supernatant decreased with reduced reference concentration, while the CPM in the lysate fractions stayed the same. This fact allowed the conclusion that in the chosen concentration range a saturation of the FAP

protease was reached. Here, the absolute amount of [^{177}Lu]Lu-FAPI-04 bound to FAP was independent of the concentration applied, as even with 3.125 pmol per well a ligand excess was present and thus all binding sites were occupied. To leave this saturation area and reach an area of equilibrium with dynamic exchange between bound and unbound states, the concentration of [^{177}Lu]Lu-FAPI-04 per well was further decreased, as depicted in part **B** of Figure 75. The concentration was stepwise lowered from 3.125 to 0.391 pmol per well, which resulted in further increasing cell uptake up to 58%, respectively. Here, the reduction of concentration by half did not demonstrate twice as high cellular uptake and the absolute bound activity of [^{177}Lu]Lu-FAPI-04 decreased, while the ratio of lysate to supernatant increased, which resulted in higher cell uptake. This indicated that the goal of reaching the desired concentration range, where there was no saturation of FAP binding sites was achieved, while simultaneously reaching high cellular uptakes of up to 58% (DMEM GlutaMAX at 4 °C with 5×10^4 cells and 0.391 pmol [^{177}Lu]Lu-FAPI-04 per well).

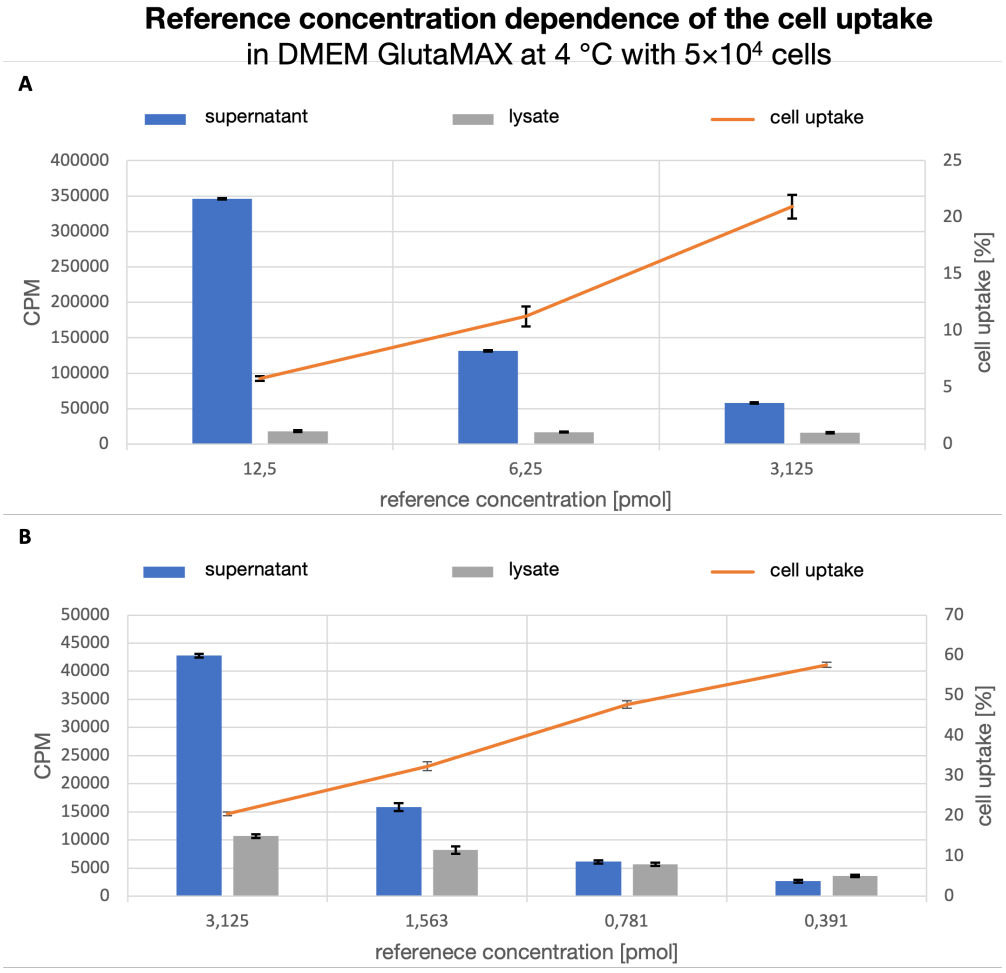

Figure 75: Cell uptake and respective CPM for supernatant and lysate at 4 °C and 5×10^4 cells per well in DMEM GlutaMAX after 1 h incubation time for different amounts of [^{177}Lu]Lu-FAPI-04. **A** shows saturation area. **B** shows concentration range leaving the saturation area.

The influence of the concentration of added radioligand [^{177}Lu]Lu-FAPI-04 was then further investigated for the affinity determinations, as described in chapter 3.4.3. An amount of

1.563 pmol of reference per well was first selected as starting point for these investigations, because it was certain that no FAP binding site saturation through an excess of ligand was occurring (Figure 75). For the affinity studies the cell number and the concentration of the reference were approximately halved to reduce the required quantity of the reference compound. Furthermore, lower cell numbers per well had benefits regarding the cultivation of HT-1080hFAP cells and the handling of the cell tests itself, as higher cell numbers can lead to detachment of the cell pellet in washing steps when using 24-well plates. This resulted in affinity studies, which were carried out with 2.5×10^4 HT-1080hFAP cells and varying amounts of reference [^{177}Lu]Lu-FAPI-04 per well for 2 h incubation time at a temperature of 4 °C. The reference ligand amount was stepwise reduced by half, from 0.7 to 0.075 pmol and the cell uptake and IC_{50} values were determined (Table 12). Additionally, the cell-bound activity at a ligand concentration of 10^{-5} M was investigated. This concentration of the tested ligand was chosen because here the cell-bound activity of the reference ligand was at its lowest, raising the question if the specific activity of the reference ligand was sufficient to obtain high enough CPM for being detectable by the gamma counter used.

Table 12: Cell uptake and affinities to FAP (IC_{50} [nM]) on 2.5×10^4 HT-1080hFAP cells per well after incubation at 4 °C for 2 h of Lu-FAPI-04 against different concentrations of [^{177}Lu]Lu-FAPI-04 and the CPM values for cell-bound activity at ligand concentration of 10^{-5} M.

[^{177}Lu]Lu-FAPI-04 ligand concentration [pmol]	cell uptake	IC_{50} [nM]	CPM for cell-bound activity at ligand concentration of 10^{-5} M
0.7	46%	6.4	3500
0.3	60%	7.1	1900
0.15	70%	7.0	1000
0.075	73%	7.7	300

If the specific activity of the reference ligand is too low, the CPM of the cell bound activity gets too low to be detectable by the used gamma counter. Additionally, the time period in which the reference ligand can be used shortens, because of the halftime of the used radioisotope for labeling. To achieve the highest possible specific activities several labeling experiments were performed resulting in a procedure where 0.5 nmol of FAPI-04 was labeled with 20 MBq of $^{177}LuCl_3$ according to GSP15 resulting in a specific activity of 40 GBy/µmol and no byproducts during labeling. Any increase in activity resulted in emerging byproducts, which would result in a necessary purification step after labeling. For the affinity studies, it could be shown that reducing the concentration of the reference only had an influence on the cell uptake but not on the IC_{50} values received for Lu-FAPI-04. The cell uptake could be increased from 46% up to 73%, while the affinity in average was 7.1 nM with a standard deviation of ± 0.5 nM. Most relevant values here were the CPM for cell-bound activities, which were 3500 CPM for 0.7 pmol and decreased to 300 CPM for 0.075 pmol. Because the labeled reference should be able to be used for at least one week and the half-life of lutetium-177 is 6.647 days, only the cell-bound activity for 0.7 pmol of [^{177}Lu]Lu-FAPI-04 seemed sufficient. Here, the activity received at a ligand concentration of 10^{-5} M one week after labeling of the

reference should still be approximately 1750 CPM, which would still be in an adequate measuring range of the gamma counter. Therefore, an amount of 0.7 pmol per well of [^{177}Lu]Lu-FAPI-04 was used for the final cell assay conditions for affinity determinations.

4.5.4 Investigation of BSA Dependency of the Cell Assay

Finally, the influence of BSA on the affinity to FAP was investigated for the reference compound Lu-FAPI-04 and Lu-rhFAPI-04. This was done because the SiFA-containing rhFAPI ligands showed high binding to the plasma protein HSA and therefore it was suspected that binding to BSA might also occur, which could affect the results of the affinity studies. BSA often is added into the medium of cell assays to reduce unspecific binding to charged plastic surfaces of tubes or well plates. Thus, the effect of using DMEM GlutaMAX with and without addition of 1% BSA as cell assay medium was investigated. The results are presented in Table 13 and showed a clear influence of BSA on the IC_{50} values resulting from the affinity studies. While this influence was marginal or non-existing for Lu-FAPI-04, the IC_{50} value of Lu-rhFAPI-04 showed a 4-fold decreased affinity when adding 1% BSA to the assay medium. This might be explainable with results of HSA binding studies conducted earlier, where Lu-FAPI-04 showed very low and Lu-rhFAPI-04 showed high binding to the plasma protein. To minimize falsification of the results by unwanted binding to BSA, the final affinity studies were performed without addition of BSA in the medium. This ensured that different binding strength of ligands to BSA did not influence the results of affinity studies.

Table 13: Influence of BSA on affinities to FAP (IC_{50} [nM]) with 2.5×10^4 HT-1080hFAP cells per well after incubation at 4 °C for 2 h of Lu-FAPI-04 and Lu-rhFAPI-04.

FAPI ligand	IC_{50} in DMEM GlutaMAX	IC_{50} in DMEM GlutaMAX + 1% BSA
Lu-FAPI-04	6.25 ± 0.7 nM	7.2 ± 0.3 nM
Lu-rhFAPI-04	53.2 ± 5.6 nM	212 ± 18 nM

4.5.5 Summary and Conclusion of the Cell Assay Development

Over the cause of the cell assay development process several parameters such as media composition, cell number, temperature and the concentration of the reference compound could be optimized to implement a reliable cell assay with consistent results. The most promising conditions were found to be DMEM GlutaMAX as media, a cell number of 2.5×10^4 HT-1080hFAP cells and 0.7 pmol of [^{177}Lu]Lu-FAPI-04 per well. Depending on the intended cell studies, the other conditions can be adjusted. However, since affinity studies were the primary goal of the development process, the parameters were mainly investigated for this purpose, resulting in an optimal temperature of 4 °C and an incubation time of 2 hours.

Finally, affinity studies were performed following the subsequent procedure. Cells were harvested 24 ± 2 h prior to the experiment and seeded into 24-well plates (2.5×10^5 cells in 1 mL/well). Following the removal of the culture medium, the cells were carefully washed with 500 µL of DMEM and left on ice for 15 min in 200 µL DMEM to equilibrate. Afterwards, 25 µL

per well of solution containing either HBSS (1% BSA, control) or the respective ligand in increasing concentrations (10^{-10} to 10^{-4} M in HBSS with 1% BSA) were added with subsequent addition of 25 µL of [^{177}Lu]Lu-FAPI-04 (0.7 pmol/well, SA: 40 GBq/µmol) in DMEM. Following incubation on ice for 120 min, the experiment was terminated by removal of the medium and consecutive rinsing with 250 µL of ice-cold PBS. The medium of both steps was combined in one fraction and represents the amount of free radioligand. Next, the cells were lysed with 250 µL of 1 M aq. NaOH for at least 15 min. After removing the lysate and a consecutive washing step (250 µL of 1 M aq. NaOH), both fractions representing the amount of bound ligand were combined. Quantification of all collected fractions was accomplished in a gamma counter. All affinity studies and other cell experiments were carried out with at least threefold repetition per ligand and are described in detail in chapters 3.4.3 and 3.4.4.

For further cell assay developments, the research process should be changed regarding the order of investigated parameter. In the first step of development a greater emphasis should be placed on the examination of the reference concentration in combination with the cell number. Here instead, the media composition, temperature and cell number were investigated first. Because the amount of ligand per well was too high, an excess was present and thus all binding sites were occupied resulting in complete saturation. Thus, the parameters for cell uptake were not really optimized because higher cell uptake would not have been possible. Therefore, an assay development should always start with investigation on the availability of binding sites and which ligand concentration can be added, while remaining an equilibrium with dynamic exchange between bound and unbound states. All other parameters should be optimized afterwards, to ensure that the selected conditions provide optimal outcomes for the cell assay. An interesting result of the BSA dependency studies was the realization that results for ligands that have strong binding to plasma proteins can in fact be massively influenced when adding BSA into an assay medium. Here, the affinity of Lu-rhFAPI-04 towards FAP showed a 4-fold decrease when 1% BSA was present in the medium. This influence should be considered when evaluating ligands with structural moieties that exhibit strong binding to HSA or other plasma proteins, such as the SiFA moiety.

In conclusion, a reliable cell assay was developed, which allowed fast execution of uptake, internalization, or affinity studies for FAP-addressing ligands, which provided our chair with the ability to evaluate the rhFAPI, transFAPI and tecFAPI ligands developed in this thesis.

5 Summary and Conclusion

In this work three new classes of FAP-addressing radiopharmaceuticals were developed, preclinically evaluated and assessed in first biodistribution studies in mice. The first two classes (rhFAPI and transFAPI) incorporated the radiohybrid concept developed at our chair. These ligands feature a Silicon-Fluoride Acceptor (SiFA) moiety and a chelator and therefore can be labeled in an independent manner. Depending on the radioisotope, the resulting series of radiopharmaceuticals ([^{18}F][free]-rh/transFAPI-n, ([^{18}F][$M_{1\text{-}2}$]-rh/transFAPI-n were M = metal and ([^{18}F][$RM_{1\text{-}2}$]-rh/transFAPI-n were RM = radiometal) can be used for PET-imaging (e.g. ^{18}F, ^{44}Sc, ^{68}Ga), for SPECT-imaging (e.g. ^{111}In), and for radioligand therapy with either β^--emitters (e.g. ^{47}Sc, ^{90}Y, ^{177}Lu) or α-emitters (e.g. ^{212}Pb, $^{212/213}$Bi, ^{227Th}, ^{225}Ac). Accordingly, this concept represents a true theranostic approach between ^{18}F- and radiometal-labeled tracers. The third class of ligands (tecFAPI) incorporated a N4-chelator for labeling with radiometals, providing the opportunity of a theranostic ^{99m}Tc/$^{186/188}$Re-pair, either for SPECT-imaging with technetium-99m or for radioligand therapy with the β^--emitters rhenium-186 and -188. Because of the presence of FAP in many different tumor entities this provides universal radiopharmaceuticals for SPECT imaging with the possibility of therapeutic applications.

Especially the tracers [^{177}Lu]Lu-rhFAPI-04+E and [^{177}Lu]Lu-rhFAPI-20, as representatives of the theranostic rhFAPI ligands, proved to be a promising starting point for further investigations into radiohybrid FAP-addressing radiopharmaceuticals. All different generations of rhFAPI ligand developments are differing mostly in varied composition of amino acids in the hydrophilic modification site and the selection of the SiFA moiety. Detailed analysis of the relevant *in vitro* parameters (binding affinities, lipophilicities, bindings to HSA) surprisingly revealed incoherencies between promising *in vitro* data and subsequent results from biodistribution studies in mice.

[^{177}Lu]Lu-rhFAPI-04+E exhibited a relatively low affinity and strong binding to HSA but demonstrated the best *in vivo* performance of all investigated rhFAPI ligands, which might be attributed to its extraordinary low lipophilicity. Therefore, an optimum *in vivo* performance was believed to be gained by further increasing the hydrophilicity by incorporation of different amino acids, metal-chelates and the use of the SIFAN$^+$ moiety. Despite all efforts, the high lipophilicity of the SiFA moiety, which is regarded as a key limitation of the SiFA technology in current literature, could not be effectively outbalanced for the developed sets of FAP-addressing ligands. In conclusion, no rhFAPI ligand proved to demonstrate equal or better characteristics than the established FAP-addressing ligand [^{68}Ga/^{177}Lu]Ga/Lu-FAPI-04.

Improved results for biodistribution studies, while simplifying the structural design of the FAP-addressing ligands, could be achieved with the transFAPI ligand [^{18}F]F-Ga_2-transFAPI-03. Here, favorable *in vivo* distribution with increased uptake in tumor tissue and low background accumulation at early imaging time points was demonstrated. During its development

process, the assumption was made that not the overall measured lipophilicity of a ligand was the most important property for beneficial pharmacokinetic behavior, but rather the compensation of the local lipophilicity of the SiFA moiety itself. This was most likely achieved through the new ligand design incorporating a symmetric SiFA moiety between two hydrophilic and sterically demanding chelators. Despite being the most promising SiFA-containing ligand, [^{18}F]F-Ga$_2$-transFAPI-03 still demonstrated less favorable tumor-to-background ratios compared to [^{68}Ga/^{177}Lu]Ga/Lu-FAPI-04, questioning the feasibility of introducing the radiohybrid concept into FAP-addressing ligands.

The labeling of rhFAPI and transFAPI ligands with fluorine-18 could successful be performed in high yields of 23.0 ± 12.1% by optimizing the previously developed *Di Carlo* Method. Further investigations into optimizing the isotopic exchange reaction conditions for labeling of rhFAPI and transFAPI ligands are needed to achieve highest possible radiochemical yields. In another part of this work, ^{99m}Tc-labled FAP-addressing ligands (tecFAPI) based on the N4-chelator were developed and preclinically evaluated. The tecFAPI ligands demonstrated excellent *in vitro* characteristics in HT-1080hFAP cells, similar to the state-of-the art ligands [^{99m}Tc]Tc-FAPI-34 and [^{99m}Tc]Tc-FL-L3. Surprisingly, the newly developed compounds showed, however, a decreased stability in murine serum, resulting in high activity accumulation in the thyroid gland and blood in tumor-bearing mice.

The *in vivo* data suggest, that the interaction of the [^{99m}Tc]Tc-N4-chelate with negatively charged carboxylic acids of the pharmacokinetic modifier decreased stability of the [^{99m}Tc]Tc-complex. Due to these results, further structural relationship studies must be conducted to improve the stability of FAP-addressing ligands bearing a N4-chelator. As quality control of [^{99m}Tc]Tc-tecFAPIs proved to be challenging in general, further studies at this chair have been initiated to optimize the ^{99m}Tc-labelling of N4-containing ligands.

Lastly, the development of a reliable HT-1080hFAP cell assay was accomplished successfully, which allowed cell-based characterizations of all evaluated ligands in this thesis. Here, several parameters as temperature, incubation time, cell number and concentration of the reference were varied and optimized to obtain an assay, which was simple and fast to perform and produced consistent results for uptake, internalization, or affinity studies.

In summary of all results within this thesis, no further investigations were initiated into developing new FAP-addressing ligands incorporating the radiohybrid concept. Here, the properties of the SiFA moiety, especially the high lipophilicity, seemed to be an unsolvable problem, especially when considering a potential application of the ligands for ^{18}F-imaging. High blood activity accumulations after 1 h p.i. in mice suggested not yet completed tracer distribution, which might provide the possibility for more favorable tumor-to-background ratios for latter time points and therefore, a potential therapeutic use case. Thus, then questioning the utilization of the radiohybrid concept with its intended ^{18}F-labelling functionality. Here, it remains to be seen if FAP-addressing ligands in general provide benefits

compared to tumor-specific tracers because of overall low observed SUVs in the tumors. Especially the previously discussed biology-guided radiotherapy (BgRT) might be an ideal opportunity to use FAPIs in a therapeutic setting. The application of ^{99m}Tc-labelled FAP-addressing compounds remain promising, because of their usability as a [^{18}F]FDG-like pan tumoral universal agent for SPECT imaging. When using the N4-chelator, however, further labeling studies with potential cartridge purification and *in vivo* stability studies must be conducted to ensure the safe application of this new chelating moiety.

6 Bibliography

1. Powell, D. W.; Mifflin, R. C.; Valentich, J. D.; Crowe, S. E.; Saada, J. I.; West, A. B., Myofibroblasts. I. Paracrine cells important in health and disease. *Am J Physiol* **1999,** *277* (1), C1-9.
2. Darby, I. A.; Laverdet, B.; Bonté, F.; Desmoulière, A., Fibroblasts and myofibroblasts in wound healing. *Clin Cosmet Investig Dermatol* **2014,** *7*, 301-311.
3. Tomasek, J. J.; Gabbiani, G.; Hinz, B.; Chaponnier, C.; Brown, R. A., Myofibroblasts and mechano-regulation of connective tissue remodelling. *Nature Reviews Molecular Cell Biology* **2002,** *3* (5), 349-363.
4. Sriram, G.; Bigliardi, P. L.; Bigliardi-Qi, M., Fibroblast heterogeneity and its implications for engineering organotypic skin models in vitro. *Eur J Cell Biol* **2015,** *94* (11), 483-512.
5. Driskell, R. R.; Watt, F. M., Understanding fibroblast heterogeneity in the skin. *Trends Cell Biol* **2015,** *25* (2), 92-9.
6. Öhlund, D.; Elyada, E.; Tuveson, D., Fibroblast heterogeneity in the cancer wound. *The Journal of experimental medicine* **2014,** *211* (8), 1503-1523.
7. Dvorak, H. F., Tumors: wounds that do not heal. Similarities between tumor stroma generation and wound healing. *N Engl J Med* **1986,** *315* (26), 1650-9.
8. Kalluri, R., The biology and function of fibroblasts in cancer. *Nature Reviews Cancer* **2016,** *16* (9), 582-598.
9. Hanahan, D.; Weinberg, R. A., Hallmarks of cancer: the next generation. *Cell* **2011,** *144* (5), 646-74.
10. Rønnov-Jessen, L.; Petersen, O. W.; Bissell, M. J., Cellular changes involved in conversion of normal to malignant breast: importance of the stromal reaction. *Physiol Rev* **1996,** *76* (1), 69-125.
11. Vong, S.; Kalluri, R., The role of stromal myofibroblast and extracellular matrix in tumor angiogenesis. *Genes Cancer* **2011,** *2* (12), 1139-1145.
12. Quail, D. F.; Joyce, J. A., Microenvironmental regulation of tumor progression and metastasis. *Nat Med* **2013,** *19* (11), 1423-37.
13. Kalluri, R., Basement membranes: structure, assembly and role in tumour angiogenesis. *Nat Rev Cancer* **2003,** *3* (6), 422-33.
14. Hanahan, D.; Coussens, L. M., Accessories to the crime: functions of cells recruited to the tumor microenvironment. *Cancer Cell* **2012,** *21* (3), 309-22.
15. Pietras, K.; Ostman, A., Hallmarks of cancer: interactions with the tumor stroma. *Exp Cell Res* **2010,** *316* (8), 1324-31.
16. Giussani, M.; Merlino, G.; Cappelletti, V.; Tagliabue, E.; Daidone, M. G., Tumor-extracellular matrix interactions: Identification of tools associated with breast cancer progression. *Semin Cancer Biol* **2015,** *35*, 3-10.
17. Zi, F.; He, J.; He, D.; Li, Y.; Yang, L.; Cai, Z., Fibroblast activation protein α in tumor microenvironment: recent progression and implications (review). *Molecular medicine reports* **2015,** *11* (5), 3203-3211.
18. Bhowmick, N. A.; Chytil, A.; Plieth, D.; Gorska, A. E.; Dumont, N.; Shappell, S.; Washington, M. K.; Neilson, E. G.; Moses, H. L., TGF-beta signaling in fibroblasts modulates the oncogenic potential of adjacent epithelia. *Science* **2004,** *303* (5659), 848-51.
19. Lujambio, A.; Akkari, L.; Simon, J.; Grace, D.; Tschaharganeh, D. F.; Bolden, J. E.; Zhao, Z.; Thapar, V.; Joyce, J. A.; Krizhanovsky, V.; Lowe, S. W., Non-cell-autonomous tumor suppression by p53. *Cell* **2013,** *153* (2), 449-60.
20. Bussard, K. M.; Mutkus, L.; Stumpf, K.; Gomez-Manzano, C.; Marini, F. C., Tumor-associated stromal cells as key contributors to the tumor microenvironment. *Breast Cancer Research* **2016,** *18* (1), 84.
21. Coussens, L. M.; Werb, Z., Inflammation and cancer. *Nature* **2002,** *420* (6917), 860-7.

22. Kalluri, R.; Zeisberg, M., Fibroblasts in cancer. *Nat Rev Cancer* **2006,** *6* (5), 392-401.
23. De Wever, O.; Van Bockstal, M.; Mareel, M.; Hendrix, A.; Bracke, M., Carcinoma-associated fibroblasts provide operational flexibility in metastasis. *Semin Cancer Biol* **2014,** *25*, 33-46.
24. Dumont, N.; Liu, B.; Defilippis, R. A.; Chang, H.; Rabban, J. T.; Karnezis, A. N.; Tjoe, J. A.; Marx, J.; Parvin, B.; Tlsty, T. D., Breast fibroblasts modulate early dissemination, tumorigenesis, and metastasis through alteration of extracellular matrix characteristics. *Neoplasia* **2013,** *15* (3), 249-62.
25. Ostman, A.; Augsten, M., Cancer-associated fibroblasts and tumor growth--bystanders turning into key players. *Curr Opin Genet Dev* **2009,** *19* (1), 67-73.
26. Augsten, M., Cancer-Associated Fibroblasts as Another Polarized Cell Type of the Tumor Microenvironment. *Frontiers in Oncology* **2014,** *4*.
27. Cortez, E.; Roswall, P.; Pietras, K., Functional subsets of mesenchymal cell types in the tumor microenvironment. *Seminars in Cancer Biology* **2014,** *25*, 3-9.
28. Ishii, G.; Ochiai, A.; Neri, S., Phenotypic and functional heterogeneity of cancer-associated fibroblast within the tumor microenvironment. *Advanced Drug Delivery Reviews* **2016,** *99*, 186-196.
29. Räsänen, K.; Vaheri, A., Activation of fibroblasts in cancer stroma. *Experimental Cell Research* **2010,** *316* (17), 2713-2722.
30. Shiga, K.; Hara, M.; Nagasaki, T.; Sato, T.; Takahashi, H.; Takeyama, H., Cancer-Associated Fibroblasts: Their Characteristics and Their Roles in Tumor Growth. *Cancers* **2015,** *7* (4), 2443-2458.
31. Alexander, J.; Cukierman, E., Stromal dynamic reciprocity in cancer: intricacies of fibroblastic-ECM interactions. *Current Opinion in Cell Biology* **2016,** *42*, 80-93.
32. Madar, S.; Goldstein, I.; Rotter, V., ‘Cancer associated fibroblasts’ – more than meets the eye. *Trends in Molecular Medicine* **2013,** *19* (8), 447-453.
33. Shiga, K.; Hara, M.; Nagasaki, T.; Sato, T.; Takahashi, H.; Takeyama, H., Cancer-Associated Fibroblasts: Their Characteristics and Their Roles in Tumor Growth. *Cancers (Basel)* **2015,** *7* (4), 2443-58.
34. Potenta, S.; Zeisberg, E.; Kalluri, R., The role of endothelial-to-mesenchymal transition in cancer progression. *British Journal of Cancer* **2008,** *99* (9), 1375-1379.
35. Kalluri, R.; Weinberg, R. A., The basics of epithelial-mesenchymal transition. *The Journal of Clinical Investigation* **2009,** *119* (6), 1420-1428.
36. Cirri, P.; Chiarugi, P., Cancer-associated-fibroblasts and tumour cells: a diabolic liaison driving cancer progression. *Cancer and Metastasis Reviews* **2012,** *31* (1), 195-208.
37. Marsh, T.; Pietras, K.; McAllister, S. S., Fibroblasts as architects of cancer pathogenesis. *Biochim Biophys Acta* **2013,** *1832* (7), 1070-8.
38. Raz, Y.; Erez, N., An inflammatory vicious cycle: Fibroblasts and immune cell recruitment in cancer. *Experimental Cell Research* **2013,** *319* (11), 1596-1603.
39. Harper, J.; Sainson, R. C. A., Regulation of the anti-tumour immune response by cancer-associated fibroblasts. *Seminars in Cancer Biology* **2014,** *25*, 69-77.
40. Hematti, P., Mesenchymal stromal cells and fibroblasts: a case of mistaken identity? *Cytotherapy* **2012,** *14* (5), 516-521.
41. Bainbridge P.1 , B. B. C., Wound healing and the role of fibroblasts. *Journal of Wound Care* **2013,** *22* (8), 407-412.
42. Rinn, J. L.; Bondre, C.; Gladstone, H. B.; Brown, P. O.; Chang, H. Y., Anatomic Demarcation by Positional Variation in Fibroblast Gene Expression Programs. *PLOS Genetics* **2006,** *2* (7), e119.
43. Öhlund, D.; Handly-Santana, A.; Biffi, G.; Elyada, E.; Almeida, A. S.; Ponz-Sarvise, M.; Corbo, V.; Oni, T. E.; Hearn, S. A.; Lee, E. J.; Chio, I. I. C.; Hwang, C.-I.; Tiriac, H.; Baker, L. A.; Engle, D. D.; Feig, C.; Kultti, A.; Egeblad, M.; Fearon, D. T.; Crawford, J. M.; Clevers, H.; Park, Y.; Tuveson, D. A., Distinct populations of inflammatory fibroblasts and myofibroblasts in pancreatic cancer. *Journal of Experimental Medicine* **2017,** *214* (3), 579-596.

44. LeBleu, V. S.; Kalluri, R., A peek into cancer-associated fibroblasts: origins, functions and translational impact. *Dis Model Mech* **2018,** *11* (4).
45. O'Connell, J. T.; Sugimoto, H.; Cooke, V. G.; MacDonald, B. A.; Mehta, A. I.; LeBleu, V. S.; Dewar, R.; Rocha, R. M.; Brentani, R. R.; Resnick, M. B.; Neilson, E. G.; Zeisberg, M.; Kalluri, R., VEGF-A and Tenascin-C produced by S100A4⁺ stromal cells are important for metastatic colonization. *Proceedings of the National Academy of Sciences* **2011,** *108* (38), 16002-16007.
46. Erez, N.; Truitt, M.; Olson, P.; Hanahan, D., Cancer-Associated Fibroblasts Are Activated in Incipient Neoplasia to Orchestrate Tumor-Promoting Inflammation in an NF-κB-Dependent Manner. *Cancer Cell* **2010,** *17* (2), 135-147.
47. Orimo, A.; Gupta, P. B.; Sgroi, D. C.; Arenzana-Seisdedos, F.; Delaunay, T.; Naeem, R.; Carey, V. J.; Richardson, A. L.; Weinberg, R. A., Stromal Fibroblasts Present in Invasive Human Breast Carcinomas Promote Tumor Growth and Angiogenesis through Elevated SDF-1/CXCL12 Secretion. *Cell* **2005,** *121* (3), 335-348.
48. Sotgia, F.; Del Galdo, F.; Casimiro, M. C.; Bonuccelli, G.; Mercier, I.; Whitaker-Menezes, D.; Daumer, K. M.; Zhou, J.; Wang, C.; Katiyar, S.; Xu, H.; Bosco, E.; Quong, A. A.; Aronow, B.; Witkiewicz, A. K.; Minetti, C.; Frank, P. G.; Jimenez, S. A.; Knudsen, E. S.; Pestell, R. G.; Lisanti, M. P., Caveolin-1^{−/−} Null Mammary Stromal Fibroblasts Share Characteristics with Human Breast Cancer-Associated Fibroblasts. *The American Journal of Pathology* **2009,** *174* (3), 746-761.
49. Sugimoto, H.; Mundel, T. M.; Kieran, M. W.; Kalluri, R., Identification of fibroblast heterogeneity in the tumor microenvironment. *Cancer Biology & Therapy* **2006,** *5* (12), 1640-1646.
50. Council, L.; Hameed, O., Differential expression of immunohistochemical markers in bladder smooth muscle and myofibroblasts, and the potential utility of desmin, smoothelin, and vimentin in staging of bladder carcinoma. *Modern Pathology* **2009,** *22* (5), 639-650.
51. Mezawa, Y.; Orimo, A., The roles of tumor- and metastasis-promoting carcinoma-associated fibroblasts in human carcinomas. *Cell and Tissue Research* **2016,** *365* (3), 675-689.
52. Yu, Y.; Xiao, C. H.; Tan, L. D.; Wang, Q. S.; Li, X. Q.; Feng, Y. M., Cancer-associated fibroblasts induce epithelial–mesenchymal transition of breast cancer cells through paracrine TGF-β signalling. *British Journal of Cancer* **2014,** *110* (3), 724-732.
53. Jung, D.-W.; Che, Z. M.; Kim, J.; Kim, K.; Kim, K.-Y.; Williams, D.; Kim, J., Tumor-stromal crosstalk in invasion of oral squamous cell carcinoma: a pivotal role of CCL7. *International Journal of Cancer* **2010,** *127* (2), 332-344.
54. Zhuang, J.; Lu, Q.; Shen, B.; Huang, X.; Shen, L.; Zheng, X.; Huang, R.; Yan, J.; Guo, H., TGFβ1 secreted by cancer-associated fibroblasts induces epithelial-mesenchymal transition of bladder cancer cells through lncRNA-ZEB2NAT. *Scientific Reports* **2015,** *5* (1), 11924.
55. Bai, Y.-P.; Shang, K.; Chen, H.; Ding, F.; Wang, Z.; Liang, C.; Xu, Y.; Sun, M.-H.; LI, Y.-Y., FGF-1/-3/FGFR4 signaling in cancer-associated fibroblasts promotes tumor progression in colon cancer through Erk and MMP-7. *Cancer Science* **2015,** *106* (10), 1278-1287.
56. Henriksson, M. L.; Edin, S.; Dahlin, A. M.; Oldenborg, P.-A.; Öberg, Å.; Van Guelpen, B.; Rutegård, J.; Stenling, R.; Palmqvist, R., Colorectal Cancer Cells Activate Adjacent Fibroblasts Resulting in FGF1/FGFR3 Signaling and Increased Invasion. *The American Journal of Pathology* **2011,** *178* (3), 1387-1394.
57. Sun, Y.; Fan, X.; Zhang, Q.; Shi, X.; Xu, G.; Zou, C., Cancer-associated fibroblasts secrete FGF-1 to promote ovarian proliferation, migration, and invasion through the activation of FGF-1/FGFR4 signaling. *Tumor Biology* **2017,** *39* (7), 1010428317712592.
58. Jedeszko, C.; Victor, B. C.; Podgorski, I.; Sloane, B. F., Fibroblast Hepatocyte Growth Factor Promotes Invasion of Human Mammary Ductal Carcinoma In situ. *Cancer Research* **2009,** *69* (23), 9148-9155.
59. Kikuchi, Y.; Kashima, T. G.; Nishiyama, T.; Shimazu, K.; Morishita, Y.; Shimazaki, M.; Kii, I.; Horie, H.; Nagai, H.; Kudo, A.; Fukayama, M., Periostin Is Expressed in Pericryptal Fibroblasts

and Cancer-associated Fibroblasts in the Colon. *Journal of Histochemistry & Cytochemistry* **2008,** *56* (8), 753-764.

60. Ratajczak-Wielgomas, K.; Grzegrzolka, J.; Piotrowska, A.; Gomulkiewicz, A.; Witkiewicz, W.; Dziegiel, P., Periostin expression in cancer-associated fibroblasts of invasive ductal breast carcinoma. *Oncol Rep* **2016,** *36* (5), 2745-2754.
61. Gascard, P.; Tlsty, T. D., Carcinoma-associated fibroblasts: orchestrating the composition of malignancy. *Genes & Development* **2016,** *30* (9), 1002-1019.
62. Han, Y.; Zhang, Y.; Jia, T.; Sun, Y., Molecular mechanism underlying the tumor-promoting functions of carcinoma-associated fibroblasts. *Tumor Biology* **2015,** *36* (3), 1385-1394.
63. Albrengues, J.; Bertero, T.; Grasset, E.; Bonan, S.; Maiel, M.; Bourget, I.; Philippe, C.; Herraiz Serrano, C.; Benamar, S.; Croce, O.; Sanz-Moreno, V.; Meneguzzi, G.; Feral, C. C.; Cristofari, G.; Gaggioli, C., Epigenetic switch drives the conversion of fibroblasts into proinvasive cancer-associated fibroblasts. *Nature Communications* **2015,** *6* (1), 10204.
64. Lisanti, M. P.; Martinez-Outschoorn, U. E.; Sotgia, F., Oncogenes induce the cancer-associated fibroblast phenotype: Metabolic symbiosis and "fibroblast addiction" are new therapeutic targets for drug discovery. *Cell Cycle* **2013,** *12* (17), 2723-2732.
65. Brennen, W. N.; Isaacs, J. T.; Denmeade, S. R., Rationale behind targeting fibroblast activation protein-expressing carcinoma-associated fibroblasts as a novel chemotherapeutic strategy. *Mol Cancer Ther* **2012,** *11* (2), 257-66.
66. O'Brien, P.; O'Connor, B. F., Seprase: an overview of an important matrix serine protease. *Biochim Biophys Acta* **2008,** *1784* (9), 1130-45.
67. Kelly, T., Fibroblast activation protein-alpha and dipeptidyl peptidase IV (CD26): cell-surface proteases that activate cell signaling and are potential targets for cancer therapy. *Drug Resist Updat* **2005,** *8* (1-2), 51-8.
68. Loktev, A.; Lindner, T.; Mier, W.; Debus, J.; Altmann, A.; Jager, D.; Giesel, F.; Kratochwil, C.; Barthe, P.; Roumestand, C.; Haberkorn, U., A Tumor-Imaging Method Targeting Cancer-Associated Fibroblasts. *J Nucl Med* **2018,** *59* (9), 1423-1429.
69. Garin-Chesa, P.; Old, L. J.; Rettig, W. J., Cell surface glycoprotein of reactive stromal fibroblasts as a potential antibody target in human epithelial cancers. *Proc Natl Acad Sci U S A* **1990,** *87* (18), 7235-9.
70. Aertgeerts, K.; Levin, I.; Shi, L.; Snell, G. P.; Jennings, A.; Prasad, G. S.; Zhang, Y.; Kraus, M. L.; Salakian, S.; Sridhar, V.; Wijnands, R.; Tennant, M. G., Structural and Kinetic Analysis of the Substrate Specificity of Human Fibroblast Activation Protein α *. *Journal of Biological Chemistry* **2005,** *280* (20), 19441-19444.
71. Hamson, E. J.; Keane, F. M.; Tholen, S.; Schilling, O.; Gorrell, M. D., Understanding fibroblast activation protein (FAP): substrates, activities, expression and targeting for cancer therapy. *Proteomics Clin Appl* **2014,** *8* (5-6), 454-63.
72. Edosada, C. Y.; Quan, C.; Wiesmann, C.; Tran, T.; Sutherlin, D.; Reynolds, M.; Elliott, J. M.; Raab, H.; Fairbrother, W.; Wolf, B. B., Selective inhibition of fibroblast activation protein protease based on dipeptide substrate specificity. *J Biol Chem* **2006,** *281* (11), 7437-44.
73. Edosada, C. Y.; Quan, C.; Tran, T.; Pham, V.; Wiesmann, C.; Fairbrother, W.; Wolf, B. B., Peptide substrate profiling defines fibroblast activation protein as an endopeptidase of strict Gly(2)-Pro(1)-cleaving specificity. *FEBS Lett* **2006,** *580* (6), 1581-6.
74. Meadows, S. A.; Edosada, C. Y.; Mayeda, M.; Tran, T.; Quan, C.; Raab, H.; Wiesmann, C.; Wolf, B. B., Ala657 and conserved active site residues promote fibroblast activation protein endopeptidase activity via distinct mechanisms of transition state stabilization. *Biochemistry* **2007,** *46* (15), 4598-605.
75. Sounni, N. E.; Noel, A., Targeting the tumor microenvironment for cancer therapy. *Clin Chem* **2013,** *59* (1), 85-93.
76. Santos, A. M.; Jung, J.; Aziz, N.; Kissil, J. L.; Puré, E., Targeting fibroblast activation protein inhibits tumor stromagenesis and growth in mice. *The Journal of clinical investigation* **2009,** *119* (12), 3613-3625.

77. Busek, P.; Mateu, R.; Zubal, M.; Kotackova, L.; Sedo, A., Targeting fibroblast activation protein in cancer - Prospects and caveats. *Front Biosci (Landmark Ed)* **2018,** *23*, 1933-1968.
78. Lindner, T.; Loktev, A.; Giesel, F.; Kratochwil, C.; Altmann, A.; Haberkorn, U., Targeting of activated fibroblasts for imaging and therapy. *EJNMMI Radiopharmacy and Chemistry* **2019,** *4* (1), 16.
79. Lindner, T.; Giesel, F. L.; Kratochwil, C.; Serfling, S. E., Radioligands Targeting Fibroblast Activation Protein (FAP). *Cancers* **2021,** *13* (22), 5744.
80. Welt, S.; Divgi, C. R.; Scott, A. M.; Garin-Chesa, P.; Finn, R. D.; Graham, M.; Carswell, E. A.; Cohen, A.; Larson, S. M.; Old, L. J.; et al., Antibody targeting in metastatic colon cancer: a phase I study of monoclonal antibody F19 against a cell-surface protein of reactive tumor stromal fibroblasts. *J Clin Oncol* **1994,** *12* (6), 1193-203.
81. Scott, A. M.; Wiseman, G.; Welt, S.; Adjei, A.; Lee, F. T.; Hopkins, W.; Divgi, C. R.; Hanson, L. H.; Mitchell, P.; Gansen, D. N.; Larson, S. M.; Ingle, J. N.; Hoffman, E. W.; Tanswell, P.; Ritter, G.; Cohen, L. S.; Bette, P.; Arvay, L.; Amelsberg, A.; Vlock, D.; Rettig, W. J.; Old, L. J., A Phase I dose-escalation study of sibrotuzumab in patients with advanced or metastatic fibroblast activation protein-positive cancer. *Clin Cancer Res* **2003,** *9* (5), 1639-47.
82. Hofheinz, R. D.; al-Batran, S. E.; Hartmann, F.; Hartung, G.; Jager, D.; Renner, C.; Tanswell, P.; Kunz, U.; Amelsberg, A.; Kuthan, H.; Stehle, G., Stromal antigen targeting by a humanised monoclonal antibody: an early phase II trial of sibrotuzumab in patients with metastatic colorectal cancer. *Onkologie* **2003,** *26* (1), 44-8.
83. Zhang, J.; Valianou, M.; Simmons, H.; Robinson, M. K.; Lee, H. O.; Mullins, S. R.; Marasco, W. A.; Adams, G. P.; Weiner, L. M.; Cheng, J. D., Identification of inhibitory scFv antibodies targeting fibroblast activation protein utilizing phage display functional screens. *FASEB J* **2013,** *27* (2), 581-9.
84. Schmidt, A.; Muller, D.; Mersmann, M.; Wuest, T.; Gerlach, E.; Garin-Chesa, P.; Rettig, W. J.; Pfizenmaier, K.; Moosmayer, D., Generation of human high-affinity antibodies specific for the fibroblast activation protein by guided selection. *Eur J Biochem* **2001,** *268* (6), 1730-8.
85. Mersmann, M.; Schmidt, A.; Rippmann, J. F.; Wuest, T.; Brocks, B.; Rettig, W. J.; Garin-Chesa, P.; Pfizenmaier, K.; Moosmayer, D., Human antibody derivatives against the fibroblast activation protein for tumor stroma targeting of carcinomas. *Int J Cancer* **2001,** *92* (2), 240-8.
86. Fischer, E.; Chaitanya, K.; Wuest, T.; Wadle, A.; Scott, A. M.; van den Broek, M.; Schibli, R.; Bauer, S.; Renner, C., Radioimmunotherapy of fibroblast activation protein positive tumors by rapidly internalizing antibodies. *Clin Cancer Res* **2012,** *18* (22), 6208-18.
87. Hornig, N.; Kermer, V.; Frey, K.; Diebolder, P.; Kontermann, R. E.; Muller, D., Combination of a bispecific antibody and costimulatory antibody-ligand fusion proteins for targeted cancer immunotherapy. *J Immunother* **2012,** *35* (5), 418-29.
88. Wang, L. C.; Lo, A.; Scholler, J.; Sun, J.; Majumdar, R. S.; Kapoor, V.; Antzis, M.; Cotner, C. E.; Johnson, L. A.; Durham, A. C.; Solomides, C. C.; June, C. H.; Pure, E.; Albelda, S. M., Targeting fibroblast activation protein in tumor stroma with chimeric antigen receptor T cells can inhibit tumor growth and augment host immunity without severe toxicity. *Cancer Immunol Res* **2014,** *2* (2), 154-66.
89. Wen, Y.; Wang, C. T.; Ma, T. T.; Li, Z. Y.; Zhou, L. N.; Mu, B.; Leng, F.; Shi, H. S.; Li, Y. O.; Wei, Y. Q., Immunotherapy targeting fibroblast activation protein inhibits tumor growth and increases survival in a murine colon cancer model. *Cancer Sci* **2010,** *101* (11), 2325-32.
90. Lee, J.; Fassnacht, M.; Nair, S.; Boczkowski, D.; Gilboa, E., Tumor immunotherapy targeting fibroblast activation protein, a product expressed in tumor-associated fibroblasts. *Cancer Res* **2005,** *65* (23), 11156-63.
91. Brennen, W. N.; Rosen, D. M.; Wang, H.; Isaacs, J. T.; Denmeade, S. R., Targeting carcinoma-associated fibroblasts within the tumor stroma with a fibroblast activation protein-activated prodrug. *J Natl Cancer Inst* **2012,** *104* (17), 1320-34.

92. Ostermann, E.; Garin-Chesa, P.; Heider, K. H.; Kalat, M.; Lamche, H.; Puri, C.; Kerjaschki, D.; Rettig, W. J.; Adolf, G. R., Effective immunoconjugate therapy in cancer models targeting a serine protease of tumor fibroblasts. *Clin Cancer Res* **2008,** *14* (14), 4584-92.
93. Narra, K.; Mullins, S. R.; Lee, H. O.; Strzemkowski-Brun, B.; Magalong, K.; Christiansen, V. J.; McKee, P. A.; Egleston, B.; Cohen, S. J.; Weiner, L. M.; Meropol, N. J.; Cheng, J. D., Phase II trial of single agent Val-boroPro (Talabostat) inhibiting Fibroblast Activation Protein in patients with metastatic colorectal cancer. *Cancer Biol Ther* **2007,** *6* (11), 1691-9.
94. Eager, R. M.; Cunningham, C. C.; Senzer, N.; Richards, D. A.; Raju, R. N.; Jones, B.; Uprichard, M.; Nemunaitis, J., Phase II trial of talabostat and docetaxel in advanced non-small cell lung cancer. *Clin Oncol (R Coll Radiol)* **2009,** *21* (6), 464-72.
95. Eager, R. M.; Cunningham, C. C.; Senzer, N. N.; Stephenson, J., Jr.; Anthony, S. P.; O'Day, S. J.; Frenette, G.; Pavlick, A. C.; Jones, B.; Uprichard, M.; Nemunaitis, J., Phase II assessment of talabostat and cisplatin in second-line stage IV melanoma. *BMC Cancer* **2009,** *9*, 263.
96. Cunningham, C. C., Talabostat. *Expert Opin Investig Drugs* **2007,** *16* (9), 1459-65.
97. Adams, S.; Miller, G. T.; Jesson, M. I.; Watanabe, T.; Jones, B.; Wallner, B. P., PT-100, a small molecule dipeptidyl peptidase inhibitor, has potent antitumor effects and augments antibody-mediated cytotoxicity via a novel immune mechanism. *Cancer Res* **2004,** *64* (15), 5471-80.
98. Tran, E.; Chinnasamy, D.; Yu, Z.; Morgan, R. A.; Lee, C. C.; Restifo, N. P.; Rosenberg, S. A., Immune targeting of fibroblast activation protein triggers recognition of multipotent bone marrow stromal cells and cachexia. *J Exp Med* **2013,** *210* (6), 1125-35.
99. Lee, K. N.; Jackson, K. W.; Christiansen, V. J.; Lee, C. S.; Chun, J. G.; McKee, P. A., Antiplasmin-cleaving enzyme is a soluble form of fibroblast activation protein. *Blood* **2006,** *107* (4), 1397-404.
100. Keane, F. M.; Yao, T. W.; Seelk, S.; Gall, M. G.; Chowdhury, S.; Poplawski, S. E.; Lai, J. H.; Li, Y.; Wu, W.; Farrell, P.; Vieira de Ribeiro, A. J.; Osborne, B.; Yu, D. M.; Seth, D.; Rahman, K.; Haber, P.; Topaloglu, A. K.; Wang, C.; Thomson, S.; Hennessy, A.; Prins, J.; Twigg, S. M.; McLennan, S. V.; McCaughan, G. W.; Bachovchin, W. W.; Gorrell, M. D., Quantitation of fibroblast activation protein (FAP)-specific protease activity in mouse, baboon and human fluids and organs. *FEBS Open Bio* **2013,** *4*, 43-54.
101. Pandya, D. N.; Sinha, A.; Yuan, H.; Mutkus, L.; Stumpf, K.; Marini, F. C.; Wadas, T. J., Imaging of Fibroblast Activation Protein Alpha Expression in a Preclinical Mouse Model of Glioma Using Positron Emission Tomography. *Molecules* **2020,** *25* (16).
102. Hintz, H. M.; Gallant, J. P.; Vander Griend, D. J.; Coleman, I. M.; Nelson, P. S.; LeBeau, A. M., Imaging Fibroblast Activation Protein Alpha Improves Diagnosis of Metastatic Prostate Cancer with Positron Emission Tomography. *Clin Cancer Res* **2020,** *26* (18), 4882-4891.
103. Osterkamp, F. Z. D.; Schneider, E.; Haase, C.; Paschke, M.; Hoehne, A.; Ungewiss, J.; Smerling, C.; Reineke, U.; Bredenbeck, A. Compounds Comprising a Fibroblast Activation Protein Ligand and Use Thereof. WO2021005131A1, 2021. Available online: https://worldwide.espacenet.com (accessed on 08. April 2022).
104. Zboralski, D.; Osterkamp, F.; Simmons, A. D.; Bredenbeck, A.; Schumann, A.; Paschke, M.; Beindorff, N.; Mohan, A. M.; Nguyen, M.; Xiao, J.; Harding, T. C.; Hoehne, A.; Reineke, U.; Smerling, C., 571P Preclinical evaluation of FAP-2286, a peptide-targeted radionuclide therapy (PTRT) to fibroblast activation protein alpha (FAP). *Annals of Oncology* **2020,** *31*, S488.
105. Jansen, K.; Heirbaut, L.; Cheng, J. D.; Joossens, J.; Ryabtsova, O.; Cos, P.; Maes, L.; Lambeir, A. M.; De Meester, I.; Augustyns, K.; Van der Veken, P., Selective Inhibitors of Fibroblast Activation Protein (FAP) with a (4-Quinolinoyl)-glycyl-2-cyanopyrrolidine Scaffold. *ACS Med Chem Lett* **2013,** *4* (5), 491-6.
106. Jansen, K.; Heirbaut, L.; Verkerk, R.; Cheng, J. D.; Joossens, J.; Cos, P.; Maes, L.; Lambeir, A. M.; De Meester, I.; Augustyns, K.; Van der Veken, P., Extended structure-activity relationship and pharmacokinetic investigation of (4-quinolinoyl)glycyl-2-cyanopyrrolidine inhibitors of fibroblast activation protein (FAP). *J Med Chem* **2014,** *57* (7), 3053-74.

107. Lee, K. N.; Jackson, K. W.; Christiansen, V. J.; Dolence, E. K.; McKee, P. A., Enhancement of fibrinolysis by inhibiting enzymatic cleavage of precursor α2-antiplasmin. *J Thromb Haemost* **2011,** *9* (5), 987-96.
108. Poplawski, S. E.; Lai, J. H.; Li, Y.; Jin, Z.; Liu, Y.; Wu, W.; Wu, Y.; Zhou, Y.; Sudmeier, J. L.; Sanford, D. G.; Bachovchin, W. W., Identification of selective and potent inhibitors of fibroblast activation protein and prolyl oligopeptidase. *J Med Chem* **2013,** *56* (9), 3467-77.
109. Thomas, L.; Eckhardt, M.; Langkopf, E.; Tadayyon, M.; Himmelsbach, F.; Mark, M., (R)-8-(3-amino-piperidin-1-yl)-7-but-2-ynyl-3-methyl-1-(4-methyl-quinazolin-2-ylmethyl)-3,7-dihydro-purine-2,6-dione (BI 1356), a novel xanthine-based dipeptidyl peptidase 4 inhibitor, has a superior potency and longer duration of action compared with other dipeptidyl peptidase-4 inhibitors. *J Pharmacol Exp Ther* **2008,** *325* (1), 175-82.
110. Tsai, T. Y.; Yeh, T. K.; Chen, X.; Hsu, T.; Jao, Y. C.; Huang, C. H.; Song, J. S.; Huang, Y. C.; Chien, C. H.; Chiu, J. H.; Yen, S. C.; Tang, H. K.; Chao, Y. S.; Jiaang, W. T., Substituted 4-carboxymethylpyroglutamic acid diamides as potent and selective inhibitors of fibroblast activation protein. *J Med Chem* **2010,** *53* (18), 6572-83.
111. Lindner, T.; Loktev, A.; Altmann, A.; Giesel, F.; Kratochwil, C.; Debus, J.; Jager, D.; Mier, W.; Haberkorn, U., Development of Quinoline-Based Theranostic Ligands for the Targeting of Fibroblast Activation Protein. *J Nucl Med* **2018,** *59* (9), 1415-1422.
112. Loktev, A.; Lindner, T.; Burger, E.-M.; Altmann, A.; Giesel, F.; Kratochwil, C.; Debus, J.; Marme, F.; Jaeger, D.; Mier, W.; Haberkorn, U., Development of novel FAP-targeted radiotracers with improved tumor retention. *Journal of Nuclear Medicine* **2019**.
113. Kratochwil, C.; Flechsig, P.; Lindner, T.; Abderrahim, L.; Altmann, A.; Mier, W.; Adeberg, S.; Rathke, H.; Roehrich, M.; Winter, H.; Plinkert, P.; Marme, F.; Lang, M.; Kauczor, H. U.; Jaeger, D.; Debus, J.; Haberkorn, U.; Giesel, F., FAPI-PET/CT: Mean intensity of tracer-uptake (SUV) in 28 different kinds of cancer. *J Nucl Med* **2019**.
114. Watabe, T.; Liu, Y.; Kaneda-Nakashima, K.; Shirakami, Y.; Lindner, T.; Ooe, K.; Toyoshima, A.; Nagata, K.; Shimosegawa, E.; Haberkorn, U.; Kratochwil, C.; Shinohara, A.; Giesel, F.; Hatazawa, J., Theranostics targeting fibroblast activation protein in the tumor stroma: 64Cu and 225Ac labelled FAPI-04 in pancreatic cancer xenograft mouse models. *Journal of Nuclear Medicine* **2019**.
115. Toms, J.; Kogler, J.; Maschauer, S.; Daniel, C.; Schmidkonz, C.; Kuwert, T.; Prante, O., Targeting Fibroblast Activation Protein: Radiosynthesis and Preclinical Evaluation of an (18)F-labeled FAP Inhibitor. *J Nucl Med* **2020**.
116. Lindner, T.; Altmann, A.; Giesel, F.; Kratochwil, C.; Kleist, C.; Krämer, S.; Mier, W.; Cardinale, J.; Kauczor, H.-U.; Jäger, D.; Debus, J.; Haberkorn, U., 18F-labeled tracers targeting fibroblast activation protein. *EJNMMI Radiopharmacy and Chemistry* **2021,** *6* (1), 26.
117. Giesel, F.; Adeberg, S.; Syed, M.; Lindner, T.; Jimenez, L. D.; Mavriopoulou, E.; Staudinger, F.; Tonndorf-Martini, E.; Regnery, S.; Rieken, S.; ElShafie, R.; Röhrich, M.; Flechsig, P.; Kluge, A.; Altmann, A.; Debus, J.; Haberkorn, U. A.; Kratochwil, C., FAPI-74 PET/CT Using Either 18F-AlF or Cold-kit 68Ga-labeling: Biodistribution, Radiation Dosimetry and Tumor Delineation in Lung Cancer Patients. *Journal of Nuclear Medicine* **2020**.
118. Lindner, T.; Altmann, A.; Kraemer, S.; Kleist, C.; Loktev, A.; Kratochwil, C.; Giesel, F.; Mier, W.; Marme, F.; Debus, J.; Haberkorn, U., Design and development of 99mTc labeled FAPI-tracers for SPECT-imaging and 188Re therapy. *Journal of Nuclear Medicine* **2020**.
119. Roy, J.; Hettiarachchi, S. U.; Kaake, M.; Mukkamala, R.; Low, P. S., Design and validation of fibroblast activation protein alpha targeted imaging and therapeutic agents. *Theranostics* **2020,** *10* (13), 5778-5789.
120. Millul, J.; Bassi, G.; Mock, J.; Elsayed, A.; Pellegrino, C.; Zana, A.; Dakhel Plaza, S.; Nadal, L.; Gloger, A.; Schmidt, E.; Biancofiore, I.; Donckele, E. J.; Samain, F.; Neri, D.; Cazzamalli, S., An ultra-high-affinity small organic ligand of fibroblast activation protein for tumor-targeting applications. *Proceedings of the National Academy of Sciences* **2021,** *118* (16), e2101852118.

121. Slania, S. L.; Das, D.; Lisok, A.; Du, Y.; Jiang, Z.; Mease, R. C.; Rowe, S. P.; Nimmagadda, S.; Yang, X.; Pomper, M. G., Imaging of Fibroblast Activation Protein in Cancer Xenografts Using Novel (4-Quinolinoyl)-glycyl-2-cyanopyrrolidine-Based Small Molecules. *Journal of Medicinal Chemistry* **2021,** *64* (7), 4059-4070.
122. Moon, E. S.; Elvas, F.; Vliegen, G.; De Lombaerde, S.; Vangestel, C.; De Bruycker, S.; Bracke, A.; Eppard, E.; Greifenstein, L.; Klasen, B.; Kramer, V.; Staelens, S.; De Meester, I.; Van der Veken, P.; Rösch, F., Targeting fibroblast activation protein (FAP): next generation PET radiotracers using squaramide coupled bifunctional DOTA and DATA5m chelators. *EJNMMI Radiopharmacy and Chemistry* **2020,** *5* (1), 19.
123. Langer, L. B. N.; Hess, A.; Korkmaz, Z.; Tillmanns, J.; Reffert, L. M.; Bankstahl, J. P.; Bengel, F. M.; Thackeray, J. T.; Ross, T. L., Molecular imaging of fibroblast activation protein after myocardial infarction using the novel radiotracer [⁶⁸Ga]MHLL1. *Theranostics* **2021,** *11* (16), 7755-7766.
124. Kelly, J. M.; Jeitner, T. M.; Ponnala, S.; Williams, C.; Nikolopoulou, A.; DiMagno, S. G.; Babich, J. W., A Trifunctional Theranostic Ligand Targeting Fibroblast Activation Protein-α (FAPα). *Molecular Imaging and Biology* **2021**.
125. Grus, T.; Lahnif, H.; Klasen, B.; Moon, E. S.; Greifenstein, L.; Roesch, F., Squaric Acid-Based Radiopharmaceuticals for Tumor Imaging and Therapy. *Bioconjug Chem* **2021**.
126. Tredwell, M.; Gouverneur, V., 18F labeling of arenes. *Angew Chem Int Ed Engl* **2012,** *51* (46), 11426-37.
127. Yusubov, M. S.; Svitich, D. Y.; Yoshimura, A.; Nemykin, V. N.; Zhdankin, V. V., 2-Iodoxybenzoic acid organosulfonates: preparation, X-ray structure and reactivity of new, powerful hypervalent iodine(V) oxidants. *Chem Commun (Camb)* **2013,** *49* (96), 11269-71.
128. Serdons, K.; Verbruggen, A.; Bormans, G. M., Developing new molecular imaging probes for PET. *Methods* **2009,** *48* (2), 104-111.
129. Wester, H. J.; Schottelius, M. In *Fluorine-18 Labeling of Peptides and Proteins*, Berlin, Heidelberg, Springer Berlin Heidelberg: Berlin, Heidelberg, 2007; pp 79-111.
130. Sanchez-Crespo, A., Comparison of Gallium-68 and Fluorine-18 imaging characteristics in positron emission tomography. *Applied Radiation and Isotopes* **2013,** *76*, 55-62.
131. Maecke, H. R.; André, J. P. In *68Ga-PET Radiopharmacy: A Generator-Based Alternative to 18F-Radiopharmacy*, Berlin, Heidelberg, Springer Berlin Heidelberg: Berlin, Heidelberg, 2007; pp 215-242.
132. Notni, J.; Wester, H.-J., Re-thinking the role of radiometal isotopes: Towards a future concept for theranostic radiopharmaceuticals. *Journal of Labelled Compounds and Radiopharmaceuticals* **2018,** *61* (3), 141-153.
133. Kuker, R.; Sztejnberg, M.; Gulec, S., I-124 Imaging and Dosimetry. *Mol Imaging Radionucl Ther* **2017,** *26* (Suppl 1), 66-73.
134. Müller, C.; Zhernosekov, K.; Köster, U.; Johnston, K.; Dorrer, H.; Hohn, A.; van der Walt, N. T.; Türler, A.; Schibli, R., A unique matched quadruplet of terbium radioisotopes for PET and SPECT and for α- and β- radionuclide therapy: an in vivo proof-of-concept study with a new receptor-targeted folate derivative. *J Nucl Med* **2012,** *53* (12), 1951-9.
135. Bé, M.-M., *Table of radionuclides*. Sèvres: BIPM: 2016.
136. Bé, M.-M., *Table of radionuclides*. Sèvres: BIPM: 2013.
137. Bé, M.-M., *Table of radionuclides*. Sèvres: BIPM: 2004.
138. Coenen, H. H. In *Fluorine-18 Labeling Methods: Features and Possibilities of Basic Reactions*, Berlin, Heidelberg, Springer Berlin Heidelberg: Berlin, Heidelberg, 2007; pp 15-50.
139. Guillaume, M.; Luxen, A.; Nebeling, B.; Argentini, M.; Clark, J. C.; Pike, V. W., Recommendations for fluorine-18 production. *International Journal of Radiation Applications and Instrumentation. Part A. Applied Radiation and Isotopes* **1991,** *42* (8), 749-762.
140. Cai, L.; Lu, S.; Pike, V. W., Chemistry with [18F]Fluoride Ion. *European Journal of Organic Chemistry* **2008,** *2008* (17), 2853-2873.

141. Jacobson, O.; Kiesewetter, D. O.; Chen, X., Fluorine-18 Radiochemistry, Labeling Strategies and Synthetic Routes. *Bioconjugate Chemistry* **2015,** *26* (1), 1-18.
142. McBride, W. J.; Sharkey, R. M.; Karacay, H.; D'Souza, C. A.; Rossi, E. A.; Laverman, P.; Chang, C.-H.; Boerman, O. C.; Goldenberg, D. M., A Novel Method of ¹⁸F Radiolabeling for PET. *Journal of Nuclear Medicine* **2009,** *50* (6), 991-998.
143. D'Souza, C. A.; McBride, W. J.; Sharkey, R. M.; Todaro, L. J.; Goldenberg, D. M., High-Yielding Aqueous 18F-Labeling of Peptides via Al18F Chelation. *Bioconjugate Chemistry* **2011,** *22* (9), 1793-1803.
144. Archibald, S. J.; Allott, L., The aluminium-[18F]fluoride revolution: simple radiochemistry with a big impact for radiolabelled biomolecules. *EJNMMI Radiopharmacy and Chemistry* **2021,** *6* (1), 30.
145. Ting, R.; Adam, M. J.; Ruth, T. J.; Perrin, D. M., Arylfluoroborates and Alkylfluorosilicates as Potential PET Imaging Agents: High-Yielding Aqueous Biomolecular 18F-Labeling. *Journal of the American Chemical Society* **2005,** *127* (38), 13094-13095.
146. Li, Y.; Liu, Z.; Harwig, C. W.; Pourghiasian, M.; Lau, J.; Lin, K.-S.; Schaffer, P.; Benard, F.; Perrin, D. M., (18)F-click labeling of a bombesin antagonist with an alkyne-(18)F-ArBF(3) (-): in vivo PET imaging of tumors expressing the GRP-receptor. *American journal of nuclear medicine and molecular imaging* **2013,** *3* (1), 57-70.
147. Li, Y.; Guo, J.; Tang, S.; Lang, L.; Chen, X.; Perrin, D. M., One-step and one-pot-two-step radiosynthesis of cyclo-RGD-(18)F-aryltrifluoroborate conjugates for functional imaging. *Am J Nucl Med Mol Imaging* **2013,** *3* (1), 44-56.
148. Ting, R.; Harwig, C.; auf dem Keller, U.; McCormick, S.; Austin, P.; Overall, C. M.; Adam, M. J.; Ruth, T. J.; Perrin, D. M., Toward [18F]-Labeled Aryltrifluoroborate Radiotracers: In Vivo Positron Emission Tomography Imaging of Stable Aryltrifluoroborate Clearance in Mice. *Journal of the American Chemical Society* **2008,** *130* (36), 12045-12055.
149. Bernard-Gauthier, V.; Bailey, J. J.; Liu, Z.; Wängler, B.; Wängler, C.; Jurkschat, K.; Perrin, D. M.; Schirrmacher, R., From Unorthodox to Established: The Current Status of 18F-Trifluoroborate- and 18F-SiFA-Based Radiopharmaceuticals in PET Nuclear Imaging. *Bioconjugate Chemistry* **2016,** *27* (2), 267-279.
150. Kumar, K.; Ghosh, A., 18F-AlF Labeled Peptide and Protein Conjugates as Positron Emission Tomography Imaging Pharmaceuticals. *Bioconjugate Chemistry* **2018,** *29* (4), 953-975.
151. Mu, L.; Höhne, A.; Schubiger, P. A.; Ametamey, S. M.; Graham, K.; Cyr, J. E.; Dinkelborg, L.; Stellfeld, T.; Srinivasan, A.; Voigtmann, U.; Klar, U., Silicon-Based Building Blocks for One-Step 18F-Radiolabeling of Peptides for PET Imaging. *Angewandte Chemie International Edition* **2008,** *47* (26), 4922-4925.
152. Al-huniti, M. H.; Lu, S.; Pike, V. W.; Lepore, S. D., Enhanced nucleophilic fluorination and radiofluorination of organosilanes appended with potassium-chelating leaving groups. *Journal of Fluorine Chemistry* **2014,** *158*, 48-52.
153. Schirrmacher, R.; Bradtmöller, G.; Schirrmacher, E.; Thews, O.; Tillmanns, J.; Siessmeier, T.; Buchholz, H. G.; Bartenstein, P.; Wängler, B.; Niemeyer, C. M.; Jurkschat, K., 18F-labeling of peptides by means of an organosilicon-based fluoride acceptor. *Angewandte Chemie - International Edition* **2006,** *45* (36), 6047-6050.
154. Wängler, C.; Niedermoser, S.; Chin, J.; Orchowski, K.; Schirrmacher, E.; Jurkschat, K.; Iovkova-Berends, L.; Kostikov, A. P.; Schirrmacher, R.; Wängler, B., One-step 18F-labeling of peptides for positron emission tomography imaging using the SiFA methodology. *Nature Protocols* **2012,** *7* (11), 1946-1955.
155. Liu, Z.; Pourghiasian, M.; Radtke, M. A.; Lau, J.; Pan, J.; Dias, G. M.; Yapp, D.; Lin, K.-S.; Bénard, F.; Perrin, D. M., An Organotrifluoroborate for Broadly Applicable One-Step 18F-Labeling. *Angewandte Chemie International Edition* **2014,** *53* (44), 11876-11880.
156. Luo, Y.-R., *Comprehensive Handbook of Chemical Bond Energies*. CRC Press: 2007.
157. Allred, A. L.; Rochow, E. G., A scale of electronegativity based on electrostatic force. *Journal of Inorganic and Nuclear Chemistry* **1958,** *5* (4), 264-268.

158. Rosenthal, M. S.; Bosch, A. L.; Nickles, R. J.; Gatley, S. J., Synthesis and some characteristics of no-carrier added [18F]fluorotrimethylsilane. *The International Journal of Applied Radiation and Isotopes* **1985,** *36* (4), 318-319.
159. Bernard-Gauthier, V.; Wängler, C.; Schirrmacher, E.; Kostikov, A.; Jurkschat, K.; Wängler, B.; Schirrmacher, R., 18F-Labeled Silicon-Based Fluoride Acceptors: Potential Opportunities for Novel Positron Emitting Radiopharmaceuticals. *BioMed Research International* **2014,** *2014*, 20-20.
160. Huheey, J. E.; Keiter, E. A.; Keiter, R. L., *Anorganische Chemie: Prinzipien von Struktur und Reaktivität*. De Gruyter: 2012.
161. Gens, T. A.; Wethongton, J. A.; Brosi, A. R., The Exchange of F18between Metallic Fluorides and Silicon Tetrafluoride. *The Journal of Physical Chemistry* **1958,** *62* (12), 1593-1593.
162. Poole, R. T.; Winfield, J. M., Radiotracers in fluorine chemistry. Part IV. Fluorine-18 exchange between labelled alkylfluorosilanesand fluorides, or fluoride methoxides, of tungsten(VI), molybdenum(VI), tellurium(VI), and iodine(V). *Journal of the Chemical Society, Dalton Transactions* **1976,** (16), 1557-1560.
163. Winfield, J. M., Preparation and use of 18-fluorine labelled inorganic compounds. *Journal of Fluorine Chemistry* **1980,** *16* (1), 1-17.
164. Cacace, F.; Speranza, M.; Wolf, A. P.; Fowler, J. S., Labelling of fluorinated aromatics by isotopic exchange with [18F]fluoride. *Journal of Labelled Compounds and Radiopharmaceuticals* **1981,** *18* (12), 1721-1730.
165. Farrokhzad, S.; Diksic, M., The syntheses of no-carrier-added and carrier-added 18F-labelled haloperidol. *Journal of Labelled Compounds and Radiopharmaceuticals* **1985,** *22* (7), 721-733.
166. Kilbourn, M. R.; Welch, M. J.; Dence, C. S.; Tewson, T. J.; Saji, H.; Maeda, M., Carrier-added and no-carrier-added syntheses of [18F]spiroperidol and [18F]haloperidol. *The International Journal of Applied Radiation and Isotopes* **1984,** *35* (7), 591-598.
167. Schirrmacher, R.; Bernard-Gauthier, V.; Schirrmacher, E.; Bailey, J. J.; Jurkschat, K.; Wängler, C.; Wängler, B., 15 - Silicon-based 18F-radiopharmaceuticals: from basic SiFA chemistry toward its clinical application. In *Fluorine in Life Sciences: Pharmaceuticals, Medicinal Diagnostics, and Agrochemicals*, Haufe, G.; Leroux, F. R., Eds. Academic Press: 2019; pp 551-574.
168. Choudhry, U.; Martin, K. E.; Biagini, S.; Blower, P. J., A49 Alkoxysilane groups for instant labelling of biomolecules with 18F. *Nuclear Medicine Communications* **2006,** *27* (3).
169. Höhne, A.; Yu, L.; Mu, L.; Reiher, M.; Voigtmann, U.; Klar, U.; Graham, K.; Schubiger, P. A.; Ametamey, S. M., Organofluorosilanes as Model Compounds for 18F-Labeled Silicon-Based PET Tracers and their Hydrolytic Stability: Experimental Data and Theoretical Calculations (PET=Positron Emission Tomography). *Chemistry – A European Journal* **2009,** *15* (15), 3736-3743.
170. Schirrmacher, E.; Wängler, B.; Cypryk, M.; Bradtmöller, G.; Schäfer, M.; Eisenhut, M.; Jurkschat, K.; Schirrmacher, R., Synthesis of p-(Di-tert-butyl[18F]fluorosilyl)benzaldehyde ([18F]SiFA-A) with High Specific Activity by Isotopic Exchange: A Convenient Labeling Synthon for the 18F-Labeling of N-amino-oxy Derivatized Peptides. *Bioconjugate Chemistry* **2007,** *18* (6), 2085-2089.
171. Brefort, J. L.; Corriu, R. J. P.; Guerin, C.; Henner, B. J. L.; Wong Chi Man, W. W. C., Pentacoordinated silicon anions: synthesis and reactivity. *Organometallics* **1990,** *9* (7), 2080-2085.
172. Corriu, R. J. P., Hypervalent species of silicon: structure and reactivity. *Journal of Organometallic Chemistry* **1990,** *400* (1), 81-106.
173. Kostikov, A. P.; Iovkova, L.; Chin, J.; Schirrmacher, E.; Wängler, B.; Wängler, C.; Jurkschat, K.; Cosa, G.; Schirrmacher, R., N-(4-(di-tert-butyl[18F]fluorosilyl)benzyl)-2-hydroxy-N,N-dimethylethylammonium bromide ([18F]SiFAN+Br−): A novel lead compound for the development of hydrophilic SiFA-based prosthetic groups for 18F-labeling. *Journal of Fluorine Chemistry* **2011,** *132* (1), 27-34.

174. Block, D.; Coenen, H. H.; Stöcklin, G., The N.C.A. nucleophilic 18F-fluorination of 1,N-disubstituted alkanes as fluoroalkylation agents. *Journal of Labelled Compounds and Radiopharmaceuticals* **1987,** *24* (9), 1029-1042.
175. Atkins, P. W. D. P. J., *Physical chemistry for the life sciences*. W.H. Freeman and Co. ; Oxford University Press: New York; Oxford, 2011.
176. Iovkova, L.; Wängler, B.; Schirrmacher, E.; Schirrmacher, R.; Quandt, G.; Boening, G.; Schürmann, M.; Jurkschat, K., para-Functionalized Aryl-di-tert-butylfluorosilanes as Potential Labeling Synthons for 18F Radiopharmaceuticals. *Chemistry – A European Journal* **2009,** *15* (9), 2140-2147.
177. Iovkova, L.; Könning, D.; Wängler, B.; Schirrmacher, R.; Schoof, S.; Arndt, H. D.; Jurkschat, K., SiFA-Modified Phenylalanine: A Key Compound for the Efficient Synthesis of 18F-Labelled Peptides. *European Journal of Inorganic Chemistry* **2011,** *2011* (14), 2238-2246.
178. Niedermoser, S.; Chin, J.; Wangler, C.; Kostikov, A.; Bernard-Gauthier, V.; Vogler, N.; Soucy, J. P.; McEwan, A. J.; Schirrmacher, R.; Wangler, B., In Vivo Evaluation of 18F-SiFAlin-Modified TATE: A Potential Challenge for 68Ga-DOTATATE, the Clinical Gold Standard for Somatostatin Receptor Imaging with PET. *Journal of Nuclear Medicine* **2015,** *56* (7), 1100-1105.
179. Wängler, B.; Quandt, G.; Iovkova, L.; Schirrmacher, E.; Wängler, C.; Boening, G.; Hacker, M.; Schmoeckel, M.; Jurkschat, K.; Bartenstein, P.; Schirrmacher, R., Kit-Like 18F-Labeling of Proteins: Synthesis of 4-(Di-tert-butyl[18F]fluorosilyl)benzenethiol (Si[18F]FA-SH) Labeled Rat Serum Albumin for Blood Pool Imaging with PET. *Bioconjugate Chemistry* **2009,** *20* (2), 317-321.
180. Wängler, B.; Kostikov, A. P.; Niedermoser, S.; Chin, J.; Orchowski, K.; Schirrmacher, E.; Iovkova-Berends, L.; Jurkschat, K.; Wängler, C.; Schirrmacher, R., Protein labeling with the labeling precursor [18F]SiFA-SH for positron emission tomography. *Nature Protocols* **2012,** *7* (11), 1964-1969.
181. Kostikov, A. P.; Chin, J.; Orchowski, K.; Schirrmacher, E.; Niedermoser, S.; Jurkschat, K.; Iovkova-Berends, L.; Wängler, C.; Wängler, B.; Schirrmacher, R., Synthesis of [18F]SiFB: a prosthetic group for direct protein radiolabeling for application in positron emission tomography. *Nature Protocols* **2012,** *7* (11), 1956-1963.
182. Rosa-Neto, P.; Wängler, B.; Iovkova, L.; Boening, G.; Reader, A.; Jurkschat, K.; Schirrmacher, E., [18F]SiFA-isothiocyanate: A New Highly Effective Radioactive Labeling Agent for Lysine-Containing Proteins. *ChemBioChem* **2009,** *10* (8), 1321-1324.
183. Wängler, C.; Kostikov, A.; Zhu, J.; Chin, J.; Wängler, B.; Schirrmacher, R., Silicon-[18F]Fluorine Radiochemistry: Basics, Applications and Challenges. *Applied Sciences* **2012,** *2* (2), 277-302.
184. Gower-Fry, L.; Kronemann, T.; Dorian, A.; Pu, Y.; Jaworski, C.; Wängler, C.; Bartenstein, P.; Beyer, L.; Lindner, S.; Jurkschat, K.; Wängler, B.; Bailey, J. J.; Schirrmacher, R., Recent Advances in the Clinical Translation of Silicon Fluoride Acceptor (SiFA) 18F-Radiopharmaceuticals. *Pharmaceuticals* **2021,** *14* (7), 701.
185. Litau, S.; Niedermoser, S.; Vogler, N.; Roscher, M.; Schirrmacher, R.; Fricker, G.; Wängler, B.; Wängler, C., Next Generation of SiFAlin-Based TATE Derivatives for PET Imaging of SSTR-Positive Tumors: Influence of Molecular Design on in Vitro SSTR Binding and in Vivo Pharmacokinetics. *Bioconjugate Chemistry* **2015,** *26* (12), 2350-2359.
186. Wängler, C.; Waser, B.; Alke, A.; Iovkova, L.; Buchholz, H.-G.; Niedermoser, S.; Jurkschat, K.; Fottner, C.; Bartenstein, P.; Schirrmacher, R.; Reubi, J.-C.; Wester, H.-J.; Wängler, B., One-step ^{18}F-labeling of carbohydrate-conjugated octreotate-derivatives containing a silicon-fluoride-acceptor (SiFA): in vitro and in vivo evaluation as tumor imaging agents for positron emission tomography (PET). *Bioconjugate chemistry* **2010,** *21*, 2289-2296.
187. Kostikov, A. P.; Iovkova, L.; Chin, J.; Schirrmacher, E.; Wängler, B.; Wängler, C.; Jurkschat, K.; Cosa, G.; Schirrmacher, R., N-(4-(di-tert-butyl[18F]fluorosilyl)benzyl)-2-hydroxy-N,N-dimethylethylammonium bromide ([18F]SiFAN+Br-): A novel lead compound for the development of hydrophilic SiFA-based prosthetic groups for18F-labeling. *Journal of Fluorine Chemistry* **2011,** *132* (1), 27-34.

188. Ilhan, H.; Lindner, S.; Todica, A.; Cyran, C. C.; Tiling, R.; Auernhammer, C. J.; Spitzweg, C.; Boeck, S.; Unterrainer, M.; Gildehaus, F. J.; Böning, G.; Jurkschat, K.; Wängler, C.; Wängler, B.; Schirrmacher, R.; Bartenstein, P., Biodistribution and first clinical results of 18F-SiFAlin-TATE PET: a novel 18F-labeled somatostatin analog for imaging of neuroendocrine tumors. *European Journal of Nuclear Medicine and Molecular Imaging* **2020,** *47* (4), 870-880.
189. Lindner, S.; Michler, C.; Leidner, S.; Rensch, C.; Wängler, C.; Schirrmacher, R.; Bartenstein, P.; Wängler, B., Synthesis and in Vitro and in Vivo Evaluation of SiFA-Tagged Bombesin and RGD Peptides as Tumor Imaging Probes for Positron Emission Tomography. *Bioconjugate Chemistry* **2014,** *25* (4), 738-749.
190. Dialer, L. O.; Selivanova, S. V.; Müller, C. J.; Müller, A.; Stellfeld, T.; Graham, K.; Dinkelborg, L. M.; Krämer, S. D.; Schibli, R.; Reiher, M.; Ametamey, S. M., Studies toward the Development of New Silicon-Containing Building Blocks for the Direct 18F-Labeling of Peptides. *Journal of Medicinal Chemistry* **2013,** *56* (19), 7552-7563.
191. Lindner, S.; Simmet, M.; Gildehaus, F. J.; Jurkschat, K.; Wängler, C.; Wängler, B.; Bartenstein, P.; Schirrmacher, R.; Ilhan, H., Automated production of [18F]SiTATE on a Scintomics GRP™ platform for PET/CT imaging of neuroendocrine tumors. *Nuclear Medicine and Biology* **2020,** *88-89*, 86-95.
192. Höhne, A.; Mu, L.; Honer, M.; Schubiger, P. A.; Ametamey, S. M.; Graham, K.; Stellfeld, T.; Borkowski, S.; Berndorff, D.; Klar, U.; Voigtmann, U.; Cyr, J. E.; Friebe, M.; Dinkelborg, L.; Srinivasan, A., Synthesis, 18F-Labeling, and in Vitro and in Vivo Studies of Bombesin Peptides Modified with Silicon-Based Building Blocks. *Bioconjugate Chemistry* **2008,** *19* (9), 1871-1879.
193. Hazari, P. P.; Schulz, J.; Vimont, D.; Chadha, N.; Allard, M.; Szlosek-Pinaud, M.; Fouquet, E.; Mishra, A. K., A New SiF–Dipropargyl Glycerol Scaffold as a Versatile Prosthetic Group to Design Dimeric Radioligands: Synthesis of the [18F]BMPPSiF Tracer to Image Serotonin Receptors. *ChemMedChem* **2014,** *9* (2), 337-349.
194. Iovkova-Berends, L.; Wängler, C.; Zöller, T.; Höfner, G.; Wanner, K. T.; Rensch, C.; Bartenstein, P.; Kostikov, A.; Schirrmacher, R.; Jurkschat, K.; Wängler, B., t-Bu2SiF-Derivatized D2-Receptor Ligands: The First SiFA-Containing Small Molecule Radiotracers for Target-Specific PET-Imaging. *Molecules* **2011,** *16* (9), 7458-7479.
195. Oh, S. W.; Wurzer, A.; Teoh, E. J.; Oh, S.; Langbein, T.; Krönke, M.; Herz, M.; Kropf, S.; Wester, H.-J.; Weber, W. A.; Eiber, M., Quantitative and Qualitative Analyses of Biodistribution and PET Image Quality of a Novel Radiohybrid PSMA, ¹⁸F-rhPSMA-7, in Patients with Prostate Cancer. *Journal of Nuclear Medicine* **2020,** *61* (5), 702-709.
196. Eiber, M.; Kroenke, M.; Wurzer, A.; Ulbrich, L.; Jooß, L.; Maurer, T.; Horn, T.; Schiller, K.; Langbein, T.; Buschner, G.; Wester, H.-J.; Weber, W., ¹⁸F-rhPSMA-7 PET for the Detection of Biochemical Recurrence of Prostate Cancer After Radical Prostatectomy. *Journal of Nuclear Medicine* **2020,** *61* (5), 696-701.
197. Kroenke, M.; Wurzer, A.; Schwamborn, K.; Ulbrich, L.; Jooß, L.; Maurer, T.; Horn, T.; Rauscher, I.; Haller, B.; Herz, M.; Wester, H.-J.; Weber, W. A.; Eiber, M., Histologically Confirmed Diagnostic Efficacy of ¹⁸F-rhPSMA-7 PET for N-Staging of Patients with Primary High-Risk Prostate Cancer. *Journal of Nuclear Medicine* **2020,** *61* (5), 710-715.
198. Wurzer, A.; Di Carlo, D.; Herz, M.; Richter, A.; Robu, S.; Schirrmacher, R.; Mascarin, A.; Weber, W.; Eiber, M.; Schwaiger, M.; Wester, H.-J., Automated synthesis of [18F]Ga-rhPSMA-7/ -7.3: results, quality control and experience from more than 200 routine productions. *EJNMMI Radiopharmacy and Chemistry* **2021,** *6* (1), 4.
199. Wurzer, A.; DiCarlo, D.; Schmidt, A.; Beck, R.; Eiber, M.; Schwaiger, M.; Wester, H. J., Radiohybrid ligands: a novel tracer concept exemplified by (18)F- or (68)Ga-labeled rhPSMA-inhibitors. *J Nucl Med* **2019**.
200. Wurzer, A.; Di Carlo, D.; Schmidt, A.; Beck, R.; Eiber, M.; Schwaiger, M.; Wester, H. J., Radiohybrid Ligands: A Novel Tracer Concept Exemplified by (18)F- or (68)Ga-Labeled rhPSMA Inhibitors. *J Nucl Med* **2020,** *61* (5), 735-742.

201. Wadas, T. J.; Wong, E. H.; Weisman, G. R.; Anderson, C. J., Coordinating radiometals of copper, gallium, indium, yttrium, and zirconium for PET and SPECT imaging of disease. *Chem Rev* **2010,** *110* (5), 2858-902.
202. Umbricht, C. A.; Benešová, M.; Schmid, R. M.; Türler, A.; Schibli, R.; van der Meulen, N. P.; Müller, C., (44)Sc-PSMA-617 for radiotheragnostics in tandem with (177)Lu-PSMA-617-preclinical investigations in comparison with (68)Ga-PSMA-11 and (68)Ga-PSMA-617. *EJNMMI Res* **2017,** *7* (1), 9.
203. Roxin, Á.; Zhang, C.; Huh, S.; Lepage, M.; Zhang, Z.; Lin, K.-S.; Bénard, F.; Perrin, D. M., A Metal-Free DOTA-Conjugated 18F-Labeled Radiotracer: [18F]DOTA-AMBF3-LLP2A for Imaging VLA-4 Over-Expression in Murine Melanoma with Improved Tumor Uptake and Greatly Enhanced Renal Clearance. *Bioconjugate Chemistry* **2019,** *30* (4), 1210-1219.
204. Roxin, Á.; Zhang, C.; Huh, S.; Lepage, M. L.; Zhang, Z.; Lin, K. S.; Bénard, F.; Perrin, D. M., Preliminary evaluation of (18)F-labeled LLP2A-trifluoroborate conjugates as VLA-4 (α(4)β(1) integrin) specific radiotracers for PET imaging of melanoma. *Nucl Med Biol* **2018,** *61*, 11-20.
205. Lepage, M. L.; Kuo, H.-T.; Roxin, Á.; Huh, S.; Zhang, Z.; Kandasamy, R.; Merkens, H.; Kumlin, J. O.; Limoges, A.; Zeisler, S. K.; Lin, K.-S.; Bénard, F.; Perrin, D. M., Toward 18F-Labeled Theranostics: A Single Agent that Can Be Labeled with 18F, 64Cu, or 177Lu. *ChemBioChem* **2020,** *21* (7), 943-947.
206. Benešová, M.; Schäfer, M.; Bauder-Wüst, U.; Afshar-Oromieh, A.; Kratochwil, C.; Mier, W.; Haberkorn, U.; Kopka, K.; Eder, M., Preclinical Evaluation of a Tailor-Made DOTA-Conjugated PSMA Inhibitor with Optimized Linker Moiety for Imaging and Endoradiotherapy of Prostate Cancer. *Journal of Nuclear Medicine* **2015,** *56* (6), 914-920.
207. Banerjee, S. R.; Pullambhatla, M.; Foss, C. A.; Nimmagadda, S.; Ferdani, R.; Anderson, C. J.; Mease, R. C.; Pomper, M. G., ^{64}Cu-labeled inhibitors of prostate-specific membrane antigen for PET imaging of prostate cancer. *Journal of medicinal chemistry* **2014,** *57* (6), 2657-2669.
208. Han, X.-D.; Liu, C.; Liu, F.; Xie, Q.-H.; Liu, T.-L.; Guo, X.-Y.; Xu, X.-X.; Yang, X.; Zhu, H.; Yang, Z., 64 Cu-PSMA-617: A novel PSMA-targeted radio-tracer for PET imaging in gastric adenocarcinoma xenografted mice model. *Oncotarget* **2017,** *8* (43).
209. Cui, C.; Hanyu, M.; Hatori, A.; Zhang, Y.; Xie, L.; Ohya, T.; Fukada, M.; Suzuki, H.; Nagatsu, K.; Jiang, C.; Luo, R.; Shao, G.; Zhang, M.; Wang, F., Synthesis and evaluation of [(64)Cu]PSMA-617 targeted for prostate-specific membrane antigen in prostate cancer. *American journal of nuclear medicine and molecular imaging* **2017,** *7* (2), 40-52.
210. Grubmüller, B.; Baum, R. P.; Capasso, E.; Singh, A.; Ahmadi, Y.; Knoll, P.; Floth, A.; Righi, S.; Zandieh, S.; Meleddu, C.; Shariat, S. F.; Klingler, H. C.; Mirzaei, S., (64)Cu-PSMA-617 PET/CT Imaging of Prostate Adenocarcinoma: First In-Human Studies. *Cancer Biother Radiopharm* **2016,** *31* (8), 277-286.
211. Chen, Y.; Pullambhatla, M.; Foss, C. A.; Byun, Y.; Nimmagadda, S.; Senthamizhchelvan, S.; Sgouros, G.; Mease, R. C.; Pomper, M. G., 2-(3-{1-Carboxy-5-[(6-[18F]Fluoro-Pyridine-3-Carbonyl)-Amino]-Pentyl}-Ureido)-Pentanedioic Acid, [18F]DCFPyL, a PSMA-Based PET Imaging Agent for Prostate Cancer. *Clinical Cancer Research* **2011,** *17* (24), 7645-7653.
212. Harada, N.; Kimura, H.; Onoe, S.; Watanabe, H.; Matsuoka, D.; Arimitsu, K.; Ono, M.; Saji, H., Synthesis and Biologic Evaluation of Novel ¹⁸F-Labeled Probes Targeting Prostate-Specific Membrane Antigen for PET of Prostate Cancer. *Journal of Nuclear Medicine* **2016,** *57* (12), 1978-1984.
213. Garrison, J. C.; Rold, T. L.; Sieckman, G. L.; Figueroa, S. D.; Volkert, W. A.; Jurisson, S. S.; Hoffman, T. J., In Vivo Evaluation and Small-Animal PET/CT of a Prostate Cancer Mouse Model Using ⁶⁴Cu Bombesin Analogs: Side-by-Side Comparison of the CB-TE2A and DOTA Chelation Systems. *Journal of Nuclear Medicine* **2007,** *48* (8), 1327-1337.
214. Bass, L. A.; Wang, M.; Welch, M. J.; Anderson, C. J., In Vivo Transchelation of Copper-64 from TETA-Octreotide to Superoxide Dismutase in Rat Liver. *Bioconjugate Chemistry* **2000,** *11* (4), 527-532.

215. Boswell, C. A.; Sun, X.; Niu, W.; Weisman, G. R.; Wong, E. H.; Rheingold, A. L.; Anderson, C. J., Comparative in Vivo Stability of Copper-64-Labeled Cross-Bridged and Conventional Tetraazamacrocyclic Complexes. *Journal of Medicinal Chemistry* **2004,** *47* (6), 1465-1474.
216. Abiraj, K.; Mansi, R.; Tamma, M. L.; Forrer, F.; Cescato, R.; Reubi, J. C.; Akyel, K. G.; Maecke, H. R., Tetraamine-derived bifunctional chelators for technetium-99m labelling: synthesis, bioconjugation and evaluation as targeted SPECT imaging probes for GRP-receptor-positive tumours. *Chemistry* **2010,** *16* (7), 2115-24.
217. Wurzer, A.; Di Carlo, D.; Schmidt, A.; Beck, R.; Schwaiger, M.; Herz, M.; Eiber, M.; Wester, H., PSMA-targeted 18F-labeled Radiohybrid Inhibitors: Labeling chemistry and automated GMP production of 18F-rhPSMA-7. *Journal of Nuclear Medicine* **2019,** *60* (supplement 1), 342.
218. Weineisen, M.; Schottelius, M.; Simecek, J.; Baum, R. P.; Yildiz, A.; Beykan, S.; Kulkarni, H. R.; Lassmann, M.; Klette, I.; Eiber, M.; Schwaiger, M.; Wester, H. J., 68Ga- and 177Lu-Labeled PSMA I&T: Optimization of a PSMA-Targeted Theranostic Concept and First Proof-of-Concept Human Studies. *J Nucl Med* **2015,** *56* (8), 1169-76.
219. Sosabowski, J. K.; Mather, S. J., Conjugation of DOTA-like chelating agents to peptides and radiolabeling with trivalent metallic isotopes. *Nat Protoc* **2006,** *1* (2), 972-6.
220. Nock, B. A.; Charalambidis, D.; Sallegger, W.; Waser, B.; Mansi, R.; Nicolas, G. P.; Ketani, E.; Nikolopoulou, A.; Fani, M.; Reubi, J. C.; Maina, T., New Gastrin Releasing Peptide Receptor-Directed [(99m)Tc]Demobesin 1 Mimics: Synthesis and Comparative Evaluation. *J Med Chem* **2018,** *61* (7), 3138-3150.
221. Valko, K.; Nunhuck, S.; Bevan, C.; Abraham, M. H.; Reynolds, D. P., Fast gradient HPLC method to determine compounds binding to human serum albumin. Relationships with octanol/water and immobilized artificial membrane lipophilicity. *J Pharm Sci* **2003,** *92* (11), 2236-48.
222. Yamazaki, K.; Kanaoka, M., Computational prediction of the plasma protein-binding percent of diverse pharmaceutical compounds. *J Pharm Sci* **2004,** *93* (6), 1480-94.
223. Miksch, J.; Prasad, V.; Di Carlo, D.; Strauss, A.-S.; Grunert, M.; Steinacker, J.; Thaiss, W.; Solbach, C.; Bolenz, C.; Beer, M.; Wiegel, T.; Wester, H.; Eiber, M.; Beer, A., Novel [F-18]siPSMA-14 shows favourable kinetics and high interobserver agreement in staging of prostate cancer patients. *Journal of Nuclear Medicine* **2021,** *62* (supplement 1), 1328-1328.
224. Löffler, J.; Hamp, C.; Scheidhauer, E.; Di Carlo, D.; Solbach, C.; Abaei, A.; Hao, L.; Glatting, G.; Beer, A. J.; Rasche, V.; Winter, G., Comparison of Quantification of Target-Specific Accumulation of [(18)F]F-siPSMA-14 in the HET-CAM Model and in Mice Using PET/MRI. *Cancers (Basel)* **2021,** *13* (16).
225. Ghuman, J.; Zunszain, P. A.; Petitpas, I.; Bhattacharya, A. A.; Otagiri, M.; Curry, S., Structural basis of the drug-binding specificity of human serum albumin. *J Mol Biol* **2005,** *353* (1), 38-52.
226. Dumelin, C. E.; Trussel, S.; Buller, F.; Trachsel, E.; Bootz, F.; Zhang, Y.; Mannocci, L.; Beck, S. C.; Drumea-Mirancea, M.; Seeliger, M. W.; Baltes, C.; Muggler, T.; Kranz, F.; Rudin, M.; Melkko, S.; Scheuermann, J.; Neri, D., A portable albumin binder from a DNA-encoded chemical library. *Angew Chem Int Ed Engl* **2008,** *47* (17), 3196-201.
227. Deberle, L. M.; Benešová, M.; Umbricht, C. A.; Borgna, F.; Büchler, M.; Zhernosekov, K.; Schibli, R.; Müller, C., Development of a new class of PSMA radioligands comprising ibuprofen as an albumin-binding entity. *Theranostics* **2020,** *10* (4), 1678-1693.
228. Martínez-Gómez, M. A.; Sagrado, S.; Villanueva-Camañas, R. M.; Medina-Hernández, M. J., Characterization of basic drug-human serum protein interactions by capillary electrophoresis. *Electrophoresis* **2006,** *27* (17), 3410-3419.
229. Ballal, S.; Yadav, M. P.; Moon, E. S.; Kramer, V. S.; Roesch, F.; Kumari, S.; Tripathi, M.; ArunRaj, S. T.; Sarswat, S.; Bal, C., Biodistribution, pharmacokinetics, dosimetry of [(68)Ga]Ga-DOTA.SA.FAPi, and the head-to-head comparison with [(18)F]F-FDG PET/CT in patients with various cancers. *Eur J Nucl Med Mol Imaging* **2020**.
230. Busek, P.; Hrabal, P.; Fric, P.; Sedo, A., Co-expression of the homologous proteases fibroblast activation protein and dipeptidyl peptidase-IV in the adult human Langerhans islets. *Histochem Cell Biol* **2015,** *143* (5), 497-504.

231. Zorzi, A.; Linciano, S.; Angelini, A., Non-covalent albumin-binding ligands for extending the circulating half-life of small biotherapeutics. *Medchemcomm* **2019,** *10* (7), 1068-1081.
232. Gotthardt, M.; van Eerd-Vismale, J.; Oyen, W. J.; de Jong, M.; Zhang, H.; Rolleman, E.; Maecke, H. R.; Béhé, M.; Boerman, O., Indication for different mechanisms of kidney uptake of radiolabeled peptides. *J Nucl Med* **2007,** *48* (4), 596-601.
233. Akizawa, H.; Arano, Y.; Mifune, M.; Iwado, A.; Saito, Y.; Mukai, T.; Uehara, T.; Ono, M.; Fujioka, Y.; Ogawa, K.; Kiso, Y.; Saji, H., Effect of molecular charges on renal uptake of 111In-DTPA-conjugated peptides. *Nucl Med Biol* **2001,** *28* (7), 761-8.
234. Kratochwil, C.; Flechsig, P.; Lindner, T.; Abderrahim, L.; Altmann, A.; Mier, W.; Adeberg, S.; Rathke, H.; Röhrich, M.; Winter, H.; Plinkert, P. K.; Marme, F.; Lang, M.; Kauczor, H.-U.; Jäger, D.; Debus, J.; Haberkorn, U.; Giesel, F. L., 68Ga-FAPI PET/CT: Tracer Uptake in 28 Different Kinds of Cancer. *Journal of nuclear medicine : official publication, Society of Nuclear Medicine* **2019,** *60* (6), 801-805.
235. Scheinberg, D. A.; McDevitt, M. R., Actinium-225 in targeted alpha-particle therapeutic applications. *Curr Radiopharm* **2011,** *4* (4), 306-20.
236. Radchenko, V.; Schaffer, P.; Knapp, F. F., The Evolving Clinical Role of Actinium-225 and Bismuth-213 for Targeted Alpha Therapy (TAT) - Production, Radiopharmaceutical Development and Clinical Applications. *Current Radiopharmaceuticals* **2018,** *11* (3), 154-155.
237. Robertson, A. K. H.; Ramogida, C. F.; Schaffer, P.; Radchenko, V., Development of (225)Ac Radiopharmaceuticals: TRIUMF Perspectives and Experiences. *Current radiopharmaceuticals* **2018,** *11* (3), 156-172.
238. Shirvani, S. M.; Huntzinger, C. J.; Melcher, T.; Olcott, P. D.; Voronenko, Y.; Bartlett-Roberto, J.; Mazin, S., Biology-guided radiotherapy: redefining the role of radiotherapy in metastatic cancer. *Br J Radiol* **2021,** *94* (1117), 20200873.
239. Oderinde, O. M.; Shirvani, S. M.; Olcott, P. D.; Kuduvalli, G.; Mazin, S.; Larkin, D., The technical design and concept of a PET/CT linac for biology-guided radiotherapy. *Clin Transl Radiat Oncol* **2021,** *29*, 106-112.
240. Hwang, M. S.; Lalonde, R.; Huq, M. S., A detailed process map for clinical workflow of a new biology-guided radiotherapy (BgRT) machine. *J Appl Clin Med Phys* **2022,** *23* (6), e13606.
241. Gaudreault, M.; Chang, D.; Hardcastle, N.; Jackson, P.; Kron, T.; Hofman, M. S.; Siva, S., Feasibility of biology-guided radiotherapy using PSMA-PET to boost to dominant intraprostatic tumour. *Clin Transl Radiat Oncol* **2022,** *35*, 84-89.
242. Wild, D.; Fani, M.; Fischer, R.; Del Pozzo, L.; Kaul, F.; Krebs, S.; Rivier, J. E. F.; Reubi, J. C.; Maecke, H. R.; Weber, W. a., Comparison of Somatostatin Receptor Agonist and Antagonist for Peptide Receptor Radionuclide Therapy: A Pilot Study. *Journal of nuclear medicine : official publication, Society of Nuclear Medicine* **2014,** *55* (8), 1248-1252.
243. Fani, M.; Nicolas, G. P.; Wild, D., Somatostatin Receptor Antagonists for Imaging and Therapy. *Journal of Nuclear Medicine* **2017,** *58* (Supplement 2), 61S-66S.
244. Esser, J. P.; Krenning, E. P.; Teunissen, J. J. M.; Kooij, P. P. M.; van Gameren, A. L. H.; Bakker, W. H.; Kwekkeboom, D. J., Comparison of [177Lu-DOTA0,Tyr3]octreotate and [177Lu-DOTA0,Tyr3]octreotide: which peptide is preferable for PRRT? *European Journal of Nuclear Medicine and Molecular Imaging* **2006,** *33* (11), 1346-1351.
245. Dude, I.; Zhang, Z.; Rousseau, J.; Hundal-Jabal, N.; Colpo, N.; Merkens, H.; Lin, K.-S.; Bénard, F., Evaluation of agonist and antagonist radioligands for somatostatin receptor imaging of breast cancer using positron emission tomography. *EJNMMI Radiopharmacy and Chemistry* **2017,** *2* (1), 4-4.
246. Bodei, L.; Cremonesi, M.; Grana, C. M.; Fazio, N.; Iodice, S.; Baio, S. M.; Bartolomei, M.; Lombardo, D.; Ferrari, M. E.; Sansovini, M.; Chinol, M.; Paganelli, G., Peptide receptor radionuclide therapy with (1)(7)(7)Lu-DOTATATE: the IEO phase I-II study. *Eur J Nucl Med Mol Imaging* **2011,** *38* (12), 2125-2135.

247. Osl, T.; Schmidt, A.; Schwaiger, M.; Schottelius, M.; Wester, H.-J., A new class of PentixaFor- and PentixaTher-based theranostic agents with enhanced CXCR4-targeting efficiency. *Theranostics* **2020,** *10* (18), 8264-8280.
248. Opalinska, M.; Hubalewska-Dydejczyk, A.; Sowa-Staszczak, A., Radiolabeled peptides: current and new perspectives. *Q J Nucl Med Mol Imaging* **2017,** *61* (2), 153-167.
249. Lapa, C.; Kircher, S.; Schirbel, A.; Rosenwald, A.; Kropf, S.; Pelzer, T.; Walles, T.; Buck, A. K.; Weber, W. A.; Wester, H. J.; Herrmann, K.; Lückerath, K., Targeting CXCR4 with [(68)Ga]Pentixafor: a suitable theranostic approach in pleural mesothelioma? *Oncotarget* **2017,** *8* (57), 96732-96737.
250. Kircher, M.; Herhaus, P.; Schottelius, M.; Buck, A. K.; Werner, R. A.; Wester, H. J.; Keller, U.; Lapa, C., CXCR4-directed theranostics in oncology and inflammation. *Ann Nucl Med* **2018,** *32* (8), 503-511.
251. Müller, C.; Farkas, R.; Borgna, F.; Schmid, R. M.; Benešová, M.; Schibli, R., Synthesis, Radiolabeling, and Characterization of Plasma Protein-Binding Ligands: Potential Tools for Modulation of the Pharmacokinetic Properties of (Radio)Pharmaceuticals. *Bioconjugate Chemistry* **2017,** *28* (9), 2372-2383.
252. Callahan, R. J.; Froelich, J. W.; McKusick, K. A.; Leppo, J.; Strauss, H. W., A modified method for the in vivo labeling of red blood cells with Tc-99m: concise communication. *Journal of nuclear medicine : official publication, Society of Nuclear Medicine* **1982,** *23* (4), 315-318.
253. Zuckier, L. S.; Dohan, O.; Li, Y.; Chang, C. J.; Carrasco, N.; Dadachova, E., Kinetics of Perrhenate Uptake and Comparative Biodistribution of Perrhenate, Pertechnetate, and Iodide by NaI Symporter–Expressing Tissues In Vivo. *Journal of Nuclear Medicine* **2004,** *45* (3), 500-507.
254. Papagiannopoulou, D., Technetium-99m radiochemistry for pharmaceutical applications. *Journal of Labelled Compounds and Radiopharmaceuticals* **2017,** *60* (11), 502-520.
255. Loktev, A.; Lindner, T.; Mier, W.; Debus, J.; Altmann, A.; Jäger, D.; Giesel, F.; Kratochwil, C.; Barthe, P.; Roumestand, C.; Haberkorn, U., A Tumor-Imaging Method Targeting Cancer-Associated Fibroblasts. *J Nucl Med* **2018,** *59* (9), 1423-1429.
256. De Decker, A.; Vliegen, G.; Van Rompaey, D.; Peeraer, A.; Bracke, A.; Verckist, L.; Jansen, K.; Geiss-Friedlander, R.; Augustyns, K.; De Winter, H.; De Meester, I.; Lambeir, A.-M.; Van der Veken, P., Novel Small Molecule-Derived, Highly Selective Substrates for Fibroblast Activation Protein (FAP). *ACS Medicinal Chemistry Letters* **2019**.
257. Baum, R. P.; Schuchardt, C.; Singh, A.; Chantadisai, M.; Robiller, F. C.; Zhang, J.; Mueller, D.; Eismant, A.; Almaguel, F.; Zboralski, D.; Osterkamp, F.; Hoehne, A.; Reineke, U.; Smerling, C.; Kulkarni, H. R., Feasibility, Biodistribution and Preliminary Dosimetry in Peptide-Targeted Radionuclide Therapy (PTRT) of Diverse Adenocarcinomas using (177)Lu-FAP-2286: First-in-Human Results. *J Nucl Med* **2021**.
258. Baum, R.; Chantadisai, M.; Smerling, C.; Schuchardt, C.; SINGH, A.; Eismant, A.; Almaguel, F.; Mueller, D.; Zboralski, D.; Osterkamp, F.; Hoehne, A.; Reineke, U.; Kulkarni, H., Peptide-Targeted Radionuclide Therapy (PTRT) using Lu-177 FAP-2286 in Diverse Adenocarcinomas: Feasibility, Biodistribution and Preliminary Dosimetry in a First-in-human study. *Journal of Nuclear Medicine* **2020,** *61* (supplement 1), 633-633.
259. Fani, M.; Weingaertner, V.; Kolenc Peitl, P.; Mansi, R.; Gaonkar, R. H.; Garnuszek, P.; Mikolajczak, R.; Novak, D.; Simoncic, U.; Hubalewska-Dydejczyk, A.; Rangger, C.; Kaeopookum, P.; Decristoforo, C., Selection of the First 99mTc-Labelled Somatostatin Receptor Subtype 2 Antagonist for Clinical Translation—Preclinical Assessment of Two Optimized Candidates. *Pharmaceuticals* **2021,** *14* (1), 19.
260. Abiraj, K.; Ursillo, S.; Tamma, M. L.; Rylova, S. N.; Waser, B.; Constable, E. C.; Fani, M.; Nicolas, G. P.; Reubi, J. C.; Maecke, H. R., The tetraamine chelator outperforms HYNIC in a new technetium-99m-labelled somatostatin receptor 2 antagonist. *EJNMMI Research* **2018,** *8* (1), 75.
261. Wessmann, S. H.; Henriksen, G.; Wester, H. J., Cryptate mediated nucleophilic 18F-fluorination without azeotropic drying. *Nuklearmedizin* **2012,** *51* (1), 1-8.

262. Kostikov, A. P.; Chin, J.; Orchowski, K.; Niedermoser, S.; Kovacevic, M. M.; Aliaga, A.; Jurkschat, K.; Wängler, B.; Wängler, C.; Wester, H.-J.; Schirrmacher, R., Oxalic acid supported Si-18F-radiofluorination: one-step radiosynthesis of N-succinimidyl 3-(di-tert-butyl[18F]fluorosilyl)benzoate ([18F]SiFB) for protein labeling. *Bioconjugate chemistry* **2012,** *23* (1), 106-114.

7 Supplemental Information

7.1 Abbreviation

α_1-AGP ..... *alpha1-acid glycoprotein*
αSMA ..... *alpha smooth muscle actin*
2-CTC ..... *2-Chlorotrityl chloride*
AA ..... *amino acid*
A_M ..... *molar activity*, *molar activity*
AMSEC ..... *albumin mediated size exclusion chromatography*
APCE ..... *antiplasmin-cleaving enzyme*
BgRT ..... *biology-guided radiotherapy*
BM ..... *basement membrane*
BMPR I/II ..... *bone morphogenetic protein receptor I/II*
BMSCs ..... *bone marrow stem cells*
Boc ..... *tert-butyloxycarbonyl*
BSA ..... *bovine serum albumin*
Ca ..... *carcinoma*
CAFs ..... *or cancer-associated fibroblasts*
CAV1 ..... *caveolin-1*
CCC ..... *cholangiocellular carcinoma*
CLL ..... *chronic lymphocytic leukemia*
CPM ..... *counts per minute*
CTGF ..... *connective tissue growth factor*
CUP ..... *carcinoma of unknown primary*
DCM ..... *dichloromethane*
Dde ..... *N-[1-(4,4-dimethyl-2,6-dioxocyclohex-1-ylidene)ethyl]*
DDR2 ..... *discoidin domain-containing receptor 2*
DFO ..... *desferrioxamine*
DFT ..... *density-functional theory*
DIPEA ..... *N,N-Diisopropylethylamine*
DMEM ..... *Dulbecco's modified Eagle's medium*
DMF ..... *dimethylformamide*
DOTA ..... *2,2',2",2"'-(1,4,7,10-tetraazacyclododecane-1,4,7,10-tetrayl)tetraacetic acid*
DOTAGA ..... *2-(4,7,10-tris(carboxymethyl)-1,4,7,10-tetraazacyclododecan-1-yl)pentanedioic acid*
DPP ..... *dipeptidyl peptidase*
DPP IV ..... *dipeptidyl peptidase IV*
DR5 ..... *death receptor 5*
EC ..... *endothelial cell*
ECM ..... *extracellular matrix*
EDA ..... *ethylenediamine*
EGF ..... *epithelial to mesenchymal program*
EGFR ..... *epidermal growth factor receptor*
EMT ..... *epithelial to mesenchymal transition*
EndMT ..... *endothelial-to-mesenchymal transition*
eq. ..... *equivalent*

ESI-MS ..... *electrospray ionization mass spectrometry*
Et_2O ..... *diethyl ether*
FAP ..... *fibroblast activation protein*, *fibroblast activation protein*
FBS ..... *fetal bovine serum*
FGF ..... *fibroblast growth factor*
FGFR ..... *fibroblast growth factor receptor*
Fmoc ..... *fluorenylmethoxycarbonyl*
FN ..... *fibronectin*
FSP1/S100A4 ..... *fibroblast specific protein-1*
FTMS ..... *Fluorotrimethylsilane*
GABA ..... *gamma-aminobutyric acid*
GRPr ..... *gastrin releasing peptide receptor*
GSP ..... *general synthesis procedure*
HATU ..... *1-[Bis(dimethylamino)methylene]-1H-1,2,3-triazolo[4,5-b]pyridinium-3-oxide hexafluoro-phosphate*
HBSS ..... *Hank´s balanced salt solution*
HFIP ..... *hexafluoroisopropanol*
HOAt *1-hydroxy-7-azabenzotriazol*
HOBt *1-hydroxybenzotriazol*
HPLC ..... *high-performance liquid chromatography*
HSA ..... *human serum albumin*
hTTR ..... *human transthyretin*
IC_{50} ..... *half-maximal inhibitory concentration*
INFγ ..... *interferon gamma*
K' ..... *capacity factor*
KB ..... *ketone bodies*
LMW ..... *low molecular weight*
LOX ..... *lysyl oxidase*
MDSC ..... *myeloid-derived suppressor cell*, *myeloid-derived suppressor cells*
MeOH ..... *methanol*
MIP ..... *maximum intensity projection*
MMPs ..... *matrix metalloproteinases*
$NaHCO_3$ ..... *sodium bicarbonate*, *sodium bicarbonate*, *sodium bicarbonate*
NIS ..... *sodium-iodide symporter*
NK ..... *natural killer*
NMP *N-methyl-2-pyrrolidone*
NMR ..... *nuclear magnetic resonance*
NSCLC ..... *non-small cell lung tumors*
p.i. ..... *post injection*
PBS ..... *phosphate buffered saline*
PDGF ..... *platelet-derived growth factor*
PDGFR α/β ..... *platelet-derived growth factor receptor alpha/beta*
PET ..... *positron emission tomography*
Pfp ..... *pentafluorophenyl*
PGE2 ..... *prostaglandin E2*
POSTN ..... *periostin*

PRRT ..... *peptide radionuclide receptor therapy*
RCC ..... *radiochemical conversion*
rt ..... *roomtemperature*
S_A ..... *specific activity*
SDF-1 (CXCL 12) ..... *stromab cell-derived factor 1*
SiFA ..... *Silicon fluorine acceptors*
SPPS ..... *solide-phase peptide synthesis*
sym-collidine *2,4,6-trimethylpyridine*
$t_{1/2}$ ..... *half-life*
TAM ..... *tumor-associated macrophages*
TBTU ..... *O-(Benzotriazol-1-yl)-N,N,N',N'-tetramethyluronium tetrafluoroborat*
*t*Bu ..... *tert-butyl*
*t*BuOH ..... *tert-butanol*
TFA ..... *trifluoroacetic acid*, *trifluoroacetic acid*
TGFβ ..... *transforming growth factor beta*
TGFβR I/II ..... *transforming growth factor beta receptor I/II,*
THF ..... *tetrahydrofuran*
TIMPs ..... *tissue inhibitor of metalloproteinases*
TIPS ..... *triisopropylsilane*
TLC ..... *radio-thin layer chromatography*
TME ..... tumor microenvironment
TN-C ..... *tenacin-C*
TNFα ..... *tumor necrosis factor alpha*
t_R ..... *retention time*
VBM ..... *vascular basement membrane*
VCAM1 ..... *vascular cell adhesion protein 1*
VEGF ..... *vascular endothelial growth factor*
WNTs ..... *wingles-related integration site*

7.2 List of Figures

7.3 List of Schemes

7.4 List of Tables

7.5 Publications

Fahnauer M., Parzinger M., Wester H.-J., European Patent WO 2022/238553 A1, *Radiopharmaceutical Somatostatin Receptor Ligands and Precursors thereof*, International Publication Date 17 November 2022 (17.11.2022).

Fahnauer M., Stopper L., Kunert J.-P., Fischer S., Fenzl S., Holzleithner N., Deiser S., Beck R., Günther T., Utz-Urban N., Wester H.-J., European Patent registered 08/2022.

7.6 Supplemental Information

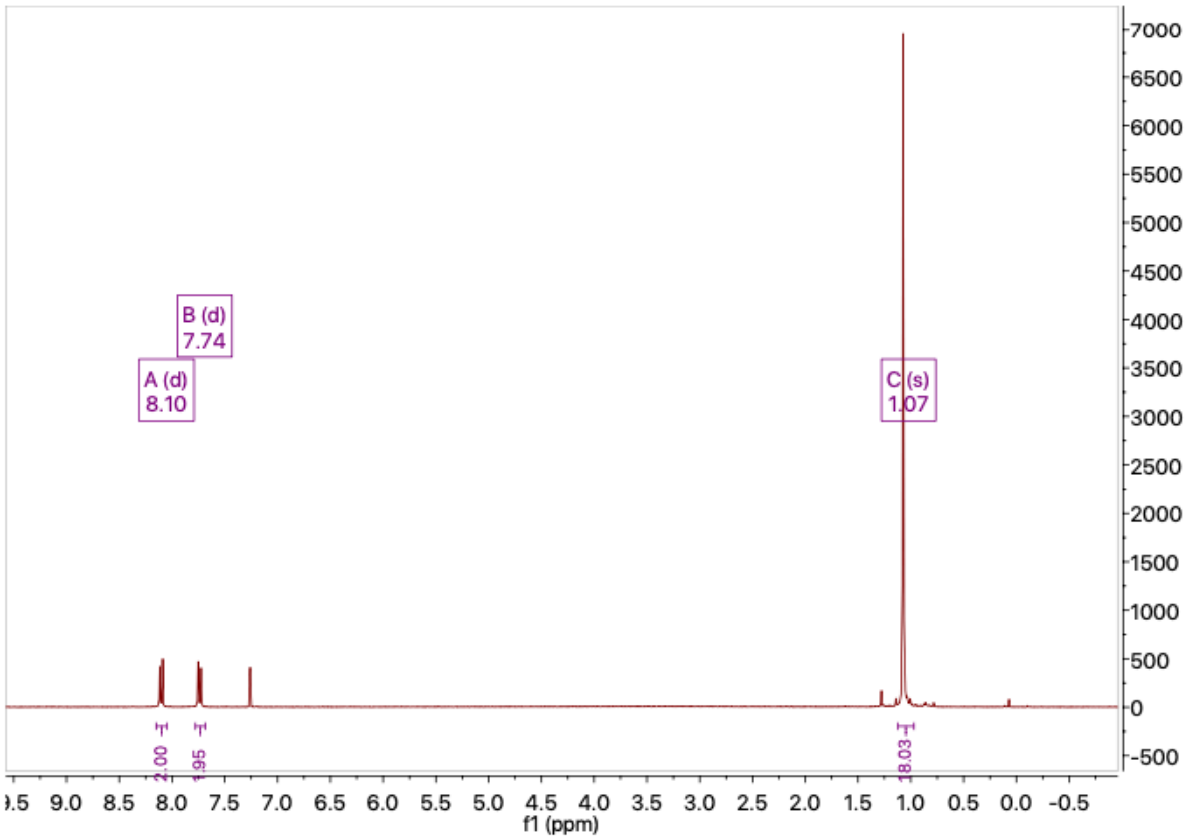

Supplemental Information 1: ^{1}H-NMR of 4-(di-*tert*-butylfluorosilyl)benzoic acid (12) (300 MHz, $CDCl_3$, 300 K): δ = 8.10 (2H, d, C_6H_4), 7.74 (2H, d, C_6H_4), 1.07 (18H, s, Si(*t*Bu)$_2$) ppm.

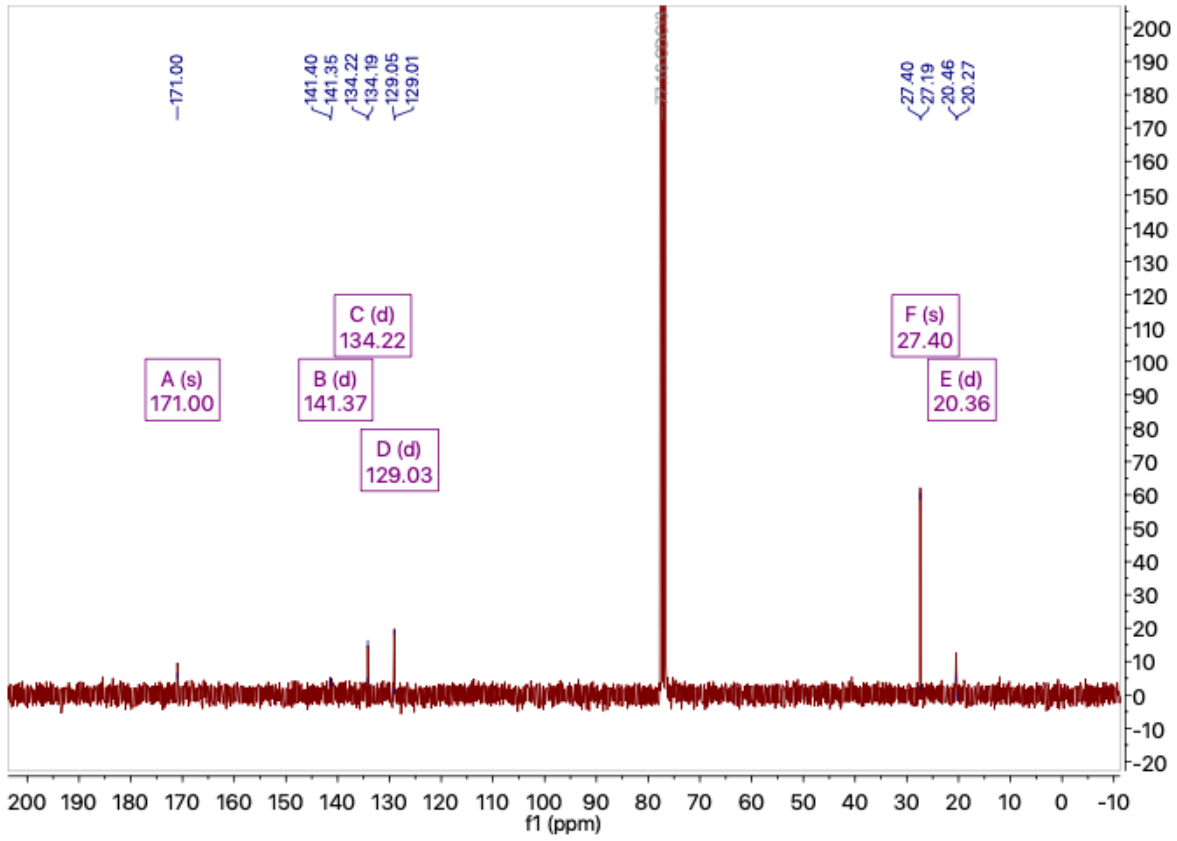

Supplemental Information 2: ^{13}C-NMR of 4-(di-*tert*-butylfluorosilyl)benzoic acid (12) (75 MHz, $CDCl_3$, 300 K): δ = 171.00 (a, COOH), 141.37 (d, C_p), 134.22 (d, C_m), 129.03 (d, $C_{i,o}$), 27.40 (d, CCH_3), 20.36 (d, CCH_3) ppm.

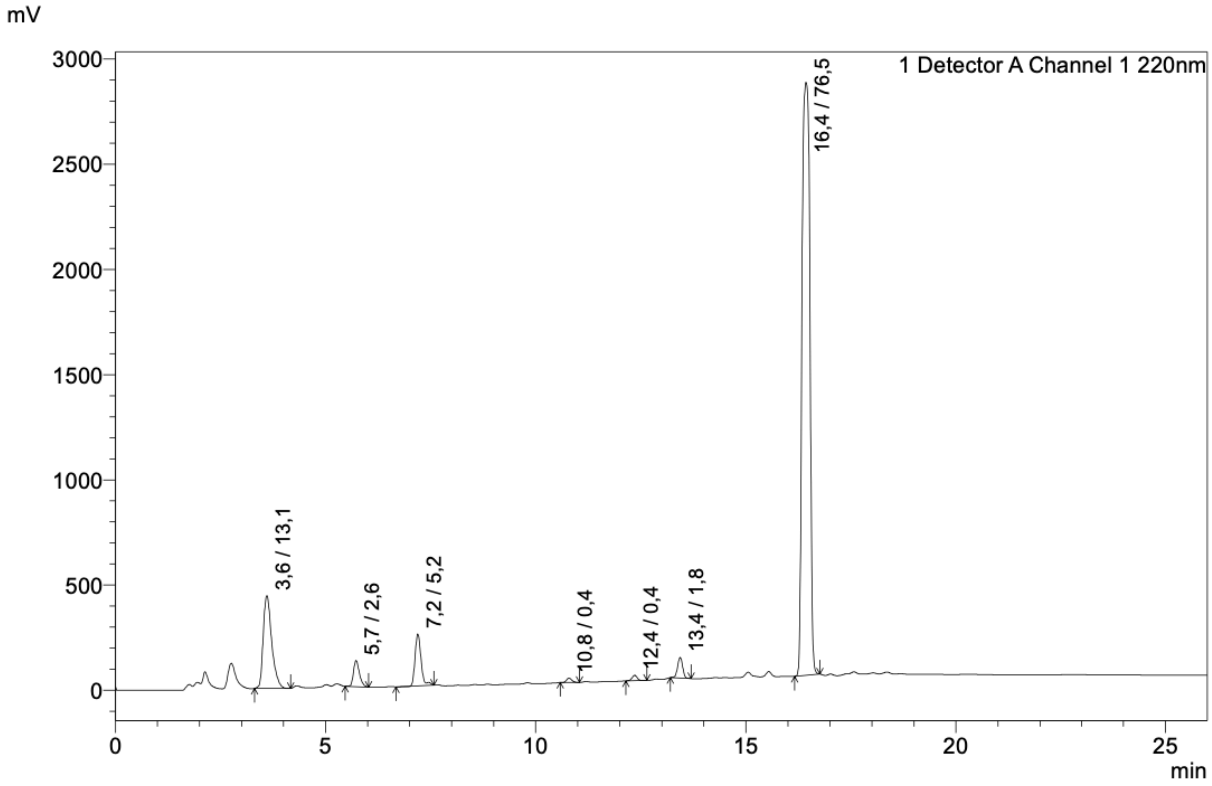

Supplemental Information 3: Reversed phase HPLC of di-*tert*-butyl(3,5-dimethylphenyl)fluorosilane (14) (50 to 100 in 15 min): t_R = 16.5 min.

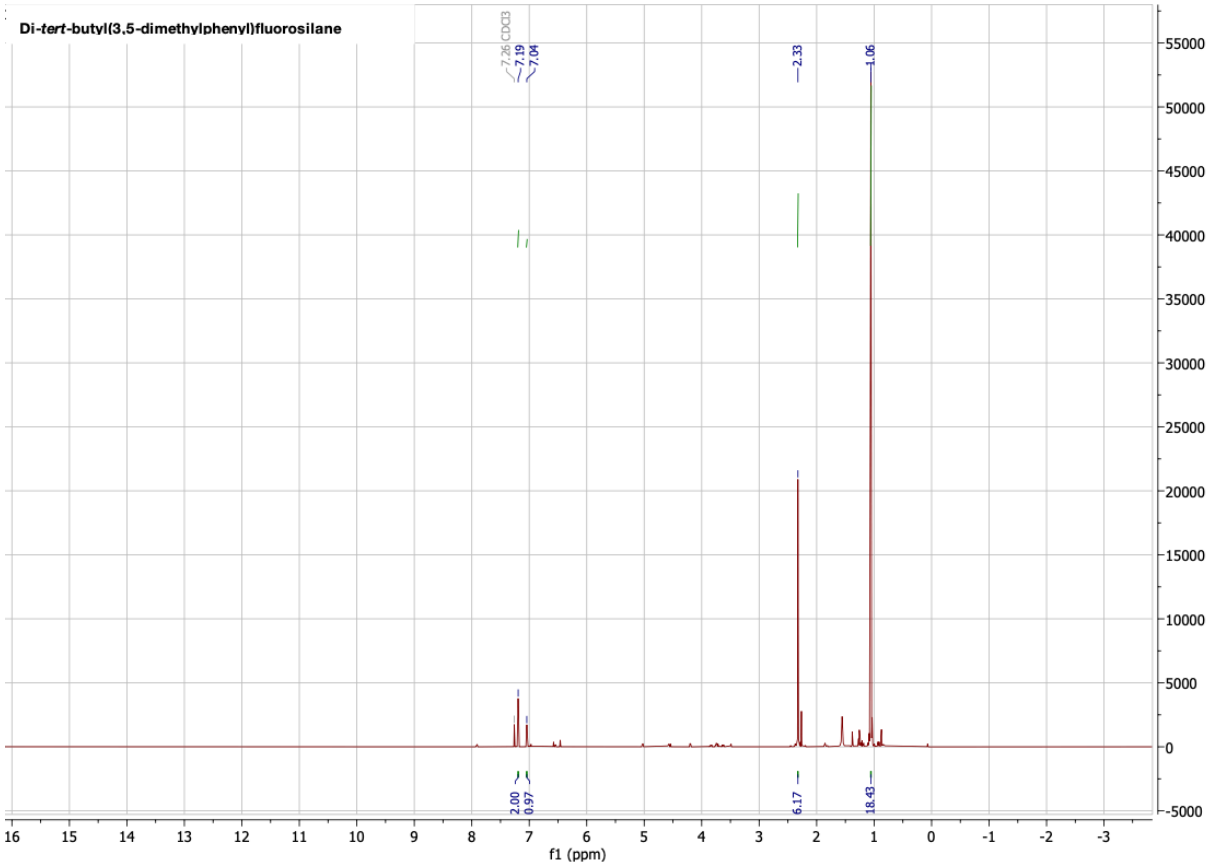

Supplemental Information 4: ^{1}H-NMR of di-*tert*-butyl(3,5-dimethylphenyl)fluorosilane (14) (500 MHz, $CDCl_3$, 300 K): δ = 7.19 (2H, s, H_O), 7.04 (1H, s, H_p), 2.33 (6H, s, CH_3), 1.06 (18H, s, Si(*t*Bu)$_2$) ppm.

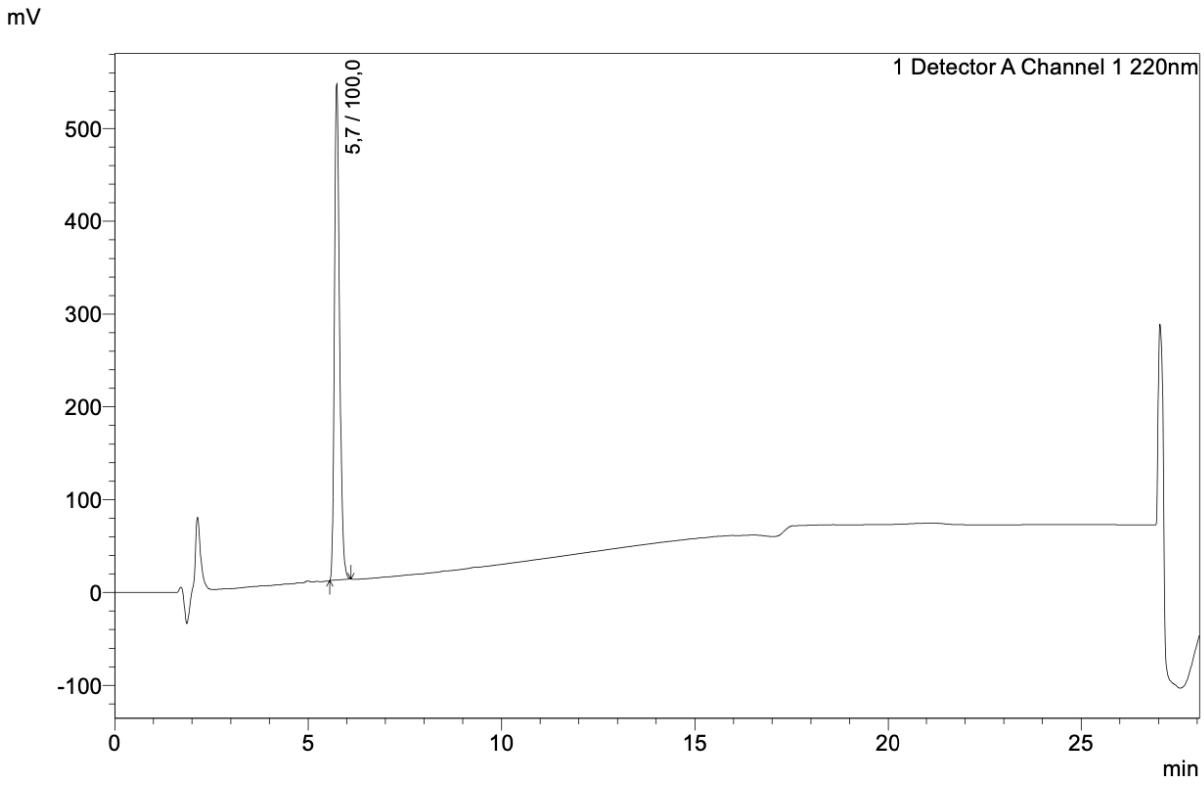

Supplemental Information 5: Reversed phase HPLC of 5-(di-*tert*-butylfluorosilyl)isophthalic acid (15) (50 to 100 in 15 min): t_R = 5.7 min (Mono acid: 9.6 min).

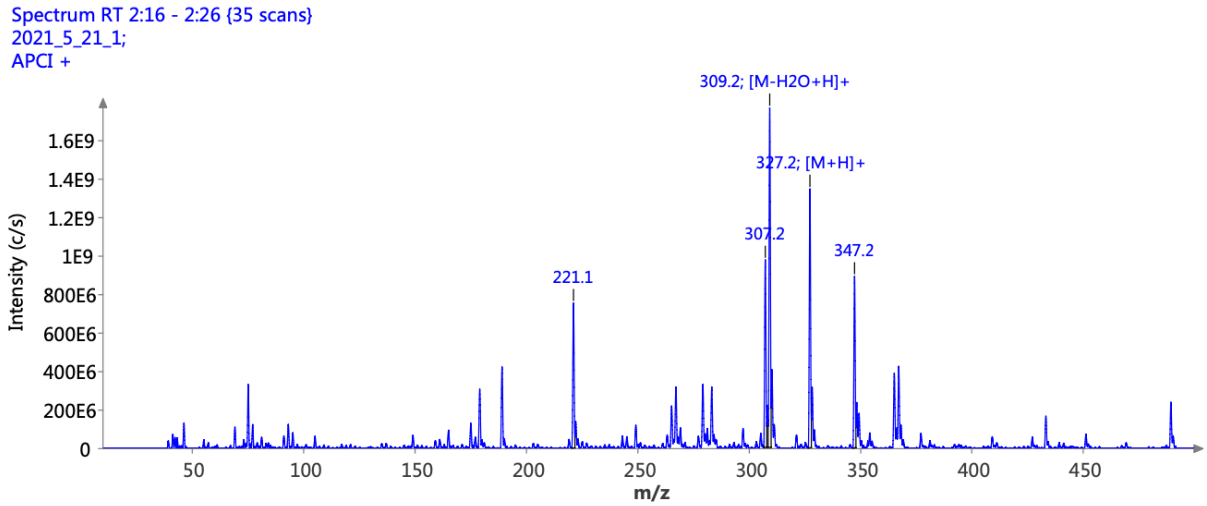

Supplemental Information 6: ESI-MS of 5-(di-*tert*-butylfluorosilyl)isophthalic acid (15) with Calculated monoisotopic mass ($C_{16}H_{23}FO_4Si$): 326.13; found: m/z = 327.2 $[M+H]^+$, 309.2 $[M-H_2O+H]^+$.

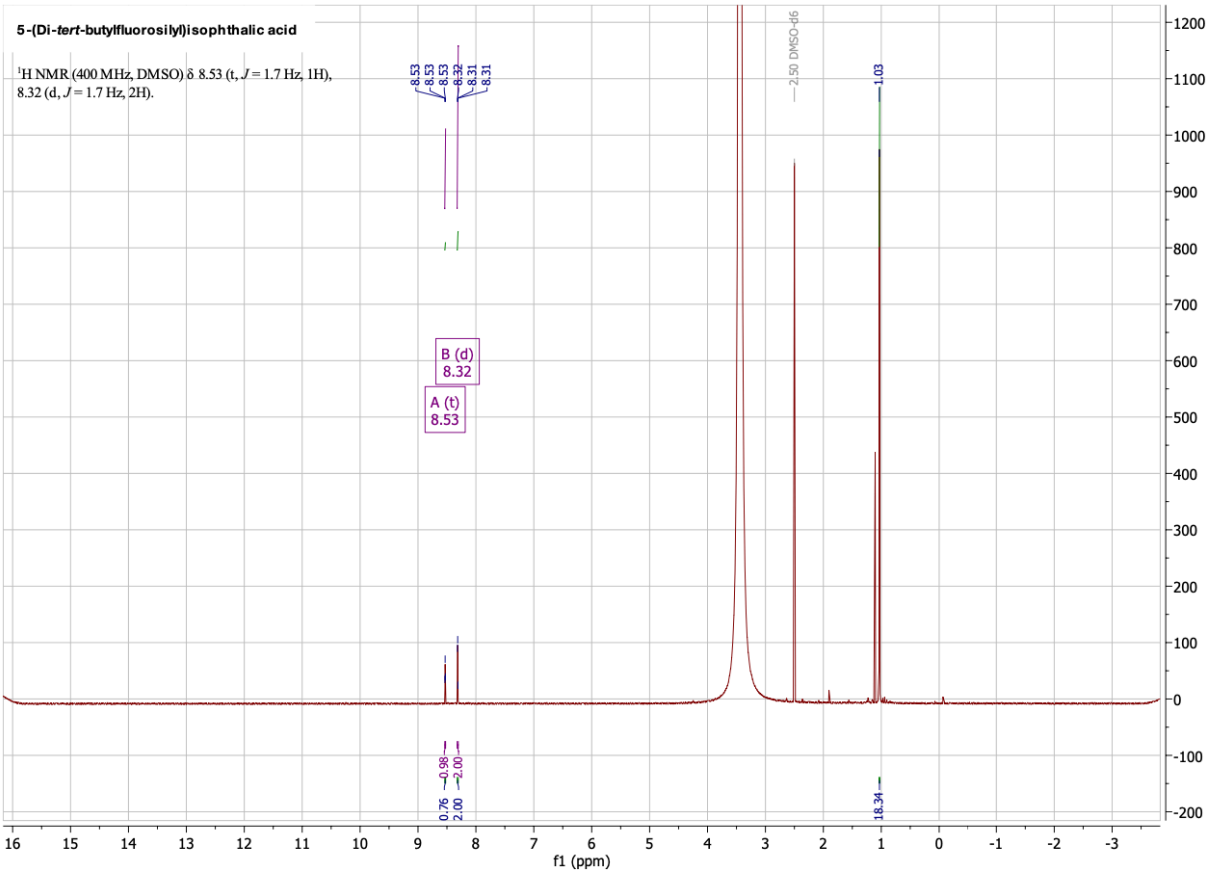

Supplemental Information 7: ^{1}H-NMR of 5-(di-*tert*-butylfluorosilyl)isophthalic acid (15) (400 MHz, DMSO-D_6, 300 K): δ = 8.53 (t, 1 H, $^{4}J(^{1}H,^{1}H)$ = 1.7 Hz; $H_{Ar\text{-}2}$), 8.32 (d, 2 H, $^{4}J(^{1}H,^{1}H)$ = 1.6 Hz; $H_{Ar\text{-}4,\text{-}6}$), 1.03 (s, 18 H; CH_3).

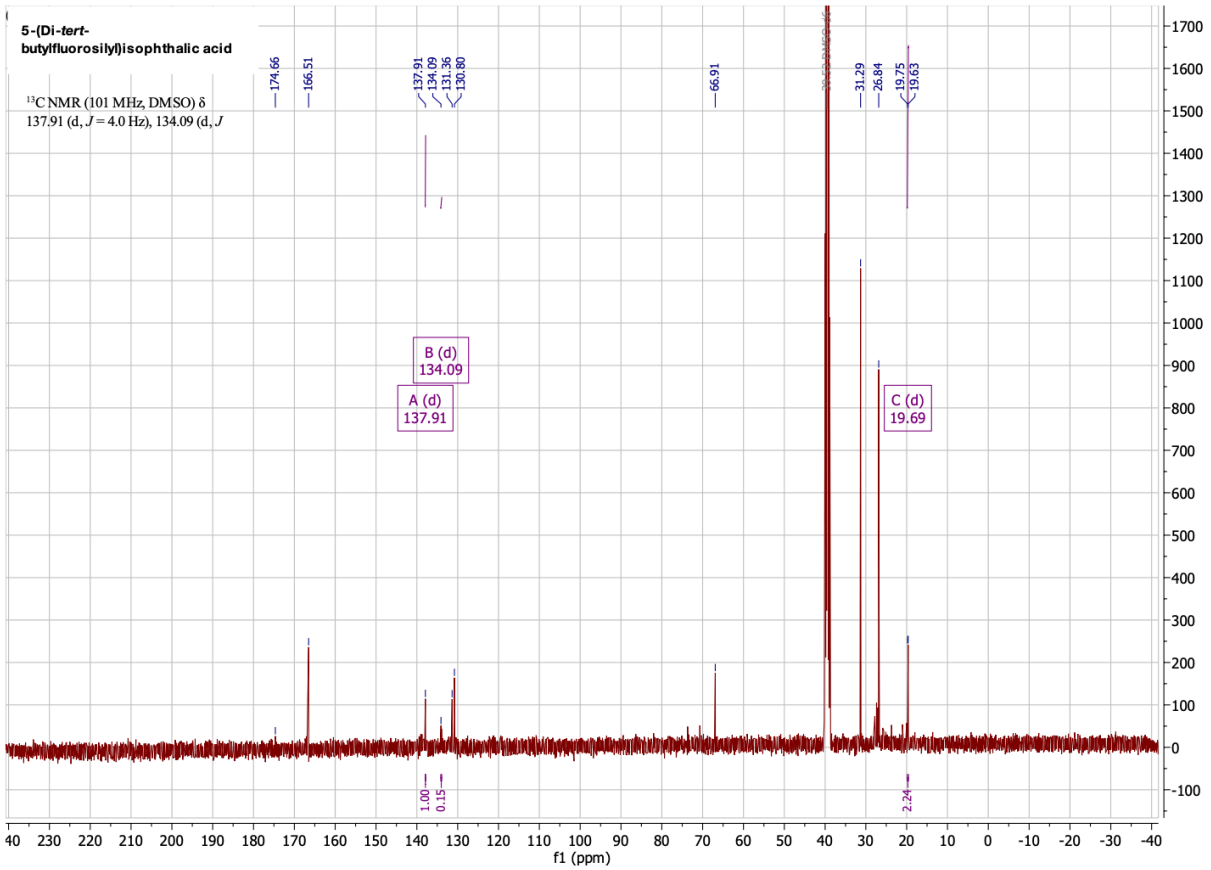

Supplemental Information 8: $^{13}C[^{1}H]$-NMR of 5-(di-*tert*-butylfluorosilyl)isophthalic acid (15) (101 MHz, DMSO-D_6): δ [ppm] = 166.5 (s; COOH), 137.9 (d, $^{3}J(^{13}C,^{19}F)$ = 4 Hz; $C_{Ar\text{-}4,\text{-}6}$), 134.0 (d, $^{2}J(^{13}C,^{19}F)$ = 14 Hz; $C_{Ar\text{-}5}$), 131.4 (s; $C_{Ar\text{-}2}$), 130.8 (s; $C_{Ar\text{-}1,\text{-}3}$), 26.8 (s; CCH_3), 19.7 (d, $^{2}J(^{13}C,^{19}F)$ = 12 Hz; CCH_3).

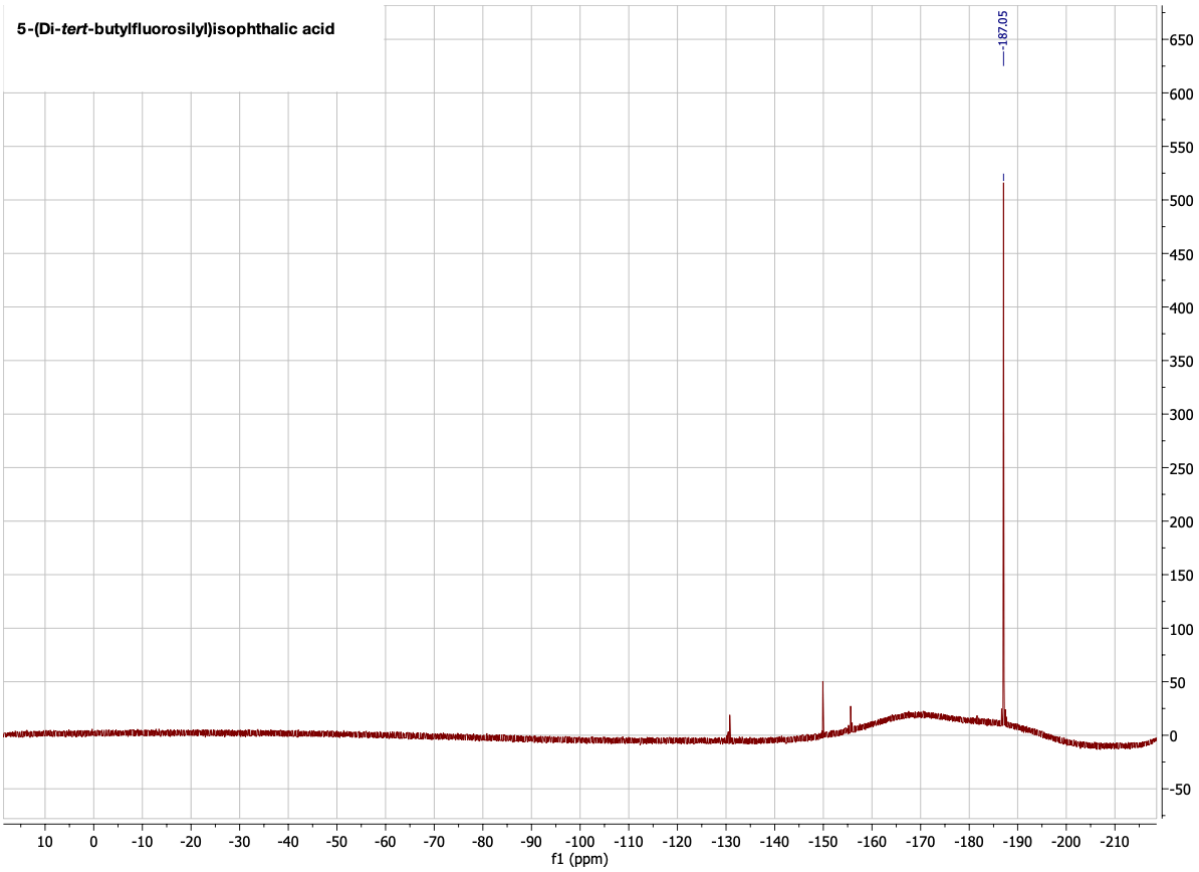

Supplemental Information 9: $^{19}F[^{29}Si]$-NMR of 5-(di-*tert*-butylfluorosilyl)isophthalic acid (15) (376 MHz, DMSO-D_6): δ = –187.1 ppm.

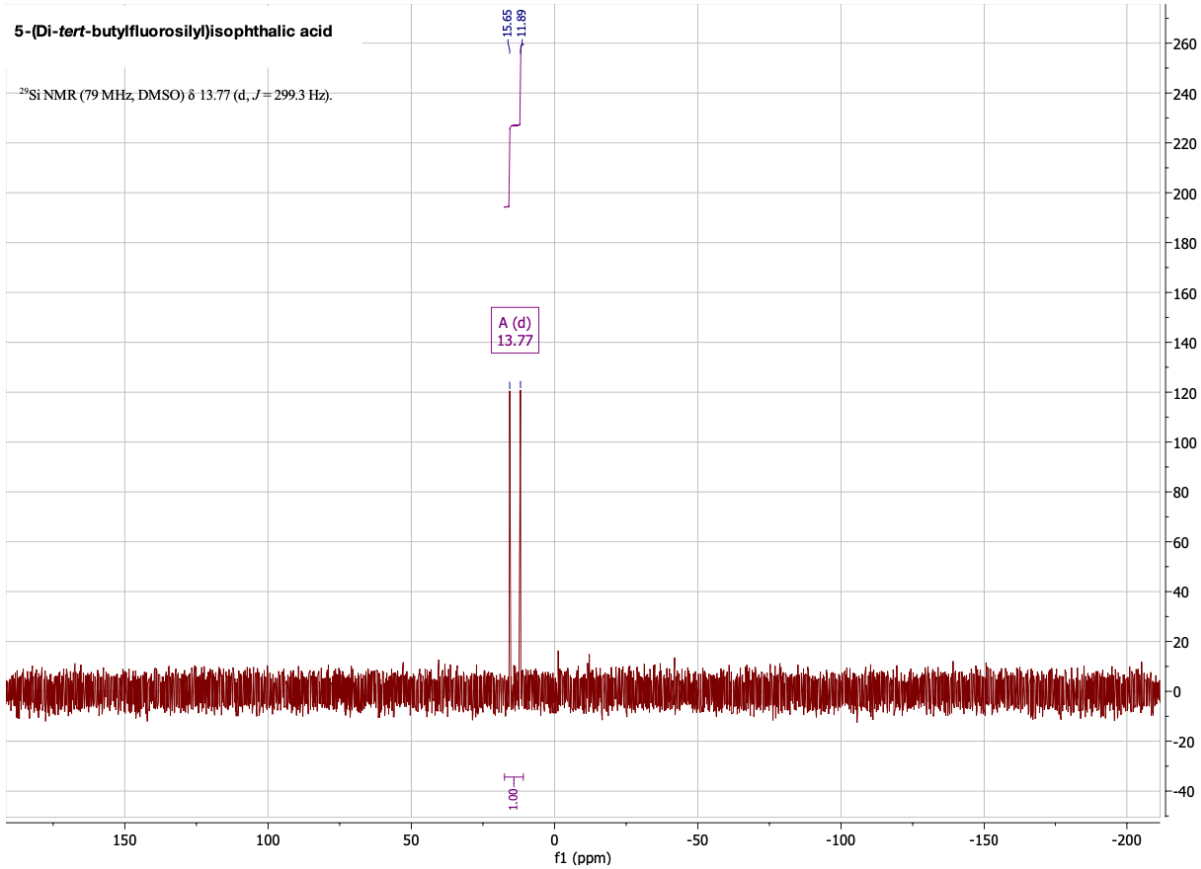

Supplemental Information 10: ^{29}Si[^{1}H]INEPT-NMR of 5-(di-*tert*-butylfluorosilyl)isophthalic acid (15) (79 MHz, DMSO-D_6): δ = 13.8 (d, $^{1}J(^{19}F,^{29}Si)$ = 299 Hz) ppm.

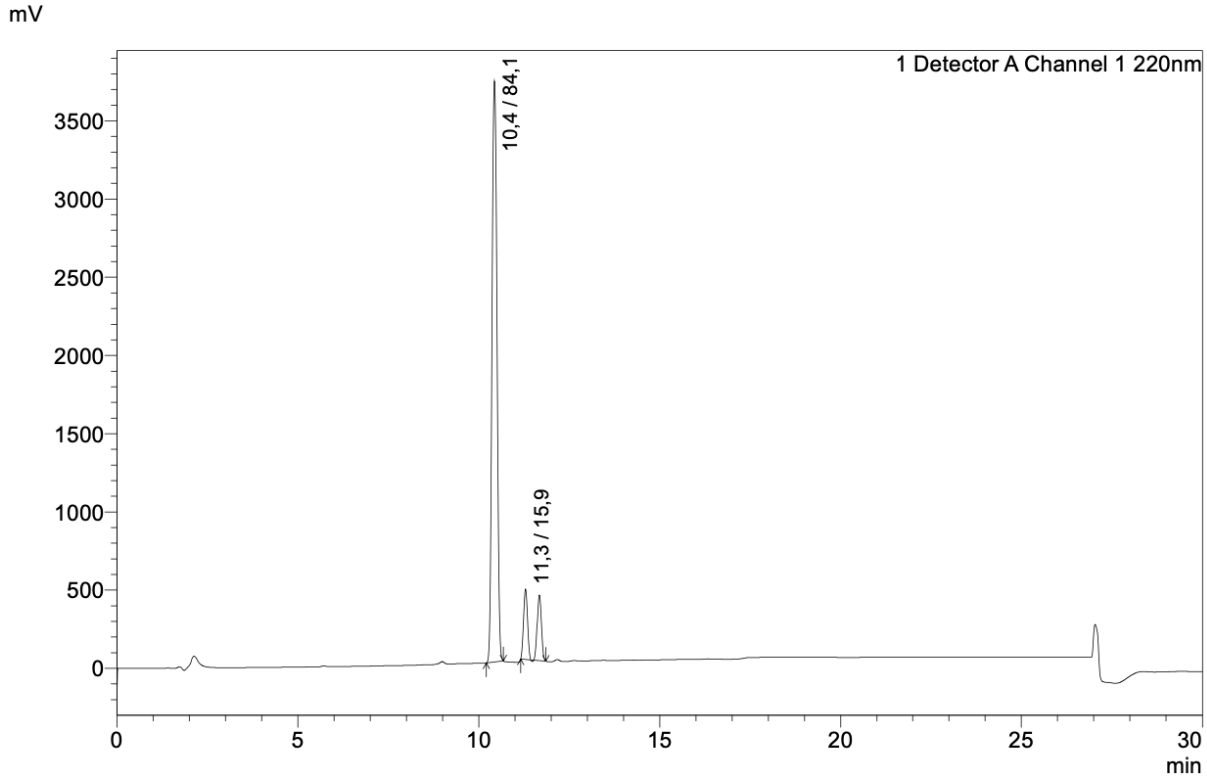

Supplemental Information 11: Reversed phase HPLC of 3-(di-*tert*-butylfluorosilyl)-5-((vinyloxy)carbonyl)benzoic acid (16) (50 to 100 in 15 min): t_R = 10.4 min.

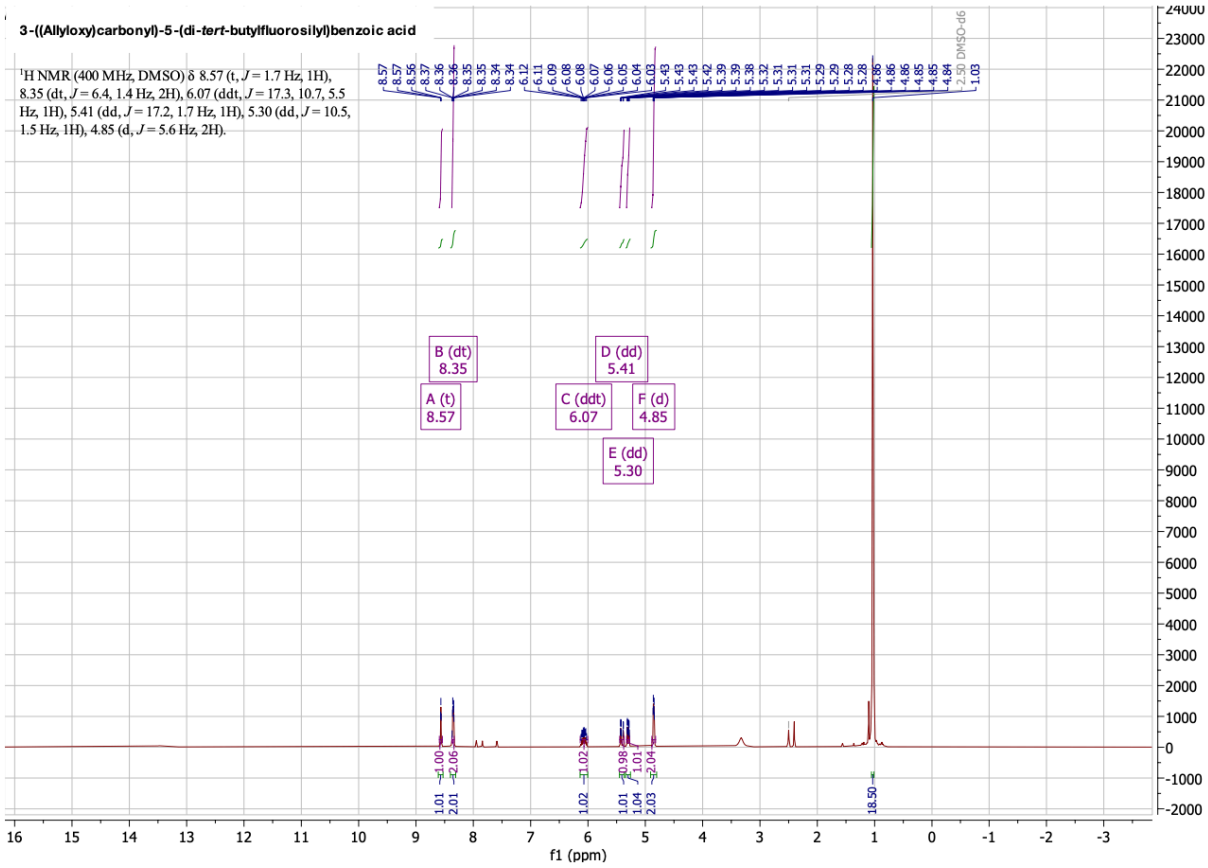

Supplemental Information 12: ^{1}H-NMR of 3-(di-*tert*-butylfluorosilyl)-5-((vinyloxy)carbonyl)benzoic acid (16) (400 MHz, DMSO-D$_6$): δ = 8.57 (t, 1H, $^4J(^1H,^1H)$ = 1.5 Hz; $H_{Ar\text{-}6}$), 8.36 (t, 1H, $^4J(^1H,^1H)$ = 1.5 Hz; $H_{Ar\text{-}2}$), 8.34 (t, 1H,

$^{4}J(^{1}H,^{1}H)$ = 1.5 Hz; H_{Ar-4}), 6.07 (ddt, 1H, $^{3}J(^{1}H,^{1}H)$ = 17.3, 10.7, 5.5 Hz; CH_2–C*H*=CH_2), 5.41 (dd, 1H, $^{3}J(^{1}H,^{1}H)$ = 17.2 Hz, $^{2}J(^{1}H,^{1}H)$ = 1.7 Hz; CH_2–CH=CH_2 (*E*)), 5.30 (dd, 1H, $^{3}J(^{1}H,^{1}H)$ = 10.3 Hz, $^{2}J(^{1}H,^{1}H)$ = 1.6 Hz; CH_2–CH=CH_2 (*Z*)), 4.85 (d, 2H, $^{3}J(^{1}H,^{1}H)$ = 5.6 Hz; CH_2–CH=CH_2), 1.03 (s, 18H; CCH_3) ppm.

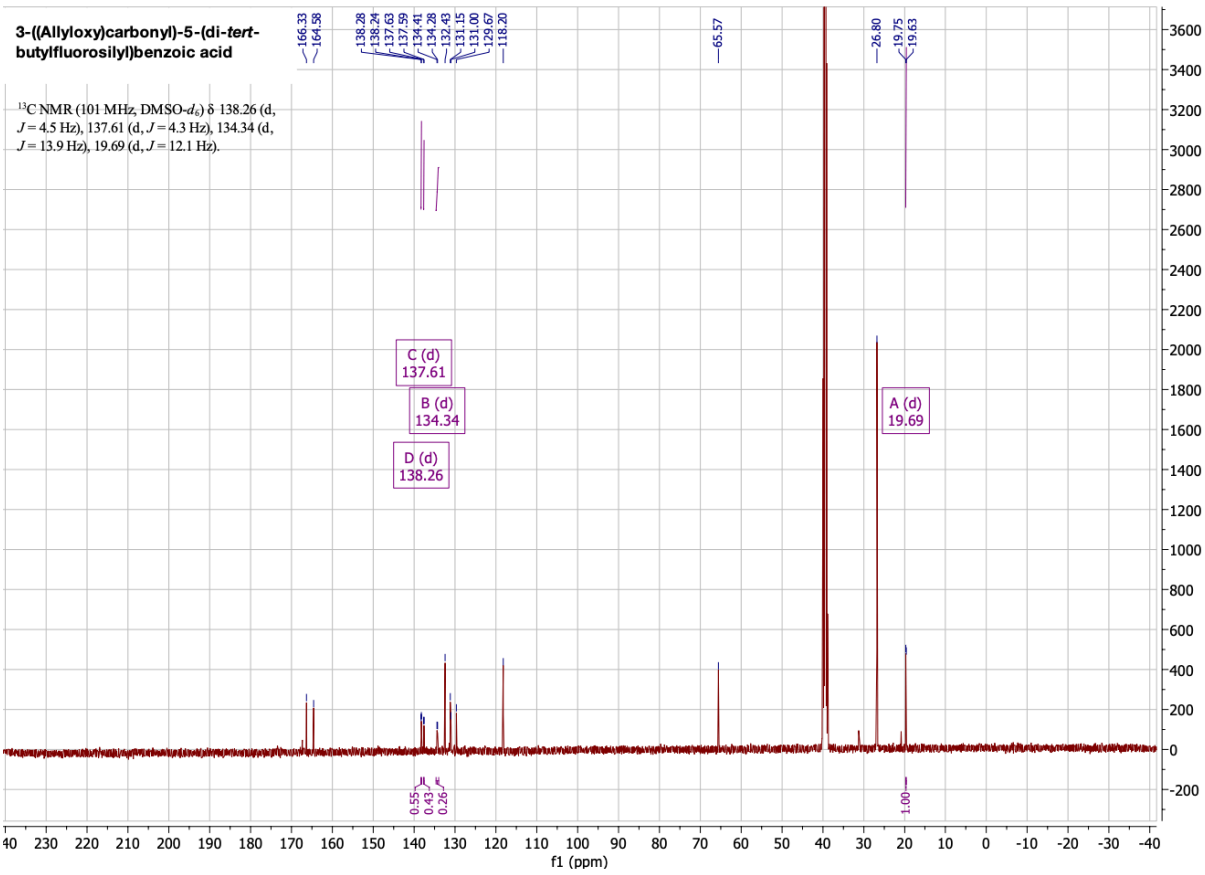

Supplemental Information 13: ^{13}C-NMR of 3-(di-*tert*-butylfluorosilyl)-5-((vinyloxy)carbonyl)benzoic acid (16) (101 MHz, DMSO-D_6): δ = 166.3 (COOH), 164.6 (*C*O-OAll), 138.3 (d, $^{3}J(^{13}C,^{19}F)$ = 4 Hz; C_{Ar-4}), 137.6 (d, $^{3}J(^{13}C,^{19}F)$ = 4 Hz; C_{Ar-6}), 134.3 (d, $^{2}J(^{13}C,^{19}F)$ = 14 Hz; C_{Ar-5}), 132.4 (CH_2–*C*H=CH_2), 131.2 (C_{Ar-2}), 131.0 (C_{Ar-1}), 129.7 (C_{Ar-3}), 118.2 (CH_2–CH=*C*H_2), 65.6 (*C*H_2–CH=CH_2), 26.8 (s; *C*CH_3), 19.7 (d, $^{2}J(^{13}C,^{19}F)$ = 12 Hz; *C*CH_3) ppm.

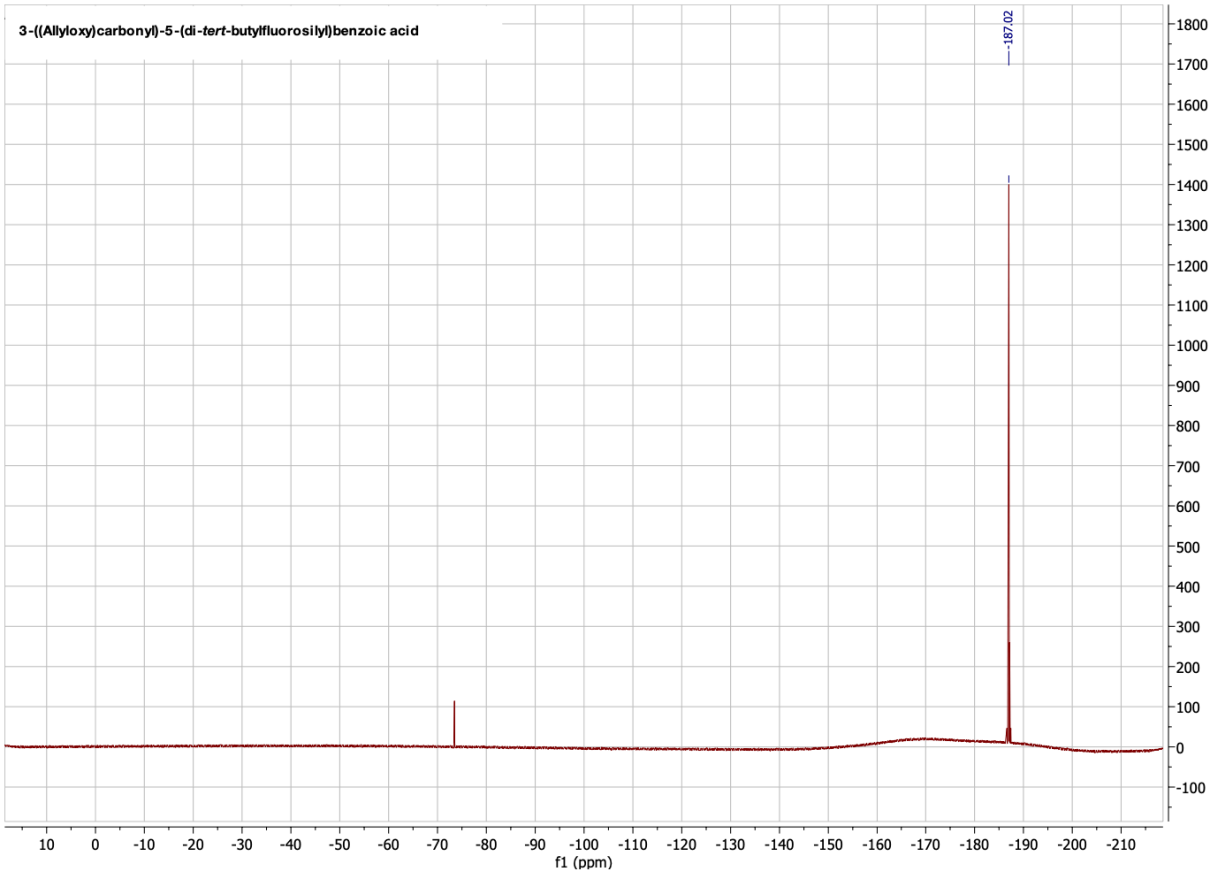

Supplemental Information 14: $^{19}F[^{29}Si]$-NMR of 3-(di-*tert*-butylfluorosilyl)-5-((vinyloxy)carbonyl)benzoic acid (16) (376 MHz, DMSO-D_6): $\delta = -187.0$ ppm.

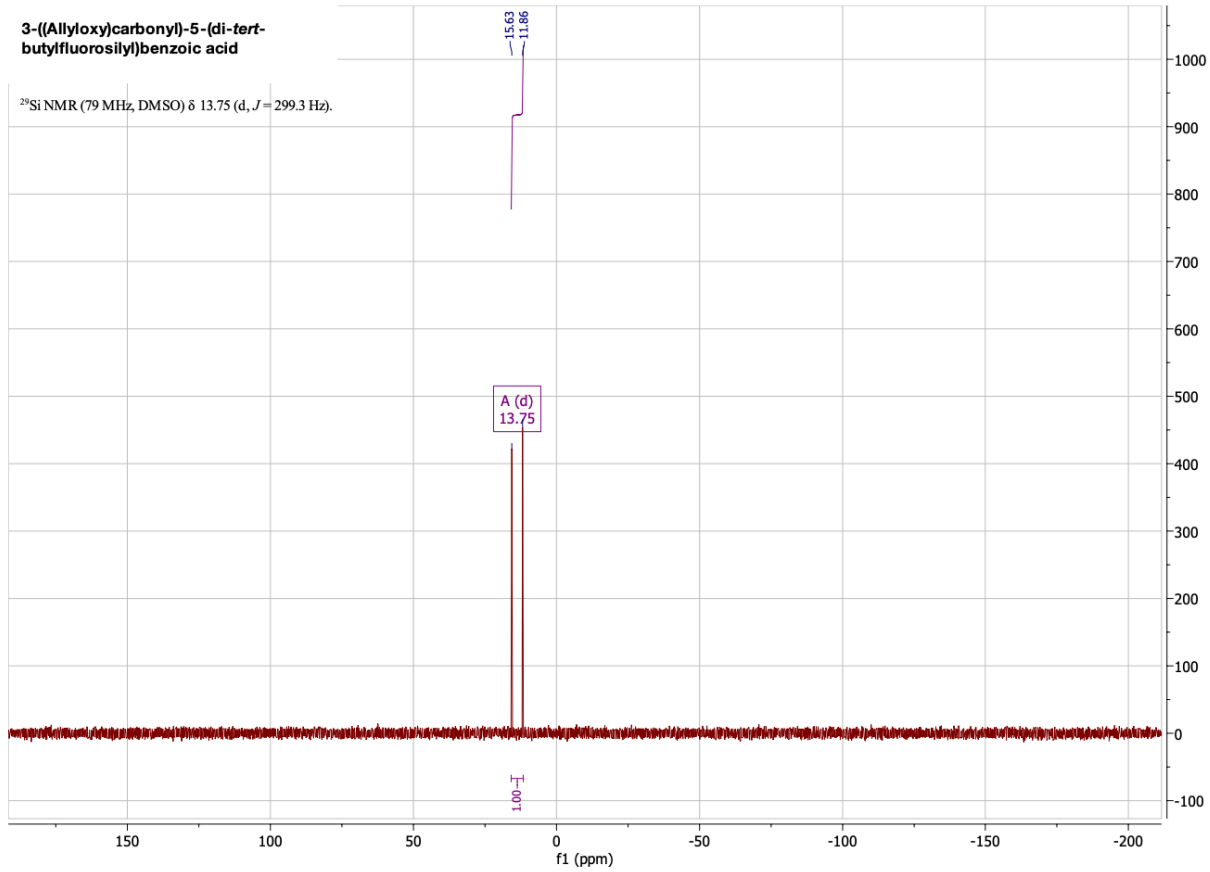

Supplemental Information 15: ^{29}Si[^{1}H]INEPT-NMR of 3-(di-*tert*-butylfluorosilyl)-5-((vinyloxy)carbonyl)benzoic acid (16) (79 MHz, DMSO-D$_6$): δ = 13.8 (d, ^{1}J(^{19}F,^{29}Si) = 299 Hz) ppm.

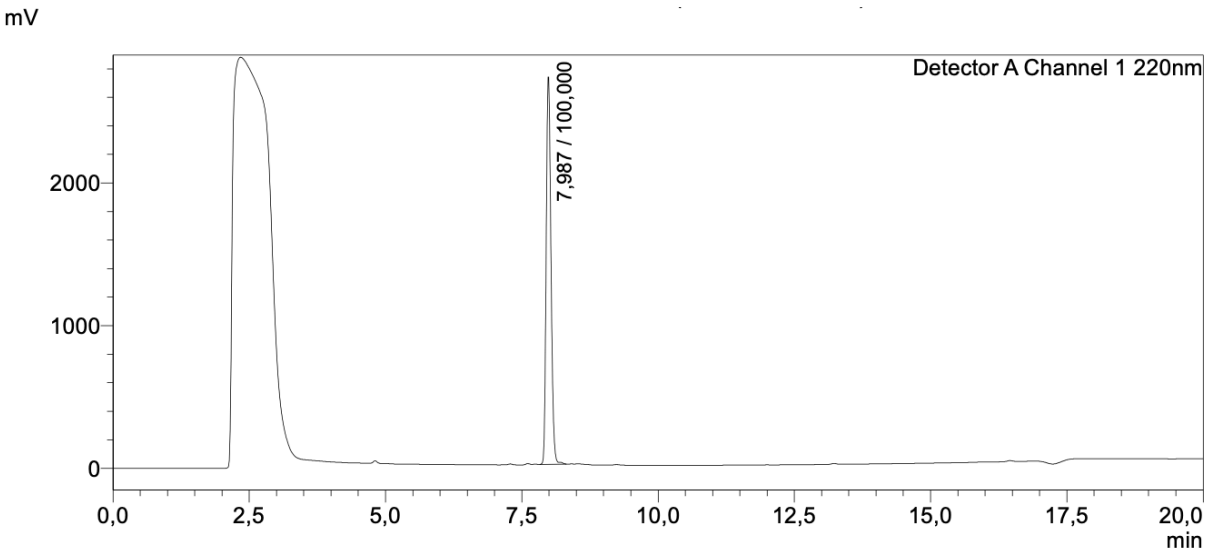

Supplemental Information 16: Quality control of rhFAPI-01 with RP-HPLC (10 to 90% B in 15 min): t_R = 7.99 min.

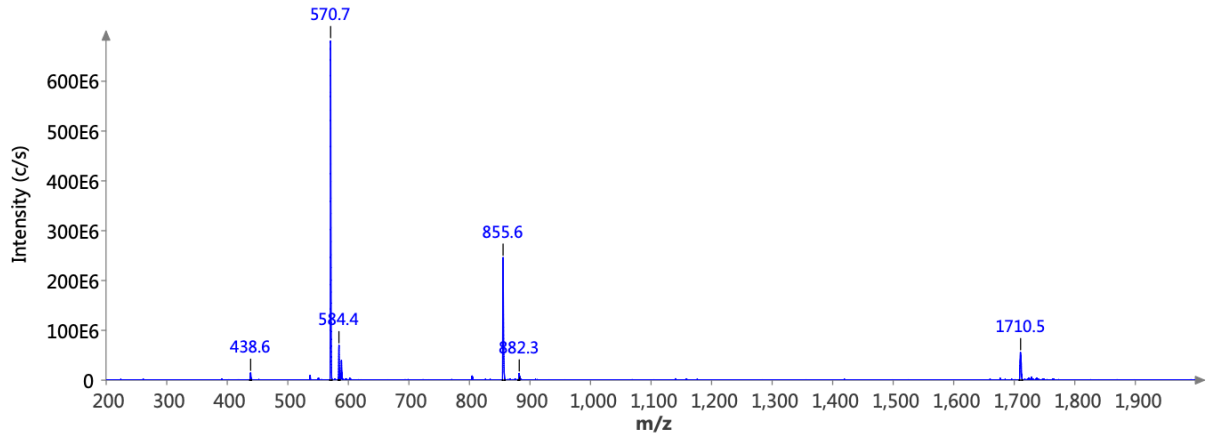

Supplemental Information 17: Mass spectrum of quality control of rhFAPI-01. ESI-MS: Calculated monoisotopic mass ($C_{78}H_{115}F_3N_{18}O_{20}Si$): 1708.83; found: m/z = 1710.5 $[M+H]^+$, 855.6 $[M+2H]^{2+}$, 570.7 $[M+3H]^{3+}$.

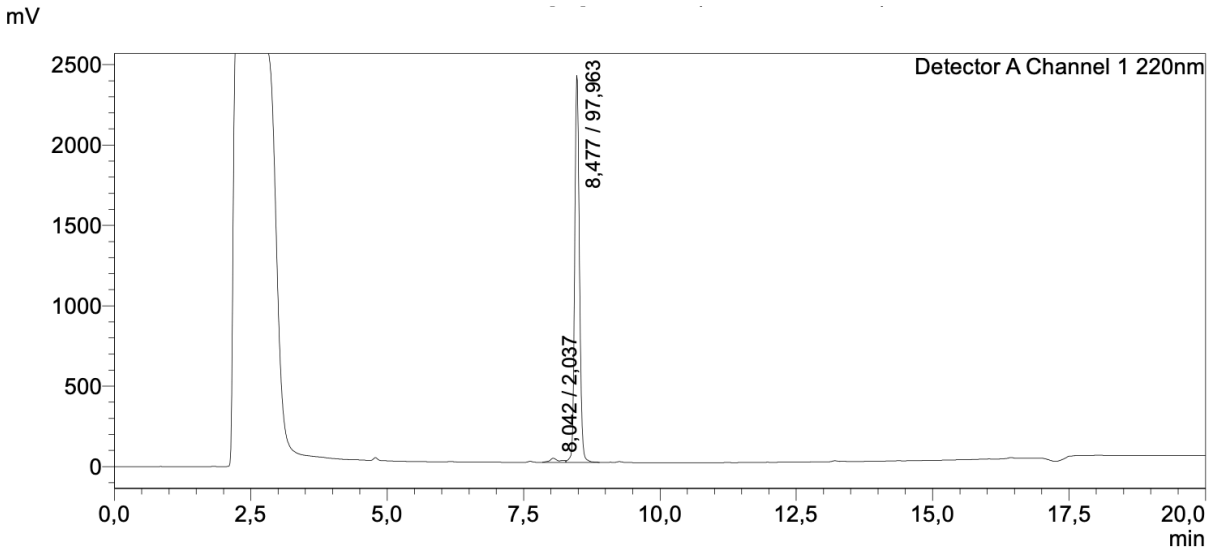

Supplemental Information 18: Quality control of [^{nat}Lu]Lu-rhFAPI-01 with RP-HPLC (10 to 90% B in 15 min): t_R = 8.48 min.

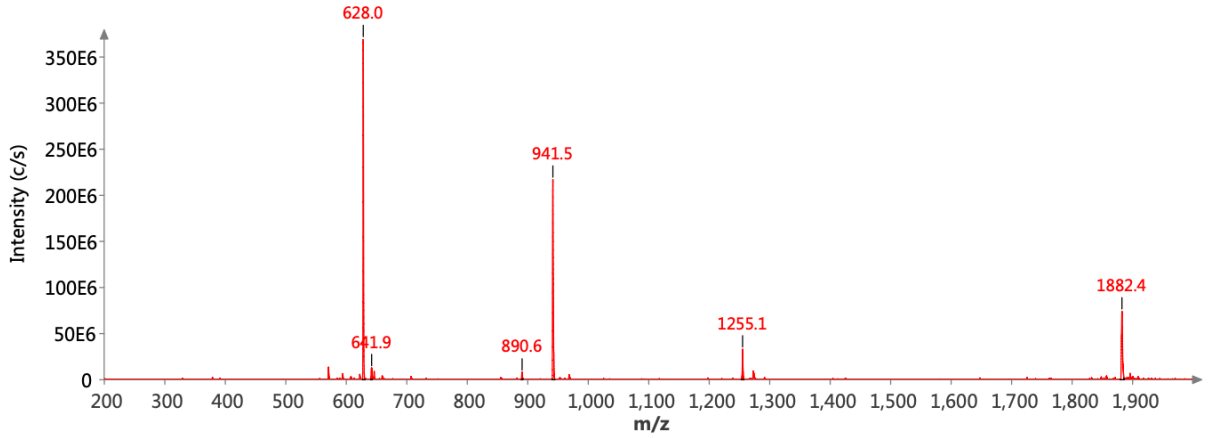

Supplemental Information 19: Mass spectrum of quality control of [^{nat}Lu]Lu-rhFAPI-01. ESI-MS: Calculated monoisotopic mass ($C_{78}H_{112}F_3LuN_{18}O_{20}Si$): 1880.74; found: m/z = 1882.4 $[M+H]^+$, 941.5 $[M+2H]^{2+}$, 628.0 $[M+3H]^{3+}$.

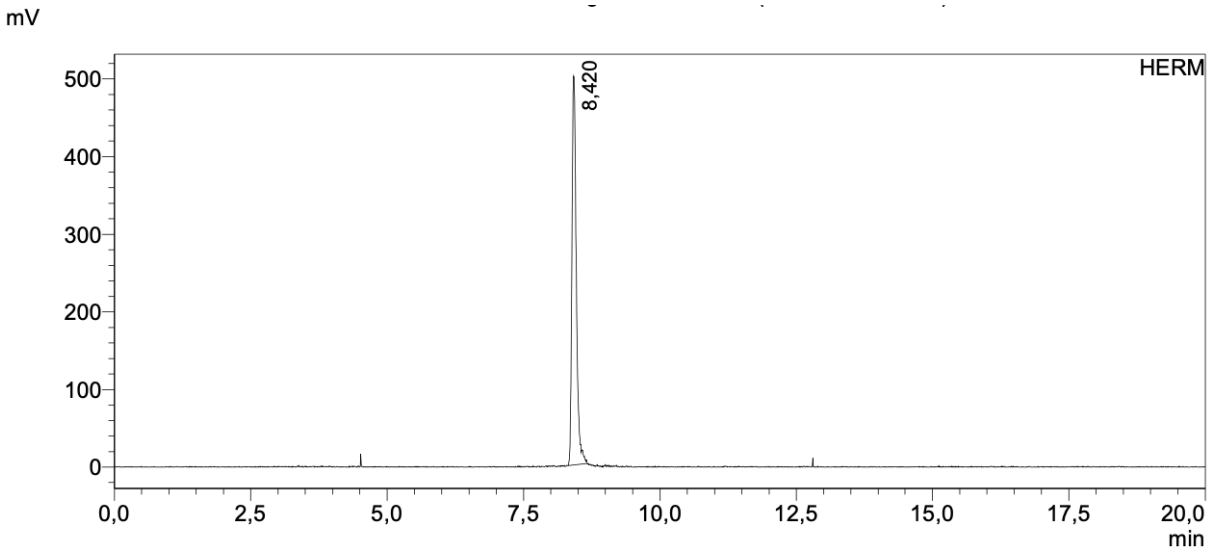

Supplemental Information 20: Quality control of [^{177}Lu]Lu-rhFAPI-01 with radio-HPLC (10 to 90% B in 15 min): t_R = 8.42 min.

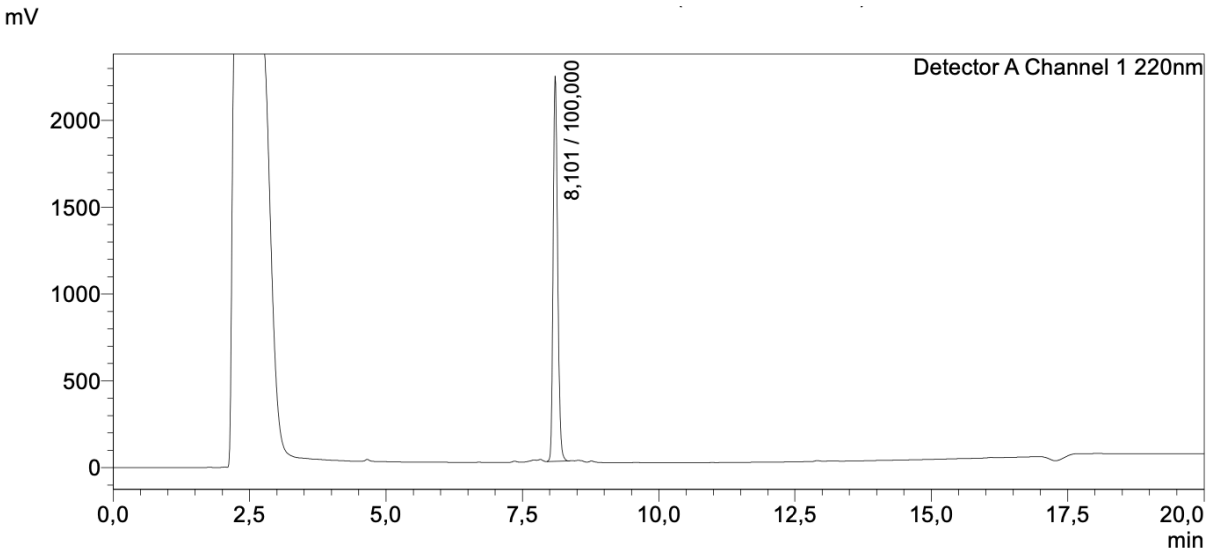

Supplemental Information 21: Quality control of rhFAPI-02 with RP-HPLC (10 to 90% B in 15 min): t_R = 8.10 min.

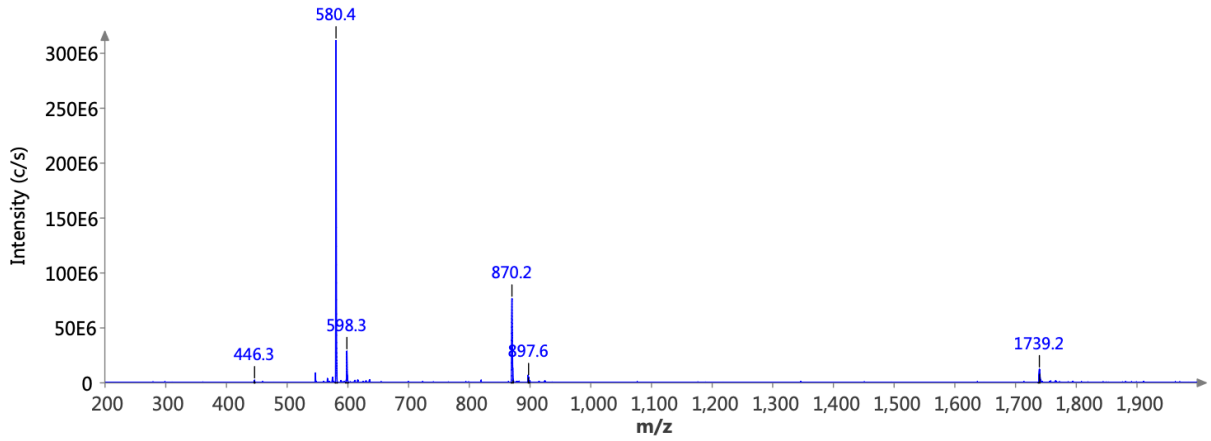

Supplemental Information 22: Mass spectrum of quality control of rhFAPI-02. ESI-MS: Calculated monoisotopic mass ($C_{78}H_{114}F_3N_{19}O_{21}Si$): 1737.82; found: m/z = 1739.2 $[M+H]^+$, 870.2 $[M+2H]^{2+}$, 580.4 $[M+3H]^{3+}$.

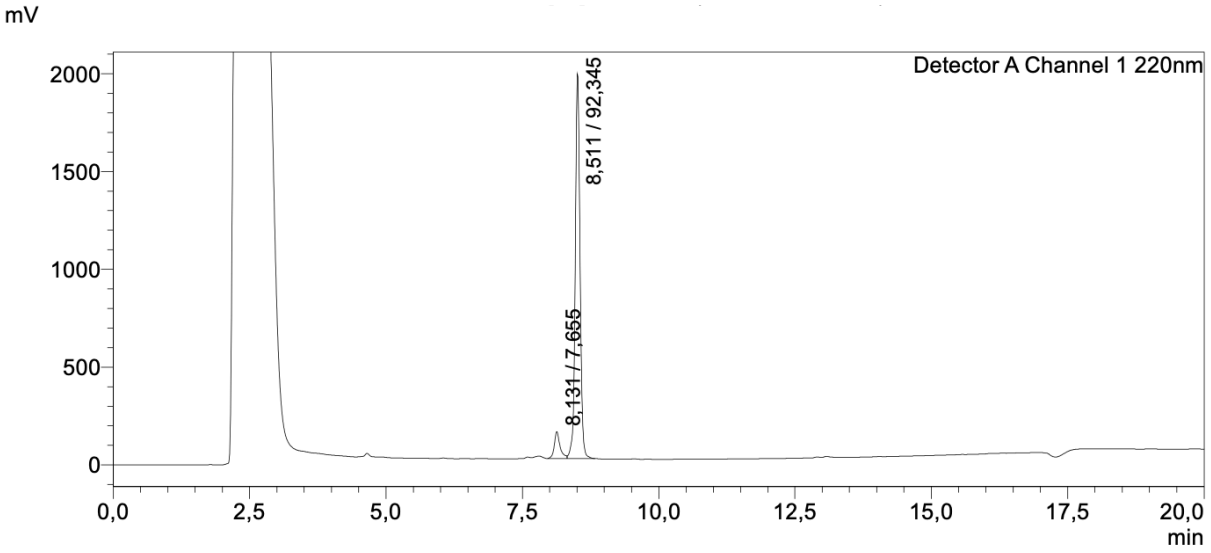

Supplemental Information 23: Quality control of [^{nat}Lu]Lu-rhFAPI-02 with RP-HPLC (10 to 90% B in 15 min): t_R = 8.51 min.

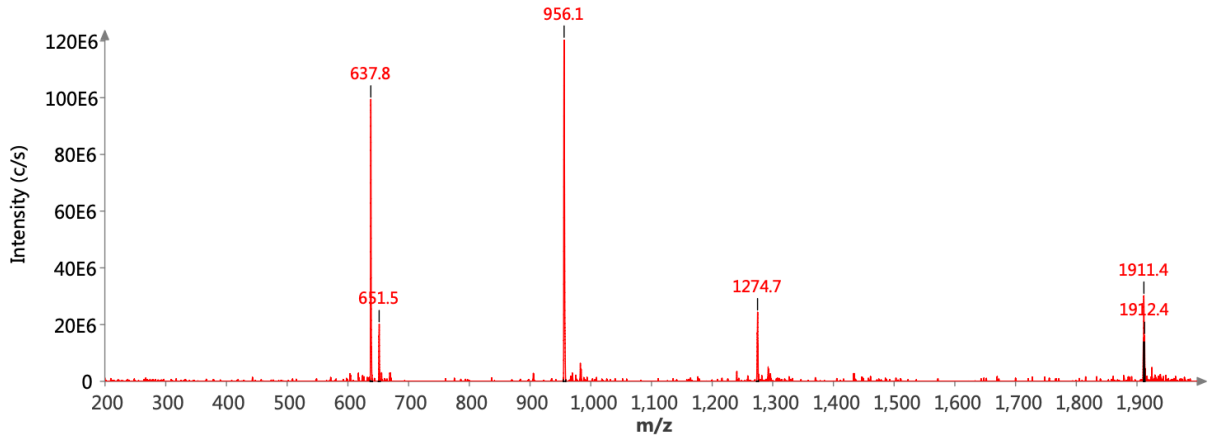

Supplemental Information 24: Mass spectrum of quality control of [^{nat}Lu]Lu-rhFAPI-02. ESI-MS: Calculated monoisotopic mass ($C_{78}H_{111}F_3LuN_{19}O_{21}Si$): 1909.73; found: m/z = 1911.4 $[M+H]^+$, 956.1 $[M+2H]^{2+}$, 637.8 $[M+3H]^{3+}$.

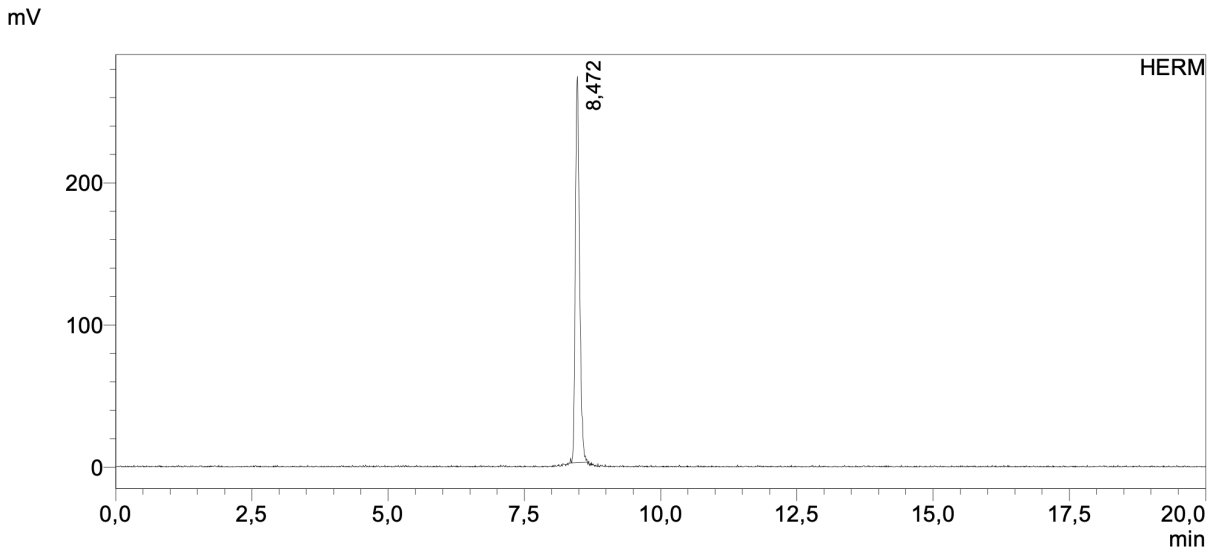

Supplemental Information 25: Quality control of [^{177}Lu]Lu-rhFAPI-02 with radio-HPLC (10 to 90% B in 15 min): t_R = 8.47 min.

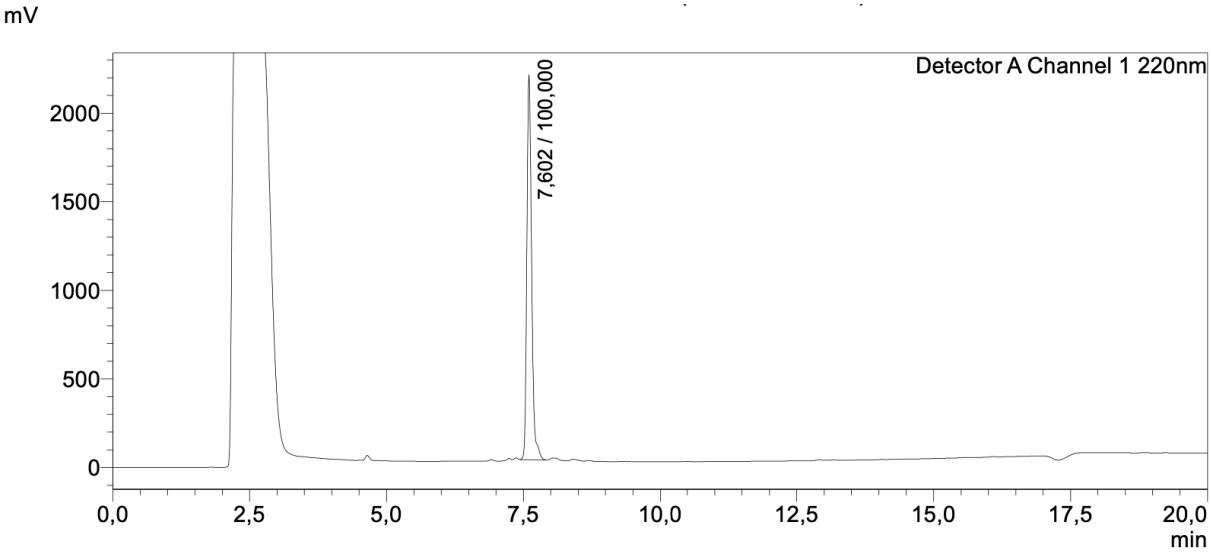

Supplemental Information 26: Quality control of rhFAPI-03 with RP-HPLC (10 to 90% B in 15 min): t_R = 7.60 min.

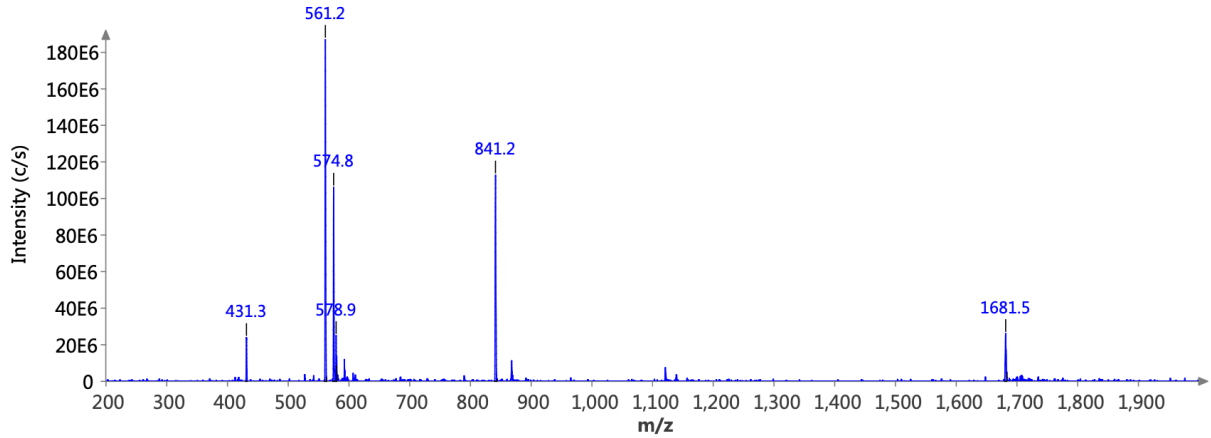

Supplemental Information 27: Mass spectrum of quality control of rhFAPI-03. ESI-MS: Calculated monoisotopic mass ($C_{78}H_{116}F_3N_{17}O_{19}Si$): 1679.84; found: m/z = 1681.5 $[M+H]^+$, 841.2 $[M+2H]^{2+}$, 561.2 $[M+3H]^{3+}$.

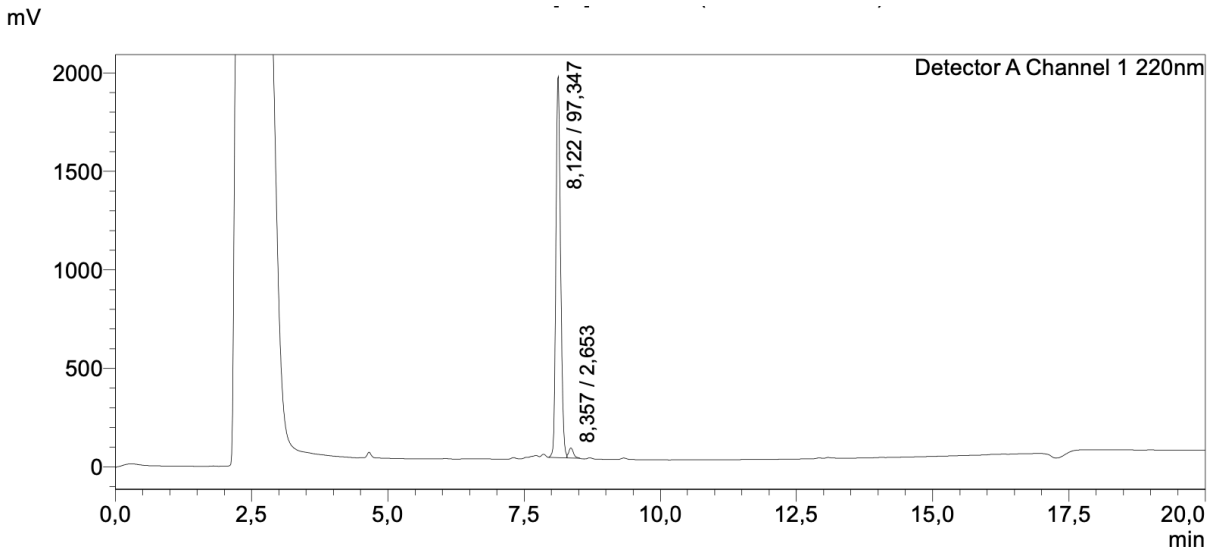

Supplemental Information 28: Quality control of [^{nat}Lu]Lu-rhFAPI-03 with RP-HPLC (10 to 90% B in 15 min): t_R = 8.12 min.

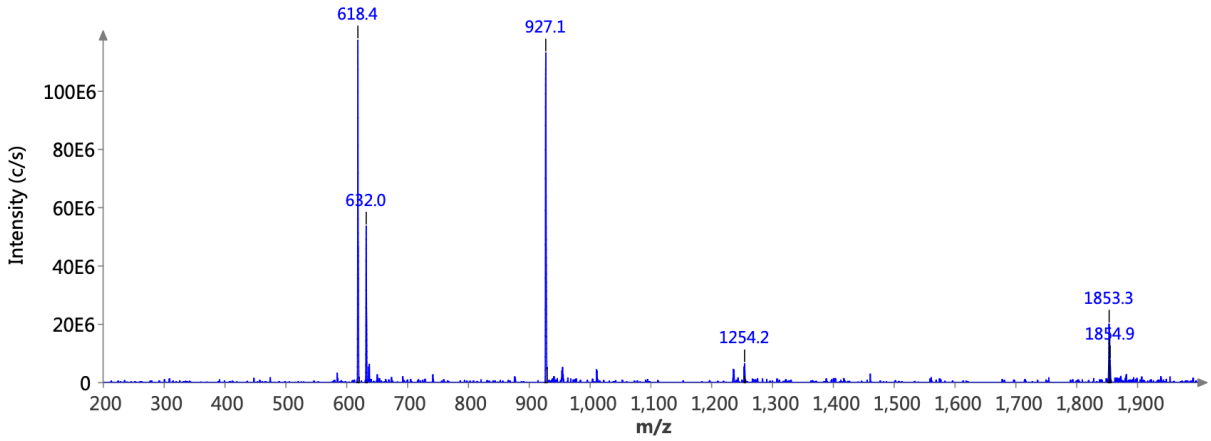

Supplemental Information 29: Mass spectrum of quality control of [^{nat}Lu]Lu-rhFAPI-03. ESI-MS: Calculated monoisotopic mass ($C_{76}H_{113}F_3LuN_{17}O_{19}Si$): 1851.75; found: m/z = 1853.3 $[M+H]^+$, 927.0 $[M+2H]^{2+}$, 618.4 $[M+3H]^{3+}$.

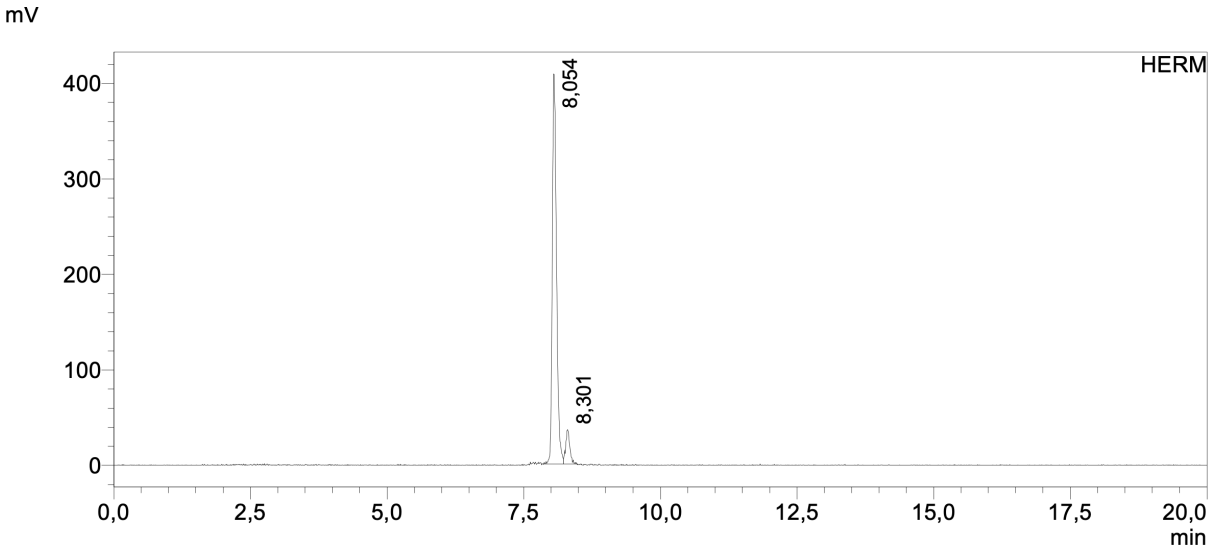

Supplemental Information 30: Quality control of [^{177}Lu]Lu-rhFAPI-03 with radio-HPLC (10 to 90% B in 15 min): t_R = 8.05 min.

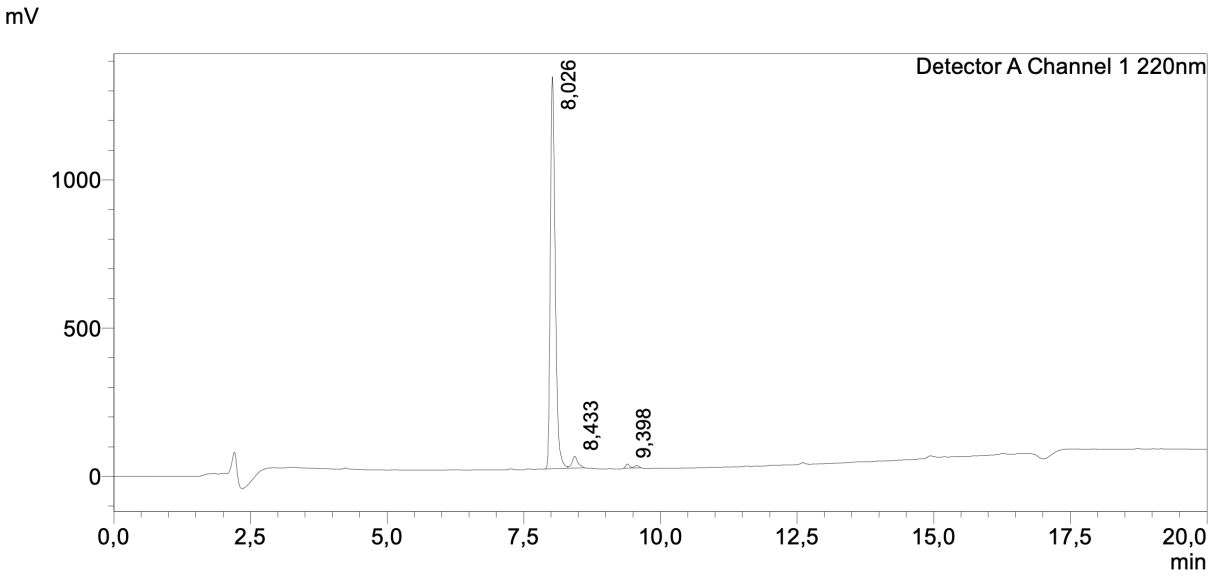

Supplemental Information 31: Quality control of rhFAPI-04 with RP-HPLC (10 to 90% B in 15 min): t_R = 8.03 min.

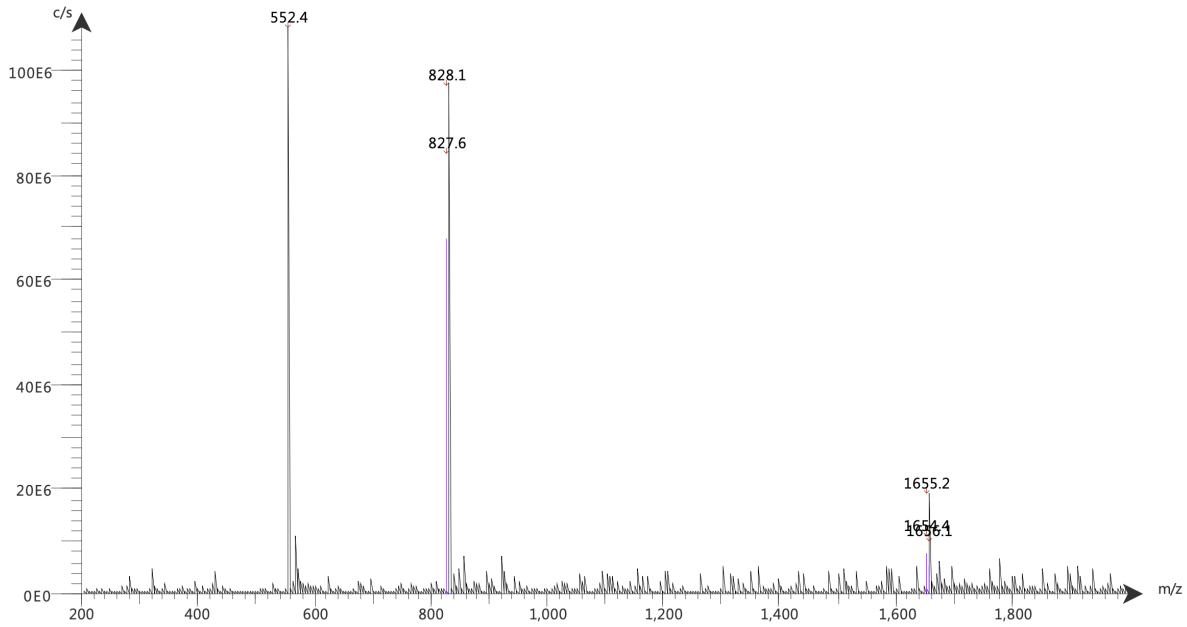

Supplemental Information 32: Mass spectrum of quality control of rhFAPI-04. ESI-MS: Calculated monoisotopic mass ($C_{74}H_{102}F_3N_{17}O_{23}Si$): 1653.7; found: m/z = 1655.2 $[M+H]^+$, 828.1 $[M+2H]^{2+}$, 552.4 $[M+3H]^{3+}$.

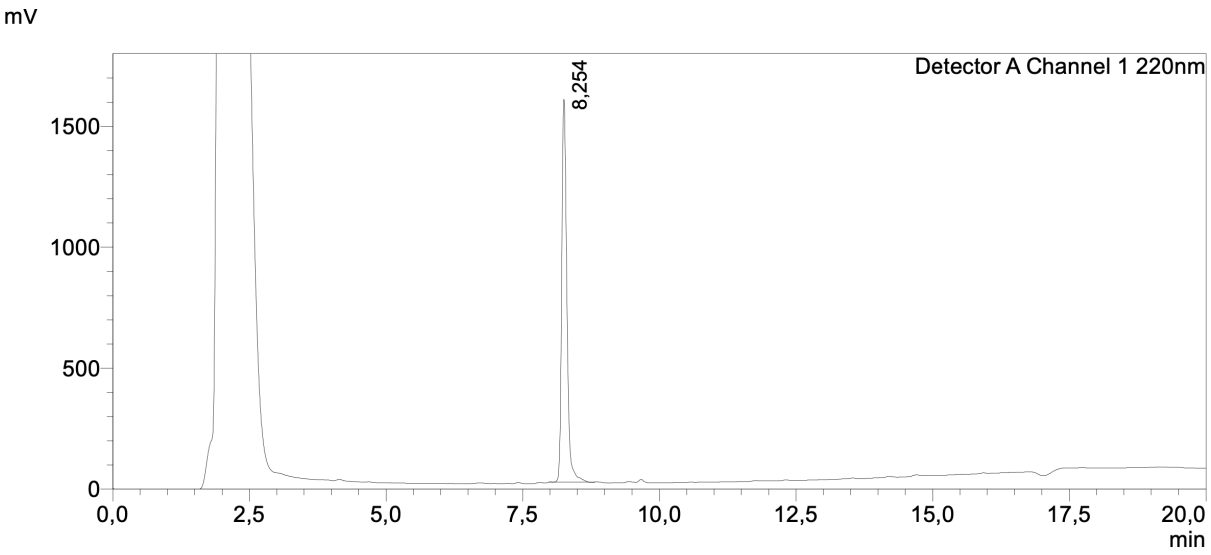

Supplemental Information 33: Quality control of [^{nat}Ga]Ga-rhFAPI-04 with RP-HPLC (10 to 90% B in 15 min): t_R = 8.25 min.

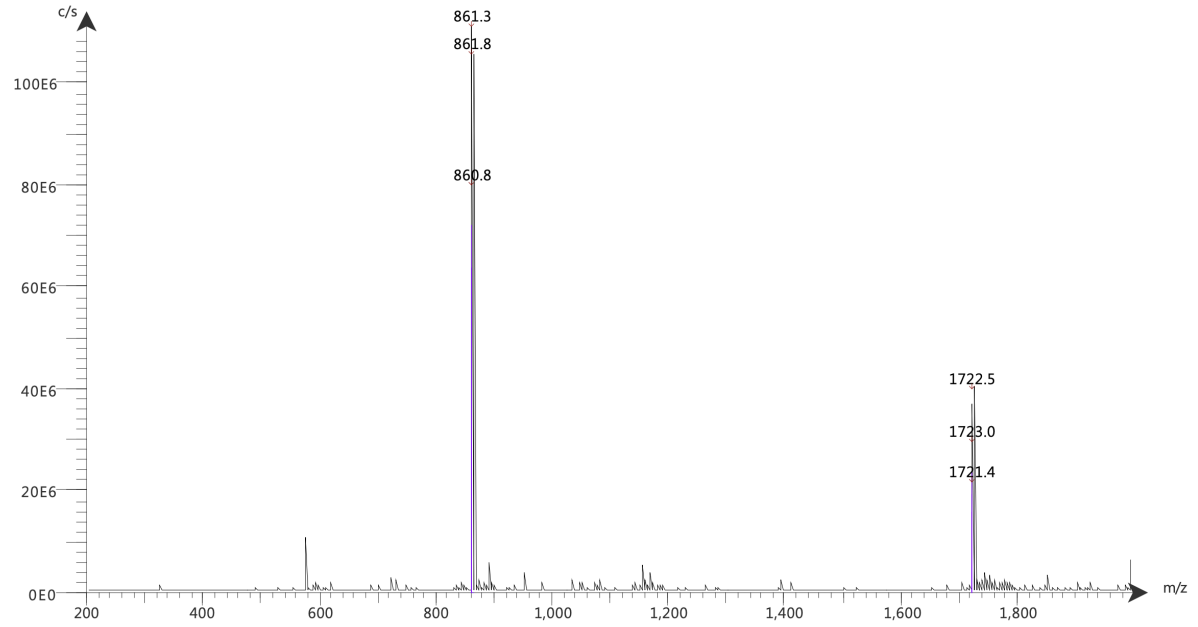

Supplemental Information 34: Mass spectrum of quality control of [^{nat}Ga]Ga-rhFAPI-04. ESI-MS: Calculated monoisotopic mass ($C_{74}H_{99}F_3GaN_{15}O_{23}Si$): 1721.49; found: m/z = 1722.5 $[M+H]^+$, 861.3 $[M+2H]^{2+}$.

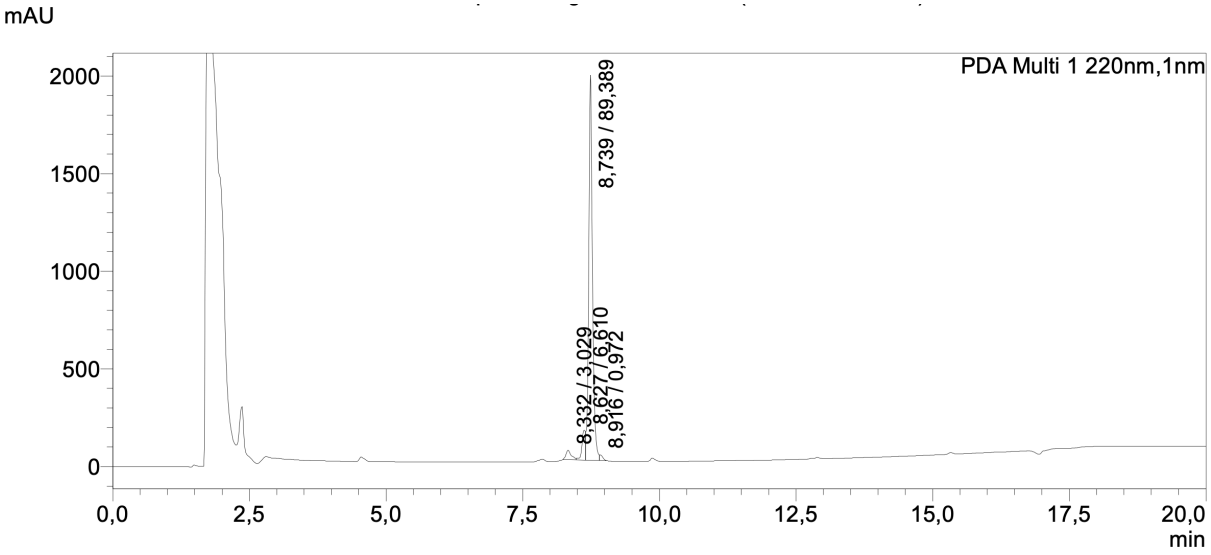

Supplemental Information 35: Quality control of [^{nat}Lu]Lu-rhFAPI-04 with RP-HPLC (10 to 90% B in 15 min): t_R = 8.74 min.

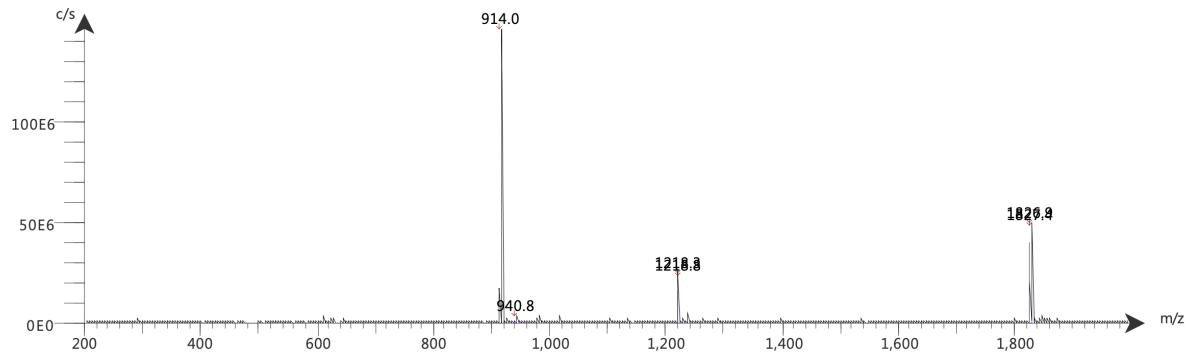

Supplemental Information 36: Mass spectrum of quality control of [^{nat}Lu]Lu-rhFAPI-04. ESI-MS: Calculated monoisotopic mass ($C_{74}H_{99}F_3LuN_{15}O_{23}Si$): 1825.49; found: m/z = 1826.5 $[M+H]^+$, 913.7 $[M+2H]^{2+}$.

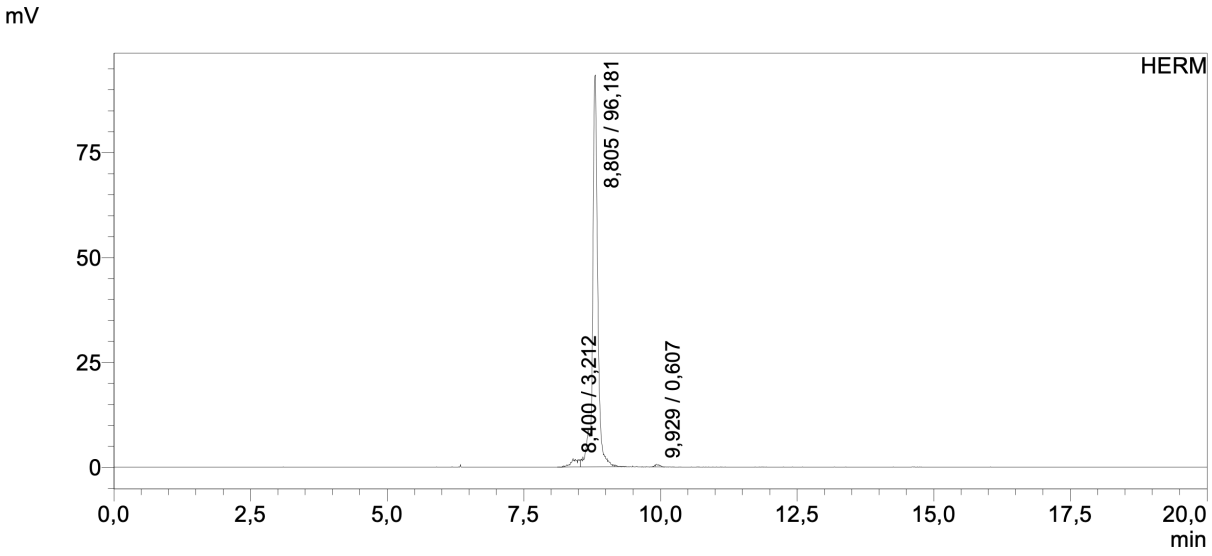

Supplemental Information 37: Quality control of [^{18}F]F-Lu-rhFAPI-04 with radio-HPLC (10 to 90% B in 15 min): t_R = 8.81 min.

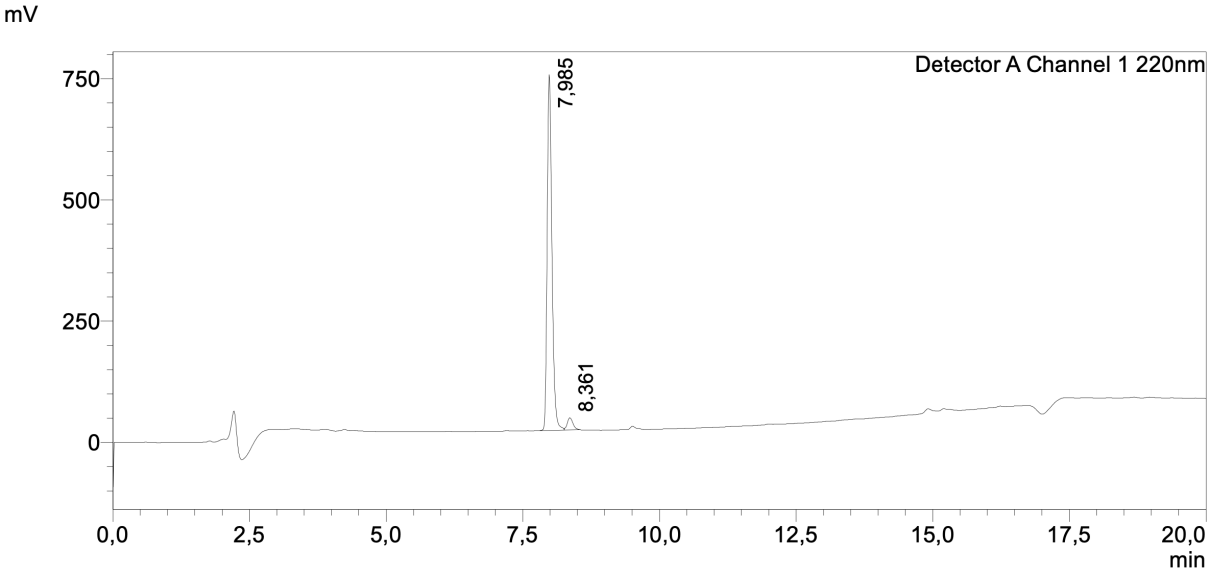

Supplemental Information 38: Quality control of rhFAPI-04+E with RP-HPLC (10 to 90% B in 15 min): t_R = 7.99 min.

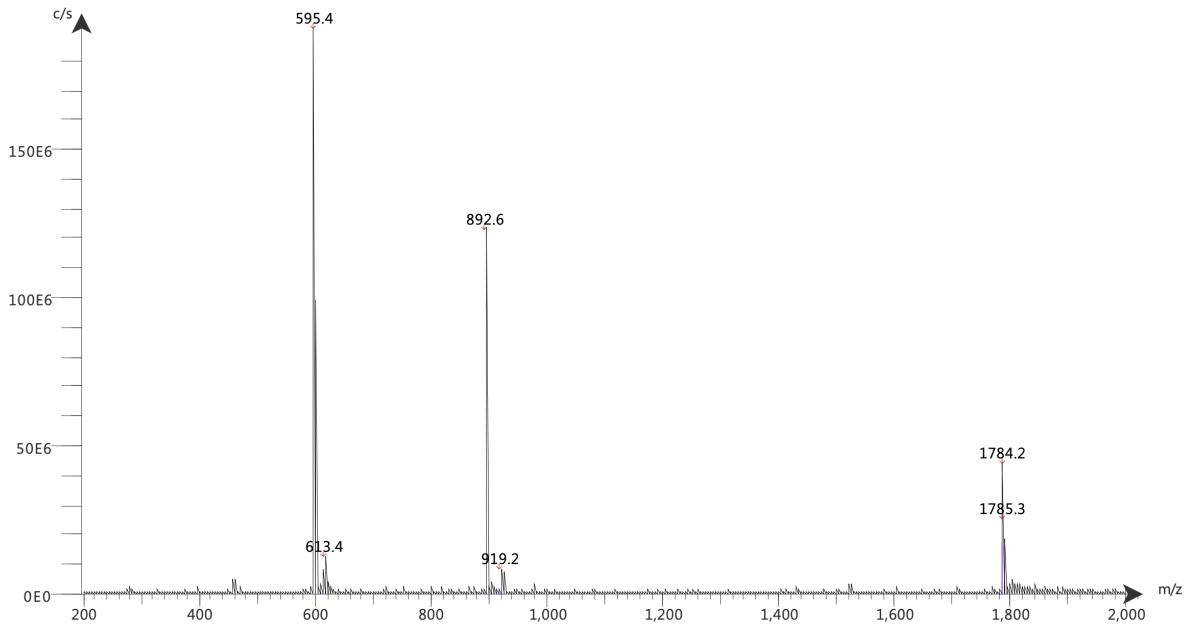

Supplemental Information 39: Mass spectrum of quality control of rhFAPI-04+E. ESI-MS: Calculated monoisotopic mass ($C_{79}H_{109}F_3N_{16}O_{26}Si$): 1782.74; found: m/z = 1784.2 $[M+H]^+$, 892.6 $[M+2H]^{2+}$, 595.4 $[M+3H]^{3+}$.

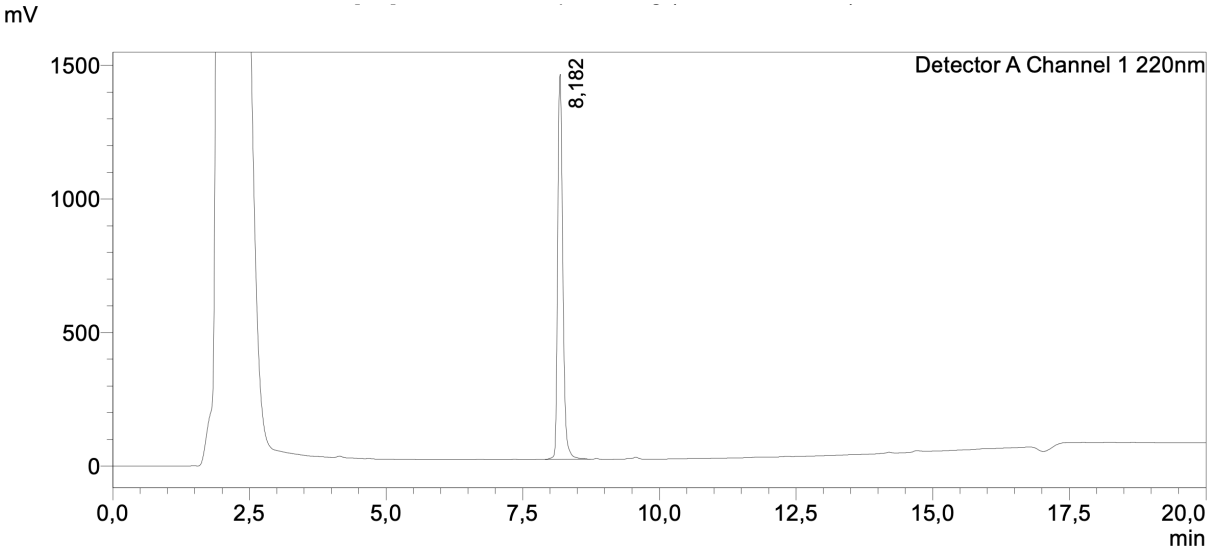

Supplemental Information 40: Quality control of [^{nat}Ga]Ga-rhFAPI-04+E with RP-HPLC (10 to 90% B in 15 min): t_R = 8.18 min.

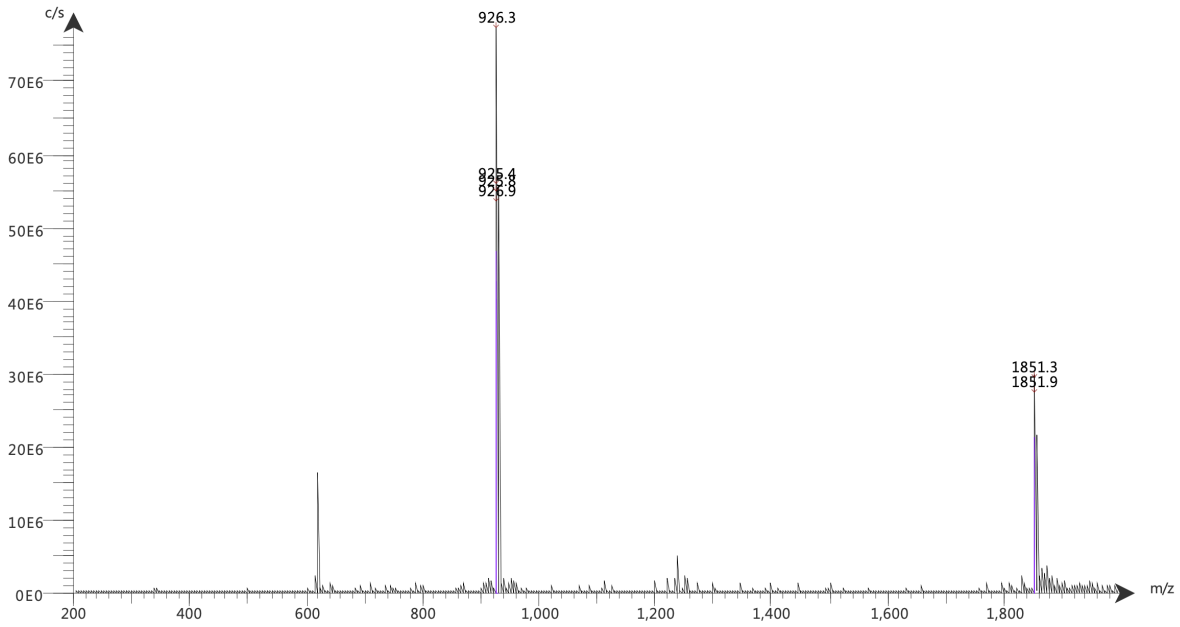

Supplemental Information 41: Mass spectrum of quality control of [^{nat}Ga]Ga-rhFAPI-04+E. ESI-MS: Calculated monoisotopic mass ($C_{79}H_{106}F_3GaN_{16}O_{26}Si$): 1850.61; found: m/z = 1851.3 $[M+H]^+$, 926.3 $[M+2H]^{2+}$.

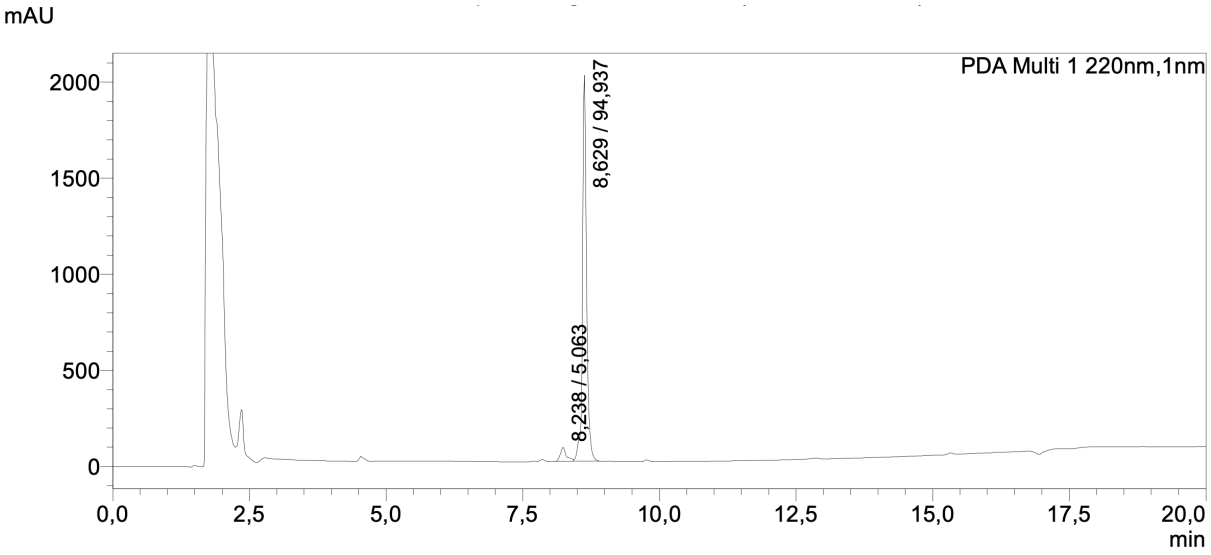

Supplemental Information 42: Quality control of [^{nat}Lu]Lu-rhFAPI-04+E with RP-HPLC (10 to 90% B in 15 min): t_R = 8.63 min.

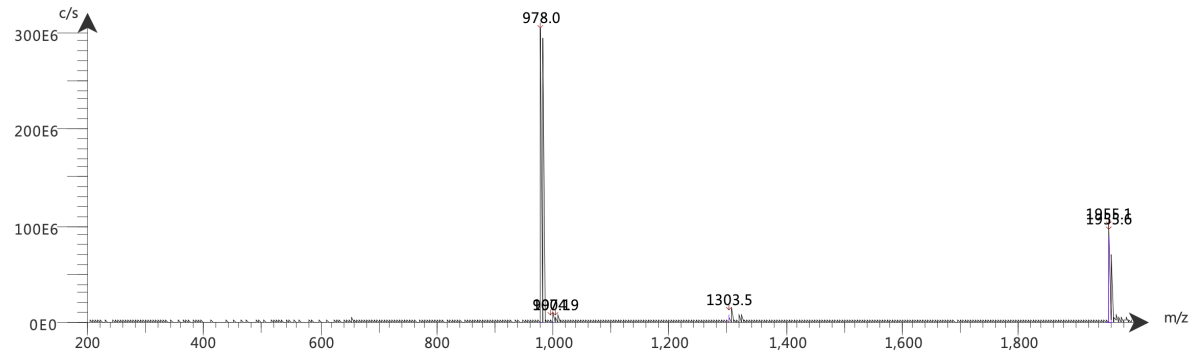

Supplemental Information 43: Mass spectrum of quality control of [^{nat}Ga]Ga-rhFAPI-04+E. ESI-MS: Calculated monoisotopic mass ($C_{79}H_{106}F_3GaN_{16}O_{26}Si$): 1955.85; found: m/z = 1956.2 $[M+H]^+$, 978.5 $[M+2H]^{2+}$.

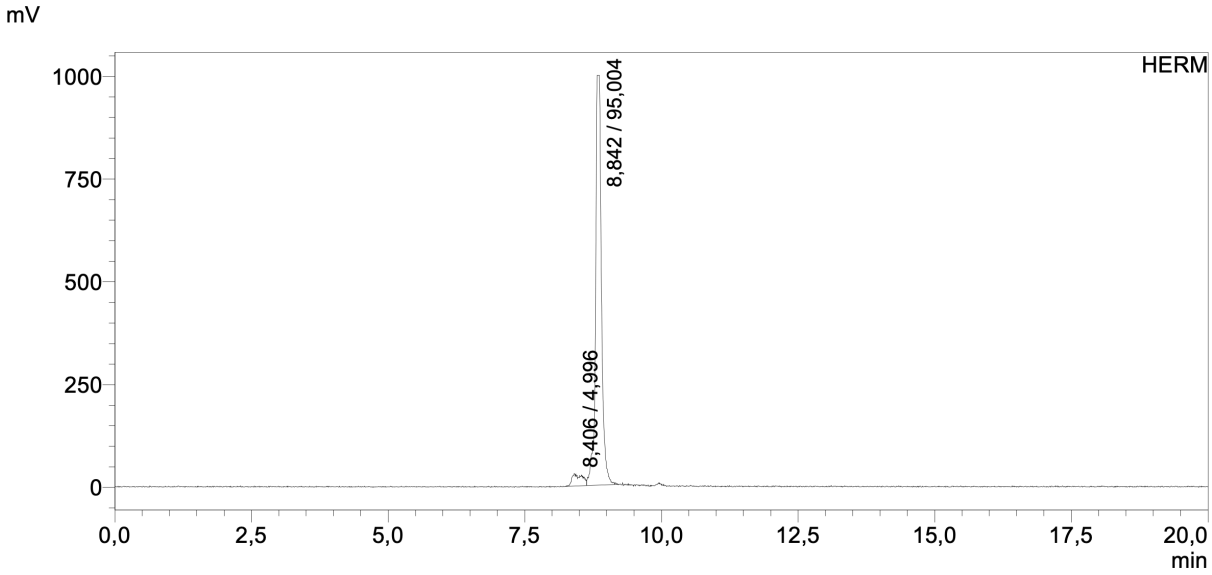

Supplemental Information 44: Quality control of [^{177}Lu]Lu-rhFAPI-04+E with radio-HPLC (10 to 90% B in 15 min): t_R = 8.84 min.

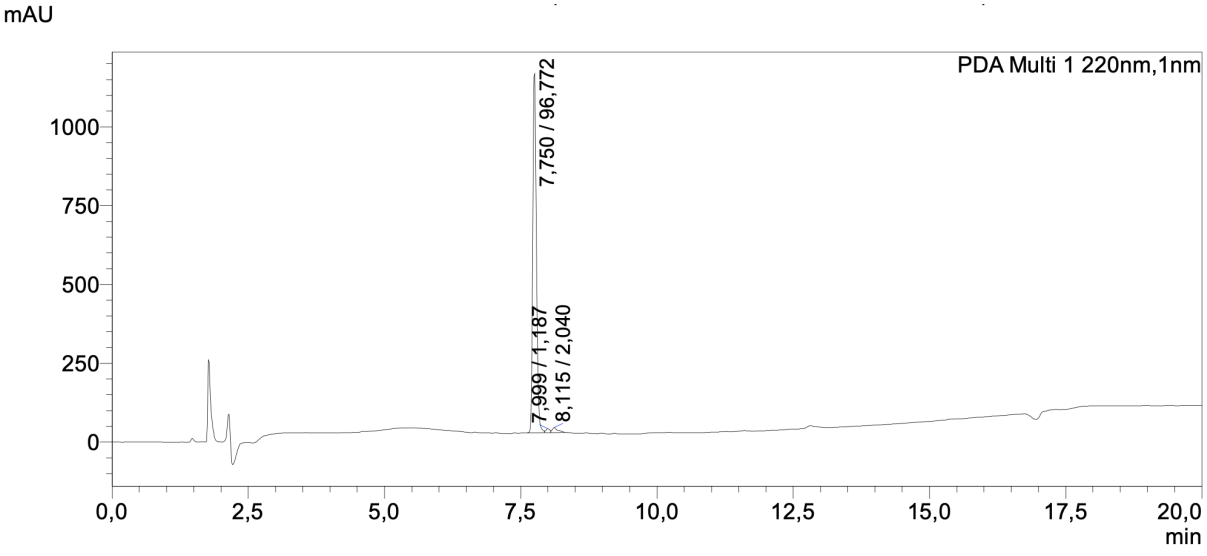

Supplemental Information 45: Quality control of rhFAPI-05 with RP-HPLC (10 to 90% B in 15 min): t_R = 7.75 min.

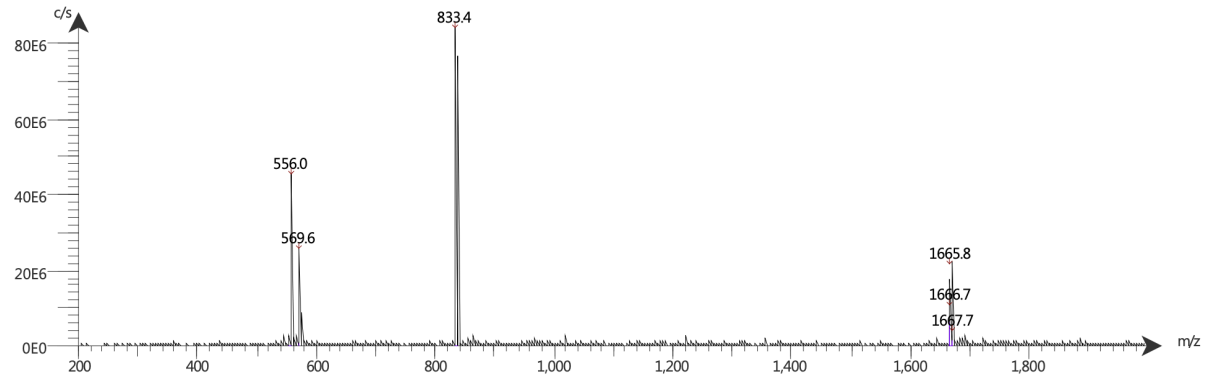

Supplemental Information 46: Mass spectrum of quality control of rhFAPI-05. ESI-MS: Calculated monoisotopic mass ($C_{77}H_{115}F_3N_{18}O_{18}Si$): 1664.84; found: m/z = 1666.7 $[M+H]^+$, 833.4 $[M+2H]^{2+}$, 556.0 $[M+3H]^{3+}$.

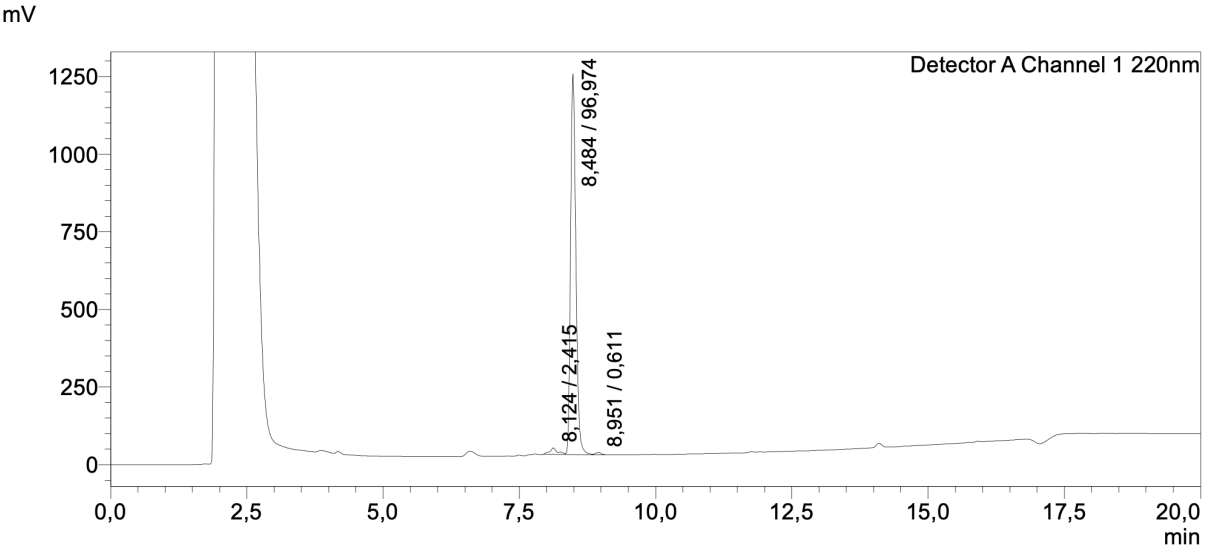

Supplemental Information 47: Quality control of [^{nat}Lu]Lu-rhFAPI-05 with RP-HPLC (10 to 90% B in 15 min): t_R = 8.48 min.

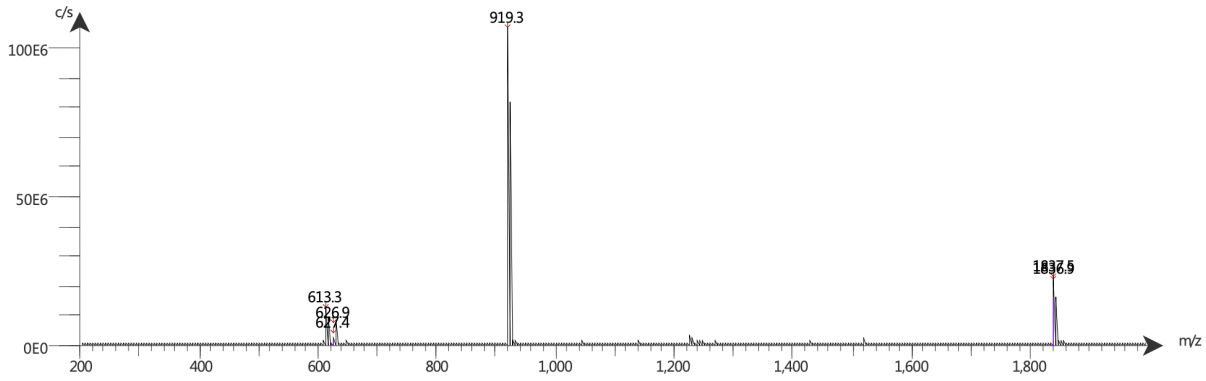

Supplemental Information 48: Mass spectrum of quality control of [^{nat}Lu]Lu-rhFAPI-05. ESI-MS: Calculated monoisotopic mass ($C_{77}H_{112}F_3LuN_{18}O_{18}Si$): 1835.75; found: m/z = 1836.9 $[M+H]^+$, 919.3 $[M+2H]^{2+}$, 613.3 $[M+3H]^{3+}$.

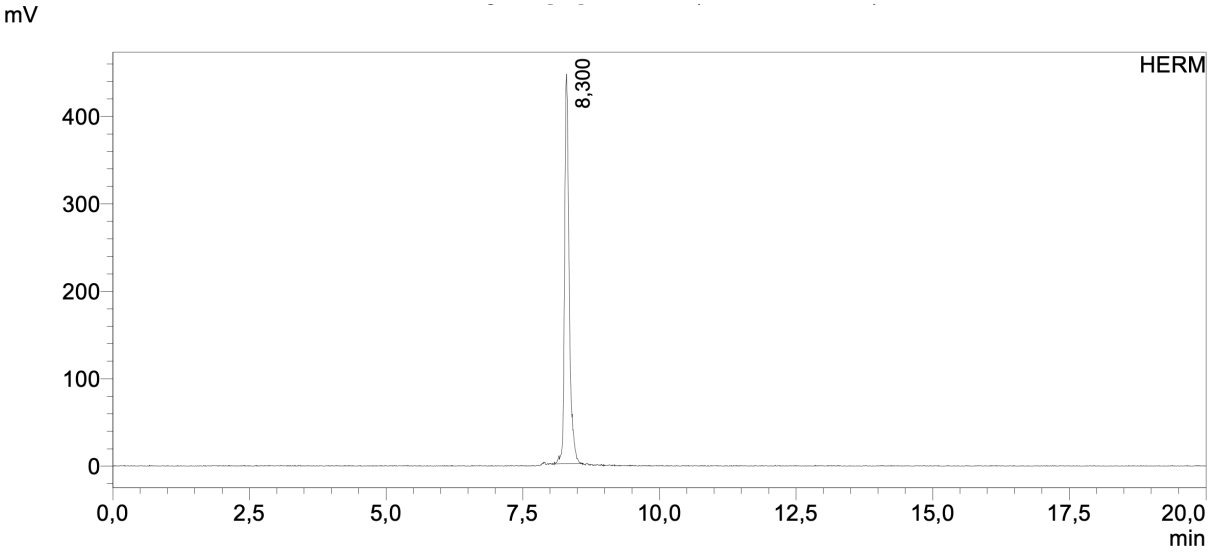

Supplemental Information 49: Quality control of [^{18}F]F-Lu-rhFAPI-05 with radio-HPLC (10 to 90% B in 15 min): t_R = 8.30 min.

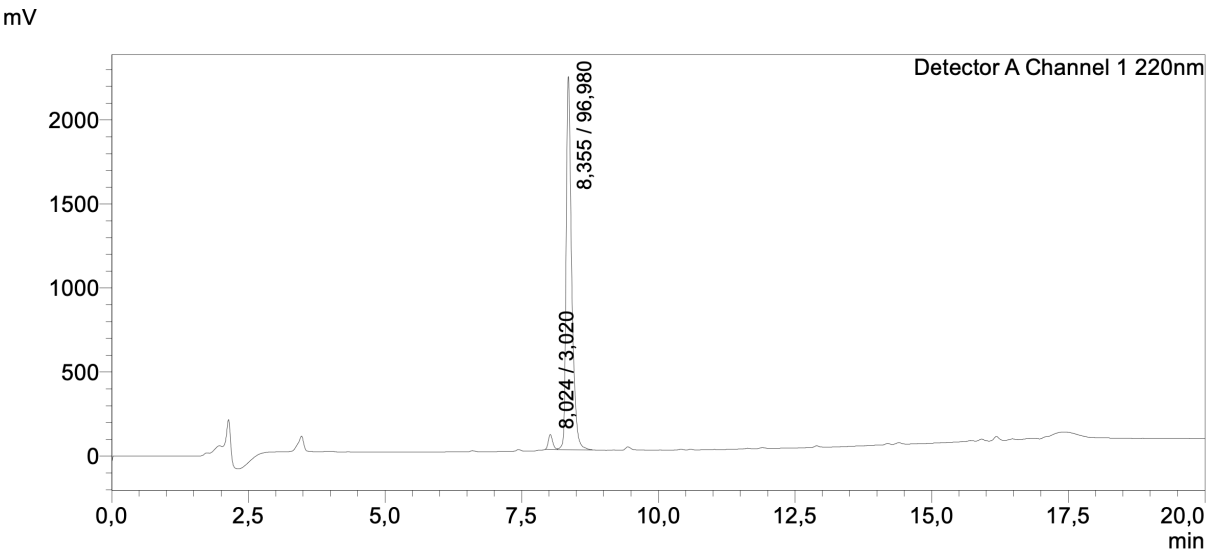

Supplemental Information 50: Quality control of rhFAPI-06 with RP-HPLC (10 to 90% B in 15 min): t_R = 8.36 min.

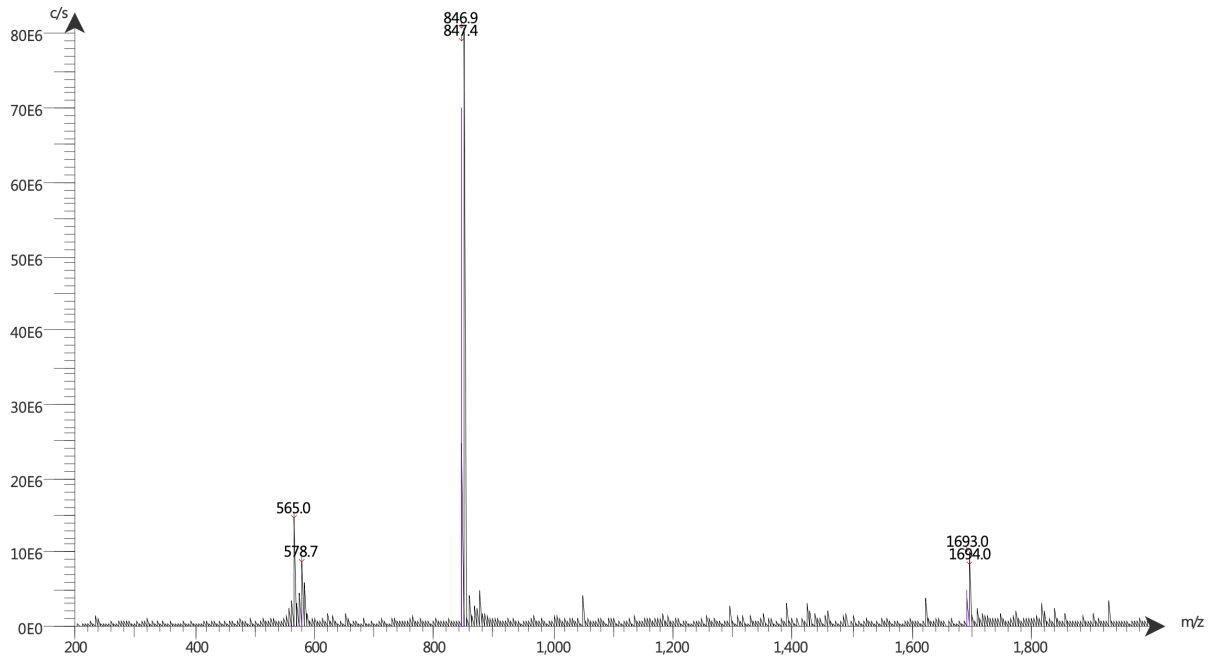

Supplemental Information 51: Mass spectrum of quality control of rhFAPI-06. ESI-MS: Calculated monoisotopic mass ($C_{77}H_{114}F_3N_{19}O_{19}Si$): 1693.83; found: m/z = 847.9 $[M+2H]^{2+}$, 565.9 $[M+3H]^{3+}$.

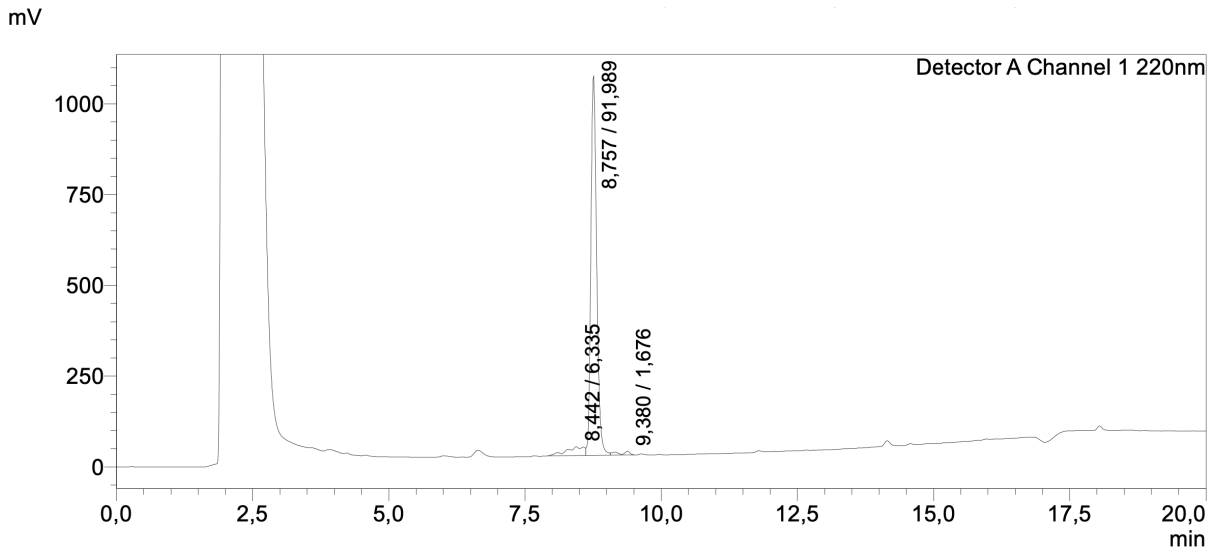

Supplemental Information 52: Quality control of [^{nat}Lu]Lu-rhFAPI-06 with RP-HPLC (10 to 90% B in 15 min): t_R = 8.76 min.

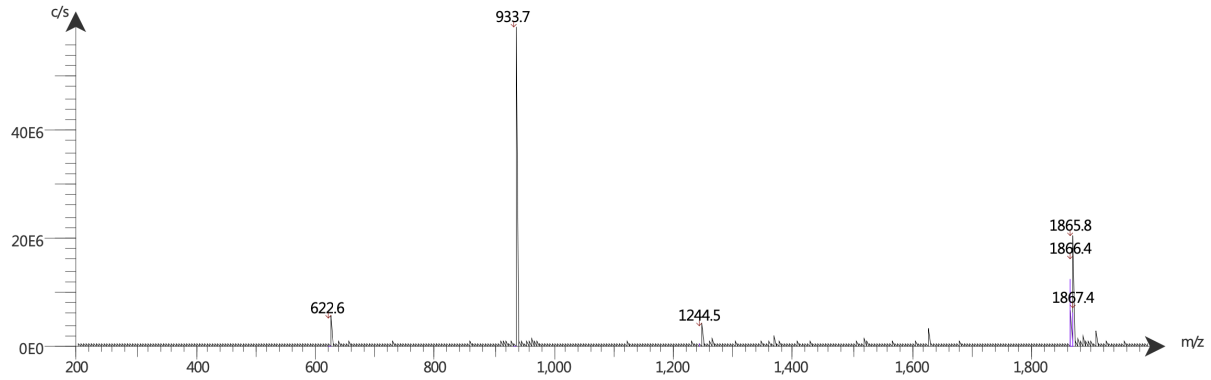

Supplemental Information 53: Mass spectrum of quality control of [^{nat}Lu]Lu-rhFAPI-06. ESI-MS: Calculated monoisotopic mass ($C_{77}H_{111}F_3LuN_{19}O_{19}Si$): 1865.90; found: m/z = 1865.8 $[M+H]^+$, 933.7 $[M+2H]^{2+}$, 622.6 $[M+3H]^{3+}$.

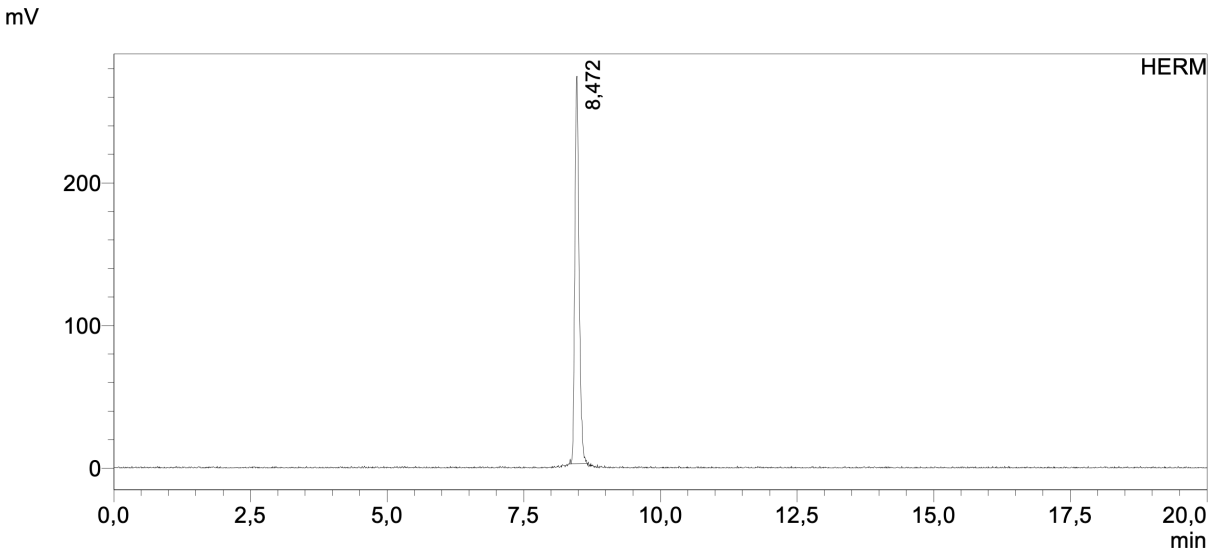

Supplemental Information 54: Quality control of [^{18}F]F-Lu-rhFAPI-06 with radio-HPLC (10 to 90% B in 15 min): t_R = 8.47 min.

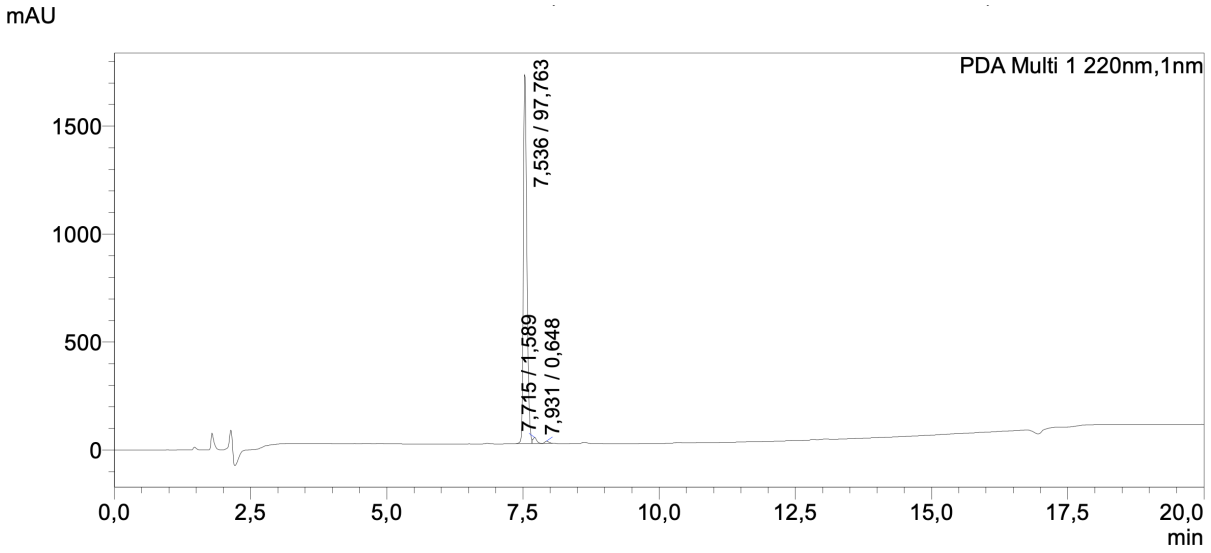

Supplemental Information 55: Quality control of rhFAPI-07 with RP-HPLC (10 to 90% B in 15 min): t_R = 7.54 min.

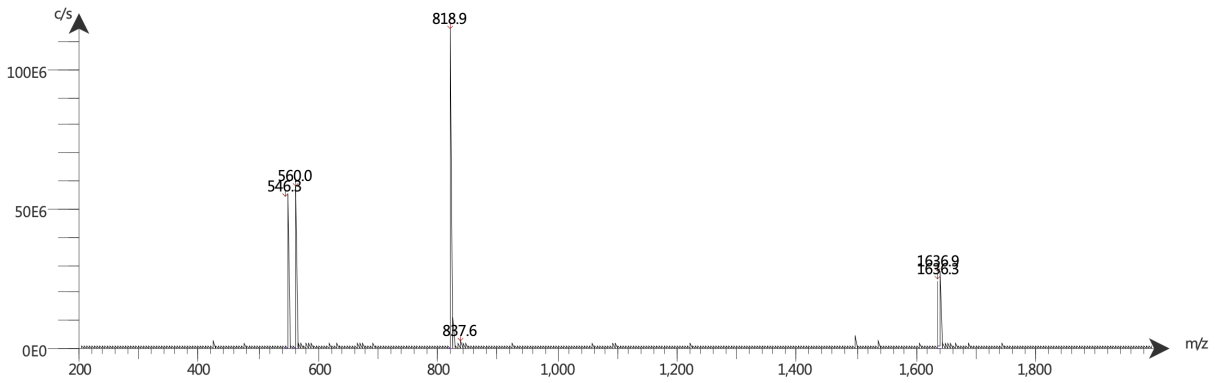

Supplemental Information 56: Mass spectrum of quality control of rhFAPI-07. ESI-MS: Calculated monoisotopic mass ($C_{77}H_{116}F_3N_{17}O_{17}Si$): 1635.85; found: m/z = 1636.9 $[M+H]^+$, 818.9 $[M+2H]^{2+}$, 546.3 $[M+3H]^{3+}$.

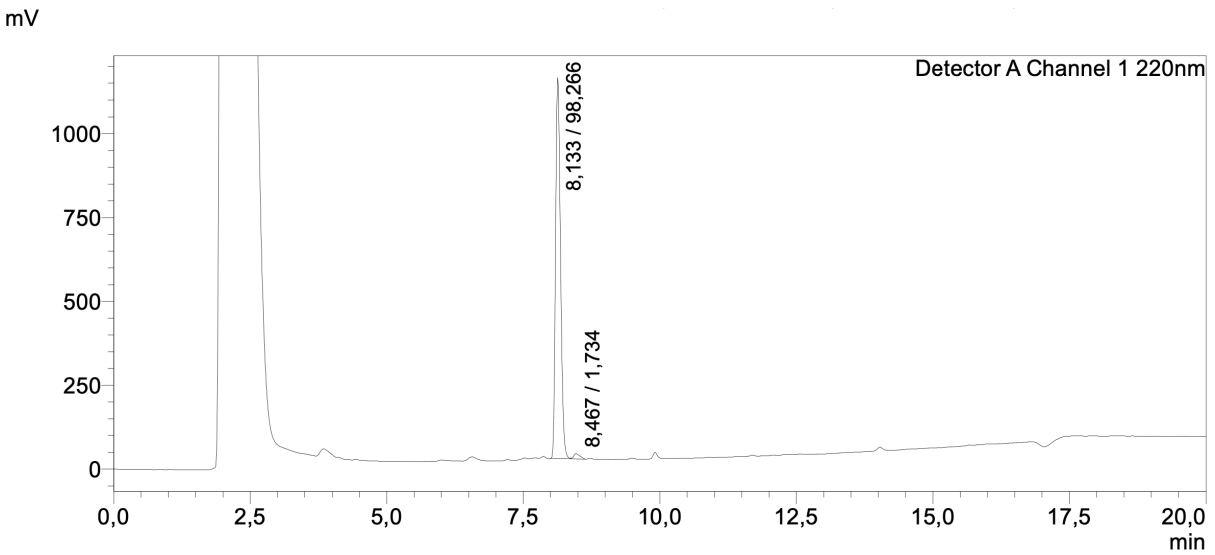

Supplemental Information 57: Quality control of [^{nat}Lu]Lu-rhFAPI-07 with RP-HPLC (10 to 90% B in 15 min): t_R = 8.13 min.

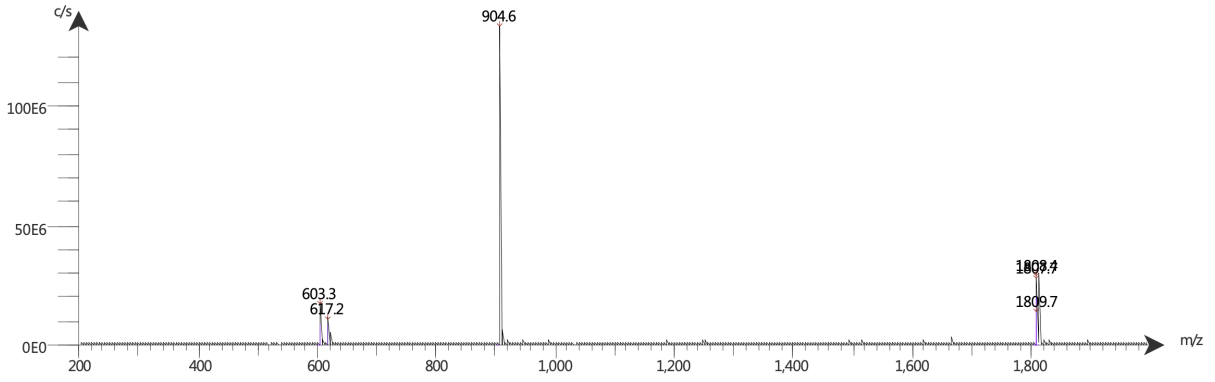

Supplemental Information 58: Mass spectrum of quality control of [^{nat}Lu]Lu-rhFAPI-07. ESI-MS: Calculated monoisotopic mass ($C_{77}H_{113}F_3LuN_{17}O_{17}Si$): 1807.90; found: m/z = 1807.7 $[M+H]^+$, 904.6 $[M+2H]^{2+}$, 603.3 $[M+3H]^{3+}$.

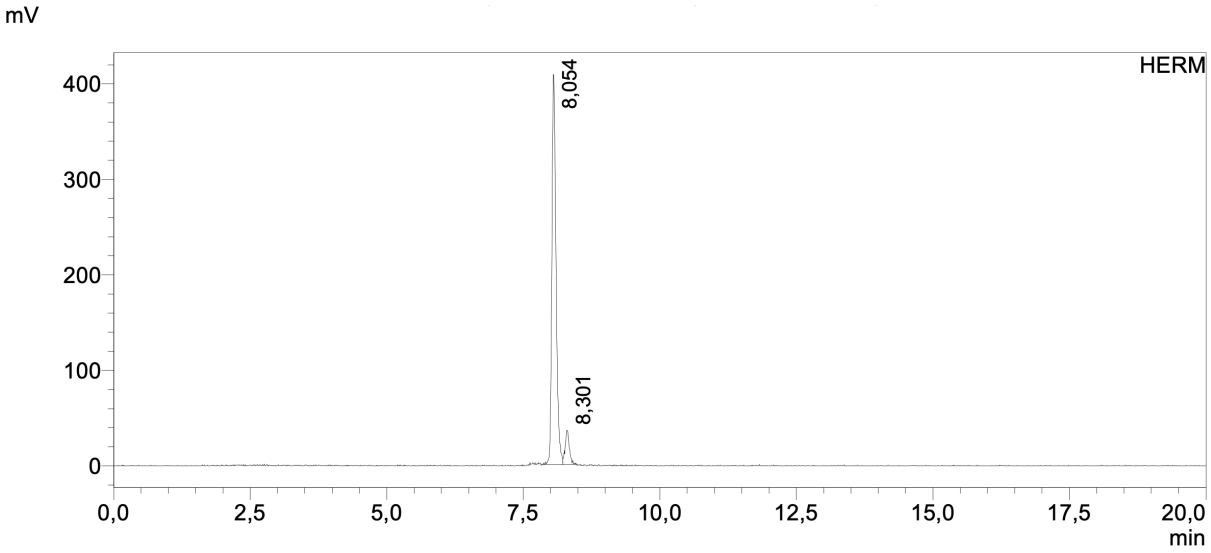

Supplemental Information 59: Quality control of [^{18}F]F-Lu-rhFAPI-07 with radio-HPLC (10 to 90% B in 15 min): t_R = 8.05 min.

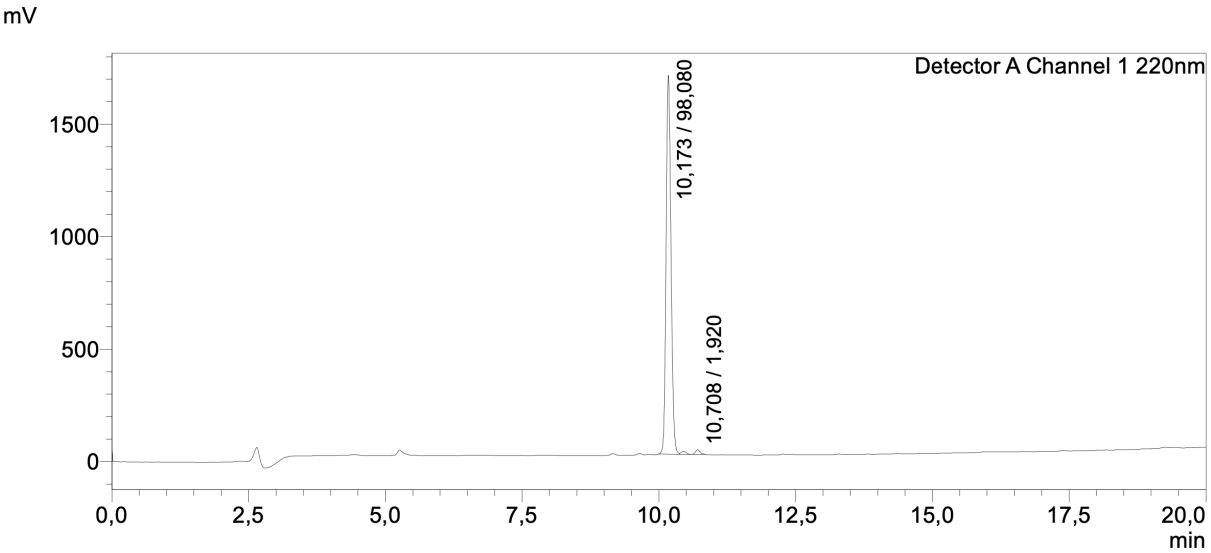

Supplemental Information 60: Quality control of rhFAPI-08 with RP-HPLC (10 to 90% B in 15 min): t_R = 10.17 min.

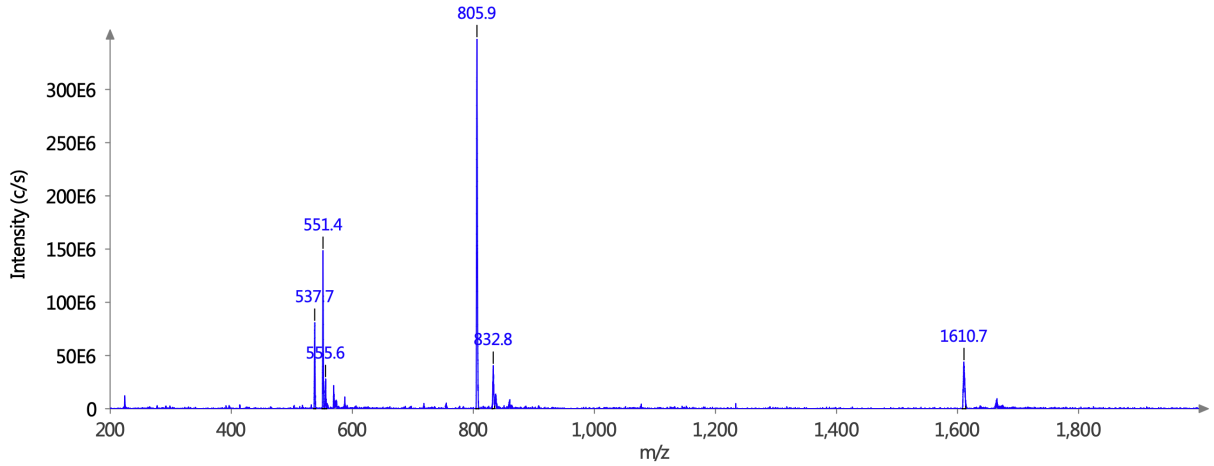

Supplemental Information 61: Mass spectrum of quality control of rhFAPI-08. ESI-MS: Calculated monoisotopic mass ($C_{73}H_{102}F_3N_{15}O_{21}Si$): 1609.71; found: m/z = 1610.8 $[M+H]^+$, 805.7 $[M+2H]^{2+}$.

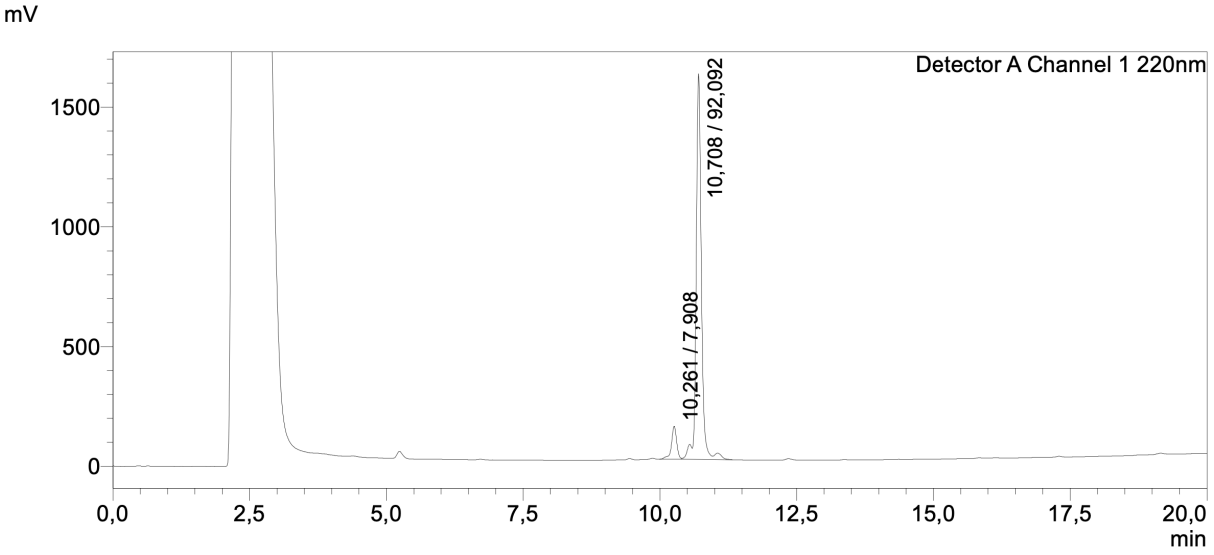

Supplemental Information 62: Quality control of [^{nat}Lu]Lu-rhFAPI-08 with RP-HPLC (10 to 90% B in 15 min): t_R = 10.71 min.

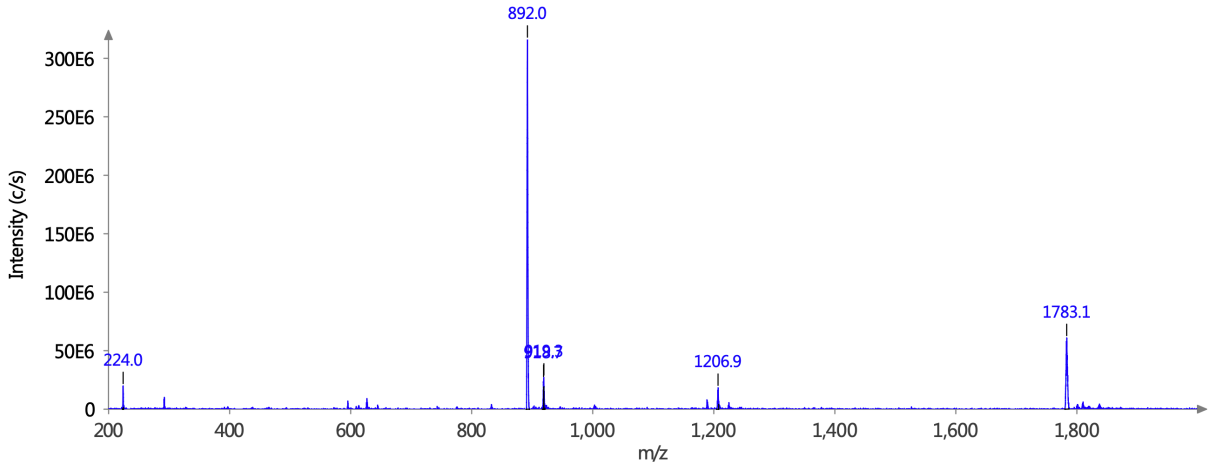

Supplemental Information 63: Mass spectrum of quality control of [^{nat}Lu]Lu-rhFAPI-08. ESI-MS: Calculated monoisotopic mass ($C_{73}H_{99}F_3LuN_{15}O_{21}Si$): 1781.63; found: m/z = 1783.1 $[M+H]^+$, 892.0 $[M+2H]^{2+}$.

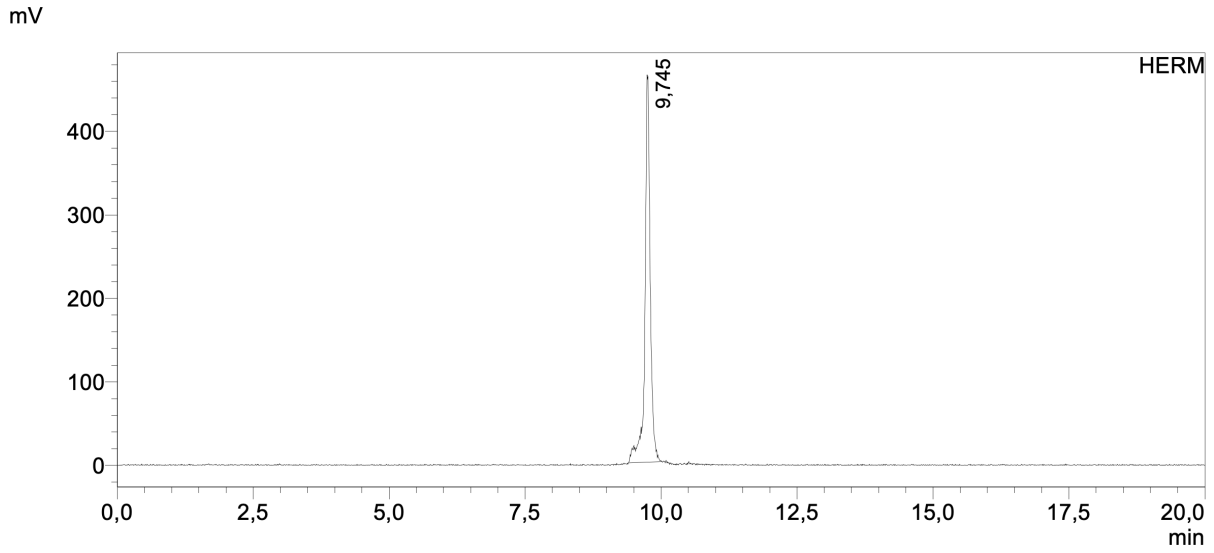

Supplemental Information 64: Quality control of [^{177}Lu]Lu-rhFAPI-08 with radio-HPLC (10 to 90% B in 15 min): t_R = 9.75 min.

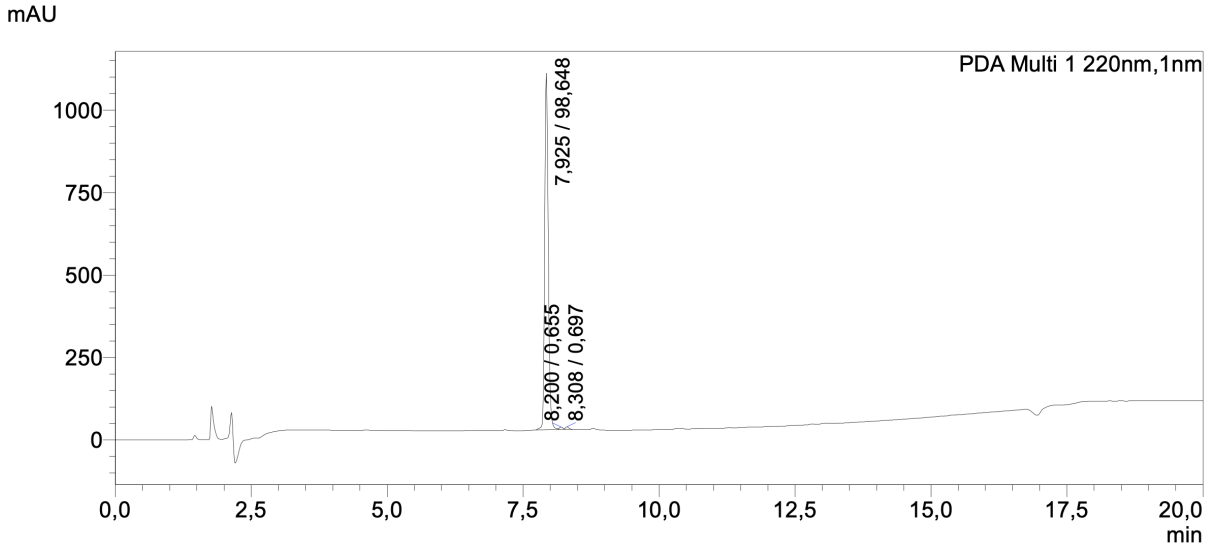

Supplemental Information 65: Quality control of rhFAPI-09 with RP-HPLC (10 to 90% B in 15 min): t_R = 7.93 min.

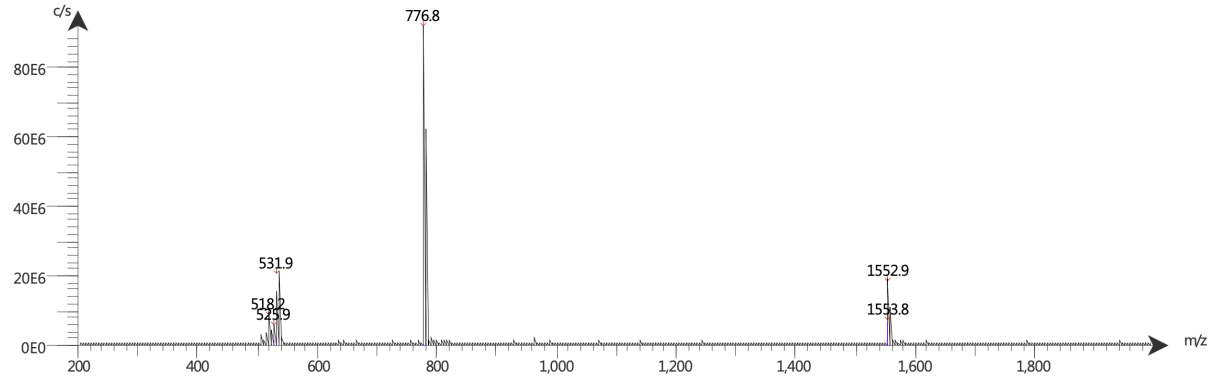

Supplemental Information 66: Mass spectrum of quality control of rhFAPI-09. ESI-MS: Calculated monoisotopic mass ($C_{71}H_{104}F_3N_{17}O_{17}Si$): 1551.75; found: m/z = 1552.9 $[M+H]^+$, 776.8 $[M+2H]^{2+}$, 531.9 $[M+3H]^{3+}$.

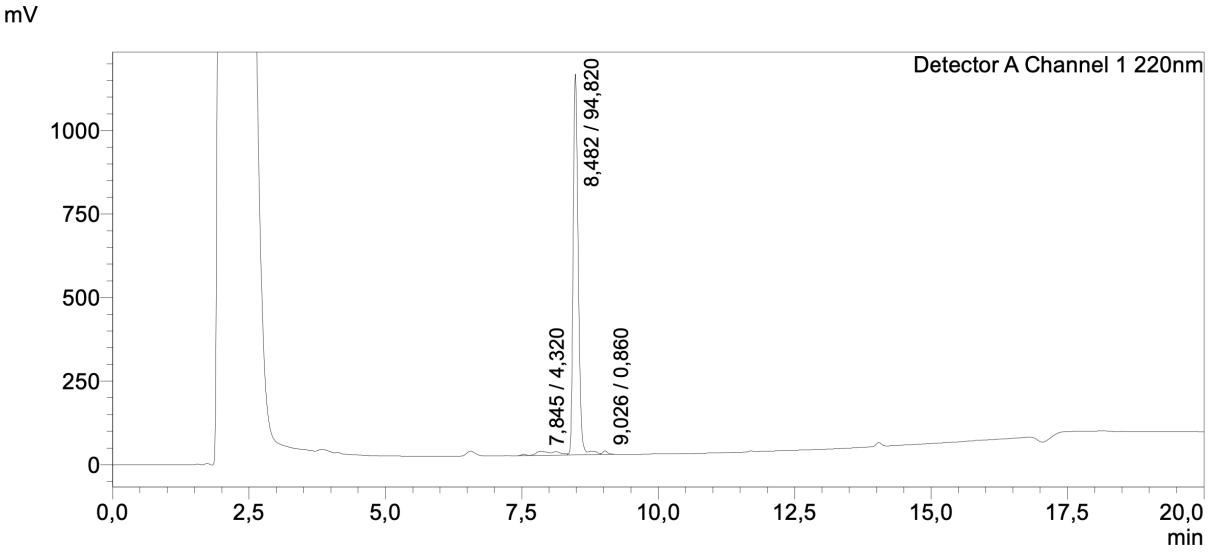

Supplemental Information 67: Quality control of [^{nat}Lu]Lu-rhFAPI-09 with RP-HPLC (10 to 90% B in 15 min): t_R = 8.48 min.

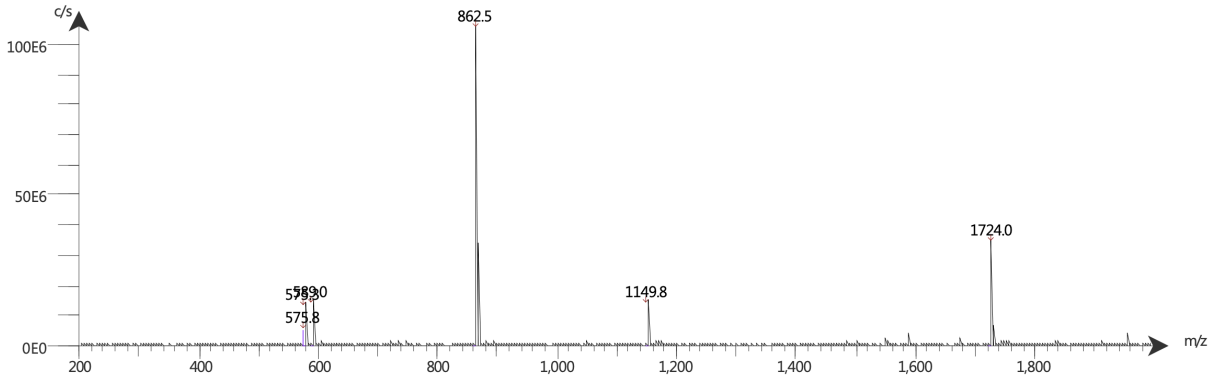

Supplemental Information 68: Mass spectrum of quality control of [^{nat}Lu]Lu-rhFAPI-09. ESI-MS: Calculated monoisotopic mass ($C_{71}H_{101}F_3LuN_{17}O_{17}Si$): 1723.74; found: m/z = 1724.0 $[M+H]^+$, 862.5 $[M+2H]^{2+}$, 575.3 $[M+3H]^{3+}$.

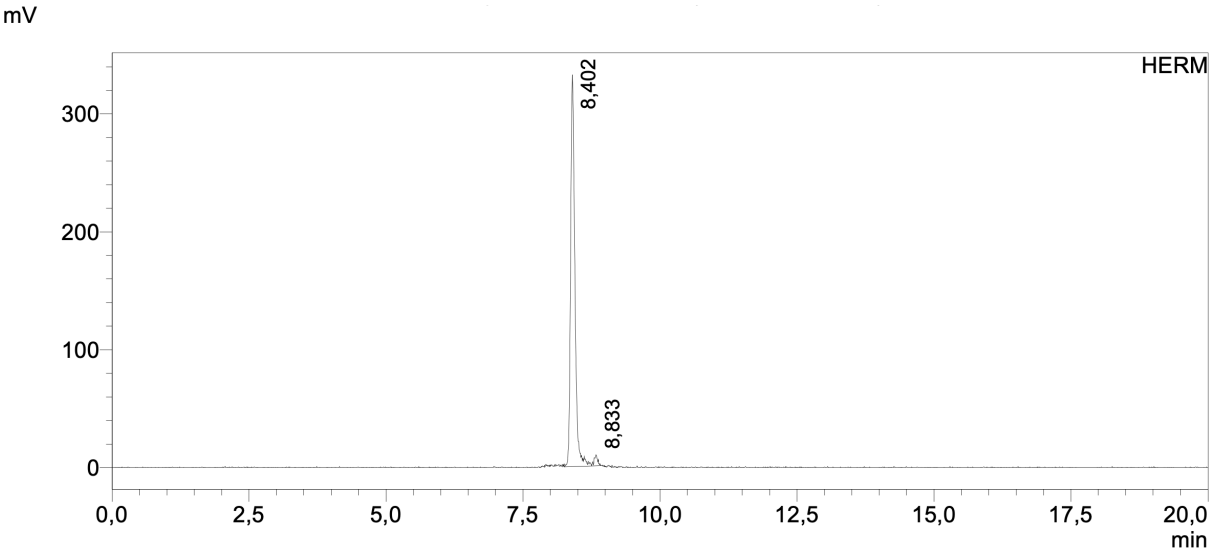

Supplemental Information 69: Quality control of [^{177}Lu]Lu-rhFAPI-09 with radio-HPLC (10 to 90% B in 15 min): t_R = 9.64 min.

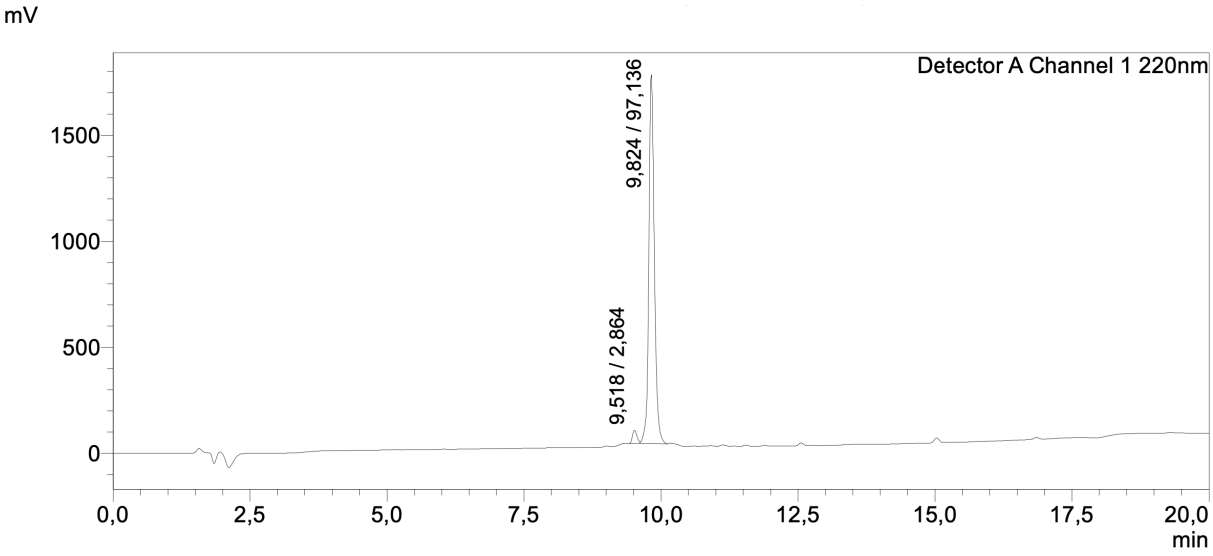

Supplemental Information 70: Quality control of rhFAPI-10 with RP-HPLC (10 to 90% B in 15 min): t_R = 9.82 min.

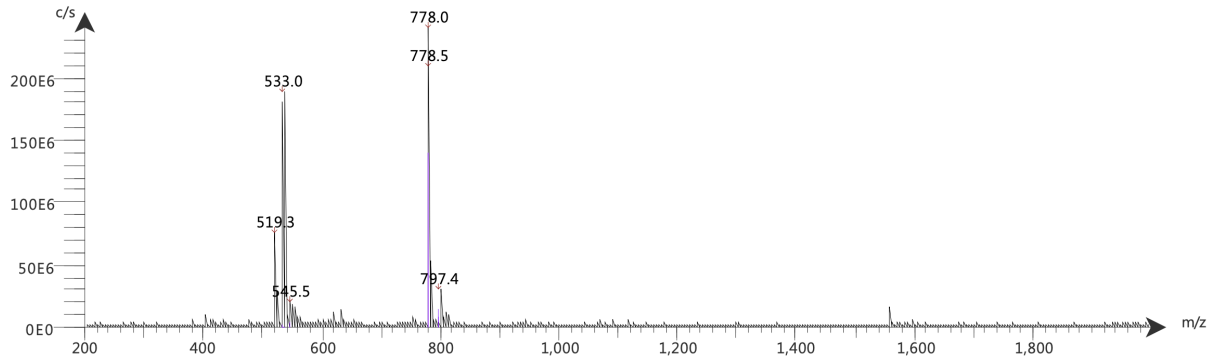

Supplemental Information 71: Mass spectrum of quality control of rhFAPI-10. ESI-MS: Calculated monoisotopic mass ($C_{71}H_{102}F_3N_{15}O_{19}Si$): 1553.72; found: m/z = 1554.7 $[M+H]^+$, 778.0 $[M+2H]^{2+}$, 519.3 $[M+3H]^{3+}$.

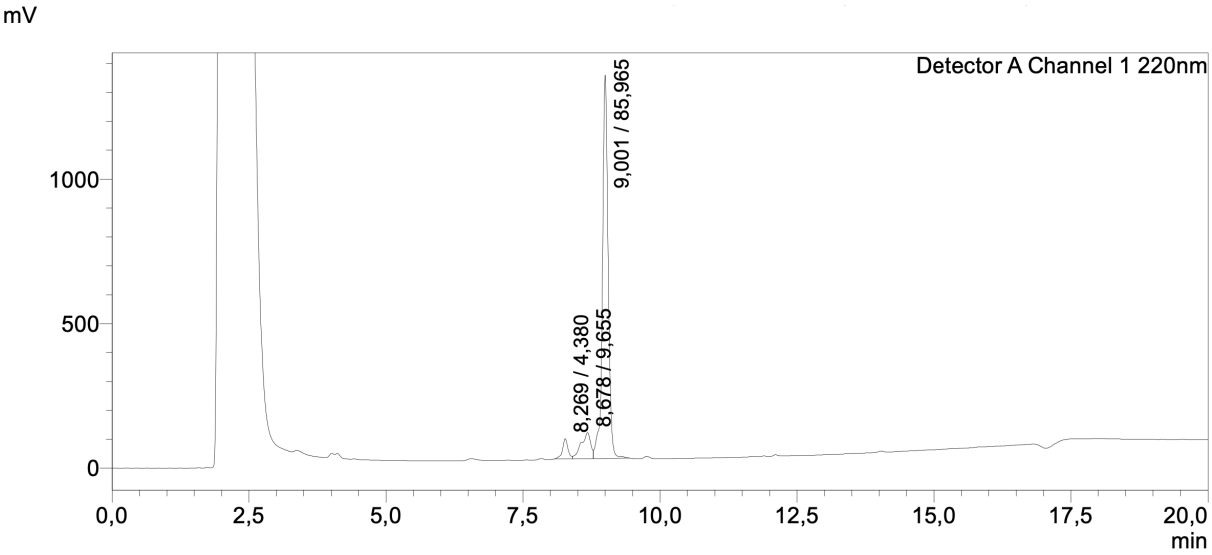

Supplemental Information 72: Quality control of [^{nat}Lu]Lu-rhFAPI-10 with RP-HPLC (10 to 90% B in 15 min): t_R = 9.00 min.

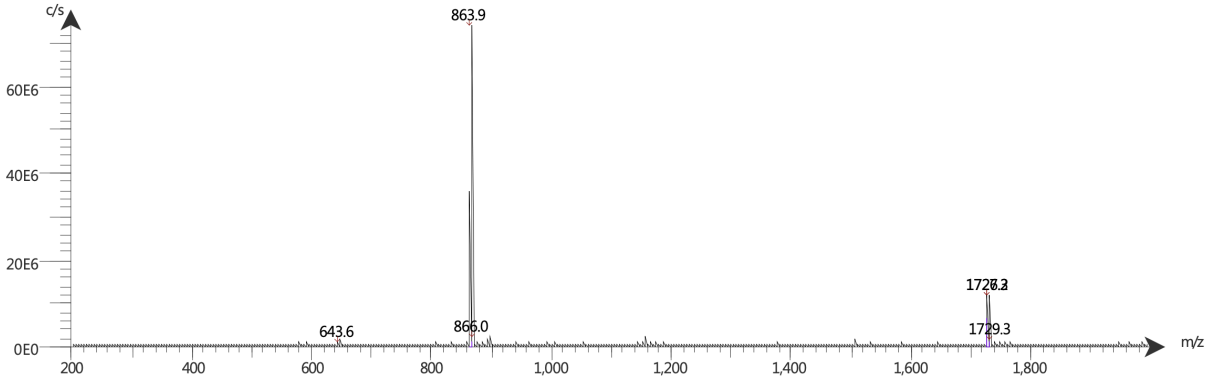

Supplemental Information 73: Mass spectrum of quality control of [^{nat}Lu]Lu-rhFAPI-10. ESI-MS: Calculated monoisotopic mass ($C_{71}H_{99}F_3LuN_{15}O_{19}Si$): 1725.71; found: m/z = 1726.3 $[M+H]^+$, 863.9.5 $[M+2H]^{2+}$.

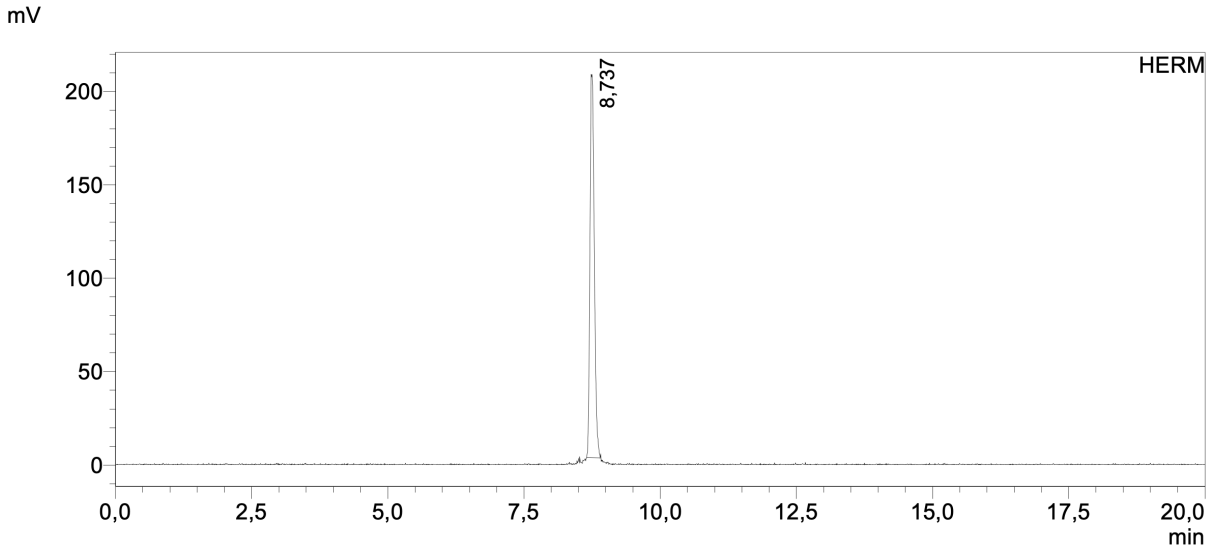

Supplemental Information 74: Quality control of [^{177}Lu]Lu-rhFAPI-10 with radio-HPLC (10 to 90% B in 15 min): t_R = 8.74 min.

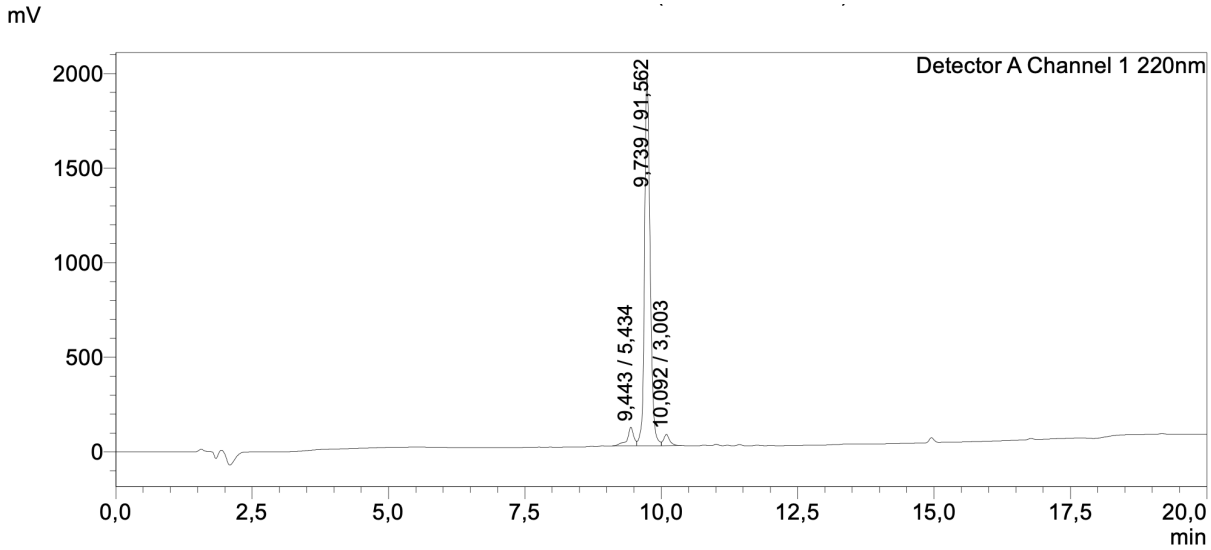

Supplemental Information 75: Quality control of rhFAPI-11 with RP-HPLC (10 to 90% B in 15 min): t_R = 9.74 min.

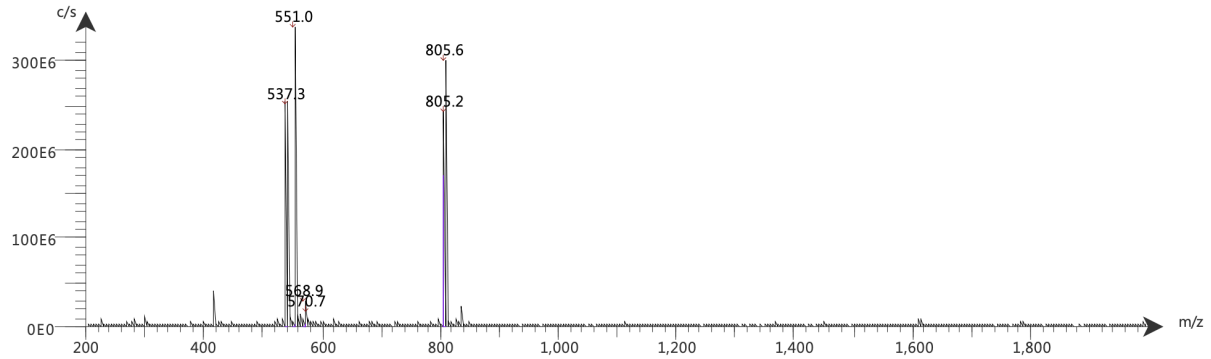

Supplemental Information 76: Mass spectrum of quality control of rhFAPI-11. ESI-MS: Calculated monoisotopic mass ($C_{73}H_{104}F_3N_{17}O_{19}Si$): 1607.74; found: m/z = 805.1 $[M+2H]^{2+}$, 537.3 $[M+3H]^{3+}$.

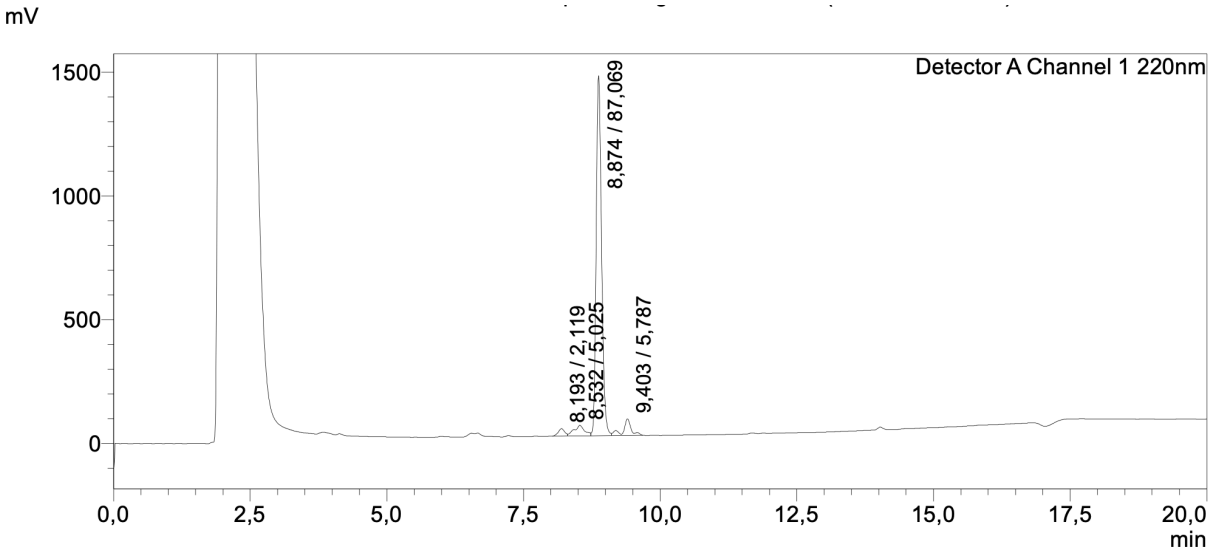

Supplemental Information 77: Quality control of [^{nat}Lu]Lu-rhFAPI-11 with RP-HPLC (10 to 90% B in 15 min): t_R = 8.87 min.

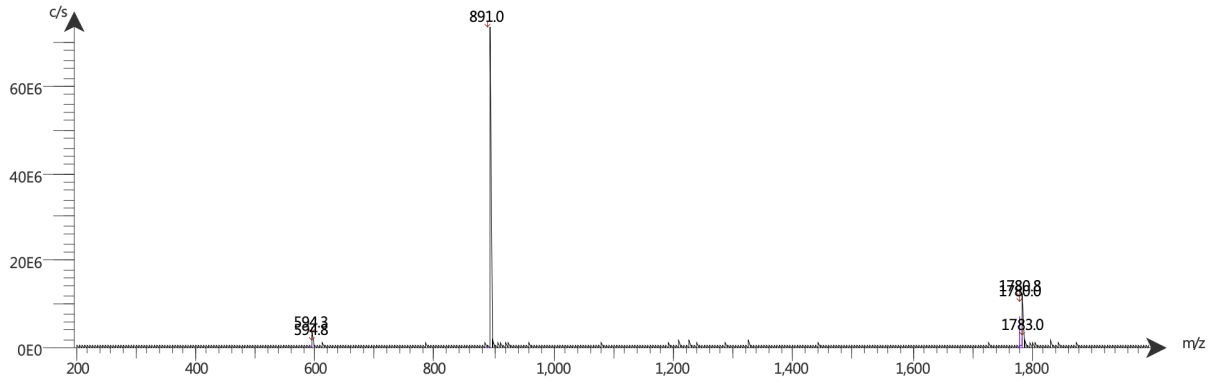

Supplemental Information 78: Mass spectrum of quality control of [^{nat}Lu]Lu-rhFAPI-11. ESI-MS: Calculated monoisotopic mass ($C_{73}H_{101}F_3LuN_{17}O_{19}Si$): 1779.76; found: m/z = 1780.0 $[M+H]^+$, 891.0 $[M+2H]^{2+}$, 594.3 $[M+3H]^{3+}$.

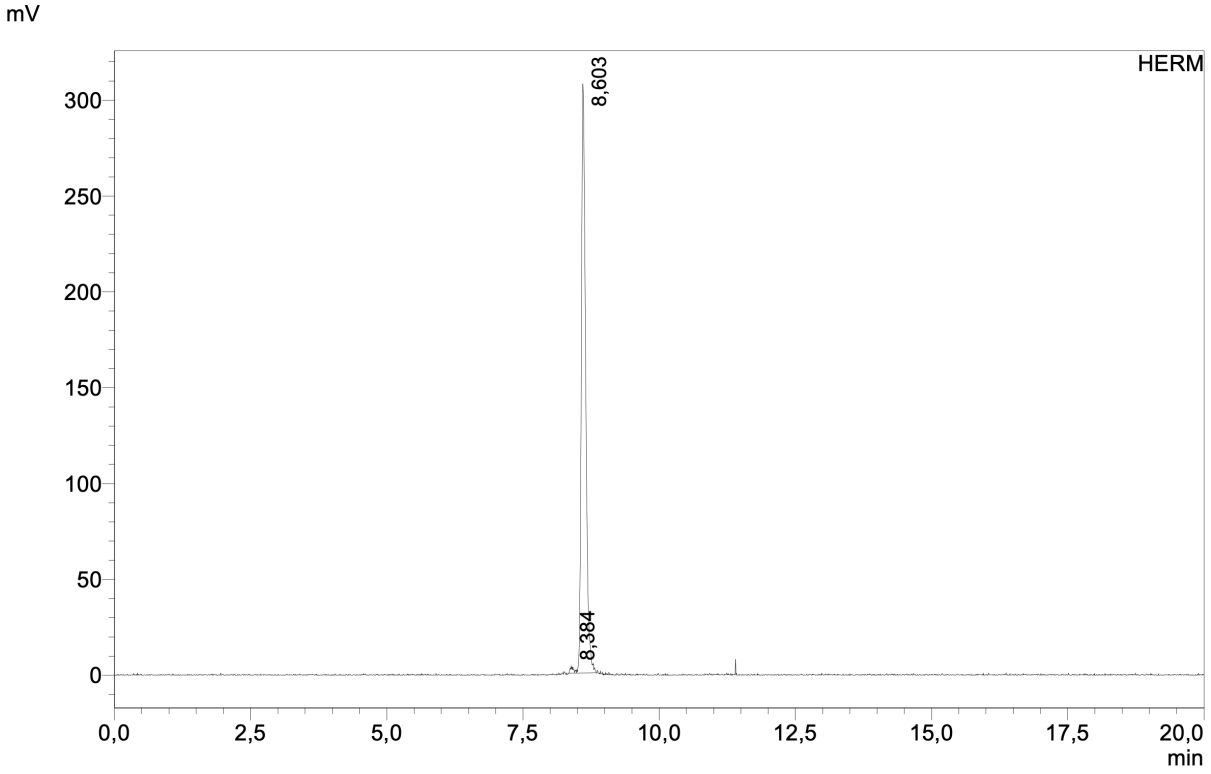

Supplemental Information 79: Quality control of [^{177}Lu]Lu-rhFAPI-11 with radio-HPLC (10 to 90% B in 15 min): t_R = 8.60 min.

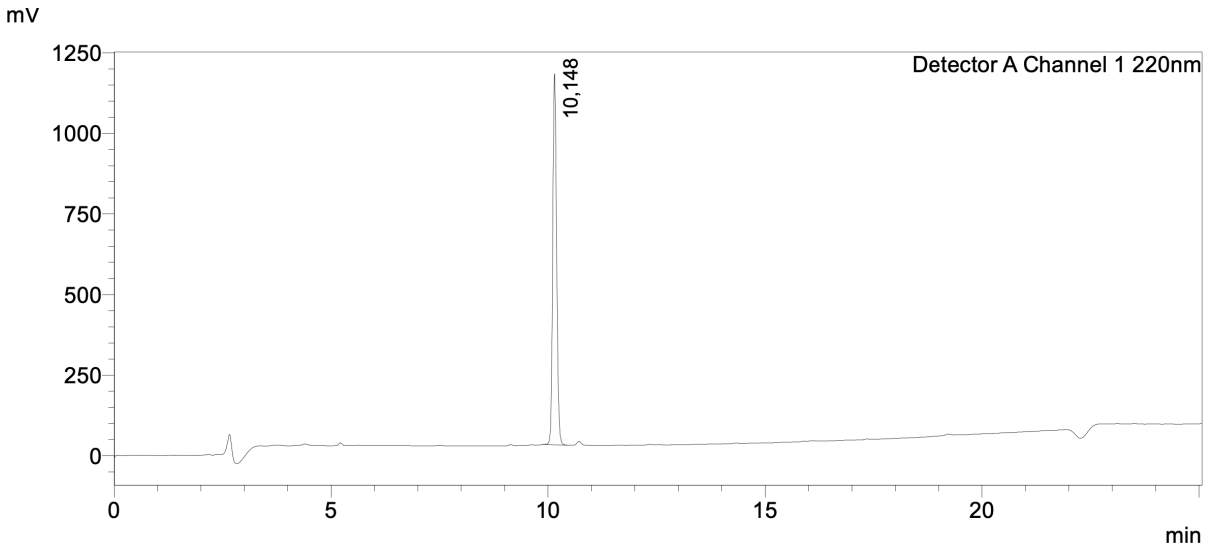

Supplemental Information 80: Quality control of rhFAPI-12 with RP-HPLC (10 to 90% B in 15 min): t_R = 10.15 min.

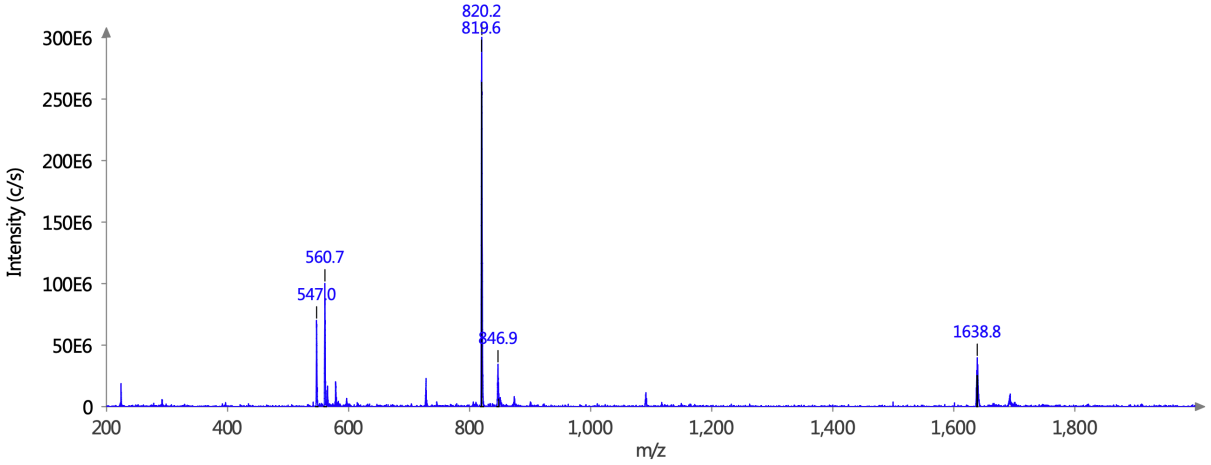

Supplemental Information 81: Mass spectrum of quality control of rhFAPI-12. ESI-MS: Calculated monoisotopic mass ($C_{75}H_{106}F_3N_{15}O_{21}Si$): 1637.74; found: m/z = 1638.6 $[M+H]^+$, 819.7 $[M+2H]^{2+}$.

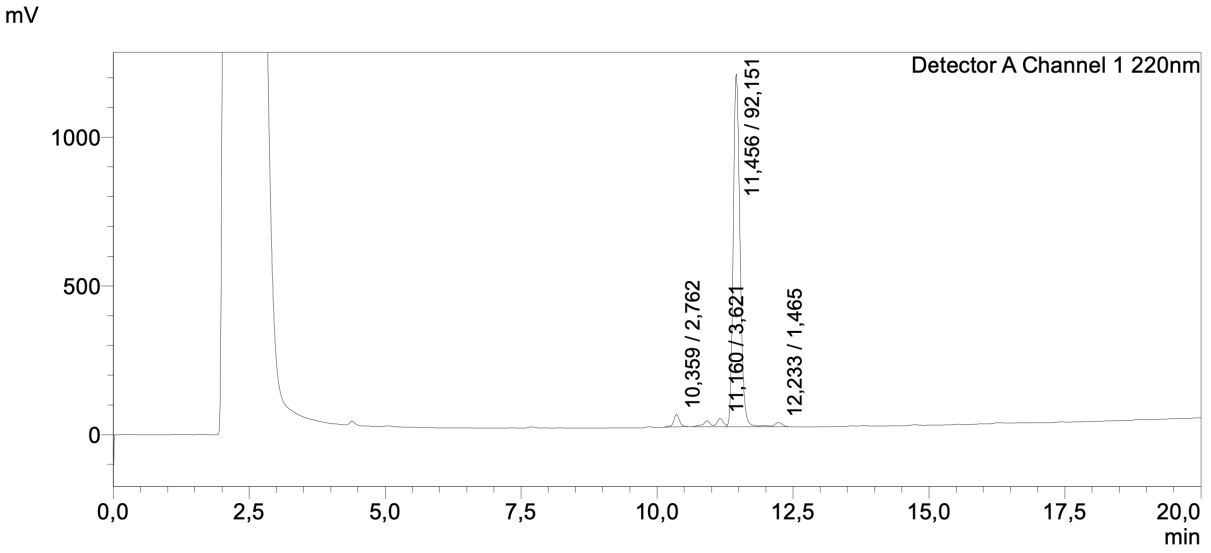

Supplemental Information 82: Quality control of [^{nat}Lu]Lu-rhFAPI-12 with RP-HPLC (10 to 90% B in 15 min): t_R = 11.46 min.

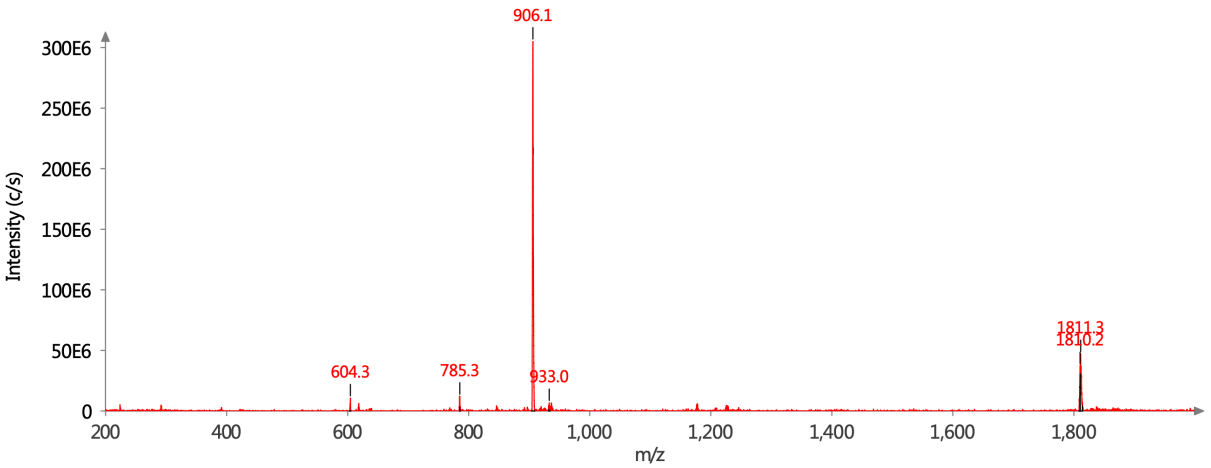

Supplemental Information 83: Mass spectrum of quality control of [^{nat}Lu]Lu-rhFAPI-12. ESI-MS: Calculated monoisotopic mass ($C_{75}H_{103}F_3LuN_{15}O_{21}Si$): 1809.66; found: m/z = 1811.3 $[M+H]^+$, 906.1 $[M+2H]^{2+}$.

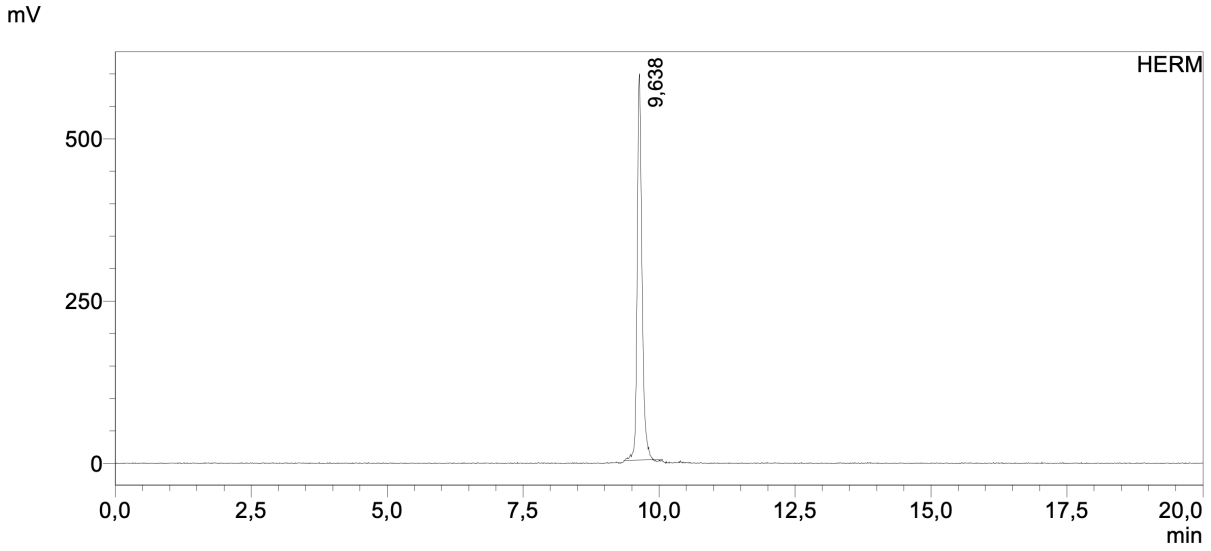

Supplemental Information 84: Quality control of [^{177}Lu]Lu-rhFAPI-12 with radio-HPLC (10 to 90% B in 15 min): t_R = 9.64 min.

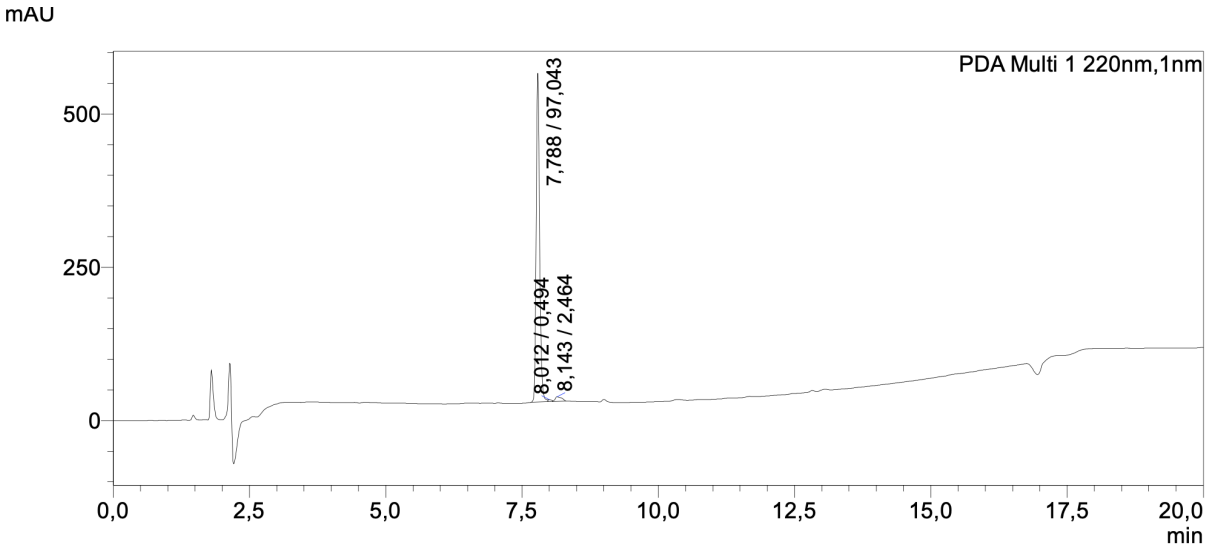

Supplemental Information 85: Quality control of rhFAPI-13 with RP-HPLC (10 to 90% B in 15 min): t_R = 7.79 min.

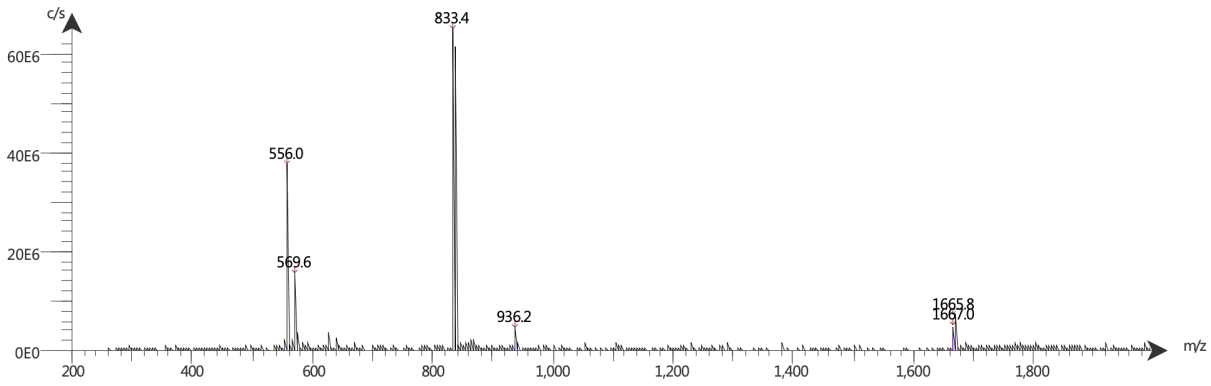

Supplemental Information 86: Mass spectrum of quality control of rhFAPI-13. Calculated monoisotopic mass ($C_{77}H_{115}F_3N_{18}O_{18}Si$): 1664.84; found: m/z = 1665.8 $[M+H]^+$, 833.4 $[M+2H]^{2+}$, 556.0 $[M+3H]^{3+}$.

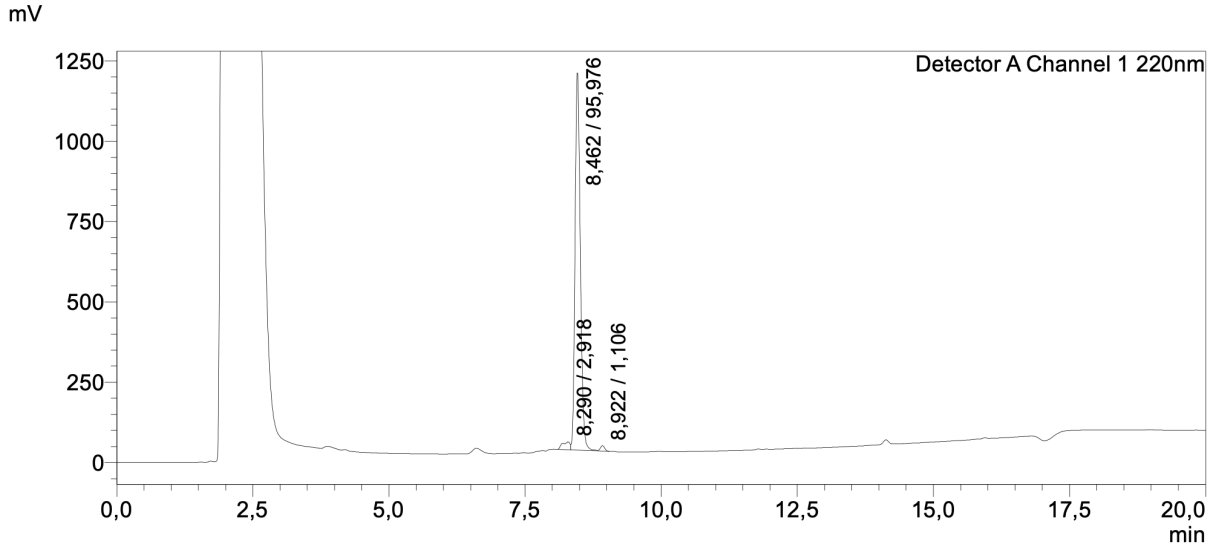

Supplemental Information 87: Quality control of [^{nat}Lu]Lu-rhFAPI-13 with RP-HPLC (10 to 90% B in 15 min): t_R = 8.46 min.

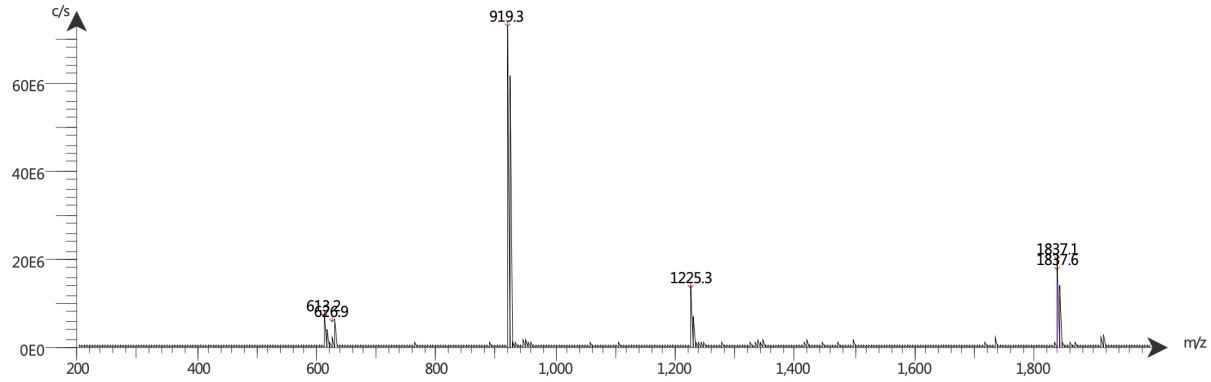

Supplemental Information 88: Mass spectrum of quality control of [^{nat}Lu]Lu-rhFAPI-13. ESI-MS: Calculated monoisotopic mass ($C_{77}H_{112}F_3LuN_{18}O_{18}Si$): 1835.75; found: m/z = 1837.1 $[M+H]^+$, 919.3 $[M+2H]^{2+}$, 613.2 $[M+3H]^{3+}$.

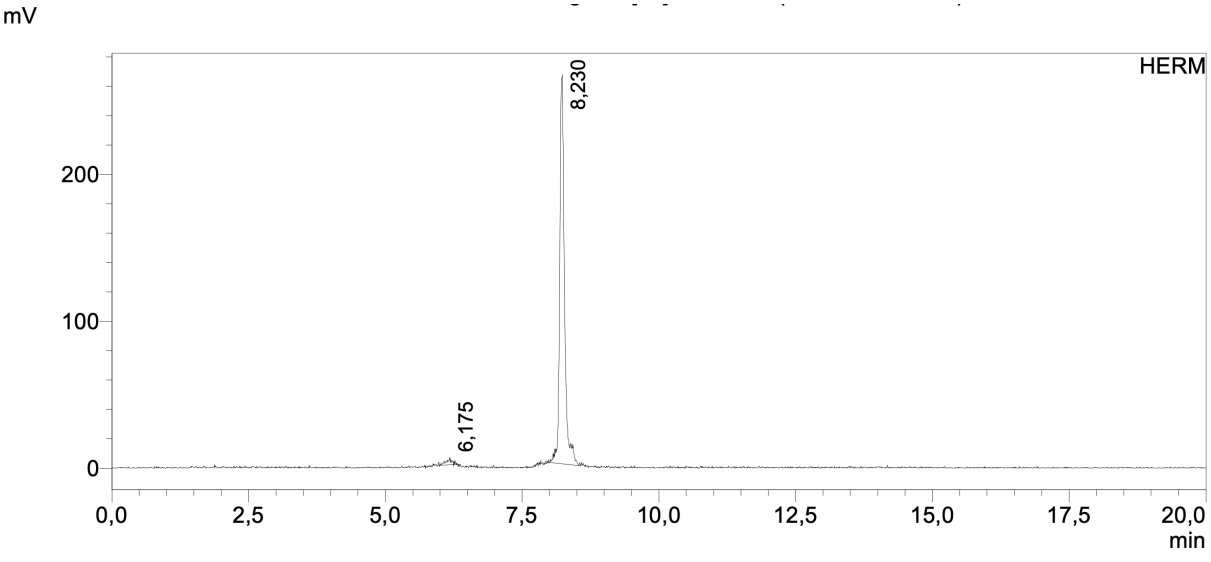

Supplemental Information 89: Quality control of [^{177}Lu]Lu-rhFAPI-13 with radio-HPLC (10 to 90% B in 15 min): t_R = 8.23 min.

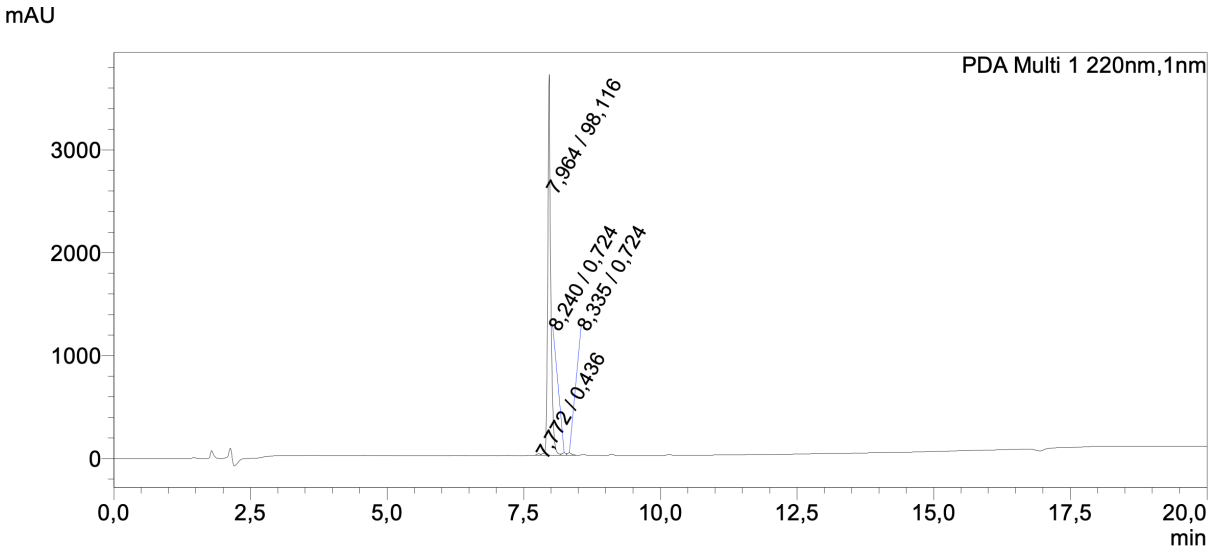

Supplemental Information 90: Quality control of rhFAPI-14 with RP-HPLC (10 to 90% B in 15 min): t_R = 7.96 min.

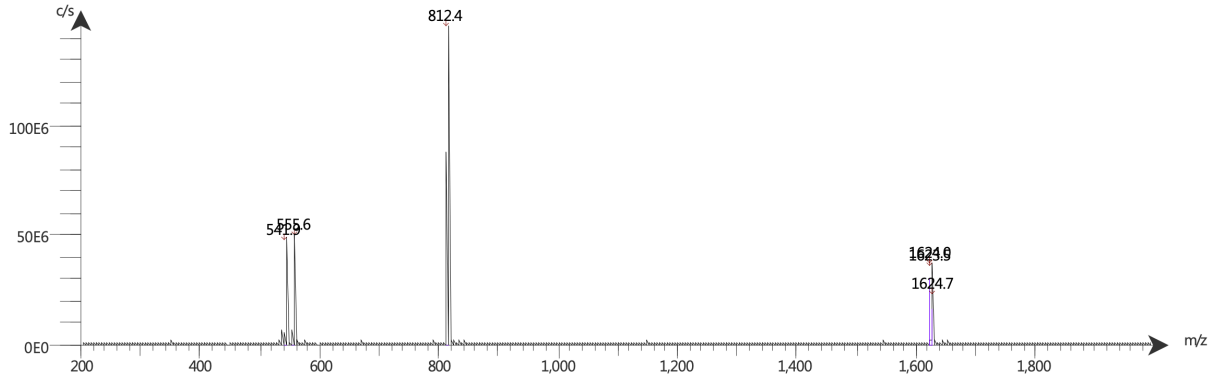

Supplemental Information 91: Mass spectrum of quality control of rhFAPI-14. Calculated monoisotopic mass ($C_{74}H_{109}F_3N_{18}O_{18}Si$): 1622.79; found: m/z = 1624.0 $[M+H]^+$, 812.4 $[M+2H]^{2+}$, 541.9 $[M+3H]^{3+}$.

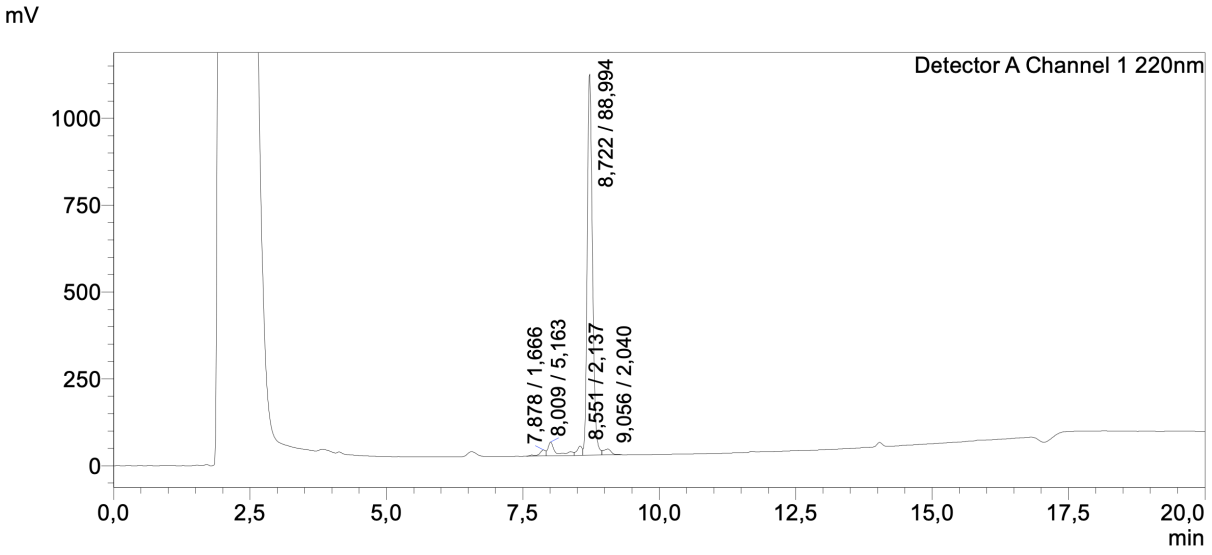

Supplemental Information 92: Quality control of [^{nat}Lu]Lu-rhFAPI-14 with RP-HPLC (10 to 90% B in 15 min): t_R = 8.72 min.

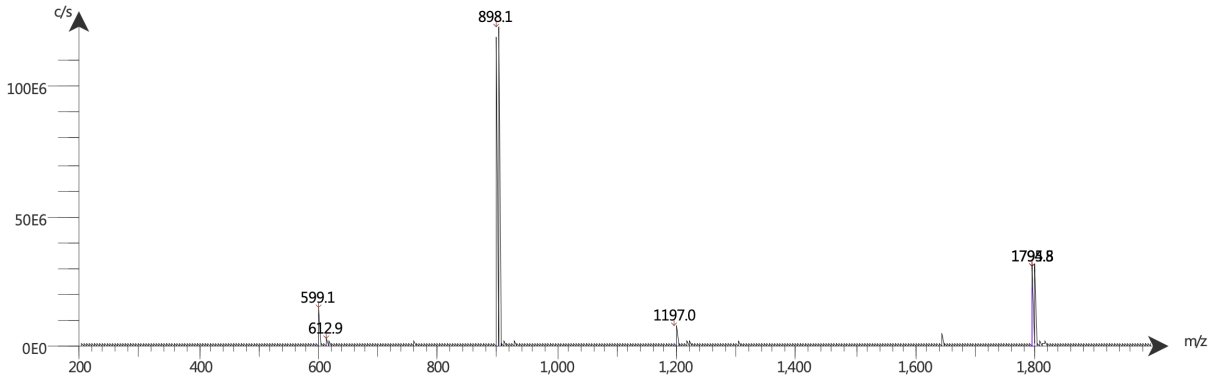

Supplemental Information 93: Mass spectrum of quality control of [^{nat}Lu]Lu-rhFAPI-14. ESI-MS: Calculated monoisotopic mass ($C_{74}H_{106}F_3LuN_{18}O_{18}Si$): 1794.82; found: m/z = 1794.8 $[M+H]^+$, 898.1 $[M+2H]^{2+}$, 599.1 $[M+3H]^{3+}$.

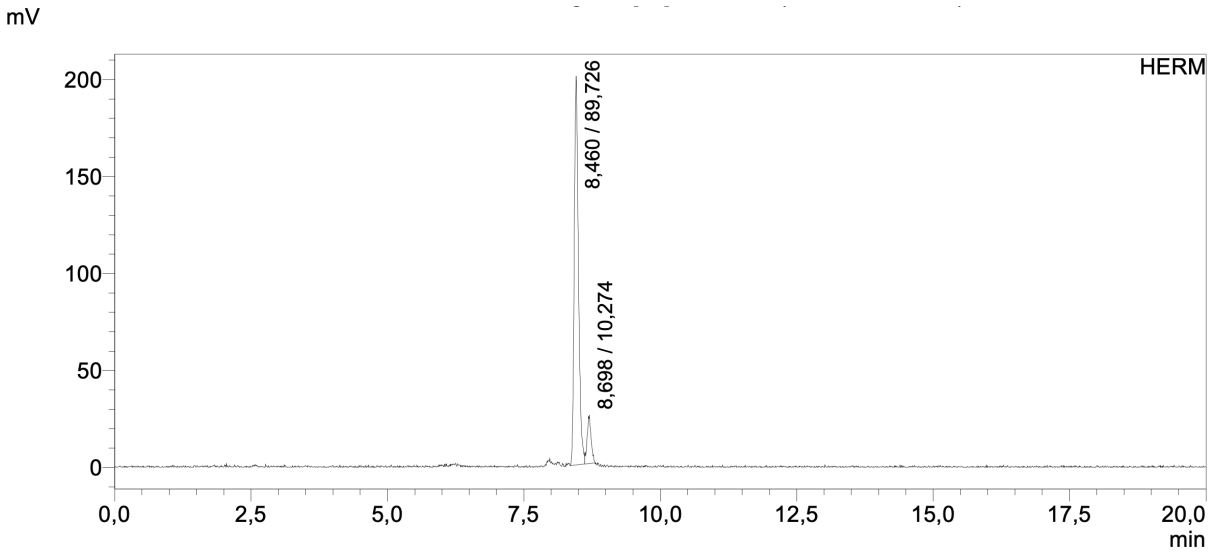

Supplemental Information 94: Quality control of [^{18}F]F-Lu-rhFAPI-14 with radio-HPLC (10 to 90% B in 15 min): t_R = 8.60 min.

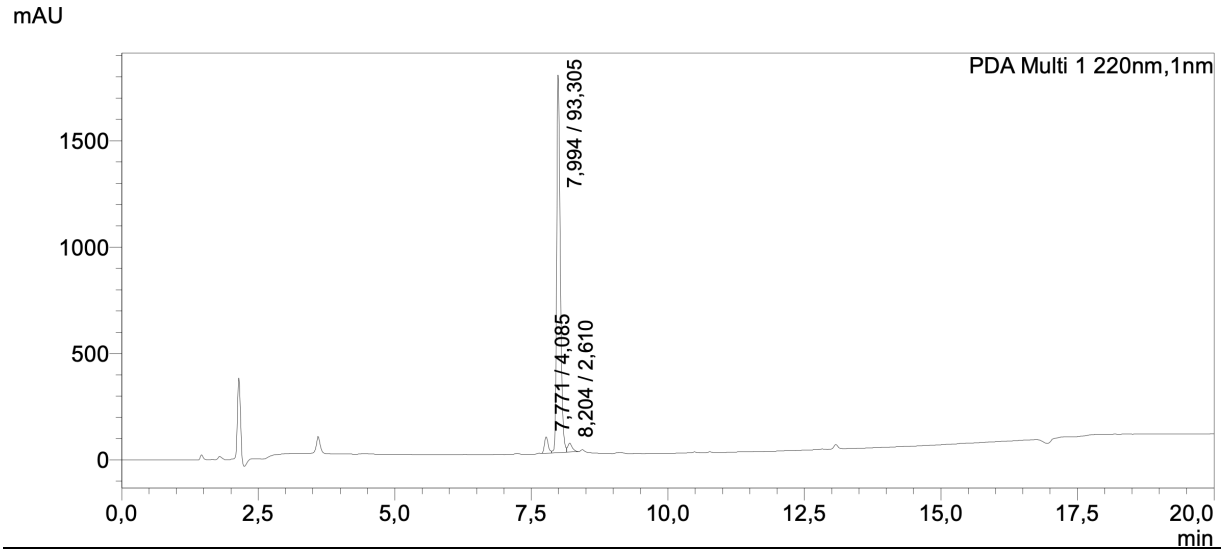

Supplemental Information 95: Quality control of rhFAPI-15 with RP-HPLC (10 to 90% B in 15 min): t_R = 7.99 min.

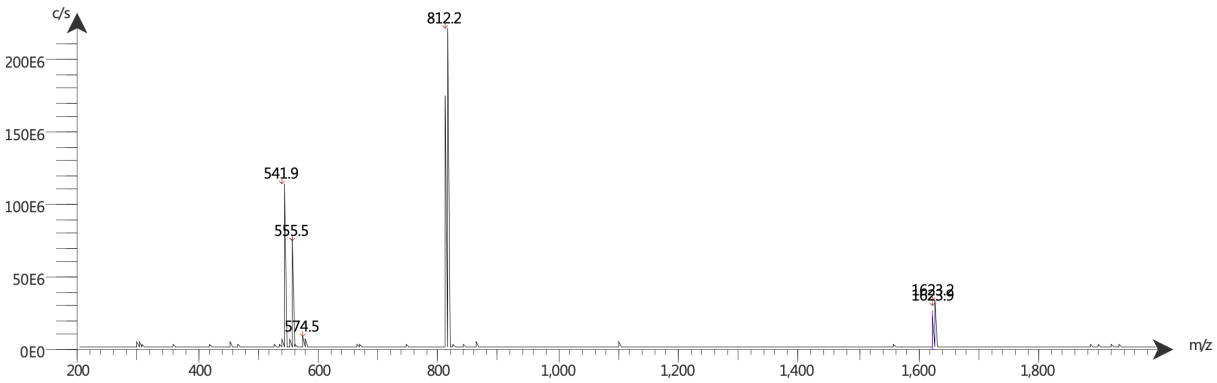

Supplemental Information 96: Mass spectrum of quality control of rhFAPI-15. ESI-MS: Calculated monoisotopic mass ($C_{74}H_{109}F_3N_{18}O_{18}Si$): 1622.79; found: m/z = 1623.9 $[M+H]^+$, 812.2 $[M+2H]^{2+}$, 541.9 $[M+3H]^{3+}$.

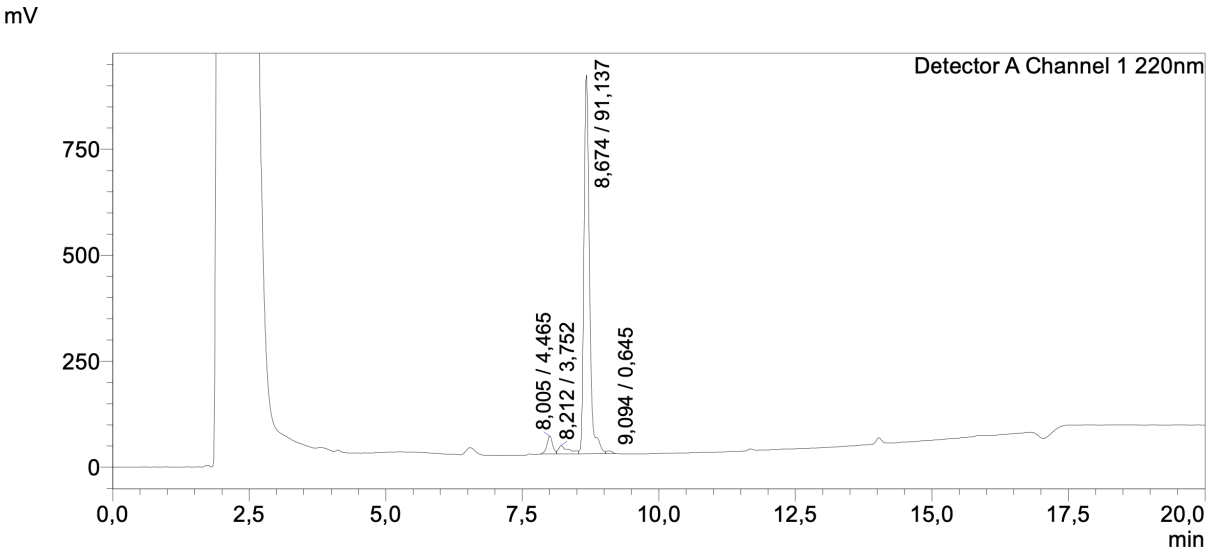

Supplemental Information 97: Quality control of [^{nat}Lu]Lu-rhFAPI-15 with RP-HPLC (10 to 90% B in 15 min): t_R = 8.67 min.

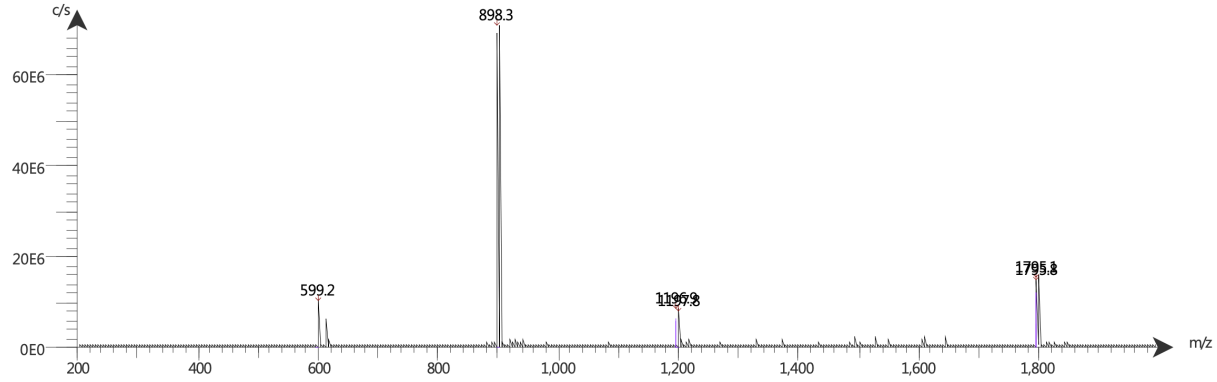

Supplemental Information 98: Mass spectrum of quality control of [^{nat}Lu]Lu-rhFAPI-15. ESI-MS: Calculated monoisotopic mass ($C_{74}H_{106}F_3LuN_{18}O_{18}Si$): 1794.82; found: m/z = 1795.1 $[M+H]^+$, 898.3 $[M+2H]^{2+}$, 599.2 $[M+3H]^{3+}$.

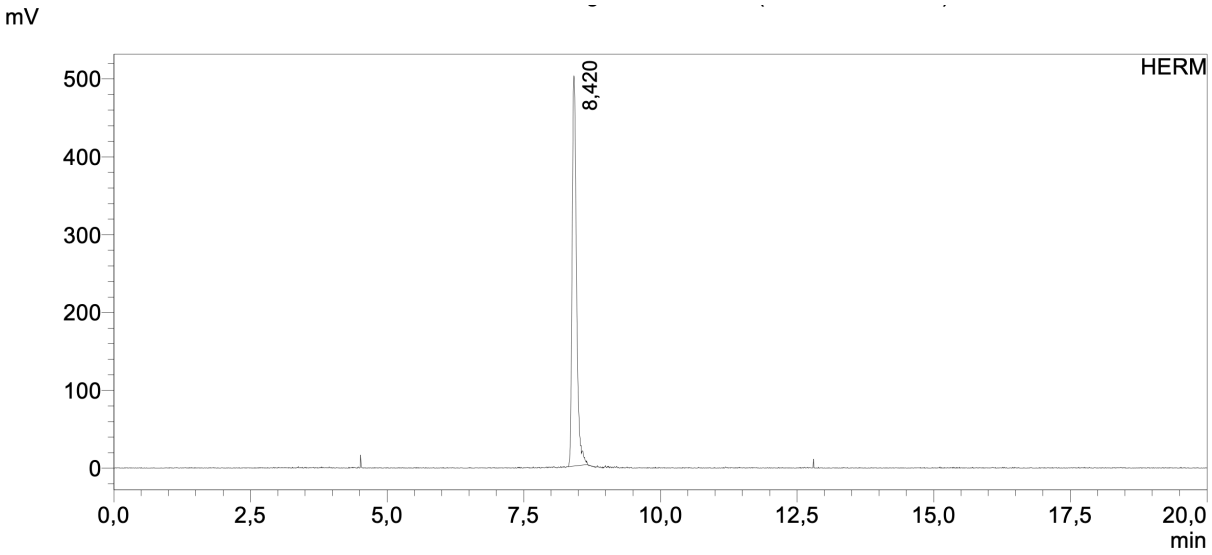

Supplemental Information 99: Quality control of [^{18}F]F-Lu-rhFAPI-15 with radio-HPLC (10 to 90% B in 15 min): t_R = 8.42 min.

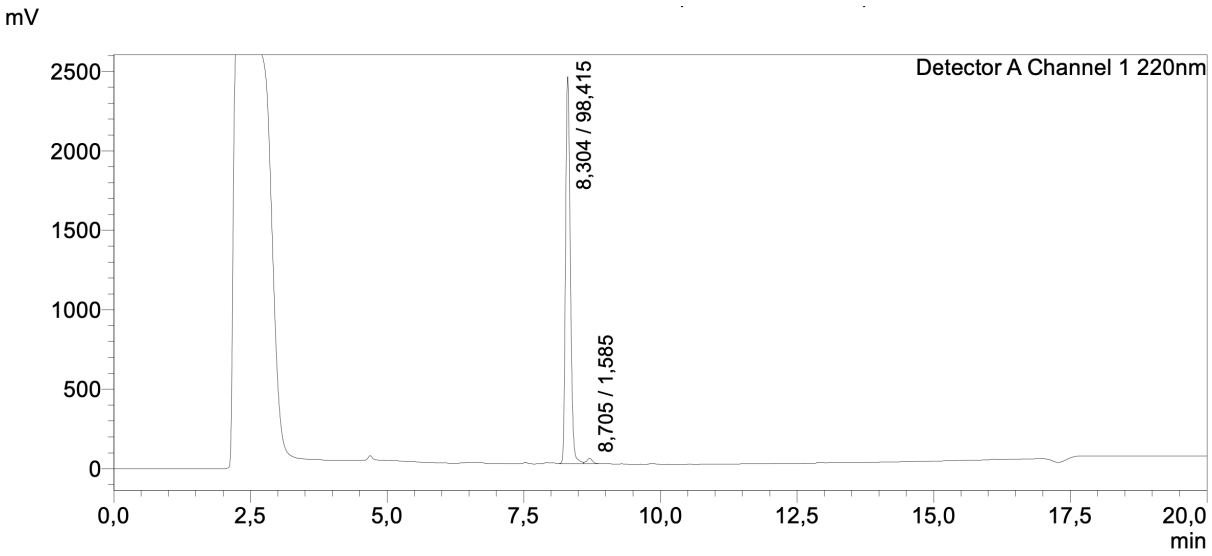

Supplemental Information 100: Quality control of rhFAPI-16 with RP-HPLC (10 to 90% B in 15 min): t_R = 8.30 min.

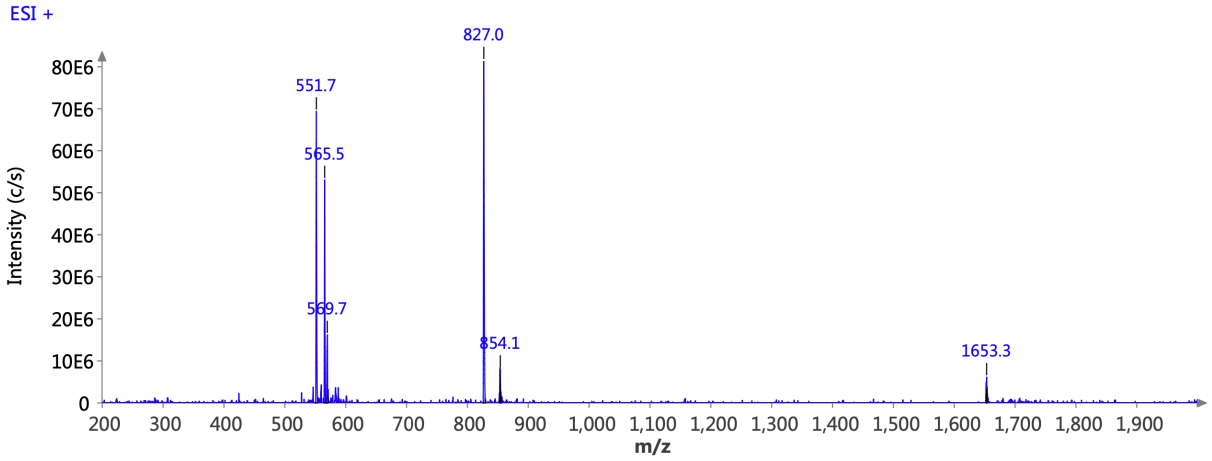

Supplemental Information 101: Mass spectrum of quality control of rhFAPI-16. ESI-MS: Calculated monoisotopic mass ($C_{75}H_{108}F_3N_{17}O_{20}Si$): 1651.77; found: m/z = 1653.3 $[M+H]^+$, 827.0 $[M+2H]^{2+}$, 551.7 $[M+3H]^{3+}$.

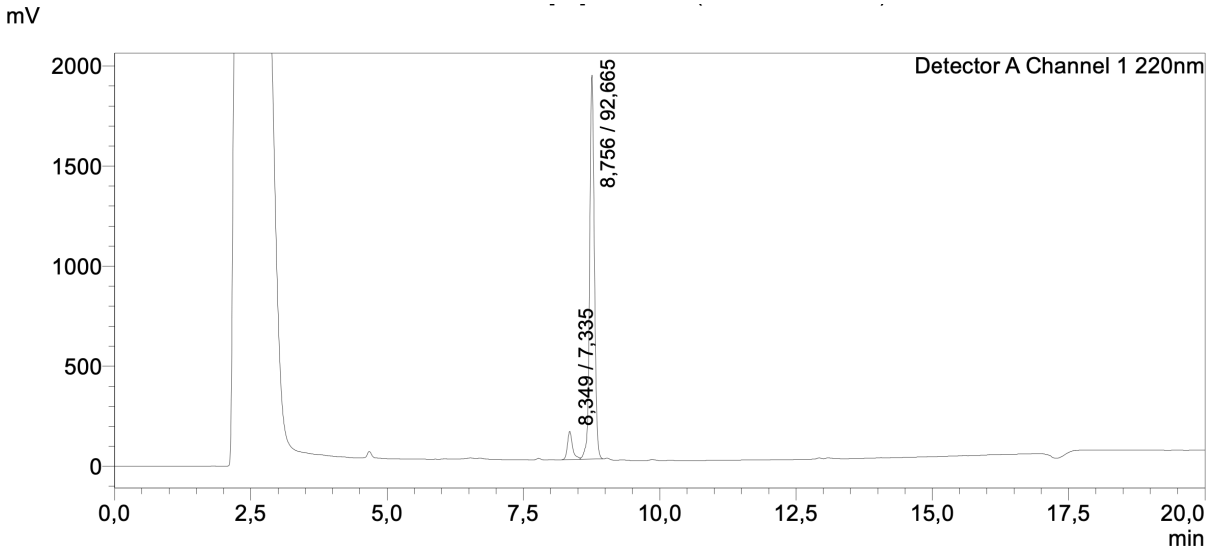

Supplemental Information 102: Quality control of [^{nat}Lu]Lu-rhFAPI-16 with RP-HPLC (10 to 90% B in 15 min): t_R = 8.76 min.

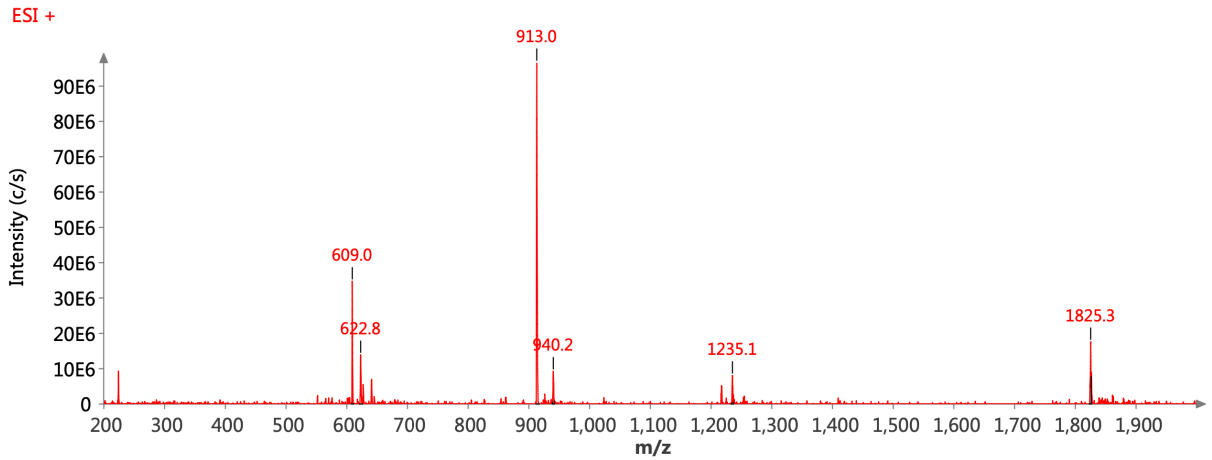

Supplemental Information 103: Mass spectrum of quality control of [^{nat}Lu]Lu-rhFAPI-16. ESI-MS: Calculated monoisotopic mass ($C_{75}H_{105}F_3LuN_{17}O_{20}Si$): 1823.69; found: m/z = 1825.3 $[M+H]^+$, 913.0 $[M+2H]^{2+}$, 609.0 $[M+3H]^{3+}$.

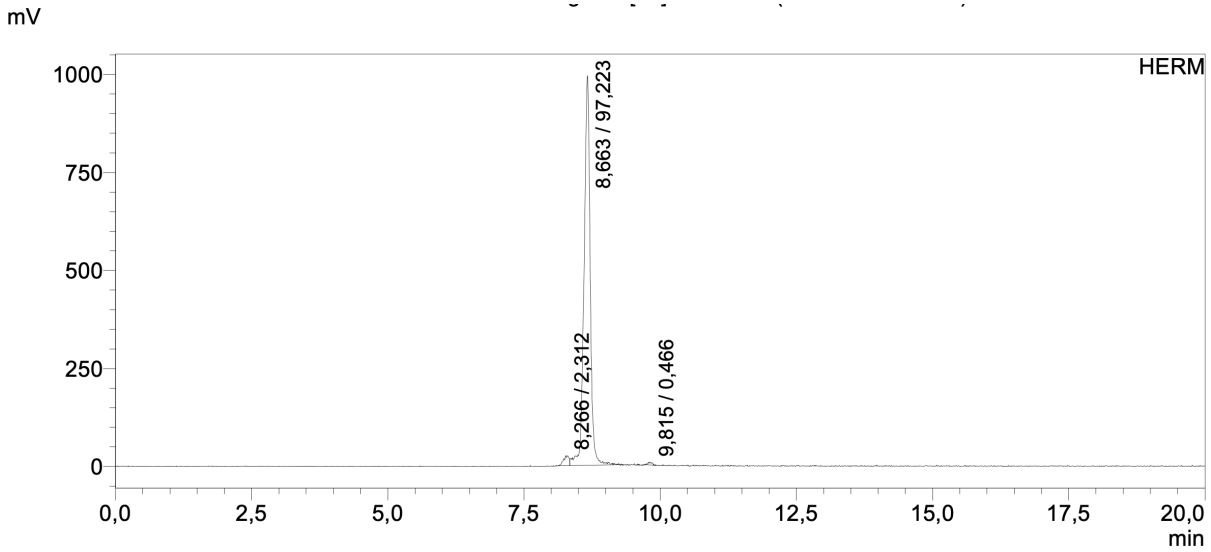

Supplemental Information 104: Quality control of [^{177}Lu]Lu-rhFAPI-16 with radio-HPLC (10 to 90% B in 15 min): t_R = 8.66 min.

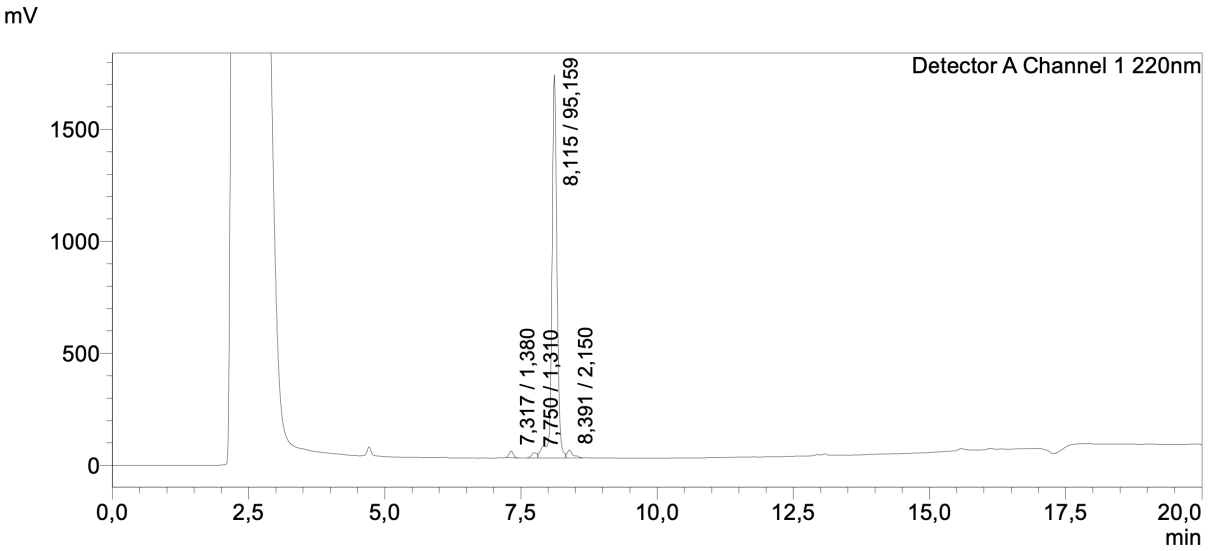

Supplemental Information 105: Quality control of [^{nat}Lu]Lu-rhFAPI-17 with RP-HPLC (10 to 90% B in 15 min): t_R = 8.12 min.

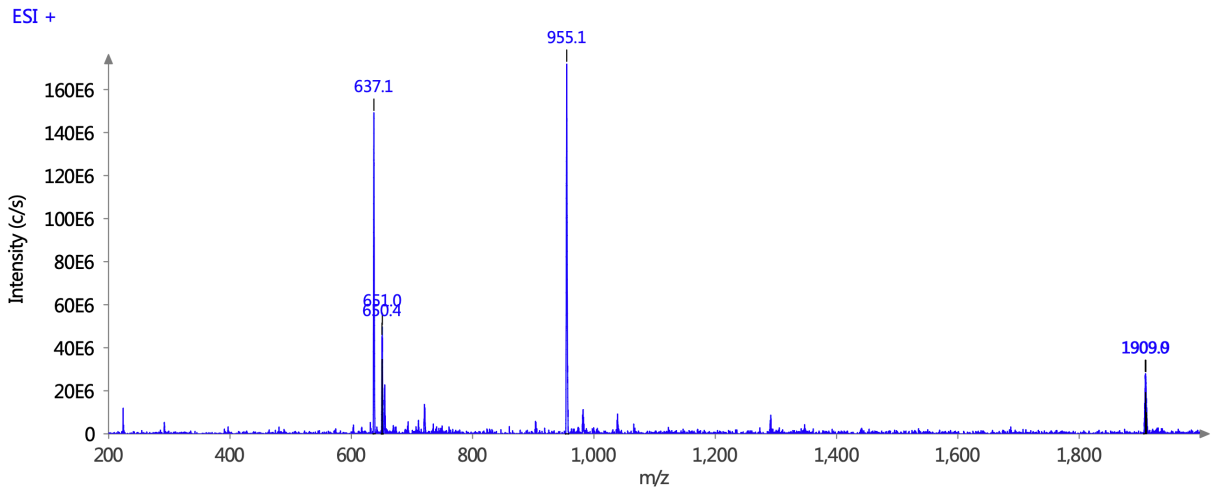

Supplemental Information 106: Mass spectrum of quality control of [^{nat}Lu]Lu-rhFAPI-17. ESI-MS: Calculated monoisotopic mass ($C_{81}H_{122}F_3LuN_{19}O_{18}Si$): 1908.83; found: m/z = 1909.9 $[M+H]^+$, 955.1 $[M+2H]^{2+}$, 637.1 $[M+3H]^{3+}$.

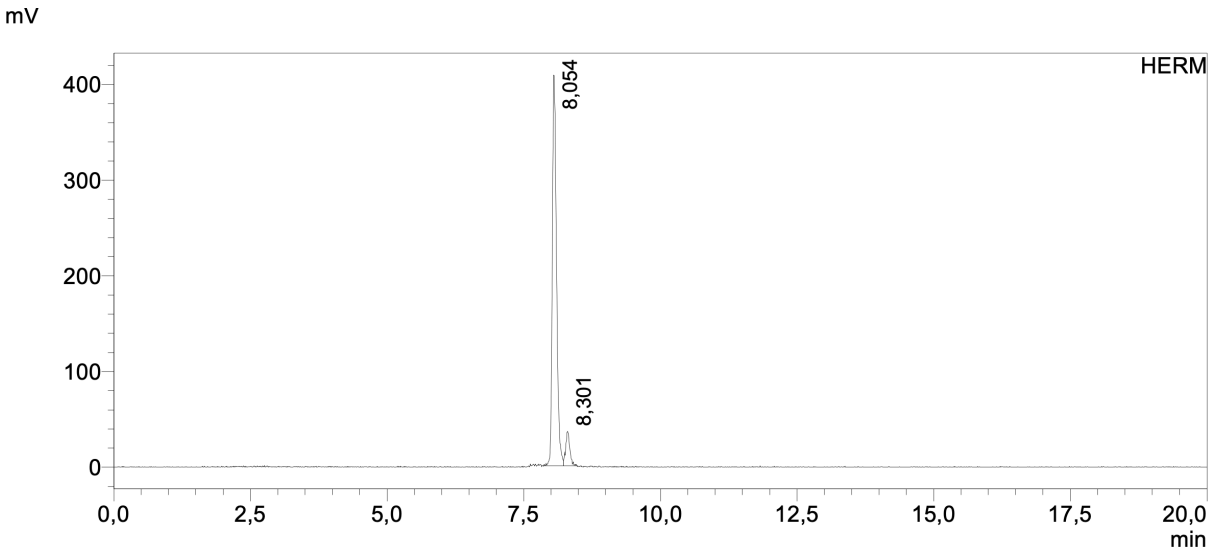

Supplemental Information 107: Quality control of [^{177}Lu]Lu-rhFAPI-17 with radio-HPLC (10 to 90% B in 15 min): t_R = 8.05 min.

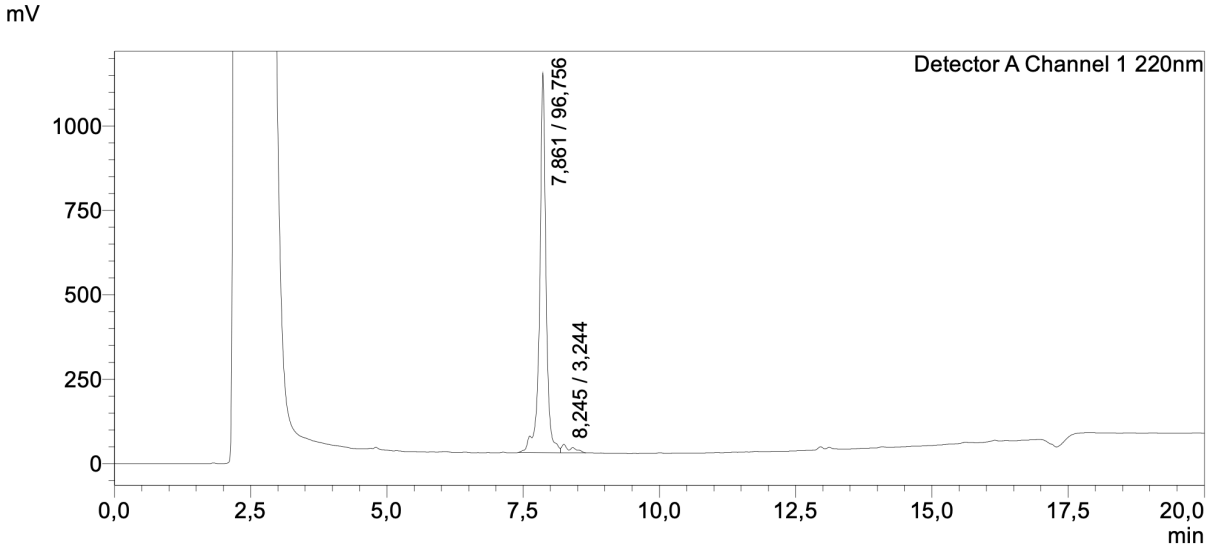

Supplemental Information 108: Quality control of [^{nat}Lu]Lu-rhFAPI-18 with RP-HPLC (10 to 90% B in 15 min): t_R = 7.86 min.

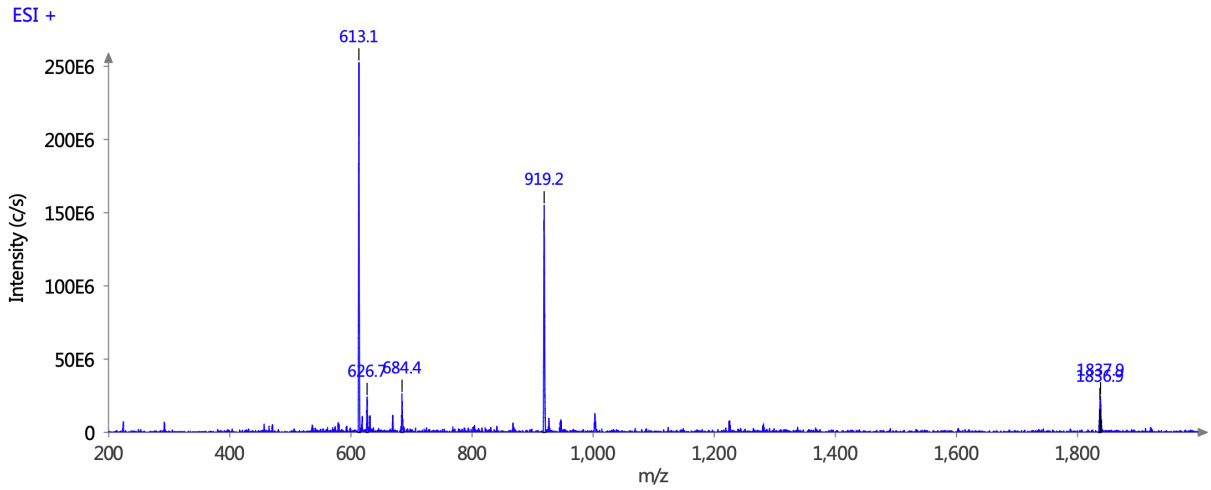

Supplemental Information 109: Mass spectrum of quality control of [^{nat}Lu]Lu-rhFAPI-18. ESI-MS: Calculated monoisotopic mass ($C_{78}H_{118}F_3LuN_{19}O_{16}Si$): 1836.81; found: m/z = 1837.9 $[M+H]^+$, 919.2 $[M+2H]^{2+}$, 613.1 $[M+3H]^{3+}$.

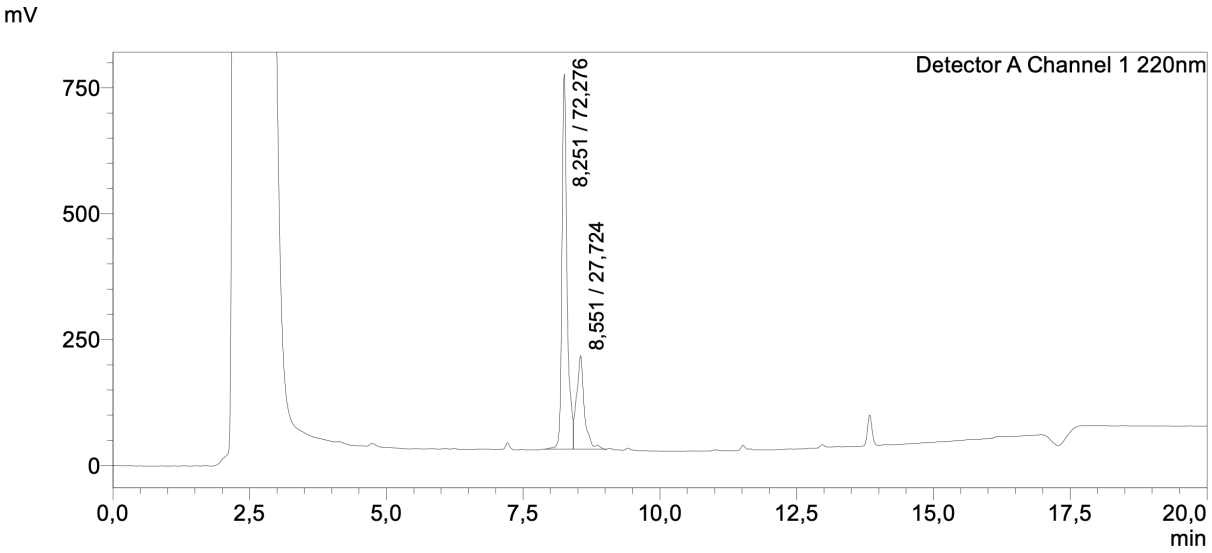

Supplemental Information 110: Quality control of rhFAPI-19 with RP-HPLC (10 to 90% B in 15 min): t_R = 8.251 min.

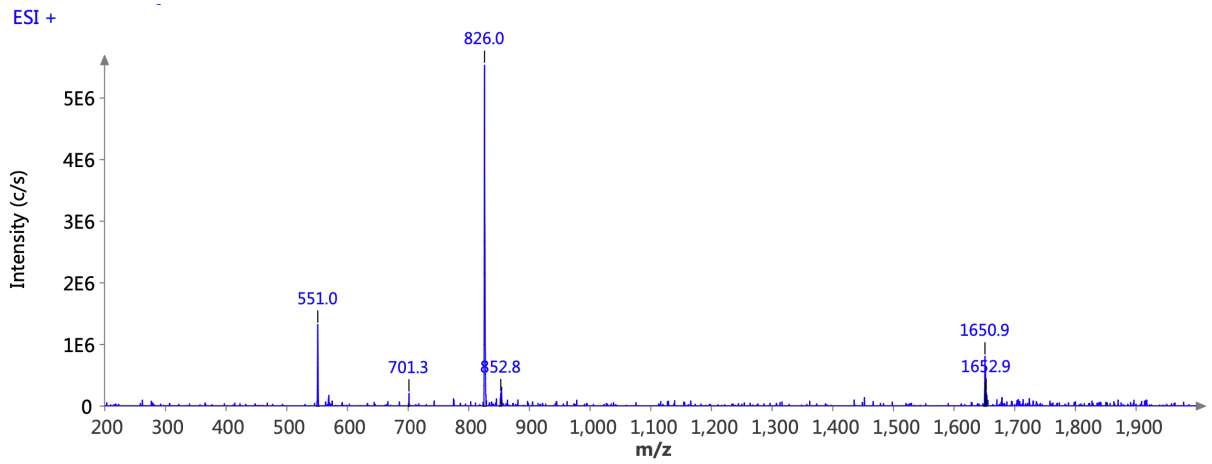

Supplemental Information 111: Mass spectrum of quality control of rhFAPI-19. ESI-MS: Calculated monoisotopic mass ($C_{76}H_{114}F_3N_{18}O_{18}Si^+$): 1651.83; found: m/z = 1652.9 $[M+H]^+$, 826.0 $[M+2H]^{2+}$, 551.0 $[M+3H]^{3+}$.

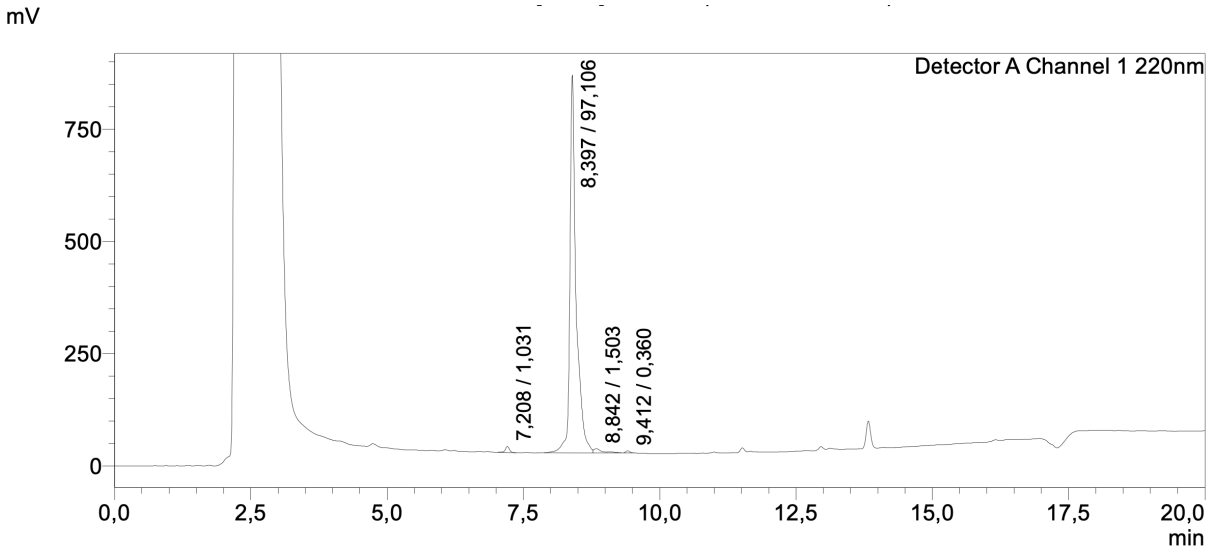

Supplemental Information 112: Quality control of [^{nat}Lu]Lu-rhFAPI-19 with RP-HPLC (10 to 90% B in 15 min): t_R = 8.40 min.

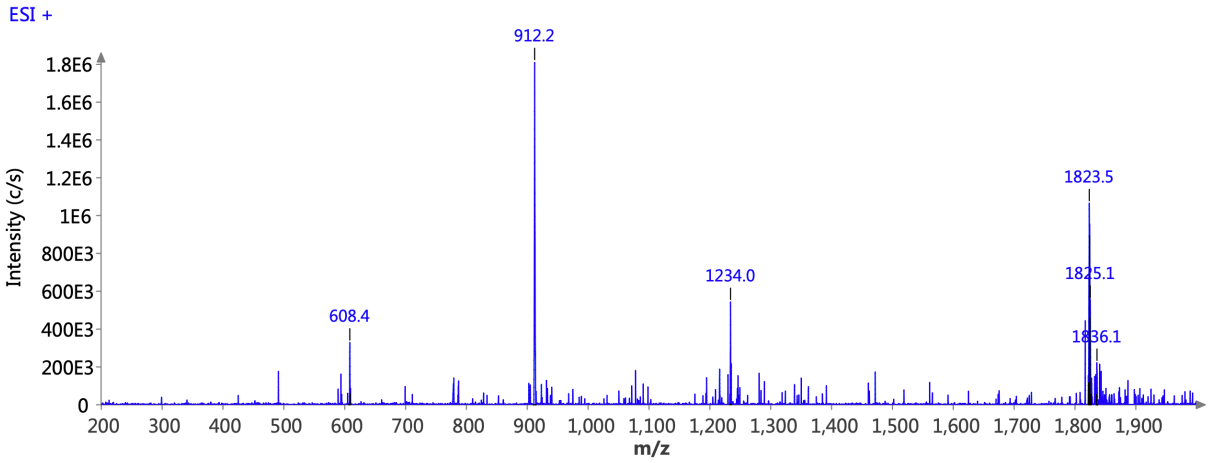

Supplemental Information 113: Mass spectrum of quality control of [^{nat}Lu]Lu-rhFAPI-19. ESI-MS: Calculated monoisotopic mass ($C_{76}H_{111}F_3LuN_{18}O_{18}Si$): 1823.74; found: m/z = 912.2 $[M+2H]^{2+}$.

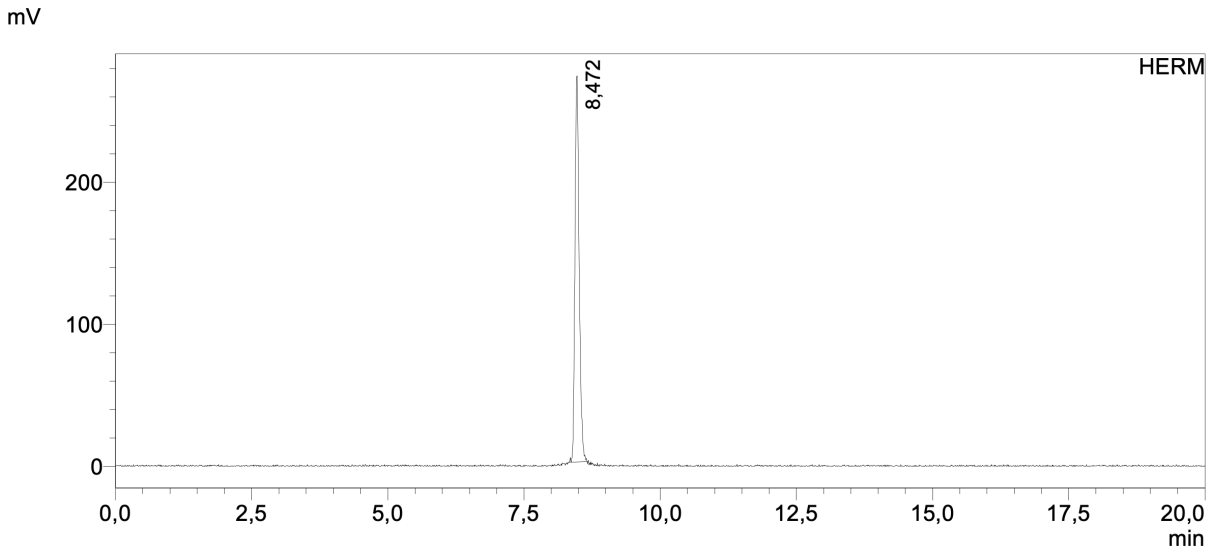

Supplemental Information 114: Quality control of [^{177}Lu]Lu-rhFAPI-19 with radio-HPLC (10 to 90% B in 15 min): t_R = 8.47 min.

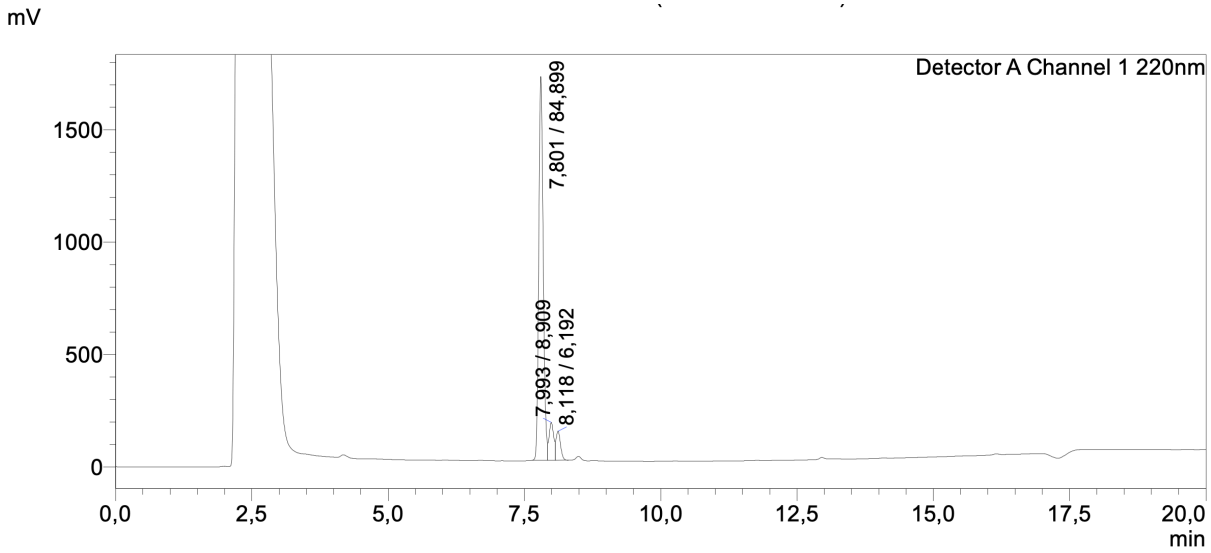

Supplemental Information 115: Quality control of rhFAPI-20 with RP-HPLC (10 to 90% B in 15 min): t_R = 7.80 min.

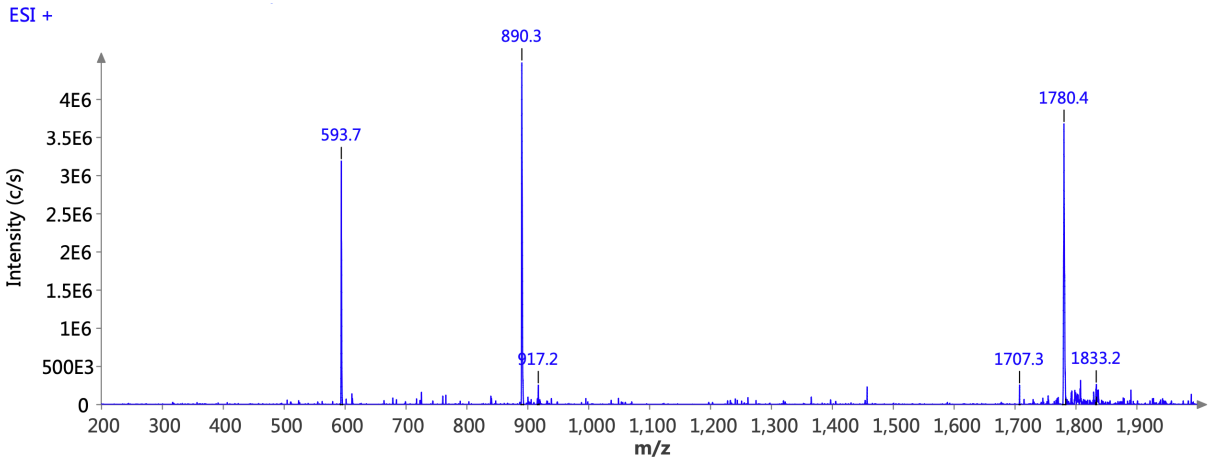

Supplemental Information 116: Mass spectrum of quality control of rhFAPI-20. ESI-MS: Calculated monoisotopic mass ($C_{82}H_{126}F_3N_{20}O_{19}Si^+$): 1779.92; found: m/z = 1780.4 $[M+H]^+$, 890.3 $[M+2H]^{2+}$, 593.7 $[M+3H]^{3+}$.

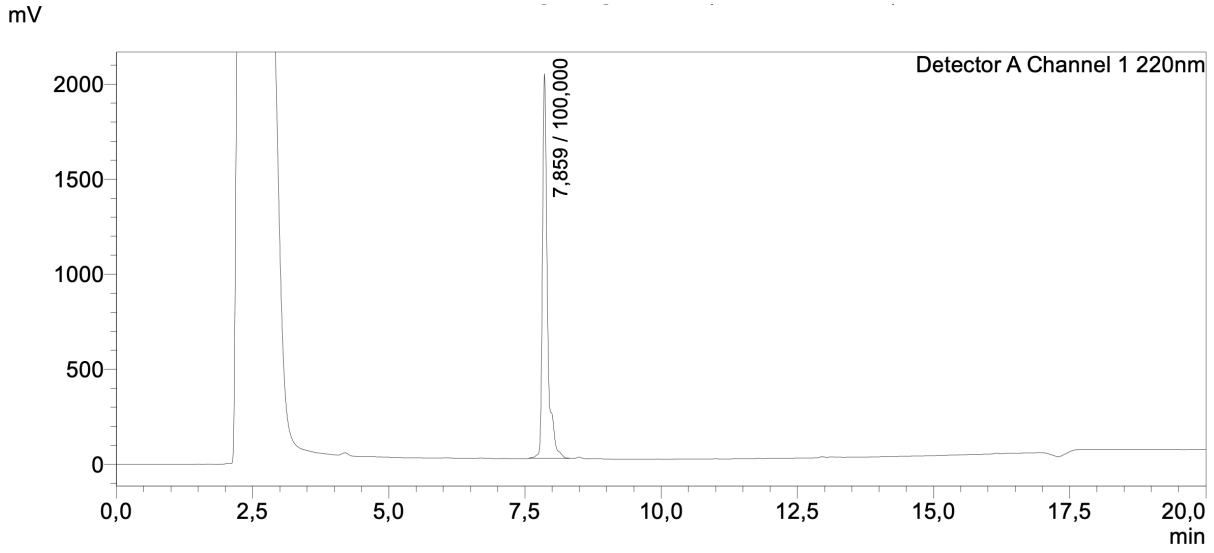

Supplemental Information 117: Quality control of [^{nat}Lu]Lu-rhFAPI-20 with RP-HPLC (10 to 90% B in 15 min): t_R = 7.86 min.

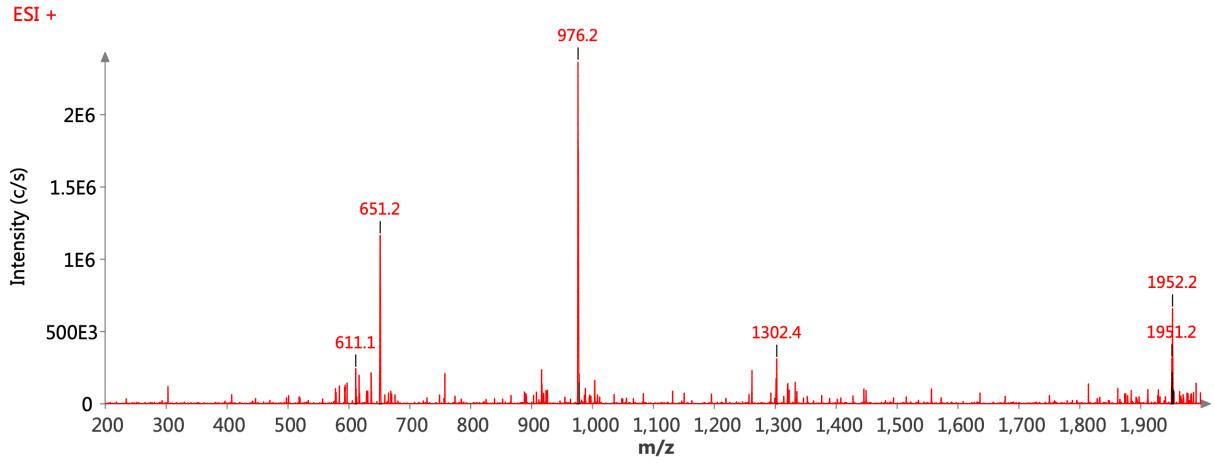

Supplemental Information 118: Mass spectrum of quality control of [^{nat}Lu]Lu-rhFAPI-20. ESI-MS: Calculated monoisotopic mass ($C_{82}H_{123}F_3LuN_{20}O_{19}Si$): 1956.12; found: m/z = 976.0 $[M+2H]^{2+}$.

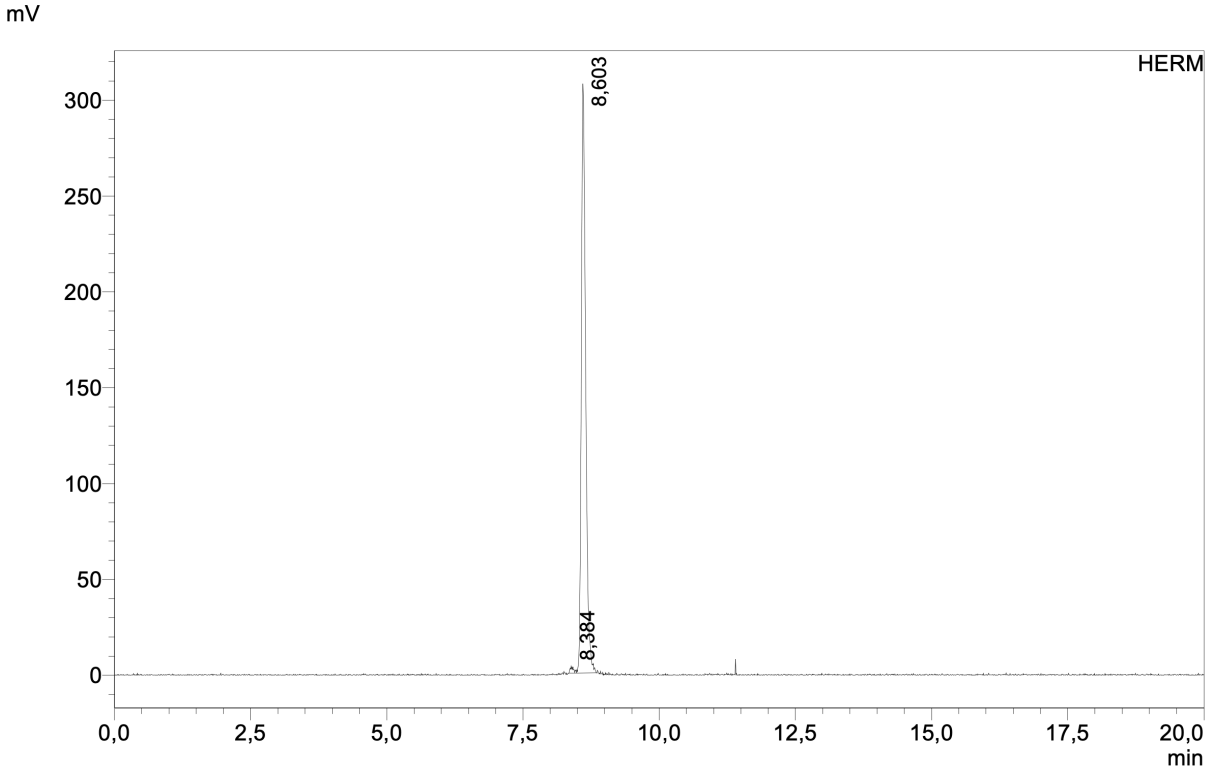

Supplemental Information 119: Quality control of [^{177}Lu]Lu-rhFAPI-20 with radio-HPLC (10 to 90% B in 15 min): t_R = 8.60 min.

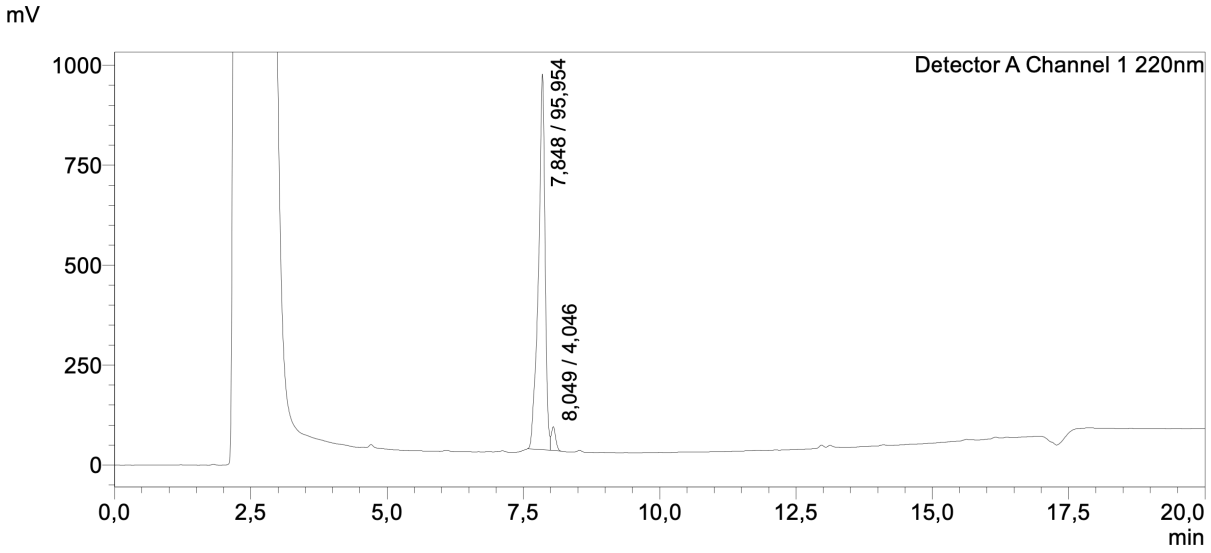

Supplemental Information 120: Quality control of [^{nat}Lu]Lu-rhFAPI-21 with RP-HPLC (10 to 90% B in 15 min): t_R = 7.85 min.

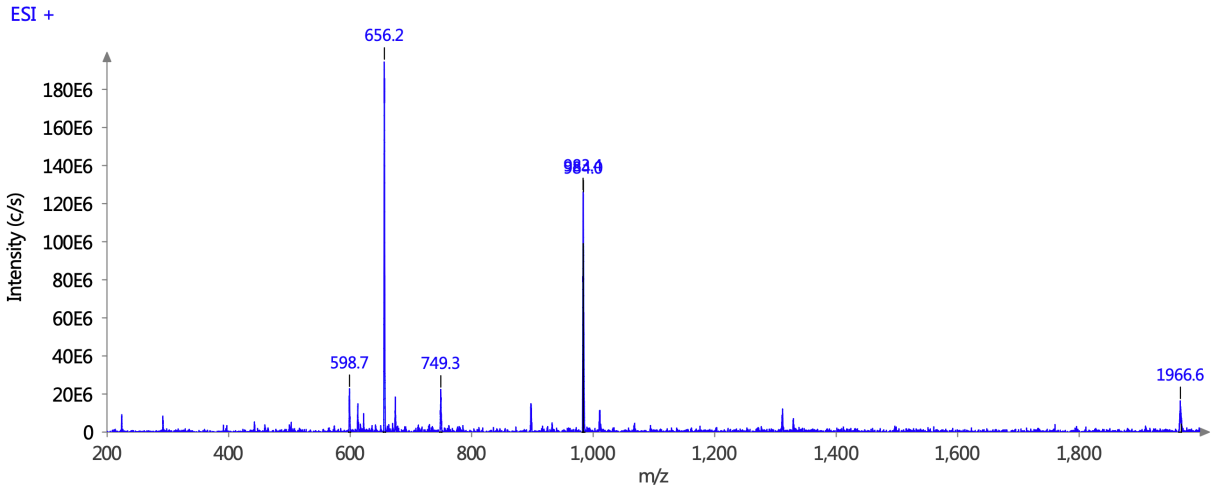

Supplemental Information 121: Mass spectrum of quality control of [^{nat}Lu]Lu-rhFAPI-21. ESI-MS: Calculated monoisotopic mass ($C_{83}H_{125}F_3LuN_{20}O_{19}Si$): 1965.86; found: m/z = 1966.6 $[M+H]^+$, 984.0 $[M+2H]^{2+}$, 656.2 $[M+3H]^{3+}$.

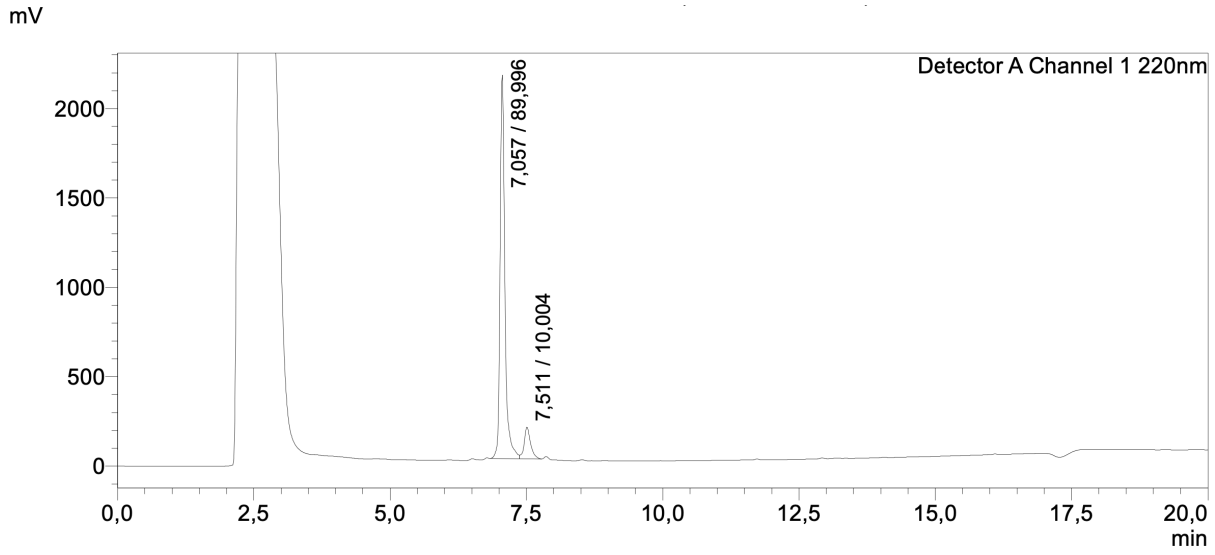

Supplemental Information 122: Quality control of transFAPI-01 with RP-HPLC (10 to 90% B in 15 min): t_R = 7.01 min.

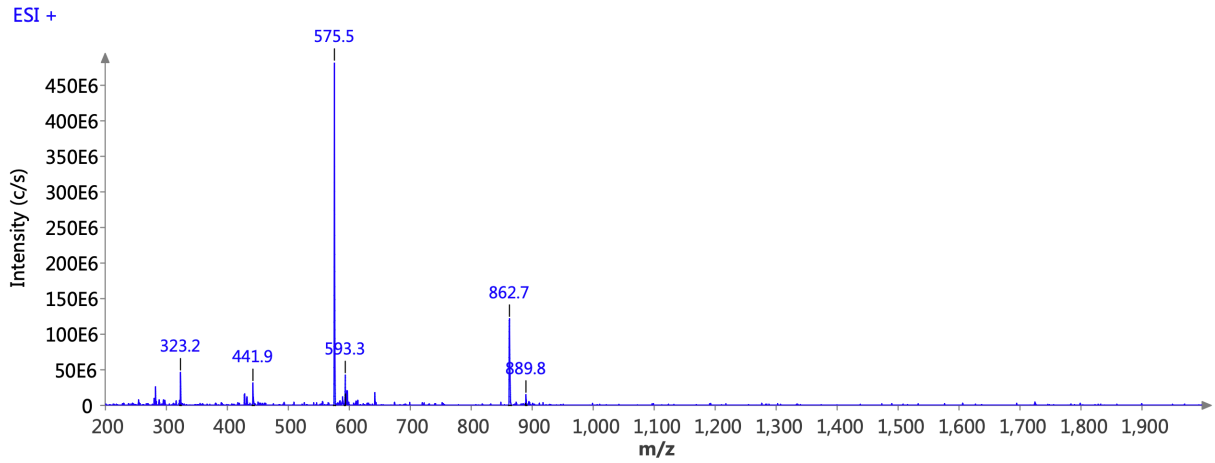

Supplemental Information 123: Mass spectrum of quality control of transFAPI-01. ESI-MS: Calculated monoisotopic mass ($C_{79}H_{117}F_3N_{18}O_{20}Si$): 1722.84; found: m/z = 862.6 $[M+2H]^{2+}$, 575.4 $[M+3H]^{3+}$.

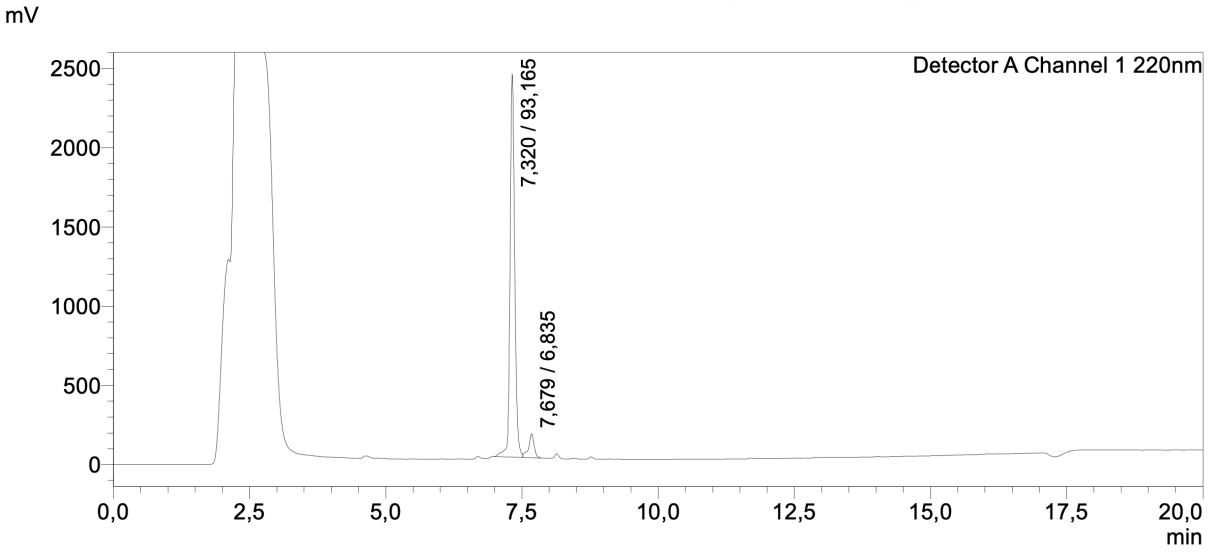

Supplemental Information 124: Quality control of [^{nat}Ga]Ga$_2$-transFAPI-01 with RP-HPLC (10 to 90% B in 15 min): t_R = 7.32 min.

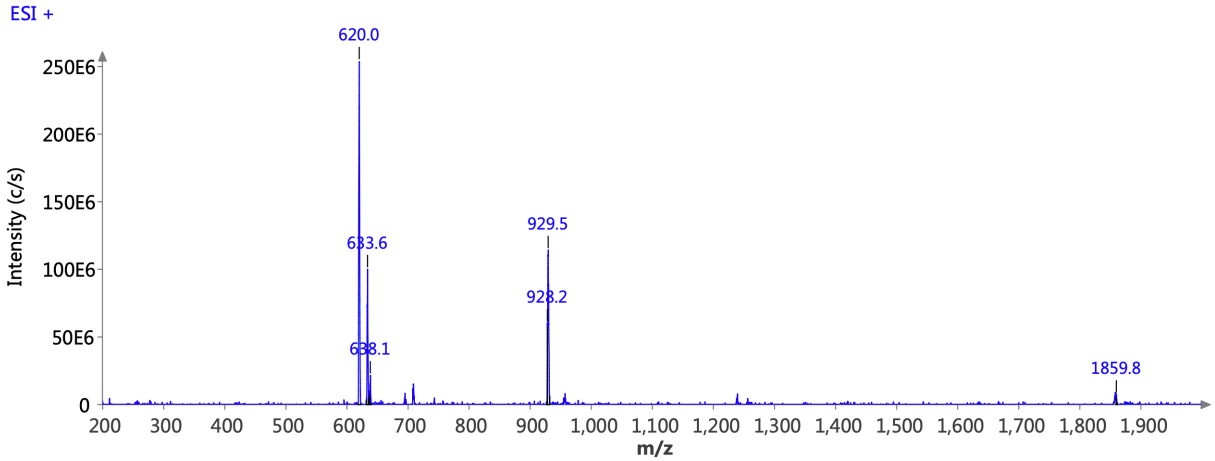

Supplemental Information 125: Mass spectrum of quality control of [^{nat}Ga]Ga$_2$-transFAPI-01. ESI-MS: Calculated monoisotopic mass ($C_{79}H_{114}F_3Ga_2N_{18}O_{20}Si$): 1857.67; found: m/z = 1859.8 $[M+H]^+$, 929.5 $[M+2H]^{2+}$, 620.0 $[M+3H]^{3+}$.

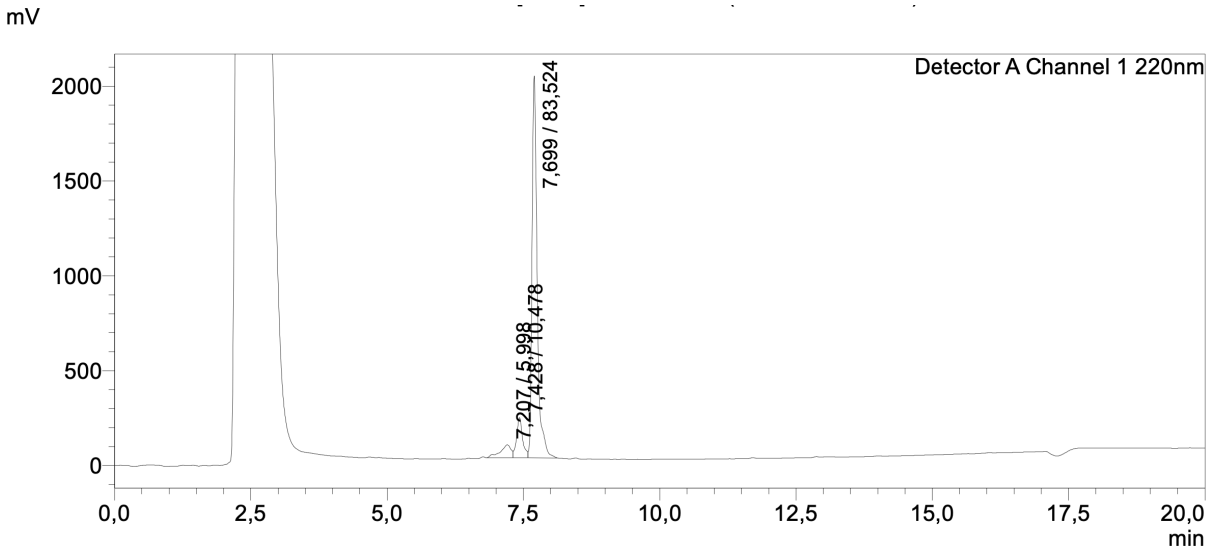

Supplemental Information 126: Quality control of [^{nat}Lu]Lu$_2$-transFAPI-01 with RP-HPLC (10 to 90% B in 15 min): t_R = 7.70 min.

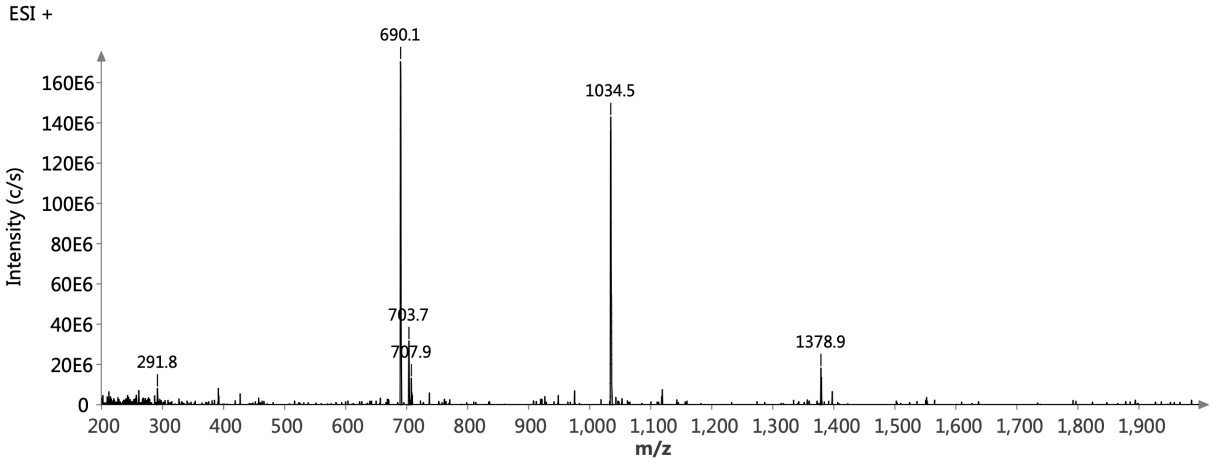

Supplemental Information 127: Mass spectrum of quality control of [^{nat}Lu]Lu$_2$-transFAPI-01. ESI-MS: Calculated monoisotopic mass ($C_{79}H_{112}F_3Lu_2N_{18}O_{20}Si$): 2067.68; found: m/z = 1034.5 $[M+2H]^{2+}$, 690.1 $[M+3H]^{3+}$.

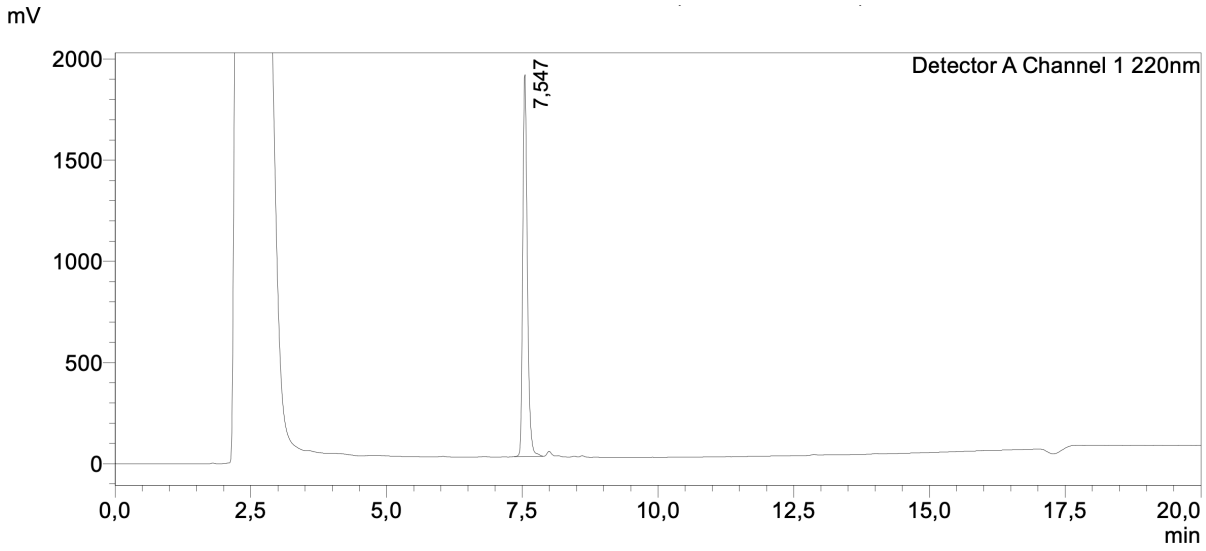

Supplemental Information 128: Quality control of transFAPI-02 with RP-HPLC (10 to 90% B in 15 min): t_R = 7.55 min.

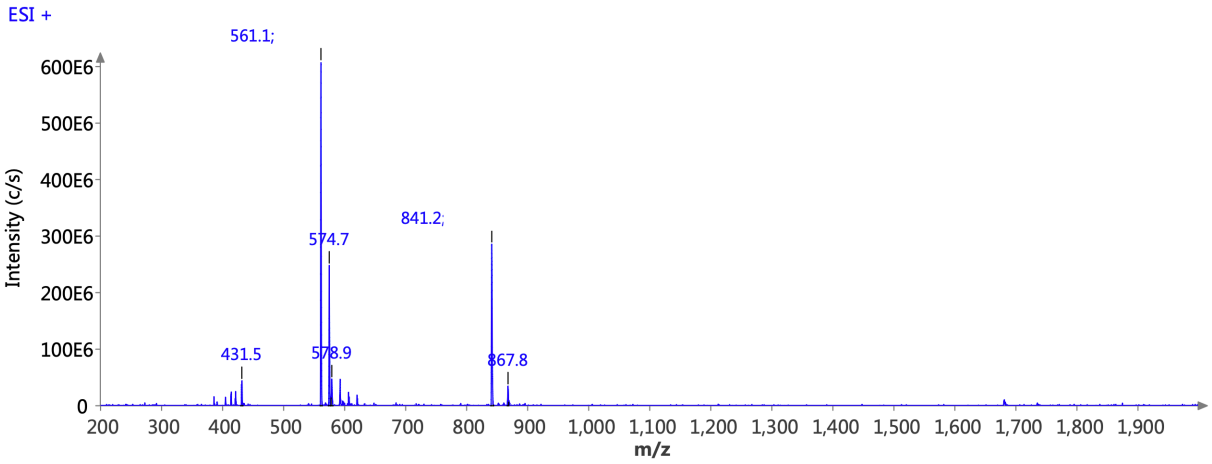

Supplemental Information 129: Mass spectrum of quality control of transFAPI-02. ESI-MS: Calculated monoisotopic mass ($C_{78}H_{116}F_3N_{17}O_{19}Si$): 1679.84; found: m/z = 841.1 $[M+2H]^{2+}$, 561.2 $[M+3H]^{3+}$.

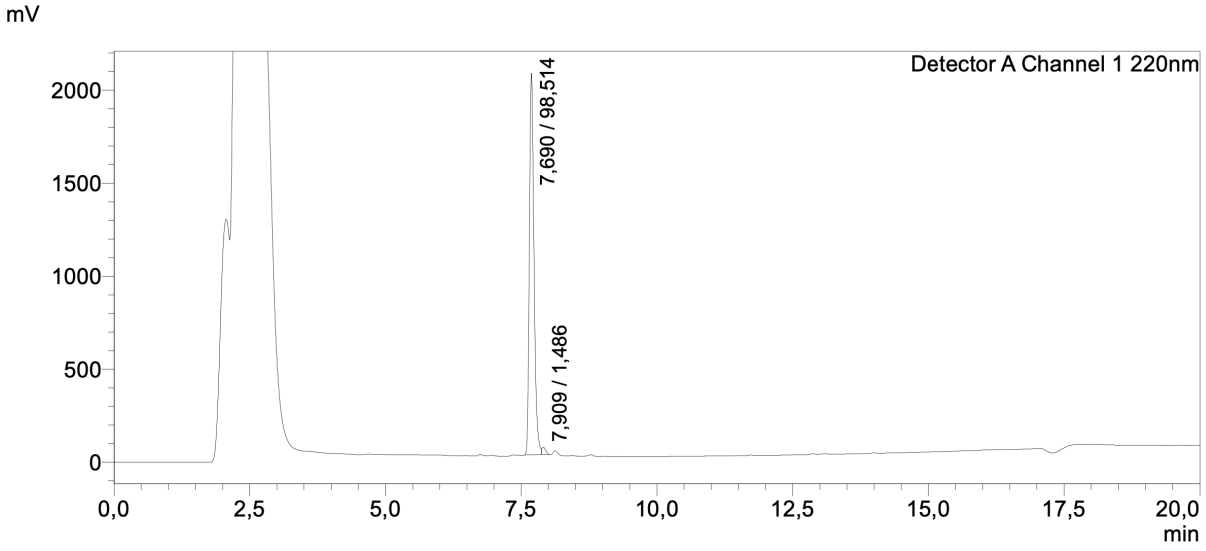

Supplemental Information 130: Quality control of [^{nat}Ga]Ga$_2$-transFAPI-02 with RP-HPLC (10 to 90% B in 15 min): t_R = 7.69 min.

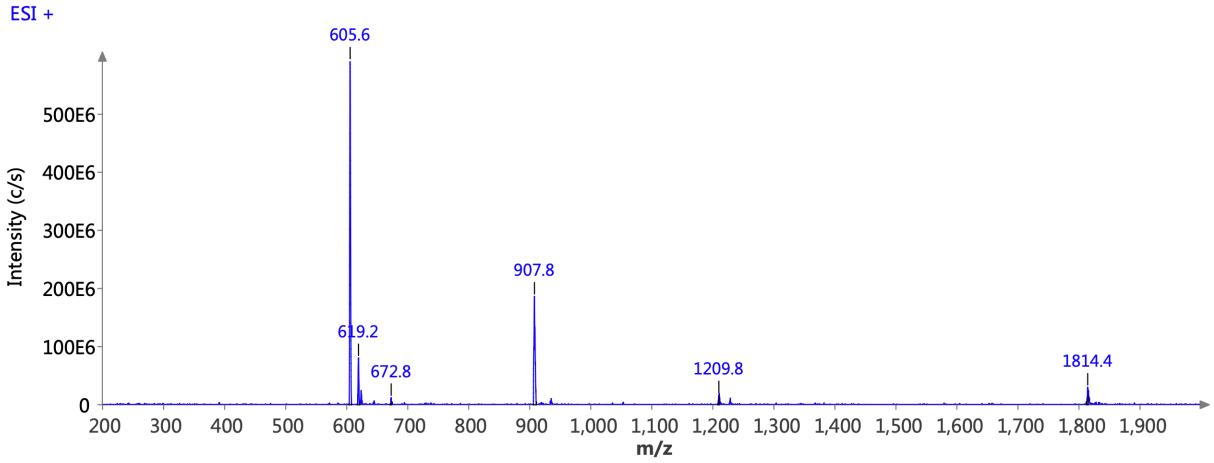

Supplemental Information 131: Mass spectrum of quality control of [^{nat}Ga]Ga$_2$-transFAPI-02. ESI-MS: Calculated monoisotopic mass ($C_{78}H_{112}F_3Ga_2N_{17}O_{19}Si$): 1813.66; found: m/z = 1814.4 $[M+H]^+$, 907.8 $[M+2H]^{2+}$, 605.6 $[M+3H]^{3+}$.

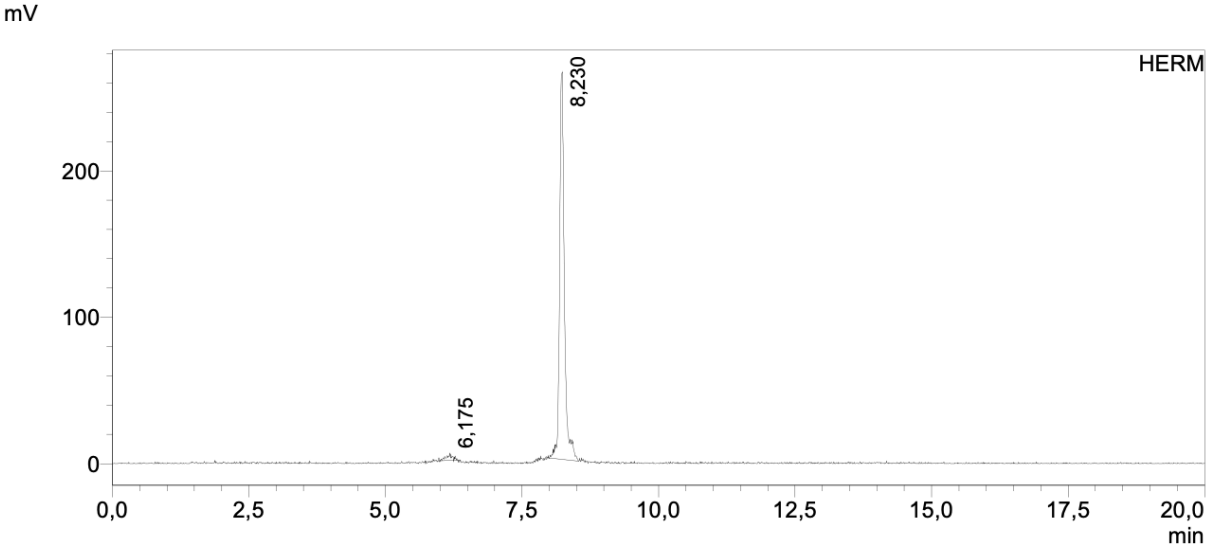

Supplemental Information 132: Quality control of [^{18}F]F-Ga$_2$-transFAPI-02 with radio-HPLC (10 to 90% B in 15 min): t_R = 8.23 min.

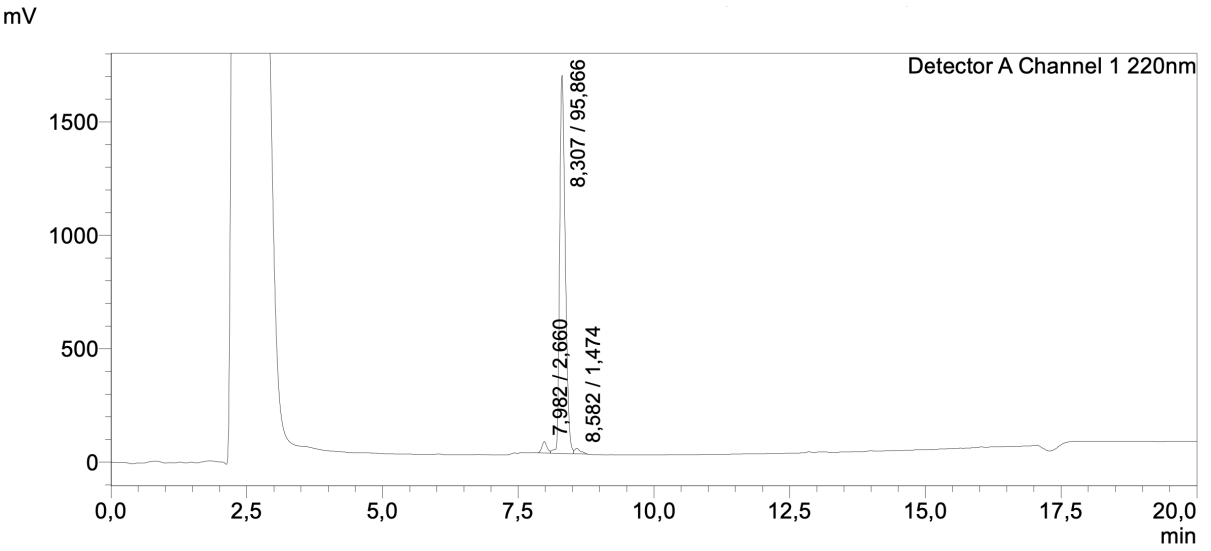

Supplemental Information 133: Quality control of [^{nat}Lu]Lu$_2$-transFAPI-02 with RP-HPLC (10 to 90% B in 15 min): t_R = 8.31 min.

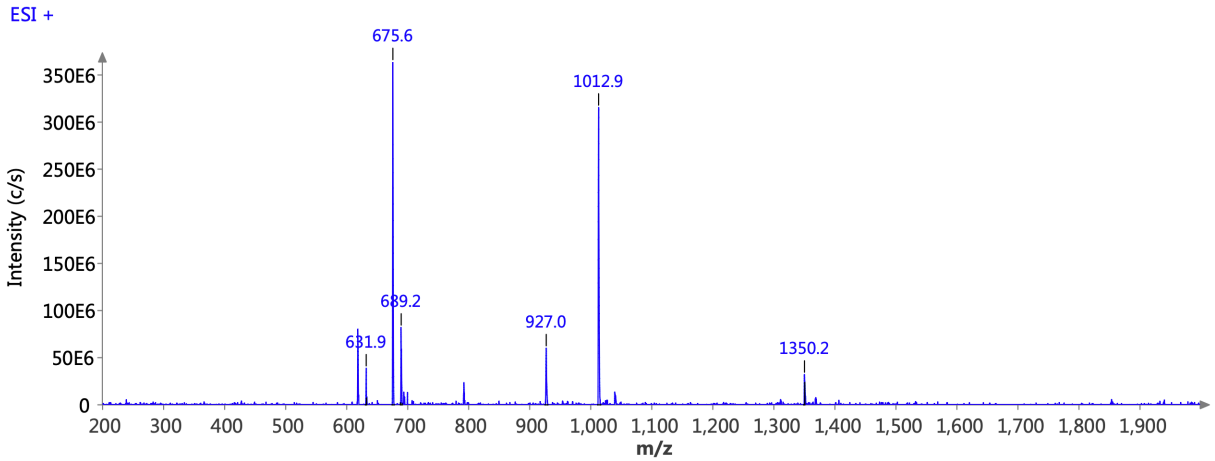

Supplemental Information 134: Mass spectrum of quality control of [^{nat}Lu]Lu$_2$-transFAPI-02. ESI-MS: Calculated monoisotopic mass ($C_{78}H_{111}F_3Lu_2N_{17}O_{19}Si$): 2024.68; found: m/z = 1012.9 $[M+2H]^{2+}$, 675.6 $[M+3H]^{3+}$.

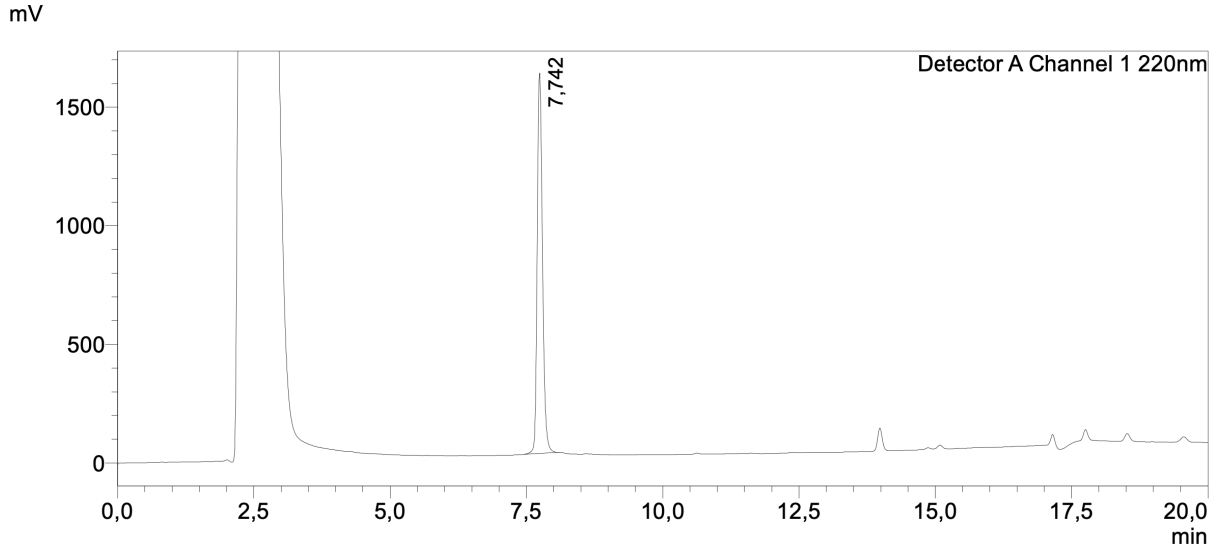

Supplemental Information 135: Quality control of transFAPI-03 with RP-HPLC (10 to 90% B in 15 min): t_R = 7.74 min.

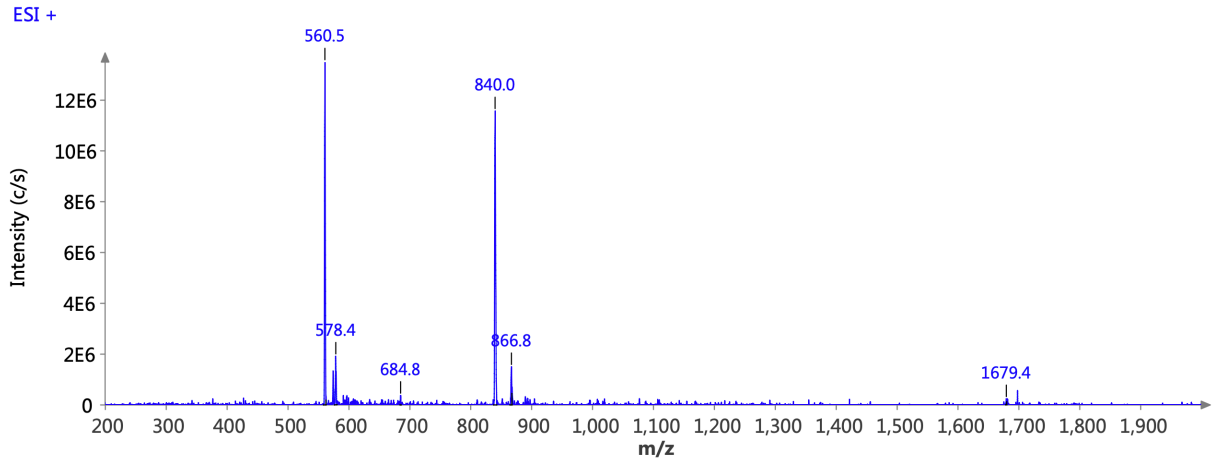

Supplemental Information 136: Mass spectrum of quality control of [^{nat}Ga]Ga$_2$-transFAPI-03. ESI-MS: Calculated monoisotopic mass ($C_{79}H_{121}F_3N_{17}O_{18}Si^+$): 1680.88; found: m/z = 1679.4 $[M+H]^+$, 840.0 $[M+2H]^{2+}$, 560.5 $[M+3H]^{3+}$.

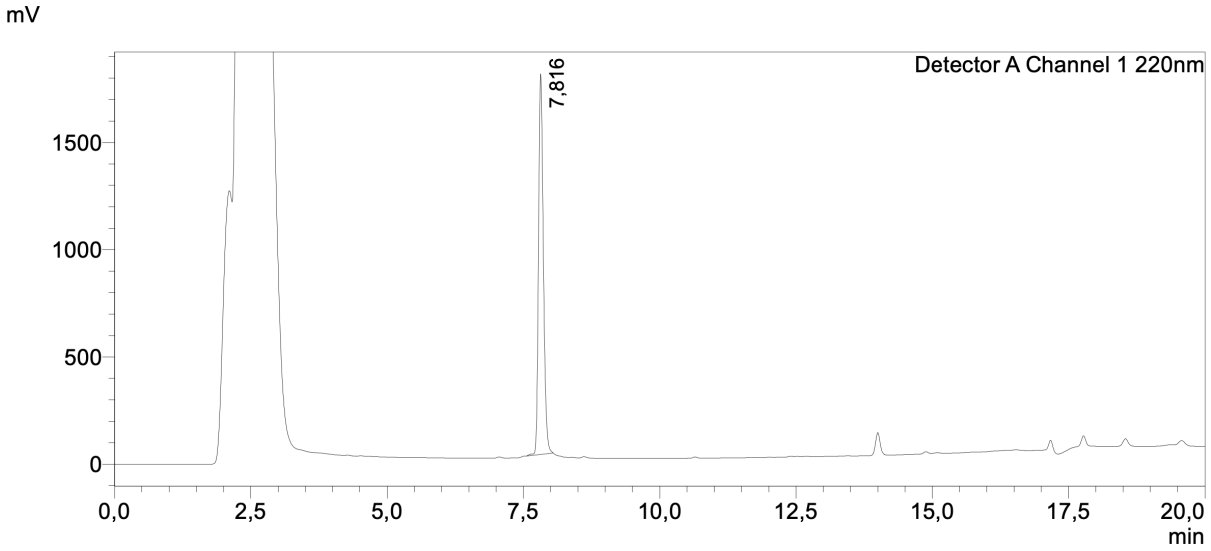

Supplemental Information 137: Quality control of [^{nat}Ga]Ga$_2$-transFAPI-03 with RP-HPLC (10 to 90% B in 15 min): t_R = 7.82 min.

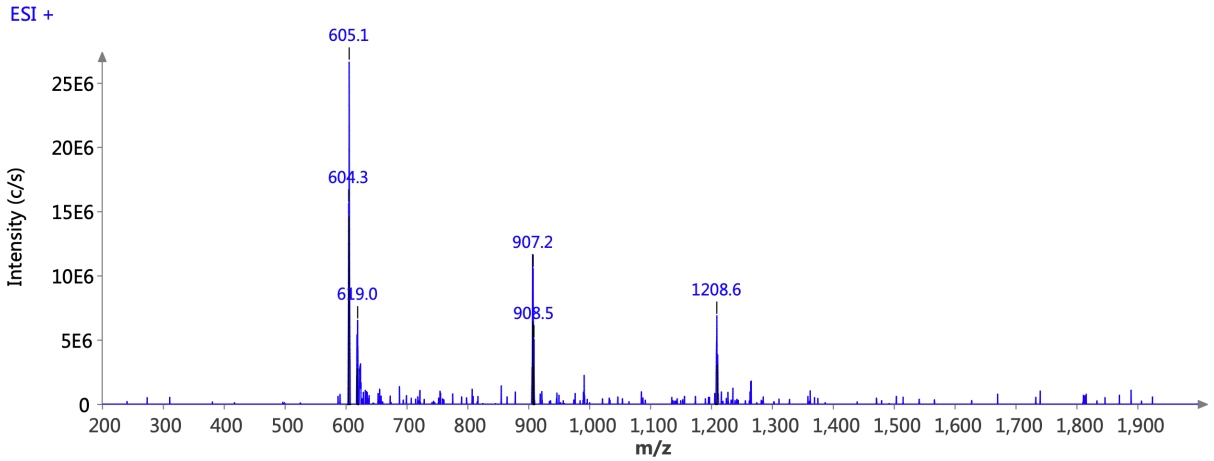

Supplemental Information 138: Mass spectrum of quality control of [^{nat}Ga]Ga$_2$-transFAPI-03. ESI-MS: Calculated monoisotopic mass ($C_{79}H_{116}F_3Ga_2N_{17}O_{18}Si$): 1813.70; found: m/z = 907.2 $[M+2H]^{2+}$, 605.1 $[M+3H]^{3+}$.

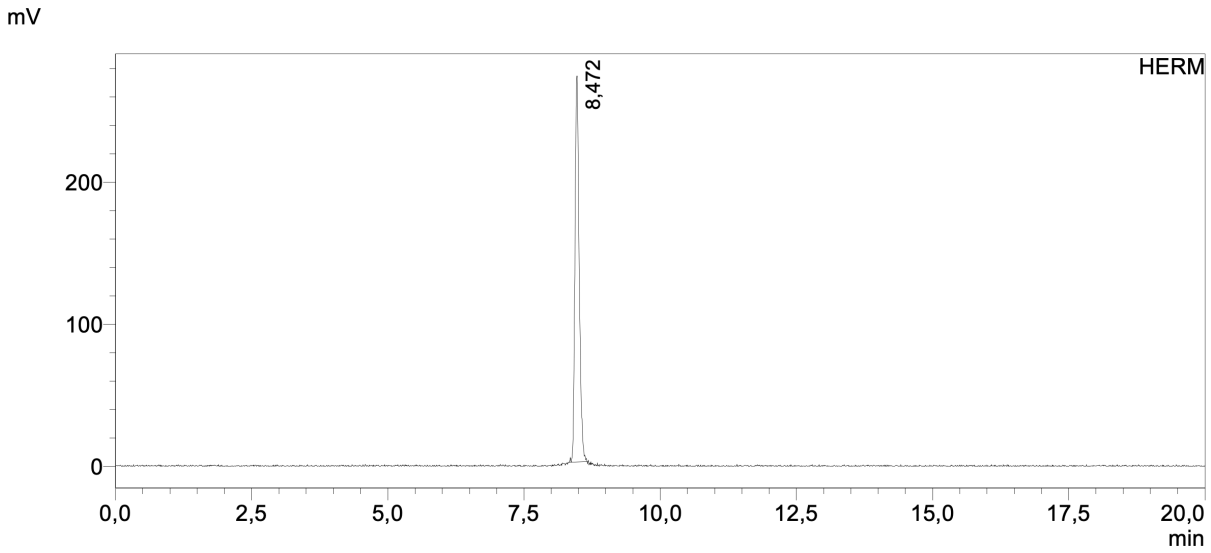

Supplemental Information 139: Quality control of [^{18}F]F-Ga$_2$-transFAPI-03 with radio-HPLC (10 to 90% B in 15 min): t_R = 8.47 min.

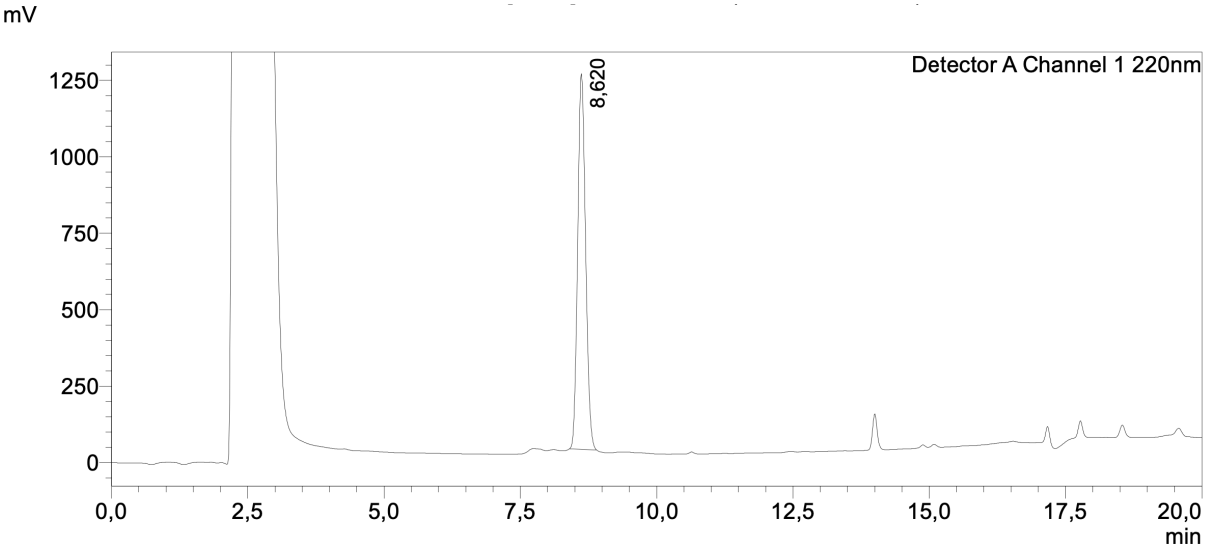

Supplemental Information 140: Quality control of [^{nat}Lu]Lu$_2$-transFAPI-03 with RP-HPLC (10 to 90% B in 15 min): t_R = 8.62 min.

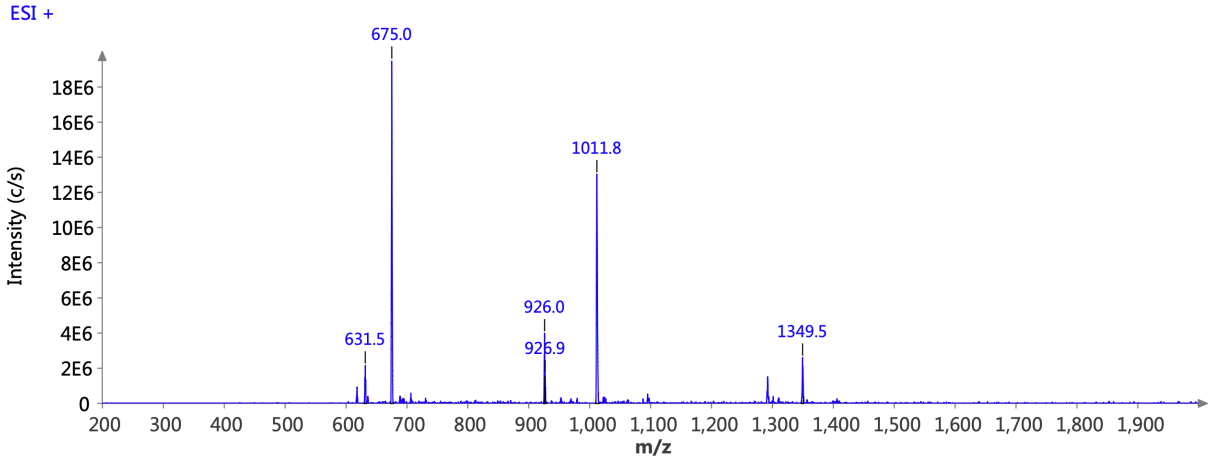

Supplemental Information 141: Mass spectrum of quality control of [^{nat}Lu]Lu$_2$-transFAPI-03. ESI-MS: Calculated monoisotopic mass ($C_{79}H_{116}F_3Lu_2N_{17}O_{18}Si$): 2025.72; found: m/z = 1011.8 $[M+2H]^{2+}$, 675.0 $[M+3H]^{3+}$.

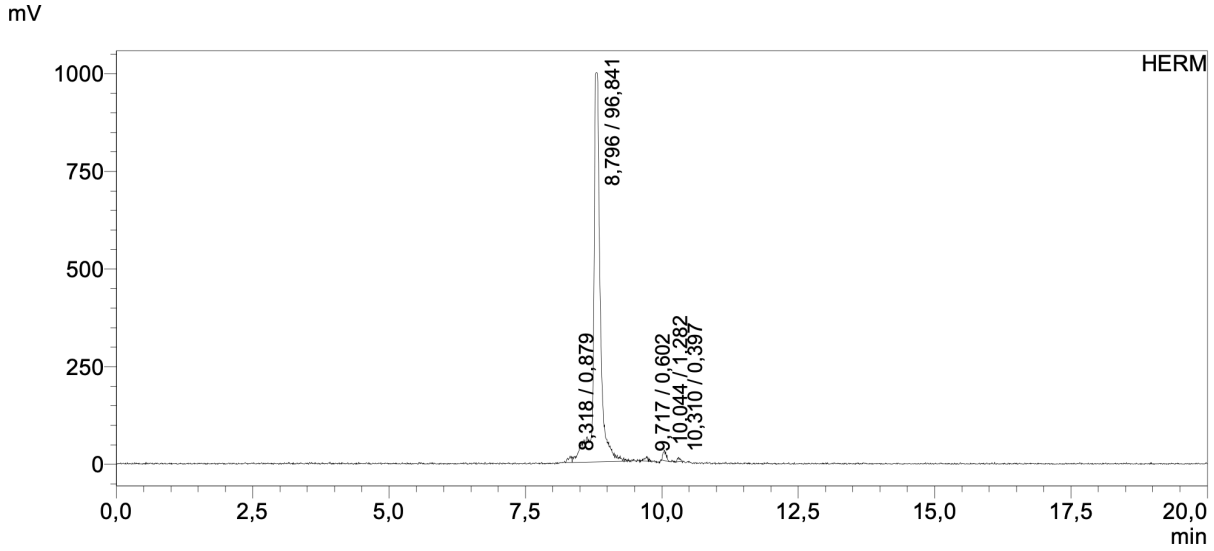

Supplemental Information 142: Quality control of [^{18}F]F-Lu$_2$-transFAPI-03 with radio-HPLC (10 to 90% B in 15 min): t_R = 8.79 min.

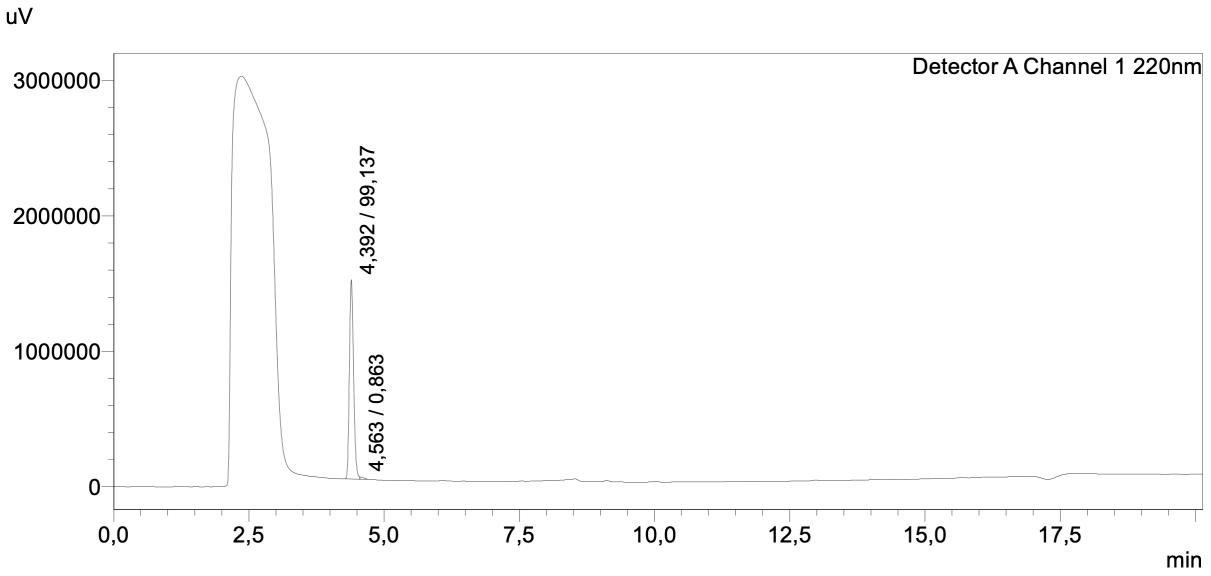

Supplemental Information 143: Quality control of tecFAPI-03 with RP-HPLC (10 to 90% B in 15 min): t_R = 4.39 min.

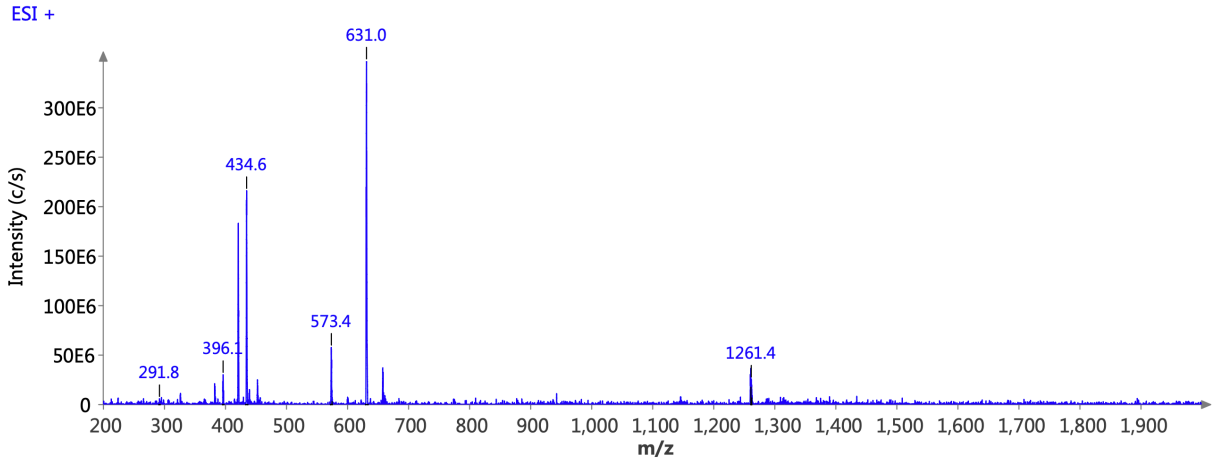

Supplemental Information 144: Mass spectrum of quality control of tecFAPI-03. ESI-MS: Calculated monoisotopic mass ($C_{55}H_{83}F_2N_{17}O_{15}$): 1259.62; found: m/z = 1261.4 $[M+H]^+$, 631.0 $[M+2H]^{2+}$, 420.6 $[M+3H]^{3+}$.

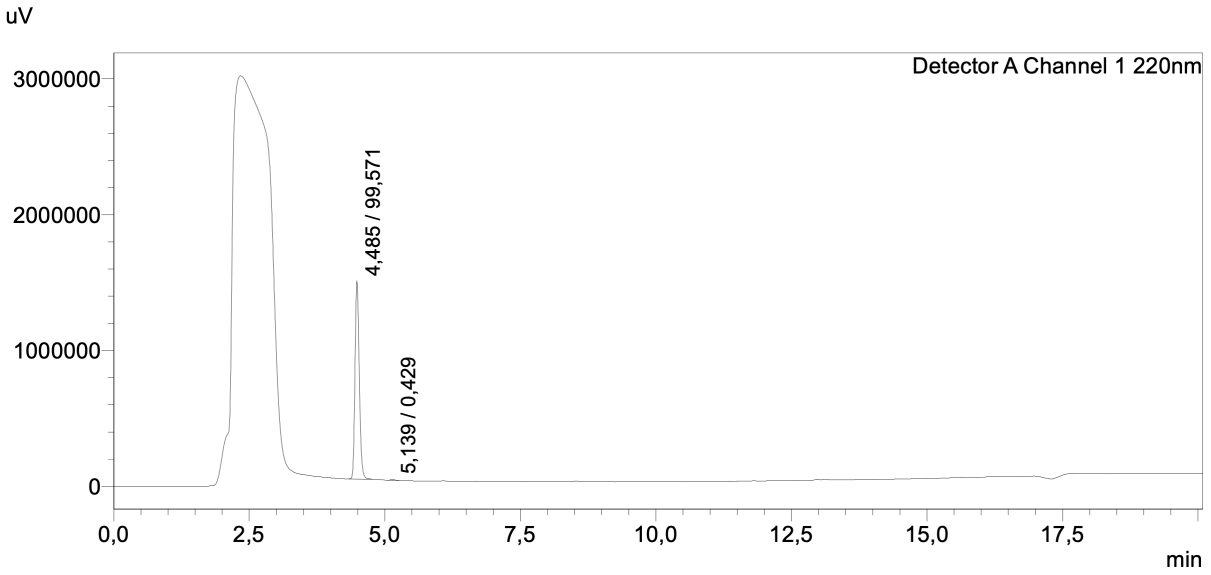

Supplemental Information 145: Quality control of [^{nat}Ga]Ga-tecFAPI-03 with RP-HPLC (10 to 90% B in 15 min): t_R = 4.46 min.

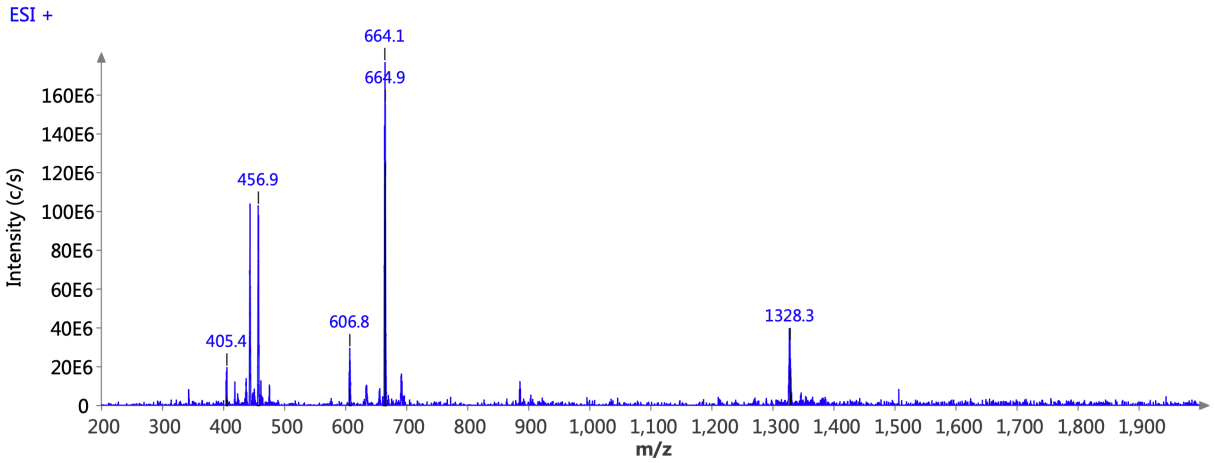

Supplemental Information 146: Mass spectrum of quality control of [^{nat}Ga]Ga-tecFAPI-03. ESI-MS: Calculated monoisotopic mass ($C_{55}H_{81}F_2GaN_{17}O_{15}$): 1326.53; found: m/z = 1328.4 $[M+H]^+$, 664.1 $[M+2H]^{2+}$, 443.2 $[M+3H]^{3+}$.

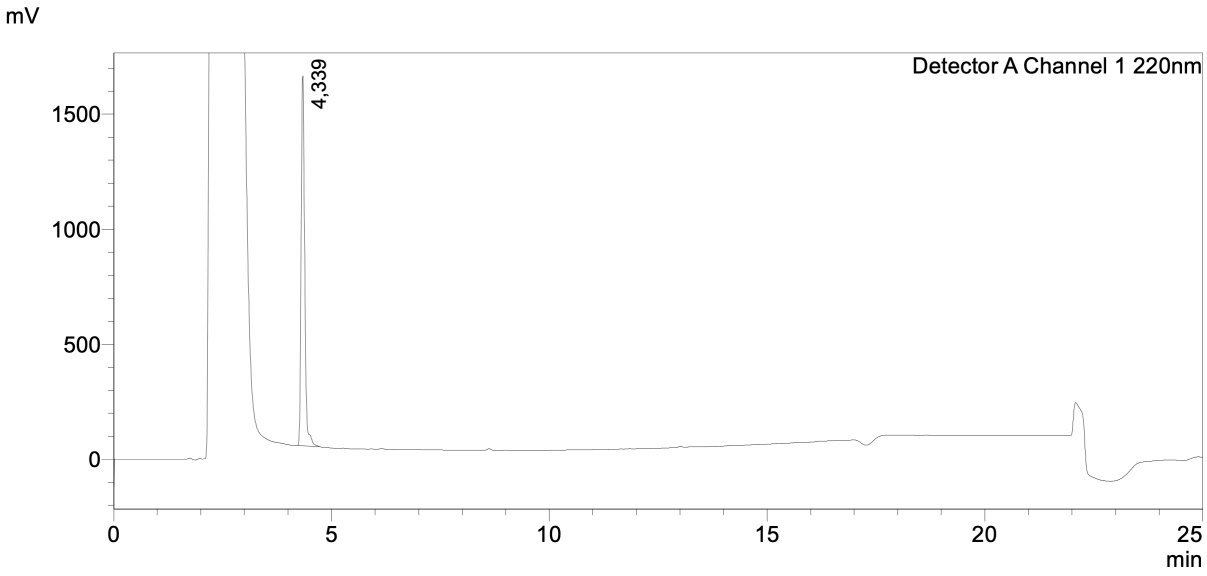

Supplemental Information 147: Quality control of tecFAPI-04 with RP-HPLC (10 to 90% B in 15 min): t_R = 4.34 min.

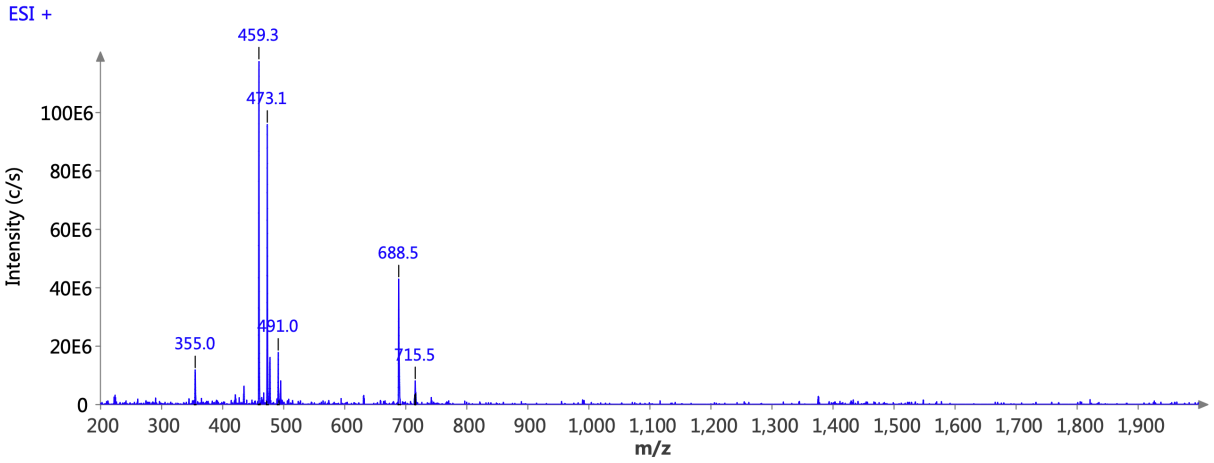

Supplemental Information 148: Mass spectrum of quality control of tecFAPI-04. ESI-MS: Calculated monoisotopic mass ($C_{59}H_{88}F_2N_{18}O_{18}$): 1374.65; found: m/z = 1376.0 $[M+H]^+$, 688.5 $[M+2H]^{2+}$, 459.4 $[M+3H]^{3+}$.

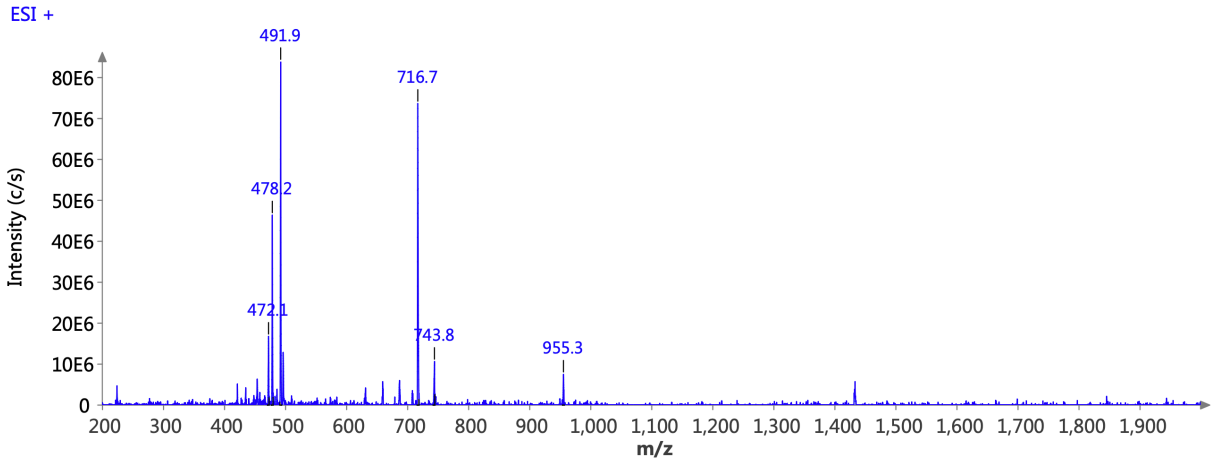

Supplemental Information 149: Mass spectrum of quality control of [^{nat}Lu]Lu-tecFAPI-03. ESI-MS: Calculated monoisotopic mass ($C_{55}H_{81}F_2LuN_{17}O_{15}$): 1432.55; found: m/z = 716.7 $[M+2H]^{2+}$, 478.2 $[M+3H]^{3+}$.

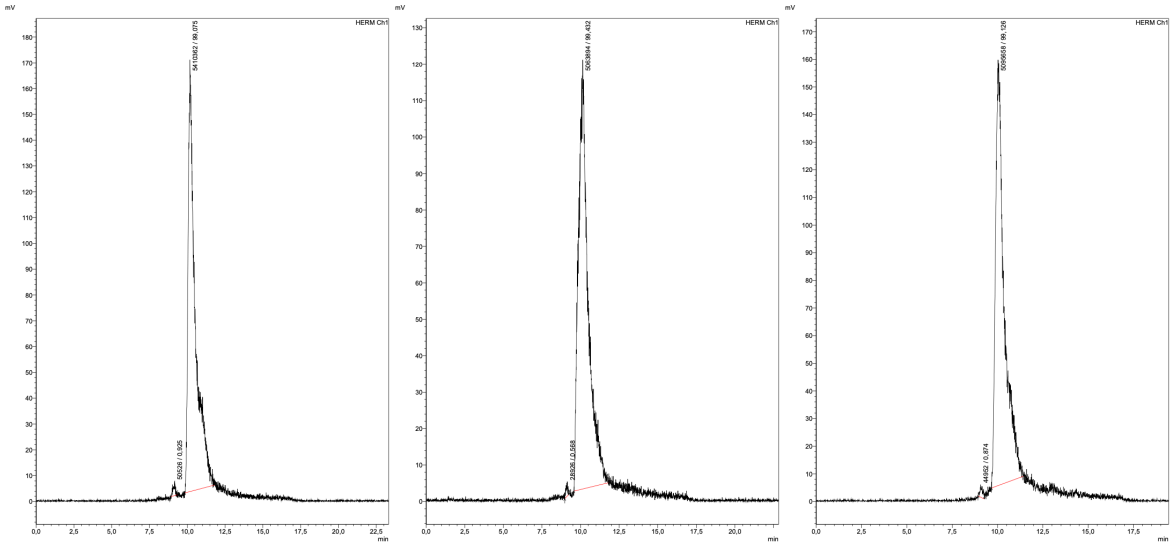

Supplemental Information 150: Quality control of [^{99m}Tc]Tc-tecFAPI-03 (left), [^{99m}Tc]Tc-Ga-tecFAPI-03 (middle) and [^{99m}Tc]Tc-Lu-tecFAPI-03 (right) with radio-HPLC (10 to 35% B in 20 min).

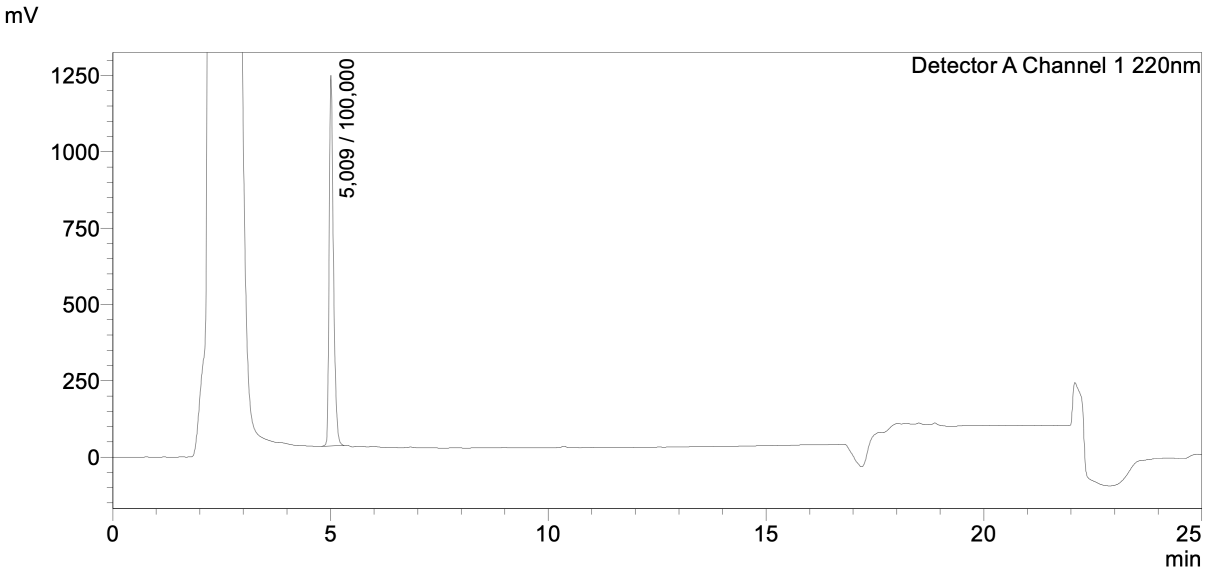

Supplemental Information 151: Quality control of [^{nat}Ga]Ga-tecFAPI-04 with RP-HPLC (10 to 60% B in 15 min): t_R = 5.01 min.

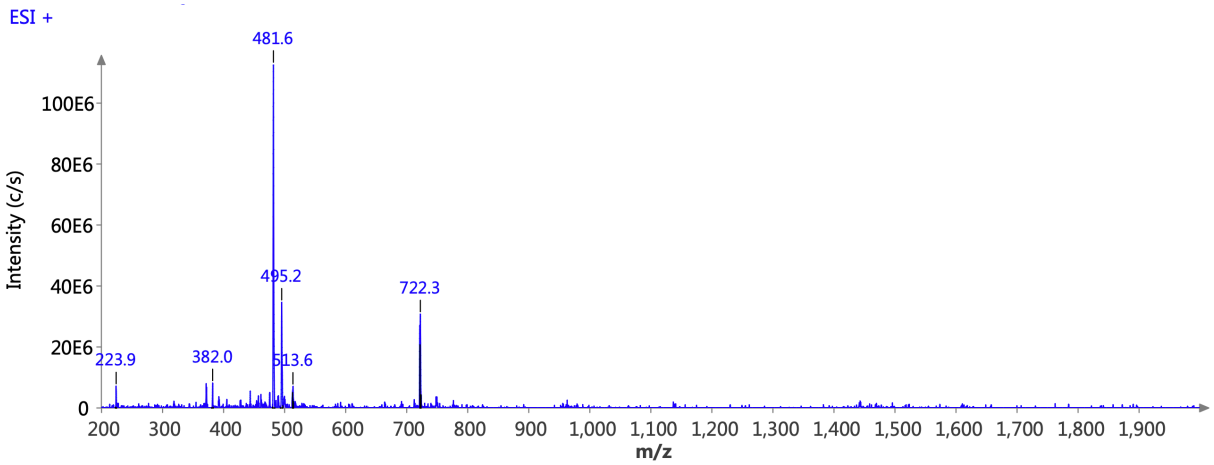

Supplemental Information 152: Mass spectrum of quality control of [^{nat}Ga]Ga-tecFAPI-04. ESI-MS: Calculated monoisotopic mass ($C_{59}H_{86}F_2GaN_{18}O_{18}$): 1441.56; found: m/z = 1443.0 $[M+H]^+$, 722.3 $[M+2H]^{2+}$, 481.6 $[M+3H]^{3+}$.

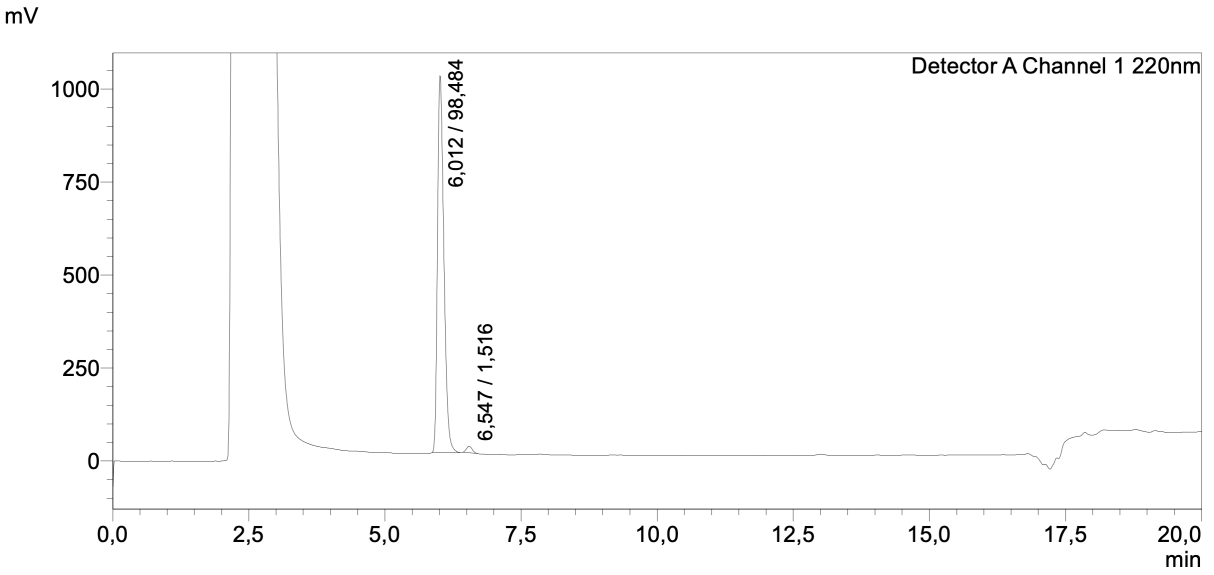

Supplemental Information 153: Quality control of tecFAPI-05 with RP-HPLC (10 to 40% B in 15 min): t_R = 6.01 min.

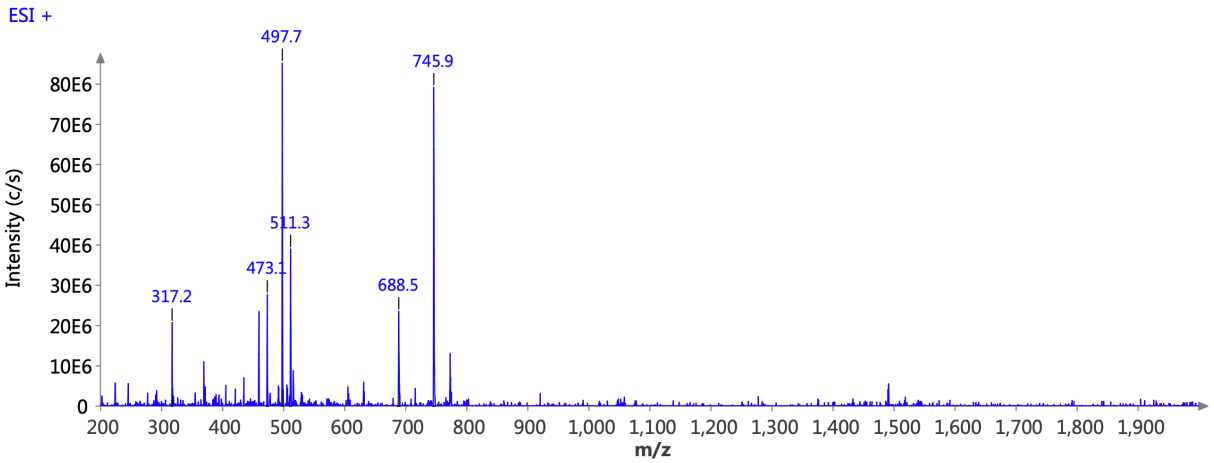

Supplemental Information 154: Mass spectrum of quality control of tecFAPI-05. ESI-MS: Calculated monoisotopic mass ($C_{63}H_{93}F_2N_{19}O_{21}$): 1489.68; found: m/z = 745.9 $[M+2H]^{2+}$, 497.8 $[M+3H]^{3+}$.

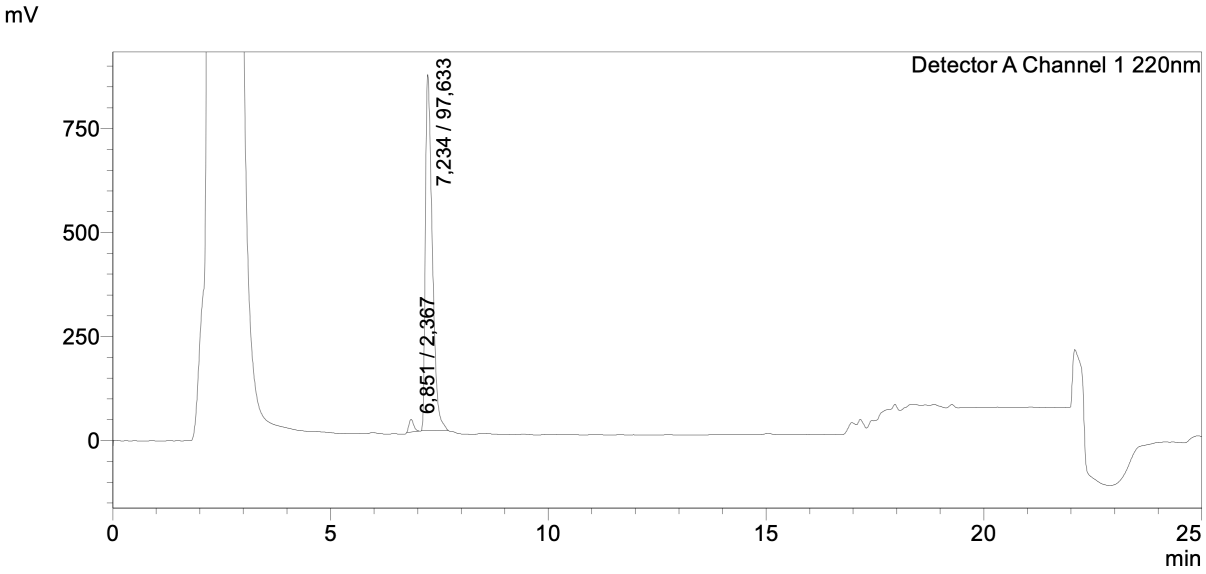

Supplemental Information 155: Quality control of [^{nat}Ga]Ga-tecFAPI-05 with RP-HPLC (10 to 30% B in 15 min): t_R = 7.23 min.

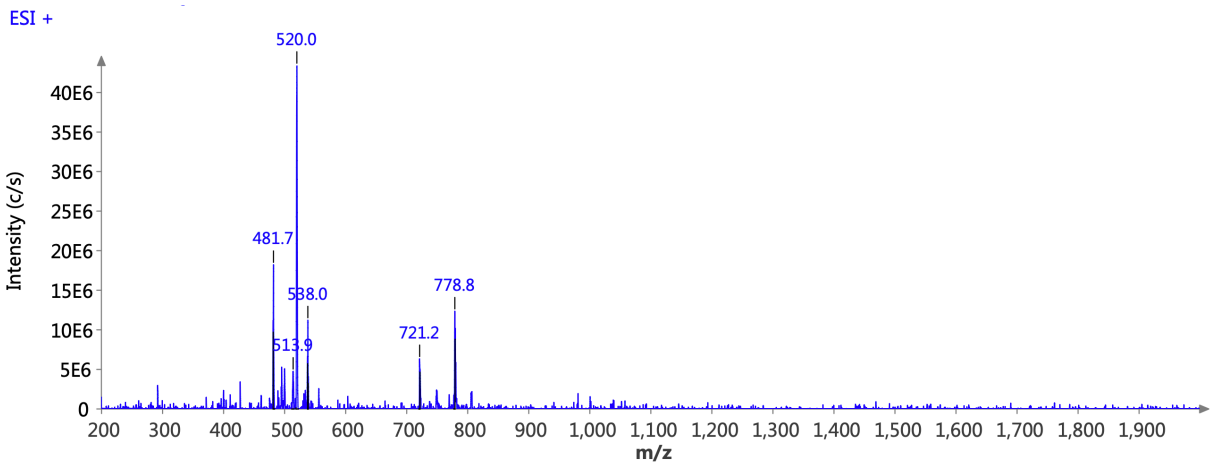

Supplemental Information 156: Mass spectrum of quality control of [^{nat}Ga]Ga-tecFAPI-05. ESI-MS: Calculated monoisotopic mass ($C_{63}H_{91}F_2GaN_{19}O_{21}$) 1556.59; found: m/z = 779.6 $[M+2H]^{2+}$, 520.0 $[M+3H]^{3+}$.